ACTA PHYSICA
ACADEMIAE SCIENTIARUM HUNGARICAE

TOMUS XLVII FASCICULI 1–3

AKADÉMIAI KIADÓ, BUDAPEST

1979

ACTA PHYS. HUNG. APAHAQ 47 (1–3) 1–274 (1979)

ACTA PHYSICA

ACADEMIAE SCIENTIARUM HUNGARICAE

SZERKESZTI
KOVÁCS ISTVÁN

Az *Acta Physica* angol, német, francia vagy orosz nyelven közöl értekezéseket. Évente két kötetben, kötetenként 4—4 füzetben jelenik meg. Kéziratok a szerkesztőség címére (1521 Budapest XI., Budafoki út 8.) küldendők.

Megrendelhető a belföld számára az Akadémiai Kiadónál (1363 Budapest Pf. 24. Bankszámla 215-11488), a külföld számára pedig a „Kultura" Külkereskedelmi Vállalatnál (1389 Budapest 62, P.O.B. 149. Bankszámla 217-10990), vagy annak külföldi képviseleteinél.

The *Acta Physica* publish papers on physics in English, German, French or Russian in issues making up two volumes per year. Distributor: "Kultura" Foreign Trading Company (1389 Budapest 62, P.O. Box 149) or its representatives abroad.

Die *Acta Physica* veröffentlichen Abhandlungen aus dem Bereich der Physik in deutscher, englischer, französischer oder russischer Sprache, in Heften, die jährlich zwei Bände bilden.

Bestellbar bei »Kultura« Außenhandelsunternehmen (1389 Budapest 62, Postfach 149) oder seinen Auslandsvertretungen.

Les *Acta Physica* publient des travaux du domaine de la physique en français, anglais, allemand ou russe, en fascicules qui forment deux volumes par an.

On peut s'abonner à l'Entreprise du Commerce Extérieur «Kultura» (1389 Budapest 62, P.O.B. 149) ou chez représentants à l'étranger.

«*Acta Physica*» публикуют трактаты из области физических наук на русском, немецком, английском и французском языках.

«*Acta Physica*» выходят отдельными выпусками, составляющими два тома в год.

Заказы принимает предприятие по внешней торговле «Kultura» (1389 Budapest 62, P.O.B. 149) или его заграничные представительства.

ACTA PHYSICA

ACADEMIAE SCIENTIARUM HUNGARICAE

TOMUS XLVII

AKADÉMIAI KIADÓ, BUDAPEST
1979

ACTA PHYS. HUNG.

INDEX

Tomus 47

ACTA PHYSICA

ACADEMIAE SCIENTIARUM HUNGARICAE

TOMUS XLVII

AKADÉMIAI KIADÓ, BUDAPEST
1979

INDEX

CONDENSED MATTER

The final manuscript was submitted for publication to Acta Physica on 21st June 1979.

PROCEEDINGS
OF THE
SECOND HUNGARIAN CONFERENCE
ON CRYSTAL GROWTH
HCCG-2
WITH INTERNATIONAL PARTICIPATION

MÁTRAFÜRED, HUNGARY

28—30 MARCH 1979

The Conference was organized by the Section of Crystal Physics of the Roland Eötvös Physical Society, Budapest

Organizing Committee:

Prof. Dr. I. TARJÁN (Honorary Chairman)
Dr. R. VOSZKA (Chairman)
Dr. E. STERK (Secretary)
Dr. E. HARTMANN (Chairman of the Programme Committee)
Dr. P. B. BARNA, Dr. P. GADÓ, Dr. G. KONCZOS, Dr. E. LENDVAY,
Dr. S. KESZTHELYI-LÁNDORI

PREFACE

Interest in crystal growth has increased considerably over the past 30 years. Characterized by the interaction of practical aims and scientific curiosity since the beginning, this field of research has been and is still progressing at a rapid pace. It was not until recently that we became aware of the fact that our field of research is a fundamental one, underlying several branches of science and, consequently, technical progress as well. This statement is especially true if we consider matters in a wider sense and take into account related problems as well which, through the study of e.g. phase transitions, of order-disorder phenomena, etc. cover a wide range of crystal structures from amorphous materials, glasses and homogeneous and heterogeneous polycrystal layers to pure and doped single crystals. The studied crystal structures cover a similarly wide range with structures built of single elements at one end of the range and macromolecules at the other. The complexity of the problem is still enhanced by the fact that a crystal sample of prescibed quality usually undergoes further processing until it is built in in an apparatus as component part. This processing may influence unfavourably the properties of the sample. Thus it is not sufficient to take care of the purity of the starting materials and of the quality of the samples produced from them, the quality control must be extended to the component parts produced from the samples as well. These questions raise numerous research problems.

Crystal physics in Hungary can rely on firm traditions in the study of crystal growth, where a number of results, both theoretical and practical, have so far been achieved. We are, however, relatively newcomers to the field of international conferences as compared to neighbourning countries. It was therefore an honour for us to organize the 2nd Hungarian Conference on Crystal Growth with international participation, Mátrafüred, 28th—30th March, 1979. The Conference gave, on the one hand a review of current work in Hungary, and on the other it offered a possibility for informal discussions on recent results, which are presented in the following papers.

Tarján Imre

(Prof. Dr. I. TARJÁN)

Acta Physica Academiae Scientiarum Hungaricae, Tomus 47 (1—3), pp. 5—11 (1979)

GROWTH OF SINGLE CRYSTALS AT THE RESEARCH LABORATORY FOR CRYSTAL PHYSICS

By

R. VOSZKA

RESEARCH LABORATORY FOR CRYSTAL PHYSICS OF THE HUNGARIAN ACADEMY OF SCIENCES, BUDAPEST, HUNGARY

A review of the research programme of the laboratory and of some results in the field of crystal growth from the melt is given.

The activities of our Laboratory, organized in 1976 from the merger of two university research groups formerly led by Academicians ZOLTÁN GYULAI and IMRE TARJÁN, cover a traditional field: the growth of optical single crystals from the melt and investigations of their defect structure.

The growth of alkali halides has been in progress since 1950. First we used the Kyropoulos method producing crystals for research and optical application. In the course of our investigations of colour centres it became clear that substitutional OH^- ions in the lattice are responsible for a number of unwanted effects. For this reason we set ourselves the task of producing OH-free high-purity alkali halides. After a few years' work this problem was solved for chlorides [1] and bromides [2] and semowhat later also for fluorides [3].

The decisive step in the solution of the problem is an OH elimination procedure, in the case of chlorides, for instance, bubbling CCl_4 vapour with Ar carrier gas through the melt contained by a quartz tube, until the surface, originally concave becomes convex, indicating that the melt no longer wets the tube wall. After sealing the quartz tube and normal freezing, the material can be purified by a vertical zone-melting method at a 60 mm/hour rate and pulled as a single crystal at a rate of 2 mm/hour. Not all impurities can be get rid of by zoning. E.g. the distribution coefficient of Ca in NaCl equals 1, thus zoning has no effect in this case, and chemical purification methods must be applied [4]. An interesting solution is the exchange of Ca^{2+} ions for Ba^{2+} ions by adding 10^{-3} mol/mol $BaCl_2$ to the aqueous solution of NaCl with subsequent precipitation of Ba^{2+} and Ca^{2+} ions in the form of carbonates by Na_2CO_3 added in excess. NaCl produced in this way can be purified by zoning.

The vertical zone growth method may be applied also for building in of cation dopants into the lattice without unwanted OH^- ions. OH^- ions may interact with divalent cations even in the lattice forming metal hydroxides. Upon annealing these may dissociate producing disturbing effects.

Fluorides can also be purified and grown as single crystals by the vertical zoning method using glassy carbon crucibles and inert atmosphere [3]. The

elimination of OH^- ions is more difficult in this case because of the lack of a direct OH elimination method available in the case of chlorides and bromides. OH elimination occurs partly by shifting of the pH towards acidity, partly by reaction with the glassy carbon crucible during the multiple zoning runs. The growth of OH-free divalent cation doped crystals, however, is still a problem, for OH gets bound by these cations.

The divalent cation content of our pure alkali halide single crystals can be characterized by ionic conductivity measurements showing an impurity content of 2×10^{-7} mol/mol for NaCl, 10^{-8} for KCl, 2×10^{-8} for RbCl, 10^{-6} for CsCl, 10^{-7} for KBr, and 10^{-8} for RbBr. OH-free high purity single crystals differ by a number of properties from nominal pure single crystals grown by the Kyropoulos method by air. Let us see the case of NaCl as an example. One of the crystals was grown from Merck p.a. material by the open-air Kyropoulos method, the other is an OH-free specimen of 2×10^{-7} mol/mol purity.

Fig. 1 shows the "self"-absorption of both crystals, shifted to shorter wavelengths in the case of the pure crystal (curve a) and displaying the OH band and a small O_2^- band in the case of the nominal pure one (curve b).

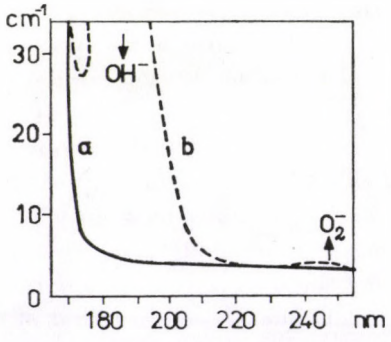

Fig. 1. Absorption curve of NaCl. a) OH-free pure, b) nominal pure

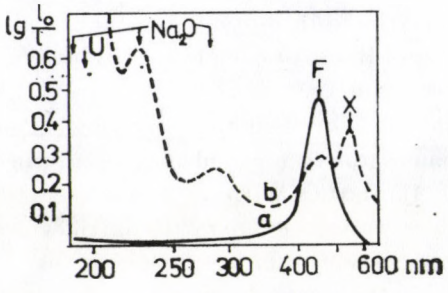

Fig. 2. Absorption curve of NaCl after electrolytical coloration.
a) OH-free pure, b) nominal pure

Fig. 2 shows the absorption of such crystals after electrolytical coloration made in order to produce F centres. In fact in the OH-free crystal exclusively F centres are generated, in contrast to the nominal pure crystal, where sodium oxide and hydride bands due to reactions with OH^- ions and also the well known X band due to F aggregation appear. Using such crystals one never obtains clear effects, and previous literature data have therefore to be revised.

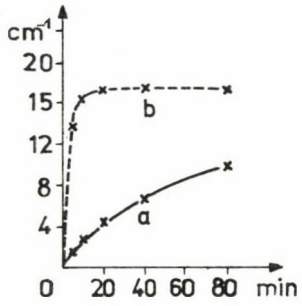

Fig. 3. The time-dependence of F absorption in NaCl. a) OH-free pure, b) nominal pure

Coloring the crystals by X-irradiation important differences in colorability can be found (Fig. 3). OH-containing crystals show fast coloration (curve b), in contrast to the slow coloration of pure ones (curve a). Coloration curves generally may be described as the sum of two exponentially saturating and one linear terms. In the case of pure crystals the exponential term due to impurities is lacking [5]. Coloration is therefore very stable, to the extent that F centres remain stable up to 250 °C and may be converted to X_k centres by bleaching light. This fact can be used for practical purposes by developing a photochromic memory based on the $F \rightarrow X_{k_2}$ conversion. For storage at 160 °C an energy density of $1 J/cm^2$ is necessary and ionizing radiation can be used for clearing the information [6]. The F and X_k bands are well separated as shown by Fig. 4. Reading without destruction and information storage for infinite time at room temperature is possible.

The remeasurement of the thermodynamic parameters of point defects in OH-free NaCl resolved a discrepancy existing in literature. One could not understand why in the series NaCl, KCl, RbCl, ordered according to cation radius, KCl has the largest enthalpy for Schottky defect formation and cation mobility. Our new values obtained on OH-free NaCl and exceeding previous literature data, solved the problem [7].

There is a further interesting difference between OH-free and nominal pure specimens from the point of view of damage by laser light. OH-free NaCl has a damage limit that is five times higher for the wavelengths of both the ruby and CO_2 laser.

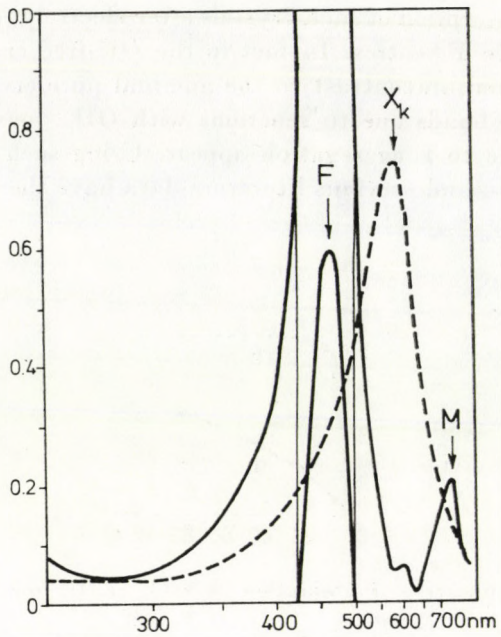

Fig. 4. Absorption curves of F and X_k centres in OH-free pure NaCl

The cutoff of self-absorption is very abrupt in the case of OH-free high-purity single crystals. Various impurities reduce its steepness extending its tail, prohibiting the investigation of exciton bands in most cases. High-purity NaF single crystals gave a possibility to study exciton bands due to Cl^- [8] and Br^- [9] ions and to determine the band parameters.

Once more it was the OH-free growth that enabled us to detect in NaCl(Ni) crystals, containing increasing amounts of Ni, the formation of $NaNiCl_3$ double salt in the course of the precipitation stages [10].

In the fifties, our laboratory was dealing with a practically important group of alkali halides, the scintillators. NaI(Tl) and CsI(Tl) single crystals were grown using the Stockbarger method, using first closed quartz crucibles and later open ceramic crucibles. The crystal dimensions were increased up to 100 mm both in diameter and length. Technology for crystal processing and casing was developed and transmitted in 1960 for production to the Gamma Works, Budapest. Meanwhile the Gamma Works introduced a number of modifications of technology resulting in a gradual improvement in the quality and in an increase of crystal sizes. Gamma scintillators are competitive on the world market.

Recently our attention was drawn to a new scintillator material, bismuth germanate ($Bi_4Ge_3O_{12}$) having various promising advantages. Due to the high effective atomic number, detector miniaturizing becomes possible which is

especially useful in geological nuclear measurements. As in this case the scintillating transition is not connected to any activator, problems arising from inhomogeneous activator distribution and afterglow do not turn up. The material is mechanically stable and chemically inert, not hygroscopic in contrast to NaI and has a low thermal expansion coefficient, thus no special handling is needed. The crystals are grown by the open-air Czochralski method in a Pt crucible. At present growth experience is being gathered.

Along with development in laser techniques oxides showing acuosto-optical, electro-optical, piezoelectric, etc. properties gained special importance. In our laboratory we started in this field by the growth of lead molibdate single crystals using the Kyropoulos method, but changed over soon to tellurium dioxide having better acuosto-optical parameters. Tellurium dioxide is a very sensitive material difficult to grow. We use for it the Czochralski method. The viscosity of the melt depends heavily on its purity. Instabilities generated in the melt, vibrations of the pulling equipment, deviations of centrality, all sensitively affect the growth process. Similar deficiencies easily result in twisted, winged and eventually in cylindrical crystals. Even in the case of excellent pulling circumstances there is still a tendency for the generation of inclusion and a great sensitivity to temperature instabilities. At present we use temperature programmers precise to 0.1 °C and carefully avoid any interference with the automatic process. The shaping of the neck, the slowness in increasing the diameter also appear to be important. We are able to produce crystals with a diameter of 3 cm, though very nice to the bare eye but very often containing inhomogeneities and microinclusions. Using our crystals the Research Institute for Computer Technique and Automation of the Hungarian Academy of Sciences developed a 7 channel modulator for its laser run line printer.

The first piezoelectric crystals produced in our laboratory were quartz single crystals grown hydrothermally as early as 1950 by the founders of the laboratory, ZOLTÁN GYULAI and IMRE TARJÁN. Unfortunately, plans for

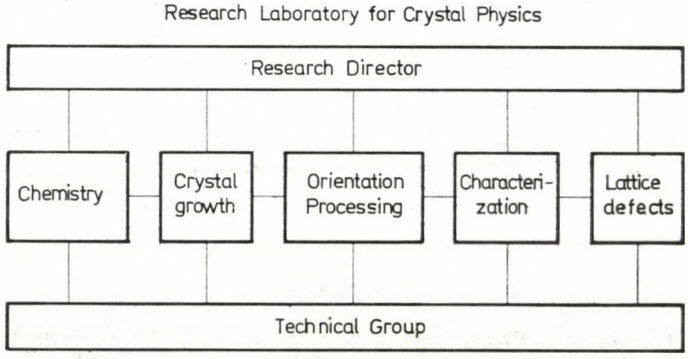

Fig. 5. The organisational pattern of the Laboratory

the creation of an experimental plant for production on a larger than laboratory scale could not be realised. At present we work on the production of piezoelectric crystals again. These are $LiNbO_3$, $Bi_{12}SiO_{20}$ and $Bi_{12}GeO_{20}$ which can be applied in SAW filters. These materials are grown also by the Czochralski method, using resistor heated furnaces and Pt crucibles. Especially interesting is $LiNbO_3$ having in addition to its piezoelectric behaviour also electro-optic, acousto-optic, piroelectric, nonlinear optic and photorefractive properties. This crystal has therefore prospective applications is various practical fields. $LiNbO_3$ can be used not only as a dynamometer, ultrasound generator, a SAW or bulk filter, due to its piezoactive behaviour, but also, due to its other properties, as a modulator, deflector or switch of laser light, as a parametric amplifier, frequency doubler, holographic memory and infrared detector, etc.

The growth of oxides raise new problems as compared to alkali halides. Such problems are the purity of the starting materials, the circumstances under which the oxide components have to react, the stoichiometry of the produced oxide, and orientation, processing and characterization of the as grown crystals.

For the solution of these problems an appropriate group scheme is being developed in our laboratory. The planned scheme is shown in Fig. 5. The Chemistry Group deals with the production, purification and analytics of the materials and also with stoichiometry problems. The Group for Crystal Growth is in charge of the growth, and the development of growth methods and equipment. The Orientation and Processing Group is responsible for X-ray orientation, cutting and polishing of the specimens. Crystals are characterized by the Characterization Group from the point of view of application. The Lattice Defects Group analyses the defect structure of crystals, the properties of artificially generated lattice defects, the general physical characteristics of our materials, and the relation between dopants and crystal properties for a thorough understanding of matter.

The Laboratory is not in charge of the actual development of equipment. This is done by cooperation with other Hungarian institutes. The development of SAW filters is carried out by the Research Institute for Technical Physics of the Hungarian Academy of Sciences. A tight collaboration between teams for crystal growth and for development is extremely important, irrespective of the fact whether they work at the same institute or not. Any step in the technology may change the defect structure and the properties of matter, therefore all physical problems arising during technological processing have to be solved jointly, to achieve the common goal, i.e. production.

REFERENCES

1. R. Voszka, I. Tarján, L. Berkes and J. Krajsovszky, Kristall u. Technik, **1**, 423, 1966.
2. R. Voszka, K. Raksányi and L. Berkes, Kristall u. Technik, **5**, 409, 1969.
3. R. Voszka, K. Raksányi and I. Földvári, Kristall u. Technik, **8**, 1347, 1973.

4. K. Raksányi and R. Voszka, Kristall u. Technik, **4**, 227, 1969.
5. G. Corradi, I. M. Gomaa and R. Voszka, phys. stat. sol. (a), **8**, K81, 1971.
6. R. Voszka, Sz. Tőkés, P. Kolin and K. Raksányi, Journal de Physique, C7, 001, 1976.
7. A. Mecseki, R. Voszka, L. Berkes and I. Földvári, phys. stat sol. (a), **30**, K87, 1975.
8. I. Földvári and R. Voszka, phys. stat. sol. (a), **28**, 249, 1975.
9. I. Földváry and R. Voszka, phys. stat sol. (a), **31**, 765, 1975.
10. I. Földvári, R. Voszka and Z. Morlin, phys. stat. sol. (b), **89**, 235, 1978.

Acta Physica Academiae Scientiarum Hungaricae, Tomus 47 (1—3), pp. 13—21 (1979)

CRYSTAL GROWTH AT THE RESEARCH INSTITUTE FOR TECHNICAL PHYSICS

By

E. LENDVAY

RESEARCH INSTITUTE FOR TECHNICAL PHYSICS OF THE HUNGARIAN ACADEMY OF SCIENCES
BUDAPEST, HUNGARY*

Crystal growing activities started at the Research Institute for Technical Physics just after the foundation of the Institute in 1958. In the first period elementary semiconductor Ge and $A^{II}B^{VI}$ compounds, mainly bulk ZnS and CdS crystals were grown. For $A^{II}B^{VI}$-s closed and open vapour phase transport systems and SSG methods have been developed and used. After finishing the research on Destriau effect and related phenomena our interest turned toward the $A^{IV}B^{VI}$ and $A^{II}B^{IV}C_2^V$ crystals and their preparation by the above mentioned methods. At the same time numerous heteroepitaxial systems containing Si, Ge, $A^{II}B^{VI}$-s, $A^{III}B^{V}$-s, etc. were prepared and investigated. In the last decade our activity was concentrated on III—V epitaxy using VPE and LPE methods. As a result different mono- and multilayer, homo- and heteroepitaxial systems have been grown for LED-s and microwave devices. The firs period was devoted to the growth of Ge and II—VI compounds, especially bulk ZnS and CdS

1. Introduction

This paper describes methods for growing different semiconductor and semiinsulator crystals as well as multilayer (homo- or heteroepitaxial) structures from liquid or vapour phase used in the Research Institute for Technical Physics (MFKI).

In a short communication it is impossible to cover the field in every detail and in all aspects for all methods and crystals or structures grown at the Institute during the last two decades.

The research and industrial trends indicate the decisive role of single crystals and epitaxial structures in electronics, especially in semiconductor technology. Consequently, we will limit ourselves to this field, neglecting numerous interesting works done on "in situ" ELMI investigations of nucleation and growth processes in thin films. This communication will describe how the activity in semiconductor crystal growth started, how it developed over the last twenty years growing semiconductor compounds and what we offer at present in the field of semiconductor materials and device technology.

2. Elementary semiconductors and $A^{II}B^{V}$ compounds

The very first experiments in crystal growing may be associated with the foundation of our Institute in 1958. At the beginning as a common project with the Industrial Research Institute for Electronics (HIKI) we had to

* Address: 1325 Budapest, Újpest 1, P.O. Box 76, Hungary.

grow Ge single crystals for semiconductor technology [1—3]. The results were soon adapted and developed by the Tungsram Works for manufacturing the first semiconductor active elements in Hungary. Work on Ge was continued on the amorphous and thin film growth.

Beside the Ge project the Groups of our Semiconductor Department developed technologies to produce $A^{II}B^{VI}$ crystals for physical investigations (mainly for electroluminescence). Particular efforts have been made to grow even larger size crystals and to produce chemically and structurally pure, as well as differently doped crystals. We had to choose techniques which did not involve the melting of high band gap materials. In order to put the techniques and crystals discussed here into a wider context, it is worth-while to mention that for $A^{II}B^{VI}$-s numerous important problems are unsolved so far, e.g. no perfect and pure ZnS crystals are available on large scale to-day, and even the "easy-to-prepare" compounds, such as CdS and selenides and tellurides raise their own unsolved theoretical and technological problems.

For the production of our $A^{II}B^{VI}$ samples chemical transport in closed and open systems, as well as the SSG (synthesis, solution, growth) method — originally developed for $A^{III}B^{V}$-s, but applied first for $A^{II}B^{VI}$-s in our Institute — were used in the production of ZnS, ZnSe, ZnTe, CdS and CdTe as it is seen in Table I. Using special closed transport systems combining transport and pulling, in the period 1970—75 we succeeded in producing cubic and hexagonal ZnS single crystals of remarkable size and a low density of stacking faults and dislocations. At the same time large semiconducting and semiinsulating CdS crystals of high perfection were grown. Using Ge, In and Sn melts pure and doped $A^{II}B^{VI}$ crystals were grown by the SSG method. This latter technology was simple and permitted to broaden substantially the range of growth methods for $A^{II}B^{VI}$ compounds.

The crystals were investigated physically and chemically enabling the determination of different polytypes and faulted structures, mechanical deformations and dislocation generation and movement. Extensive research was carried out on the photo-, and electroluminescence of these crystals (mainly of the ZnS crystals). The charge carrier transport, photo-and acoustoelectrical phenomena and the photo-decomposition were also studied as a function of the doping material quality and quantity, and more than 60 original papers were published in international journals and books in the mentioned fields.

3. $A^{IV}B^{VI}$, $A^{II}B^{IV}C_2^V$ compounds and heteroepitaxial systems

In the period 1966—75 the SSG method was also applied to crystallize different $A^{IV}B^{VI}$ compounds. As a short summary of this activity we should like to mention the growth of GaS, GaSe, GaTe and In chalcogenides. Data on these works are listed in Table I, since the method for preparation and the apparatus

Table I

MFKI publications on the growth of $A^{II}B^{VI}$ single crystals

No.	Author	Published paper	Reference
1	P. KOVÁCS, J. SZABÓ	Erfahrungen über die Herstellung von ZnS Einkristallen	Acta Phys. Hung., *14*, 131, 1962
2	P. KOVÁCS, J. SZABÓ	Erfahrungen über die Herstellung von ZnS Einkristallen	»Zur Physik und Chemie der Kristallphosphoren« Berlin, Akad. Verlag, 1962
3	M. SOMOGYI, K. RICHTER	Correlation between the methods of preparation and stoichiometry of ZnS	Acta Phys. Pol., *26*, 815, 1964
4	E. LENDVAY	On the nucleation in diffusion crystal growing	Acta Phys. Hung., *17*, 315, 1964
5	I. BERTÓTI, E. LENDVAY, M. FARKAS-JAHKNE, M. HÁRSY, P. KOVÁCS	Dendritic growth of ZnS crystals	phys. stat. sol., *12*, K1, 1965
6	E. LENDVAY, P. KOVÁCS	Growth spirals on ZnS crystals	phys. stat. sol., *8*, K125, 1965
7	LENDVAY Ö.	On the diffusion method of crystal growth (in Hungarian)	Magyar Fiz. Folyóirat, *13*, 231, 1965
8	E. LENDVAY	On the diffusion method of crystal growth	Office of Aerospace Res. U.S. Airforce, Cambridge Res. Lab. 69—0275
9	I. BERTÓTI, E. LENDVAY, M. FARKAS-JAHNKE, P. KOVÁCS, M. HÁRSY	Dendritic growth of ZnS crystals	Acta Phys. Hung., *21*, 121, 1966
10	M. HÁRSY	Growth of ZnS and CdS crystals from Ga, In, Tl and Sn melts	Krist. und Technik, *2*, 447, 1967
11	M. HÁRSY, G. GERGELY, J. SCHANDA, M. SOMOGYI, P. SVISZT, G. SZIGETI	ZnS crystals grown from Ga and In melts	Proc. Intl. Conf. of II—VI Compounds ed. D.S. Thomas Benjamin, Inc. N.Y., 1967
12	HÁRSY M., RICHTER K.	Preparation of luminescent pure ZnS raw-materials and single crystals (in Hungarian)	Fiz. Szemle, *17*, 214, 1967
13	P. KOVÁCS, K. RICHTER, F. GÁL	Some thermochemical parameters of growth of ZnS single crystals from vapor phase	Proc. ICOL, Akadémiai Kiadó, Budapest, 1968
14	E. LENDVAY, P. KOVÁCS	Luminescence and impurity precipitation in ZnS single crystals	Proc. ICOL, Akadémiai Kiadó, Budapest, 1968

Table I (continued)

No.	Author	Published paper	Reference
15	I. BERTÓTI, M. FARKAS-JAHNKE, M. HÁRSY, T. NÉMETH, K. RICHTER	Preparation, composition and structures of mixed crystals in ZnS—GaP systems	Proc. ICOL Akadémiai Kiadó, Budapest, 1968
16	M. HÁRSY	Synthesis and growth of ZnS, ZnSe, ZnTe, GaS, GaSe and InS crystals in Ga and In melts	Mat. Res. Bull., *3*, K93, 1968
17	HÁRSY M.	Crystallization of semiconductors from non-stoichiometric melts (in Hungarian)	Fiz. Szemle, *19*, 148, 1969
18	E. LENDVAY, P. KOVÁCS	Hollow single crystals of ZnS	J. Cryst. Growth, *7*, 61, 1970
19	M. HÁRSY, P. SVISZT, B. PŐDÖR, J. BALÁZS, E. LENDVAY	Growth and some physical properties of non-stoichiometric CdS single crystals	J. Cryst. Growth, *9*, 209, 1971
20	P.KOVÁCS, L. VARGA, E. LENDVAY	Growth of large dendritic ZnS crystals from the vapor phase	J. Cryst. Growth, *11*, 68, 1971
21	E. LENDVAY	Growth of structurally pure cubic and hexagonal ZnS single crystals	J. Cryst. Growth, *10*, 77, 1971
22	LENDVAY Ö.	Study of crystal surfaces and dislocations by etching (in Hungarian)	Magyar Fiz. Folyóirat, *19*, 43, 1971
23	BALÁZS J.	Semiconducting CdS crystals and their Electrical properties (in Hungarian)	Híradástechnika, *24*, 139, 1973
24	E. LENDVAY	Preparation of ZnS single crystals by chemical transport reactions	Acta Techn. Hung., *80*, 151, 1975
25	LENDVAY Ö.	On the formation of secondary phases in solids (in Hungarian)	Magyar Fiz. Folyóirat, *24*, 333, 1978

were the same as in the case of II—VI compounds. In the Ga compounds the very interesting hexagonal layer structure was investigated. Methods for GaSe chemical transport were also developed in cooperation with the Laboratoire de Luminescence II. Université de Paris VI, which substantially contributed to the more profound understanding of the growth mechanism of this material from the vapour phase [4, 5]. At that time, according to the original application of the SSG method, the synthesis, doping and crystallization of GaP were also investigated at the Institute. Research on the injection luminescence of

Table II

MFKI publications on epitaxial growth of heterojunctions

No.	Author	Published paper	Reference
1	I. BERTÓTI, M. FARKAS-JAHNKE, E. LENDVAY, T. NÉMETH	Heteroepitaxial growth of ZnS on GaP	J. Mater. Sci., *4*, 699, 1969
2	I. BERTÓTI	Heteroepitaxial growth of Si on $ZnSiP_2$	J. Mater. Sci., *5*, 1073, 1970
3	M. HÁRSY, E. LENDVAY	Heteroepitaxial overgrowth of ZnS on GaS single crystals	J. Mater. Sci., *5*, 988, 1970
4	E. LENDVAY, J. BALÁZS, M. GÁL, G. GERGELY, J. SCHANDA	Preparation and properties of Si/ZnS heterojunctions	"Proc. Intl. Conference on the Physics and Chemistry of Semicond. Heterojunctions" Akadémiai Kiadó, Budapest, 1971. Vol. 1., p. 263
5	I. BERTÓTI, L. VARGA, M. FARKAS-JAHNKE, T. NÉMETH, N. A. GORYUNOVA	Heteroepitaxy involving $ZnSiP_2$, $ZnGeP_2$ and $CdSnAs_2$ Compounds	see (4), Vol. 1, p. 107
6	I. BERTÓTI, C. SZÉKELY, G. STUBNYA, L. VARGA, L. GÚTAI	Preparation, structure and some properties of Si/Ge and $Si/Si_{1-x}Ge_x$ heterojunctions	see (4), Vol. 1, p. 341
7	I. BERTÓTI, T. NÉMETH, G. STUBNYA, M. FARKAS-JAHNKE, T. GÖRÖG	Investigation of Si epitaxial growth on single crystalline quartz substrate	see (4), vol. III., p. 191
8	L. GÚTAI, J. PFEIFER, I. MARKÓ	Some properties of Si/Ge heterojunctions obtained by vacuum evaporation	see (4), Vol. II., p. 301
9	M. HÁRSY, N. VARGHA, E. LENDVAY, L. VARGA	Preparation and structure of ZnS/GaS heterojunctions	see (4), Vol. I., p. 179
10	J. RÓNAI-PFEIFER, E. HARASZTI-SZABÓ M. FARKAS-JAHNKE	Oriented growth of Si layers on ZnS single crystal substrates	Thin Solids Films, *11*, 71, 1972
11	J. RÓNAI-PFEIFER, L. VARGA, B. SZENTPÁLI	Si/Ge heteroepitaxial structures evaporated in ultra-high vacuum	Thin Solid Films, *11*, 59, 1972
12	J. RÓNAI-PFEIFER, E. HARASZTI-SZABÓ	The investigation of Ge/Si layer structures by means of the ERM	Thin Solid Films, *20*, 31, 1974

$A^{III}B^{V}$-s, the detailed study of the physical properties of GaP also began and led to the present wide activity in the III—V field.

Between 1965 and 1970 our interest turned toward heteroepitaxial systems and ternary chalcopyrites. In this connection Si being generally available offered us a good quality substrate material, so heteroepitaxial systems based on silicon as Si/ZnS were under investigation. Original works published in this field are listed in Table II. During this period both the heteroepitaxial system of ZnS/GaP and the alloyed phase of the two compounds were discovered. Different methods for growing the mentioned systems containing ZnS and Ge/Si; Ge/GeSi alloy; SOS (silicon on sapphire) and other systems were developed and studied.

On the other hand, similar investigations have been made on ternary $A^{III}B^{IV}C_2^V$ chalcopyrites as $ZnSiP_2$; $ZnGeP_2$ and $ZnSnAs_2$, as well as heteroepitaxial systems with Si and the different $A^{II}B^{IV}C_2^V$-s. Promising early results with ternary chalcopyrites suggested a wide future application, but owing to the difficulties in technology these hopes have not been realized so far. The Groups of our Semiconductor Department search for other materials and applications.

4. $A^{III}B^{V}$ compounds

In the last two decades Si has become the basic material in semiconductor technology. However, the next important materials for semiconductor application are the $A^{III}B^{V}$, mostly the Ga compounds. In the cases of $A^{III}B^{V}$ compounds melting and stoichiometry problems occur. Serious considerations have led to the conclusion that these problems will be solved on industrial scale using Bridgman and LEC (liquid encapsulated Czochralski) methods, but the epitaxial processes will attract increasing research interest. That is, if device development arrived at a certain level, techniques for growing epitaxial structures with different topology (lateral and vertical dimensions, etc.) and other characteristics (concentration, dislocation density, etc.) will be required. Really, $A^{III}B^{V}$ epitaxy rapidly becomes an important and inherent branch of the research and development of different solid state elements as LED-s as well as lasers, microwave and other devices. These developments originated from the new possibilities offered by the extensive research on $A^{III}B^{V}$-s. Although most of the epitaxial possibilities, even molecular beam epitaxy have been recognized for a long time, numerous modifications of vapour phase and liquid phase epitaxy have been described. These improvements of epitaxial methods had the most far reaching impact on our crystal growth activities. First, we grew InSb and InSb—NiSb crystals for producing different magnetoresistors. 10 years ago we built up our first VPE and LPE systems for $A^{III}B^{V}$-s, in which GaP and GaAsP layers were grown onto GaAs substrates. Our deve-

lopments in both VPE and LPE fields, the knowledge of $A^{III}B^{V}$ epitaxy and the equipment designed enabled us to solve such problems as the production of GaP and GaAsP LED-s of different kinds, IR light sources and microwave Gunn diodes. These investigations and technological developments form a solid basis for our present work on $A^{III}B^{V}$ technologies.

Nowadays we are working on several versions of microwave devices such as high-power Gunn diodes, Schottky mixers and detectors. The family of different LED-s has been completed using LPE methods; red, green, orange and IR diodes of different kinds were developed. To satisfy the requirements imposed on the design of high-energy light sources and microwave devices it was of particular importance to develop VPE and LPE methods providing fairly well reproducible and precisely controlled results. It has been established that oxygen plays an essential role as background impurity in GaAs and affects crucially the conductivity of undoped epilayers. So, to get pure (10^{-14}–10^{-15} cm^{-3}) layers, we have to develop methods to purify our materials, especially for microwave purposes. Similarly, microwave applications require very definite and thin epilayers, the reproducible production of which is also a very complicated problem, strongly connected with the stability and the precise regulation of the growth system. It has always been important to eliminate random variations in temperature or composition. Thus, temperature control and program systems, as well as complete gas mixer stands, using mass flow controllers, were developed in our Laboratory.

One of the most efficient methods used is the LPE. Since the early Nelson experiments a great number of horizontal and vertical systems have been published. The vertical dip techniques in our Laboratory gave unsatisfactory results, therefore, horizontal slider methods and rotating systems have been applied. During LPE growth the real processes involve many interacting mechanisms, and it is difficult to decide without experimental data which is significant in a given case. To eliminate undesired effects, we have examined the role of the constructions and boat materials in surface morphology and in doping of the grown layers, the role of under- and supersaturation, the cooling rate and the different possibilities of contacting the melts with the wafers. As most of the devices require predetermined levels of dopants, extensive work was devoted to the investigation of doping processes and the determination of impurity distribution (lateral and normal, the so-called profile measurements).

To exclude oxygen-containing atmospheres, gas-tight valves and joints were developed for LPE systems, which contain flowing H_2 or can be evacuated. Both the rotational and slider systems are the usual graphite multiple bin systems, because this method has advantages when multilayer structures are required. Temperature was measured by MFKI (Research Institute for Technical Physics) digital thermometers of 0.1 °C accuracy, the regulation and prog-

Table III

MFKI publications on crystal and epitaxial layer growth of $A^{III}B^{V}$-s

No.	Author	Published paper	Reference
1	M. HÁRSY	Separation of GaP crystals from Ga	Krist. und Technik, *3*, K93 1963
2	PAPP E.,* PŐDÖR B., ZSINDELY,* S. LEGÁT* T.	Preparation and properties of GaAs single crystals (in Hungarian)	Híradástechnika, *20*, 369, 1969
3	BERTÓTI I., SOMOGYI K.	Preparation and study of GaP single crystals (in Hungarian)	Híradástechnika, *21*, 133, 1970
4	E. PAPP,* B. PŐDÖR, S. ZSINDELY,* T. LEGÁT*	Preparation and properties of GaAs single crystals	Acta Techn. Hung., *68*, 245, 1970
5	PŐDÖR B., ZSINDELY S.,* PAPP E.	Preparation and properties of doped semiconducting and semiinsulating GaAs crystals (in Hungarian)	MFKI Közl., *0—3*, 43, 1971
6	GÖRÖG T., KOCSIS ZS.	Preparation of epitaxial GaP layers and study of their electrical parameters (in Hungarian)	MFKI Közl., *0—14*, 47, 1974
7	GÖRÖG T.	Method and apparatus for preparation of $A^{III}B^{V}$ semiconductor structures (in Hungarian)	Bp., 1974
8	L. VARGA, A. T. NAGY, T. GÖRÖG, E. LENDVAY	On the characterization of heterostructures by X-ray diffraction	Acta Techn. Hung., *80*, 293, 1975
9	T. GÖRÖG, E. LENDVAY,	Epitaxial growth of $A^{III}B^{V}$ semiconductors from vapor phase	Acta Phys. Hung., *44*, 13, 1978
10	J. PFEIFER, L. CSONTOS, B. SZENTPÁLI	Investigation of the doping level in overcompensated p-GaP layers grown by liquid phase epitaxy	Acta Phys. Hung., *44*, 29, 1978
11	V. V. JEVSZTROPOV, A. N. IMENKOV, B. N. KALININ, J. PFEIFER, L. CSONTOS, JU. P. JAKOVLEV	Ob oszobennoszt'áh elektroljumineszcencii p-n GaP-nGaAlP sztruktur	Elektronnaja Techn. szer. 6., Materialü, 1978
12	V. V. JEVSZTROPOV, A. N. IMENKOV, B. N. KALININ, J. PFEIFER, L. CSONTOS, JU. P. JAKOVLEV	Szpektrü ljumineszcencii p-nGaP-nGaAlp-n n-pGaP-nGaP sztruktur legirovannüh Si	FTP, *12*, 1017, 1978
13	J. PFEIFER, B. PŐDÖR, L. CSONTOS, N. NÁDOR	Observations on residual donors in GaP LPE	Revue de Phys. Applique, *13*, 741, 1978

*Coworkers of Res. Inst. of Metals (FKI), Budapest

ram was also realized by using MFKI equipment. We have already discussed some of the major problems in the growth of high-quality epitaxial layers, but some problems remain to be solved in the VPE processes, too.

Thus, e.g. in LPE systems the random temperature variations or dissipation processes, while in VPE systems the concentration variations influence the grown morphology and the doping homogeneity.

For regulation and the temperature program also MFKI systems have been applied, but for flow rate measuring and gas mixing mass flow controllers are used. The gas unit built at our Institute is able to control and regulate the gas composition (involving the dopant lines) throughout the whole epitaxial process. Our results have been summarized in several publications listed in Table III and reports have been published concerning the growth processes. More than 50 original papers have been published by our coworkers on the application of the semiconductor systems measuring transport and domain properties, the formation and properties of metal semiconductor systems, recombination, deep level spectroscopy as well as device physics; the optical, electrical and microwave properties of solid state devices built in our laboratories.

As a closing remark, we should like to mention that now, after ten years' work, we are aware of the problems of $A^{III}B^{V}$ technology, and in some important cases have solved the problem of growth layers with definite properties. Our present facilities make it possible to focus our attention on the different fields of $A^{III}B^{V}$ technologies. Our crystals and multilayer structures will subsequently be the subject of further investigations aimed at the production of different solid state devices.

REFERENCES

1. T. Németh, A. Lőrinczy and P. Szebeni, Magy. Fiz. Folyóirat, **10**, 293, 1962 (in Hungarian); Acta Phys. Hung., **16**, 63, 1963.
2. J. Rónai-Pfeifer, phys. stat. sol., **17**, K15, 1966.
3. T. Németh, M. Németh-Sallay and B. Sallay, "Technology of Ge" in Technology of Semiconductor Materials ed. by I. Szép, Tankönyvkiadó, Budapest, 1963. (in Hungarian).
4. E. Lendvay, A. Kuhn, A. Chevy and T. Ceva, J. Mater., **6**, 305, 1971.
5. A. Kuhn, A. Chevy and E. Lendvay, J. Cryst. Growth, **13/14**, 380, 1972.

Acta Physica Academiae Scientiarum Hungaricae, Tomus 47 (1—3), p. 23 (1979)

CRYSTAL GROWTH AT THE CENTRAL RESEARCH INSTITUTE FOR PHYSICS

By

G. KONCZOS

CENTRAL RESEARCH INSTITUTE FOR PHYSICS, HUNGARIAN ACADEMY OF SCIENCES
BUDAPEST, HUNGARY

A short review of some results in crystal growth is given.

At our Institute crystal growth began in the early sixties with the preparation of metallic single crystals. These crystals were used in various kinds of basic studies, e.g. determination of magnetic structure, crystal anisotropy and phase transitions. Single crystals of pure metals like Cu, Ni, Pb [1—3] and Fe—Al, Fe—Ni [4] Mn—As [5—6] alloys were grown by the Bridgman method.

A research project was organized in 1970 for the study of magnetic bubble memories. First, rare earth orthoferrites [7] were grown from high temperature solvents (flux method) between 1969—1972. In an endeavour to decrease bubble domain diameter, magnetic garnet films [8] were grown by liquid phase epitaxy on gadolinium gallium garnet (GGG) single crystal substrates (1974). GGG crystals of 1″ diameter have been grown by the Czochralski method since 1973. For the improvement of crystal quality a diameter control was developed by the measurement of weight change of the melt (1976) [9]. The cutting and polishing of GGG crystals have also been elaborated. Crystal defects in the substrate and in the garnet films are determined by X-ray topography, selective etching, and by optical and magnetic measurement techniques [10—12].

Current main aims are: production of GGG crystals and garnet films with larger diameter (2″ and more), improvement of cyrstal quality by the better control of the environment (clean rooms, laminary flow boxes).

REFERENCES

1. E. KRÉN and P. SZABÓ, Magy. Fiz. Folyóirat **9**, 161, 1961.
2. P. SZABÓ and E. KRÉN, KFKI Közlemények, **7**, 366, 1959.
3. P. SZABÓ and E. KRÉN, Prib. Techn. Exper., 76, 1961.
4. G. KONCZOS and J. TAKÁCS, unpublished results.
5. J. PAITZ, J. Crystal Growth, **11**, 218, 1971.
6. J. PAITZ, Kristall und Technik, **7**, 999, 1972.
7. B. KESZEI, Thesis 1972. ELTE Budapest.
8. B. KESZEI and M. PARDAVI-HORVÁTH, IEE Trans. Magn. Vol. MAG-14. 605, 1978.
9. J. PAITZ and L. GOSZTONYI, Acta Phys. Hung., this issue, p. 233.
10. C. BECKER, E. ZSOLDOS and E. VÁZSONYI, phsy. stat. sol. (a), **32**, K17 1975.
11. C. BECKER, E. ZSOLDOS and A. WEBER, phys. stat. sol. (a), **34**, 519, 1976.
12. E. ZSOLDOS and C. BECKER, Kristall und Technik, **11**, 1275, 1976.

Acta Physica Academiae Scientiarum Hungaricae, Tomus 47 (1—3), pp. 25—31 (1979)

SYNTHESIS AND CRYSTAL GROWTH OF $A^{III}B^{V}$ COMPOUNDS FROM ELEMENTS

By

T. GÖRÖG and E. LENDVAY

RESEARCH INSTITUTE FOR TECHNICAL PHYSICS OF THE HUNGARIAN ACADEMY OF SCIENCES
BUDAPEST, HUNGARY*

Compact, inclusion-free GaAs and GaP ingots were synthetized and crystalline boules were grown using modified Bridgman and SSD methods. Preliminary investigations showed that in case of GaAs using travelling boat system after the synthesis semiconductor grade macrocrystalline ingots can be prepared by oriented freeze. For GaP the modified SSD (Synthesis Solution Diffusion) method proved to be useful producing macrocrystalline, pure materials.

1. Introduction

$A^{III}B^{V}$ compounds are widely used in the electronic device industry. As applications require good quality crystalline materials, there is considerable interest for synthesis and crystal growth in the literature. Great efforts were made partly to produce high purity materials, partly to grow crystals with sufficient surface and quality for mass producing devices as LED-s, microwave diodes, MESFETS, etc. As a starting material solid ingots were synthetized from the elements under high temperatures and pressures, and single crystals were pulled from the ingots by Liquid Encapsulated Czochralski (LEC) or Bridgman methods.

The physical properties of $A^{III}B^{V}$ crystals as well as the quality of $A^{III}B^{V}$-based devices are strongly affected by the growth processes, i.e. by the crystal perfection. It is generally known e.g. that the highest quantum efficiency was achieved on LED-s having active region grown from Ga-rich solutions (solution grown, SG or liquid phase epitaxy, LPE) [1]. In LEC crystals the quantum efficiency of a p—n junction is rather low [2] so one must build up layers using epitaxial methods. Similarly to radiative recombination the noise properties in microwave devices can also be affected by choosing the proper growth method. LPE-grown structures generally have better properties than VPE-built structures, etc. From these experimental data and theoretical considerations one can state that the efficient and economical solution is to grow bulk crystals from Ga-rich solution combining synthesis and crystal growth. Numerous attempts have been made to perform bulk growth and several methods have been described, e.g. travelling solvent [3], horizontal gradient freeze [4]

* Address: 1325 Budapest, Újpest 1, P.O. Box 76, Hungary

and Bridgman techniques [5]. The modifications of the Bridgman method have proved to be the most useful ones [6, 7]. Recent increasing interest in synthesis and growth is stimulated by the fact that gallium is an industrial product of the Ajka Aluminium Works (Hungary).

The aim of this work is to investigate the methods of synthesis and the role of the different materials used such as quartz, graphite, etc. in the impurity contents of the synthetized $A^{III}B^{V}$ compounds.

2. General principles and growth methods

The preparation methods of $A^{III}B^{V}$ ingots from high temperature Ga melts are based on previous investigations of the phase diagram as well as the partial pressures along the $A^{III}B^{V}$ liquidus curve [8, 9]. It is well known that above the Ga-rich melts (in the case of high mole fraction of Ga) the equilib-

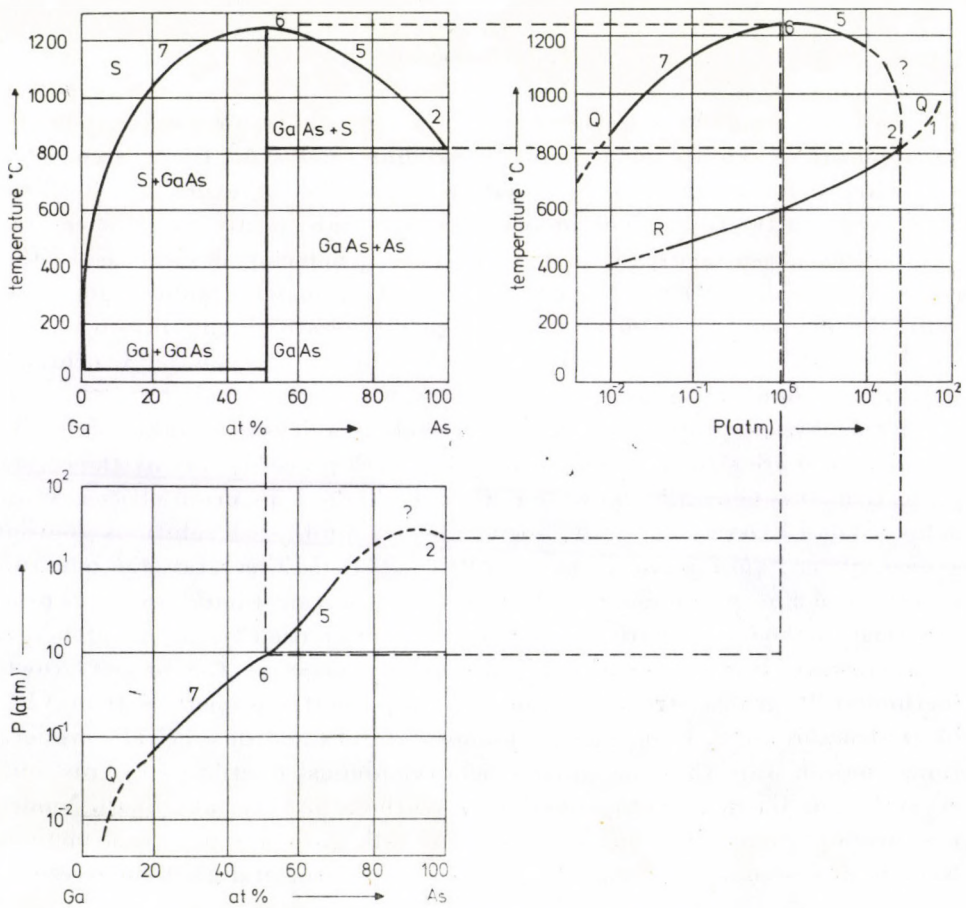

Fig. 1. Phase diagram of the GaAs and equilibrium pressures

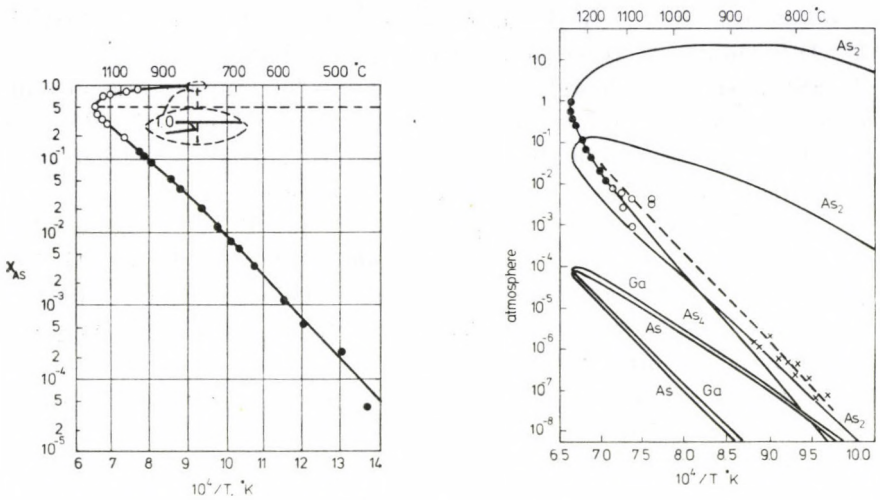

Fig. 2. The liquidus curve of the GaAs and the corresponding vapour pressure values

rium vapour pressure is low, therefore the difficulties caused by the high dissociation pressure of $A^{III}B^{V}$-s above stoichiometric melts can be avoided. The situation is illustrated in Fig. 1, where the phase diagram of the GaAs is seen. At Ga mole fraction $X_{Ga} = 0.5$ (the stoichiometric composition) above the melt GaAs the equilibrium pressure is 0.9 atm. The main components of the vapour are As_2 and As_4 molecules, according to Fig. 2. Starting from the As side of the phase diagram, along the liquidus curve the high pressure of the V. column element is dominant. In the case of GaP the situation is more pronounced because at the melting point the equilibrium vapour pressure of the volatile P component is 35 atm. Another difficulty is that at about the melting point of the $A^{III}B^{V}$, both the As and P are extremely reactive, so it is necessary to apply special materials. From these facts the advantages of the Ga-rich melt are clearly seen.

Of the various possibilities the proper method of synthesis and growth can be selected by the chemical character of the $A^{III}B^{V}$ compound. For these semiconductors both horizontal and vertical methods have been developed. For the most important compound, GaAs, horizontal techniques have been applied using two or three principal heat zones: a low temperature region for the V. element source, and a high-temperature region for the Ga. The system is closed, and after completing the procedure of synthesis, one can grow" in situ" macro-, or single crystalline ingots from the dense, inclusion-free polycrystalline material using a third travelling zone along the ingot or pulling the ingot through the temperature gradient.

For GaP the vertical systems proved to be the most useful. Similarly to the GaAs, synthesis and growth take place in a closed system containing a phos-

phorus source and the Ga. In the past few years the method called "Synthesis Solution Diffusion" (SSD) has found wide application.

In SSD systems, although the growth rate is low, the equipment and the procedure are relatively simple and economical. A container with gallium is located at the upper part of the reactor tube. The Ga surface is held at an elevated temperature T_s (1200 °C), the bottom is at a lower temperature T_c so there is a temperature gradient along the Ga column. The P source is situated under the Ga in a constant temperature region at about 400—420 °C. In this arrangement the continuous generation of P is maintained. The phosphorus reacts with Ga at the melt surface and diffuses toward the lower temperature region. Reaching the suitable supersaturation conditions, nucleation and crystal growth begins at the bottom of the gallium. The process takes place continuously until one of the components is exhausted.

3. Synthesis and growth of GaAs and GaP

In our Laboratory the horizontal method was used for GaAs synthesis. The raw materials were 6N quality Ga (Alutröszt—FKI, Hungary) and As (Freiberg Spure Metall, GDR). Our method was principally based on the Bridgman process, however, there were deviations and modifications. The closed quartz ampoule charged with Ga and As was placed into a two-zone system in which the As source was held in a low temperature (610—640 °C) zone. This zone was heated by a resistance furnace regulating the temperature as well as the partial pressure of the As in the system with sufficient ($\pm$1 °C) accuracy. The gallium container was placed in a high temperature zone (1250 °C). The heating of this zone was not performed by the usual resistance heating but by an RF generator applied to maintain gallium temperature at a relatively high level (1200—1500 °C). The As source and the ampoule itself were made of quartz (Hereaus OFHC quality), while for the Ga boat in which the synthesis took place OFHC quartz and high purity graphite (type 556 Ringsdorf, FRG) were used. The ampoule was charged in a nitrogen filled box. Before synthesis a special treatment was introduced; after charging, the system was heat-treated for 3 hours at 650 °C in H_2 stream to remove arsenic and gallium oxide. After evacuation the ampoule was closed by sealing and the Ga source was heated up to 1245 °C and held at this temperature for further 3 hours. The vacuum before sealing was 10^{-5} torr.

For synthesis first the Ga source was heated to 1250 °C and then, in a second step, the As source reached a temperature of 610—640 °C. The RF heating produced a strong turbulence in the Ga melt promoting the intense reaction between the Ga and the As. This is one of the main deviations as compared to the classical Bridgman method. The mixing increases the reaction

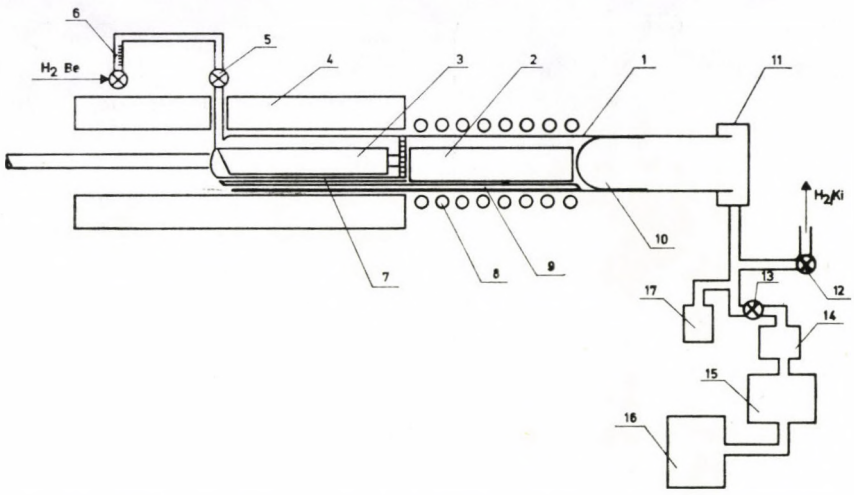

Fig. 3. Apparatus for the growth of GaAs macrocrystalline ingots by synthesis and oriented freeze

1. Reactor tube; 2.Ga container; 3. As container; 4. Resistance heated furnace; 5. Valve; 6. Rotameter; 7. Thermocouple for the As source; 8. RF coil; 9. Thermocouple for the Ga source; 10. Quartz plug; 11. Vacuum tight screw-cup; 12. H_2 output valve; 13. Vacuum valve; 14. Liquid N_2 trap; 15. Diffusion pump; 16. Vacuum (rotation) pump; 17. Pirani gauge

rate which is normally a diffusion-controlled process. The synthesis time was 8—24 hours depending on the quantity of the Ga charge. Another modification was that after the reaction was completed the GaAs melt was pulled through the temperature gradient between the reaction region and the As container producing an oriented freeze of the GaAs. The system is seen in Fig. 3.

It was observed that owing to the strong turbulence effect even in case of a synthesis of short duration the resulting GaAs ingot was a dense Ga inclusion-free material. Using for the synthesis a travelling boat and oriented freezing, the ingot consists of crystallites of an average size of some mm;. Both quartz and graphite were suitable to produce semiconductor grade material as the photoluminescence and free carrier concentration measurements suggested 10^{17}—10^{18} cm^{-3} concentration. The synthetized ingots were 100—300 g in weight, and they could be applied for LEC growing.

For GaP the SSD system represented in Fig. 4 was used in our experiments. The Ga was heated similarly to the GaAs by an RF coil allowing the Ga temperature to rise. The surface temperature of the Ga was 1240—1245 °C while the P source was held at 420—440 °C by a resistance furnace. Contrary to the usual systems between the P zone and the Ga column we applied a graphite cylinder to prevent the condensation of the P vapour. This graphite was also heated by the lower part of the RF coil, the construction of which produced a temperature gradient along the Ga column.

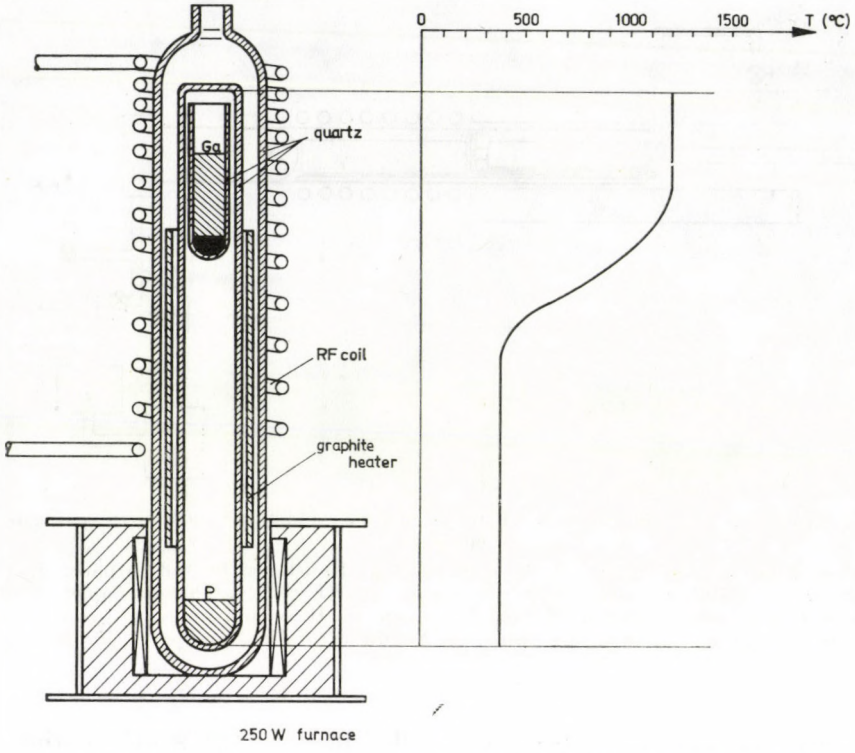

Fig. 4. Closed reactor system for SSD growth of GaP macrocrystalline ingots.

6N quality Ga (Aluterv—FKI) and red P (BDH 5N) were used. The P source temperature was regulated with ± 1 °C accuracy using a temperature programmer developed at this Institute. The preparation of the Ga and P sources as well as the charging process and prepurification of the quartz ampoule and the materials were similar the GaAs synthesis. After sealing the ampoule the system was placed in a vertical crystal growing apparatus (type BCG 265 Metal Research Ltd.) and heated up to the synthesis temperature. After two hours reaction the first GaP crystals appeared at the ampoule tip and the lowering of the system started. With a lowering rate approximately corresponding to the rate of the growing crystal front (5—10 mm/hour) depending on the Ga volume the metal was transformed into GaP. The resulting ingot was a macrocrystalline, inclusion-free material with an average crystallite size of 1 cm^3. Cutting down slices from the boule, after polishing, transparent, optically clear wafers with free carrier concentration of about 10^{17}—10^{19} cm^{-3} could be produced. Using this material as a source of LPE we obtained epitaxial layers of high purity showing low-temperature (4 K) photoluminescence spectra characteristic of pure GaP materials.

REFERENCES

1. I. LADANYI and H. KRESSEL, RCA Rev., **33,** 517, 1972.
2. R. A. LOGAN, H. G. WHITE and W. WIEGMANN, Solid State Electronics, **17,** 55, 1971.
3. K. KURATA, J. SHIZAFUJI and T. ENDO, Japan. J. Appl. Phys., **2,** 65, 1963.
4. T. S. PLASKETT, S. E. BLUM and L. M. FOSTER, J. Electrochem. Soc., **114,** 1303, 1967. G. BOUGNOT and A. JOULLIE, C. R. Acad. Sci. Paris, **269,** 884, 1969.
5. L. R. WEISBERG, F. D. ROSI and P. G. HERHART, Properties of Elemental and Compound Semiconductors, Interscience Publishers, New York, 1959.
6. H. RODOT, A. HRUBY and M. SCHNEIDER, J. Cryst. Growth, **3/4,** 305, 1969.
7. K. KANEKO, M. AYABE, M. DOSEN, K. MORIZANE, S. USUI and N. WATANABE, Proc. IEEE, **61,** 884, 1973.
8. W. D. LAWSON and S. NIELSON, The Art and Science of Growing Crystals, Ed. J. J. Gilman, John Wiley and Sons, New York, 1963.
9. C. P. THURMOND, J. Phys. Chem. Solids, **26,** 785, 1965.

Acta Physica Academiae Scientiarum Hungaricae, Tomus 47 (1—3), pp. 33—44 (1979)

QUICK AND AUTOMATIC DETERMINATION OF THE DOPANT CONCENTRATION PROFILE OF GaAs EPITAXIAL LAYERS

By

T. SEBESTYÉN, E. LENDVAY and T. GÖRÖG

RESEARCH INSTITUTE FOR TECHNICAL PHYSICS OF THE HUNGARIAN ACADEMY OF SCIENCES
BUDAPEST, HUNGARY*

An automatic instrument called Post Office Profile Plotter is used at this Institute for the quick estimate of the crystal quality and the determination of the impurity profile between $4 \cdot 10^{14}$ and $4 \cdot 10^{18}$ cm^{-3} with an in-depth resolution of about 10 nm.

This equipment automatically and continuously registers the dopant concentration profile by measuring photo capacitance, photo current and photo voltage of a Schottky contact formed between the semiconductor material and a transparent electrolyte during the photo-electrochemical etching of the semiconductor.

In this paper an assessment of this method as well as measurement results on VPE and LPE n, n^+-n, p^+-n GaAs and $GaAs_{1-x}P_x$ ($c = 0.38$) structures are presented.

Changes of the dopant profiles due to mechanical polishing or annealing were also measured near the surface of the samples.

1. Introduction

GaAs is the most widely used III—V compound semiconductor because of its well-developed technology and many advantageous properties. For most applications the active layer of the GaAs devices (e.g. Gunn diodes, Schottky diodes, IMPATT diodes and infrared light emitting diodes) is made by liquid or vapour phase epitaxy on highly doped n GaAs substrates. We also use both liquid and vapour phase epitaxy [1, 2] for preparing epitaxial GaAs, GaAsP and GaP for microwave and optoelectrical devices.

The characterization of epitaxial layers has an important role in linking crystal growth with device making by feeding back information to technology and construction about the starting and formed materials or in checking the effects of device processing.

Assuming that the intrinsic properties (such as band structure) are known, only the extrinsic properties, such as resistivity, dopant concentration, carrier mobility, the energies of the shallow and deep acceptor and donor levels, the lifetime and diffusion length of the minority carriers, have to be characterized.

The requirement for the characterization of the various properties of semiconductor materials had led to the development of a very wide range of measurement techniques over the last ten years. A good review is given on these techniques in a paper recently published by BLOOD and ORTON [3].

* Address: 1325 Budapest, Újpest 1, P.O. Box 76 Hungary.

In our Institute an automatic Van der Pauw measuring system and an automatic angle dependent geometrical magnetoresistance, MR, measuring system [4] are used for evaluating the epitaxial layers formed on semi-insulating GaAs substrates and for determining the mobility and the average dopant concentration in epitaxial layers on n^+ GaAs substrates, respectively.

Generally, the depth distribution of dopant concentration must be known for the thin layer structures made by epitaxy, diffusion or ion implantation where the abruptness of the high-low interfaces and the profile shapes have importance in specific applications. On the other hand, the determination of the doping profile is necessary both for a complete evaluation of the epitaxial layer and for device modelling.

By using continuous electrolytic etching to remove material and a simultaneous fixed-bias C-V measurement to determine the doping level the two components in that product are separated and a wide range of doping concentrations can be continuously profiled over an unlimited depth [5].

The Schottky barriers formed at a contact between an electrolyte and a semiconductor have recently found wide interest among physicists because this type of Schottky barrier is easily formed. These Schottky barriers are suitable not only for material characterization by C-V method but also for generating photovoltage at illumination trough the transparent electrolyte. Such systems have been studied as converters of solar energy into chemical energy by photoelectrolysis of water or as photovoltaic power generators [6, 7, 8]. The greatest obstacle for the practical application of such systems is their susceptibility to photoelectrochemical decomponsition. There is ample experimental evidence showing that all non-oxide, n-type semiconductors undergo photoanodic decomposition. The reaction rate is proportional to the surface concentration of holes in the n-type semiconductors. In wide band gap n-type materials the quantity of thermally generated holes is negligible and other exitation e.g. by light, is needed to get anodic dissolution. Two examples [7] are given in the following anodic reactions

$$\mathrm{GaAs} + 6\mathrm{h}^+ + 2\,\mathrm{H_2O} + \mathrm{solv} \rightarrow \mathrm{Ga^{3+}} \cdot \mathrm{solv} + \mathrm{AsO_2^-} + 4\,\mathrm{H^+} \cdot \mathrm{solv}$$

$$\text{or} \quad \mathrm{GaAs} + 6\mathrm{h}^+ + 12\,\mathrm{OH^-} \rightarrow \mathrm{Ga(OH)_6^{3-}} + \mathrm{As(OH)_6^{3-}}$$

$$\text{and} \quad \mathrm{GaP} + 6\mathrm{h}^+ + 3\,\mathrm{H_2O} + \mathrm{solv} \rightarrow \mathrm{Ga^{3+}} \cdot \mathrm{solv} + \mathrm{H_2PO_3^-} + 4\,\mathrm{H^+} \cdot \mathrm{solv}$$

where h^+ denotes the positive holes participating in the anodic dissolution. The solvent materials used in profiling GaAs are 0.1 M Tiron (1,2 dihydroxy-benzene-3,5 disulfonic acid disodium salt, i.e. $C_6H_4Na_2O_8S_2$) or 10% KOH. Tiron gives slower etching rate but better area control than the 10% KOH. The complexant electrolyte Tiron has a strict six-electron equivalence which allows the integrated current density to be converted automatically to the dissolution depth by making use of Faraday law. Tiron and KOH, too, allows

the electroetching to occur without interference from insoluble products at the electrode surface, in contrast to, say, sulfuric acid solutions which leave precipitated arsenious oxide [9].

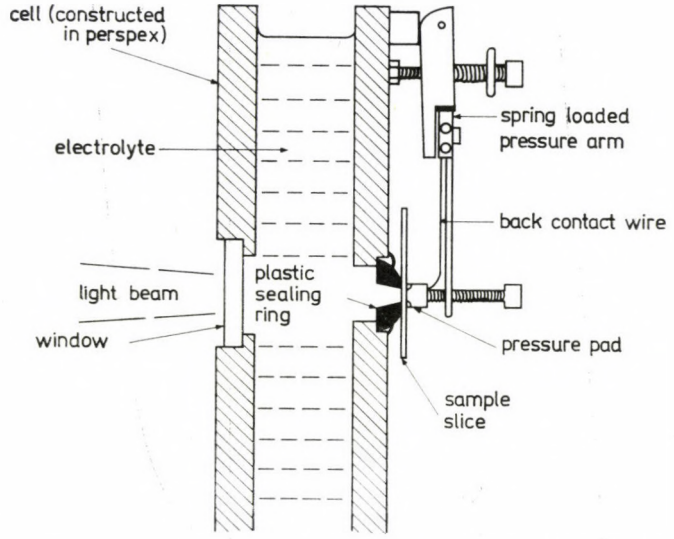

Fig. 1. The electrochemical cell of the Post Office Profile Plotter. The sample slice is pressed onto the sealing ring (Neopreme or Polythene) having a diameter of 3.5 mm. Ohmic contact is made by a current pulse flowing through the two back contact wires. Light having a photon energy higher than the energy band gap of the semiconductor illuminates the electrolyte-semiconductor interface by passing through the window and the transparent electrolyte

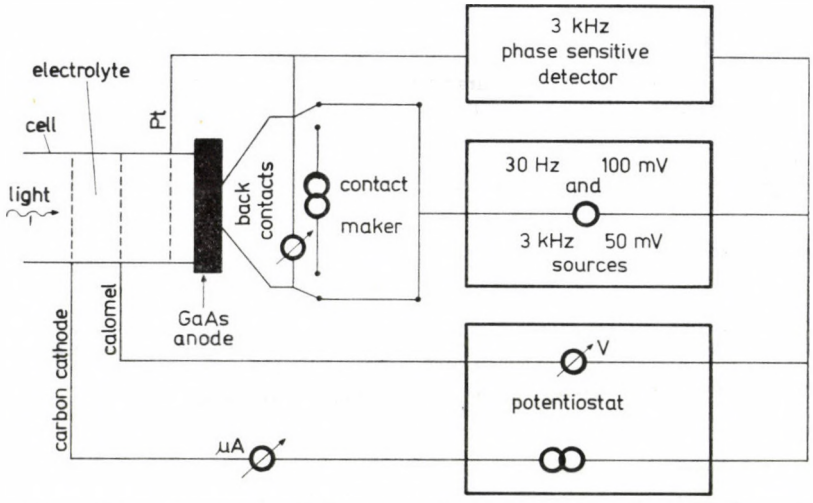

Fig. 2. Schematic representation of the connections of the electrolyte cell shown in Fig. 1. The dissolution current is passed via a back contact and the carbon cathode, whilst the potential is measured via the other back contact with respect to a saturated calomel electrode. Capacitance measurements are made via a back contact and an auxiliary cathode of platinum wire [5]

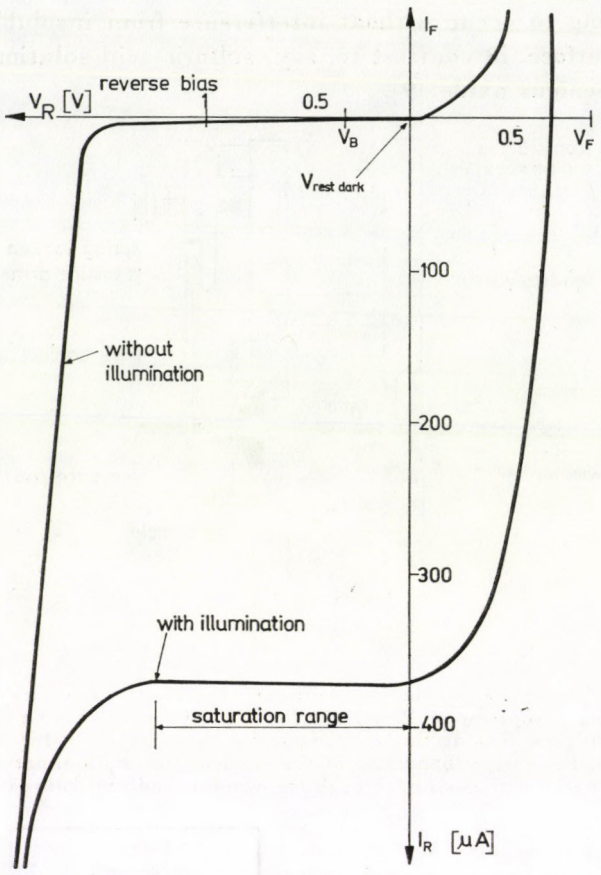

Fig. 3. The typical current-voltage characteristics of the Schottky diodes formed as the interface between 10% KOH and n-type GaAs, according to AMBRIDGE and FAKTOR [5]

The electrolyte cell of the Profile Plotter is schematically shown in Fig. 1. The schematic representation of the cell connection is shown in Fig. 2.

The typical voltage-current curve for a reverse biased junction formed between an n-type GaAs sample and a 10% KOH electrolyte is shown in Fig. 3. according to AMBRIDGE and FAKTOR [5].

Fig. 4. shows the energy band structure of n-type GaAs in contact with complexant Tiron electrolyte, as it was suggested by FAKTOR and STEVENSON [9]. The built-in potential is about 1 V in equilibrium. The level R in Tiron is determined by the redox interaction taking place between the electrolyte and the semiconductor. The level R conincides with the Fermi level of the semiconductor in equilibrium (Fig. 4a). Under reverse bias the voltage drop, V_B, in the depletion layer is added to the built-in potential, V_{bi}, and the depletion width is increased. It is supposed that the band edges, E_c and E_v, are pinned

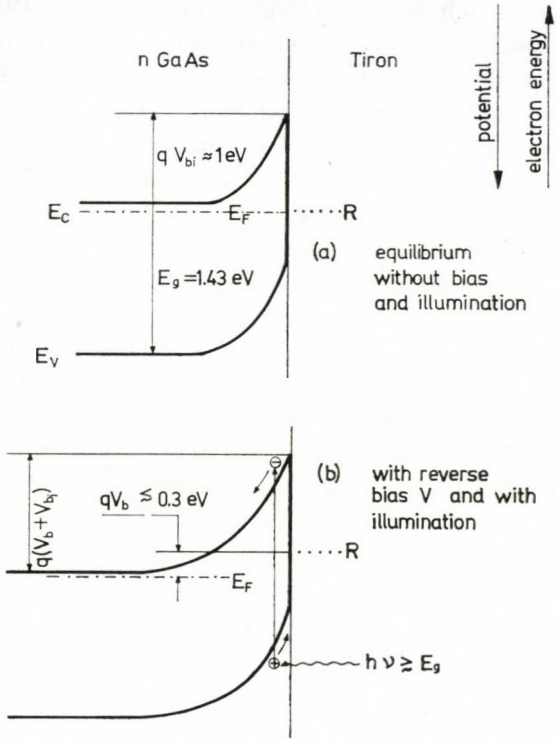

Fig. 4. The equilibrium band structure diagram of the Schottky barrier formed between the complexant Tiron electrolyte and n-type GaAs [9]. (a) The band edges, Ec and Ev, of GaAs are pinned relative to level R determined by the redox interaction between the electrolyte and the semiconductor. (b) The incident light excites electrons from the valence band into the conduction band. The holes created move towards the interface and promote the anodic dissolution of the GaAs material

relative to level R under bias, too, as it is experienced in the case of metal-GaAs junctions. We shall discuss elsewhere the nature and the role of level R. It is also illustrated in Fig. 4 that the incident light with an energy of $h\nu \gtrsim$ Eg excites an electron into the conduction band and the hole created is forced towards the interface. This process promotes the anodic dissolution of n-type GaAs.

2. A quick evaluation of the purity of epitaxial reactors

It is a general experience that there is a self-cleaning effect during the first few runs of VPE and LPE reactors after their set up or cleaning. This effect could be observed very quickly by the profile plotter and the dopant concentration range of the next run could be predicted. This prediction can be used for a proper choice of the layer thickness to the dopant concentration expected, or to avoid the wasting of a large quantity of good substrate material if the expectable dopant concentration range is good for nothing.

Fig. 5 shows the self-cleaning effect found with our VPE reactor. Dotted line shows the impurity concentrations obtained after the first set up to the VPE reactor. As can be seen in the Figure, the self cleaning taking place during the first six runs was followed by three runs with a rather uniform dopant concentration of about $8 \cdot 10^{15}$ cm^{-3}. Beginning with the tenth run the dopant concentration increased again and a cleaning process was necessary.

After the first cleaning of the reactor tube the concentration decreased very quickly from a high value of above 10^{19} cm^{-3}, as it is shown by the solid line. The useful range of runs with dopant concentrations of about 10^{15} cm^{-3} was rather large starting at the 3rd run and ending at the 9th run. Then, a fast rise of the dopant concentration took place, which necessitated a new cleaning process again. There are a number of possibilities to make use of these measuring results. Two of these were mentioned at the beginning of this paraghraph. Another possibility is to make "phantom epitaxies" with no or very small samples. It can be also seen in Fig. 5 that in the second run (denoted by ⊗) of a given day samples with lower dopant concentration can generally be obtained. All these suggest that a continuous operation of the epitaxial reactors can produce purer epitaxial layers, than epitaxial runs with long intervals.

The explanation of these effects can be based on the following. Before the first set up everything is thoroughly cleaned and baked out. There is a strong interaction between the cleaned internal surfaces and the transport medium, i.e. the vapour or liquid phase from which the epitaxy takes place. As a result of this interaction the transport medium becomes contaminated and the unintentional dopant concentration will be high. During a few runs, however, the internal surfaces become passivated against these interactions, and the quantity of contamination getting into the transport medium is smaller than that of the contamination getting out of it. If a dynamic equilibrium can be reached at a low contamination level for many runs, the ratio of the useful runs to the total number of runs between two cleanings can be high and the cleaning before the cycle of the runs is successful, as in the case of the second cycle shown in Fig 5. There must be, however, other factors causing other types of contaminations able to accumulate in the transport medium and/or on the internal surfaces. These contaminations can arise e.g. from the flushing gases, the substrate surfaces, source materials, the back-diffusion of the reaction product accumulating at the output side of the reactor. These accumulations of the contamination result in an increase of the unintentional dopant concentration at the end of the cycle of runs between two cleanings, as can be seen in Fig. 5. After the next cleaning the internal surfaces can again interact with the transport medium but the accumulated contaminations are removed and the phenomena repeat themselves in the next cycle. It is interesting to note that both cycles shown in Fig. 5 consist of about 10—11 runs. This means that the accumulation of the contamination is independent of the minimum

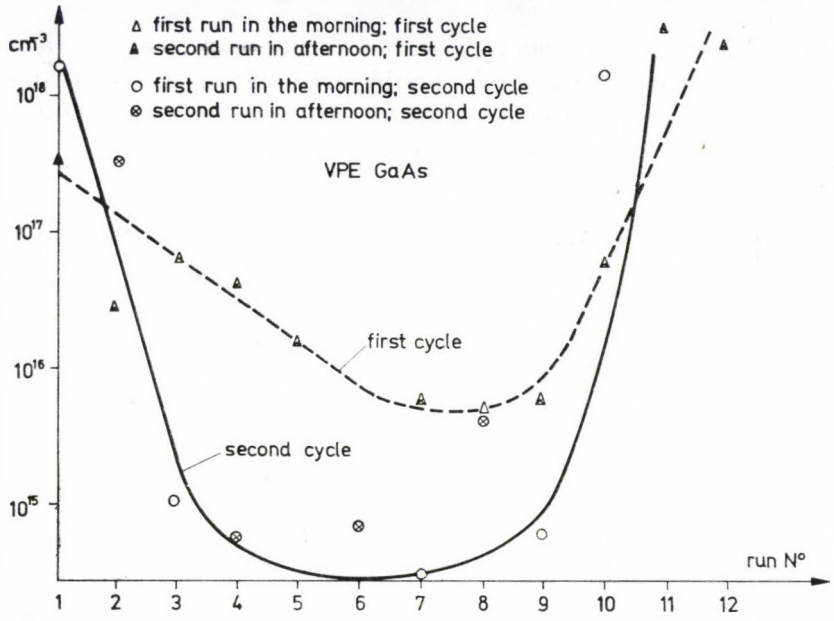

Fig. 5. The dopant concentration as a function of run No. during the first and second cycle after setting up the VPE reactor. In the first part of a cycle between two cleaning processes the concentration decreases. At the end of the cycle a fast rise of the concentration takes place, which necessitates a new cleaning process.

level of contamination and the number of runs with low dopant concentration. The steep rise of concentration at the end of the second cycle shown in Fig. 5 demonstrates that a drastic effect is responsible for the ending of the cycle.

All this was related to runs producing 7—8 μm thick epitaxial layers. If the thickness of VPE layers is different the accumulated layer thickness can be used instead of run No.

3. Measurement results on epitaxial GaAs layers

Fig. 6 shows some results obtained by measuring GaAs layers prepared by vapour phase epitaxy [2] on GaAs substrates. As can be seen in the Figure, the homogeneity of the dopant concentration and the reproducibility of layer thickness were rather good. Sample GB 56/II had the most inhomogeneous dopant concentration of the four samples. This type of profile showing a decreasing dopant concentration towards the surface might be attributed to a self-cleaning effect during the epitaxial growth. The steeply decreasing tail near the surface of this sample was also typical for such types of profiles. It may be considered to be due to a non-stoichiometric (arsenic-poor) post-growth at the end of the process. On the other hand, the indicated dopant concentration in such samples shows a dependence on the light intensity and the bias voltage applied during the measurement.

Fig. 7 shows a more complex profile obtained by measuring an n^+—n GaAs multilayer structure made by liquid phase epitaxy [1] on a GaAs substrate. The n^+ layer at the surface was grown for promoting the formation of a good ohmic contact during preparing Gunn diodes from this structure.

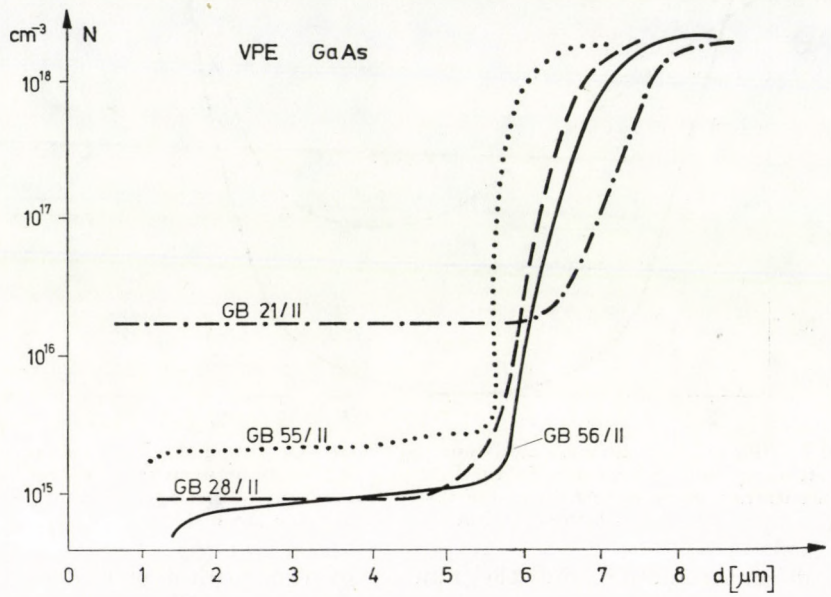

Fig. 6. Measurement results obtained on GaAs layers prepared in our laboratory by vapour phase epitaxy [2]

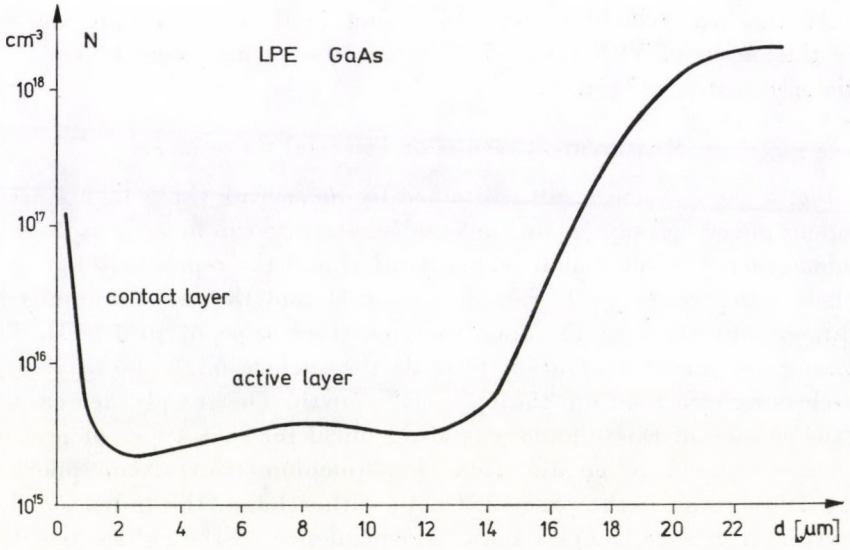

Fig. 7. Measurement result obtained on n^+-n LPE layers made in our laboratory

The active layer shows a decrease of dopant concentration towards the surface of the sample. This is advantageous in respect of domain formation and extinction as well as the temperature distribution and the efficiency of Gunn diode.

4. Measurement of p-n structures

AMBRIDGE and FAKTOR [5] did not propose to profile p-type GaAs in a similar way as that used for n-type GaAs. For profiling p-type GaAs a repeated switching from anodic potential to cathodic one was applied by them. Cathodic voltage of -1.3 V relative to the saturated calomel electrode, with a duration of smaller than 1 : 100 of the switching cycle, was applied to measure the capacitance of the well-defined Schottky barrier reverse biased by this voltage. After switching back the dissolution took place during the rest of the switching cycle at the usual anodic potential. The values of carrier concentration obtained by them agree to within the usual tolerance levels (about $\pm 20\%$), with values derived from Hall-effect measurements.

We have made profiling in both GaAs and $GaAs_{1-x}P_x$ ($x = 0.38$) $p^+ - n$ structures where the p^+ layer was formed by Zn diffusion. But we did not switch the potential to a cathodic one. The measurement was made under a continuously maintained anodic current, as in the case of n-type GaAs. One of the profiles obtained by us is shown in Figs. 8 and 9. The p-type layer was dissolved in dark. During approaching the $p-n$ junction the current decreased to zero (Fig. 9c). This made possible a very convenient measuring process since the dissolution stopped automatically when the p-type layer was

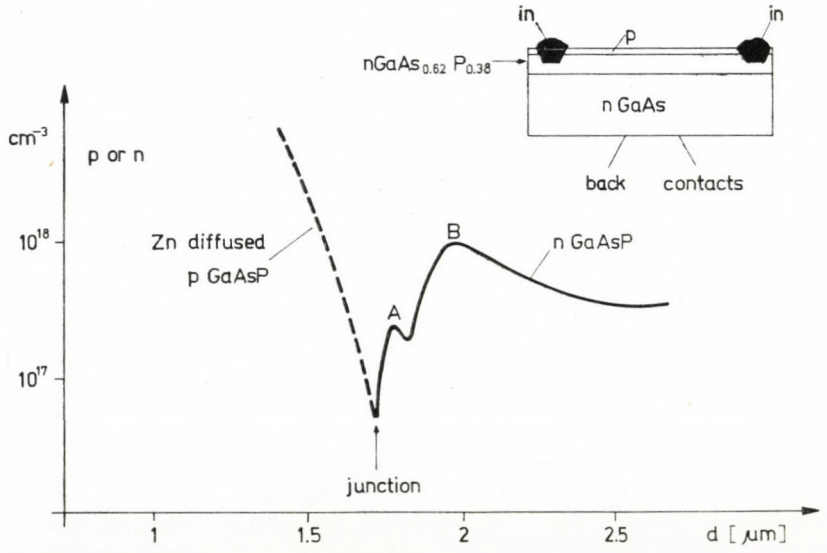

Fig. 8. Profile obtained on p-n $GaAs_{0.62}P_{0.38}$ structure shortened by alloyed In beads. The p layer was made by Zn diffusion. Insert shows schematically the structure measured

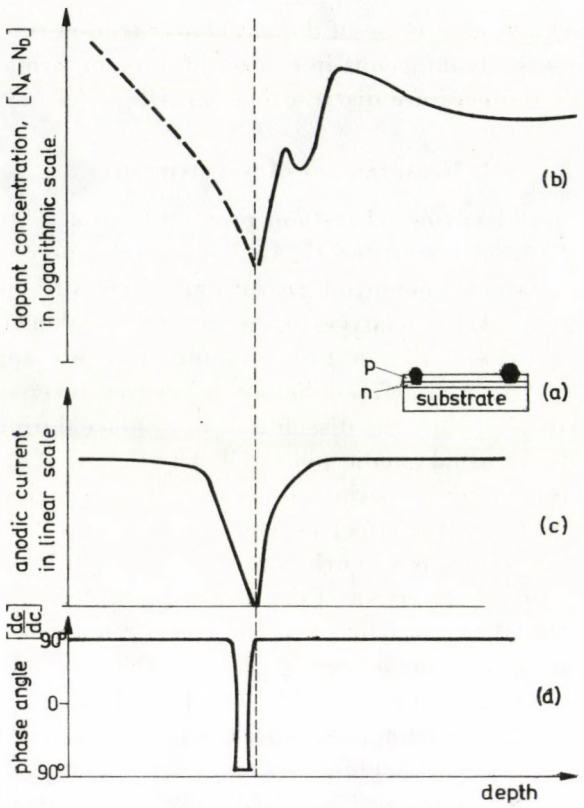

Fig. 9. (a) Scheme of the structure measured. (b) Profile shown in Fig. 8. (c) The current measured during profiling. (d) The "phase angle", dC/dV, measured during profiling

etched over. Therefore, there was no need to wait for the moment when the p—n junction was reached. On the other hand, a self-delineation in respect of the etching front took place at the p—n junction.

To improve the results we made a short-circuit at the p—n junction by alloying indium beads deeply enough into the epitaxial layer. As is known, the In gives ohmic contact to both n- and p-type GaAs, GaAsP, GaP, etc., therefore it makes a short-circuit at the p—n junction.

The "phase angle", dC/dV, changed also very abruptly near the p—n junction (Fig. 9d). This is suspected to be due to overlapping of the two depletion layers.

The circumtances for profiling p-type GaAs and other III—V compounds are worse than those for n-type materials because the Schottky barrier height in p-type semiconductor is inherently lower in equilibrium than that in n-type material. But in spite of this disadvantage, the p-type semiconductor can be profiled by C—V method even in the slightly forward biased range. During electrochemical profiling the n-type material can be also a slightly forward

biased by illumination alone or even by applying forward bias, too. With well-behaving semiconductors the value of the dopant concentration does not change when the bias is changed from 2 V reverse bias to a forward bias having a value of a few tenths of volt.

With p-type semiconductors anodic dissolution can be achieved by maintaining a small forward bias without using light. The width of the depletion layer and rest of the built-in potential ($\approx$0.3 V) in this slightly forward-biased state can be still enough to accommodate the 50 mV RMS 3 kHz test signal modulated at 30 Hz, 100 mV RMS, and to give results of reasonable accuracy for the "well-behaving" crystals.

Reverting to our measured profile shown in Fig. 8 the depth of the p—n junction determined from the profile was the same within 0.1 μm as that obtained by SEM measurements on cleaved and etched surfaces. The concentration of the substrate obtained by the profile was also the same as that obtained from Hall-effect measurement. It is not clear yet, however, whether the features denoted by A and B in Fig. 9 have any physical sense or they are artifacts.

Similar results have also been obtained on GaAs p—n junctions where both the p- and the n-type layer were made by multilayer vapour phase epitaxy.

5. Dopant profiles near the substrate surface

Photoelectrochemical profiling can help the epitaxial technology in assessing the substrate surface onto which the epitaxial layer is to be deposited. Two examples are given in this paragraph.

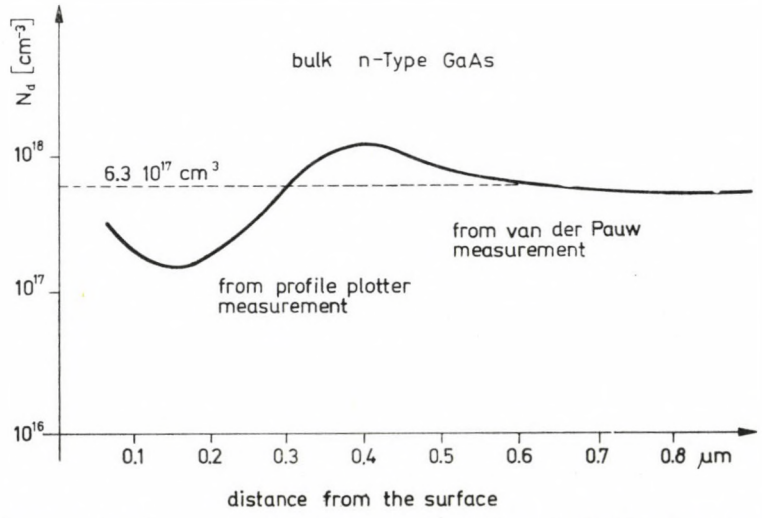

Fig. 10. Change of the dopant concentration near the surface of a bulk n-type GaAs polished mechanically and chemically before profiling. The bulk value of concentration determined by Van der Pauw measurement is shown by dashed line

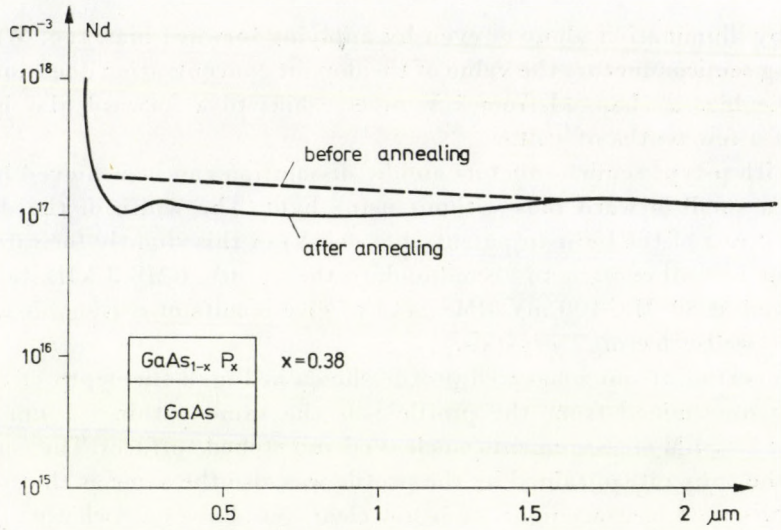

Fig. 11. Dopant concentration near the surface of an epitaxial $GaAs_{0.62}P_{0.38}$ layer before and after annealing at 700 °C for 3 hours in saturated As_4 vapour

Dopant distribution profile in a bulk GaAs near the surface polished first mechanically and then chemically is shown in Fig. 10. As can be seen in the Figure the dopant concentration obtained by Hall-effect measurement is the same as that obtained by the electrochemical profiling, but only for regions being well (at least 0.6 μm deep) beneath the surface. In this case the surface preparation of the substrate was not good.

In another case we wanted to separate the effect of annealing on $GaAs_{0.62}P_{0.38}$ epitaxial layer. The heat cycle simulated that used for Zn diffusion (700 °C for 3 hours in saturated As_4 vapour. As can be seen in Fig. 11 the dopant profile changed drastically due to annealing only in a region a few tenths of micrometer beneath the surface. In regions more than 1.5 μm deep beneath the surface the dopant concentration profiles coincide.

REFERENCES

1. E. Lendvay, Acta Phys. Hung., this issue, p. 13.
2. T. Görög and E. Lendvay, Acta Phys. Hung., **44**, 13, 1978.
3. P. Blood and J. W. Orton, Rep. Prog. Phys., **41**, 157, 1978.
4/a. L. Gútai and I. Mojzes, Appl. Phys. Lett., **26**, 325, 1975.
4/b. L. Gútai and T. Görög, Acta Phys. Hung. **44**, 69, 1978.
5. T. Ambridge and M. M. Factor, in Inst. Phys. Conf. Ser. No. 24. 1975. pp. 320—330.
6. H. Gerischer, J. Electrochem. Soc., **125**, 218C, 1978.
7. H. Gerischer, J. Vac. Sci. Technol., **15**, 1422, 1978.
8. M. S. Wrighton, J. M. Bolts, A. B. Bocarsly, M. C. Palazzotto and E. G. Walter, J. Vac. Sci. Technol. **15**, 1429, 1978.
9. M. M. Faktor and J. L. Stevenson, J. Electrochem. Soc., **125**, 621, 1978.

Acta Physica Academiae Scientiarum Hungaricae, Tomus 47 (1—3), pp. 45—50 (1979)

N DOPING IN THE LIQUID PHASE EPITAXIAL GROWTH OF GaP : N LIGHT EMITTING DIODES

By

J. PFEIFER, L. CSONTOS and M. GÁL

RESEARCH INSTITUTE FOR TECHNICAL PHYSICS OF THE HUNGARIAN ACADEMY OF SCIENCES
BUDAPEST, HUNGARY*

GaP:N green light emitting p—n junction diodes with quantum efficiencies at 20 mA d.c. of 0.1% have been reproducible grown in a modified LPE slider system. A correlation between growth defects caused by solid GaN traces present in the melt and lg $I-V$ and η_q-I characteristics of the diodes has been found.

Introduction

Recombination at the isoelectronic trap nitrogen occupying phosphorus sites significantly increases the external quantum efficiency of green emitting electroluminescent junctions formed in GaP [1, 2].

The most efficient green light emitting diodes utilize liquid phase epitaxial (LPE) layers grown from Ga melts doped with N by adding NH_3 to the gas ambient [3—16].

Owing to the chemical reaction

$$NH_3^g + Ga^l \rightleftharpoons GaN^l + \frac{3}{2} H_2^g$$

GaN is forming in the growth solution. The solid solubility limit of N in GaP is higher than the value corresponding to the partial pressure of NH_3 over liquid Ga in equilibrium with solid GaN [17].

Nitrogen concentration in the grown layers is controlled by the concentration of GaN in the Ga solution. It increases linearly with P_{NH_3} until P_{NH_3} equals the above mentioned limit at which time the N concentration reaches a constant value. The morphology of the LPE layers becomes disturbed at this and higher values of P_{NH_3} [18]. In this aspect it makes no sense to increase the percentage of the NH_3 in the inlet gas over the equilibrium value. There are, however, arguments in favour of an inlet of NH_3 pressures higher than the equilibrium into the growth system. NH_3 is not stable at the growth temperatures. Quartz and graphite have catalytic effect on NH_3 decomposition [19]. The actual value of P_{NH_3} over the growth solution can be substantially lower

* Address: 1325 Budapest, Újpest 1, P.O. Box 76 Hungary.

than the value calculated from the relative inlet NH_3 and H_2 flow rates [18]. Therefore an experimental optimalization is needed in every growth system.

In this paper we report on the effect of NH_3 pressure varied in the range of the GaN solubility limit on the growth of GaP LPE layers and on some of the diode parameters e.g. quantum efficiency and lg $I-V$ characteristics.

Experimental procedure

The LPE method used to grow junctions shown in Fig. 1 utilizes the slider system in which a (111) B n-type S-doped LEC substrate is moved under a Ga-rich solution of GaP. The dopants were S for the n-type layers originally present in the melt as a background impurity and Zn for the p-type layers

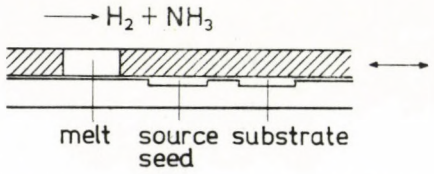

Fig. 1. Schematic representation of the slider boat used for the growth of GaP light emitting junctions

introduced from the gas phase during the cooling cycle. Details of the Zn doping have been published elsewhere [20].

The growth runs were started typically at 990 °C after the desired period of saturation with NH_3 at the same temperature. Cooling rates of 1 °C min^{-1}—3 °C min^{-1} were used and the layers were grown over temperature intervals of 140 °C. The growth technique used here is similar to that described by [10—15]. However, for the diodes described in this paper, two variants of the Ga melts were used. Several growth runs were made using near equilibrium solutions of GaP. In another series of growth runs two seeds were used. The first seed is used as the source to equilibrate the bottom of the melt saturated with nitrogen but containing no phosphorus and the second seed as the substrate for the desired growth. The length of the time when the slider is positioned so that the source seed in under the melt is not long enough to ensure the total saturation of the melt. It remains quasi-saturated.

Figs. 2 and 3 show the schematic representation of the boat and the concentration profile of phosphorus for growth runs with quasisaturated melt. After the completion of the growth cycle the slices were removed from the furnace, cleaned, thinned and provided with evaporated gold alloy contacts (n-type: Au—Ge—Ni, p-type: Au—Be) which were alloyed into the crystal

at 600 °C and 500 °C, respectively. Chips were then obtained from the contacted slice by scribing on the p surface and breaking. The chips were then bonded to diode headers and the p-side contact was made by thermocompression of gold wire.

After a light etching the diodes were covered by an epoxy resin. However, the fabrication of the diodes was identical for every slice. The cleaving process does not ensure the standardized sample geometry necessary for a meaningful comparison of the external quantum efficiency of individual diodes. Therefore groups of nonselected diodes were measured and compared.

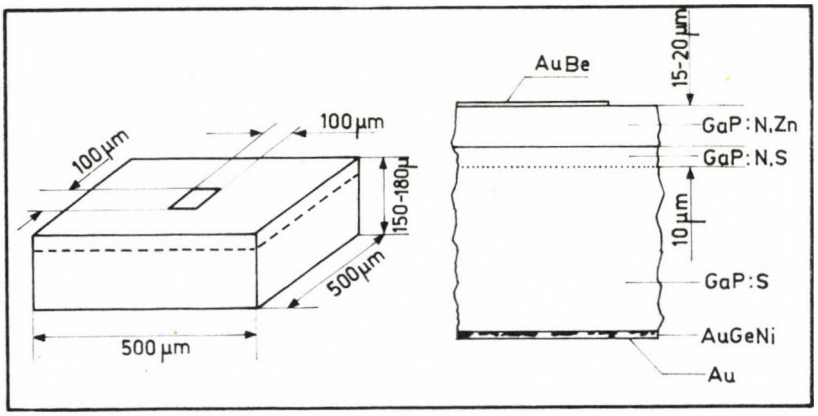

Fig. 2. Junction structure with metal contacts of a green LED. Double epitaxial layers of n- and p-type GaP are grown on n-type GaP substrate.

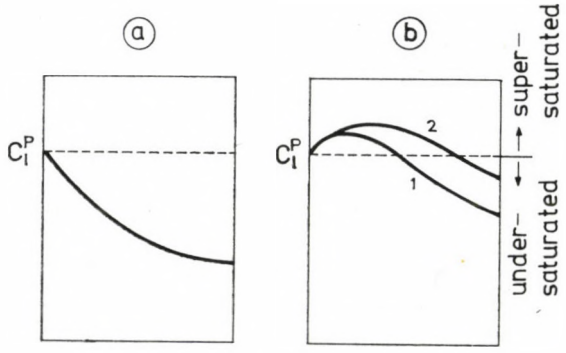

Fig. 3. The distribution of phosphorus in the melt being in contact with the source seed (a). The distribution of phosphorus in the melt being in contact with the substrate during the cooling cycle (b). Profile 2 is more developed in time than profile 1. C_l^P = liquidus concentration of phosphorus

Results and discussion

Fig. 4 shows the quantum efficiencies of the devices which were fabricated from different runs as a function of diode current. In Fig. 4a the results of non-nitrogen-doped devices are presented for comparison. In Fig. 4b the results of very highly doped devices are presented. The nitrogen concentration in these samples was established by maintaining a partial pressure of NH_3 over the melt higher than sufficient to form GaN. A one-step growth process onto the substrate seed was used in this run. Moving the melt over the substrate according to the one-step process the separated solid particles of GaN originally floating on the top of the solution would get into contact with the surface of the substrate and give rise to growth defects shown in Fig. 5. This type of growth defects behave like short-circuits in the p—n junction. The leakage current of the short circuits is high, as shown in Fig. 6a, and a significant portion of the diode current gives no contribution to the emission (Fig. 4b, initial part of the $\eta_q - I$ curves).

However, some of the devices of this growthr un are efficient. The growth from nitrogen-saturated and phosphorus-quasisaturated melt, i.e. the use of a two-step process eliminates the growth defects and the high leakage current

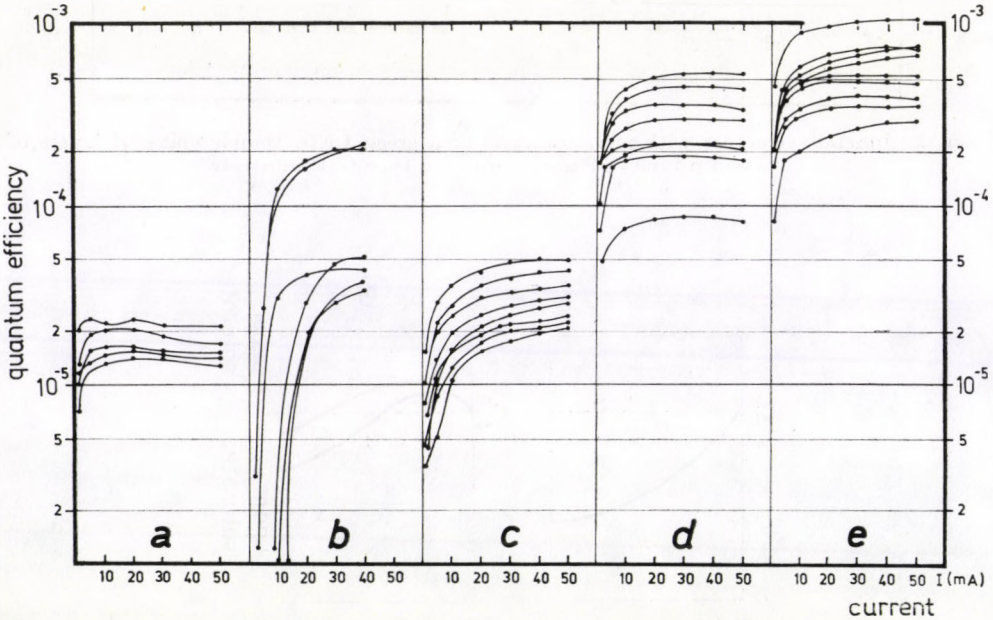

Fig. 4. The quantum efficiency for groups of diodes from different growth runs as a function of current. a) K428: without N addition; b) K423: uncontrolled NH_3 flow, disturbed layer; c) NK609: N concentration: 1.10^{17} cm^{-3}; d) NK1102: N concentration: 5.10^{18} cm^{-3}, saturation time: 15 min; e) NK1108: N concentration: 5.10^{18} cm^{-3}, saturation time: 60 min

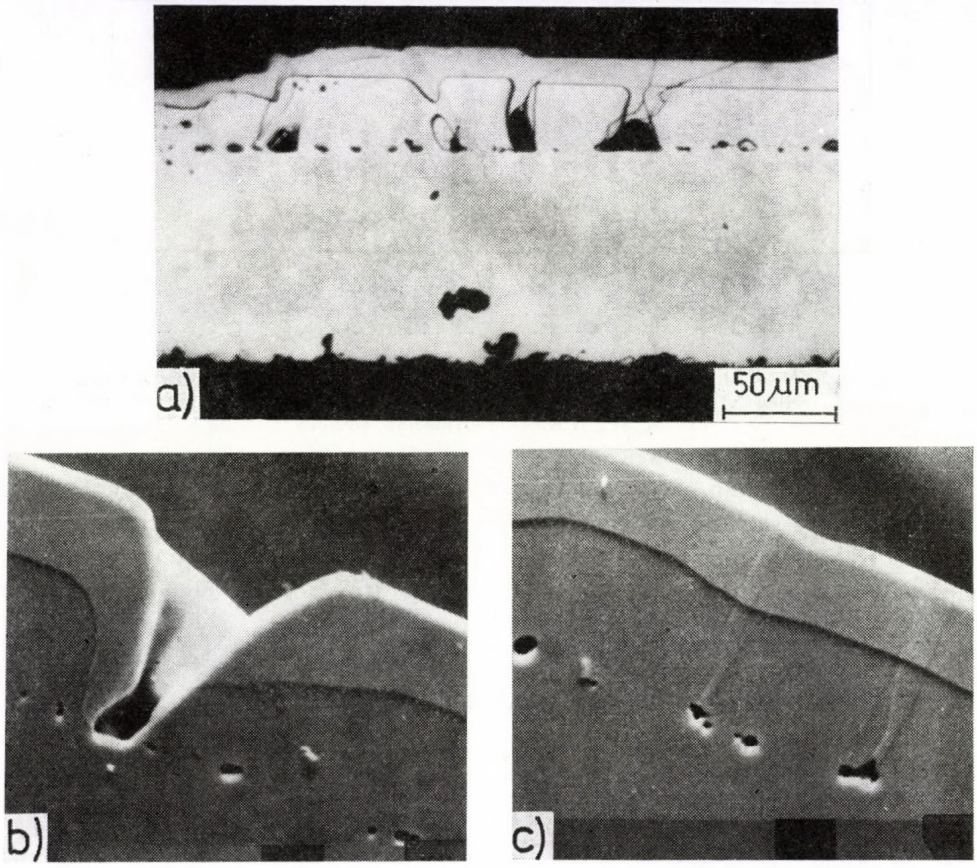

Fig. 5. Growth defects caused by GaN in GaP:N epitaxial junctions. a) Optical micrograph; b), c) SEM micrographs. The cleaved junctions are delineated in a $KOH-K_3(Fe(CN)_6)$ etchant

of the junctions (Fig. 6b and c) and increases the average quantum efficiency of the devices.

The measured dependence of the quantum efficiency upon diode current and nitrogen doping level for devices fabricated from runs by two-step growth process is shown in Figs. 4c, 4d and 4e. The increase in the efficiency was achieved by variation of the percentage of NH_3 in the gas ambient and the saturation time used in the layer growth. Nitrogen concentration was determined by the measurement of the optical absorption [21] in the layers. Little is known on the distribution of incorporated nitrogen in the layers and the value of the nitrogen concentration at the p—n junction could only be estimated from the electroluminescent spectra.

The maximum value of external quantum efficeincy (0.1%) was obtained with diodes from runs characterized by a saturation time of 60 minutes in

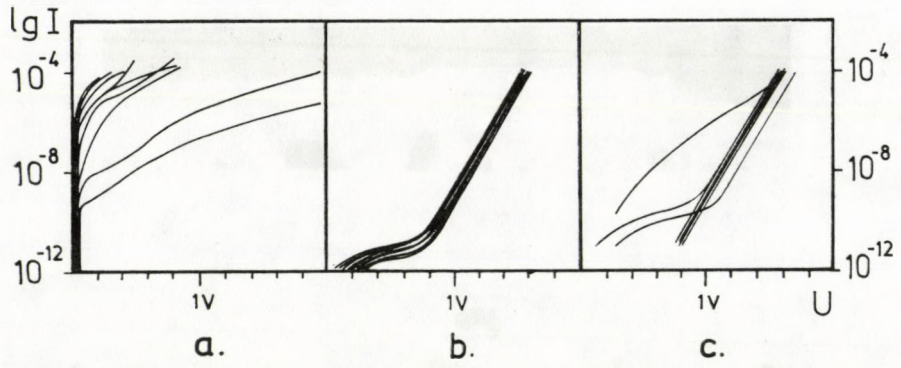

Fig. 6. lg $I-V$ characteristics for groups of diodes from different growth runs. a) K423 uncontrolled NH_3 flow, disturbed layer; b) NK1108 N concentration: $5 \cdot 10^{18}$ cm^{-3}; c) NK1102 N concentration: $5 \cdot 10^{18}$ cm^{-3}

a 0.1% NH_3 containing ambient (Fig. 4e). The average nitrogen concentration for the devices shown in Fig. 4e was $5 \cdot 10^{18}$ cm^{-3}. Lower percentage of NH_3 (Fig. 4c) and shorter saturation time (Fig. 4d) yielded lower quantum efficiencies. However, the average nitrogen concentration for the devices presented in Fig. 4d was $5 \cdot 10^{18}$ cm^{-3} likewise.

Acknowledgement

The authors are indebted to Drs. Yu. P. Yakovlev and V. V. Evstropov for valuable discussions and to Dr. E. Lendvay for encouragement during the course of this work.

We wish to thank Mr. I. Bárdi for technical assistance. Thanks are also due to Mrs. K. Horacsek for SEM pictures.

REFERENCES

1. D. G. Thomas, J. J. Hopfield and C. J. Frosch, Phys. Rev. Letters, **15**, 857, 1965.
2. R. A. Logan, H. G. White and W. Wiegmann, Appl. Phys. Lett., **13**, 139, 1968.
3. R. A. Logan, H. G. White and W. Wiegmann, Sol-Sate El., **14**, 55, 1971.
4. I. Ladany and H. Kressel, RCA Rev., **33**, 517, 1972.
5. P. D. Sudlow, A. Mottram and A. R. Peaker, J. Mat. Sci., **7**, 168, 1972.
6. P. C. Mürau and R. N. Bhargava, J. Electrochemical Soc., **123**, 728, 1976.
7. A. H. Herzog and H. F. McLain, J. Electronic Mat., **3**, 265, 1974.
8. D. R. Wight, J. C. H. Birbeck, J. W. A. Trussler and M. L. Young, J. Phys. D. Appl. Phys., **6**, 1622, 1973.
9. K. K. Shih, J. M. Woodall, S. E. Blum and L. M. Foster, J. Appl. Phys., **39**, 2962, 1968.
10. R. S. M. Ignatkina et al., FTP, **5**, 626, 1971.
11. T. Beppu, A. Kasami and M. Toyama, Jap. J. Appl. Phys., **11**, 1331, 1972.
12. A. A. Bergh, R. H. Saul and C. R. Paola, J. Electrochem. Soc., **120**, 1558, 1973.
13. R. H. Saul and D. D. Roccasecca, J. Electrochem. Soc., **120**, 1128, 1973.
14. R. H. Saul and O. G. Lorimor, J. Cryst. Growth, **27**, 183, 1974.
15. Takao Yamaguchi and Tatsihiko Niina, Jap. J. Appl. Phys., **15**, 1219, 1976.
16. C. Weyrich, G. H. Winstel, K. Mettler and M. Plihal, Inst. Phys. Conf. Ser., **24**, 145, 1975.
17. O. G. Lorimor and M. E. Weiner, J. Electrochem. Soc., **119**, 1576, 1972.
18. D. D. Roccasecca, R. H. Saul and O. G. Lorimor, J. Electrochem. Soc., **121**, 962, 1974.
19. C. N. Hinshelwood, The Kinetics of Chemical Change, Clarendon Press, Oxford, 1940.
20. J. Pfeifer, L. Csontos and B. Szentpáli, Acta Phys. Hung., **44**, 29, 1978.
21. M. Gál, K. Németh and G. Eppeldauer, J. Phys. E. Scientific Instruments, **9**, 484, 1976.

Acta Physica Academiae Scientiarum Hungaricae, Tomus 47 (1—3), pp. 51—67 (1979)

THIN PHASE EPITAXY OF III—V COMPOUND SEMICONDUCTORS

By

T. SEBESTYÉN

RESEARCH INSTITUTE FOR TECHNICAL PHYSICS OF THE HUNGARIAN ACADEMY OF SCIENCES
BUDAPEST, HUNGARY*

The main point of similarity between Solid Phase Epitaxy (SPE) and Thin Phase Epitaxy (TPE) developed by the author et al for making good ohmic contacts to low-doped n-type GaAs is that both have a thin (≈ 1 μm) phase from which the epitaxy of a semiconductor material takes place. However, in contrast to solid phase epitaxy an additional vapour, "beam" or solid phase is involved, too. The role of the additional phase is to prevent the loss or to supply an excess of the volatile component(s), such as arsenic and phosphorous, during the epitaxial growth. The non-volatile component, such as Ga, Al or In, is deposited into the thin phase prior to TPE.

The basic concepts and realizations of SPE and TPE are summarized. After reviewing the experimental results of TPE on making ohmic contacts to GaAs and InP the application of TPE in the GaAs MOSFET technology is described. Then, related experiments and processes as well as alloying with short-duration, spike-type heat cycles by using furnace heating or pulsed laser or electron beams are reviewed.

1. Introduction

Compound semiconductor devices, such as light emitting diodes, field effect transistors and Gunn diodes, provide efficient and long-life operation only if they have low-resistance ohmic contacts with high metallurgical stability. The most reliable devices can be obtained by ohmic contacts having a highly doped and sufficiently thick semiconductor contact layer between the contact metal and the active semiconductor region. For many devices the thickness of the semiconductor contact layer has to be in the range of 0.01—1 μm. The dopant concentration in the contact layer must be above 10^{19} cm^{-3} for most device applications. Such contact layers are not produced by vapour phase epitaxy (VPE) or liquid phase epitaxy (LPE) which are generally used for the production of the active epitaxial layers. One of the usual ways is to prepare LPE or VPE contact layers so thin and highly doped as possible (e.g. with a thickness of a few tenths of microns and with a concentration of about 10^{18} cm^{-3};) and then to raise the concentration near its surface by alloying a suitable contact metal on it. This combination of epitaxy and alloying generally gives very good results, but as a process it is sometimes too sophisticated for practical applications because of the multilayer epitaxy and the separate contacting process involved. This is why there is an interest in producing both

* Address: 1325 Budapest, Újpest 1, P.O. Box 76 Hungary.

the contact metal and the highly doped contact layer in one processing step. This can be done by thin phase epitaxy described in the following.

The other usual way of making ohmic contact is the well known contact alloying. This is also good for compound semiconductor material having a not too low dopant concentration. The alloying is, however, a very crucial processing step since the opimum alloying temperature range is narrow and depending on many processing parameters. Long alloying times or temperatures differing from the optimum one result in high specific contact resistance due to incomplete alloying or because of the volatile component evaporating out of the metal system. The evaporation loss of the volatile component of the compound semiconductor prevents the regrowth of a sufficiently thick semiconductor contact layer.

In the thin phase epitaxy the loss of the volatile component is prevented by applying an encapsulation or/and an overpressure of the volatile component. Instead of having evaporation loss even a continuous supply of the volatile component is possible in this way. If, before alloying, the nonvolatile component is deposited into the metal system, a synthesis of the semiconductor mate-

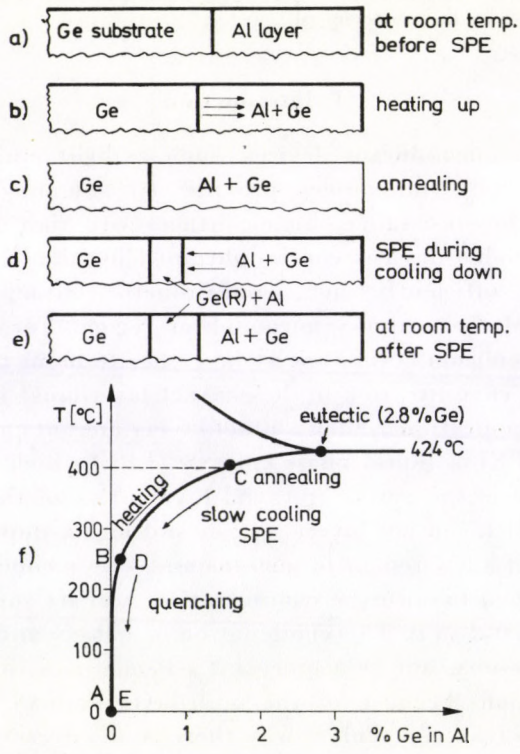

Fig. 1. Illustration of the several phases a, b, c, d, e of solid phase epitaxy (SPE) of a simple eutectic system (f). In this case SPE is a separation of a crystalline Ge layer, Ge(R), from the Al + Ge solid solution. SPE occurs during cooling down (d).

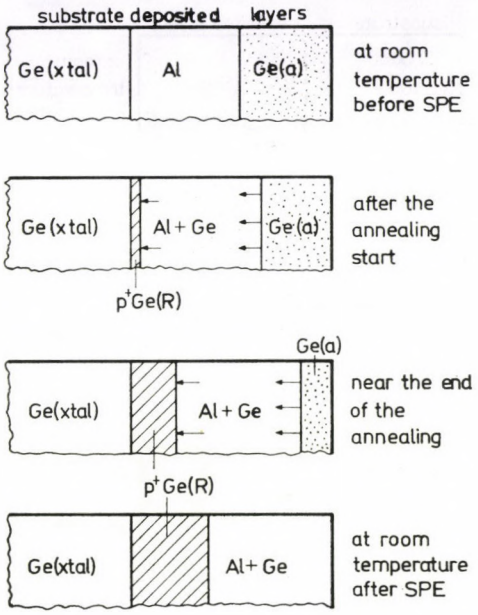

Fig. 2. Isothermal SPE for making thick ($\approx$1 μm) regrown layer, p$^+$Ge(R), due to the transport of amorphous Ge layer, Ge(a), through the Al layer. The transport process consists of dissolution of Ge(a) by Al, the diffusion and the precipitation of Ge atoms.

rial is possible from the separately supplied elements. This synthesis is taking place as an epitaxial process promoted by the metal-semiconductor interface. The thin phase epitaxy (TPE) is in some respects similar to solid phase epitaxy (SPE) and also to the other epitaxies. TPE is sometimes confused with SPE because of the similarities.

Therefore, before reviewing the developments in TPE the main concepts and realizations of SPE will be summarized to make clear the aspects for the comparison of TPE.

2. Solid phase epitaxy (SPE)

The basic goal of SPE is to achieve epitaxial growth by means of solid-state reactions at much lower temperatures than those needed for the formation of eutectic or compound compositions [1, 2].

SPE can be realized

— by using transport medium, such as thin elemental or compound metal layers, or

— by applying no metal transport medium.

In the first case, e.g. a thin Al layer (100—1500 nm) on a Ge single crystal SPE is basically a separation process of crystals out of solid solution (Fig. 1).

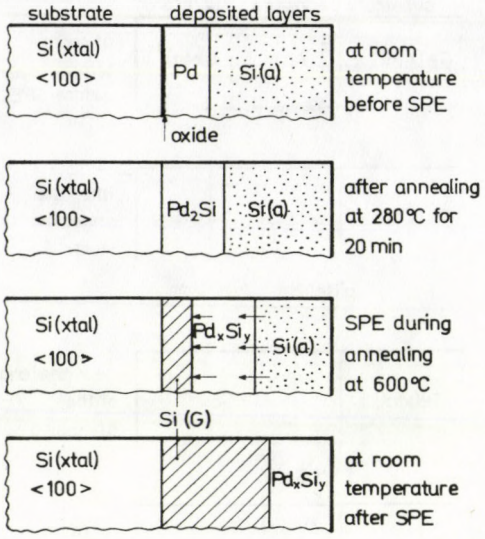

Fig. 3. To remove the thin oxide layer Pd is used for making SPE on Si substrates. $PdSi_2$ is easily formed through silicon oxide, too. Palladium silicide Pd_xSi_y can serve as a transport medium during isothermal SPE. During SPE amorphous silicon, Si(a), dissolved and transported through the Pd_xSi_x layer and as a result a silicon layer, Si(G), is grown on the crystalline substrate, Si(xtal).

If the solid solution is formed by dissolution of the semiconductor into the metal layer during the heating up or the annealing part of the heat cycle, upon cooling the metal layer becomes supersaturated and recrystallization at the metal-semiconductor interface takes place. In this case SPE is very similar to the well-known alloying process. The main differences are that the temperature is low and no melting takes place, i.e. instead of alloying this is a sintering process. However, to get an epitaxial growth a slow cooling rate and the proper choice of the metal layer are needed. Generally, this simplest realization of SPE results in a very thin regrown layer because of the low solubility limit.

To get thicker SPE layers an excess of the semiconductor material must be supplied during the epitaxial growth. An ingenious solution of this problem was to deposit the semiconductor material in amorphous state onto the top of the metal layer (Fig. 2). In this case the metal layer acts both as a solvent and as a transport medium between the amorphous and the crystalline phase of the semiconductor material. Since the amorphous phase of the semiconductor has a higher free energy than its crystalline phase, a transport process may take place from the amorphous to the crystalline phase at a *constant* (elevated) temperature, too [3].

The surfaces of silicon substrates generally contain a thin, native oxide layer even after careful cleanings. This oxide layer prevents uniform interac-

tions (i.e. a good wetting) between the substrate and the metal layer. This results in an island structure of the SPE layer. An excellent solution of this problem is based on the choice of contact metal able to interact with silicon substrate even through the intentionally grown oxide layer made by boiling the Si Substrate in HNO_3 or H_2O_2. The best choice for this aim is a thin Pd layer (Fig. 3). The interaction between Pd and Si results in a Pd_2Si silicide layer which allows the transport of Si atoms through itself [4]. The Si(a)—Pd—Si(xtal) structure becomes a Si(a)—Pd_2Si—Si(xtal) structure due to an annealing process at 280 °C for 20 minutes and the increase of temperature of 600 °C facilitates the Si transport through the silicide layer and the SPE growth on the silicon substrate, as illustrated in Fig. 3.

If oxide-free interfaces are produced by using an ultrahigh vacuum system or by heating the substrates to high temperatures homo- or hetero-epitaxial growth can be made by well-known methods, such as vacuum evaporation, pyrolysis of silane, ion sputtering. Ion implantation offers a new way for getting interfaces free of any oxide or dirty layers. Bipolar structures, buried collector layers and greater throughput in production runs require high-dose (10^{15} to 10^{16} cm^{-2}) ion implantation which produces an amorphous

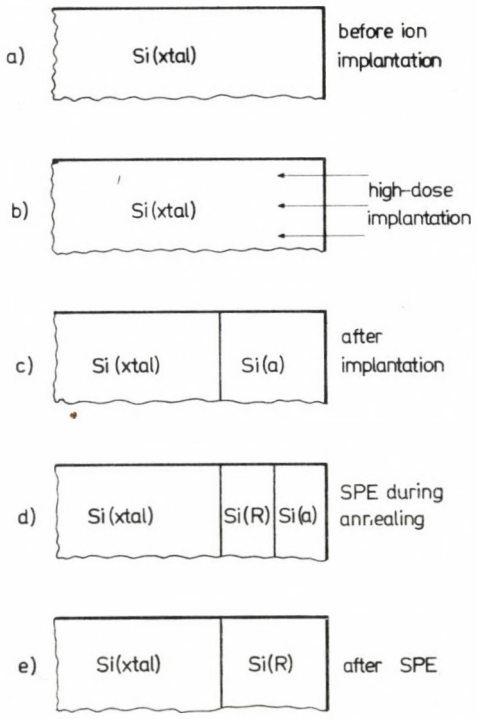

Fig. 4. Amorphous Si layer, Si(a), produced by high-dose implantation has a very pure interface with the substrate. The regrown Si layer, Si(R), is readily formed without any transport medium. SPE is in this case an interface crystallization process.

layer on the surface of the semiconductor materials. In this case, the interface between the amorphous and the crystalline phase is inherently clean, free of any oxide or dirty layers since it is never exposed to ambient. During the annealing following the ion implantation an SPE process takes place (Fig. 4).

3. The basic concepts of thin phase epitaxy (TPE)

To overcome the technological difficulties in getting good ohmic contacts to low-doped n-type GaAs, the author et al developed a process in 1974 which is often considered to be a special case of SPE [5, 6]. We have called this process Thin Phase Epitaxy (TPE) because it was proposed for both thin solid phase and thin liquid phase. In comparison with liquid phase epitaxy this name emphasizes that the phase from which the epitaxy takes place is thin. Some-

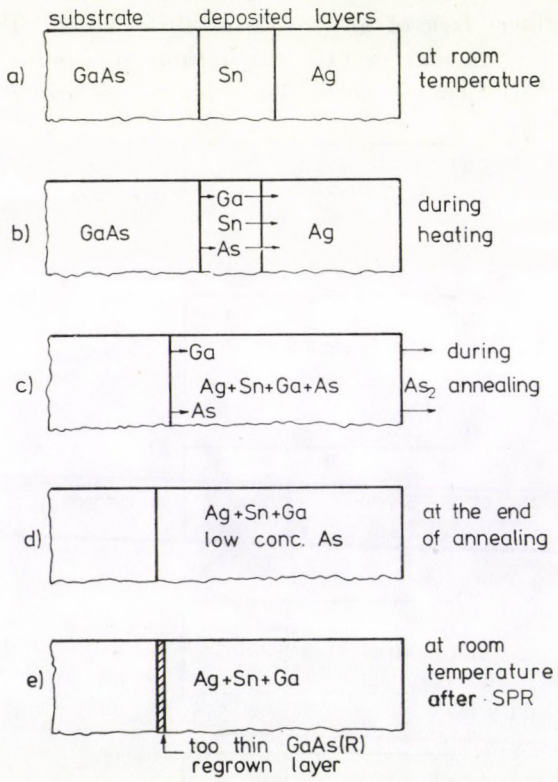

Fig. 5. Illustration of the disadvantage of solid phase epitaxy in the case of GaAs and other III—V or II—VI compound semiconductors having a volatile component. At elevated temperatures the volatile component evaporates out of the thin metal layer having a high surface to volume ratio. During cooling down only a very thin regrown layer, GaAs(R), can be obtained because in the metal layer no arsenic oversaturation can be achieved at elevated temperatures suitable for effective regrowth.

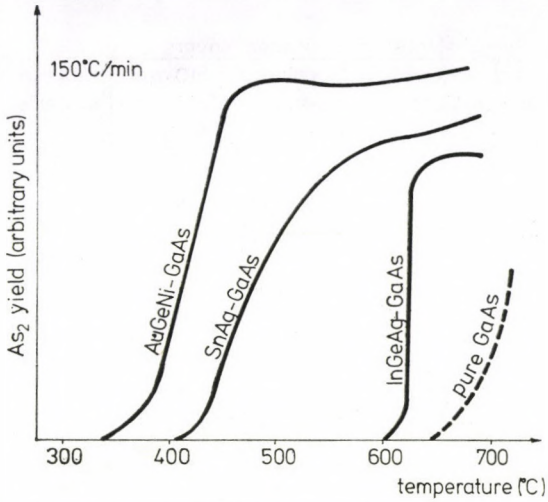

Fig. 6. One of the first measurement results illustrating the excess arsenic loss over the usua contact metal systems of GaAs [8]. For comparison the arsenic evaporation rate over the pure GaAs is also shown.

times this process has also been regarded as thin film epitaxy (HARTNAGEL and co-workers [7]). The term thin film epitaxy is, however, a denomination for any kind of epitaxial growth involved in thin film technology, e.g. an epitaxial growth of metal films on semiconductors, insulators, etc. during or after deposition.

Fig. 5 illustrates the consequence of the excess arsenic loss during the annealing process. The arsenic loss has been measured by us in situ using a quadrupole mass spectrometer. Fig. 6 shows some of the first results obtained [6]. A regrown contact layer thinner than the screening length results in a non-ohmic behaviour [9]. To get a thicker regrown layer the excess arsenic loss must be avoided by using very short alloying time, as will be discussed later, or by preventing the evaporation of the volatile components.

Fig. 7 schematically shows the versions of TPE. The encapsulation shown in Fig. 7a can be based on silicon oxide, aluminium oxide or silicon nitride etc. layers deposited on the top of the metal systems. This can be regarded as IMS encapsulation. Such insulation layers are widely used for preventing the arsenic loss during an epitaxial regrowth of amorphous compound semiconductor layers made by high dose implantation or during the post implantation annealing to make the implanted species electrically active. This version of TPE can easily be realized in all laboratories where post-implantation annealing of this type is facilitated. Them ain disadvantage of this method is that it is a rather sophisticated one and needs generally an excess high-temperature process to deposit the insulating layer. The anodic oxidation of the metal layer to be discussed later is, however, a low temperature process for insulator layer production.

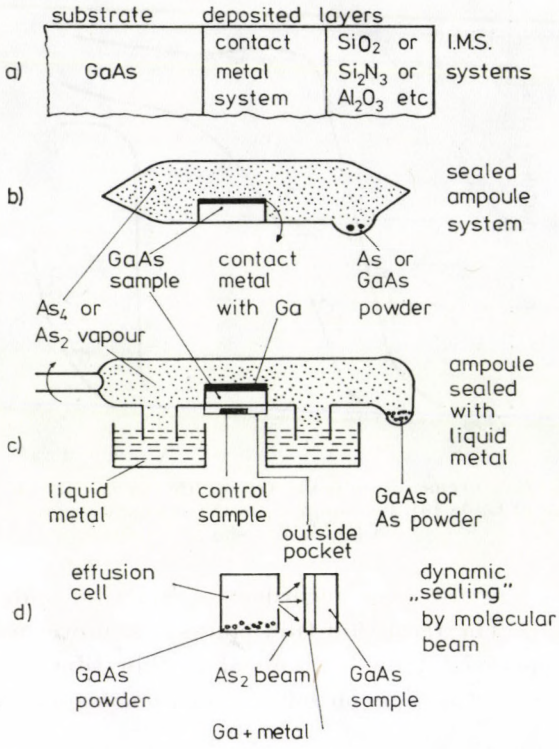

Fig. 7. The versions of TPE avoiding the excess arsenic loss at elevated temperatures by applying: (a) solid phase, (b, c) vapour phase and (d) "beam phase" over the contact metal system. The epitaxial synthesis on the GaAs substrate takes place from Ga deposited into the contact metal and from As supplied by the vapour (b, c) phase or "beam" (d) phase at elevated temperatures.

Sealed quartz ampoules are widely used for the diffusion of compound semiconductors. The realization of TPE with a sealed quartz ampoule (Fig. 7b) is a straightforward possibility in any laboratory where diffusion is made in this way. The main differences are that instead of a naked crystal a metal-covered sample is used and lower temperature is needed. We plan to use this version of TPE in the near future since our Laboratory is equipped with all facilities.

The realization of TPE by the method illustrated in Fig. 7 and Fig. 8 was made by the author et al in 1974 [5, 6]. In this method the sealing is made by dipping the openings of the ampoule into liquid In or Ga. Dipping into or out of liquid metal is made by rotating the push rod via a Wilson seal. Another but very similar realization of TPE was later described by HARTNAGEL [10]. Fig. 7d shows a dynamic sealing system which can be realized in laboratories where molecular beam technology is used. In this version of TPE, instead of

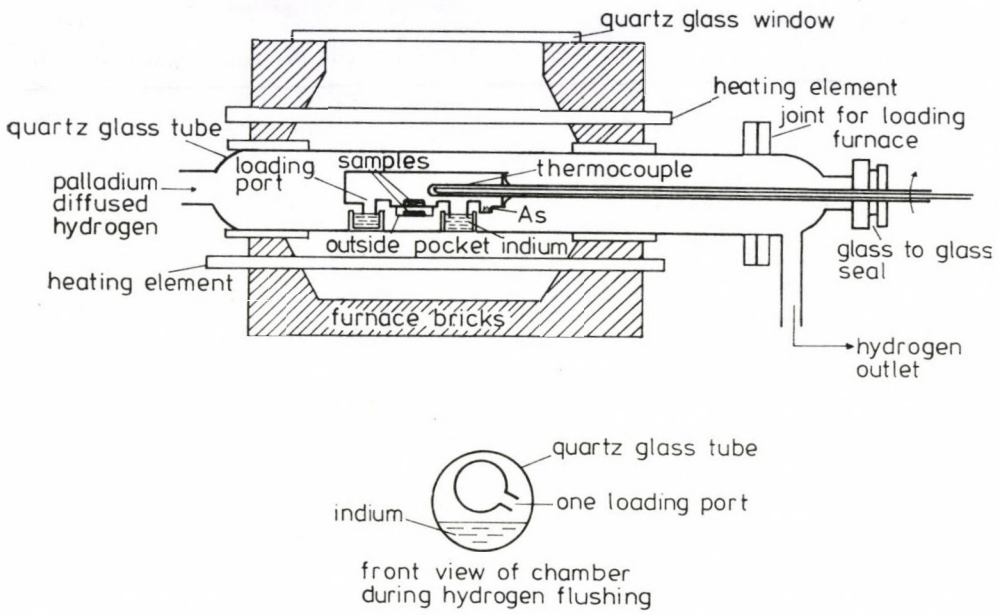

Fig. 8. The system used in the first realization of TPE [5, 6]. The sample holder is shown in detail in Fig. 7c.

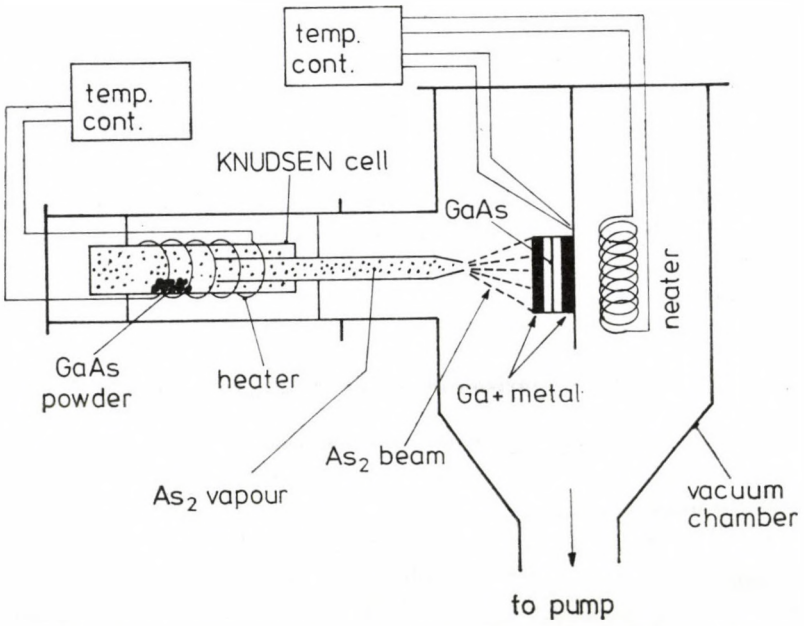

Fig. 9. The newest realization of TPE corresponding to Fig. 7d [12]

Table I

A summary of the main characteristics and

Epitaxial process	Phases involved	Type phase thickness (cm)	Type semicond.	Type temperatures (°C)
LPE	Liquid	0.1—1	III—V	700—800
VPE	Vapour	1—10	Si III—V	700—800
MBE	"Beam"	1—10	III—V	350—450
SPE	Thin solid	10^{-5}—10^{-4}	Si Ge	350—600
TPE	Thin solid or liquid	10^{-5}—10^{-4}	III—V	350—600
	Additional solid vapour or "beam"	10^{-5}—10^{-4} or 1—10		

arsenic vapour, an arsenic molecular beam is used to prevent the arsenic loss from the thin metallic phase. This method of TPE has been developed at our Institute in 1978 [11, 12] and is illustrated in more detail in Fig. 9. The difference between molecular beam epitaxy and this version of TPE is that MBE is a surface process since no transport medium is used. TPE is, however, an interface process since a liquid or solid transport medium is used.

Fig. 10 schematically shows the versions of TPE and the abbreviations proposed for them.

4. A comparison of the epitaxial processes

Table I gives a summary of the main characteristics and the important parameters of the epitaxial process. LPE and VPE are well developed and widely used epitaxial processes in the fabrication of semiconductor devices. MBE is now under development for solving special problems encountered in semiconductor technology. MBE have been also successfully used for nonalloyed ohmic contacts by making very highly doped ($>10^{19}$ cm^{-3}) semiconductor contact layers and depositing in situ the contact metal layer, too [13, 14].

important parameters of epitaxial processes

Type thickness of epilayer (μm)	Contamination	No. of dimensions controllable	Formation of ohmic contacts on epilayer	Typical applications
10—100	low	1	difficult or easy	layers or multilayers for GaP, GaAsP, GaP, GaAlAs devices
2—20	low	1	difficult or easy	layers or multilayers for Si, GaAs, InP devices
0.01—1	not bad	1	very difficult or very easy	very thin multilayers ohmic contacts
0.01—1	high	3	during SPE	ohmic contacts to Si; Schottky diodes shallow p-n junctions
		photolithography		
0.01—0.5	high	3	during TPE	ohmic contacts to III—V and II—VI semiconductors; shallow p-n junctions

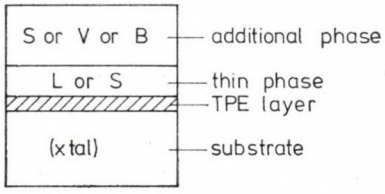

notation	thin phase	additional phase
$T_L PE(S)$	liquid	solid
$T_S PE(S)$	solid	(Fig. 7a)
$T_L PE(V)$	liquid	vapour(Fig. 8.)
$T_S PE(V)$	solid	(Fig. 7.b or c)
$T_L PE(B)$	liquid	"beam" (Fig. 9.)
$T_S PE(B)$	solid	(Fig. 7. d)

Fig. 10. Summary of the realization possibilities and notations of TPE

The other promising application of MBE is to prepare a very thin multilayer structure to get a supperlattice. SPE is recently under investigation to understand the metallurgical processes involved and to look for its capabilities [2]. The TPE process has not been thoroughly investigated yet. Some demonstrative experiments and research work will be reviewed in the following.

Table I shows that the most distinctive feature of TPE is the complexity and variety of phases that can be involved. The thickness of the phase from which the epitaxy takes place is in the same range as that with SPE, and is many orders of magnitude smaller than that used in the other epitaxial process. TPE makes no sense for Si and Ge and other semiconductors having no volatile component e.g. SiC, since TPE is needed, and can be applied, only for semiconductors such as III—V or II—VI compound semiconductors, having volatile component. It is attributted to TPE that either one of component is supplied from an additional vapour or beam phase during the epitaxial deposition or the volatile component loss is prevented by an additional solid phase. The temperatures and the thickness of the epitaxial layer are about the same as with SPE and MBE and are well lower than those with LPE and VPE. As regards the contamination of epitaxial layers TPE and SPE are inferior to MBE, LPE and VPE. This feature limits the application of TPE ans SPE to the preparation of highly doped thin contact layers or asymmetrically doped shallow p—n junctions. In respect of the dimension control the TPE and the SPE are superior to the other epitaxial processes, since they are compatible with photolithography and a three-dimensional control of the geometry of the epitaxial layers can easily be realized with them This offers good prospects for their application in IC technology. Ohmic contacts can be readily obtained with SPE and TPE. The difficulty of getting ohmic contact to LPE, VPE and MBE layers depends on the semiconductor and the dopant concentration near the surface of the epitaxial layers. Using multilayer techniques, a highly doped thin contact layer can be made on the top of a low-doped epitaxial layer by VPE, LPE or MBE processes to facilitate the formation of an ohmic metal contact. This is one of the usual solutions of the contacting problem. As it was mentioned, especially good ohmic contact layers have been recently obtained by MBE followed by in situ metallization [13, 14]. Without using multi layer techniques, the formation of ohmic contacts to low-doped VPE, LPE and MBE layers may be very difficult. It is especially so with GaAs, GaP, etc. semiconductor materials.

5. The first demonstrative experiments of TPE

The first experiments demonstrating the possibility of the thin phase epitaxial process were performed in 1974 [5, 6]. An alloying furnace was redesigned for the purpose of TPE as is shown in Fig. 8. The ampoule sealed with

liquid metal shown in Fig. 7c also had an outside pocket for a control sample. The influence of the arsenic vapour can be seen by comparing the parameters of the sample inside the ampoule containing arsenic vapour and of the sample in the outside pocket containing no arsenic vapour. Of course, the control sample originated from the same slice and was handled in exactly the same way as the sample in the TPE process. The characteristics of the heating cycle employed by us were the following:

heating rate: 60 °C/min,
annealing time at 620 °C: 5 min,
cooling rate during TPE: 2 °C min^{-1} (from 620 °C to 580 °C),
cooling after TPE: very quick (quenching).

The contact metal system was a layered structure deposited in the order and thickness:

20 nm In + 20 nm Ga + 100 nm Ge + 200 nm Ag.

Control samples without Ga were also prepared. The qualitative effects shown in Table II are:

1. both Ga and As are needed to get good ohmic contacts;
2. the effect of Ga and As can be based on the formation of a sufficiently thick contact layer formed by the epitaxial process;
3. good ohmic contacts can be obtained with an alloying time much longer than the usual one minute.

Table II

Qualitative effects obtained in the first demonstrative experiments of TPE using n-type GaAs epitaxial layer with a dopant concentration of about $5 \cdot 10^{15}$ cm^{-3} and the equipment shown in Figs. 7c and 8

Metal system	In + Ga + Ge + Ag		In + Ge + Ag	
Placing of the sample in the rig (inside the ampoule is arsenic vapour, in the outside pocket is no arsenic vapour)	in the arsenic vapour	out of the arsenic vapour	in the arsenic vapour	out of the arsenic vapour
Sample No.	1	2	3	4
Ohmic character after the first heat cycle	good	bad	bad	bad
Change of the place of the samples	2	1	4	3
Ohmic character after the second heat cycle	good	good	good	bad

Sample No. 1 shows that TPE can be repeated, since the prolonged heat cycle does not harm the ohmic character of the sample. (It is trivially so with Ge and Si but not with GaAs, GaP, etc. semiconductor materials having a volatile component).

It was demonstrated by Sample No. 2 and 4 that the samples can even be "repared" after an unsuccessful alloying by realloying them in arsenic vapour!

The bad result obtained with sample No. 3 after the first heat cycle could be due to the excess arsenic diffused into the metal system. Because of this arsenic saturation no or very little Ga may be dissolved (arsenic-rich but Ga-poor metal system). On the other hand, the arsenic evaporated out of the metal contact and Ga dissolved into the metal system (becoming arsenic-poor but Ga-rich) during the second heat cycle when the sample was placed out of arsenic vapour. Therefore, the metal system contained at the same time *both* Ga and As in neither case sufficient for TPE.

The contact layers made by TPE were analyzed by several methods. Microprobe analysis of cleaved edges of GaAs samples containing the cross-section of ohmic contacts has shown the complex distribution of the five elements involved [15, 16]. Two coincident Ga, As and In peaks were also found. This suggested that a ternary compound of $In_{0,4}\,Ga_{0,6}\,As$ precipitated in the contact metal system [16]. Accumulation of Ge near the metal-GaAs interface was also observed. It was concluded that heterojunction effects could play a role in the formation of the ohmic contacts.

It was shown that the oxide growth or the dissolution due to an anodic current can be made over thicknesses of about 10 to 70 nm at a constant rate, characteristic of the material composition anodized, if carefully controlled conditions are employed [7]. This method was also applied for analysing the Ga content in the contact metal on a GaAs sample. The sample was treated as Sample No. 2 in Table II and was analyzed after both the first and the second heat cycles. Less gallium was found in the metal system after the second heat cycle than after the first one. This was accounted for by the TPE process which could convert Ga into GaAs.

The possibility of a TPE process was also demonstrated with InP [17]. A layered structure of contact metals, i.e.

$$20\text{ nm In} + 75\text{ nm Sn} + 255\text{ nm Ag}$$

and an ambient containing hydrogen and phosphorous vapour as well as an alloying system similar to that shown in Fig. 8 were used for the experiments [10, 17]. The problems with InP are similar to those with GaAs. The phosphorous is very volatile and can be supplied from vapour phase during TPE. The In deposited into the contact metal system before the TPE process is much

less volatile. The contact produced had an ohmic character and low specific contact resistance. By using TPE contacts Gunn diodes with an instantaneous efficiency of about 3% could be produced, too [17].

6. TPE in the MOSFET technology

GaAs MOSFETs are advantageous for microwave analogue and digital applications because of the high electron mobility and the high value of the drift velocity at saturation. TPE was also used for making the drain and source islands of enhacement-type MOSFET devices [10, 18, 19].

20 nm In + 100 nm Sn + 50 nm Al metal system was deposited on p-type GaAs. Then, the surface of GaAs and the Al layer on the top of the contact metal system were anodically oxidized. The role of the Al_2O_3 layer obtained by oxidation of the Al layer was to prevent the arsenic loss during alloying.

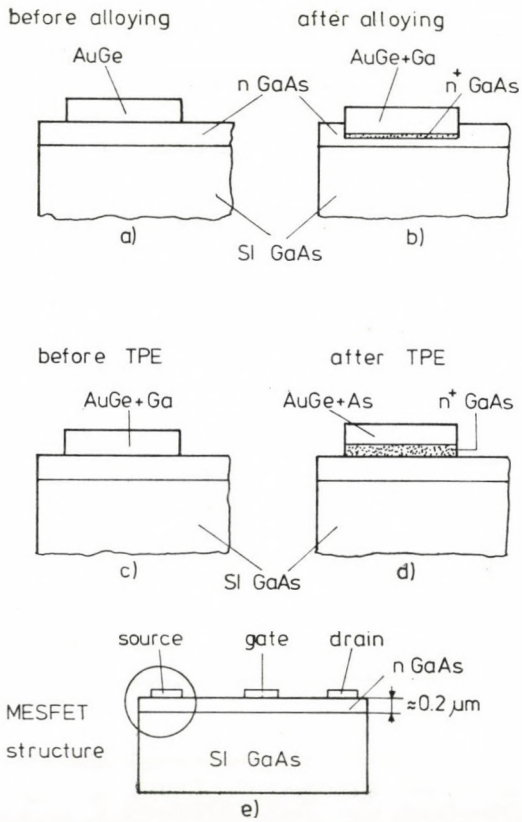

Fig. 11. GaAs MESFET structure (e) and the details of the source region before (a) and after (b) a usual alloying process as well as before (c) and after (d) a TPE process obtained by OTSUBO et al [20]

This structure was an IMS system illustrated in Fig. 7a. The alloying was performed in an N_2 ambient at 600 °C for 5 minutes. At this temperature the contact metal is a melt and dissolves a thin layer of GaAs. During cooling down a regrowth of GaAs dissolved in the metal takes place. By the notation introduced in Fig. 10 this process can be regarded as a T_LPE(S) process (i.e. thin liquid phase epitaxy with an additional solid phase). The n^+GaAs layer regrown during the TPE process formed an n^+—p junction with the p-type substrate and an ohmic contact with the InSn contact metal. Completing the preparation by other suitable processing steps MOSFET devices with good properties could be fabricated. The electrical characteristics were better with MOSFET devices made by using TPE than those with devices fabricated by employing a VPE layer [10, 18, 19].

The use of TPE was proposed also for the cases, where very thin VPE layers having a thickness of about a few tenths of micrometer were used to prepare GaAs MOSFET devices, as illustrated in Fig. 11e [20]. The very thin n-type epitaxial active layer on semi-insulating substrate can be dissolved by the contact material consisting of Au—Ge, and due to the incomplete regrowth of GaAs dissolved both the regrown n^+GaAs and the active n GaAs layer which remained undissolved become too thin (Fig. 11a and b). This results in an increase in source and drain resistances and gives devices with poorer microwave performances [20]. On the other hand, the TPE process results in thick n^+ GaAs on the top of the active n GaAs layer and a geometry more advantageous in view of lower specific contact resistance, as it is illustrated in Figs. 11c and d.

7. Further prospects

TPE is still in its infancy. Further work is still needed to reveal the metallurgical processes and to explain the phenomena in detail. TPE seems to be a useful tool for making ohmic contacts for good quality and high reliability III—V and II—VI compound semiconductor devices. Of course, TPE has to compete with other processes, especially with the pulsed laser or pulsed electron beam techniques being also candidates for improving the quality and reliability of these devices. The results of this competition will depend very much on economical factors. TPE is not an expensive process where the facilities are developed for other purposes e.g. for diffusion, MBE or post-implantation annealing.

REFERENCES

1. Thin Films — Interdiffusion and Reactions, Edited by J. M. Poate, K. N. Tu and J. W. Mayer, Wiley-Interscience, New York, 1978.
2. S. S. Lau and W. F. van der Weg, Chapter 12 in Ref. [1].
3. G. Ottiviani, D. Sigurd, V. Marello, J. W. Mayer and J. O. McCaldin, J. Appl. Phys., **45**, 1730, 1974.

4. C. Canali, J. W. Mayer, G. Ottiviani, D. Sigurd and W. F. Van der Weg, Appl. Phys Lett., **25**, 3, 1974.
5. T. Sebestyen, H. Hartnagel and L. H. Herron, Electronics Letters, **10**, 372, 1974.
6. T. Sebestyen, H. L. Hartnagel and L. H. Herron, IEEE Trans. on Electron Devices, ED-**22**, 1073, 1975.
7. A. F. A. B. El-Safti, B. L. Weiss and H. L. Hartnagel, Electronics Letters, **12**, 322, 1976.
8. T. Sebestyen, M. Menyhard and D. Szigethy, Electronics Letters, **12**, 96, 1976.
9. T. Sebestyen, H. Hartnagel and L. H. Herron, in Inst. Physics. Conf. Ser. No. 24, Institute of Physics, London and Bristol, 1975, pp. 77—88.
10. H. L. Hartnagel, Electronics and Power, **22**, 765, 1976.
11. T. Sebestyen, I. Mojzes and D. Szigethy, presented at 5th Specialist Workshop on Active Microwave Semiconductor Devices, Venice, Oct. 11—13, 1978.
12. I. Mojzes, T. Sebestyen, P. B. Barna, G. Gergely and D. Szigethy, Thin Solid Films, 61, 1979.
13. W. T. Tsang, Appl. Phys. Letters, **33**, 1022, 1978.
14. J. V. Dilorenzo, N. C. Niehaus and A. Y. Cho, J. Appl. Phys., **50**, 951, 1979.
15. B. L. Weiss and H. L. Hartnagel, Electronics Letters, **11**, 263, 1975.
16. H. Hartnagel, K. Tomizawa, L. H. Herron and B. L. Weiss, Thin Solid Films, **36**, 393, 1976.
17. H. T. Mills and H. L. Hartnagel, Electronics Letters, **11**, 621, 1975.
18. B. Bayraktaroglu, E. Kohn and H. L. Hartnagel, Electronics Letters, **12**, 53, 1976.
19. H. L. Hartnagel, J. Vac. Sci. Technol., **13**, 860, 1976.
20. M. Otsubo, H. Kumabe and H. Miki, Solid State Electronics, **20**, 617, 1977.

Acta Physica Academiae Scientiarum Hungaricae, Tomus 47 (1—3), pp. 69—74 (1979)

OPTICAL EXCITATION OF ELECTRONS BOUND TO SHALLOW DONORS IN GaP

By

B. PŐDÖR and Z. LACZKÓ

RESEARCH LABORATORY FOR INORGANIC CHEMISTRY OF THE HUNGARIAN ACADEMY OF SCIENCES
BUDAPEST, HUNGARY

Infrared transmission measurements of GaP with S, Te and Si donor impurities revealed absorption lines due to the excitation of electrons bound to lower lying ls like states to higher lying p like states. $1s \rightarrow 2p_{\pm}$ transitions were observed for S, Te and Si donors as well as transitions to other p_0 and $p_{\pm}$ states. Optical ionization energies of S, Te and Si were determined as 891 ± 5 cm^{-1}, 776 ± 5 cm^{-1} and 713 ± 5 cm^{-1}, respectively, using the effective mass approximation.

1. Introduction

Due to the excitation of electrons from ground states of donors to the higher lying excited states of the same impurity centres, characteristic absorption lines can be observed in the energy range beyond the ionization energy of the impurities. As the ionization energies of shallow donors and acceptors of the different semiconductors are mostly in the range from 10 to 1000 meV, these absorption lines fall into the infrared spectral region, well beyond 10 μm wavelengths.

The infrared absorption spectra of different shallow donors (S, Se, Te and Si) in GaP have been reported by various authors [1—9]. Nevertheless there exists no agreement either in the assignment of the observed lines, or in their theoretical interpretation. The former is caused by the fact that in the spectral region of interest, i.e. from about 400 to 800 cm^{-1}, strong two-phonon absorption bands are present, whose assignment is also by no means unambiguous [10—14]. The theoretical interpretation is made more difficult by the complicated structure of the conduction band minimum of GaP [6, 7, 9].

In this paper some preliminary results concerning infrared absorption due to the excitation of electrons from donor ground states to higher lying excited states of S, Te and Si donors in GaP are presented, together with the results of a tentative theoretical interpretation based on the effective mass theory (EMT), anticipating all of the shortcomings of the application of this model to our case.

2. Experimental results

The infrared transmission measurements were performed on liquid phase epitaxial GaP layers grown on semiinsulating GaP substrates. These layers contain predominantly S or Si donors [15]. Bulk grown GaP samples doped with Te or S were also investigated.

Dominant donors were identified by their thermal ionization energies obtained from Hall effect measurements [15]. Infrared transmission spectra at room temperature were recorded on a Perkin-Elmer 225 grating spectrophotometer between 1000 and 400 cm^{-1} with a resolution of better than 1 cm^{-1}.

In Figs. 1 and 2 typical infrared transmission spectra are presented. In the spectrum shown in Fig. 1 the broad band between about 750 and 700 cm^{-1} is due to two-phonon absorption involving longitudinal and transversal zone-edge phonons at the X and L points of the Brillouin zone. Absorption lines attributed to the excitation of electrons bound to S and Si donors are marked

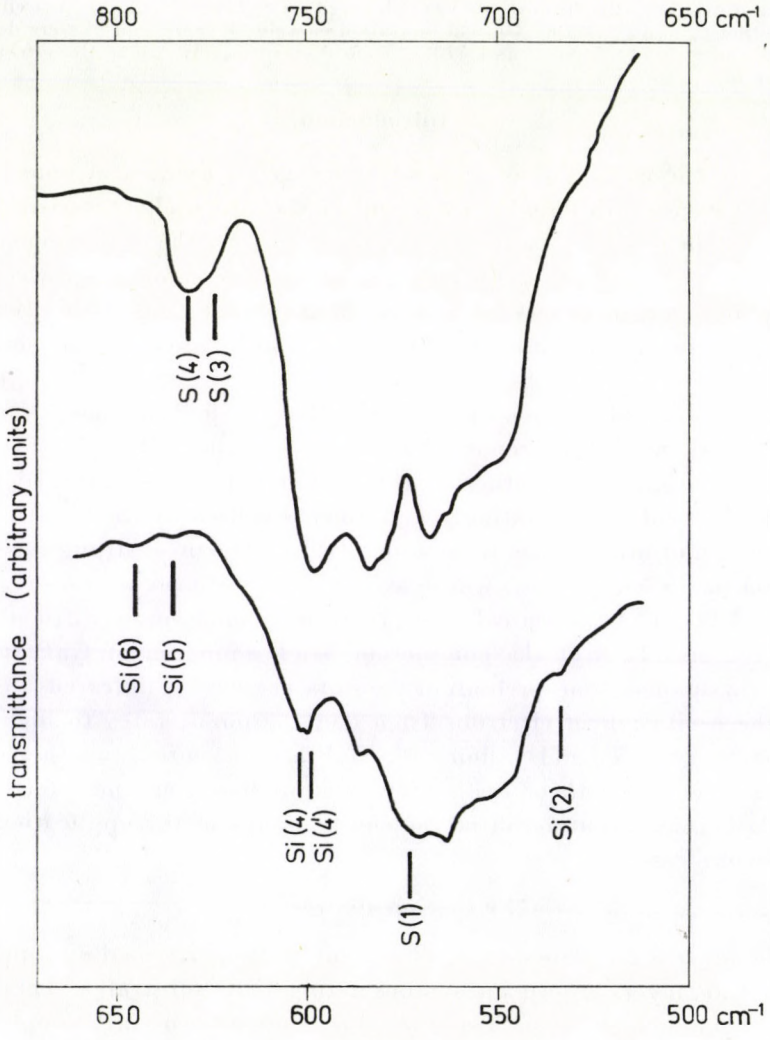

Fig. 1. Infrared transmission spectrum of bulk grown S-doped GaP containing also Si as residual donor

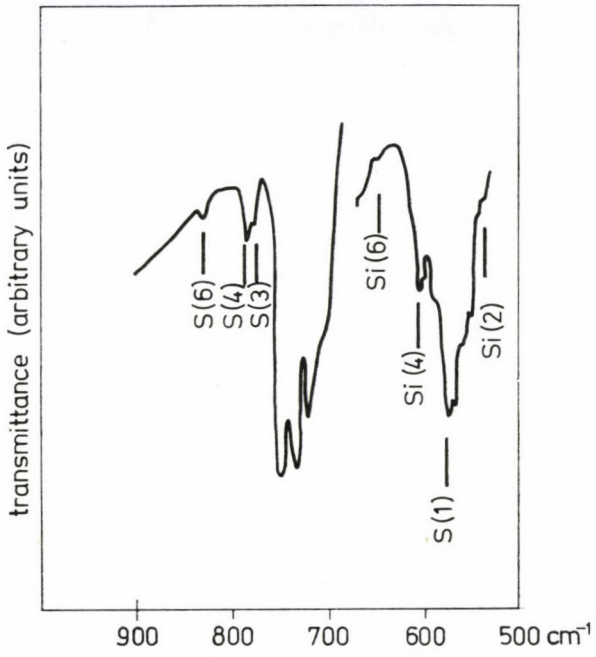

Fig. 2. Infrared transmission spectrum of LPE GaP layer. The dominant donor is S with $N_D = 9 \times 10^{16}$ cm^{-3}, but some Si is also present.

accordingly. The strongest lines belong to the $1s \rightarrow 2p_{\pm}$ transition [16, 17]. Three lines due to S and five lines due to Si are identified on this spectrum.

In Fig. 2 a spectrum taken on a LPE layer is presented. According to the Hall effect and photoluminescence measurements [15] the dominant donor in this sample is S. But besides lines due to S, absorption lines belonging to Si are also present in this spectrum. All of the observed absorption lines, in

Table I

Observed absorption lines for S and Te donors

Line	Assignment	Excitation energy (cm^{-1})	
		S	Te
7	$1s(A_1) \rightarrow 5p_0$	—	—
6	$1s(A_1) \rightarrow 3p_{\pm}$	826	—
5	$1s(A_1) \rightarrow 4f_0$	808	—
4	$1s(A_1) \rightarrow 2p_{\pm}$	781	666
3	$1s(A_1) \rightarrow 4p_0$	774	—
2	$1s(A_1) \rightarrow 3p_0$	—	—
1	$1s(A_1) \rightarrow 2p_0$	571	454

Table II

Observed absorption lines for Si donors

Line	Assignment	Excitation energy (cm^{-1})
7	$1s(\Gamma_8) - 5p_0$	653
6	$1s(\Gamma_8) - 3p_\pm$	647
5	$1s(\Gamma_8) - 4f_0$	630
4	$1s(\Gamma_8) - 2p_\pm$	603
4′	$1s(\Gamma_7) - 2p_\pm$	599
3	$1s(\Gamma_8) - 4p_0$	—
2	$1s(\Gamma_8) - 3p_0$	539
2′	$1s(\Gamma_7) - 3p_0$	534
1	$1s(\Gamma_8) - 2p_0$	—

analogy with the hydrogen spectrum, can be classified as belonging to the Lyman spectrum.

In Tables I and II we summarize the observed absorption lines of S and Te donors, and that of Si donors, respectively, as well as the proposed assignments based on the EMT [9, 16, 17]. The relative intensities of the absorption lines roughly correspond to the theoretical estimations [17] thus lending support to our assignments.

3. Discussion

In the effective mass approximation the binding energies of p-like excited states should not depend on the donor species. The data presented in Table III show that the positions of the observed absorption lines relative to the $2p_\pm$ lines do not depend on the donor species in the limits of the present experiments.

A tentative fit using the EMT of FAULKNER [16] which in turn is based on a multi-ellipsoidal model of the conduction band minimum, resulted in the theoretical line separations also given in Table III. The following parameter values were obtained: effective mass anisotropy parameter $\gamma^{-1} = m_l/m_t = 22 \pm 2$, effective Rydberg constant $R_t^* = 301 \pm 10\ cm^{-1}$. The anisotropy parameter agrees well with the value of $20\ ^{+10}_{-\ 6}$ deduced from recent cyclotron resonance measurements [17]. All of the six identified line separations belonging to different donors agree with the theoretical predictions. The theoretical fit resulted in the binding energy of the $2p_\pm$ state a value of $110 \pm 4\ cm^{-1}$. This adds up with the observed $1s \rightarrow 2p_\pm$ transition energies of the different donors (see Table IV) to give the following ground state ionization energies for S, Te and Si, respectively: $891 \pm 5\ cm^{-1}$, $776 \pm 5\ cm^{-1}$ and $713 \pm 5\ cm^{-1}$. These

Table III

Separation between the donor lines (cm^{-1})

Assignment	Effective mass theory	Experiment		
		S	Te	Si
$4p_{\pm} - 2p_{\pm}$	63 ± 3			
$5f_0 - 2p_{\pm}$	60 ± 3			
$5p_0 - 2p_{\pm}$	54 ± 3			50
$3p_{\pm} - 2p_{\pm}$	44 ± 2	45		44
$4f_0 - 2p_{\pm}$	31 ± 3	27		34
$2p_{\pm} - 4p_0$	4 ± 3	7		
$2p_{\pm} - 3p_0$	67 ± 6			65
$2p_{\pm} - 2p_0$	211 ± 5	210	212	

$\gamma^{-1} = 22 \pm 2$ $\quad R_I^* = 301 \pm 10\ cm^{-1}$

values are about 2 meV higher than the currently suggested optical ionization energies [7, 9], and they are about 2 to 5 meV higher than the thermal ionization energies derived from our Hall effect measurements [15].

Table IV

Binding energy of the $2p_{\pm}$ state, and donor ground state ionization energies

Donor	Transition	Observed energy (cm^{-1})	$2p_{\pm}$ binding energy (cm^{-1})	Ground state ionization energy (cm^{-1})
S	$1s(A_1) \rightarrow 2p_{\pm}$	781 ± 1	110 ± 4	891 ± 5
Te	$1s(A_1) \rightarrow 2p_{\pm}$	666 ± 1	110 ± 4	776 ± 5
Si	$1s(\Gamma_8) \rightarrow 2p_{\pm}$	603 ± 1	110 ± 4	713 ± 5

Finally we should like to dis cussan interesting feature of the Si spectra. Si, being a Ga site donor has a ground state symmetry different from that of the P site donors, S and Te. Its ground state is splitted into two 1s states having symmetries of Γ_8 and Γ_7, respectively. According to photoluminescence measurements [18] this splitting amounts to about 4.0 cm^{-1}. Closer examination of our spectra (see Fig. 1) has shown that the Si $2p_{\pm}$ line as well as the $3p_0$ line seems to be a doublet. A separation of about 3—5 cm^{-1} can be inferred from our measurements, in agreement with the expectations.

Grateful acknowledgements are due to Dr. J. PFEIFER for providing the GaP samples and to Dr. S. DOBOS for making available the infrared measuring equipment.

REFERENCES

1. A. ONTON, Phys. Rev., **186,** 786, 1969.
2. A. ONTON and R. C. TAYLOR, Phys. Rev., **B1,** 2587, 1970.
3. T. ARAI, N. ASAMURA, K. KUDO and S. UMEMOTO, Jap. J. Appl. Phys., **11,** 106, 1972.
4. W. SCOTT and J. R. ONFFROY, Phys. Rev., **B13,** 1664, 1976.
5. В. Берндт, А. А. Копылов, А. Н. Пихтин, Письма в ЖЭТФ, **22,** 587, 1975.
6. A. C. CARTER, M. S. SKOLNICK, R. A. STRADLING, J. P. LEOTIN and S. ASKENAZY, Proc. Int. Conf. Phys. Semicond. Rome, 1976.
7. А. А. Копылов, А. Н. Пихтин, ФТП, **11,** 867, 1977.
8. W. SCOTT, J. Appl. Phys., **48,** 3173, 1977.
9. A. C. CARTER, P. J. DEAN, M. S. SKOLNICK and R. A. STRADLING, J. Phys. C, **10,** 5111, 1977.
10. R. M. HOFF and J. C. IRWIN, Canad. J. Phys., **51,** 63, 1973.
11. E. S. KOTELES and W. R. DATARAS, Solid State Comm., **19,** 221, 1976.
12. В. И. Закржевский, А. Н. Пихтин, Д. А. Яськов, ФТТ, **13,** 2635, 1971.
13. B. ULRICI and E. JAHNE, phys. stat. sol. (b), **86,** 517, 1978.
14. R. BESERMAN and D. SCHMELTZER, Solid State Comm., **24,** 793, 1977.
15. J. PFEIFER, B. PŐDÖR, L. CSONTOS and N. NÁDOR, Revue de Physique Appliquée, **13,** 741, 1978.
16. R. FAULKNER, Phys. Rev., **184,** 713, 1969.
17. W. KOHN, in Solid State Physics, Ed. F. Seitz and D. Turnbull, Academic Press, New York, 1957, Vol. 5. p. 257.
18. J. LEOTIN, J. C. OUSSET, R. BARBASTE, S. ASKENAZY, M. S. SKOLNICK, R. A. STRADLING and G. POIBLAUD, Solid State Comm., **16,** 363, 1975.
19. P. J. DEAN, W. SCHAIRER, M. LORENZ and T. N. MORGAN, J. Lumin., **9,** 343, 1974.

Acta Physica Academiae Scientiarum Hungaricae, Tomus 47 (1—3), pp. 75—81 (1979)

RESIDUAL DONORS IN LIQUID PHASE EPITAXIAL GaP*

By

B. PŐDÖR

RESEARCH LABORATORY FOR INORGANIC CHEMISTRY OF THE HUNGARIAN ACADEMY OF SCIENCES
BUDAPEST, HUNGARY

and

J. PFEIFER

RESEARCH INSTITUTE FOR TECHNICAL PHYSICS OF THE HUNGARIAN ACADEMY OF SCIENCES
BUDAPEST, HUNGARY

Identification of the nature and sources of residual impurities in intentionally non-doped $A^{III}B^{V}$ type semiconductor epitaxial layers is of great importance in order to grow high purity or controllably doped epitaxial layers. In this paper results of a systematic study of the electrical properties and nature of residual donors in liquid phase epitaxial GaP layers grown under different conditions are presented. S and Si were found as main residual donors in LPE layers. Electrical properties of S, Si and Te in GaP are discussed, and methods of the electrical characterization of donors are presented.

1. Introduction

In this paper some results concerning the electrical properties of donor impurities in liquid phase epitaxial GaP layers, as well as some results as to their nature and sources will be presented. The identification of the nature and sources of chemical impurities in intentionally non-doped $A^{III}B^{V}$-type semiconductors is of great importance in order to grow high purity or controllably doped epitaxial layers. This applies especially to the case of GaP, where the main residual donors are believed to be S and Si.

We have carried out a systematic study on the characterization of donors and more generally of electrically active impurities in GaP epitaxial layers, as well as on the incorporation of residual impurities into the epitaxial layers under different conditions. Based on these results GaP epitaxial layers were grown with total concentration of electrically active impurities as low as 3×10^{16} cm^{-3} and with electron mobility, measured at liquid nitrogen temperature, as high as 1900 cm^2/Vs [1].

Because of lack of space and time, only a limited selection of problems can be dealt with here. A more detailed account of our results can be found in our papers already published [1, 2], and under preparation [3].

* Work performed at the Research Institute for Technical Physics of the Hungarian Academy of Sciences, Budapest.

In this paper the following subjects are dealt with:

i) Analysis of donor impurities using electrical methods;

ii) Some results concerning the incorporation of S and Si donors into GaP epitaxial layers.

2. Analysis of donors using electrical methods

To identify the donors in GaP epitaxial layers, electron concentration versus temperature curves deduced from Hall effect data were analysed. The identification of impurities was also greatly aided by low temperature photoluminescence spectra measurements.

The dominant donors can be identified with the help of their thermal activation energies deduced from the analysis of electron concentration versus temperature curves, like those shown in Fig. 1. All Hall effect measurements

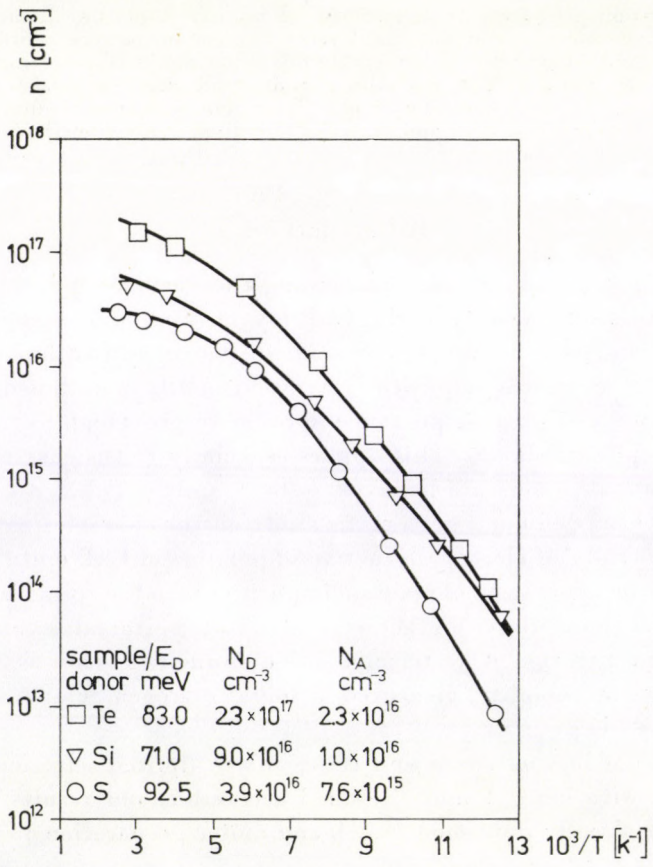

Fig. 1. Electron concentration versus reciprocal temperature in GaP containing S, Te and Si donors. Full lines are theoretical curves calculated with the parameters indicated.

were carried out using the Van der Pauw method in the temperature range from 77 to 400 K. The estimated error of the measured electrical parameters (Hall constant, conductivity, mobility) was less than 10 per cent.

Because of chemical shifts, the difference in the donor ground state energies of S, Te and Si, the donors which are dealt with in this work, differ by about 10 meV, more exactly $E_D(S) > E_D(Te) > E_D(Si)$ and $E_D(S) - E_D(Te) \simeq 14$ meV and $E_D(Te) - E_D(Si) \simeq 8$ meV (values derived from published optical data [4, 5, 6]). The analysis is complicated by the fact that the observed thermal ionization energies show a concentration dependence, which we found to be about 10 meV for ionized donor concentrations of about 10^{16} cm^{-3}, quite comparable with the difference in the ionization energies themselves.

In order to be able to identify residual donors only with the help of the measured thermal ionization energies, we have studied the dependence of ionization energies of S, Te and Si in function of the ionized donor concentration in GaP. The measurements were carried out on carefully selected and characterized LPE layers grown by us (S and Si donors). LEC crystals (Te donors) and SG crystals (Si donors). Methods of sample characterization, etc. are described in [3].

The dependence of thermal ionization energies on the ionized donor concentration, as established by us, is presented in Figs. 2 and 3. Typical standard errors of the points are also indicated. For single donors, the thermal ionization energy should depend linearly on the cubic root of the ionized donor concentration, as found here. From the data presented in these Figures we can deduce the following relationships (energies are in meV, concentrations are in cm^{-3})

$$E_D(S) = (105 \pm 2) - (3.8 \pm 0.7) \times 10^{-5} \; N_A^{1/3}$$

$$E_D(Te) = (94.5 \pm 2) - (3.8 \pm 0.4) \times 10^{-5} \; N_A^{1/3}$$

$$E_D(Si) = (83.5 \pm 2) - (4.6 \pm 0.2) \times 10^{-5} \; N_A^{1/3}$$

The thermal ionization energies (E_D), donor and acceptor concentrations (N_D and N_A) were deduced from the electron concentration versus temperature curves using a non-linear least-squares fit to a single donor — single acceptor model [1, 3] (details of the model are to be found in the Appendix). The standard errors are $\pm(2-3)$ meV for E_D, $\pm(10-20)$ per cent for N_D and $\pm(20-50)$ per cent for N_A, respectively.

As such relationships obtained on well characterized samples are not available from the literature, except those of VINK et al [7] obtained for Si donors in GaP, we should like to assess their relevance.

The ionization energies extrapolated to infinite dilution agree within experimental errors with the optical ionization energies of about 107 meV,

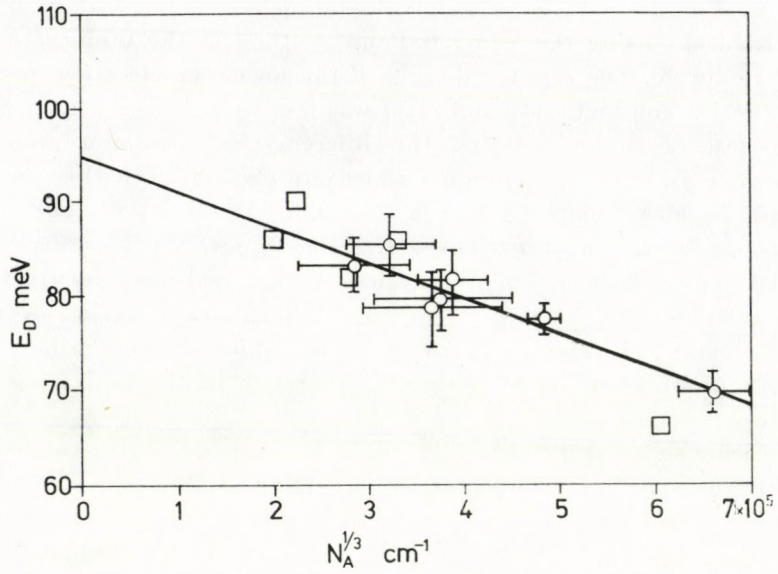

Fig. 2. Plot of donor ionization energy (E_D) versus cubic root of ionized donor concentration (N_A) of Te donors in GaP. Circles are our data, bars represent the standard errors. Squares are the data from [9]

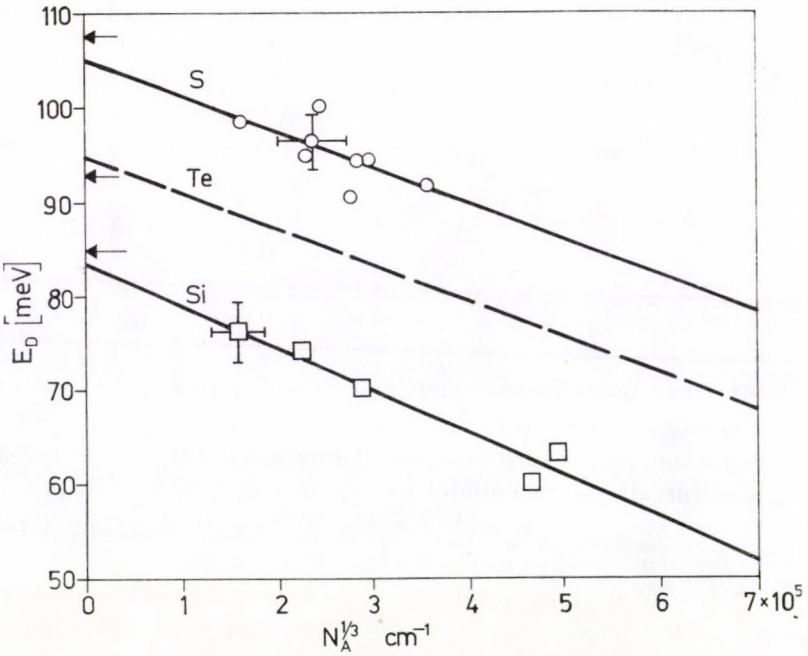

Fig. 3. Plot of donor ground state ionization energies versus cubic root of ionized donor concentrations of S, Te and Si donors in GaP. Bars represent typical standard errors. Arrows indicate the corresponding optical ionization energies

93 meV and 85 meV, respectively, reported in the current literature [5, 6]. But preliminary results of infrared excitation spectra measurements on these donors [8] resulted in optical ionization energies for S, Te and Si, which are about 2 to 3 meV higher than those referred to above.

We think that the results for Te are the most realiable among our thermal ionization energies. It seems to be very improbable that both S and Si should be present in these crystals in such concentrations as to cause a fortuitous coincidence of the apparent ionization energies with those of Te. The ionization energies obtained for S donors seem to be a little low in the light of the optical data. This could be attributed to a minute Si contamination of the S containing LPE layers, which is quite plausible according to our experience. The data for Si donors are thought to be the least reliable, because most of them were obtained on SG samples, not so well characterized as the other ones.

3. Behaviour of residual donors in LPE layers

Now we will discuss the observations concerning the behaviour of residual impurities in intentionally non-doped GaP layers. These epitaxial layers were grown on semiinsulating GaP substrates with starting temperatures and cooling rates corresponding to the values used to prepare green light emitting diodes. Horizontal graphite slider boats were used [1]. The doped crystals were used as source material at the epitaxial growth. Three kinds of graphite materials were used, but most of the measurements were made on layers grown in morganite graphite slider boats. Mass spectrometric analysis showed traces of S in this material. $N_D - N_A$ of the layers ranged from 2×10^{16} cm^{-3} to 4×10^{17} cm^{-3}, electron mobility measured at 77 K ranged from 600 to 1900 cm^2/Vs.

The dominant residual donors were found to be S or Si depending on the growth conditions. Photoluminescence measurements performed at liquid helium temperatures on samples identified as S-doped, showed strong donor-acceptor pair band at 2.200 eV attributed to Zn—S pairs as well as a set of strong Zn—S pair lines. Nevertheless in samples where the electrical properties were dominated by Si donors, weak Zn—S pair luminescence band and lines were also detected.

Te was not identified in the epitaxial layers even if the source crystals were doped with Te to a level of $(3-5) \times 10^{17}$ cm^{-3}. This statement needs some specifications. In the great majority of cases the electrical properties of LPE layers could be understood on the basis of incorporation of a single species of donor, either S or Si. In some cases intermediate donor energies were seen, which at first sight could be assigned to Te; but these samples could be reinterpreted either as containing Si, or it was concluded that two donor species are present, for which case our model does not apply.

The main source of the S contamination of the layers was the graphite material of the boats used. But some of the S donors comes from the gallium melt. From boats made from morganite graphite the first layers grown contained S at the level of $(2 - 5) \times 10^{17}$ cm^{-3}. With increasing cumulative annealing time at the growth temperature (two series at 900 and 990 °C) in consecutive runs the S contamination gradually decreased to a level below of somewhat 10^{17} cm^{-3}. Then in the subsequent runs already Si appeared as major donor dominating the electrical properties [1].

The second kind of graphite material resulted in residual S concentrations at the level of $(1-2) \times 10^{17}$ cm^{-3}, and this value has also shown a gradual decrease in consecutive growth runs, witnessing also the depletion of S contents of the graphite material.

In both cases the acceptor concentration deduced from the Hall data ranged from $(1-5) \times 10^{16}$ cm^{-3} and $(1 - 2) \times 10^{16}$ cm^{-3}, respectively. It did not show systematic changes in the different runs. According to the low temperature photoluminescence results the main acceptor is Zn. It is possible, however, that also Si acts as acceptor in our samples, but it does not affect the photoluminescence spectra.

From the boat made from a third graphite material layers were grown with very low S content. The electrical properties were dominated by Si donors reaching a level less than 3×10^{16} cm^{-3}.

4. Conclusions

Summing up we can conclude that the main residual donors in non doped GaP are S and Si. Most of the S comes from the graphite boats, and its concentration can be strongly decreased when annealing the boat and melt prior to growth. After sufficiently long annealing time, or using graphite boats depleted of S, the major donor impurities in the layers are Si.

Careful analysis of electrical measurements, coupled with photoluminescence spectrum measurements are able to identify the different donors in GaP epitaxial layers.

*

Grateful acknowledgements are due to Mrs. L. CSONTOS, Mrs. N. NÁNDOR and Mrs. S. PÜSPÖKI for participating in the experimental work. Photoluminescence spectra were measured by Dr. M. GÁL.

Appendix

For a multi-ellipsoidal model from charge neutrality we have

$$\frac{n(n + N_A)}{(N_D - N_A - n)} = \frac{v}{g} N_c' \left(\frac{m_\perp^* \, m_{II}^*}{m_0^3}\right)^{1/2} \frac{\exp(-E_D/kT)}{g_D},$$

here $v = 6$ is the number of equivalent valleys in the conduction band minimum of GaP, $g = 2$ is the spin degeneracy factor, E_D is the donor ground state ionization energy, n, N_D and N_A are the electron, donor and acceptor concentrations, respectively, $N_c' = 4.829 \times 10^{15}$

$T^{3/2}\,\mathrm{cm}^{-3}$ is the reduced density of states. The effective mass parameters used here are $m_{\perp}^{*}/m_0 = 0.25$ and $m_{\parallel}^{*}/m_0 = 2.5$.

g_D is the degeneracy factor of the donor ground state. For P-site donors as S or Te, the donor ground state has a symmetry of $1s(A_1)$, and lies well below the other 1s states, so in a good approximation we can put $g_D = 1$. For Ga site donors as Si the donor ground state has a symmetry of $1s(\Gamma_8)$, and a degeneracy of 3. But very close above it is the other state $(1s(\Gamma_7))$ with a degeneracy of 3 that for all practical purposes they can be lumped together to a ground state with $g_D = 6$.

REFERENCES

1. J. Pfeifer, B. Pődör, L. Csontos and N. Nádor, Revue de Physique Appliquée, **13**, 741, 1978.
2. В. В. Евстропов, А. Н. Именков, Б. Н. Калинин, Й. Пфайфер, Л. Чонтош, Ю. П. Яковлев, ФТП, **12**, 1017, 1978.
3. B. Pődör, J. Pfeifer, L. Csontos, N. Nádor and F. Deák, phys. stat. sol. (a) to be published.
4. W. Scott, J. Appl. Phys., **48**, 3173, 1977.
5. А. А. Копылов, А. Н. Пихтин, ФТП, **11**, 867, 1977.
6. P. J. Dean, D. Bimberg and E. Mansfield, Phys. Rev., **B15**, 3096, 1977.
7. A. T. Vink, A. J. Bosman, J. A. van der Does de Bye and R. C. Peters, J. Luminescence, **5**, 57, 1972.
8. B. Pődör and Z. Laczkó, Acta Phys. Hung., this issue, p. 69.
9. M. Toyama, K. Unno and A. Kasami, Jap. J. Appl. Phys., **7**, 1418, 1968.

Acta Physica Academiae Scientiarum Hungaricae, Tomus 47 (1—3), pp. 83—91 (1979)

DIRECT SYNTHESIS OF EPITAXIAL $A^{II}B^{VI}$ SEMICONDUCTOR THIN LAYERS ON METAL SINGLE CRYSTAL SUBSTRATES

By

D. IWANOV and CHR. NANEV

INSTITUTE OF PHYSICAL CHEMISTRY, BULGARIAN ACADEMY OF SCIENCES, 1040 SOFIA, BULGARIA

The method of direct synthesis of $A^{II}B^{VI}$ thin layers on metal single crystal substrates enables us to obtain the whole set of compounds of Zn and Cd with S, Se and Te. The morphology and the structure (texture and epitaxy) of the layers were investigated by means of TEM, SEM, X-ray and electron diffraction methods. The epitaxial layers have been synthesized at relatively low temperatures on the basal faces of the supporting single crystals.

I. Introduction

Interest in $A^{II}B^{VI}$ thin layers has gradually increased in the last decade due to their semiconductor and optoelectronic properties [1, 2, 3]. For example there is a certain possibility to use CdS, CdTe and other $A^{II}B^{VI}$ layers for the direct conversion of the solar energy into electricity [4, 5]. The solar cells produced on such basis may become important power sources due to the relatively low production costs [6].

There are various methods for the deposition of $A^{II}B^{VI}$ thin layers such as vacuum evaporation, chemical transport reaction, etc. [7]. They all are characterized by the high deposition temperatures. In the Institute of Physical Chemistry a method has been developed of obtaining $A^{II}B^{VI}$ thin layers on metal single crystal substrates at relatively low temperatures [8, 9]. According to this method metalloid vapours such as sulphur, selenium and tellurium react with the surface of zinc and cadmium single crystals. For example in this way we were able to produce epitaxial CdS layers even at a substrate temperature of 150 °C.

II. Experimental

The apparatus for growing zinc and cadmium single crystals and $A^{II}B^{VI}$ layers is shown in Fig. 1. It consists of: furnace 1 for obtaining zinc and cadmium single crystal substrates and the $A^{II}B^{VI}$ layers, furnace 2 for heating the metalloids, the cooling finger C, the Zn (Cd) single crystal. T_1, T_1, T_3 are the thermocouples, M is a stereomicroscope for observation and BS is a break-off glass tip.

One example of the zinc and cadmium single crystals used as substrates is shown in Fig. 2. The crystals have been obtained by the STRANSKI—KAISCHEW method [10, 11] in sealed glass ampoules evacuated to 10^{-6} torr. Now we

should like to describe briefly the preparation of the substrate: the zinc (and cadmium) single crystals were obtained by freezing a molten droplet and then exposing it to the vapours of the same substance. A constant temperature difference between the furnace 1 and the cooling finger which defined the super-

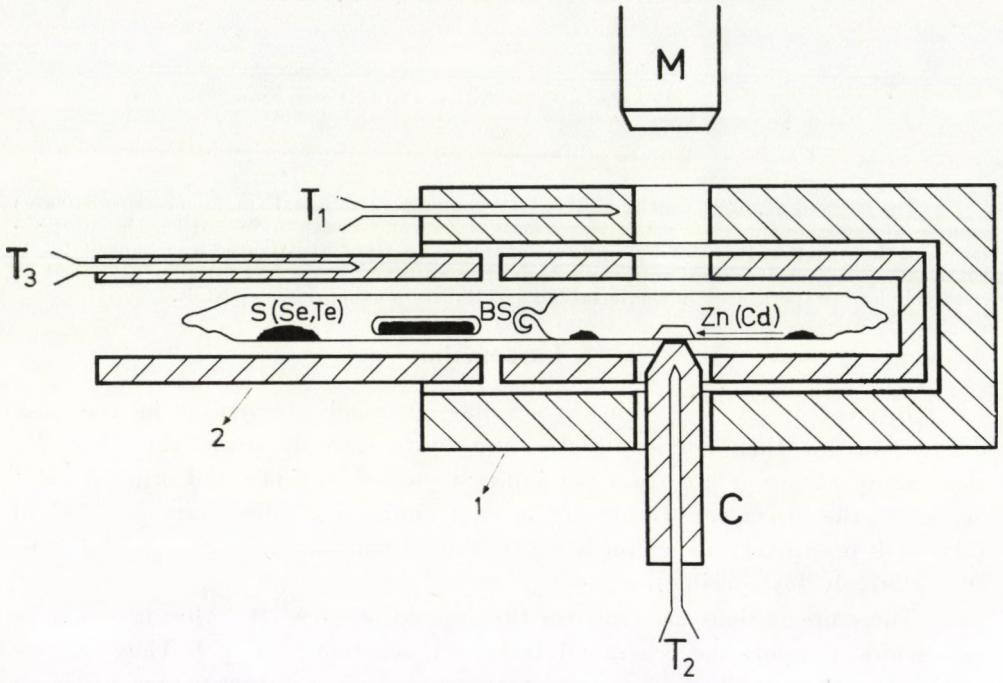

Fig. 1. Apparatus for growing zinc and cadmium single crystal substrates and $A^{II}B^{VI}$ layers: 1 — furnace for obtaining the crystals; 2 — furnace for heating the metalloids; C — cooling finger; Zn (Cd) — zinc (cadmium) single crystal; S, Se, Te — sulphur, selenium, tellurium; M — stereomicroscope; T_1, T_2, T_3 — thermocouples; BS — break-off glass tip

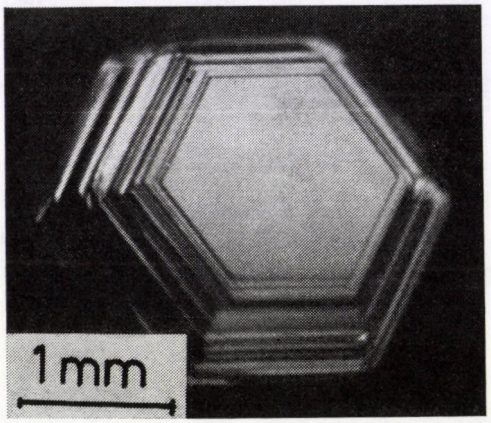

Fig. 2. Zinc single crystal grown from the vapour phase

saturation was maintained during every experiment. The zinc single crystals grew at temperatures of about 400 °C while the cadmium single crystals grew at relatively lower temperatures 300 °C. As a result of the growth of the crystal, the so-called end-growth form is obtained. It exhibits only the basal $\{0001\}$ face, the pyramidal $\{10\bar{1}1\}$ and the prismatic $\{10\bar{1}0\}$ faces. One can recognize that only the basal face is very smooth but the other faces have many steps.

On obtaining the end-growth form of the metal single crystal, metalloid vapours were introduced through the broken-off glass tip BS. They react with the hot surface of the metal single crystal following the general reaction equation:

$$A + B \rightarrow A^{II}B^{VI},$$

where A is Zn or Cd and B is S or Se or Te. In this way thin chalcogenide films (several hundred to two thousands Å thick) were obtained for 2 to 6 hours. The substances used were 99.9999% Zn, 99.999% Cd, 99.999% Se, spectrally pure S and pure Te. They were additionally purified by repeated vacuum (10^{-6} torr) distillation and sublimation.

The chalcogenide growth conditions are summarized in Table I, the temperatures of the furnaces 1 and 2 and of the cooling finger being kept constant during the whole reaction time. These three temperatures were predetermined in order to obtain metalloid vapour pressure 5 to 10 times higher than the corresponding metal vapour pressure which is important especially for the first moment of the reaction.

The layers were investigated either together with the supporting crystals (by means of reflection electron diffraction, scanning electron microscopy and X-ray texture goniometer), or after their removal from the substrates (by transmission electron microscopy, electron and X-ray diffraction). The chalcogenide layers have been detached from the supporting metal crystals by

Table I

Chalcogenide growth conditions

Single crystals	Substrate temperature (°C)	Metalloids	Source temperature (°C)	Chalcogenides	Colour
Zn	250—400	S	50—250	ZnS	grey, blue, green
		Se	215—370	ZnSe	yellow, red, brown
		Te	450—500	ZnTe	red, black
Cd	150—300	S	50—210	CdS	yellow, red
		Se	220—350	CdSe	red, dark red
		Te	450—530	CdTe	black, brown

the electrochemical dissolution of the latter. An 1n sulphate solution found application in such cases. The sulphidation kinetics of zinc has also been investigated ellipsometrically.

III. Results and discussion

III. 1. *Morphology*

During the reaction with S, Se and Te the zinc and cadmium single crystals lost their initial metallic glitter which fact referred to the formation of $A^{II}B^{VI}$ layers on them. The colours of the layers are shown in Table I.

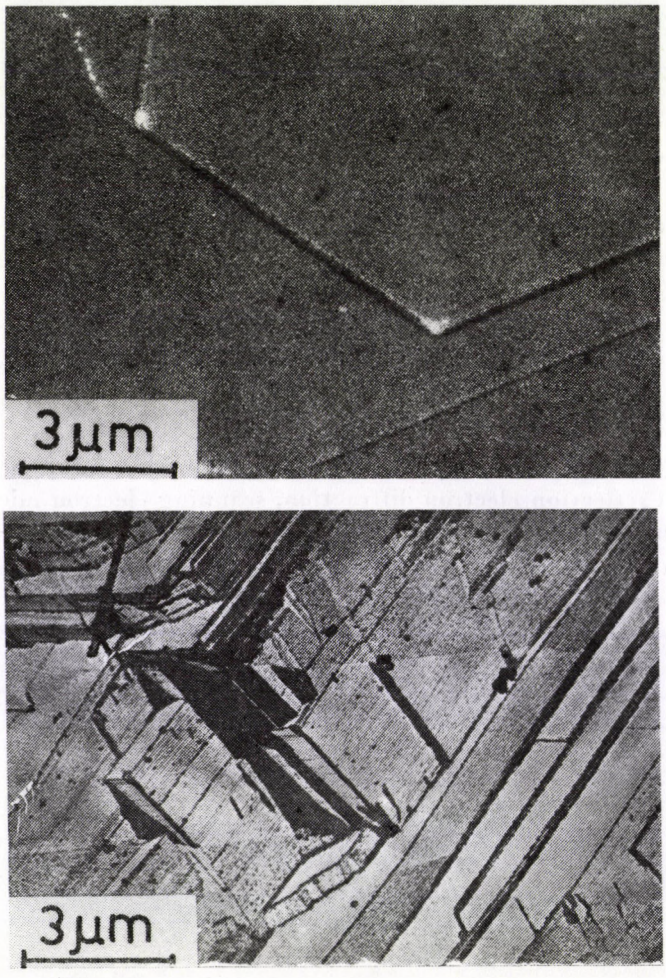

a)

b)

Fig. 3. Transmission electron micrographs of ZnS layers: a) obtained on the basal face at a substrate temperature of 355 °C with a sulphur vapour pressure of $7 \cdot 10^{-1}$ torr. b) obtained on the pyramidal face at a substrate temperature of 254 °C with a sulphur vapour pressure of $3 \cdot 10^{-3}$ torr

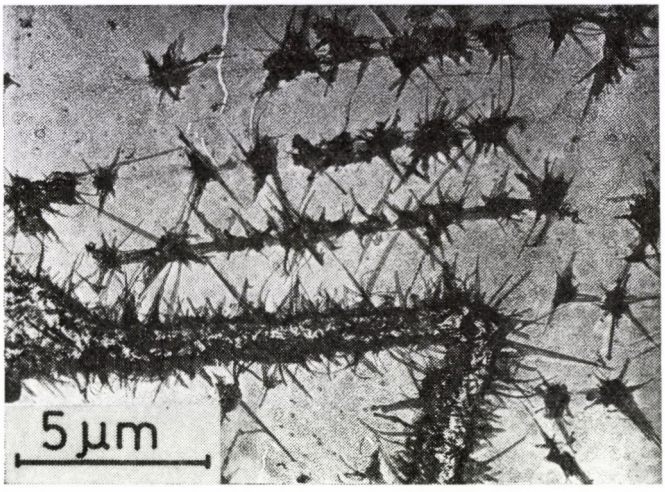

Fig. 4. CdS whiskers observed by TEM. The whiskers grow from the CdS layer on the basal face of the cadmium single crystal. Growth conditions: substrate temperature 310 °C, sulphur vapour pressure $1.5 \cdot 10^{-1}$ torr

Optical and scanning electron microscope investigations showed that the layers reproduced well the steps on the single crystal substrates as well as all peculiarities of their surface structure. Transmission electron microscopy confirms this conclusion (Fig. 3a, b). It is seen that the films obtained on the basal face exhibit a uniform structure. The layers removed from the pyramidal and the prismatic faces reproduced the surface morphology of the crystal substrate including numerous steps and growth details. As a general conclusion we can point out here that the sulphides reproduced better the surface structure than the selenides and tellurides. Nevertheless all of the layers can be used as electron microscopic replicas of the growing zinc and cadmium single crystals. For example this procedure may appear as a convenient replication method at elevated temperatures. Moreover, the possibility to use the ZnS and CdS layers as replicas of the substrate enables the direct determination of their azimuthal orientation by comparing it with the electron diffraction pattern. In this way we found that the steps on the basal faces of the Cd single crystals oriented along $\langle 11\bar{2}0\rangle$ are parallel to the $\langle 11\bar{2}0\rangle$ crystallographic direction in the CdS layers; The steps on the basal faces of the Zn single crystals oriented along $\langle 11\bar{2}0\rangle$ are parallel to the $\langle 110\rangle$ in ZnS layers.

In conclusion some peculiarities of the layers, e.g. the growth of whiskers on the CdS layers (Fig. 4) and so on, have to be mentioned.

III. 2. *Phase structure and epitaxy*

The results obtained by the electron microscopic, electron and X-ray diffraction investigations of the layers, obtained on the basal faces of the Zn

and Cd single crystals are shown in Table II. It is seen that some of the layers have cubic (sphalerite type) structure (ZnS, ZnSe, ZnTe and CdTe), the others being of hexagonal (wurtzite type structure (CdS and CdSe). This was confirmed by means of the Debye-Scherrer method, transmission and reflection electron diffraction and X-ray texture goniometer investigations. We suggest that the layers have the thermodynamically stable structure typical for the synthesis temperatures.

The following epitaxial relations were established for the layers with cubic phase structure:

$$\{111\}\ \text{ZnS(ZnSe, ZnTe)} \parallel \{0001\}\ \text{Zn with } \langle 110\rangle\ \text{ZnS (ZnSe, ZnTe)} \parallel \langle 11\bar{2}0\rangle\ \text{Zn},$$
$$\{111\}\ \text{CdTe} \parallel \{0001\}\ \text{Cd with } \langle 110\rangle\ \text{CdTe} \parallel \{11\bar{2}0\rangle\ \text{Cd}$$

and for the layers with hexagonal structure:

$$\{0001\}\ \text{CdS (CdSe)} \parallel \{0001\}\ \text{Cd with } \langle 11\bar{2}0\rangle\ \text{CdS} \parallel \text{(CdSe)}\ \langle 11\bar{2}0\rangle\ \text{Cd}.$$

Table II

A(II)B(VI) layer structure

A(II)B(VI) Compounds	Phase structure	Investigation methods	Epitaxial relations	Investigation methods	Lattice parameters (Å)	Investigation methods
ZnS	Sphalerite	1, 2, 3, 4	111 ZnS II 0001 Zn 110 ZnS II $11\bar{2}0$ Zn	3, 4 3, 5	$a = 5.40 \pm 0.01$	1, 2, 3
CdS	Wurtzite	1, 2, 3, 4	0001 CdS II 0001 Cd $11\bar{2}0$ CdS II $11\bar{2}0$ Cd	3, 4 3, 4, 5	$a = 4.13 \pm 0.01$ $c = 6.70 \pm 0.01$	1, 2, 3 1, 2, 3
ZnSe	Sphalerite	1, 2, 4	111 ZnSe II 0001 Zn 110 ZnSe II 0001 Zn	2, 4 4	$a = 5.66 \pm 0.01$	1, 2
CdSe	Wurtzite	1, 2, 4	0001 CdSe 0001 Cd	2, 4	$a = 4.23 \pm 0.01$ $c = 6.85 \pm 0.01$	1, 2
ZnTe	Sphalerite	1, 2, 3, 4	111 ZnTe II 0001 Zn 110 ZnTe II $11\bar{2}0$ Zn	3, 4 3	$a = 6.08 \pm 0.01$	1, 2, 3
CdTe	Sphalerite	1, 2, 3, 4	111 CdTe II 0001 Cd 110 CdTe II $11\bar{2}0$ Cd	3, 4 3	$a = 6.47 \pm 0.01$	1, 2, 3

Investigation methods:
1. Debye-Scherrer
2. Transmission electron diffraction
3. Reflection electron diffraction
4. X-ray texture goniometer
5. Comparison of the transmission electron diffraction pattern with the replica

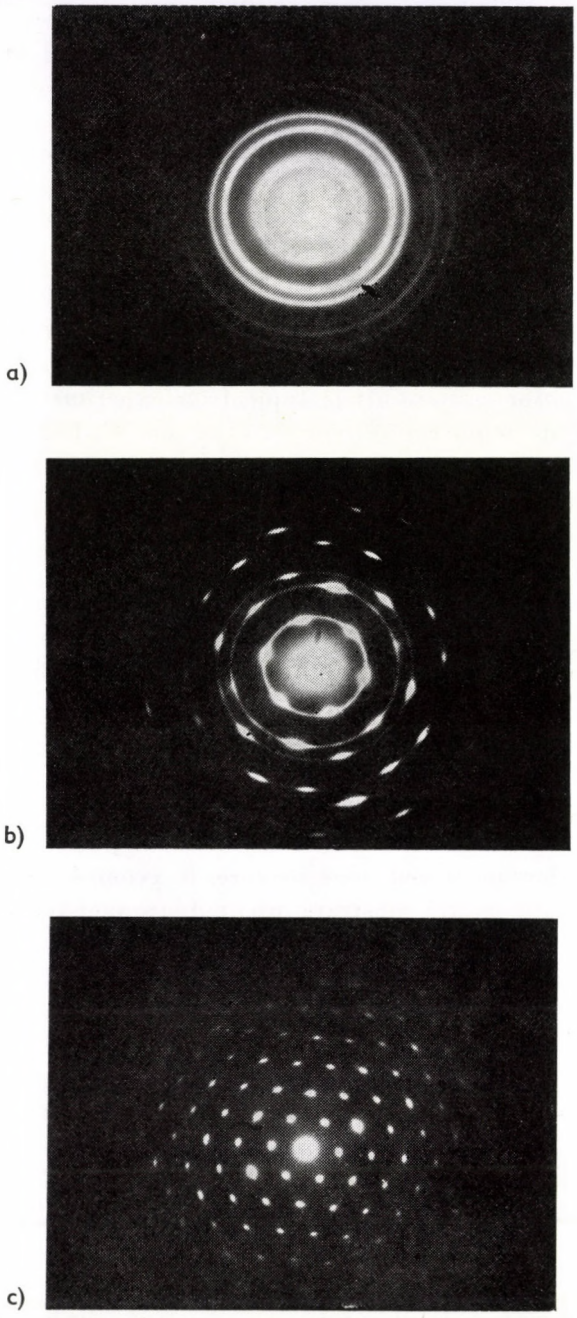

Fig. 5. Transmission electron diffraction patterns of ZnS layers obtained under the following conditions: a) substrate temperature 260 °C, sulphur vapour pressure $4 \cdot 10^{-4}$ torr; b) substrate temperature 320 °C, sulphur vapour pressure $5 \cdot 10^{-3}$ torr; c) substrate temperature 380 °C, sulphur vapour pressure 1 torr

These epitaxial relations were established by reflection and transmission electron diffraction, X-ray texture goniometer and by the above mentioned comparison of the transmission electron diffraction with the electron micrograph of the substrate.

The lattice parameters (see Table II) of the $A^{II}B^{VI}$ layers calculated from the X-ray and the electron diffraction patterns agree fairly well with the data in the literature [1].

Summarizing we can point out that there is some gradation in the structural perfection of the layers. For example the degree of structural perfection of the ZnS layers is rising on the one hand with the substrate temperature and on the other hand with decreasing thicknesses. In Fig. 5a one can see the ring electron diffraction pattern. It is typical for experiments performed in the range of substrate temperature from 250 to 300 °C. Fig. 5b shows some mosaic structure. This is typical for temperatures from 300 to 350 °C of the substrates. Epitaxial layers were obtained on substrates heated above 370 to 400 °C (Fig. 5c). The same temperature dependence of the layer structure was found also for ZnTe and CdTe [12].

On the other hand epitaxial CdS [9] and CdSe [13] layers were obtained in the whole temperature interval from 150 to 300 °C investigated by us. This fact may be employed for the production of CdS epitaxial layers at low temperatures.

Thin layers of ZnSe change their texture from {111} at low temperatures into {110} texture at high temperatures [14].

The $A^{II}B^{VI}$ layers obtained on the pyramidal and on the prismatic faces of the substrates were hardly oriented. They were very often polycrystalline and in other cases they possessed some texture. In general we got an impression that the Cd single crystal substrate oriented stronger than the Zn single crystal substrate. This holds true for the basal face of the crystals as well as for the pyramidal and prismatic faces.

III. 3. *Kinetics and mechanism of the layer formation*

An ellipsometric study of the zinc sulphidation kinetics has recently been started in our laboratory. The first data show a parabolic dependence of the layer thickness versus reaction time. These data are in a good agreement with WAGNER's theory [15] for metal oxidization.

The experimental results obtained on $A^{II}B^{VI}$ layers lead to the conclusion that the reaction proceeds through diffusion of interstitial metal ions in the chalcogenide thin film. WEISSMANTEL et al [16] were the first to suggest this mechanism for the formation of CdS layers on evaporated Cd layers. Some of the facts which confirm this suggestion in our case are summarized as follows:

1) The diffusion coefficients for Cd and Zn in chalcogenides are greater than those for metalloids [17].

2) The parabolic dependence established for the ZnS layer thickness as a function of the reaction time indicates that metal ions diffuse through the ZnS layer [18].

3) The observed growth of CdS whiskers shows that Cd is transported to the surface of the overgrown CdS film where it reacts with the sulphur.

4) As mentioned above the $A^{II}B^{VI}$ layers reproduced perfectly well the surface structure of the metal single crystals. Evidently the metal surface has been blocked by the first stages of the chalcogenide film formation. For the further growth of the layer metal ions have to diffuse through it. Otherwise, if the metalloid diffuses through the $A^{II}B^{VI}$/metal interface, the latter will be penetrating deeply the bulk of the metal single crystal and will change its form.

IV. Conclusion

Epitaxial $A^{II}B^{VI}$ thin layers were obtained on metal single crystal substrates at relatively low temperatures. We can expect that the metal/semiconductor interface in the case under consideration may exhibit interesting properties due to the lack of impurities since the whole procedure takes place in vacuum sealed glass ampoules.

REFERENCES

1. Physics and Chemistry of II—VI Compounds M. Aven and J. S. Prener, Editors, North-Holland Publ. Co., Amsterdam, 1967.
2. J. I. Pankove, Optical Processes in Semiconductors, Prentice-Hall, New Jersey, 1971.
3. D. B. Holt, Thin Solid Films, **24,** 1, 1974.
4. J. Du Bow, Electronics, **23,** 86, 1976.
5. L. Curran, Electronics, **23,** 91, 1976.
6. A. Rothwart and K. W. Böer, Progress in Solid State Chemistry, **10,** 71, 1975.
7. Handbook of Thin Film Technology, L. Maissel and R. Glang, Editors, McGraw-Hill Book Company, New York, 1970.
8. Chr. Nanev and D. Iwanov, Thin Solid Films, **35,** 155, 1975.
9. D. Iwanov and Chr. Nanev, J. Mat. Sci., **13,** 1449, 1978.
10. I. N. Stranski, Zs. Phys. Chem., B **38,** 451, 1938.
11. R. Kaischew and Chr. Nanev, phys. stat. sol., **10,** 779, 1965.
12. D. Iwanov and Chr. Nanev, to be published.
13. D. Iwanov, to be published.
14. D. Iwanov and Chr. Nanev, to be puslished.
15. Chemistry of the Solid State, W. E. Garner, Editor, Butterworths, London, 1955.
16. G. Hecht, J. Herberger and C. Weissmantel, Thin Solid Films, **2,** 293, 1968.
17. Atomic Diffusion in Semiconductors, D. Shaw, Editor, Plenum Press, London and New York, 1973.
18. K. Meyer, Physikalisch-chemische Kristallographie, VEB Deutscher Verlag für Grundstoffindustrie, Leipzig, 1968.

Acta Physica Academiae Scientiarum Hungaricae, Tomus 47 (1—3), pp. 93—105 (1979)

EPITAXIAL GROWTH OF SILICON SINGLE CRYSTAL LAYERS

By

G. Kósza, T. Kormány and L. Nagy

RESEARCH INSTITUTE FOR TELECOMMUNICATION, BUDAPEST, HUNGARY

CVD growth of Si on highly doped (111) Si substrates using the $SiCl_4-Si-H_2$ open tube system has been studied in a horizontal reactor by means of one-factorial experiments. It was recognized that for realizing a uniform growth rate in the samples not only deposition temperature but also the temperature distribution of the system characterized by the parameters T_{max} and x_t has to be considered.

From these experiments the central point for the multifactorial investigations could be located.

1. Introduction

In the last twenty years the epitaxial layer-growth process has been investigated from several aspects (thermodynamics, kinetics, autodoping, determination of layer characteristics, etc.) The optimization of this process, however, was a somewhat neglected field. To get the optimum conditions for the Si-layer growth by chemical vapour deposition (CVD) it is necessary to perform thermodynamical analysis, one-factor and multifactorial investigations. After performing the thermodynamical analysis of the system there are two ways for optimization: the numerical optimization of a possible theoretical model or the experimental optimization [1, 2]. In spite of many efforts a complete theoretical model of the epitaxial silicon layer growth does not exist presently, therefore the optimization has to be based on experimental results.

The growth rate of the epitaxial layer grown by the CVD process has been analysed and modelled by several authors. Previous theoretical results were reviewed of Bloem [3] to explain the kinetics of silicon growth from the vapour phase. A generalised equation was given by him for the growth rate as a function of position (x) along the susceptor. Unfortunately, the calculated growth rate values differ by a factor 3 or 4 from each other and therefore they cannot be used for design purposes. The importance of entry effects and their influence on the development of velocity and temperature profiles has been suggested by Ban [4]. Based on his measurements of transport phenomena the growth rate values, however, cannot be calculated from his model. Manke and Donaghey [5] used a model of "developing temperature" to calculate the mean gas-phase temperature and deposition rate distribution of silicon which gives the growth-rate values in case of a vertical cylinder reactor.

In this contribution the Si epitaxial layer growth in a horizontal reactor will be considered. In the course of our work a series of one-factorial experiments

were performed making use of some basic facts from the previous theories. As a consequence of the studies a suitable range of parameters, resulting in a uniform Si growth rate in horizontal reactors could be established. The experimental results could also be used to deduce some conclusions on the process parameters influencing the layer thickness and the dopant distribution uniformity.

2. Experimental work

A self-built RF-heated horizontal reactor was used in the experiments. The substrate was homogeneous, (111) oriented, As doped Si single crystal, free of dislocations (according to X-ray topography) with a specific resistance of $4-5 \cdot 10^{-3}$ ohmcm. Epitaxial layers were grown by the $SiCl_4$-procedure. In the process RS—Q quality $SiCl_4$ and electronic grade HCl gas was used, the H_2-gas has been Pd-purified.

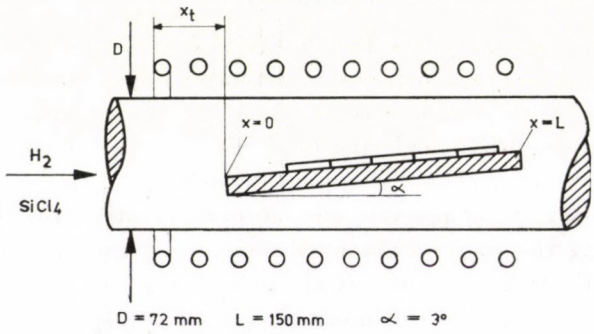

Fig. 1. Reactor tube and the main parameters

Before each growth cycle fresh Si has been deposited onto the etched graphite susceptor. The used wafers were backside lapped, without deposition. HCl-etching has been carried out for 1 minute, with 1% HCl in H_2, at the growth temperature, followed by annealing for 5 minutes in H_2. After completing the layer growth the annealing has been repeated. The pressure was approximately 1 atm because of the open tube system. No dopant gas has been added. Additive process parameters are summarised in Table I and in Fig. 2.

In Table I both the possible parameter ranges for the given layer growth system and the actually realized parameter values are indicated.

The following notations were used:

T_{max} maximum temperature measured at the crystal surface (°C),
V flow rate of hydrogen (lit/hour),
t_g time of the layer growth (min),
M_{SiCl_4} concentration of $SiCl_4$ in the input gas (molfraction).

Table I
Process parameters

Parameter	Range		Realized values
x_t (cm)	−10	18	−2; 8
T_{max} (°C)	900	1250	1100; 1200
V (l/n)	300	3000	800; 1300; 1800
t_g (min)		100	10; 20; 30
M_{SiCl_4} (molfraction)	$1 \cdot 10^{-4}$	$3 \cdot 10^{-3}$	$7.5 \cdot 10^{-4}$; $1.2 \cdot 10^{-3}$; $1.5 \cdot 10^{-3}$; $5.5 \cdot 10^{-4}$x; $2.5 \cdot 10^{-3}$x

x only in the case $V = 800$ l/h

The sketch of the experimental reactor tube is shown in Fig. 1, where X_t denotes the distance between the susceptor leading edge — and the edge of the RF coil.

$D = 72$ mm is the diameter of the quartz tube, $L = 150$ mm is the length of the graphite susceptor, $\alpha = 3^0$ is the tilting angle of the susceptor.

The Si-wafer position on the susceptor was characterized by the distance (x) from the leading edge.

The time dependence of the process parameters are given in Fig. 2. where C_{HCl} and M_{SiCl_4} denote the concentrations of the active components in the carrier gas measured in volume-percentage and molfraction, respectively. The parameter t stands for the complete process time which is the sum of the time intervals for the vapour phase etching, layer growth, heating and cooling cycles.

The epitaxial layer thickness was measured by IR-interference technique, the dopant distribution by a high frequency CV-method [6].

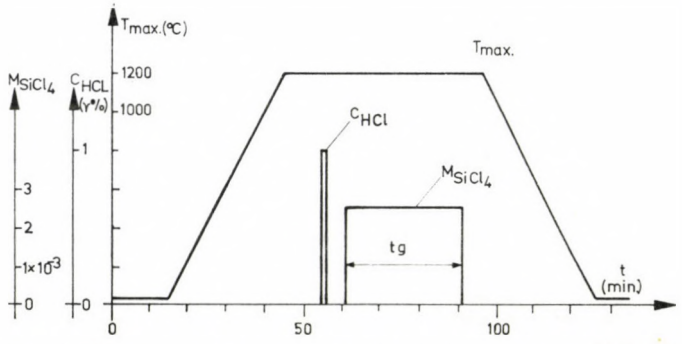

Fig. 2. Time functions and parameters of the general growth cycle

3. Results and discussion

It is well known that in case of small $SiCl_4$ concentration in the carrier H_2 gas, the layer growth rate G at a fixed wafer position x is linearly related to the mol fraction M of the $SiCl_4$:

$$G = k \cdot M. \tag{1}$$

In previous theories the constant k was supposed to be dependent on the gas flow rate V, the wafer position x and the growth temperature T, as follows:

$$k = f(V, x, T). \tag{2}$$

In our experimental work the layer growth rate G was measured for different process parameter values.

In Fig. 3 the growth rate G is given as function of the $SiCl_4$ concentration M for different gas flow rate values V. It can be seen that the increase of the gas flow rate from 800 l/h to 1800 l/h resulted in a similar increase of the k values from 246 to 364.

Next the functional dependence of the coefficient k on the process parameters has been investigated. From the experimental results it could be

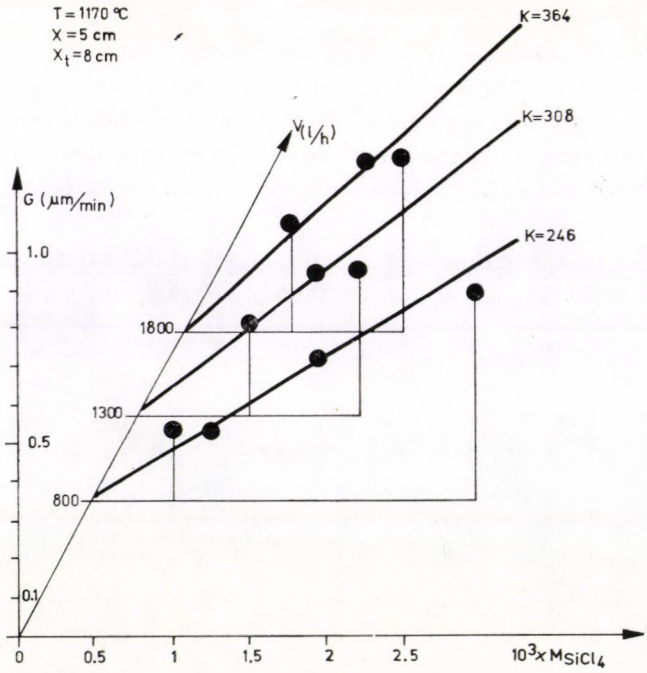

Fig. 3. The growth rate (G) as a function of the $SiCl_4$ mole fraction and hydrogen flow rate

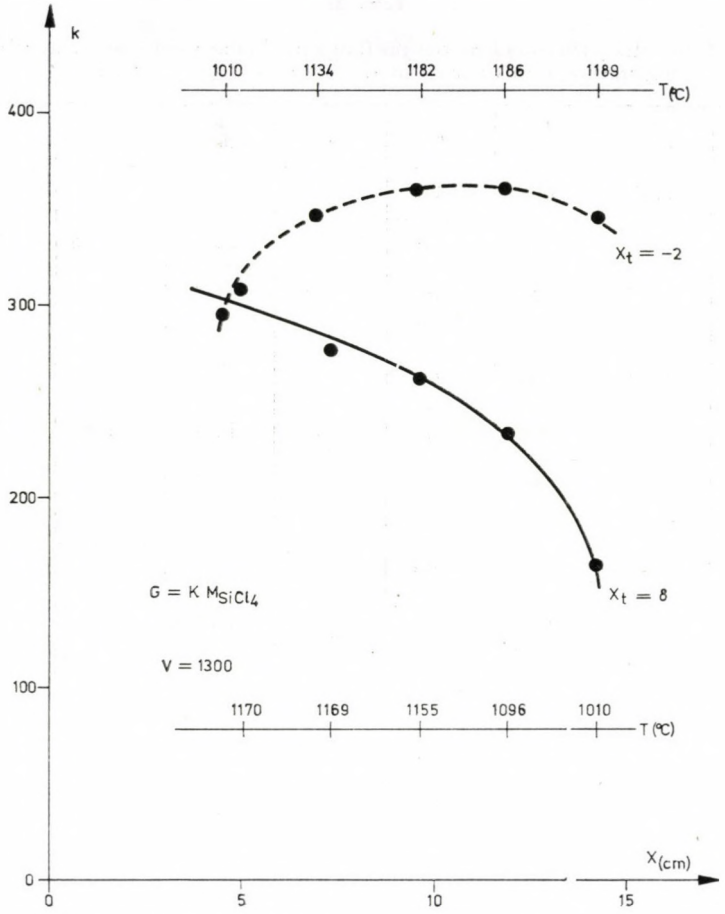

Fig. 4. Variation of k values along the graphite susceptor

recognized that the growth coefficient k was not uniquely determined by the parameters V, x and T as supposed in Eq. (2) but it was also influenced by the temperature distribution along the graphite susceptor. The measured results are summarized in Table II. The left hand side of the Table corresponds to the value $x_t = 8$ cm, on the right hand side the data for the case of $x_t = -2$ cm are given.

The experimental data have verified our assumption, that at the same temperature but at different wafer and graphite positions (x, x_t) the growth coefficients differ considerably and therefore to achieve nearly constant growth coefficients a suitable temperature distribution has to be realized. In our case placing the graphite susceptor at $x_t = -2$ cm position resulted in an almost uniform growth rate distribution (see in Fig. 4).

Table II

Dependence of growth coefficients k on the gas flow rate V, the wafer position x, and the growth temperature T in the case of $x_t = 8$ cm and $x_t = -2$ cm

x (cm)	T (°C)	V (lh^{-1})	k	k	V (l/h^{-1})	T (°C)	x (cm)
5	1169	800	246				
		1300	308	294	1300	1010	4.5
		1800	364				
7.3	1155	800	232				
		1300	277	347	1300	1134	6.9
		1800	307				
9.6	1096	800	213				
		1300	262	360	1300	1182	9.6
		1800	301				
11.9	1010	800	188				
		1300	233	361	1300	1186	11.8
		1800	268				
14.2	1170	800	141				
		1300	165	346	1300	1189	14.2
		1800	174				
$x_t = 8$ cm				$x_t = -2$ cm			

This suitable temperature distribution responsible for nearly constant growth rate values along the graphite susceptor resulted also in a layer-thickness uniformity. The growth rate distributions corresponding to the best and worst temperature distributions characterized by the parameters $x_t = -2$ cm, $T_m = 1190$ °C and $x_t = 8$ cm, $T_m = 1172$ °C, respectively, are shown in Figs. 5 and 6.

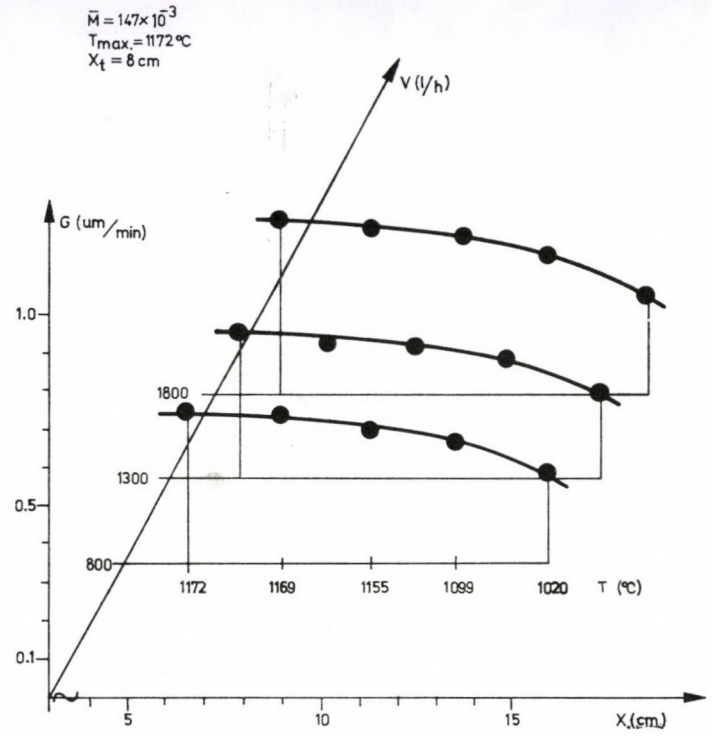

Fig. 5. Variation of growth rate (G) along the graphite susceptor using different gas flow rates, $x_t = 8$ cm

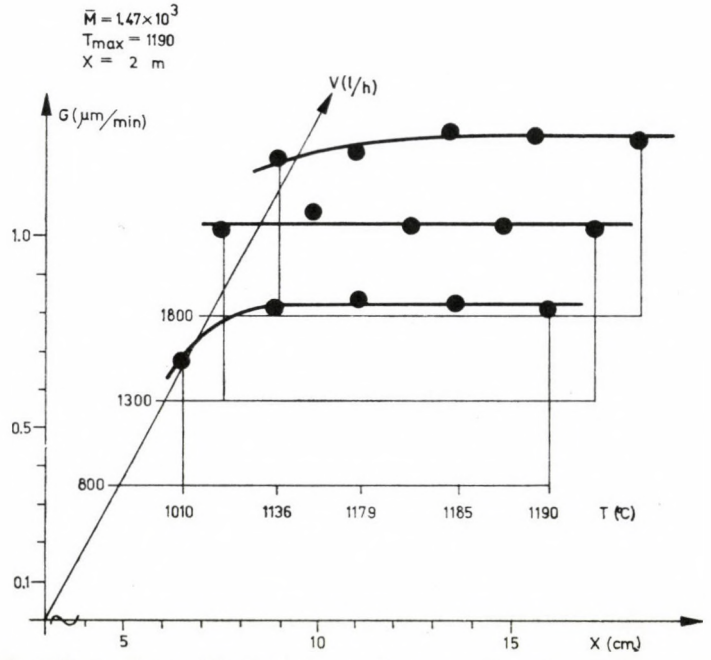

Fig. 6. Variation of growth rate (G) along the graphite susceptor using different gas flow rates, $x_t = -2$ cm

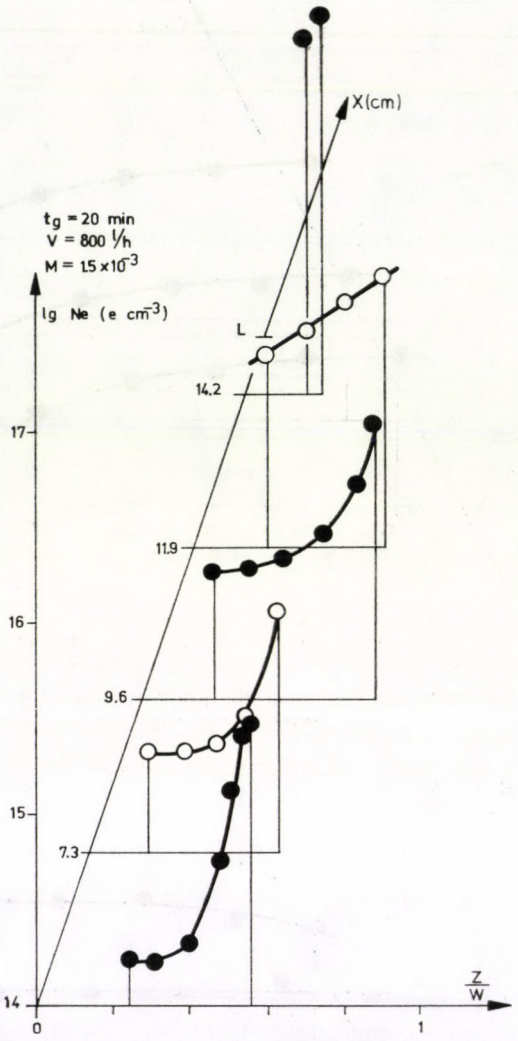

Fig. 7. Variation of dopant distribution along the graphite susceptor

Based on the measured data an experimental relationship between k and V can be formulated, as follows:

$$\log k = m \cdot \log V + b, \tag{3}$$

where the coefficients m and b depend on the temperature T and the position x. Some calculated values of m and b are summarized in Table III.

In the course of the epitaxial layer processing not only the growth rate and the epitaxial layer thickness but also the dopant distribution has to be

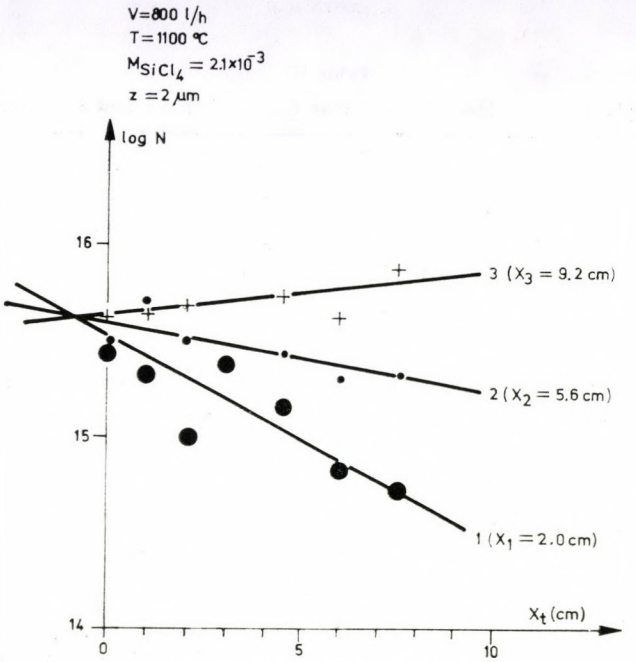

Fig. 8. Dopant concentration at $z = 2$ μm depth realizing different x_t-values (1, 2, and 3 are the wafer positions on the susceptor)

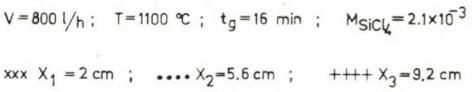

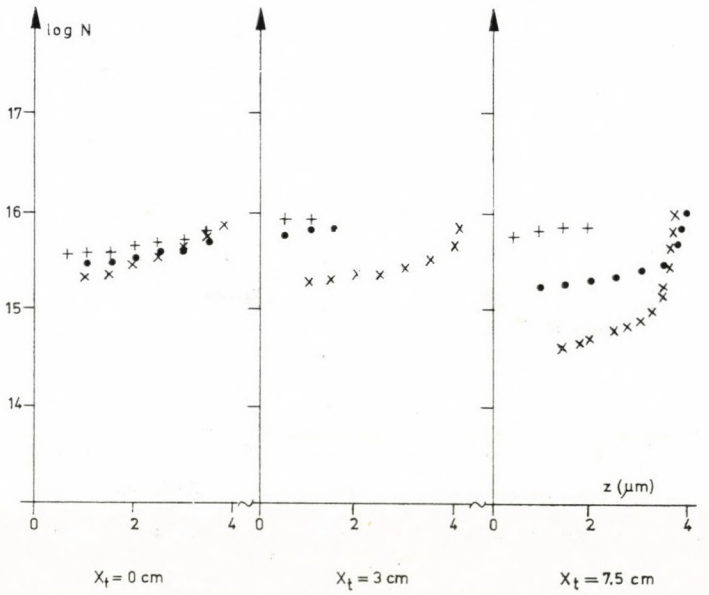

Fig. 9. Dopant distribution as a function of depth (z) at different x_t values

Table III

Experimental values of m and b at $T_{max} = 1170$ °C and $x = 8$ cm

x	T	m	b
5	1170	0.50	0.97
9.6	1155	0.41	1.16
14.2	1010	0.31	1.26

uniform. Therefore it is important to note that different susceptor positions characterized by x_t may result in considerable changes of the dopant concentration.

An unfavourable case is illustrated in Fig. 7. The dopant distribution in the epitaxial layer of the Si-wafers is strongly dependent on the position x at the susceptor. The minimum values of dopant concentration increase in the gas flow direction.

To investigate this phenomenon several graphite positions have been realized in the reactor tube and dopant profiles of the Si-epitaxial layers grown at different wafer position (x) were measured. The dopant concentration values

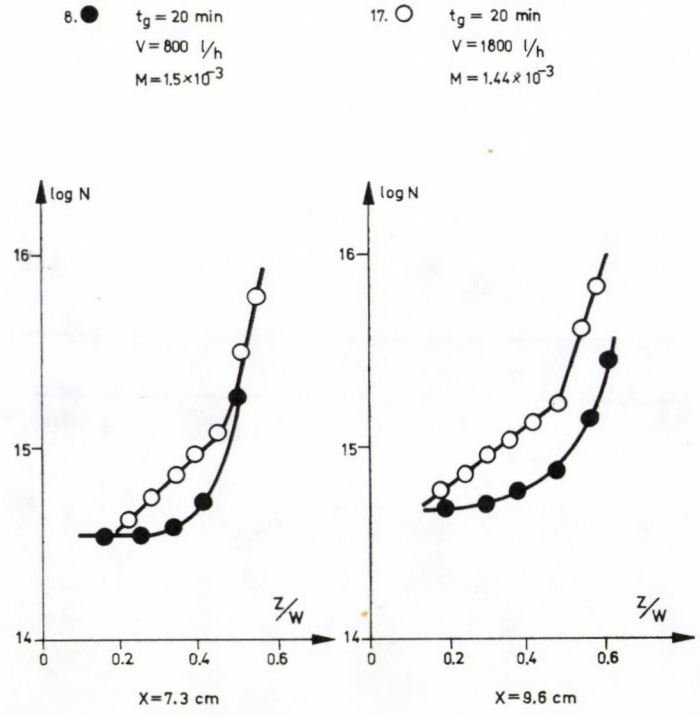

Fig. 10. Dopant distribution at different flow rates in the case of substrate positions $x = 7.3$ cm and $x = 9.6$ cm

for different wafer positions along the susceptor, measured at 2 μm depth in their epitaxial layers, are given in Fig. 8.

For the group of wafers built up in a given growth cycle the most uniform dopant concentration distribution resulted for $x_t = -1$ cm, this position being almost equal to the optimum position ($x_t = -2$ cm) for layer thickness uniformity.

The complete dopant distribution profiles for several wafers at different positions along the susceptor are compared in Fig. 9 for different x_t values. From the Figure it can be recognized that the optimum placement corrsponding to $x_t = -2$ cm results in a favourable coincidence of the dopant profiles also.

The result of the one-factorial experiments may be used to find the central point of the multifactorial investigations [1, 2]. To demonstrate this in Fig. 10 the dopant distribution is illustrated as a function of the wafer position on the graphite susceptor at two different flow rates. It is evident, that the autodoping effect has a minimum value at the lowest flow-rate

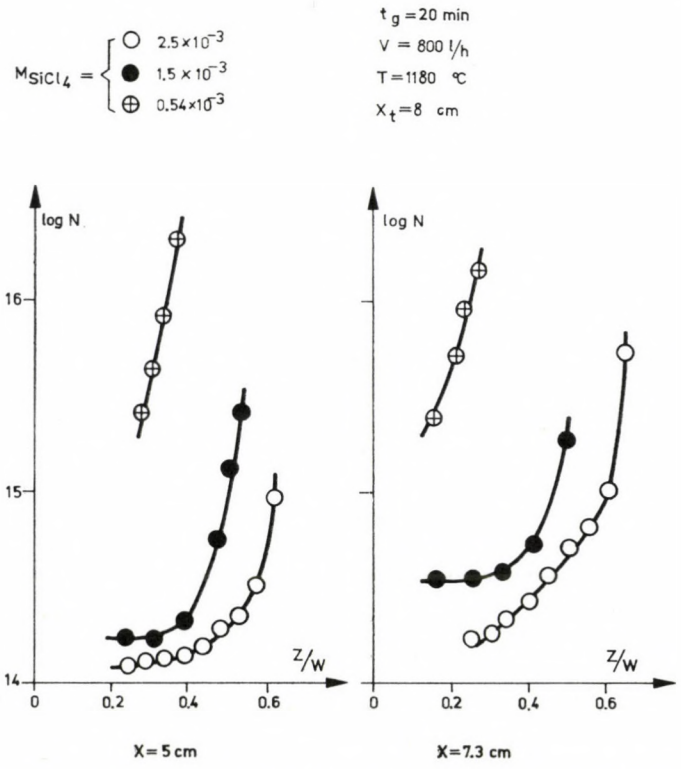

Fig. 11. Dopant distribution of different $SiCl_4$ mole fraction in the case of substrate position $x = 5$ cm and $x = 7{,}3$ cm

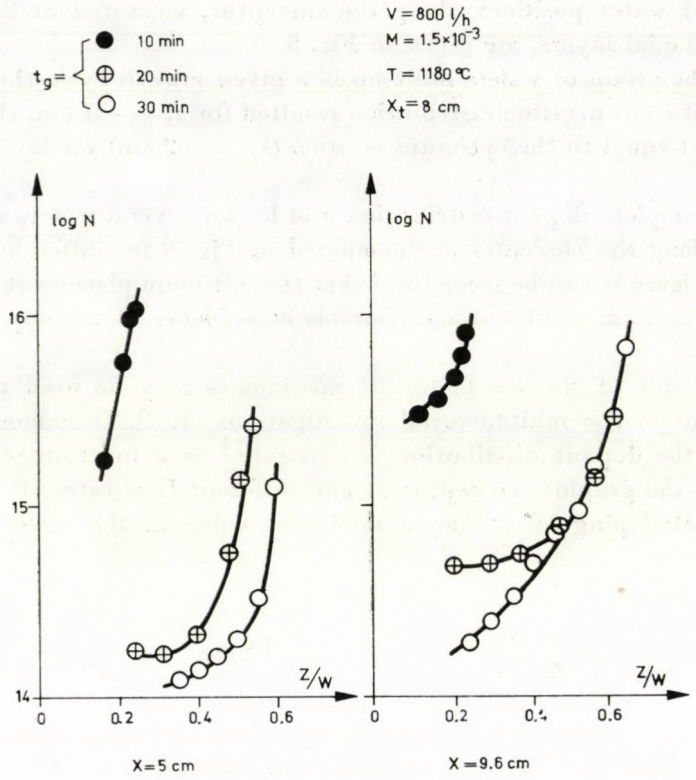

Fig. 12. Dopant distribution at different times of deposition in the case of substrate positions $x = 5$ cm and $x = 9.6$ cm

(800 l/h^{-1}) and therefore in the central point of the multifactorial investigations the flow rate value was chosen to be 800 l/h.

In view of similar considerations (see Fig. 11, 12) for the $SiCl_4$ concentration (M) and the deposition time (tg), the chosen values were $M = 2.5 \cdot 10^{-3}$ and $t_g = 30$ min, respectively.

4. Conclusions

CVD growth of Si on highly doped (111) Si substrates using the $SiCl_4$—Si—H_2 open tube system has been studied in a horizontal reactor by means of one-factorial experiments. It was recognized that for realizing a uniform growth rate in the samples not only deposition temperature but also the temperature distribution of the system characterized by the parameters T_{max} and x_t has to be considered. It is important that the uniform growth rate was in one-to-one correspondence with the uniform layer thickness and dopant distribution. Thus the process parameters established in our experiment

could be used advantageously in the technology of growing undoped silicon epitaxial layers by the CVD—$SiCl_4$-process. Introducing the new process parameter x_t the central point for the multifactorial investigations could be located.

Acknowledgements

We are grateful to Dr. F. A. KUZNETZOV and his Laboratory in Novosibirsk at the Institute of Inorganic Chemistry of the Siberian Branch of the Soviet Academy of Sciences for helpful discussions.

REFERENCES

1. G. E. P. BOX and K. B. WILSON, J. at the Royal Statistical Society, Series *B*, **13**, 1, 1951.
2. JU. P. ADLER, E. V. MARKOVA, JU. V. GRANOVSKIJ, Design of experiments to assess optimal conditions, Műszaki Könyvkiadó, Budapest, 1977 (in Hungarian).
3. J. BLOEM, Semiconductor Silicon 1977. 201, 1977. Edited by H. R. Huff and E. Sirtl, The Electrochem. Soc. Inc., Princeton, N. J.
4. V. S. BAN, J. Electrochem. Soc., **125**, 317, 1978.
5. C. W. MANKE and L. F. DONAGHEY, J. Electrochem. Soc., **124**, 561, 1977.
6. M. SIMEK, L. KÁLMÁN and T. GERŐ, Ann. of Res. Inst. Telecomm., 167—177, 1975.

Acta Physica Academiae Scientiarum Hungaricae, Tomus 47 (1—3), pp. 107—115 (1979)

ВЛИЯНИЕ ПРИМЕСИ СВИНЦА НА РАЗРУШЕНИЕ КРИСТАЛЛОВ NaCl ПОД ДЕЙСТВИЕМ ИЗЛУЧЕНИЯ РУБИНОВОГО ЛАЗЕРА

В. В. НАБАТОВ, Л. М. БЕЛЯЕВ, Н. Н. ДЫМЕНКО

ИНСТИТУТ КРИСТАЛЛОГРАФИИ АН СССР, МОСКВА, СССР

и

Р. ВОСКА

ИССЛЕДОВАТЕЛЬСКАЯ ЛАБОРАТОРИЯ ПО ФИЗИКЕ КРИСТАЛЛОВ ВАН, БУДАПЕШТ, ВЕНГРИЯ

Показано, что не вся примесь свинца, даже при малых концентрациях его в шихте находится в решетке в виде изолированного иона Pb^{2+}. Определенная часть примеси присутствует в кристалле в виде включений соединений свинца. Пороговая плотность мощности ($P_{\text{порог}}$) снижается от значения 10^9 вт/см^2 на порядок при изменении концентрации (C_{Pb}) примеси от 10^{-7} до 10^{-4} моль/моль. Эта зависимость имеет вид: $P_{\text{порог}} \sim \frac{1}{\log C_{Pb}}$.

Характерные особенности разрушения при $P = P_{\text{порог}}$: увеличение размера трещин с уменьшением концентрации примеси; появление окраски в зоне разрушения в образцах с $C_{Pb} \geq 10^{-4}$ моль/моль. Измерения микротвердости образцов подтверждают то, что эти особенности вызваны изменением механических свойств кристаллов. Рассмотрены включения различных соединений свинца. Высказано предположение, что разрушение обусловлено микровключениями интерметаллических соединений свинца размером не более 10^{-6} см.

Известно, что публикуемые экспериментальные данные о пороге разрушения прозрачных для лазерного излучения диэлектриков отличаются для одного и того же вещества [1, 2]. Это связывают с разной степенью оптической чистоты испытуемых материалов из-за возможного присутствия микроскопических включений примеси сильно поглощающих лазерное излучение [3, 4].

Теоретически задача о разрушении прозрачного диэлектрика для частного случая, когда в фокусе лазерного пучка находится единичное поглощающее включение, рассматривалась в ряде работ [5, 6, 7]. В общем случае, когда в объеме диэлектрика находится множество включений, решение ее встречает известные трудности. Точное вычисление порога пока невозможно. Оценки, сделанные на основании соотношений взятых из работы [8] показывают, что снижение порога станет заметным при плотности поглощающих включений более 10^8 см$^{-3}$ (при диаметре включения 10^{-4} см). Обычно в эксперименте пытаются установить корреляцию между порогом разрушения и числом включений. Для группы кристаллов LiF с примесями металлов (количество примеси не контролировалось) была подмечена качественная связь между порогом разрушения и числом включений и структурных не-

совершенств [9, 10]. Однако, изучение особенностей разрушения кристаллов с конкретными примесями и выяснение зависимости порога разрушения от содержания примеси в широком диапазоне концентраций ее в образцах не проводилось. С целью восполнения указанного пробела и была поставлена данная работа.

Характеристика исследуемых образцов

В качестве объекта исследования были выбраны кристаллы NaCl с примесью свинца. Кристаллы прозрачны на основной и удвоенной частоте рубинового лазера. A, B и C — полосы поглощения, обусловленные ионом свинца Pb^{2+} в анионном окружении лежат в ультрафиолетовой области [11]. Помимо изолированного иона Pb^{2+} в кристаллах NaCl: Pb в том случае, когда превышается предел растворимости примеси, присутствуют частицы фазы $PbCl_2$ [12]. Кроме того возможно существование двойных солей типа $mNaCl \cdot nPbCl_2$ [13] и агрегированных ассоциатов: примесный ион-катионная вакансия [14].

Кристаллы выращивались из расплава с помощью методики, которая позволяла производить дополнительную очистку шихты и выращиваемого кристалла [15]. Были получены 4 кристалла (№№ 1, 2, 3, 4) в виде цилиндрических стержней с концентрацией свинца в шихте соответственно 10^{-3};

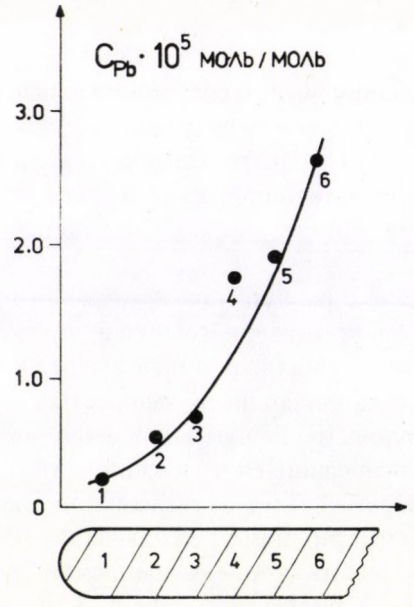

Рис. 1. Типичное распределение примеси свинца по длине стержня (на примере кристалла № 3). Цифры на кривой соответствуют номеру частей, на которые был разрезан стержень (изображен внизу).

10^{-4}; 10^{-5}; и 10^{-6} моль/моль. Кристалл № 1 в отличие от прочих был мутным, поскольку содержал включения выпавшей фазы $PbCl_2$.

Распределение примеси по длине кристаллов было неоднородным, так как оно определяется не только физико-химическими особенностями кристаллизуемой системы, но и технологическими факторами [16]. Для всех стержней концентрация примеси нарастала к части стержня, относящейся к конечной стадии кристаллизации (рис. 1).

Данные о распределении примеси были получены следующим образом. Стержень распиливался поперек, параллельно грани (100) на 5—6 (в зависимости от длины стержня) частей. Из центральной области каждой части вырезался образец. Это делалось для получения однозначных результатов, поскольку могла иметь место и радиальная зависимость распределения примеси. Предварительно для нескольких образцов концентрация свинца была определена с помощью количественного химического анализа. Эта концентрация была сопоставлена с максимумом А-полосы поглощения ($\lambda = 274$ нм) этих же образцов. Полученная графическая зависимость дала возможность с помощью только спектрофотометрических измерений получить необходимые данные о содержании свинца в любом образце. Для области малых концентраций мы сочли возможным пользоваться экстраполяционными значениями.

Исходя из пропорциональности между концентрацией иона свинца ($C_{Pb^{2+}}$) и коэффициентом поглощения $\varkappa$ в А-полосе, имеющей место при малых концентрациях примеси, были получены сведения о концентрации иона свинца. При этом $C_{Pb^{2+}}$ для 1-ой части стержня определялось из равенства $C_{Pb^{2+}} = KC_0$. Здесь: K — коэффициент распределения, который в соответствии с результатами работы [17] был взят равным 0,15, а C_0 — исходная концентрация примеси в шихте. В таблице I на примере кристалла № 3 сопоставлены для разных его частей общая концентрация свинца (C_{Pb}) и концентрация иона свинца ($C_{Pb^{2+}}$).

Таким образом, даже при малой исходной концентрации только часть примеси свинца входит в NaCl в виде иона Pb^{2+}.

Таблица I

№ части	$\varkappa$ см$^{-1} \cdot 10^2$	C_{Pb} моль/моль $\cdot 10^5$	$C_{Pb^{2+}}$ моль/моль $\cdot 10^5$
1	3,7	2,1	1,5
2	5,6	5,0	2,3
3	7,4	9,0	2,9
4	8,1	10,5	3,2
5	8,7	12,5	3,5
6	9,5	14,5	3,8

В экспериментах по лазерному разрушению использовались прямоугольные образцы размером $10\times10\times7$ мм³, полученные выкалыванием по плоскостям спайности. Поверхности, через которые проходил лазерный пучок, не полировались, поскольку было показано [18], что ступени скола не влияют на порог объемного разрушения.

Методика исследования

Использовалась общепринятая методика исследования разрушения. В качестве источника излучения использовался рубиновый лазер, добротность которого модулировалась пассивным затвором. Параметры импульса были следующие: длительность на полуширине — 50 нсек, выходная мощность, контролируемая калориметром ИКТ—1м, — $2\cdot10^6$ вт. Благодаря селекции поперечных мод, интегральное за время действия импульса распределение интенсивности по сечению пучка, описывалось гауссовым законом. Излучение фокусировалось в объем образца линзой с фокусным расстоянием $f = 2{,}1$ см. Минимум каустики располагался на расстоянии $2 \div 3$ мм от входной поверхности. Интенсивность излучения менялась нейтральными фильтрами. За порог разрушения принималась минимальная мощность ($P_{\text{порог}}$) при которой имело место разрушение. Каждая исследуемая точка объема подвергалась однократному воздействию импульса лазера. Факт разрушения устанавливался по вспышке, сопровождающей разрушение, а также по появлению рассеяния света газового лазера ЛГ-36.

Основная ошибка при оценке порога складывается из погрешности измерения мощности лазера и погрешности определения мощности, вызывающей разрушения. Последняя оценивается разностью между пороговой мощностью и мощностью, при которой в процессе эксперимента разрушение уже не происходит. Практически эта погрешность задается ступенями ослабления интенсивности пучка примененных нейтральных фильтров. Относительная ошибка измерения мощности не превышала $\pm$ 10%, а погрешность установления порога была не хуже — 10%.

Порог разрушения

Опыты показали, что порог разрушения NaCl снижается с увеличением содержания свинца (рис. 2). Нижний предел порога $0{,}1\cdot10^9$ вт/см² соответствует образцам с максимальной концентрацией примеси 10^{-3} моль/моль. В этих образцах присутствовали частицы фазы $PbCl_2$. В чистых беспримесных кристаллах порог разрушения определяется механизмом ударной ионизации [19]. Поэтому по мере уменьшения количества примеси $P_{\text{порог}}$ должен стремиться к постоянному значению. Однако, верхний предел $P_{\text{порог}}$ в эксперименте не был достигнут. Возможно здесь сказалось присутствие примесей

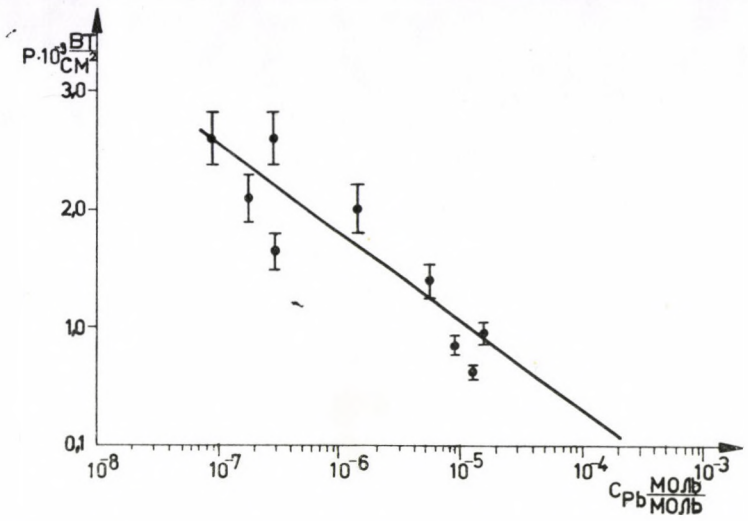

Рис. 2. Изменение пороговой плотности мощности $P_{\text{порог}}$ с концентрацией примеси свинца в NaCl

прочих 2-х валентных металлов, концентрация которых в исследуемых кристаллах не превышала 10^{-6} моль/моль.

В соответствии с теорией, в материалах, содержащих поглощающие включения, порог разрушения обратно пропорционален концентрации включений [6, 20]. В нашем случае график (рис. 2) описывается функцией вида $P_{\text{порог}} \sim \frac{1}{\log C_{\text{Pb}}}$. Таким образом в кристаллах NaCl примесь Pb влияет на оптическую прочность, но слабо: порог разрушения меняется на порядок, в то время как концентрация примеси — на три порядка.

Вид повреждений и окраска зоны разрушения

Вид повреждений исследованных образцов зависел от содержания примеси в них и мощности импульса. В области C_{Pb} $10^{-4} \div 10^{-7}$ моль/моль при $P = P_{\text{порог}}$ появляется одна, реже две зоны разрушения. Их особенность по сравнению с данными [21, 22], состоит в значительности размеров полости (40 ÷ 60 мк) в центре зоны разрушения и трещин (0,8 ÷ 1,5 мм) (рис. 3). Сопоставление длительности импульса, длины трещин и известной [23] предельной скорости их распространения дает основание считать, что развитие трещин вследствие термоупругих напряжений продолжается и после окончания лазерного имьульса.

В образцах, где C_{Pb} порядка 10^{-3} моль/моль размеры единичных трещин малы, всего лишь доли миллиметра. С повышением пороговой мощ-

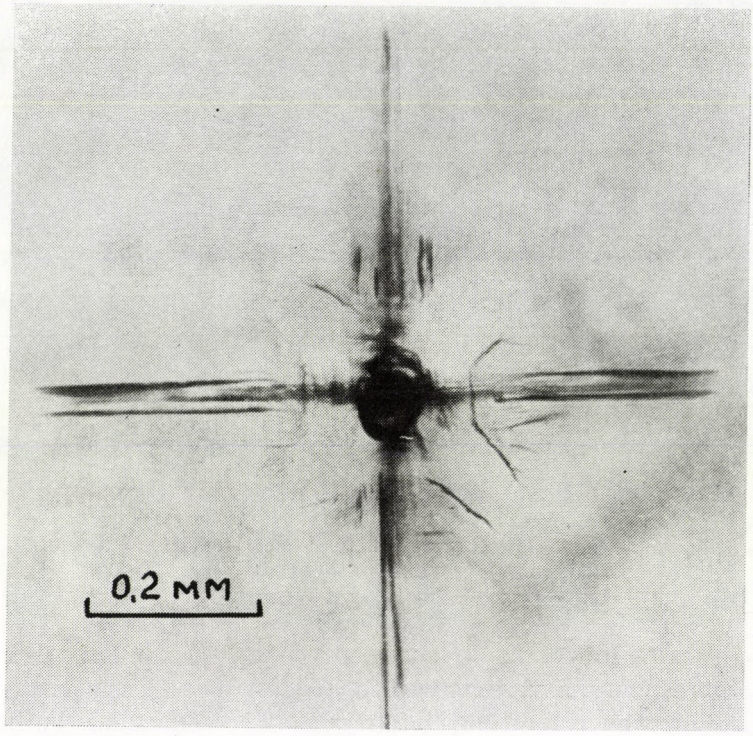

Рис. 3. Картина разрушения образца NaCl : Pb при $P = 2 \cdot 10^9$ вт/см². Концентрация примеси: $C = 3 \cdot 10^{-7}$ моль/моль. Излучение лазера направлено перпендикулярно рисунку.

ности до $P = 2P_{\text{порог}}$ в образцах с $C_{\text{Pb}} 10^{-4} \div 10^{-7}$ моль/моль увеличивается размер повреждения. Число повреждений при этом, в отличие от зафиксированных в [9] не менялось. Лишь в образцах с концентрацией примеси свинца порядка 10^{-3} моль/моль рост мощности приводит к возрастанию числа повреждений, так что образуется трек.

Ранее отмечалось появление синеватой окраски в зоне разрушения NaCl (чистота образцов указана не была). Предполагалось, что она вызвана либо возникновением электронных центров окраски [24], либо выпадением коллоидных частиц металла [25]. Нами обнаружено, что окрашивание имеет место при разрушении образцов с концентрацией Pb не менее 10^{-4} моль/моль. Окрашивается центральная часть зоны разрушения в плоскости трещины, перпендикулярной направлению пучка. Обычно окраска наблюдается на границе застывшего расплавленного вещества всей зоны или ее участка. В разных участках интенсивность окраски не одинакова (рис. 4). Распределение окраски и цвет ее говорят о том, что она обусловлена выпадением коллоидальных частиц металла.

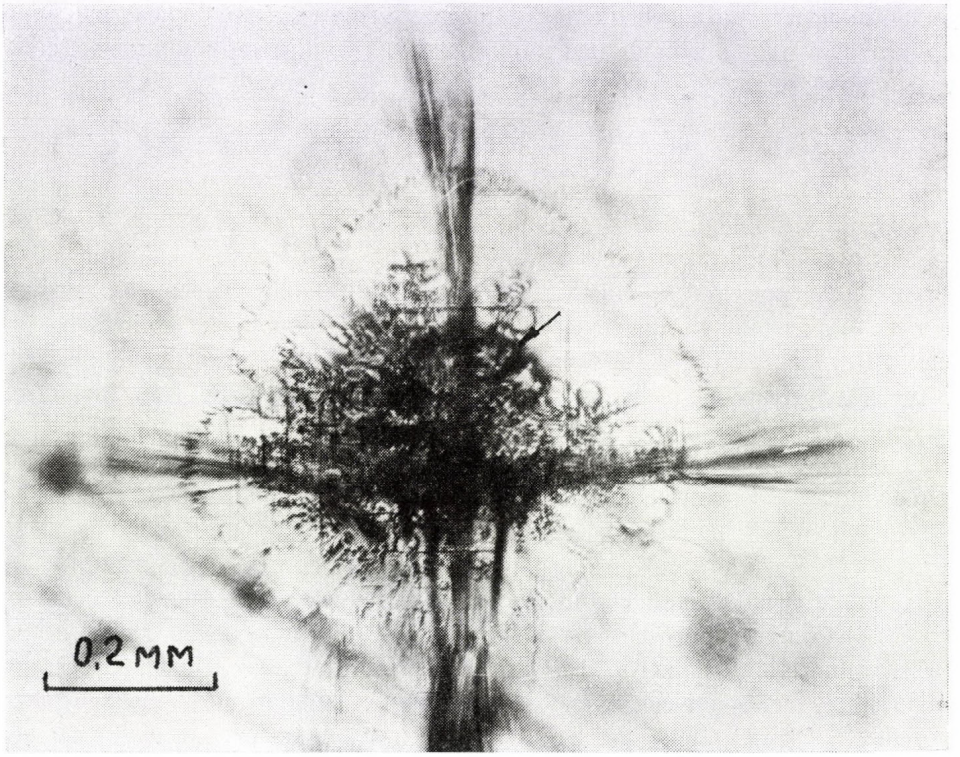

Рис. 4. Появление окраски (темная кайма, отмеченная стрелкой) в образцах NaCl : Pb при $C_{Pb} \geq 10^{-4}$ моль/моль

Не вызывает сомнений, что различный вид повреждений в зависимости от концентрации примеси обусловлен изменением механических свойств образцов. Об этом свидетельствуют полученные нами данные по микротвер-

Таблица II

Изменение микротвердости в кристаллах NaCl : Pb с концентрацией примеси

C_{Pb} моль/моль	10^{-3}	10^{-4}	10^{-5}	10^{-6}
H кг/мм^2	20,40	17,4	20,0	17,35

дости (таблица II), которая является одним из показателей механических свойств материалов [26, 27].

В явлении окрашивания механические свойства материала также играют определенную роль. Дело в том, что процесс выпадения частиц металла становится возможным при какой-то конкретной температуре и

давлении перегретого вещества в зоне разрушения. Эти параметры определяются не только мощностью импульса, но также и термоупругими свойствами материала.

Обсуждение результатов

Выше было показано, что определенная часть примеси свинца не входит в решетку NaCl и присутствует в кристалле, по-видимому, в виде включений. Изменение оптической прочности, естественно, необходимо связать с наличием этих включений. Если бы в образцах имелись включения только одного диаметра порядка 10^{-6}; 10^{-5} или 10^{-4} см, то в соответствии с количеством примеси плотность включений, к примеру, в кристалле № 3 достигала бы значения 10^{13}; 10^{10} или 10^{7} см$^{-3}$. Однако, проведенные нами эксперименты по выявлению включений методом ультрамикроскопии не подтвердили выше приведенные оценки. Рассеивающие частицы плотностью не более 10^{8} см$^{-3}$ и диаметром $10^{-5} \div 10^{-4}$ см наблюдались только вдоль границ блоков в кристалле № 2. В кристаллах № 3, 4 было отмечено полное отсутствие каких-либо рассеивающих свет частиц. Заметим, что чувствительность метода при использовании газового лазера мощностью 40 мвт обеспечивала регистрацию частиц с плотностью гораздо меньшей, чем 10^{7} см$^{-3}$. Отсутствие рассеяния в нашем случае может быть объяснено наличием включений, размер которых меньше 10^{-6} см, а также наличием включений с показателем преломления, мало отличающимся от показателя преломления основной матрицы.

Теория показывает, что чем меньше частица, тем большим должен быть ее коэффициент поглощения, чтобы частица инициировала разрушение материала. При плотности мощности в наших экспериментах 10^{9} вт/см^{2} и «опасном» радиусе частицы $2 \cdot 10^{-5}$ см, приводящем к пробою, коэффициент поглощения ее должен быть не менее 10^{4} см$^{-1}$. Оценки сделаны нами на основании соотношений, взятых из работы [8], причем фигурирующий там коэффициент α принят как и в [6] равным 0,1. Эти оценки и результаты опытов по рассеянию дают основание считать, что включения типа $PbCl_2$ и агрегированных ассоциатов не должны приводить к разрушению.

Однако, значительные коэффициенты поглощения могут иметь интерметаллические соединения свинца. Система натрий-свинец насчитывает не менее пяти соединений типа Na_xPb_y [28, 29]. К сожалению, литературные данные по исследованию этой системы в матрице NaCl отсутствуют. Возможно, что существенную долю примеси в кристаллах NaCl : Pb составляют агрегированные ассоциаты и мельчайшие включения фазы $PbCl_2$. И только незначительная доля относится к интерметаллическим соединениям. Присутствие последних и определяет наблюдаемое на опыте влияние примеси Pb на оптическую прочность. Если допустить, что плотность (n) включений интерметаллических соединений пропорциональна логарифму концентрации,

т. е. $n \sim \log C_{Pt}$, то получается $P_{\text{порог}} \sim \frac{1}{n}$. Именно такая зависимость имеет место при рассмотрении оптического пробоя на поглощающих включениях.

ЛИТЕРАТУРА

1. D. Olness, Journ. Appl. Phys., **39,** I, 1968.
2. Дж. Рэди, Действие мощного лазерного излучения, «Мир», Москва, 1974.
3. R. W. Hopper, B. R. Uhlmann, Journ. Appl. Phys., **41,** 4023, 1970.
4. Е. М. Акуленок, Ю. К. Данилейко, А. А. Маненков, В. С. Нечитайло, А. Д. Пискун, В. Я. Хаимов-Мальков, Письма в ЖЭТФ, **16,** 336, 1972.
5. Ю. К. Данилейко, А. А. Маненков, В. С. Нечитайло, А. М. Прохоров, В. Я. Хаимов-Мальков, ЖЭТФ, **63,** 1030, 1972.
6. С. И. Анисимов, Б. И. Макшанцев, ФТТ, **15,** 1090, 1973.
7. Б. И. Макшанцев, П. С. Кондратенко, Г. М. Гандельман, ФТТ, **16,** 173, 1974.
8. И. В. Алешин, С. И. Анисимов, А. М. Бонч-Бруевич, Я. А. Имас, В. А. Комолов, ЖЭТФ, **70,** 1214, 1976.
9. Н. В. Волкова, ФТТ, **12,** 616, 1970.
10. Н. В. Волкова, ФТТ, **12,** 2182, 1970.
11. J. S. Dryden, G. G. Harvay, Journ. Phys. C. Solid State Phys., **2,** 613, 1969.
12. Р. И. Гиндина, Труды Ин-та физ. и астроном. Тарту, **11,** 91, 1960; Е. К. Завадовская, М. П. Игнатьева, И. Я. Мелик-Гайказан. Изв. АН СССР сер. физич., **29,** 68, 1965. J. Baltog, C. Ghita, M. Giurgea, Journ. Phys. C. Solid State Physics. **7,** 1892, 1974.
13. A. Bohun, J. Dolejŝi, M. Simeĉkova, H. Svobodova, Z. Physik., **243,** 244, 1971.
14. M. Hartmanová, phys. stat. solidi (a), **7,** 303, 1971.
15. R. Voszka, I. Tarján, L. Berkes, J. Krajsovsky, Kristall und Technik, **1,** 423, 1966. K. Raksany, R. Voszka, Kristall und Technik, **4,** 227, 1969. R. Voszka, K. Raksany, L. Berkes, Kristall und Technik, **5,** 409, 1970.
16. В. Я. Хаимов-Мальков, В. А. Перльштейн, Кристаллография, **4,** 904, 1959.
17. О. Л. Крейнин, К. М. Розин, М. П. Шаскольская, Сб. «Рост кристаллов» IX, «Наука», стр. 167.
18. Н. А. Алексеев, Н. В. Волкова, Г. В. Степанова, Л. М. Шестопалов, ФТТ, **11,** 2720, 1969.
19. B. Bräunlich, A. Schmid, P. Kelly, Appl. Phys. Lett., **26,** 4, 150, 1975.
20. С. И. Анисимов, В. А. Комолов, ФТТ, **16,** 575, 1974.
21. D. Olness, Appl. Phys. Lett., **8,** 11, 283, 1966.
22. М. С. Бродин, В. Н. Ватулеев, А. М. Камуз, Сб. «Нелинейная оптика», стр. 267, Новосибирск, 1968.
23. J. J. Gilman, C. Knudsen, W. P. Walsch, Journ. Appl. Phys., **29,** 601, 1958.
24. Н. И. Алексеев, Н. В. Волкова, В. В. Лихачев, Л. М. Шестопалов, ФТТ, **10,** 2403, 1968.
25. М. С. Бродин, В. Н. Ватулеев, С. В. Закревский, А. М. Камуз, Квант. электроника. Тр. республиканского семинара по квант. элекронике, Киев, 1966, стр. 77.
26. J. J. Gilman, Australian Journ. Phys., **13,** 2A, 325, 1960.
27. Ю. С. Боярская, «Деформирование кристаллов при испытаниях на микротвердость». «Штиинца», Кишинев, 1972 г.
28. K. Zintl; R. Harder Z. Phys. Chem., **34,** 283, 1936.
29. В. Я. Аносов, С. А. Погодин. «Основные начала физико-химического анализа». гл. XIII, §4, М.-Л., 1947.

Acta Physica Academiae Scientiarum Hungaricae, Tomus 47 (1—3), pp. 117—123 (1979)

A NEW METHOD OF CONTROLLED DOPING OF ALKALI HALIDE CRYSTALS WITH Pb IONS

By

K.-J. BERG and F. FRÖHLICH

DEPARTMENT OF PHYSICS, MARTIN-LUTHER-UNIVERSITY, HALLE, GDR

By optical absorption measurements and by further analytical methods it is shown that by thermal treatment at temperatures above 400 °C lead evaporates from Pb doped alkali halide crystals for which the essentially higher vapour pressure of $PbCl_2$ as compared to that of the crystals is responsible. On the other hand it is possible to introduce lead into the crystals by annealing in $PbCl_2$ atmosphere. On the basis of these effects several experimental methods can be deduced by which any defined lead concentration in a given specimen of alkali halide crystals can be realized.

1. Introduction

It is well known that alkali halide crystals doped with lead exhibit characteristic absorption bands in the ultraviolet spectral region (see e.g. the review article by FOWLER [1]). According to the generally used notation the bands are designated A, B, C_1, C_2 and C_3 in the sequence of decreasing wavelength of the peak position (see Fig. 1, full line curve). Additional bands of the Pb induced absorption (D bands) are observed in vacuum ultraviolet region. The absorption coefficient at the peak of the A band is often used in the literature for the determination of the lead concentration in the crystal (see e.g. [2, 3, 4]). At least in the case of NaCl crystals one must be cautious using this method because the absorption spectrum related to the Pb incorporated is highly sensitive to the thermal treatment of the crystals (e.g. [2, 5, 6]); see also Fig. 1). Only after rapid quenching from temperatures above 400 °C can prominent A, B and C bands be measured. In a previous paper [7] therefore a different simple method was described by means of which the content of Pb in NaCl crystals can be determined quantitatively for any thermal pretreatment. On the basis of this method the distribution coefficient of Pb in NaCl crystals — grown by the Kyropoulos technique in air — was calculated [8]. During these investigations lead was found to evaporate preferentially from the melt before the growing process starts leading to a decrease of the initial concentration in the melt. As a plausible reason for this the essentially higher vapour pressure of $PbCl_2$ as compared to that of NaCl was suggested.

The aim of the paper presented is to show that also in the case of Pb doped crystals the high vapour pressure of $PbCl_2$ is responsible for a drastic decrease of the Pb content, if the crystals are annealed sufficiently long at

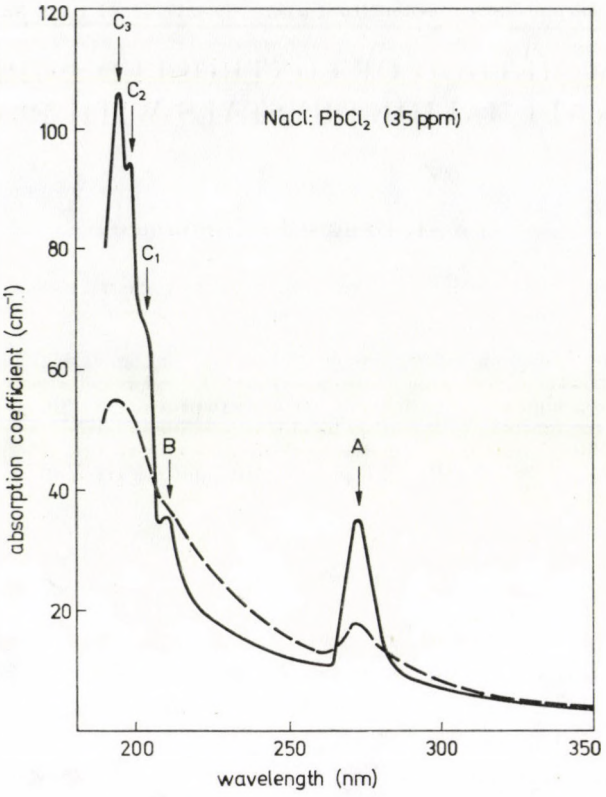

Fig. 1. Ultraviolet absorption of a sodium chloride crystal containing 35 ppm lead ions measured after quenching from 600 °C (full line curve) and after subsequent annealing at 170 °C for 22 h (dashed line curve)

temperatures above 400 °C. Using this effect several experimental methods are proposed by which any defined Pb concentration in a given specimen of alkali halide crystals can be realized.

2. Experimental

The growth of the single crystals was performed by the Kyropoulos method in air. The doping was achieved by adding $PbCl_2$ to the melt. All starting materials had analytical grade purity and were supplied by VEB Laborchemie, Apolda, GDR. One NaCl crystal was grown by the Bridgman method using starting materials purified by a method of Voszka et al [10] by which oxygen containing impurities especially OH^- ions are excluded.

The concentration of lead in the crystals was determined by measuring the Pb induced optical absorption of aqueous solutions of the crystals [7, 9]

and in some cases additionally by the spectral analysis of the crystals.* For the annealing of the specimens ($10 \times 10 \times 0.5$ mm^3 dimension) muffle furnaces with electronic temperature control (± 1 K) were used. Special openings in the furnace walls gave a direct connection with the room atmosphere. After each annealing process the specimens were quenched to room temperature (RT) on an aluminium plate. For annealing temperatures above 400 °C the absorption coefficient at the peak of the A band was used as a relative measure for the lead concentration in the specimen under investigation as explained in the introduction. All measurements of the optical absorption were carried out by a spectrophotometer DK — 2A (Beckman Instr., USA) at RT.

3. Results and discussion

Annealing of Pb doped NaCl crystals exhibiting prominent A, B and C bands (produced by short time heating at 600 °C) at temperatures above 400 °C leads to a decrease of these bands. The shape of the spectrum remains unchanged. At temperatures lower than 400 °C this effect is not so clearly evident because here one has to expect aggregation phenomena of the Pb ions inducing changes of the absorption spectrum (e.g. [5, 6]; see also Fig. 1). In Fig. 2 the

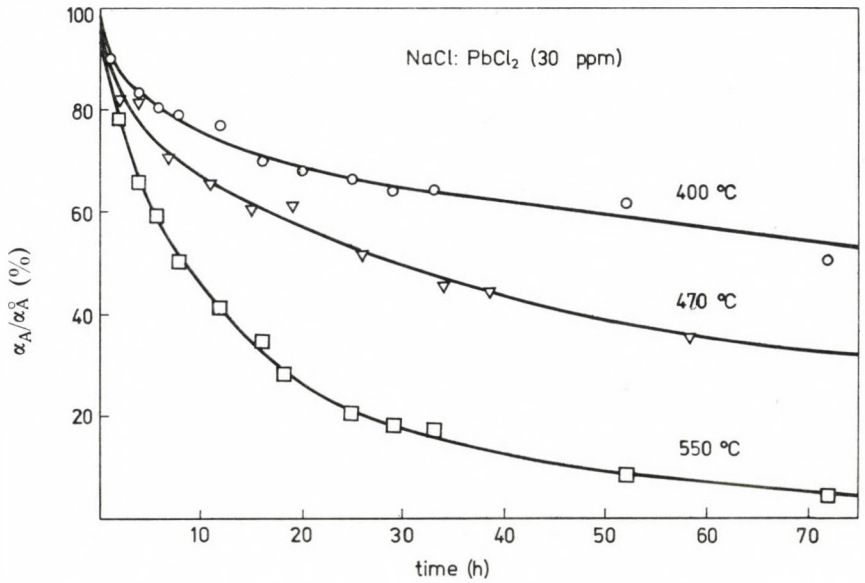

Fig. 2. Decrease of the A band absorption as a function of annealing time at different temperatures for a NaCl crystal containing 30 ppm lead ions

* We want to thank Dr. M. Bubig of the Analytical Laboratory of VEB Filmfabrik Wolfen, GDR, for performing these measurements.

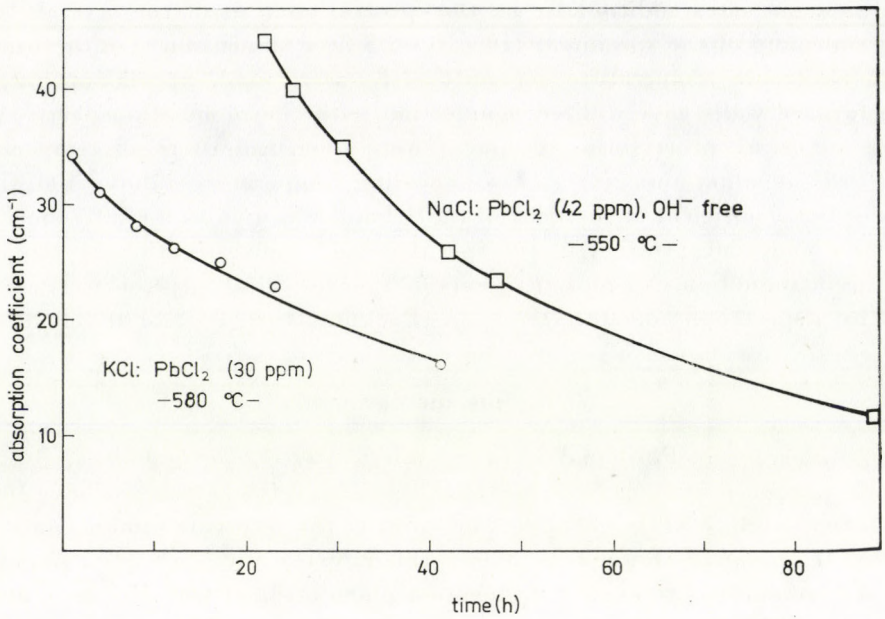

Fig. 3. Decrease of the absorption coefficient at the peak of the A band as a function of annealing time at 550 °C and 580 °C for an OH^- free NaCl crystal, containing 42 ppm lead ions and a KCl crystal containing 300 ppm lead ions, respectively

absorption coefficient α_A at the peak of the A band (normalized to α_A^0, measured after a pretreatment of 10 minutes at 600 °C) is shown as a function of the annealing time at different temperatures. One can see clearly the decrease of the A band absorption with time and the increasing rate with increasing temperatures. After an annealing time of 100 h at 550 °C the Pb induced absorption has practically disappeared.

Fig. 3 shows the same effect for the OH^- free NaCl crystal and for a Pb doped KCl crystal too.

For all NaCl crystals — after the total decay of the A band — the absolute lead content was determined in the two different ways mentioned in Chapter 2. Both methods give the same result: the crystals no longer contain lead. That can only mean that lead evaporates from the crystals during annealing. As a reason for this one can assume an essentially higher vapour pressure of $PbCl_2$ as compared to that of NaCl. In Fig. 4 the vapour pressure of $PbCl_2$, NaCl and KCl, taken from LANDOLT—BÖRNSTEIN [11] is plotted against the temperature. In the temperature region between 400 °C and 600 °C considered here the vapour pressure of $PbCl_2$ is about four orders of magnitude higher than that of NaCl. It should be noted that the vapour pressure curves of Pb and of the chlorides of divalent cations like $CaCl_2$, $BaCl_2$, and $MnCl_2$ preferentially used for doping are situated on the right hand side of the NaCl and

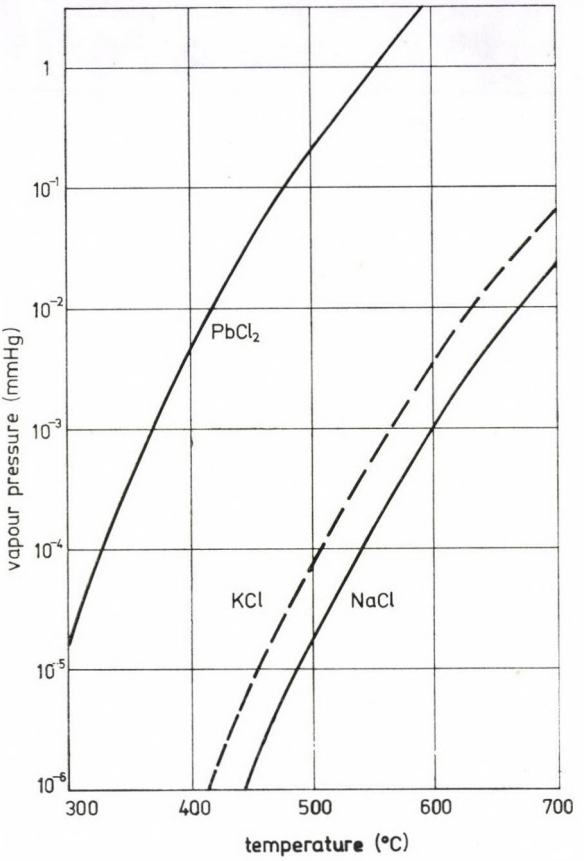

Fig. 4. Vapour pressure of $PbCl_2$, KCl and NaCl taken from LANDOLT—BÖRNSTEIN [11] plotted against the temperature

KCl curves. This means that lead is evaporated in the form of $PbCl_2$ and that one cannot expect an evaporation of e.g. $CaCl_2$, $BaCl_2$ and $MnCl_2$ from correspondingly doped crystals.

By annealing experiments in different atmospheres it could be proved that the vapour pressure actually is the responsible quantity. In contrast to the previously described heat treatments these experiments were performed in closed quartz ampoules with an annealing time of 100 h at 600 °C: If the ampoule contains air after such a treatment the absorption coefficient α_A is not changed with respect to the value α_A^0 measured after 10 minutes annealing at 600 °C before inserting the specimen into the ampoule (compare Table I, column 2). This result surprising at first sight will be clear if one calculates the partial vapour pressure at equilibrium of the $PbCl_2$ in the ampoule amounting to 3×10^{-4} mm Hg. For the formation of this pressure under the given con-

Table I

Change of the adsorption coefficient at the peak of the A band measured after annealing in different atmospheres

Atmosphere	Air	Vacuum	$PbCl_2$ vapour	Vacuum
α_A° (cm^{-1}) (crystal 1)	71	72	75	86
α_A (cm^{-1}) (crystal 1)	71	72	extremely high	39
α_A° (cm^{-1}) (crystal 2)	—	—	—	0
α_A (cm^{-1}) (crystal 2)	—	—	—	45

ditions (0.05 cm^3 volume of the crystal specimen and 36 cm^3 volume of the ampoule) only 0.05 ppm $PbCl_2$ are necessary. But this small change of concentration in the crystal is not detectable. The same is valid for the experiment performed in vacuo. Also in this case no decrease of the lead content could be observed (Table I, column 3). In a third experiment the annealing has been done in an atmosphere of saturated $PbCl_2$ vapour formed by including a sufficient quantity of $PbCl_2$ inside the ampoule. The A band increases so drastically that a quantitative measurement is impossible. Obviously, $PbCl_2$ diffuses from the atmosphere into the crystal. Finally a Pb doped sample and an undoped sample were annealed together in vacuo. During this treatment the A band intensity of the Pb doped sample decreases to half of the initial value while in the undoped sample an A band with approximately the same height arises (Table I, column 5). This means that $PbCl_2$ evaporates from the doped sample (crystal 1) producing in the ampoule an atmosphere of saturated $PbCl_2$ vapour from which lead diffuses into the undoped sample (crystal 2). The process is finished if the Pb concentrations in both samples are equal.

4. Conclusions

On the basis of the results and the corresponding explanations described in Chapter 3 one can propose three different methods by which any defined Pb concentration in specimens of alkali halide crystals can be produced.

First method: By annealing a Pb doped crystal in an open furnace at normal atmosphere any wanted concentration lower than the starting one can be realized by a suitable choice of temperature and time. In order to remove concentration gradients possibly built up in the specimen during the evaporation process an annealing at 600 °C in a closed volume should be added.

Second method: Any wanted concentration of lead can be produced by annealing of undoped specimens in a closed tube containing a sufficiently high quantity of $PbCl_2$ to maintain an atmosphere of saturated $PbCl_2$ vapour.

Third method: Crystal specimens can be doped with a defined concentration of lead by including undoped samples together with a suitable doped one in a closed tube and annealing at about 600 °C.

The application of these doping methods surely is convenient and effective for the production of well doped specimens, e.g. for the investigation of aggregation phenomena of Pb ions and their influence on structure sensitive properties of alkali halide crystals for which specimens with a special sequence of defined concentrations or several specimens with identical concentration are necessary (e.g. [3, 5, 12, 13]). Furthermore the second method seems to be especially suitable for the production of very high Pb concentrations which are difficult to get by doping of the melt.

Acknowledgements

The authors would like to thank Mrs. J. JASCHINSKY and Mrs. E. HORN for carefully performing the experiments.

REFERENCES

1. W. B. FOWLER in W. B. Fowler (Ed.), Physics of Color Centers, Academic Press, New York and London, 1968.
2. J. H. SCHULMAN, R. J. GINTHER and C. C. KLICK, J. Opt. Soc. Am., **40**, 854, 1950.
3. W. A. SIBLEY, E. SONDER and C. T. BUTLER, Phys. Rev., **136** A, 537, 1964.
4. J. Z. DAMM, W. IWANICKA, J. TRNKA and J. VELICKÁ, Kristall u. Technik, **8**, 709, 1973.
5. J. S. DRYDEN and G. G. HARVEY, J. Phys. C, **2**, 603, 1969.
6. M. FAYET-BONNEL, phys. stat. sol. (b), **60**, 713, 1973.
7. K. J. BERG and F. FRÖHLICH, Czech. J. Phys., B **28**, 1020, 1978.
8. K. J. BERG and F. FRÖHLICH, Kristall u. Technik, **12**, 1025, 1977.
9. M. L. MUKHERJEE and B. N. DAS, Indian J. Phys., **48**, 664, 1974.
10. R. VOSZKA, I. TARJAN, L. BERKES and J. KRAJSOVSZKY, Kristall u. Technik, **1**, 423, 1966.
11. LANDOLT-BÖRNSTEIN, Zahlenwerte und Funktionen, Vol. II, 2, a, Springer-Verlag, Berlin—Göttingen—Heidelberg, 1960.
12. S. B. S. SASTRY, V. VISWANATHAN and C. RAMASASTRY, J. Phys. Soc. Japan, **35**, 508, 1972.
13. J. L. PASCUAL and F. AGULLÓ-LÓPEZ, Crystal Lattice Defects, **7**, 161, 1977.

Acta Physica Academiae Scientiarum Hungaricae, Tomus 47 (1—3), pp. 125—132 (1979)

GROWTH, STOICHIOMETRY AND PROPERTIES OF $LiNbO_3$ SINGLE CRYSTALS

By

K. POLGÁR, L. JESZENSZKY, K. RAKSÁNYI and E. HARTMANN

RESEARCH LABORATORY FOR CRYSTAL PHYSICS, OF THE HUNGARIAN ACADEMY OF SCIENCES
BUDAPEST, HUNGARY

$LiNbO_3$ single crystals were grown from melt by Czochralski method, for acousto-electronic purposes. The stoichiometric problems in connection with growing were studied by chemical methods: gravimetric method, based on the determination of Nb in its $NbO(Oxine)_3$ complex; volumetric method, involving titration of peroxo-niobium(V) complex; spectrophotometric determination, in form of peroxo-niobium(V) complex in its acidic solution at 340 nm. The properties of crystals were investigated by physical methods. The inclusions, strains were studied by different microscopic investigations.

A very attractive combination of piezoelectric and optical properties has made lithium niobate one of the most extensively studied materials in recent years. Since 1965 when Ballman reported the successful growth of single crystals by the Czochralski technique [1] hundreds of papers on $LiNbO_3$ have been published.

In connection with the fast development of surface acoustic wave devices, this material now takes second place to quartz as a single crystalline piezoelectric [2].

In our laboratory we have been dealing with growing of $LiNbO_3$ crystals for about 3 years. The growth is made in a resistance heated furnace.

Growing $LiNbO_3$ crystals in a resistance heated furnace is very advantageous from the viewpoint of cooling, because in an induction heated furnace, the crystals often crack due to the large temperature gradient. In order to avoid cracking it is necessary to use an afterheater. In our resistance heated furnace the crystals have never been cracked provided the composition of the melt was good.

We have grown crystals along the [001], [012], [010] and [110] pulling axes, the most favourable direction proved to be the [001] one, which is also appropriate for poling the crystals during the growth process. Lithium metaniobate is one of the four compounds we know about in the $Li_2O—Nb_2O_5$ system.

The phase diagram of this system is shown in Fig. 1 [13]. It can be seen that in the neighbourhood of the lithium metaniobate composition there is a fairly large range of solid solubility, and the maximum melting point is at a composition of 48.6% for lithium oxide. This is known as the congruent

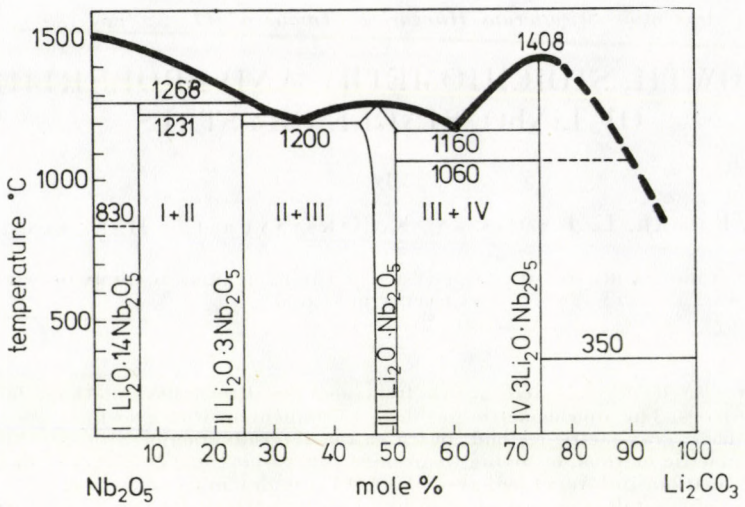

Fig. 1. Phase diagram of $Li_2O-Nb_2O_5$ system [13]

composition, which is characterized by the fact, that the distribution coefficients between melt and solid phases for all components are equal to one.

Homogeneous crystals can only be grown starting with a melt of this very composition. Growing crystals from a melt differing from the congruent composition exerts a decisive influence on the quality of the crystal involving several important physical properties. First of all we can mention the extraordinary index of refraction. This affects the double refraction, and consequently changes the temperature of phase matching for optical second harmonic generation at a given wave length [3]. The Curie temperature is also very sensitive to the change of composition. Other physical methods, for example the measurement of lattice parameters and NMR linewidth of Nb^{93} were less effective [9], [10].

It must be mentioned that in every case the physical parameters of single crystals were determined knowing the composition of the melt. The ratio Li : Nb is determined not only by weighing the components but by many factors. For instance, different compositions can be obtained by raising the temperature too fast while sintering Li_2CO_3 and Nb_2O_5 [4]. If Li_2O does not react immediately with Nb_2O_5, it can evaporate from the system resulting in Li deficiency. On the other hand, in the neighbourhood of the melting point of $LiNbO_3$, the Nb_2O_5, if not reacted, may evaporate from the system [5]. Growing under an atmosphere containing too much water vapour $LiNbO_3$ can be hydrolyzed and the composition may change [6].

A comparative study of the results obtained with the aid of the physical methods showed that the standard error in molar fraction could be kept under 1×10^{-4} only in rare cases. The efficiency of the relevant chemical methods

has not been systematically investigated until now. To fill this gap we worked out chemical analytical methods in our laboratory to measure the Nb content in undoped $LiNbO_3$ crystals. In case of very pure materials, this method is suitable to determine the Li : Nb ratio. We have elaborated three methods: a gravimetric, a volumetric and a spectrometric method.

As fas as the gravimetric method is concerned we proceed as follows: we solved the $LiNbO_3$ fused previously with $K_2S_2O_7$ in a mixture of sulphuric and oxalic acids, then by adding an excessive amount of urea we precipitated it in the form of niobium-oxinate $NbO(C_9H_6ON)_3$. In order to make the homogeneous precipitation complete we continued it over 18 hours on a water bath. After filtering and washing, the precipitate was dried at room temperature and after ingition at 950 °C we weighed it in form of Nb_2O_5. The procedure described in the literature [7] proved to be unsatisfactory from the point of view of reproducibility of results, and had to be modified in many respects.

We have found the optimal fusion conditions at a mole ratio of 1 : 10 and 1 : 15 concerning $Nb_2O_5 : K_2S_2O_7$ and $LiNbO_3 : K_2S_2O_7$, respectively. The necessary amount of urea addition was found to be 180 g to a solution containing 0.5 Nb_2O_5, and the optimal pH value for the hydrolysis was between 7 and 8.

In the volumetric determination method we measured Nb(V) in form of its peroxide complex. The main process is the adding of a known excess amount of nitrilo-triacetic acid to the $NbO_2(H_2O_2)^+$ complex. This makes a ternary complex with the former and then the excess of NTA is titrated back by a solution of $CuSO_4$. The standard procedure reported in the literature [8] was modified concerning the ratio of the reagent volumes. The end-point indication was made with a methyl calcein fluorescent indicator. The indicator was subjected to a preliminary chromatographic purification in order to give a sharp end-point.

In the spectrophotometric method our aim was to choose an absorption band having low molar absorption coefficient [11], [13], because this made it possible to determine a large amount of materials using a technique developed mainly for trace quantities. The use of the standard procedure led to a pronounced time dependence of the extinction. The crucial point for obtaining good reproducibility was to wait equal periods before each measurement.

After fusing with $K_2S_2O_7$ the material is dissolved in a mixture containing H_2O_2, sulphuric and phosphoric acids. Then we measured the extinction of this solution at 340 nm. In order to reach a higher precision we employed differential spectrophotometry.

We studied the validity of the Lambert—Beer rule and found it to be valid over a broad concentration range. We have determined the molar extinction coefficient from the data obtained with pure Nb_2O_5. The value of the latter is 906 ± 4.5 ($1\ mol^{-1}\ cm^{-1}$).

With this differential method the standard deviation of results (expressed in molar ratio of Nb), was about 8×10^{-3}. We employed all three methods for several kinds of samples: Nb_2O_5 specpure, $LiNbO_3$ crystals grown from congruent melt, and for some crystals grown from other, not congruent composition.

Our results are summarized in Table I.

The measured values of the molar fractions, with one exception, exceed the nominal ones. A careful analysis of the possible sources of error has shown that this shift cannot be attributed to errors of weighing out the reactants or to reasons resulting from the composition or purity of the latter. Nor does the standard error of the gravimetric method allow for that. In addition, the sign of this shift does not change, as it would be expected, when the niobium content of the melt exceeds that of the congruent composition. Compositions far from the congruent one, under equilibrium condition now prevailing, have no significant influence on the amount of this shift either.

To date the majority of the papers presented on this topic including the most sophisticated determinations of the congruent composition, while plotting the results of measurements against the composition of the melt, have made use of or have been based on the nominal Li or Nb content of the melt. The role of the inherent errors due to such a procedure was not analyzed in most cases, although such effects as vaporization and incomplete homogenization before sintering were frequenctly touched. Although it seems very improbable that three independent methods, one of them having a fairly good reliability, would give equally erroneous results, even in this latter case the gravimetric method can be recommended as a successful and simple tool for checking real melt compositions. Namely, allowing for an undirectional and

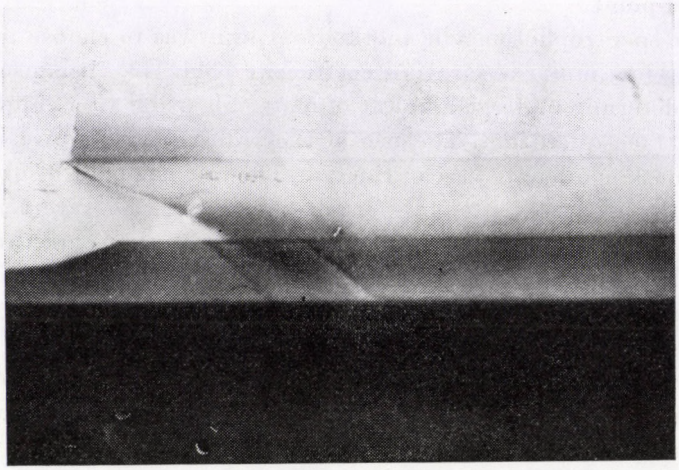

Fig. 2. Regular set of cracks along $(10\bar{1}2)$ plains (50×)

Table I

Comparison of different chemical methods

Sample		Nb content $\frac{Nb}{Li+Nb}$	Gravimetric method			Titrimetric method			Spectrophotometric method		
			I	II	III	I	II	III	I	II	III
Nb_2O_5 specpure		1	11	0.995	3×10^{-3}	15	1.003	6×10^{-3}	—	—	—
$LiNbO_3$ crystal		0.514	5	0.529	9×10^{-3}	5	0.523	6×10^{-3}	3	0.56	1.5×10^{-2}
$Li_2O-Nb_2O_5$	1	0.600	5	0.608	1.1×10^{-3}	6	0.60	1.3×10^{-2}	4	0.62	1.5×10^{-2}
$Li_2O-Nb_2O_5$	2	0.550	5	0.5211	8×10^{-4}	6	0.504	9×10^{-3}	4	0.53	1.5×10^{-2}
$Li_2O-Nb_2O_5$	3	0.450	5	0.465	1.1×10^{-3}	6	0.472	8.5×10^{-3}	4	0.47	1.5×10^{-2}
$Li_2O-Nb_2O_5$	4	0.400	5	0.411	3×10^{-3}	6	0.41	10^{-2}	4	0.41	1.6×10^{-2}
Average methodic error (in mole fraction)				10^{-3}			4×10^{-3}			8×10^{-3}	

I The number of samples

II The average of calculated molar fraction

III Standard deviation of molar fractions

fairly constant systematic error of the analytical procedures, this fact even justifies the setting up of a calibration curve. As far as the standard errors are concerned, the titrimetric and spectrophotometric methods are a bit inferior to the gravimetric one, however, in view of their relative simplicity they are very useful for obtaining a crude estimate of the composition. From the average methodic errors it can be seen that it is only the gravimetric method in the case of at least four parallels that has an accuracy comparable to that of the physical methods. The disadvantage of physical methods lies in the fact that 1) the composition of standards is not controlled by analytical methods 2) that these methods need very expensive instrumentation and very careful,

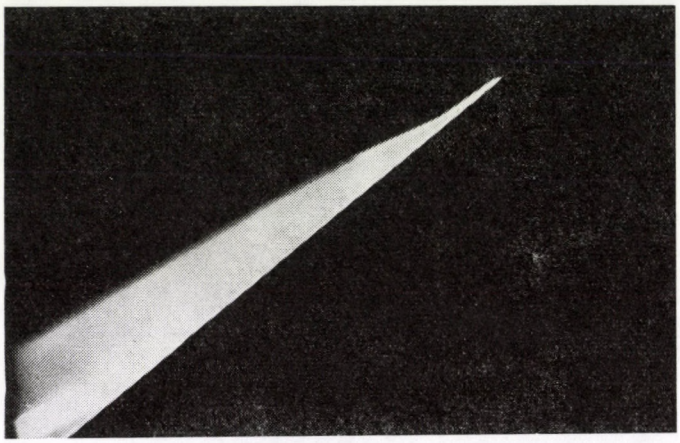

Fig. 3. Microcrack in polarized light (100×)

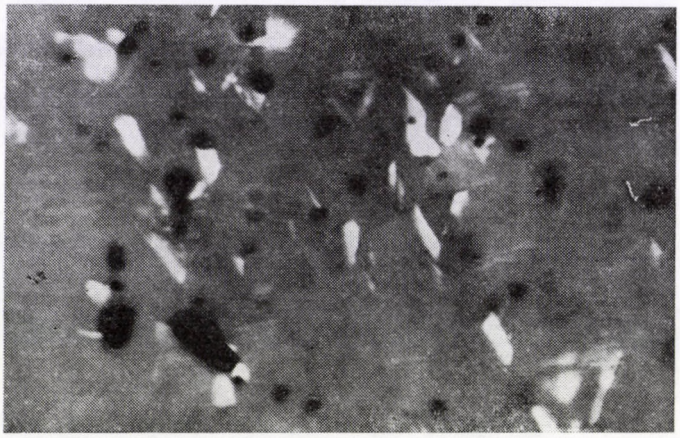

Fig. 4. Microcracks near inclusions (100×)

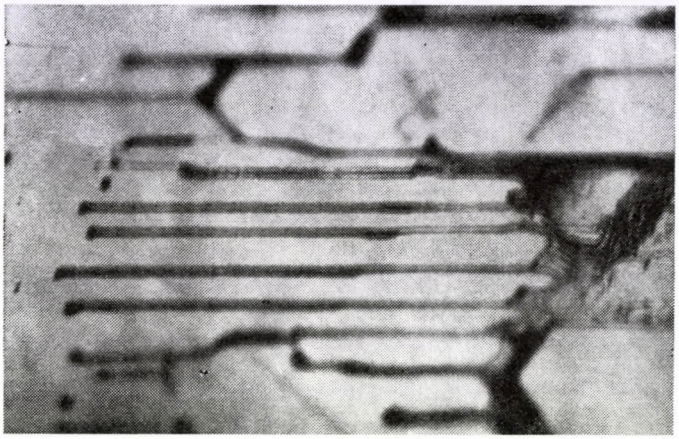

Fig. 5. Inclusions in $LiNbO_3$ crystal (100×)

crystal processing. Furthermore the physical data are microscopic in their nature, i.e. the obtained data refer to a tiny volume element of the crystal, and are very uncertain and sensitive to inhomogeneities. Only the measurement of Curie temperature yields results with a comparable rapidity and feasibility with the gravimetric method but also requires comparative basic analytical data. A systematic study of Curie temperature method is under way in our laboratory.

We have investigated the main optical features of our crystals by different microscope techniques. The defects which occurred most frequently were cracks, microcracks, inclusions and strain induced double refraction. Cracks occurred when the crystal composition differed from the congruent one, or the cooling was not appropriate. Different types of cracks were observed, as for instance a regular set of cracks along the $(10\bar{1}2)$ plains (Fig. 2) and shell shaped cracks.

The observation of these cracks was easy by a simple optical microscope but microcracks were hardly seen by this technique. An especially useful instrument for observing microcracks was the polarization microscope (Fig. 3). The microcracks occurred mostly near to inclusions and rough cracks (Fig. 4).

The formation of inclusions in our crystals originated probably from impurities and from the inappropriate rate of rotation. The inclusions found in our crystals were very different in shape and size ranging from several microns to several hundreds of microns (Fig. 5). In the vicinity of cracks and inclusions we have found areas behaving differently from their surroundings. These may be strained areas.

In summary, the chemical and microscopical methods can successfully supplement the customary ones in many respects and can effectively help the crystal grower in attaining good quality $LiNbO_3$ single crystals.

Acknowledgements

The authors would like to express their gratitude to Dr. R. VOSZKA for his expert leadership in crystal growing and to Mrs. G. LINDER and Miss Á. TÓTH for their precise assistance in chemical analytical measurements.

REFERENCES

1. A. A. BALLMAN, J. Am. Ceram. Soc., **48**, 112, 1965.
2. A. RAUBER, Chemistry and Physics of Lithium Niobate in New Topics in Matrials Science I. Edited by E. Kaldis, North Holland, Amsterdam, 1978.
3. K. G. BERGMAN, A. ASHKIN, A. A. BALLMAN, J. M. DZIEDZIC, H. J. LEVINSTEIN and R. G. SMITH, Appl. Phys. Lett., **12**, 92, 1968.
4. P. P. BUDNIKOV and A. M. GINSZTLING, Reactions in solid phase (in Hungarian), Műszaki Könyvkiadó, Budapest, 1968.
5. SH. NIIZEKI, K. KOTA and H. TOYOTA, Japan 71, 14, 825 21. 4. 1971. Patent.
6. R. M. HILTON, US Air F. Cambridge R. L. Instr. Pap. No 161, 1969.
7. L. KOSTA and M. DULAR, Talanta, **8**, 265, 1961.
8. E. LASSNER, Talanta **10**, 1229, 1863.
9. P. LERNER, C. LEGRAS and J. P. DUMAS, J. Crystal Growth, **3—4**, 231, 1968.
10. G. E. PETERSON and A. CARNEVALE, J. Chem. Phys., **56**, 4848, 1972.
11. G. TELEP and D. F. BOLTZ, Anal. Chem., **24**, 163, 1952.
12. I. M. GIBALO, Analiticseszkaja Himija Niobija i Tantala, Nauka, Moscow, 1967.
13. L. O. SVAASAND, M. ERIKSRUD, A. P. GRANDE and F. MO, J. Cryst. Growth, **18**, 179, 1973.

Acta Physica Academiae Scientiarum Hungaricae, Tomus 47 (1—3), pp. 133—138 (1979)

SOME ASPECTS OF THE MACROSCOPIC THEORY OF ORIENTED CRYSTALLIZATION FROM THE MELT

COMMUNICATION I

A GENERAL FORMULATION OF THE PROBLEM

By

E. A. BRENER and V. A. TATARCHENKO

THE SOLID STATE PHYSICS INSTITUTE, ACADEMY OF SCIENCES OF THE USSR
142432 CHERNOGOLOVKA, USSR

The stability of the crystallization process in the Czochralski, Stepanov, Verneuil and floating zone techniques is analyzed on the basis of a general approach suggested in the paper. A comparative analysis of these four techniques enables to characterize each one by the capability to grow crystals of given sizes and shapes.

The methods of oriented crystallization from the melt eliminating any contact of the side faces of a growing crystal with solid walls are now becoming increasingly widespread. These are the Czochralski, Stepanov, Verneuil and floating zone techniques, characterized by a fixed orientation of crystallization at a fixed position of the solid—liquid interface.

The common feature of these methods, each of them having a predominant field of application, is the elimination of crystal contact with a solid wall; as a result, both the shape and the size of a growing crystal are essentially determined by capillarity forces which form a meniscus in the interface boundary zone. In addition, the crystallization process also depends on the conditions of heat and mass exchange in the crystal—melt system.

A general approach developed in the present series of communications consists in analyzing jointly the capillarity phenomena and the conditions of heat and mass transfer for all four of the methods mentioned; it yields comparative characteristics of these techniques and elucidates the capabilities of each of them to grow crystals of given sizes and shapes. The approach is justified if the heat and mass transfer conditions, and not the crystallization kinetics, constitute the limiting step of the process; this is usually the case in the actual systems at typical pulling rates. Certain kinetic effects, such as a dependence of supercooling at the crystallization front on the crystallization rate, can be taken into account, however, within the framework of the outlined approach.

An analysis of the conditions of heat and mass transfer in the crystal—melt system requires that the equation of melt flow (the Navier-Stokes equation) with the boundary condition at the free meniscus surface (the Laplace capillarity equation) be solved jointly with the continuity equation (the mass

conservation law) and the heat conduction equation (the energy conservation law). This system of equations must be supplemented by an appropriate system of boundary conditions which, together with the parameters included in the equations, characterize the specific features of each of the growth techniques involved.

In principle, a solution of this equation makes it possible to determine the size of the crystal, the position of the interface with respect to the shaper edges in the Stepanov technique, with respect to the free surface in the Czochralski technique, and with respect to the burner endface in the Verneuil technique and so on, as functions of the controlled parameters of the crystallization process. It will be demonstrated later that the sought variables (x_i) satisfy the following system of differential equations:

$$\frac{dx_i}{dt} = f_i(t, x_1, \ldots, x_n) \qquad (i = 1, 2, \ldots, n) \qquad (1.1)$$

where t is time, and n is the number of variables which depends on the method of crystallization and the cross-section of the crystal obtained. The steady-state values of interest (x_{i0}) satisfy the following system of equations:

$$f_i(x_{10}, x_{20}, \ldots, x_{n0}) = 0 \qquad (i = 1, 2, \ldots, n). \qquad (1.2)$$

Only steady-state solutions of system (1.2) are physically realizable. According to Lyapunov, solutions are stable if they are stable for the corresponding linearized system

$$\frac{dx_i}{dt} = \sum_{k=1}^{n} \frac{\partial f_i}{\partial x_k} (x_k - x_{k0}). \qquad (1.3)$$

All partial derivatives in (1.3) are evaluated at $x_i = x_{i0}$. System (1.3), in its turn, is stable when all the roots of the characteristic equation

$$\det \left(\frac{\partial f_i}{\partial x_k} - s\delta_{ik} \right) = 0 \qquad (1.4)$$

have negative real parts (δ_{ik} is Kronecker's symbol).

As a rule, the difficulties involved in determining the unstationary functions f_i depending explicitly on time are considerable. The obstacles can often be overcome by using the quasistationary approach, but this calls for substantiation in each specific case. MULLINS and SEKERKA, for instance [1], used the quasistationary approach to analyze morphological stability of the crystallization front shape and obtained the results in agreement with the experimental data [2]. Explicit equations of system (1.1) are derived by using the conservation laws for mass, heat, and growth angle. It is convenient to consider the mass conservation law for each specific method of crystallization.

The condition of heat balance at the crystallization front, which enables to determine the interface position as a function of time, will be discussed later.

The condition of constancy of the growth angle, specific for crystallization from the melt and making it possible to find the crystal cross-section size and shape as functions of time, must be discussed in more detail. Let us define the growth angle as an angle between the tangents to the meniscus and the crystal side surface at the three-phase curve. This angle was shown experimentally [3, 4, 5] and theoretically [6, 7] to be an (anisotropic) constant in each material. In what follows we discuss only an isotropic model. Elementary geometric manipulations demonstrate (Fig. 1.1) that for constant growth angle, the transversal size of the crystal R depends on time according to

$$\frac{dR}{dt} = -V \tan(\alpha_0 - \alpha_e), \tag{1.5}$$

where V is the pulling rate, α_0 is an angle between the tangent to the meniscus and the horizontal line at the threephase curve, $\alpha_e = \pi/2 - \varphi_0$ where φ_0 is the growth angle. In the case of steady-state growth $\alpha_0 = \alpha_e$. In a general case, the angle α_0 as a function of crystal size, crystallization position and other factors, is found together with the meniscus shape by solving the Navier-Stokes equation with the Laplace capillarity equation serving as a boundary

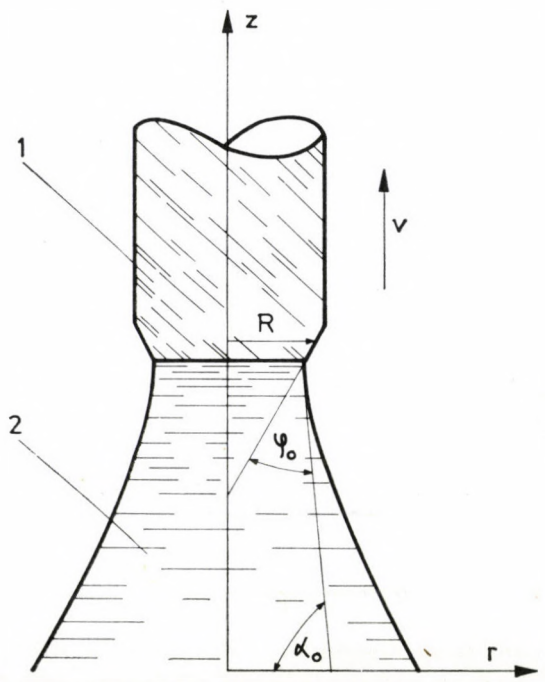

Fig. 1.1. Changes in diameter of a growing crystal for $\alpha_0 \neq \alpha_e = \pi/2 - \varphi_0$;
1 — crystal; 2 — melt

condition at the free surface. The required additional system of boundary conditions is specific for each crystallization technique. A complete solution of the problem as stated is mathematically a very difficult proposition. It is therefore of interest to estimate the effects of some factors on the crystallization process.

Let us discuss the conditions of formation of the molten column. Three types of forces participate in this: 1) the forces of inertia related to the melt flow; 2) capillarity forces; 3) gravity forces. An estimate of the effects of these forces is given by the characteristic numbers: Weber number $We = \frac{\varrho V^2 L}{\gamma}$, Froude number $Fr = \frac{V}{\sqrt{gL}}$, and Bond number $Bo = \frac{\varrho g L^2}{\gamma}$ (here ϱ is the material density, L is a characteristic linear dimension, γ is the surface tension coefficient, and g is the gravity acceleration). The flow in the melt can be neglected if the Weber and Froude numbers are small. The Bond number determines the range where capillarity and gravitational forces predominate [8].

It can be shown that the effects of the gravity and capillarity forces are much greater than that of inertia at all reasonable growth rates. In other words, the formation of a liquid column can be considered in the hydrostatics approximation up to the rates $V \sim 10 \div 10^2$ cm/s. It must be underlined that the quasiequilibrium treatment of these phenomena is justified by the fact that the capillarity equilibrium sets on practically instantaneously.

In addition to the flow caused by crystallization, convective flows with velocities substantially higher than flow velocities may appear in the system. The effects of such perturbation on the column formation and heat transfer in the melt will be discussed later in the text.

It was already mentioned above that the heat balance equation at the crystallization front makes it possible to find the interface velocity

$$\lambda_1 G_1 - \lambda_s G_s = \mathfrak{L} V_c , \tag{1.6}$$

where λ_1, λ_s are heat conductances of the liquid and solid phases, G_1 and G_s are the temperature gradients at the crystallization front in the liquid and solid phases, $\mathfrak{L}$ is the latent heat of melting per unit volume, $V_c = V - \frac{dh}{dt}$ is the crystallization rate, and h is the height of the crystallization front.

From (1.6),

$$\frac{dh}{dt} = V - \frac{1}{\mathfrak{L}} (\lambda_1 G_1 - \lambda_s G_s). \tag{1.7}$$

The quantities G_1 and G_s, being the functions of crystal size, position of the crystallization front, and other parameters of the process, have to be found by solving the heat conductance equation for the melt and crystal, respectively.

It was mentioned above that in the general case this requires that nonstationary equations be solved. A quasistationary approach used here implies that the temperature distribution at all times satisfies the stationary heat conductance equation for the instantaneous position of the crystallization front. This approach is justified if the characteristic time of temperature relaxation is much smaller than that of front relaxation, after a perturbation, back to the steady-state position. Both G_1 and G_s are then found by solving a one-dimensional convective equation taking into account heat exchange at the side surface [9]

$$\frac{d^2T_i}{dz^2} - \frac{V}{\varkappa}\frac{dT_i}{dz} - \frac{\mu_i}{\lambda_i}J(T_i - T_{en}) = 0, \tag{1.8}$$

where $i = l, s$ ($i = l$ in the melt and $i = s$ in the solid), T_i is the temperature, $\varkappa_i$ is the temperature conductivity coefficient, z is the coordinate, μ_i is the coefficient of heat exchange with the ambient medium, J is the ratio of the perimeter of the crystal cross-section to its area, and T_{en} is the ambient temperature.

The second term in (1.8) takes into account the melt flow and the crystal motion at the rate V, and the third term — the heat exchange across the side surface with the ambient medium. Several reasons are decisive in selecting this equation for a description of heat transfer in a crystal-melt system. In contrast to three-dimensional equations, Eq. (1.8) has simple solutions which furnish good fit to the true temperature distribution for small Biot numbers $\left(Bi = \frac{\mu}{\lambda}R \ll 1\right)$. Nevertheless, Eq. (1.8) gives a qualitatively correct description of G_1 and G_s as functions of the relevant parameters even for not too small Biot numbers. There can be no doubt that the defect structure of a crystal cannot be analyzed without detailed information on the temperature fields, so that solution of 3D problems is unavoidable. Still, the application of Eq. (1.8) for the purposes of this work is reasonably justified. The temperature at the interface is assumed equal to the crystallization temperature T_0. The remaining boundary conditions depend on the specific growth technique and cooling conditions.

In growing single crystals of optically transparent materials, the radiation flux is taken into account by introducing an effective thermal conductivity coefficient proportional to T^3. If the heat transfer from the side surface of the crystal proceeds radiationally according to the Stefan—Boltzmann law, we arrive at an equation of the type of (1.8) with respect to T^4. The results obtained below can therefore be applied to this case if T is replaced by $T^{1/4}$.

When opaque materials with high melting point are crystallized, linearization of the radiational heat transfer and introduction of an effective heat exchange coefficient for the side surface enable to use Eq. (1.8) up to 2000 °C [10].

REFERENCES

1. W. W. Mullins and R. F. Sekerka, J. Appl. Phys., **35,** 444, 1964.
2. W. A. Tiller and J. W. Rutter, Canad. J. Phys., **34,** 729, 1956.
3. Yu. M. Shashkov and E. V. Melnikov, Zh. Fiz. Khim., **39,** 1364, 1965.
4. T. Surek and B. Chalmers, J. Cryst. Growth, **29,** 1, 1975.
5. V. A. Tatarchenko and G. A. Satunkin, J. Cryst. Growth. **37,** 285, 1977.
6. V. V. Voronkov, FTT, **5,** 571, 1963.
7. W. Bardsley, F. G. Frank, G. W. Green and D. T. J. Hurle, J. Cryst. Growth, **23,** 341, 1974.
8. A. V. Lykov, Handbook on Heat and Mass Transfer, Energiya Publs, Moscow, 1978, p. 132 (in Russian).
9. H. S. Carslaw and J. C. Jaeger, Conduction of Heat in Solids, Oxford, 1957, p. 148.
10. F. B. Khambatta and P. J. Gelisse a.n, J. Cryst. Growth, **13/14,** 710, 1972.

Acta Physica Academiae Scientiarum Hungaricae, Tomus 47 (1—3), pp. 139—149 (1979)

SOME ASPECTS OF THE MACROSCOPIC THEORY OF ORIENTED CRYSTALLIZATION FROM THE MELT

COMMUNICATION II

THE CZOCHRALSKI AND STEPANOV GROWTH TECHNIQUES

By

E. A. BRENER and V. A. TATARCHENKO

THE SOLID STATE PHYSICS INSTUTE, ACADEMY OF SCIENCES OF THE USSR
142432 CHERNOGOLOVKA, USSR

The stability of the crystallization process, while growing crystals in the shape of circular cylinder, plate or tube by Czochralski and Stepanov techniques, was analyzed according to Lyapunov. The stability of the crystal cross-section shape, the stability of the crystallization front shape and the effect of the surface tension gradient on the formation of the meniscus and heat transfer processes in the liquid phase were investigated.

In the Czochralski growth a crystal is pulled from the free surface of the melt. In Stepanov's method, a crystal is pulled from the shaper. A condition that has to be satisfied is either that of catching at the sharp edges of the shaper or wetting at the shaper sides [1]. The size of a crystal drawn and the position of the crystallization front can be found from a solution of the problem formulated in Communication I of this paper.

As a result of the mass conservation, the melt level in these systems drops gradually as the crystal is being pulled from the crucible. If, however, the crystal cross-section area is much smaller than the melt surface area in the crucible, this effect is negligible.

Two parameters can therefore be varied independently: the crystal size and the position of the crystallization front (a two-degree-of-freedom system).

It has been mentioned above that the crystal size can be found as a function of time from the condition of constancy of the growth angle; according to Eq. (1.5),

$$\delta\dot{R} = -V \tan(\alpha_0 - \alpha_e) = -V\left(\frac{\partial\alpha_0}{\partial R}\,\delta R + \frac{\partial\alpha_0}{\partial h}\,\delta h\right). \tag{2.1}$$

A dot over $\delta\dot{R}$ denotes differentiation with respect to time, $\delta R = R - R_0$ and $\delta h = h - h_0$ are the deviations of the crystal radius R and the crystallization front position h from the respective equilibrium values.

The crystallization front position as a function of time is found from the heat balance law at the crystallization front; according to (1.7),

$$\delta\dot{h} = \frac{1}{\mathfrak{L}}\left(\frac{\delta G}{\delta R} + \frac{\delta G}{\delta h}\,\delta h\right), \tag{2.2}$$

where $G = \lambda_s G_s - \lambda_1 G_1$.

The partial derivations in Eqs. (2.1) and (2.2) are evaluated for equilibrium values of R_0 and h_0.

Equations (2.1) and (2.2) are conveniently recast to

$$\delta\dot{R} = A_{RR}\,\delta R + A_{Rh}\,\delta h, \tag{2.3}$$

$$\delta\dot{h} = A_{hR}\,\delta R + A_{hh}\,\delta h, \tag{2.4}$$

where

$$A_{RR} = -V\frac{\partial\alpha_0}{\partial R}; \qquad A_{Rh} = -V\frac{\partial\alpha_0}{\partial h};$$

$$A_{hR} = \frac{1}{\mathfrak{L}}\,\frac{\partial G}{\partial R}; \qquad A_{hh} = \frac{1}{\mathfrak{L}}\,\frac{\partial G}{\partial h}.$$

The necessary and sufficient conditions of stability of the steady-state solutios R_0 and h_0, according to Gurvitz's criterion [2], are

$$A_{RR} + A_{hh} < 0, \tag{2.5}$$

$$A_{RR}A_{hh} - A_{Rh}A_{hR} > 0. \tag{2.6}$$

A functional relationship between the angle α_0, crystal radius R, and crystallization front coordinate h can be found by solving the Laplace capillarity equation. The corresponding expressions for a number of boundary conditions were found in [3] for the Stepanov technique and in [4] for the Czochralski growth.

It was already mentioned that the temperature gradients in Eq. (2.2) as functions of R and h must be found by solving the thermal problem for the crystal—melt system. It is logical to choose the temperature at the base of the melt column T_m as one of the boundary conditions. A solution of this problem for Eq. (1.8) with different heat exchange conditions at the upper end-face of the crystal is given in [5].

The first attempt to analyze stability of the growth process in the methods under discussion was made in [6]. Only Eq. (2.4) for the rate of variation of the crystallization front coordinate was analyzed, while the deviations δR and δh were meant dependent; the relationship between them was such that at any moment the angle α_0 be equal to $\alpha_e = \pi/2 - \varphi_0$, where φ_0 is the growth angle. The results obtained in [6] were qualitatively correct although reflected only a part of the whole picture.

The solutions of the capillarity problem [3] and of the thermal problem [5] enabled the authors of the present paper to analyze the signs of coefficients

Czochralski growth		A_{RR}		A_{Rh}		A_{hh}	A_{hR}
		>0		<0			
small-diameter crystal	boundary catching condition	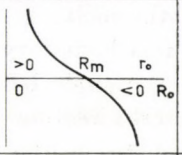		<0		<0 if $T_m \geqslant T_0$	
large diameter crystal $R > \infty$ or a plate	boundary catching condition	<0		single-valued menisci	<0	>0 if $T_m < T_0$	>0
				two-valued menisci	>0		
					>0 at $R_0 \leqslant r_0$		
	boundary wetting condition	$\alpha_0 < \alpha_1$	<0	<0			
		$\alpha_0 > \alpha_1$	<0 $r_0 - R_0 > m$				
			0 $r_0 - R_0 < m$				

A_{RR} and A_{Rh}, referred to henceforth as the capillarity coefficients, and of A_{hR} and A_{hh}, referred to as thermal coefficients (Table 2.I), to find the joint solutions of the capillarity and thermal problems, and to analyze their stability [7]. The main conclusions are as follows.

In drawing thin rods ($R_0/a \lesssim 1$, where $a = \sqrt{\frac{2\gamma}{\varrho g}}$ is the capillarity constant) at the boundary condition of catching, the crystallization is stable in the range $R_0 > R_b$, where R_b is the lower bound on stability found from conditions (2.5), (2.6). Moreover, $R_b > R_m$ for a supercooled melt and $R_b < R_m$ for a superheated one. In this case R_m is the boundary for the capillarity stability ($R_0 > R_m$ is the capillarity stability region: $A_{RR} < 0$; $R_0 < R_m$ is the capillarity instability region: $A_{RR} > 0$). In other words, the overall stability region of a superheated melt is broader than that of the capillarity stability.

When cylindrical rods are drawn by the Czochralski technique, $A_{RR} > 0$ (the capillarity instability) and the growth is stable only in a superheated melt in the range where inequalities (2.5), (2.6) are satisfied. This corresponds to large crystal diameters $R_0 \gg a$, with $A_{RR} \to 0$. When plates or large-diameter cylindrical rods ($R_0/a \gg 1$) are grown in the conditions of boundary catching, the capillarity stability is always realized ($A_{RR} < 0$). Moreover, $A_{Rh} < 0$ for single-valued menisci, which corresponds to mutual stabilization ($A_{Rh} A_{hR} < 0$). In a superheated melt $A_{hh} < 0$: in this case inequalities (2.5)—(2.6) are always satisfied so that crystallization is stable. The overall stability in a supercooled melt ($A_{hh} > 0$) is achieved when inequalities (2.5), (2.6) are satisfied. However,

for two-valued menisci (positive pressure) there is a range of parameters where $A_{Rh} > 0$ (no mutual stabilization) when crystal radius R_0 is close to the shaper size r_0. This may lead to instability which can be compensated for only by a considerable superheating of the melt.

In the case of wetting as a boundary condition, the capillarity stability is realized for $\alpha_0 < \alpha_1$ (α_1 is the angle between the tangent to the meniscus at the shaper and the horizontal direction. If $\alpha_0 > \alpha_1$, the capillarity stability is achieved for wide spacings between the crystal and the shaper wall.

An analysis of joint solutions of the thermal and capillarity problems was reported by the authors of this review in [7]. The number of solutions may be two, one, or none, depending on the crystallization parameters. Furthermore, if the number is two, one of the solutions is unstable. In principle, a single joint solution may be obtained by increasing the pulling rate; unfortunately, this solution is unstable.

The process kinetics (crystallization temperature as a function of growth rate) was taken into account in [8] (and independently in [9]), and revealed insubstantial changes caused by a decrease in A_{hh}. If the melt is slightly supercooled with respect to the equilibrium temperature, this effect may lead to an actual superheating of the melt, that is to a transition to the thermal stability region.

The results obtained enable to derive quantitative estimates which confirm applicability of the quasistationary approach to thermal phenomena when stability is analyzed. It was mentioned above that this approach is justified if the characteristic time of the crystallization front relaxation to the steady state τ_{rf} is greater than the corresponding relaxation time of temperature τ_{rT}

$$\tau_{rf} \approx \frac{1}{|A_{hh}|} \approx \frac{\mathfrak{L}h^2}{\lambda(T_m - T_0)} .$$

As follows from [10], τ_{rT} can be estimated as $\tau_{rT} \approx \frac{h^2}{\alpha}$, so that

$$\tau_{rf}/\tau_{rT} \approx \frac{\mathfrak{L}}{\varrho c(T_m - T_0)} \approx 10^2 \div 10^3 \gg 1.$$

It is also of interest to estimate the effects of various thermophysical and other constants of materials on the crystallization stability. We find that with other conditions being identical, the stability (evaluated as the inverse of the characteristic relaxation time) is higher for materials with higher thermal conductivity λ, growth angle φ_0, and with smaller latent heat of melting $\mathfrak{L}$. The stability can be increased by raising the melt superheating and by forced air cooling of the crystal in a local zone. Not only the stability is increased but the range of stable growth is widened as well. It is of interest to analyze how the type of stability changes [11] with the changing size of a crystal grown. For

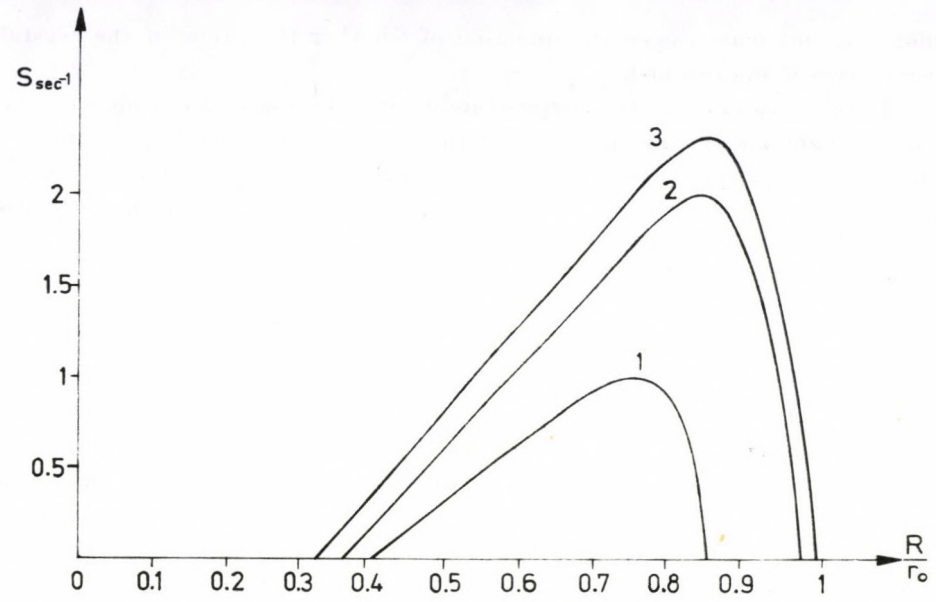

Fig. 2.1. Stability characteristic $S(s^{-1})$ as a function of the ratio of crystal radius to that of the shaper, R_0/r_0, for three materials (1 — Al, 2 — Si, 3 — Al_2O_3) grown in identical conditions

instance, when thin rods are grown by the Stepanov technique from a superheated melt, an increased rod diameter (this can be achieved, for example, by diminishing the pulling rate) changes the stability type in the following sequence: "saddle" type instability — "unstable node" — "unstable focus" — "stable focus" — "stable node". The characteristic relaxation times in a steady-state mode are, for different materials, in the range of 1 to 10 s. When the stability boundary is approached, the relaxation times increase. In principle, an optimal R_0/r_0 ratio can be determined on the basis of such calculations. Fig. 2.1 plots the stability index as a function of this ratio at a fixed thermal regime for three materials (Al, Si, Al_2O_3.)

The following may be considered as an experimental confirmation of results yielded by the above analysis: a) difficulties in drawing constant cross-section crystals by the Czochralski method; b) drawing of constant cross-section profiles by the Stepanov method when the crystal-to-shaper size ratio $R_0/r_0 \gtrsim 1/2$; *c*) improved self-stabilizing of the process when forced air cooling is employed in a local zone.

Stability of the cross-section shape in a drawn crystal

Until now we discussed stability only with respect to a uniform perturbation of the cross-section (variation of the cylinder radius or of the plate thickness). This approach elucidates the stability of the characteristic profile

dimension, but leaves open the question of whether the shape of the crystal cross-section is maintained.

In order to analyze the shape stability it is necessary to impose on the contour bounding the profile cross-section an arbitrary small perturbation which can be expanded into a series in an appropriate set of orthogonal functions (selected on the basis of the contour shape), and then to calculate its coefficients as functions of time. The cross-section shape is stable if coefficients of all the terms of the expansion diminish with time. The first term of the expansion corresponds to a uniform perturbation, that is to a variation of the cross-section dimensions with its shape unaltered. A nonperturbated contour corresponds to a nonperturbed meniscus described by a function z_0 satisfying the capillarity equation with the boundary conditions, and the angle α_e. A small deviation from the contour corresponds to a solution $z = z_0 + z_1$ which satisfies a two-dimensional capillarity equation linearized in a small correction term z_1, and to the corresponding angle $\alpha_0 = \alpha_e + \delta\alpha$. All the equations being linear with respect to z_1, the behaviour of an arbitrarily small and sufficiently smooth perturbation can be analyzed by following that of the superposition of the expansion components. For example, in the case of cylindrical crystals the perturbed contour is described by an expression $R = \Sigma a_m \cos m\varphi$, where m is an integer, and φ is the angle in a cylindrical reference frame (a uniform perturbation corresponds to $m = 0$). In the first approximation, neither the perimeter nor the cross-section area are altered by the harmonics with $m \neq 0$, so that the temperature gradients in the thermal problem under discussion remain unchanged. In addition to the conditions already derived earlier, it is necessary now to require for the steady-state growth that $\dot{a}_m/a_m < 0$ for $m \neq 0$. The ratio $\dot{a}_m/a_m$ is the already familiar coefficient $A_{RR} = \dot{a}_0/a_0 = -V\dfrac{\partial\alpha_0}{\partial R} = -V\dfrac{\partial\alpha_0}{\partial a_0}$. Similarly, $A_{Ra_m} = \dot{a}_m/a_m = -V\dfrac{\partial\alpha_0}{\partial a_m}$ for all m. The corresponding derivatives $\dfrac{\partial\alpha}{\partial a_m}$ must be found by solving a linearized two-dimensional capillarity Laplace equation. It can be shown that A_{Ra_m} diminishes with increasing m for a number of boundary conditions on the shaper both in growth of cylindrical crystals and plates. In other words, all the coefficient $A_{Ra_m} < 0$ if $A_{Ra_0} \equiv A_{RR} < 0$; hence, the additional requirements to the crystallization stability are met. Thus, A_{RR} is always negative in plate growth, so that the conditions of stability found earlier are complete. In the case of drawing thin filaments, there is a range of crystal radii in which $A_{RR} > 0$ and therefore an instability in the first harmonic may develop. A more detailed analysis shows that this instability really exists. A perturbation at the first harmonic corresponds to a small shear strain, and the instability produced thereby must result in crystal bending. This was indeed observed in growth of sapphire filaments ~ 300 μm in diameter (Fig. 2.2). A finite-width plate can

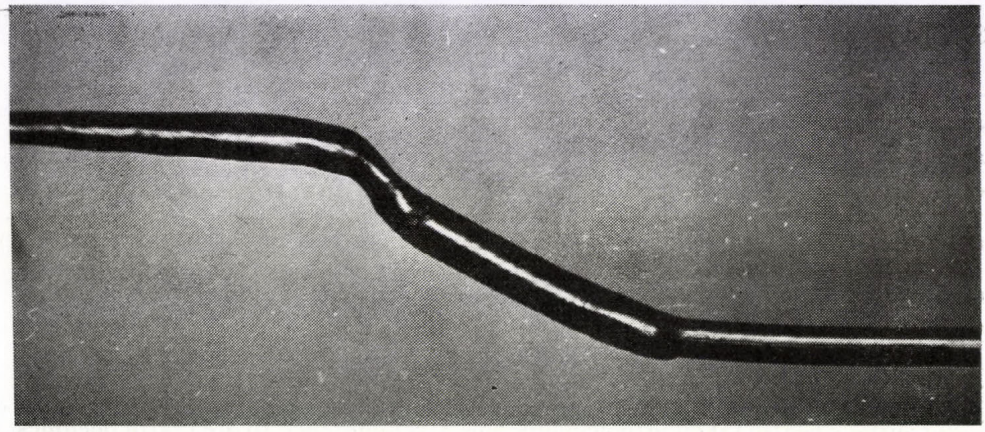

Fig. 2.2. Bending of a whisker growing in an unstable mode (instability in the first harmonic)

be regarded as consisting of semi-cylindrical boundary parts and a planar middle part. The plate growth is stable far from the edges at the catching condition. A variation in width or bending in the plane can be expressed in terms of a perturbation at the first harmonic of the semi-cylindrical boundary regions. As a result, a steady-state growth of a thin plate requires that stability conditions be satisfied for the first harmonic of the filament of the corresponding diameter.

Stability of crystallization in growth of tubular crystals

The preceding Sections treated the growth of rod- and plate-shaped crystals, with, as a result, a single characteristic dimension of the crystal cross-section: rod radius or plate thickness. A tubular crystal cross-section is characterized by two dimensions: external radius R_1 and internal radius R_2. Hence, the capillarity equation for the external portion of the meniscus and the heat balance equation have to be supplemented by the Laplace capillarity equation for the internal part of the meniscus, the pressure and growth angle being the same as for the external part. The system characterizing stability of joint solutions of these equations is

$$\begin{aligned} \delta\dot{R}_1 &= A_{R_1R_1}\delta R_1 + A_{R_1R_2}\delta R_2 + A_{R_1h}\delta h, \\ \delta\dot{R}_2 &= A_{R_2R_1}\delta R_1 + A_{R_2R_2}\delta R_2 + A_{R_2h}'\delta h, \\ \delta\dot{h} &= A_{hR_1}\delta R_1 + A_{hR_2}\delta R_2 + A_{hh}\delta h. \end{aligned} \tag{2.7}$$

Coefficients $A_{R_1R_1}$ and A_{R_1h} are equal to $-V\dfrac{\partial}{\partial R_1}$ and $-V\dfrac{\partial\alpha_0}{\partial R_2}$, respectively.

Similarly, $A_{R_2R_2} = V\dfrac{\partial\alpha_0}{\partial R_2}$, $A_{R_2h_2} = V\dfrac{\partial\alpha_0}{\partial h}$. It should be emphasized that $A_{R_1R_2} = A_{R_2R_2} = 0$; this is only natural since the internal and external menisci are independent. The thermal coefficients A_{hR_1}, A_{hR_2} and A_{hh} are determined as before. The following must, however, be underlined. The characteristic dimensions of the cross-section enter the thermal problem as a ratio of the circumference to the cross-section area. Thus, the ratio is equal to $\dfrac{2}{R_1}$ for growth of a rod with the radius R_1. If the tube's internal diameter is not too large, the heat outflux is significant only on the outer surface of the growing crystal. Hence, the ratio in question becomes $\dfrac{2R_1}{R_1^2 - R_2^2}$. If the heat outflux from the inner surface is also taken into account, the circumference to area ratio becomes $\dfrac{2}{R_1 - R_2}$. Table 2.II lists the signs of coefficients A derived by analyzing the solutions to capillarity and heat conductance equations.

According to Gurvitz's criterion, the following inequalities give the necessary and sufficient conditions of stability of system (2.7):

$$A_{R_1R_1} + A_{R_2R_2} + A_{hh} < 0, \tag{2.8}$$

$$-A_{R_1R_1}A_{R_2R_2}A_{hh} + A_{R_1R_1}A_{R_2h}A_{hR_2} + A_{R_2R_2}A_{R_1h}A_{hR_1} > 0 \tag{2.9}$$

$$-(A_{R_1R_1} + A_{R_2R_2} + A_{hh})(A_{R_1R_1}A_{R_2R_2} + A_{hh} + A_{R_2R_2}A_{hh} -$$

$$- A_{R_1h}A_{hR_1} - A_{R_2h}A_{hR_2}) - (A_{R_1R_1}A_{R_2R_2}A_{hh} +$$

$$+ A_{R_1R_1}A_{R_2h}A_{hR_2} + A_{R_2R_2}A_{R_1h}A_{hR_2}) > 0. \tag{2.10}$$

When large diameter tubes are grown ($R_2 \gg a$), the solution is always single; Table 2.II shows that inequalities (2.8)—(2.10) are satisfied and this solution is therefore stable. It is likely that this is the reason why such tubes are comparatively easier to grow than other profiles.

In the case of small-diameter tube crystallization ($R_1 \ll a$), the number of solutions depends on the process parameters (two, one, or no solutions). The process of tube crystallization is found to be stable for $R_1 > R_1^*$ and $R_2 > R_2^*$ (Table 2.II). Furthermore, if there are two solutions, one of them is unstable. The solution with $R_1 > R_1^*$, $R_2 < R_2^*$ is unstable. Indeed it can be seen from Table 2.II that inequality (2.9) is violated. The process of "shutting-down" of tubes during crystallization could then be interpreted as follows. When R_2 becomes smaller than R_2^*, the process becomes unstable, which brings about further decrease of R_2 until the tube is "shut"; after this a rod with $R_1 > R_1^*$ continues growth since this process was shown above to be stable. An intriguing possibility is that of steady-state drawing of thick-walled capil-

	$A_{R_1R_1}$	A_{R_1h}	$A_{R_2R_2}$	A_{R_2h}	A_{hR_1}	A_{hR_2}	A_{hh}
small diameter ($R_1 \ll a$) $p=0$	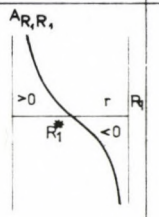	<0	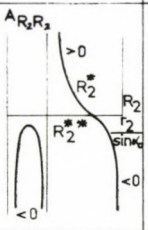	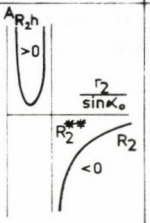	>0	<0	<0 if $T_m \gg T_0$ >0 if $T_m < T_0$
large diameter ($R_2 > a$) $p=0$	<0	<0	<0	>0			

laries with $R_2 < R_2^*$. In all likelihood, however, the growth of such profiles should meet with considerable difficulties, owing to the essential narrowness of this region; this region widens, though, for materials with high values of the growth angle.

The effect of surface tension gradient on formation of the meniscus and heat transfer processes in the liquid phase

Normally crystallization is conducted in the conditions of a temperature gradient in the liquid phase. The result is convection and, in particular, free convection involving gravity and characterized by the Rayleigh number $Re = \frac{g\beta \Delta T L^3}{\eta \varkappa}$, and the so-called Marangoni convection [12, 13] involving the surface tension gradient and characterized by the Marangoni number $Ma = \frac{\partial \gamma}{\partial T} \frac{\Delta T L}{\eta \varkappa}$. Here β is the bulk expansion coefficient, ΔT is the characteristic temperature difference, L is a characteristic linear dimension, η is the dynamic viscosity coefficient and γ is the surface tension coefficient. The number $Bo = \frac{g\beta L^2}{\partial \gamma / \partial T}$, obtained as the ratio of the Rayleigh and Marangoni numbers, characterizes the relative contributions of gravitational and capillarity forces into the formation of convective flow. The number Bo is small for small characteristic dimensions of the system, when capillarity forces predominate. It

was proved experimentally [14] that it is the Marangoni convection which develops in the zone with characteristic dimension $L \sim 5$ mm. The characteristic dimensions in the Stepanov growth being still smaller, we discuss the effects of only this convection. If the melt is superheated, the surface tension is increased at the crystallization front, and therefore the melt is transported toward the front at the free surface, and away from it at the centre because of the generated pressure gradient. This pressure gradient is directed against that produced by the gravity field, and hence increases the convexity of the molten columns. The pattern is reversed in supercooled melts. It was mentioned, however, that flow affects the meniscus form appreciably beginning with flowrates of $10 \div 10^2$ cm/s. The actual observed flowrates in a zone with $L \sim 5$ mm are $V \approx 1$ cm/s. For the reason given above, flow rates in the Stepanov techniques are still smaller, and the effects on the meniscus shape are expected to be negligible.

Convection in the liquid phase results in the melt stirring and so increases the heat influx to the crystallization front through a superheated melt. The magnitude of these flowrates can be estimated from the boundary condition at the meniscus free surface: $\eta \frac{\partial V}{\partial r} = -\frac{\partial \gamma}{\partial T} \operatorname{grad} T$, whence $V \sim \frac{\partial \gamma}{\partial T} \frac{R \Delta T}{\eta h}$, where R is the crystal radius (the characteristic transversal dimension of the meniscus), and h is the meniscus height. The Marangoni thermal number gives a characteristic of the ratio of the heat flux transferred by the melt flow at the flow rate V to that transferred by diffusion. The estimates yielded by the above formula exceed the observed values by an order of magnitude [14]. This discrepancy is caused by friction on the surface of the crystal. It was also mentioned in the cited reference that the convective contribution into heat transfer becomes essential if zones are longer than 1 mm. Note that the convective heat flux to the crystallization front increases as R rises and h diminishes; this is clear from the estimate of convective flowrates. These changes operate in the same direction as the corresponding changes in the heat flux transported by diffusion. In other words, the thermal coefficients A_{hR} and A_{hh} which are of interest in an analysis of stability, change their magnitudes but do not alter their signs. Summarizing, the effect of convective heat transfer on crystallization can be taken into account here by introducing formally the effective heat conductance and heat exchange coefficients.

Stability of the shape of the crystallization front

The crystallization front was assumed plane in the preceding Sections, and only its coordinate was analyzed for stability. In the general case an arbitrary perturbation of the front can be treated as a superposition of the shape and coordinate perturbations. Formally, this could be realized by expand-

ing the perturbation into a series in an appropriate set of orthogonal functions, with the first term taking into account the change in the crystallization front coordinate and the remaining term representing shape distortion at a constant front coordinate. All the terms of the expansion will be regarded as independent since an analysis of stability is restricted to a linearized problem. So far only the stability of the first term (the crystallization front stability) was considered. Perturbations of the front shape at constant front coordinate (perturbation of all the terms in the expansion excepting the first one) do not change the capillarity problem as discussed above, so that the shape stability is determined by the heat effects only; this was investigated by MULLINS and SEKERKA [15, 16] and by others [17, 18]. It was found that, with impurity effects neglected, a plane front is stable in the growth from a superheated melt, while the instability appearing in the case of growth from a supercooled melt can be compensated for, at low supercooling, by the Gibbs—Thompson effect (the dependence of the crystallization temperature on surface curvature) and the effect of kinetics at the crystallization front. Qualitatively, the pattern is retained if the initial front shape is not planar. The stability of the crystallization front is determined by a joint action of the capillarity and thermal conditions of the crystallization process. Obviously, the magnitudes of the thermal coefficients A_{hR} and A_{hh} must change but the signs will not be altered. The stability of the front shape must be analyzed in a manner similar to that of [15].

REFERENCES

1. V. A. TATARCHENKO, A. I. SAET and A. V. STEPANOV, Izv. AN SSSR, ser. fiz., **33,** 1954, 1969.
2. L. E. ELSGOLTS, Differential Equations and Calculus of Variations, Nauka Publs, Moscow, 1969, p. 227.
3. V. A. TATARCHENKO, J. Cryst. Growth, **37,** 272, 1977.
4. S. V. TSIVINSKY, Inzh. Fiz. Zh., **5,** 59, 1962.
5. V. A. TATARCHENKO, Inzh. Fiz. Zh. **30,** 532, 1976.
6. V. A. TATARCHENKO, Fiz. Khim. Obr. Mater., **6,** 47, 1973.
7. V. A. TATARCHENKO and E. A. BRENER, Izv. AN SSR, ser. fiz., **40,** 1456, 1976.
8. B. L. TIMAN and O. D. KOLOTII, Kristallografiya, **24,** 192, 1979.
9. V. A. TATARCHENKO and E. A. BRENER, J. Cryst. Growth, to be published.
10. H. S. CARSLAW and J. C. JAEGER, Conduction of Heat in Solids, Oxford, 1957, p. 253.
11. A. A. ANDRONOV, A. A. VITT and S. E. KHAIKIN, The Theory of Oscillations, Fizmatgiz Publs, Mocsow, 1959, p. 385 (in Russian).
12. C. E. CHANG and W. R. WILCOX, J. Cryst. Growth, **28,** 8, 1975.
13. C. E. CHANG and W. R. WILCOX, Intern. J. Heat Mass Transfer, **19,** 355, 1976.
14. D. SCHWABE, A. SCHAMENN, F. PREISSER and R. ODER, J. Cryst. Growth, **48,** 305, 1978.
15. W. W. MULLINS and R. F. SEKERKA, J. Appl. Phys., **34,** 323, 1963.
16. W. W. MULLINS and R. F. SEKERKA, J. Appl. Phys., **35,** 444, 1963.
17. S. CORIELL and E. SEKERKA, J. Cryst. Growth, **34,** 157, 1976.
18. L. A. TARSHIS and W. A. TILLER, Proceedings of an International Conference on Crystal Growth, Boston, 1966, p. 157.

Acta Physica Academiae Scientiarum Hungaricae, Tomus 47 (1—3), pp. 151—158 (1979)

SOME ASPECTS OF THE MACROSCOPIC THEORY OF ORIENTED CRYSTALLIZATION FROM THE MELT

COMMUNICATION III
THE VERNEUIL TECHNIQUE

By

V. A. BORODIN, E. A. BRENER and V. A. TATARCHENKO

THE SOLID STATE PHYSICS INSTITUTE, ACADEMY OF SCIENCES OF THE USSR
142432 CHERNOGOLOVKA, USSR

The stability of the crystallization process while growing crystals by Verneuil technique is analyzed. The growth of thin rods and plates is stable in case a heat flow from the burner to the crystal monotonously decreases.

In the Verneuil method, the material in powdered form is fed onto the molten layer kept within the torch of an oxygen-hydrogen burner or a plasma jet. Fig. 3.1a represents schematically an idealized setup for crystal growth which is used to analyse heat and mass transfer in the process of crystallization. The origin of a reference frame (z, r) is fixed at the end-face surface of the burner, and axis z is directed downward. In the Verneuil technique, the crystal radius R, position of the crystallization front x, and that of the liquid-vapour interface l can be varied independently. Let us introduce the meniscus height $h = x - l$. The rate of crystal radius variation and that of crystallization front are derived, as usual, from the conditions of the growth angle constancy and of the heat balance. The position of the liquid-vapour interface as a function of time is found from the mass conservation law. A system characterizing stability of crystallization in the Verneuil technique is

$$\delta\dot{R} = A_{RR}\,\delta R + A_{Rl}\,\delta l + A_{Rh}\,\delta h, \tag{3.1}$$

$$\delta\dot{l} = A_{lR}\,\delta R + A_{ll}\,\delta l + A_{lh}\,\delta h, \tag{3.2}$$

$$\delta\dot{h} = A_{hR}\,\delta R + A_{hl}\,\delta l + A_{hh}\,\delta h. \tag{3.3}$$

Determination of capillarity coefficients $\mathbf{A}_{RR}$, $\mathbf{A}_{Rl}$, $\mathbf{A}_{Rh}$

According to (1.5), $\delta\dot{R} = -V(\alpha_0 - \alpha_e)$, so that the capillarity coefficients are $A_{RR} = -V\dfrac{\partial\alpha_0}{\partial R}$, $A_{Rl} = 0$, $A_{Rh} = -V\dfrac{\partial\alpha_0}{\partial h}$. Here $A_{Rl} = 0$ since

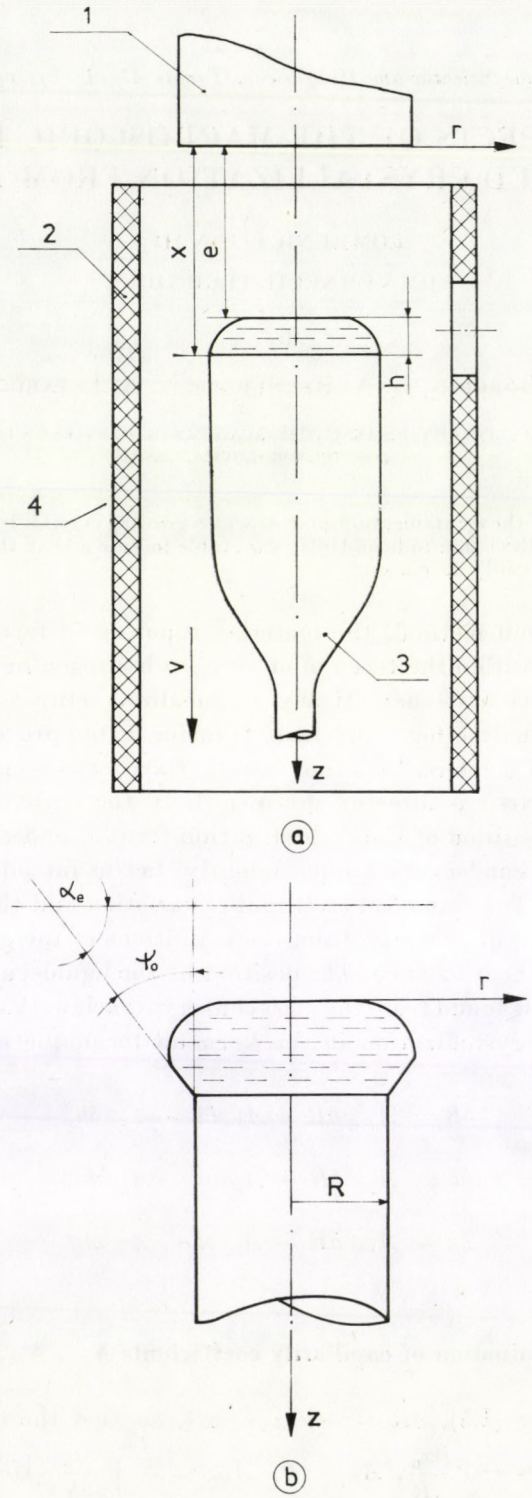

Fig. 3.1. An idealized diagram of crystal growth by the Verneuil technique.
a) A model used to analyze the heat and mass transfer in the process of crystallization. 1 — burner; 2 — furnace muffle; 3 — crystal; 4 — melt. b) A model used to analyze capillarity phenomena

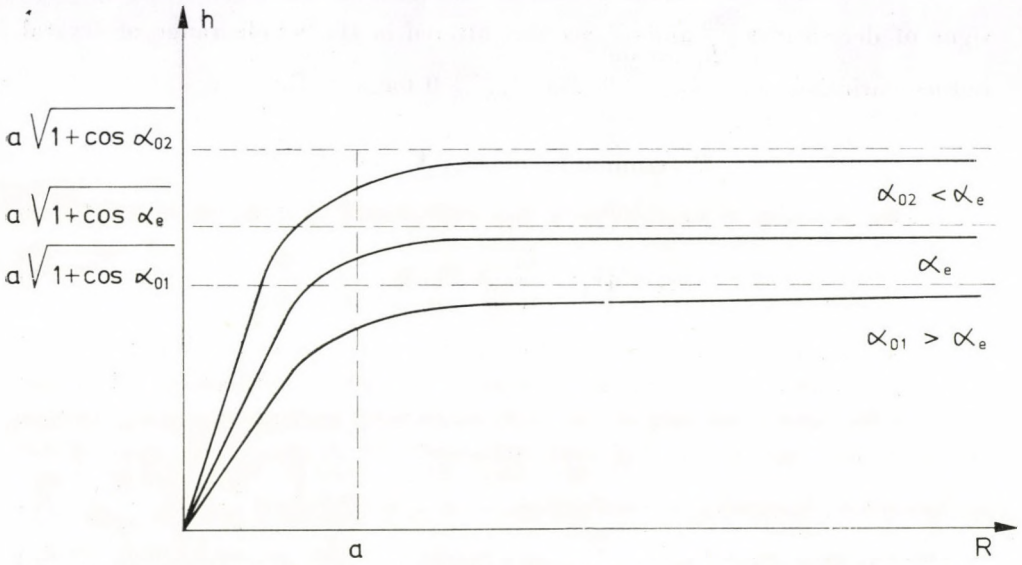

Fig. 3.2. Meniscus height h as a function of the radius of a growing crystal for different angles α_0

neither the meniscus shape nor the angle are dependent explicitly on the position of the liquid-vapour interface l. A functional relationship between α_0, R, and h is determined by solving the Laplace capillarity equation. Formally the specifics of crystallization in the Verneuil method are contained in a boundary condition for $r = 0$ (Fig. 3.1*b*). The liquid drop is symmetric: $\left.\frac{dz}{dr}\right|_{r=0} = 0$. A qualitative behaviour of h as a function of R for a number of values of α_0 is plotted in Fig. 3.2. When the crystal radius is much smaller than the capillarity constant a, we can neglect the weight of the molten column in the Laplace equation. The meniscus surface is in this case spherical, and its height h is a linear function of R; $h = R\frac{1+\cos\alpha_0}{\sin\alpha_0}$. If $R \gtrsim a$, the Laplace equation cannot be resolved in quadratures and numerical calculations are inevitable. It is possible, however, to determine a qualitative picture of $h(R)$. Analytic solutions can be obtained for the segments of the meniscus with $r \ll a$ and $r \gg a$; the general solution is then obtained by matching the functions and their derivatives at the point $r = a$. We find that as R increases, h tends asymptotically to $a\sqrt{1+\cos\alpha_0}$. The maximum deviation from the true curve $h(R)$ is observed for this method in the neighbourhood of $r = a$, but we obviate the difficulties involved in numerical calculations and obtain a qualitatively correct representation of the general trend. In the range of small R, the capillarity coefficients are: $A_{RR} = -\frac{V}{R}\sin\alpha_0$, $A_{Rh} = \frac{V}{R}\frac{\sin^2\alpha_0}{1+\cos\alpha_0}$. Fig. 3.2 shows that the

signs of derivatives $\frac{\partial \alpha_0}{\partial R}$ and $\frac{\partial \alpha_0}{\partial n}$ are not altered in the whole range of crystal radius variation, and $A_{RR} < 0$ and $A_{Rh} > 0$ for any R.

Determination of A_{lR}, A_{ll}, and A_{lh}

The condition of mass balance in a crystal-melt system can be written as

$$W_0 = \pi \varrho_s R^2 \left(V - \frac{dx}{dt}\right) + \pi \varrho_L R^2 \left(\frac{dx}{dt} - \frac{dl}{dt}\right), \tag{3.4}$$

where W_0 is the mass of powder entering the molten layer per unit time, and ϱ_s and ϱ_L are the densities of the solid and liquid phase, respectively. The first term on the right-hand side of Eq. (3.4) is the mass undergoing crystallization per unit time, and the second term represents the change in the mass of the molten layer. Assuming for simplicity $\varrho_s = \varrho_L = \varrho$, we obtain $\frac{dl}{dt} = -\frac{W_0}{\pi \varrho R^2} + V$. In a steady-state growth, $V = \frac{W_0}{\pi \varrho R_0^2}$, so that the radius of the growing crystal R_0 can be found if we know the powder feed rate W_0 and the pulling rate V. When a deviation from the equilibrium occurs, $\frac{dl}{dt} = \frac{2W_0}{\pi \varrho R_0^3} \delta R$. By comparing this expression to Eq. (3.2), we arrive at: $A_R = \frac{2W_0}{\pi \varrho R_0^3}$, $A_{ll} = 0$, $A_{th} = 0$. The coefficient A_{lR} was determined under an assumption that the density of the powder supply flow is represented by the delta function at $r = 0$. In actual conditions this density distribution is slightly "smeared". It is readily shown, however, that if the distribution has a maximum at $r = 0$, the sign of A_{lR} is not altered and only its magnitude is changed. Then, $A_{lR} = 0$ if the flux density is independent of r; finally, $A_{lR} < 0$ if the flux density has a minimum at $r = 0$. If the powder is fed through the central nozzle of the burner (this is the most frequent case), the powder flux density is maximum at the furnace muffle centre so that normally $A_{lR} > 0$.

Determination of A_{hR}, A_{hl}, and A_{hh}

It has already been mentioned that the position of the crystallization front as a function of time can be found from the equation of heat balance at the interface. This requires that the heat conduction equation (1.8) be solved with the appropriate boundary conditions. The main distinction in the formulation of the thermal problem for the Verneuil crystallization technique consists in fixing a boundary condition at the liquid-vapour interface, retaining in principle the same conditions at the crystallization front and the same heat exchange conditions at a cooled end-face of the crystal as in the Czochralski and

Stepanov techniques discussed in Communication II. The approach most suitable for the Verneuil technique is to fix the heat flux density Q at the surface of the molten layer. The heat flux density at constant flow rate of gases fed into the burner is a function of the distance between the burner and the melt surface level. The function $Q(l)$ is known [1] to be determined by the burner design and the flow rate of gases burnt. A fraction of the heat flux immediately at the melt surface is consumed for powder melting. It is given by $\eta \mathfrak{L} \varrho V$ where η is a coefficient characterizing the state of the powder ($0 \leq \eta \leq 1$). Namely, $\eta = 0$ if powder reaches the melt surface already molten, and $\eta = 1$ if powder melting starts on the melt surface. The boundary condition at the melt surface then becomes

$$\lambda_l \frac{dT_1}{dz}\bigg|_{z=l} = -Q + \eta \mathfrak{L} \varrho \left(V - \frac{dl}{dt}\right). \tag{3.5}$$

Omitting the rather straightforward intermediate manipulations, we give the final expressions for A_{hR}, A_{hl}, and A_{hh}:

$$A_{hR} = \frac{1}{\mathfrak{L}\varrho}\left[\lambda_l T_0 \xi_1^2 \frac{h}{R} + \frac{1}{2}(Q - \eta \mathfrak{L} \varrho V)\, \xi_1^2 h \frac{h}{R}\right] - A_{lR}(1-\eta), \tag{3.6}$$

$$A_{hl} = \frac{1}{\mathfrak{L}\varrho}\frac{dQ}{dl}, \tag{3.7}$$

$$A_{hh} = \frac{1}{\varrho \mathfrak{L}}\left[\lambda_l T_0 \xi_1^2 + (Q - \eta \mathfrak{L} \varrho V)\, \xi_1^2 h\right] < 0; \xi_1 = \sqrt{\frac{\mu \cdot 2}{\lambda_l R}}. \tag{3.8}$$

Two limitations were taken into consideration in the derivation of (3.6)—(3.8). Firstly, the Biot number was assumed small, that is $\xi_1 R \ll 1$. This enables to assume $\xi_1 h \ll 1$, since either $h \simeq R$ or $h < R$. Secondly, perturbations of crystal radius or crystallization front position leave the temperature gradient in the solid phase pratically unaltered because the displacement of the crystallization front is negligibly small compared to the crystal length, and the radius is changed only in the vicinity of the crystallization front.

Determination of the conditions of stability of the crystallization process

The necessary and sufficient condition of stability of system (3.1)—(3.3) is that Gurvitz's conditions be satisfied [2]; in the case in question this means

$$A_{RR} + A_{hh} < 0, \tag{3.9}$$

$$A_{Rh} A_{lR} A_{hl} < 0, \tag{3.10}$$

$$-(A_{RR} + A_{hh})(A_{hh} A_{RR} - A_{Rh} A_{hR}) + A_{Rh} A_{lR} A_{hl} > 0. \tag{3.11}$$

Both A_{RR} and A_{hh} being negative, inequality (3.9) is satisfied; A_{Rh} is positive, so that inequality (3.10) is satisfied if A_{lR} and A_{hl} have opposite signs. It was

already mentioned above that powder supply through the central nozzle of the burner results in $A_{lR} > 0$; consequently, A_{hl} must be negative. This means that the heat flux density in the vicinity of the crystallization zone satisfies the condition $\frac{dQ}{dl} < 0$, that is the heat flux density is diminishing with increasing the distance from the burner. The conditions necessary and sufficient for inequality (3.11) to hold, are

$$A_{RR} A_{hh} - A_{Rh} A_{hR} > 0, \tag{3.12}$$

$$-(A_{RR} + A_{hh})(A_{RR} A_{hh} - A_{hR} A_{Rh}) > |A_{Rh} A_{lR} A_{hl}|. \tag{3.13}$$

Taking into account that $A_{RR} = -\frac{\partial h}{\partial R} A_{Rh}$, where $\frac{\partial h}{\partial R}$ is taken from the solution of the capillarity problem (Fig. 3.2), we can write

$$A_{RR} A_{hh} - A_{hR} A_{Rh} = A_{Rh} \left\{ \frac{\partial h}{\partial R} \frac{1}{\mathfrak{L}\varrho} [\lambda_l T_0 \xi_1^2 + (Q - \eta \mathfrak{L} \varrho V) \xi_1^2 h] - \right.$$

$$\left. - \frac{1}{\mathfrak{L}\varrho} \left[\lambda_l T_0 \xi_1^2 \frac{h}{R} + \frac{1}{2} (Q - \eta \mathfrak{L} \varrho V) \xi_1^2 h \frac{h}{R} \right] + A_{lR} (1 - \eta) \right\}. \tag{3.14}$$

Let $R \ll a$; taking into account that $\frac{\partial h}{\partial R} \approx \frac{h}{R}$, we obtain from (3.14) that $A_{RR} A_{hh} - A_{Rh} A_{hR} > 0$. For (3.13) to be satisfied it is sufficient that

$$\left| \frac{dQ}{dl} \right| \ll \frac{\mathfrak{L} \varrho A}{R} \tag{3.15}$$

This approximate estimate gives a lower value than $\left| \frac{dQ}{dl} \right|$ obtainable from Eq. (3.13). This underestimation of the modulus definitely satisfies inequality (3.11); moreover, estimate (3.15) has a clear physical meaning: the process is stable if the change in the heat flux density Q along the furnace muffle of the growth zone over distances of the order of R does not exceed the crystallization heat flux. If this requirement and the condition $\frac{dQ}{dl} < 0$ are satisfied, crystallization is stable for $R \ll a$.

If $R \gg a$, then $\frac{\partial h}{\partial R}$ falls off much steeper than $\frac{h}{R}$ (Fig. 3.2); as follows from (3.14), $A_{RR} A_{hh} - A_{hR} A_{Rh} < 0$ beginning with a sufficiently large R in the range $R > a$, that is the crystallization process becomes unstable. It also follows from (3.14) that the stability region may be somewhat widened by decreasing η, that is by melting the powder before it is fed into the molten layer. The stability region is also broadened by lowering the modulus $\left| \frac{dQ}{dl} \right|$; nevertheless, these measures do not ensure the stability of the process for large-diameter crystals.

Discussion of results

In the case of corundum ($\gamma = 670$ dyne/cm, $\varrho = 3.87$ g · cm^{-3} [3]) $a = 6$ mm. An estimate on the basis of the above analysis indicates that growth of corundum crystals by the Verneuil technique is stable for crystal diameters below 10 to 12 mm. This figure is in good agreement with practical data on the growth of thin corundum rods [4].

From the standpoint of the process stability, the Verneuil technique differ from the Czochralski method in that in the former method the instability sets on in the transition from the smaller radii to the larger ones, while in the latter one the situation is quite the opposite. The principal reason is the difference in the meniscus shape. It is of interest to note that if the Verneuil crystallization were realized in the conditions of weightlessness, the surface of the molten layer would be spherical for any crystal radius, the linear relationship between the meniscus height h and the crystal radius R would be retained for any R, and stability would not break down at higher values of crystal radius as found to be the case in the gravity field.

If the crystals are grown in the instability region $R \gg a$, it is advisable that the rate of increase of a perturbation be as small as possible; it is then feasible to keep the crystal diameter within the prescribed interval by a smooth variation of the process parameters. This is essential since any sharp change in the process parameters meant to maintain the crystal diameter (such as a variation of powder supply rate in the case of ruby growth) results in local inhomogeneity of the optical parameters of the crystal. The above argumentation demonstrates that the steepness of perturbations δR, δh and δl can be diminished by a more complete melting of powder before it reaches the molten layer, by improving the burner design, and by optimizing the gas flowrate in burner tube in such manner that the heat flux density at the melt varies more smoothly at the approach to the burner $\left(\text{the conditions } \frac{dQ}{dl} < 0 \text{ and } \left|\frac{dQ}{dl}\right| \ll \frac{\mathfrak{L}\varrho V}{R}\right)$. The requirements to the conditions of the Verneuil crystallization, derived from the theoretical analysis of the flame fusion method, are in good agreement with the data available in the literature on the optimal regimes of crystallization found empirically. Flow rates of process gases through the channels of a three-tube burner were adjusted experimentally in [5] in order to satisfy the condition $\frac{dR}{dl} < 0$. The crystal thus grown had a smoother surface and improved optical and structural characteristics. The condition $\frac{dR}{dl} < 0$ is analogous to that derived in this paper, $\frac{dQ}{dl} < 0$. Indeed, a crystal grown at a closer distance from the burner will have a larger radius only if the heat flux density Q increases toward the burner (l is directed from the burner).

The condition $\left|\frac{dQ}{dl}\right| \ll \frac{\mathfrak{L}\varrho V}{R}$ indicates that the heat flux density must vary along the muffle axis the smoother the larger the crystal radius. In principle, this is achieved by increasing the contact area of oxygen and hydrogen in the flame produced by the burner, for example of a multitube type [6], or by preheating the oxygen and hydrogen before they enter the burner [7]. The authors of [7] indicate that gas preheating improved crystal quality.

The advantages of powder melting before it reaches the molten layer are also born out by experiments [8].

REFERENCES

1. Sh. O. Arzumanyan, S. N. Shorin and L. A. Litvinov, Monokristally i Tekhnika, No. 2 (9), Kharkov, 1973. p. 23.
2. L. E. Elsgolts, Differential Equations and Calculus of Variations, Nauka Publs, Moscow, 1969, p. 227.
3. E. E. Spilrain, K. A. Yakimovich and A. F. Tsitsarkin, Teplofizika visokikh temperatur, **11**, 1001, 1973.
4. S. K. Popov, in: Rost Kristallov, Vol. XI, Moscow 1959, p. 145.
5. V. A. Tatarchenko and G. I. Romanova, Monokristally i Tekhnika, No. 2 (9), Kharkov, 1973, p. 48.
6. R. A. Lefever and G. W. Clark, Rev. Scient. Instr., **33**, 769, 1962.
7. E. B. Zeligman, B. K. Kazurov, S. D. Krasnenkova, in: Rost Kristallov, Vol. IX, Moscow, 1972, p. 159.
8. FRG Patent No. 1220403, 1967.

Acta Physica Academiae Scientiarum Hungaricae, Tomus 47 (1—3), pp. 159—165 (1979)

SOME ASPECTS OF THE MACROSCOPIC THEORY OF ORIENTED CRYSTALLIZATION FROM THE MELT

COMMUNICATION IV
THE FLOATING ZONE TECHNIQUES

By

E. A. BRENER, G. A. SATUNKIN and V. A. TATARCHENKO

THE SOLID STATE PHYSICS INSTITUTE, ACADEMY OF SCIENCES OF THE USSR
142432 CHERNOGOLOVKA, USSR

The stability of the crystallization process while growing crystals by the floating zone technique is analyzed. This technique is compared with Stepanov's with respect to crystallization process stability.

An idealized diagram of crystallization by the method of floating zone is shown in Fig. 4.1, where the crystal is pulled upward. The variants of the floating zone technique with the horizontal geometry and with the vertical downward pulling direction are also widely used. Various methods of heating are employed to form a molten zone: induction, electron-beam, or laser heating. Each specific heater design produces a characteristic region of maximum temperature which suggests a convenient physical reference point when thermal phenomena accompanying crystallization are analyzed. This reference origin in the Stepanov technique is taken at the shaper edge, and in the Verneuil technique at the burner end-face.

It should be noted that the stability of the floating zone crystallization was already analyzed [1]. The approach suggested in the present paper seems to us more general since [1] does not take into account the heat effects in the process of crystallization, with the ensuing approximate character of the derived stability criteria.

In contrast to the edge-defined film-fed crystallization (the Stepanov technique), the pressure P at the meniscus in the floating zone method is not determined by the height difference between the free melt surface level and the shaper edge but by the Laplace pressure. In the case of the Verneuil method the meniscus pressure was found from an additional boundary condition at the tip of a liquid drop $\left(\left.\frac{dz}{dr}\right|_{r=0} = 0\right)$.

An analysis of the floating zone crystallization is simplified if instead of pressure we consider the melt volume W whose time variation can be found from the mass conservation law. Both this volume and the pressure are then

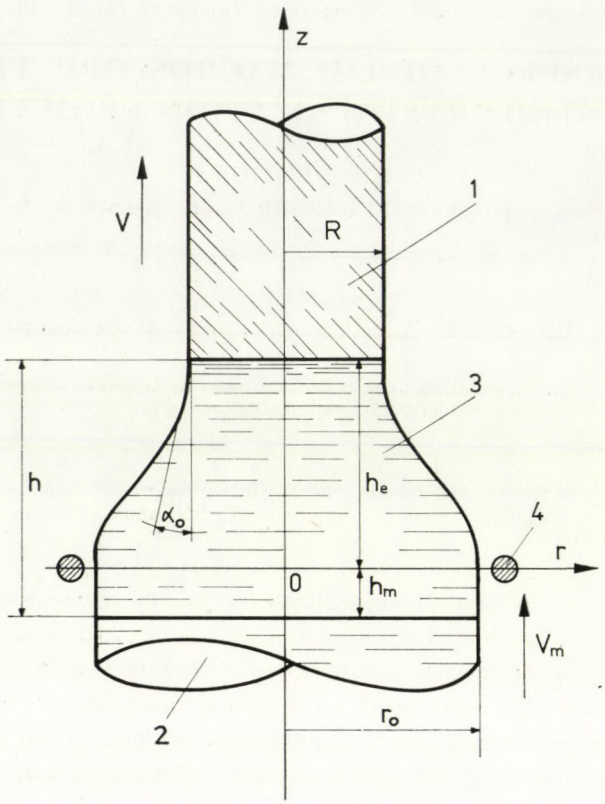

Fig. 4.1. An idealized diagram of crystal growth by the floating zone technique used to analyze the capillarity phenomena and the heat and mass transfer conditions in the process of crystallization. 1 — growing crystal; 2 — melted crystal; 3 — melt; 4 — heater

found by jointly solving the capillarity and thermal problems, taking into account the mass conservation relationship. Independently varied in the floating zone crystallization are the crystallization front position h_c and the melting front position h_m. The condition of heat balance at the melting front yields h_m as a function of time. In this case the molten zone length is $h = h_c - h_m$. Minus sign in this expression follows from h_m being negative in the reference frame of Fig. 4.1. All in all, there are therefore four independently varied characteristics: crystal radius R, crystallization front position h_c, melting front position h_m, and molten zone volume W (four-degree-of-freedom system). According to Lyapunov's theory, a system of equations determining the stability of the crystallization process in the general case is

$$\dot{\delta R} = A_{RR}\delta R + A_{Rh_e}\delta h_c + A_{Rh_m}\delta h_m + A_{RW}\delta W,$$

$$\dot{\delta h_c} = A_{h_eR}\delta R + A_{h_eh_e}\delta h_c + A_{h_eh_m}\delta h_m + A_{h_eW}\delta W,$$

$$\dot{\delta h}_m = A_{h_m R}\,\delta R + A_{h_m h_c}\,\delta h_c + A_{h_m h_m}\,\delta h_m + A_{h_m W}\,\delta W, \qquad (4.1)$$

$$\dot{\delta W} = A_{WR}\,\delta R + A_{W h_c}\,\delta h_c + A_{W h_m}\,\delta h_m + A_{WW}\,\delta W.$$

According to Eq. (1.5), the capillarity coefficients are determined, as in all the cases discussed previously by partial derivatives of the angle α_0 over an appropriate parameter: $A_{RR} = -V\frac{\partial \alpha_0}{\partial R}$, $A_{Rh_c} = -V\frac{\partial \alpha_0}{\partial h_c} = -V\frac{\partial \alpha_0}{\partial h}$, $A_{Rh_m} = -V\frac{\partial \alpha_0}{\partial h_m} = V\frac{\partial \alpha_0}{\partial h} = -A_{Rh_c}$, $A_{RW} = -V\frac{\partial \alpha_0}{\partial W}$. In contrast to the Stepanov technique, where $\frac{\partial \alpha_0}{\partial R}$ and $\frac{\partial \alpha_0}{\partial h}$ are calculated at a constant pressure, in the case in question these partial derivatives are to be found at a constant volume. In addition, $\frac{\partial \alpha_0}{\partial W}$ has to be found. An earlier publication [2] (its results were used to find capillarity coefficients for Stepanov's method) gives expressions for h as a function of R, α_0, and P. Using them, one can derive similar expressions for W; the partial derivatives in question for the floating zone crystallization are then found by writing the total differentials of dh and dW and eliminating dP in them. Details of the procedure are given in [3], and the capillarity coefficients for different types of menisci are listed in Table 4.I.

It has already been noted that an analysis of thermal phenomena in a crystal-melt-crystal system is facilitated if the reference frame origin is chosen in the maximum temperature point and if this temperature T_m is assumed

	A_{RR}	$A_{Rh}=A_{Rhe}$	A_{RW}	A_{hche}	A_{hmhm}	A_{hcR}	B	C
small-diameter crystals (R<a)	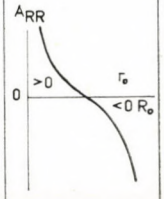	<0	>0	<0	<0	>0	<0	>0
large-diameter crystal (R>a) or plate	<0							

fixed. The thermal conditions in the growing crystal and in that portion of the molten zone which is located between the origin and the crystallization front are then quite similar to those analyzed earlier for the Stepanov techniques; consequently, A_{h_cR} and $A_{h_ch_c}$ coincide with the corresponding thermal coefficients A_{hR} and A_{hh}. Moreover, $A_{h_ch_m} = 0$, since the temperature gradients in the indicated part of the molten zone are independent of the position of the melting boundary h_m. The true shape of the meniscus is neglected in an analysis of thermal phenomena, by assuming it to be cylindrical with radius R. Under this approximation $A_{h_cW} = 0$. The next step taking into account the true shape of the meniscus consists in introducing the mean meniscus radius which should be substituted for R in the corresponding expressions for temperature gradients in the liquid phase. Such a substitution would have no principal importance in the case of Stepanov's method, since there the essential factor is the crystal radius R. In the floating zone crystallization, however, an independent variation of volume W even for fixed crystal radius R results in a changed meniscus radius and in a correspondingly changed temperature gradient in the liquid phase. Obviously, A_{h_cW} has the same sign as $A_{h_cR}(A_{h_cR} > 0)$. Indeed, an increase in W and that in R result in an increased mean radius of the meniscus and hence in an enhanced heat flux to the crystallization front and a diminished rate of crystallization. We assume in the first approximation $A_{h_cW} = 0$, and later give a qualitative analysis of the consequences of the indicated effect for the stability of the crystallization process. It has been mentioned above that the advancement rate of the melting front can be found from the heat balance condition at the melting boundary:

$$\lambda_1 G_1 - \lambda_s G_s = \mathfrak{L}\left(V_m - \frac{dh_m}{dt}\right), \tag{4.2}$$

where V_m is the velocity of the melted crystal, G_1 and G_s are temperature gradients at the melting front in the melt and crystal, respectively. The heat supplied to the crystallization front from the liquid phase flows into the growing crystal together with the liberated heat of crystallization. At the same time, the heat flux from the liquid phase to the melting front must be sufficient for melting of the crystal advancing at the velocity V_m. As a result, the temperature gradient in the liquid phase at the melting front is greater than the corresponding gradient at the crystallization front. In both cases the temperature difference $T_m - T_0$ with respect to the maximum temperature point is the same, so that we find $h_m < h_c$; this last inequality is the stronger the higher the crystallization rate and, correspondingly, the advancement rate V_m. In the first approximation, the thermal flux leaving the melt by heat exchange through the lateral surface of the meniscus is proportional to h_m and can be ignored at small h_m. Within this approximation, the temperature

gradient in the liquid phase at the melting front can be assumed equal to $G_1 = -\dfrac{T_m - T_0}{h_m}$ (the minus sign comes from $h_m < 0$). As follows from (4.2), in steady-state conditions

$$\mathfrak{L} V_m = -\lambda_1 \frac{T_m - T_0}{h_m} - \lambda_s G_s.$$

In the case of deviation from the equilibrium, we obtain

$$\delta \dot{h}_m = -\frac{\lambda_l}{\mathfrak{L}} \frac{T_m - T_0}{h_m^2} \delta h_m. \tag{4.3}$$

It can be demonstrated that from the standpoint of crystallization stability, the selected approximation with $A_{h_m R} = A_{h_m h_1} = A_{h_m W} = 0$ implies that terms proportional to h_m/h_1 are neglected. In other words, the criterion of applicability of the approximation in question is: $h_m/h_c \ll 1$. The heat flux from the lateral meniscus surface along the whole zone length must be taken into account at small growth rates and for such heat transfer conditions when $h_m \approx h_c$.

It was mentioned above that the changes in melt volume can be found by resorting to the mass conservation law:

$$\frac{dW}{dt} = \pi \frac{\varrho_s}{\varrho_l} \left[r_0^2 \left(V_m - \frac{dh_m}{dt} \right) - R^2 \left(V - \frac{dh_m}{dt} \right) \right], \tag{4.4}$$

where ϱ_s and ϱ_1 denote the solid and liquid phase densities, respectively, and r_0 is the radius of the crystal melted. With given r_0, V_m, and the pulling rate V, the radius of the growing crystal R_0 is found from the condition of the steady-state growth $r_0^2 V_m = R_0^2 V$. For deviations from the equilibrium, the corresponding coefficients in (4.1) are

$$A_{WR} = B + CA_{h_c R}, \quad A_{W h_c} = CA_{h_c h_c}, \quad A_{W h_m} = -CA_{h_m h_m},$$

$$A_{WW} = CA_{h_c W}, \quad B = -2\pi \varrho_s/\varrho_l R_0 V, \quad C = \pi \frac{\varrho_s}{\varrho_l} R_0^2$$

(we recall that at this junction $A_{h_c W} = 0$).

According to the Gurvitz criterion, the necessary and sufficient conditions of stability of system (4.1), with coefficients A as analyzed above, are

$$A_{h_m h_m} < 0, \tag{4.5}$$

$$A_{RR} + A_{h_c h_c} < 0, \tag{4.6}$$

$$BA_{RW} A_{h_c h_c} > 0, \tag{4.7}$$

$$BA_{RW} A_{RR} - (A_{RR} + A_{h_c h_c})(A_{RR} A_{h_c h_c} - A_{R h_c} A_{h_c R} - CA_{RW} A_{h_c R}) > 0. \tag{4.8}$$

If the thermal coefficients ($A_{h_e R}$ and $A_{h_e h_e}$) are formally set to zero in inequalities (4.6) and (4.8), the stability criteria derived earlier in [1] are obtained $\left(\frac{\partial \alpha_0}{\partial R} > 0 \text{ and } \frac{\partial \alpha_0}{\partial W} < 0\right)$. The conditions (4.5)—(4.8) derived in the present paper are more general. When $T_m > T_0$ (superheating of the zone, i.e. the necessary condition of growth in the floating zone method), $A_{h_m h_m}$ and $A_{h_e h_e}$ are negative, that is inequality (4.5) is always satisfied. As shown in [1, 3], A_{RW} for all zone parameters is positive $\left(\frac{\partial \alpha_0}{\partial W} < 0, \text{ see Table 4.I}\right)$, that is decreases as the zone volume increases. Since at the same time $B = -2\pi \frac{\varrho_s}{\varrho_l} R_0 V < 0$, condition (4.7) is satisfied at all times. Inequality (4.6) is also satisfied in the range of capillarity stability, $A_{RR} < 0$ $\left(\frac{\partial \alpha_0}{\partial R} > 0\right)$. It has been mentioned already [1] that $\frac{\partial \alpha_0}{\partial R} > 0$ in a wide range of zone parameters, but in [3] it was demonstrated that there are such meniscus shapes for which stability is violated $\left(\frac{\partial \alpha_0}{\partial R} < 0\right)$. Nevertheless it can be rigorously demonstrated that A_{RR} in the floating zone growth is always smaller than the corresponding A_{RR} of similar menisci in the Stepanov techniques. This means that the capillarity stability boundary $\left(\frac{\partial \alpha_0}{\partial R} = 0\right)$ in the floating zone method is shifted towards smaller crystal radii. In other words, this method may produce crystals with $r_0/R_0 > 2$.

HAGGERTY reported [4] the growth of thin sapphire filaments by the floating zone method, with r_0/R_0 reaching 10. This large difference in r_0 and R_0 is explained by the difference in growth conditions: in the Stepanov techniques the crystal radius changes at a constant pressure while in the floating zone growth it changes at a constant volume. The two methods reveal, nevertheless, some features which are qualitatively common from the point of view of crystallization stability. The growth in the range of capillarity instability is possible for both if the conditions of thermal stability are satisfied. A more detailed analysis of condition (4.8) given in [3] shows that, as in the Stepanov technique, the growth of large-diameter crystals or plates is unstable in the range of two valued menisci, for R_0 close to r_0.

It was noted above that changes in the zone volume W at fixed R and h result in changes in the temperature gradient in the liquid phase. This factor was not yet included into the analysis of crystallization stability. It is obvious, however, that this effect lowers the stability. Indeed, an increase in the zone volume enhances the heat flux to the crystallization front and diminishes the crystallization rate (see above), which in turn increases the melt volume still further. Evidently, the overall stability of crystallization may still take place.

No such effect is inherent, all other factors being equal, in the Stepanov technique; this is a definite advantage of the method as compared to the other three.

Conclusion

An analysis given enables to select optimal design and modes of crystallization for all the methods discussed and to recommend the advisable ranges of application for each of them. For instance, the Czochralski techniques are most suitable for growing large-diameter crystals, while the Verneuil techniques are favoured for small-diameter ones. When crystallization proceeds in nonsteady-state conditions, as for example, in growing large-diameter crystals by the Verneuil techniques, the automatic control units must be employed, with parameters satisfying the results given in this paper. We did not touch upon the crystal quality problems; it is nevertheless quite obvious that violation of set modes of crystallization do constitute a source of increased defect concentration in crystals. Consequently, the steady-state mode of crystallization is advantageous in growing more perfect crystals.

REFERENCES

1. T. Surek and S. R. Coriell, J. Cryst. Growth, **37**, 253, 1977.
2. V. A. Tatarchenko, J. Cryst. Growth, **37**, 272, 1977.
3. V. A. Tatarchenko, E. A. Brener and G. A. Satunkin, J. Cryst. Growth, to be published.
4. J. S. Haggerty, Production of Fibers by a Floating Zone Fiber Drawing Technique, NASA CR — 120948, May 1972.

Acta Physica Academiae Scientiarum Hungaricae, Tomus 47 (1—3), pp. 167—183 (1979)

ARTIFICIAL EPITAXY (DIATAXY) OF SILICON AND GERMANIUM

By

V. I. KLYKOV, N. N. SHEFTAL

INSTITUTE OF CRYSTALLOGRAPHY, ACADEMY OF SCIENCES OF THE USSR, MOSCOW, USSR

and

E. HARTMANN

RESEARCH LABORATORY FOR CRYSTAL PHYSICS OF THE HUNGARIAN ACADEMY OF SCIENCES
BUDAPEST, HUNGARY

The artificial epitaxy (diataxy) of silicon and germanium on amorphous quartz substrates was investigated in order to determine the best type of relief pattern, the mechanism of orientation and other regularities of the process.

Introduction

The investigation of artificial epitaxy began with experiments in 1963 [1]. The first successful results were obtained by crystallization in solution on diffraction gratings with crossing systems of lines only in 1972 [2]. Further work was carried out by the crystallization of principally semiconductor materials on special artificial surface-relief gratings [3—6].

The essence of the idea of artificial epitaxy is the growth of single crystal layers on nonoriented substrates having a relief pattern which interacts with the microcrystals appearing in the medium of crystallization. The term "artificial epitaxy" does not explain the idea of the method. Therefore it was replaced by another, shorter term — "diataxy" (drawing epitaxy).

In this work, the diataxy of silicon and germanium on amorphous quartz substrates was investigated by VLS crystallization in order to determine the best type of relief pattern, the mechanism of orientation, and other regularities of process.

Experimental part

Substrates

Four types of micropatterns were used. The first three of them (Fig. 1a, b and c) served for the orientation of crystals growing on a face (111). Among them were hexagonal patterns (Fig. 1b) for the hexagonal faces of

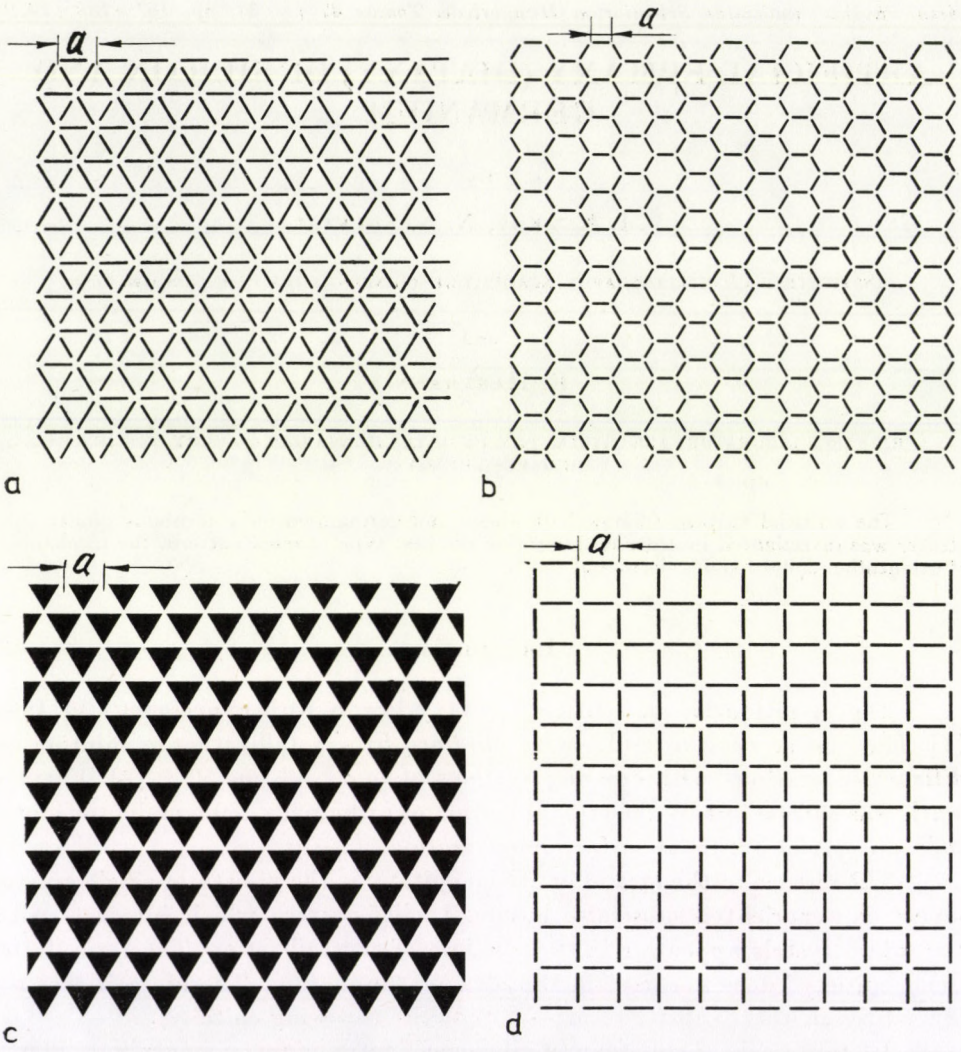

Fig. 1. The types of pattern for the diataxy

cuboctahedra. A square net (Fig. 1d) was used for the orientation of crystals that grow onto the substrate with a cube face.

The neighbouring cells of the patterns in Fig. 1a are in twin position. The pattern of Fig. 1c does not include twin cells.

The patterns on the substrates are obtained by photolithography relief etching. The dark sites in Fig. 1 correspond to the protuberances of the micro-relief, the light ones to the depressions.

The growth of silicon and germanium was accomplished by the VLS mechanism by the chloride method [7] using gold or silver as solvents. To

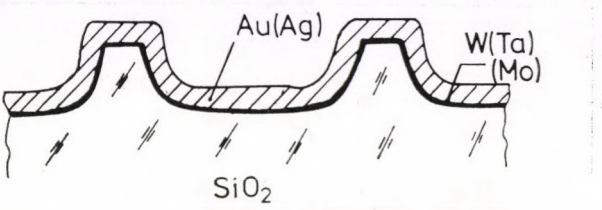

Fig. 2. The cross-section of the substrate prepared for diataxial growth

improve the adhesion of melt of gold with the substrate surface which already has a formal relief pattern, the surface was covered by a thin (2000 Å — 2 μm) layer of W by vacuum evaporation. Thin films of Mo and Ta were used, if Ag served as a solvent. Au and Ag were also deposited on the substrates by vacuum evaporation. The thicknesses of these layers were 0.1—15 μm. A cross section of the prepared substrates is shown in Fig. 2. The substrate has a surface area 15—20 mm^2 and a thickness of 1 mm.

Growth of diataxial layers

The growth of diataxial layer was performed in a vertical tube reactor having HF heating. The temperature of the specimens was measured with an optical pyrometer with $\pm 10°$ accuracy. The tetrachlorides of silicon and germanium conform to quality special class of purity and hydrogen with dew point -70 °C and oxygen content 10^{-5} % were used.

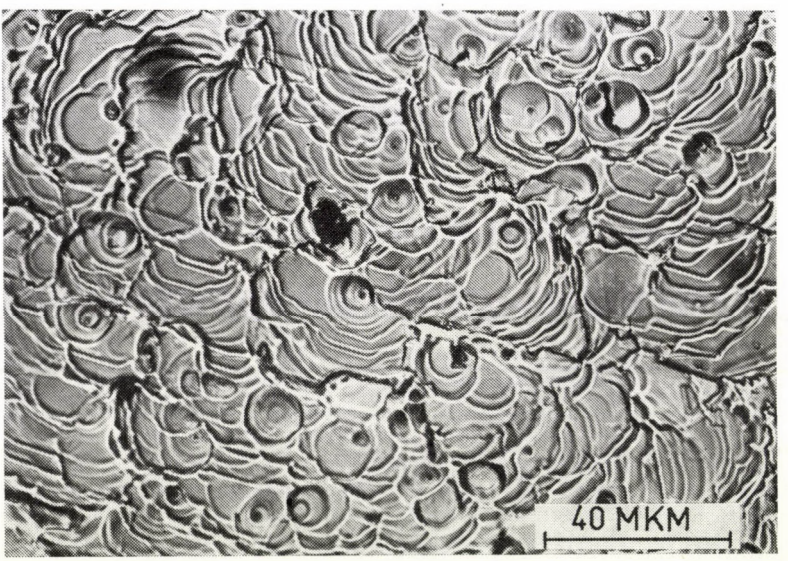

Fig. 3. Typical shape of surface of thick diataxial layer observed using interferential contrast

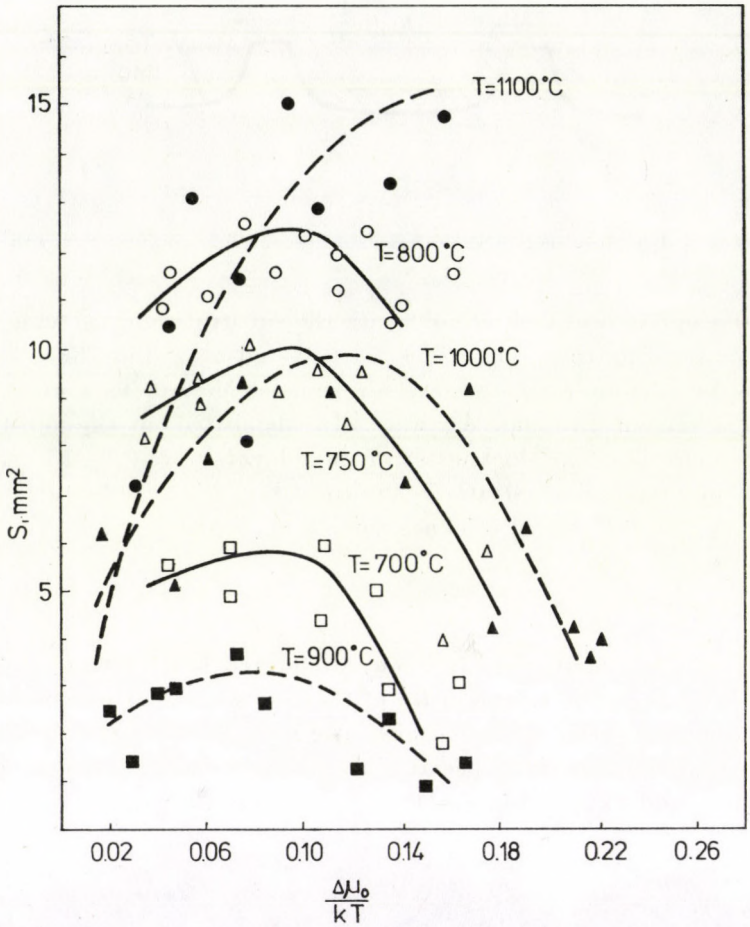

Fig 4. The dependence of area of monocrystalline layers of Si (dashed lines) and Ge (continuous lines), grew from the solution in Au on supersaturation. Size of cells 10 μm. Area of substrates 20 mm². ○, △, □ — Ge; — ●, ▲, ■ — Si

The study of the morphology of diataxial layers showed that their formation occurs according to the following scheme:

1) the formation of a supersaturated solution in the melt;

2) the appearance of the crystallization centres and their orientation by the pattern;

3) their tangential expansion and the formation of single crystal regions;

4) coalescence of the separate single crystal region into a continuous monocrystalline layer.

It was established by the method of the askew polishing that after crystallization most of the solvent (70—90%) is found between the single crystal and the substrate. The rest of the solvent is either driven back to the sides of the substrate or is squeezed out onto the surface of the diataxial layer.

If single crystal regions do not unite, the solvent remains in the form of a vein. An insignificant part of the solvent ($<0.001\%$) is captured by the single crystal in the form of solid solution.

The morphology of a diataxial layer is essentially formed by the influence of displaced droplets of metal-solvent. It consists of a great number of the little round steps (Fig. 3), whose faces are evidently covered by a thin layer of solvent ([8], p. 133). The trains are the traces of the motion of metal droplets on the surface.

Influence of supersaturation

The total sizes of single crystal areas are determined principally by the adhesion between the substrate and the liquid phase and the number of crystallization centres. Both of these factors are functions of supersaturation. The dependence of the sizes of Ge and Si diataxial layers grown from Au solutions vs the crystallization conditions is shown in Fig. 4.

At the beginning an increase of supersaturation leads to an extension of the single crystal areas. Gradually they achieve the maximum size and the subsequent increase of supersaturation increases the competition between the centres of crystallization and gives rise to the formation of the mosaic structures. The area of single crystal regions diminishes (Fig. 4) and their structural perfection decreases.

The growth of supersaturation and, correspondingly, the number of crystallization centres, leads to polycrystalline growth.

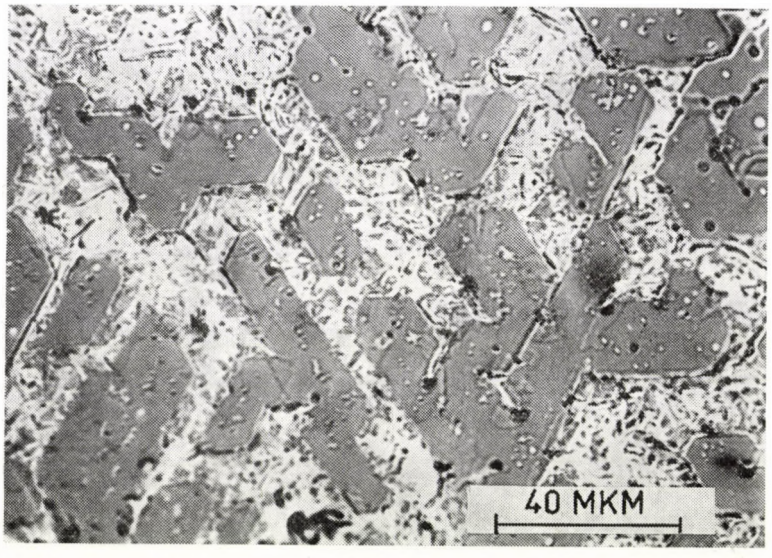

Fig. 5. Diataxial growth of Si at supersaturation <0.1

Thus there exists some optimum interval of supersaturation in which it is possible to obtain the maximum sizes of single crystal layers.

The maximum sizes of monocrystalline layers of Ge and Si, obtained from the Au solution were almost equal to the substrate sizes reaching 10—15 mm².

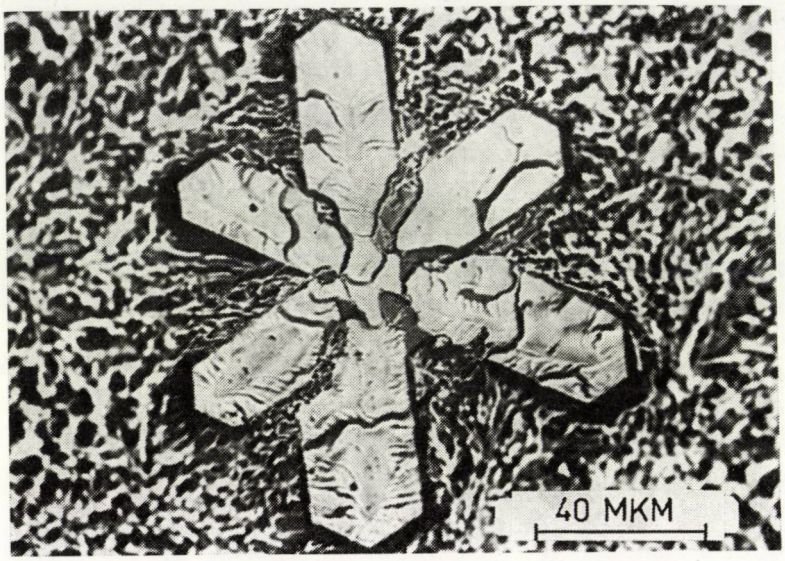

Fig. 6. An example of predendrite stage of crystallization

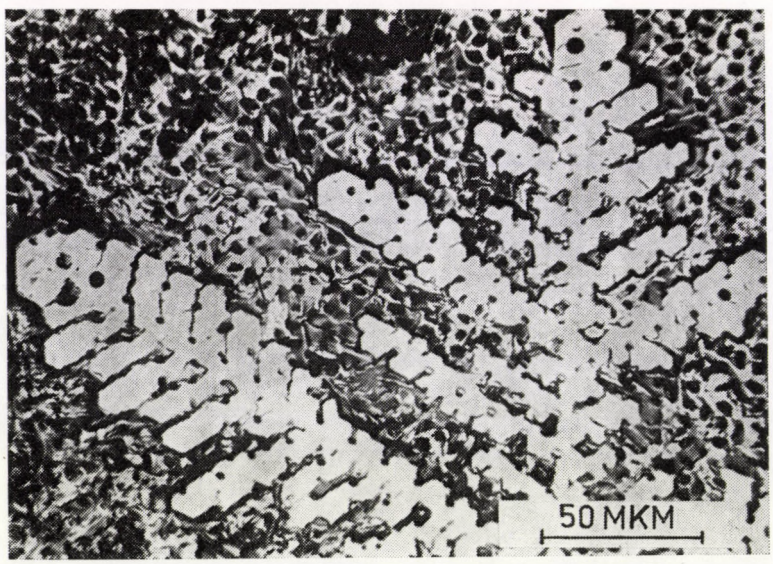

Fig. 7. Si dendrite, grown from solution in Au on the triangle net. Size of cell: 10 μm

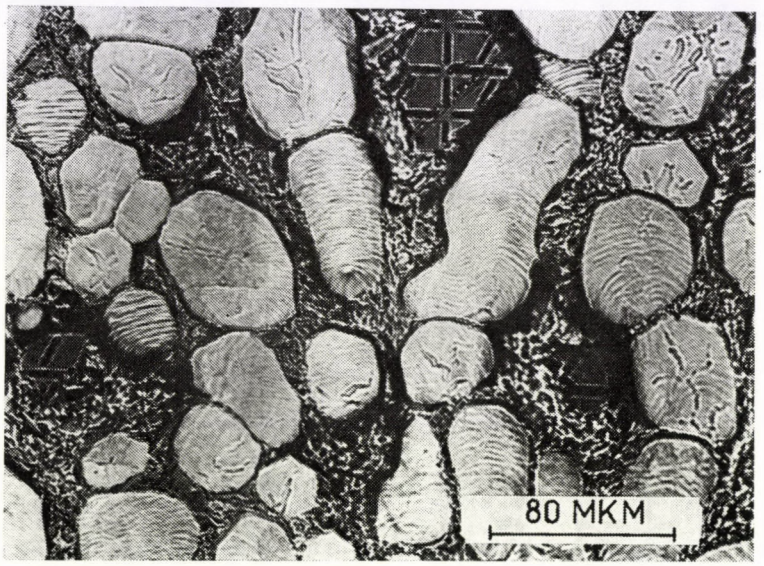

Fig. 8. Rounded growth of Ge from the solution in Au

But along the perimeter of this area too remained a polycrystalline border having a width near 1 mm. By using Ag as solvent, single crystal layers whose areas were almost twice less were obtained.

The supersaturation for the average value of the temperature 800 °C for germanium and 1000 °C for silicon significantly affected the growth of layers. At relatively small (less than 0.1) supersaturations Ge and Si form in the initial growth period well faceted crystals with smooth (111) surfaces parallel to the substrate.

These crystals grow in the monocrystalline regions retaining the facing (Fig. 5).

The increase of the supersaturation above 0.1 initiates the first manifestation of morphological instability — the "predendritic state" (Fig. 6). One can see that first a small crystallization centre is formed. Then six branches grew out from this centre, developing into well faceted crystals. Their morphologies show that in the later period the growth is smoother; this is related to the lowering of the supersaturation in the growth zone caused by the crystallization. Further increase of supersaturation induces the appearance of the well-developed dendrites (Fig. 7).

If the supersaturation continues to increase, round crystals with a large number of curvilinear steps on the surface are formed, instead of dendrites. This is especially characteristic of the growth of Ge (Fig. 8).

A very large supersaturation ($\sim$0.2) gives rise to polycrystalline growth accompanied by mass whisker growth.

The influence of temperature

The size of the single crystal areas increases continuously with a rise of temperature (Fig. 9). This can be explained by the better adhesion of the liquid phase with the substrate. The influence of the temperature on the morphology of the growing layers under different supersaturations is shown in Fig. 10 for Si (in the case of Ge the changes are similar but occur at a temperature by about 150 °C lower). Only chaotic mass whisker growth was observed below 750 °C without any principal direction. The density of the whiskers often reached 10^9 cm^{-2}. With the increase of the temperature to 1100 °C, the transition to polycrystalline and then to monocrystalline growth is gradually observed.

An increase in temperature facilitated the formation of smoother surfaces

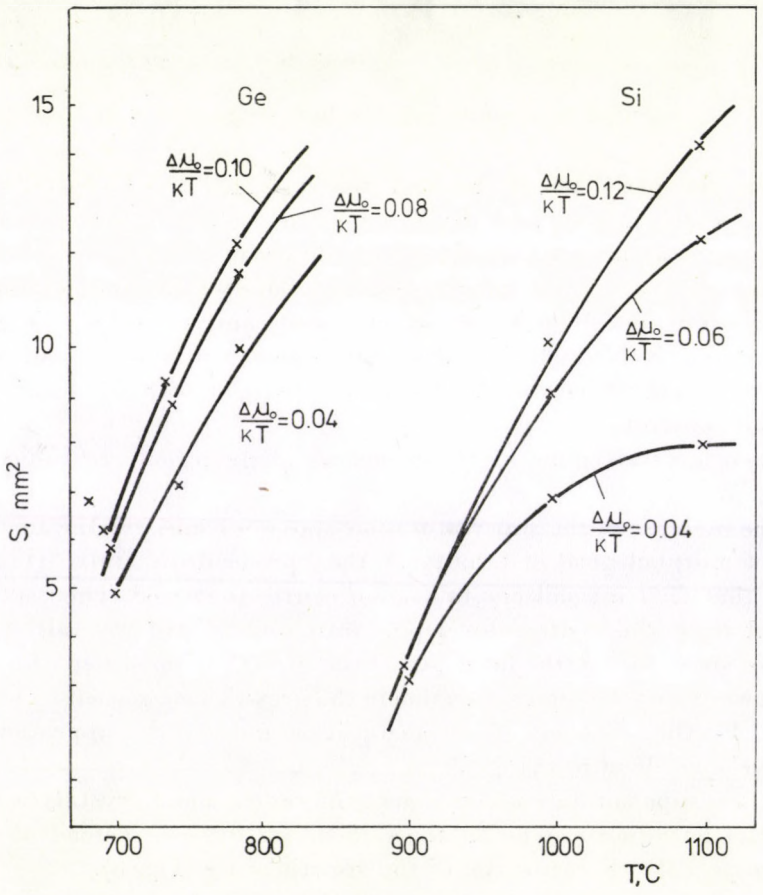

Fig. 9. The influence of temperature on the sizes of Si diataxial layers. Triangle net, size of cells — 10 μm, solvent — Au

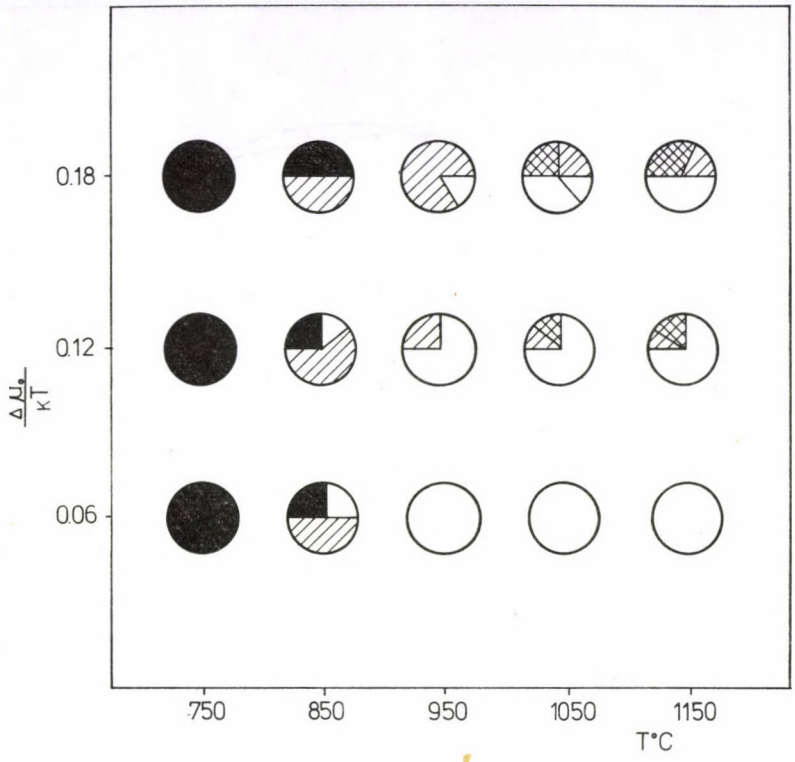

Fig. 10. The influence of temperature on the morphology of diataxial layers of Si. ○ — single crystal, ▨ — polycrystal, ⁝⁝ — dendrites, ● — whiskers

of the monocrystalline areas. The number of steps was diminished and the lateral faceting became more sharply defined.

Above 1000 °C predendritic and dendritic crystallization was observed.

Influence of the thickness of the solvent layer

The molten layers of Au or Ag tend to form droplets. The microrelief of the substrate prevents this.

Continuous layers equal to the substrate area can be obtained as a result of tangential growth and a subsequent concretion of several single crystal regions with the same orientation that were developed in different sites of substrate.

The dependence of the size of the layers on the initial thickness of the film is shown in Fig. 11.

For the orientation of the small crystals by the patterns it is necessary that the seed floating on the surface of the liquid phase be able to grow to the size of the cell while retaining high mobility. The optimum thickness of Au

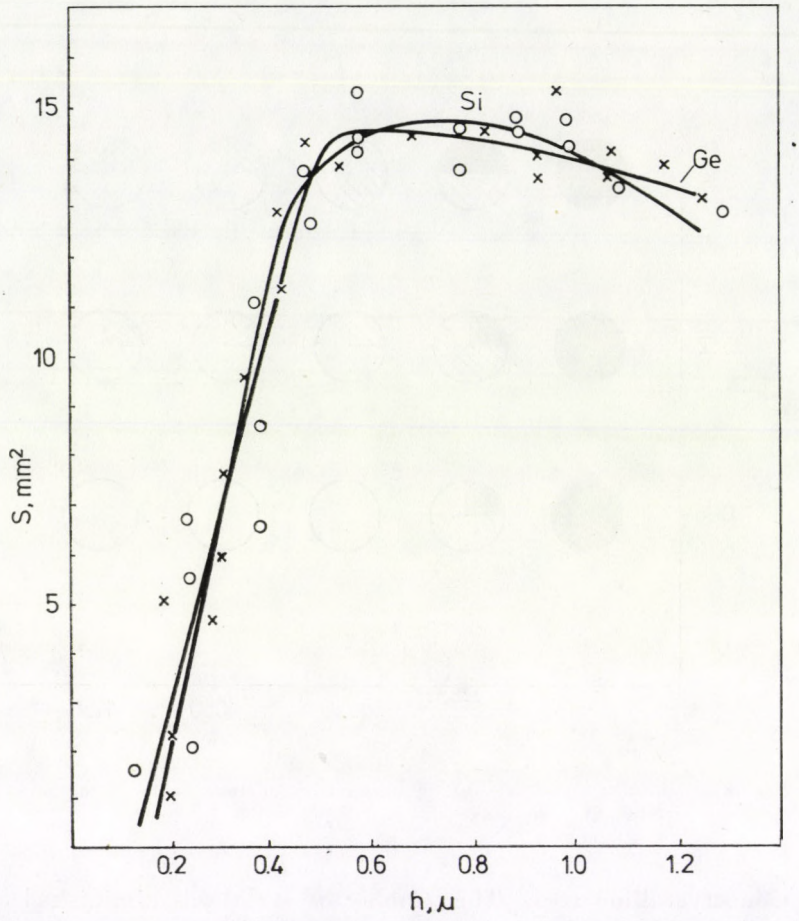

Fig. 11. The dependence of the size of diataxial layers on initial thickness of Au film. Size of cells: 20 μm

films is 0.5—0.8 μm. It approximately corresponds to the depths of the microrelief with cell site 10—40 μm. In this interval of thickness the action of the orientational mechanism is more effective and the microrelief retains the liquid phase sufficiently well.

The orienting actions of the pattern are worse if the thickness of the liquid layer is larger than the relief depth.

Influence of the pattern type

Since layers nearly always with orientation (111) have been formed on all types of substrates, the patterns which take this fact into account have been the most effective. The total area of single crystal regions served as a measure

of effectiveness. The effectiveness of the orienting action is diminished from "a" to "c", "b", "d" as shown in Fig. 1.

The orienting action of the pattern is determined in general by the form of the cells and their dimensions.

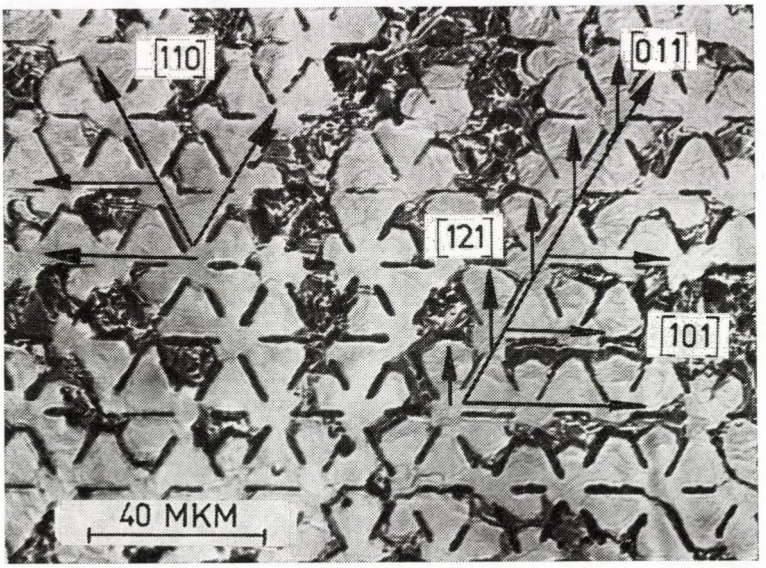

Fig. 12. The initial stage of diataxial growth of Ge from the solution in Au on a triangle net

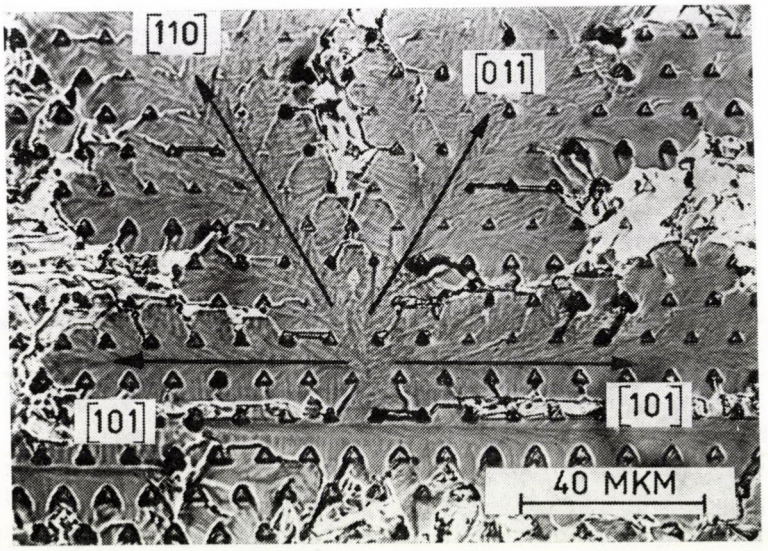

Fig. 13. The growing of a Ge crystallization centre on the pattern of Fig. 1c

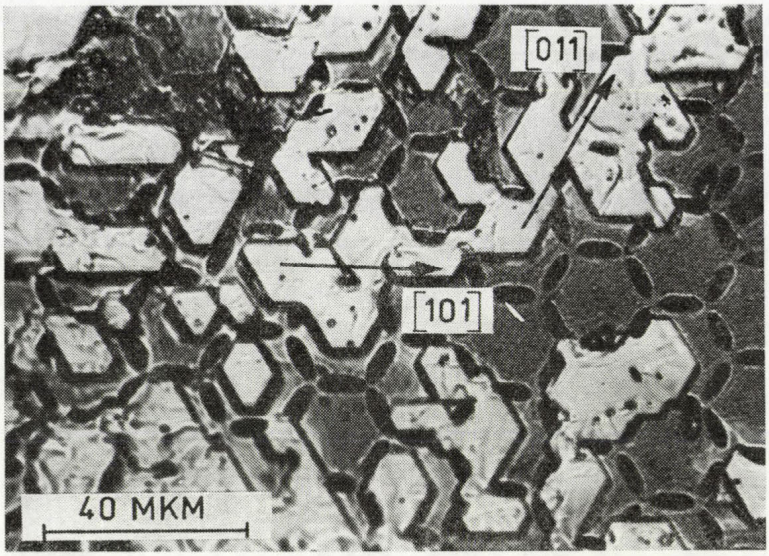

Fig 14. Ge small crystals on the substrate with hexagonal net

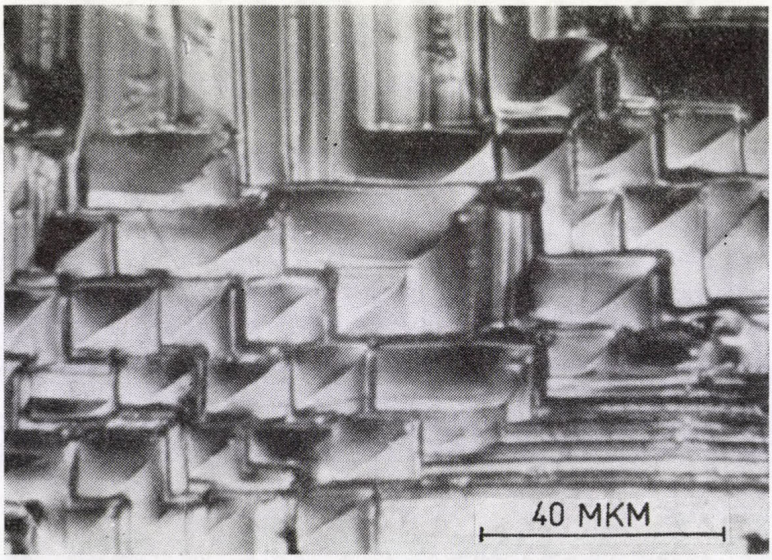

Fig. 15. Ge layer with (100) orientation

The initial stage of growth a of Ge layer on a part of a surface of the substrate with triangular pattern is shown in Fig. 12. The growth proceeds from several places simultaneously. It is possible to find the centres of growth and to observe the spread of layers by using the arrangement of the growth steps on the single crystal surface. Two such centres are shown in Fig. 12.

Using the pattern without twin cells the growth direction ⟨110⟩ is the most advantageous.

One can see that the big single crystal area developed from one centre (Fig. 13).

The small crystals of Ge which have been grown on the substrate with the hexagonal pattern area shown in Fig. 14. Iodine etchant was used to remove Au.

The part of the centres where there is a lack of crystallizing material gives almost isometrical crystals.

The appearance of regions with (100) orientation has been observed in less than 1% of the cases of the growth of single crystal layers and such layers appear more frequently on Ge than on Si. Such a region in the case of Ge is shown in Fig. 15.

The attempts to control diataxial crystallization of (100) layers on the substrates with the square patterns have not succeeded.

Influence of the cell sizes

This influence can be seen with the aid of the pattern shown in Fig. 1a (as the most effective one). The cell size is changed from 10 μm to 1 mm and the smaller the size the stronger is its orienting action. When the cells are 10—20 μm, it is possible to obtain layers of Ge and Si from Au solution which cover almost all the substrate surface. An example is shown in Fig. 16.

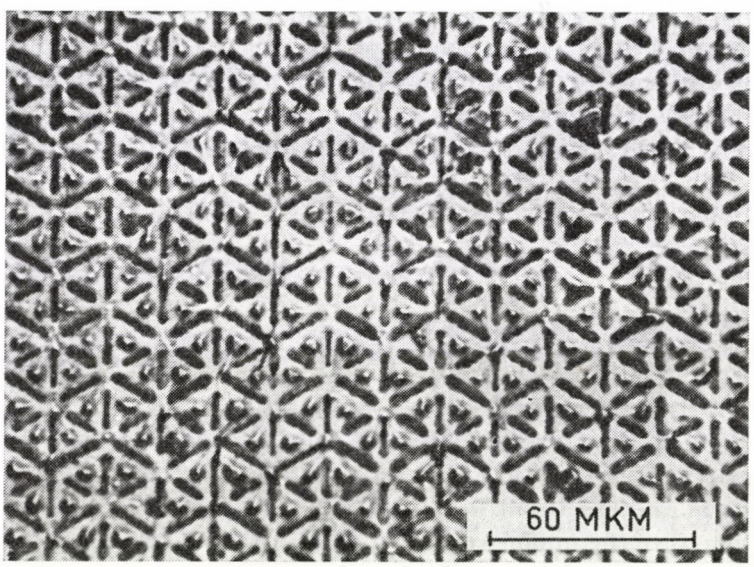

Fig. 16. The orienting action of the pattern with cells of 20 μm under high density of crystallization centres

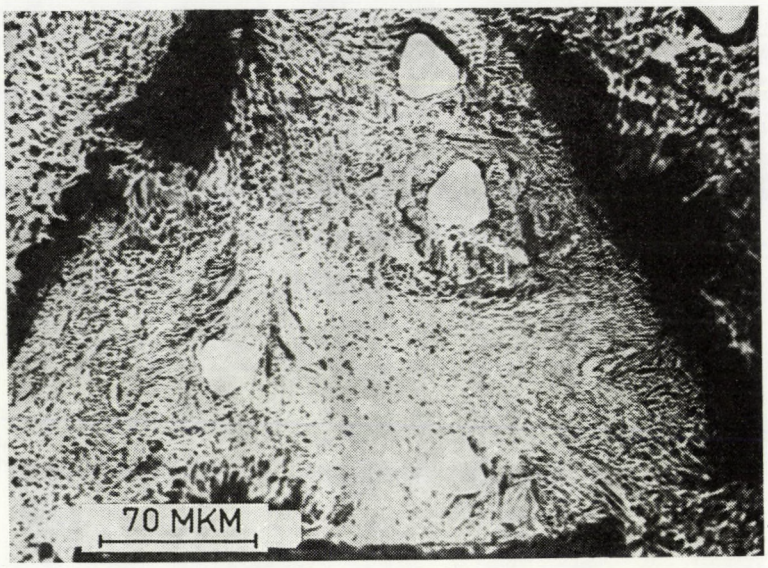

Fig. 17. Ge small crystals on the surface of Ge—Au alloys in a triangle net of 450 μm

It can be seen that every cell has a small oriented silicon crystal.

If the cell size is increased the orienting action of the pattern is gradually diminished. The areas of the single crystal regions diminish also and their quality deteriorates. In the first stages of growth the number of nonorientated small crystals increases. This occurs because the increase of the cell sizes gives rise to the weakening of the capillary forces acting as the orienting factor.

The weakening of the capillary forces becomes observable at cell sizes of 100 μm (Fig. 6). The growing crystals tend to join in places where the capillary forces are stronger, i.e. in the narrowing cell knots. With a further increase of the cell sizes several crystals tend to appear simultaneously in the cell disturbing each other (Fig. 17). In this case the cell does not act as an orienting factor.

The perfection of the layers

The structural defects appearing during the process of diataxy can be divided into two groups: defects due to the influence of the pattern, defects which are independent of the pattern. The twins and low-angle boundaries relate to the first group. The twins arise in all patterns excluding the pattern in Fig. 1c while in the case of the pattern Fig. 1a all adjacent cells are twinned.

In practice, the number of twin boundaries can be diminished if crystallization occurs with a low density of nucleation centre, when each centre can grow forming a large single crystal area.

If, accidentally, a growing crystal is not in correct position in the cell, low angle boundaries will be generated in the spreading process of the layers.

The twin and low-angle boundaries are not straight lines because they reproduce the form of crystallization front.

The second group of structural diataxial defects are dislocations, stacking faults, tripyramids, etc. Stacking faults have been observed very rarely, especially at the beginning stage of growth.

Tripyramids have been observed only in the thick layers and in very small quantity.

The defects most frequently are dislocations. Etching shows that the dislocation arrangement is very irregular. In some regions they are absent while in other regions they form large groupings. Their appearance may be caused by the capture of microdroplets of the liquid phase of the impurity particles.

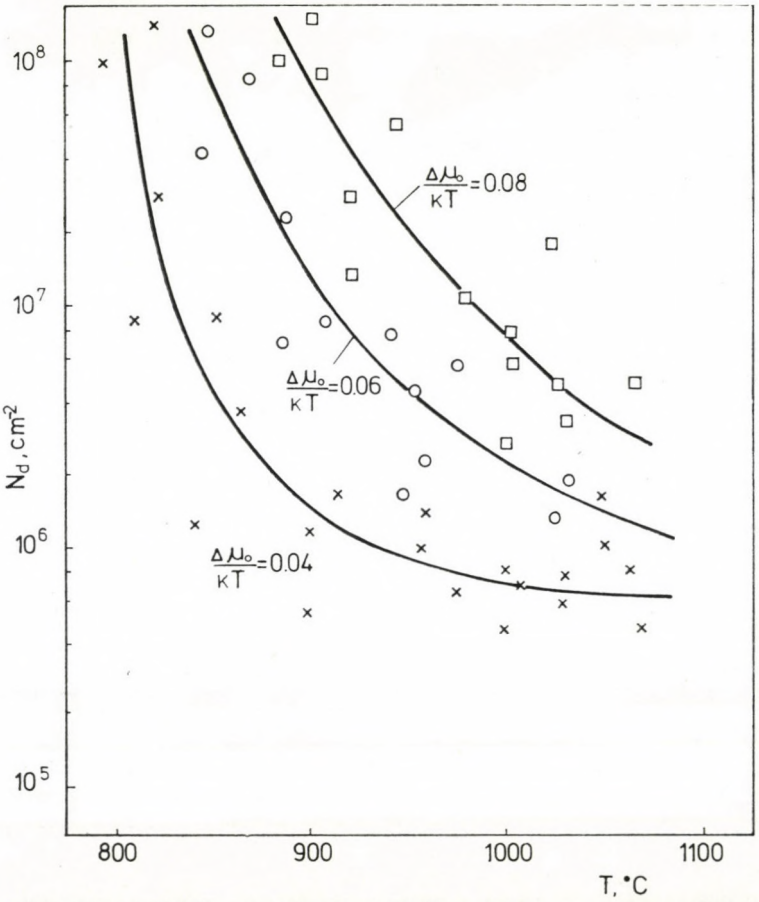

Fig. 18. The dependence of dislocation density in Si diataxial layers on the condition of growth (Triangle net, size of cells — 20 μm, solvent Au)

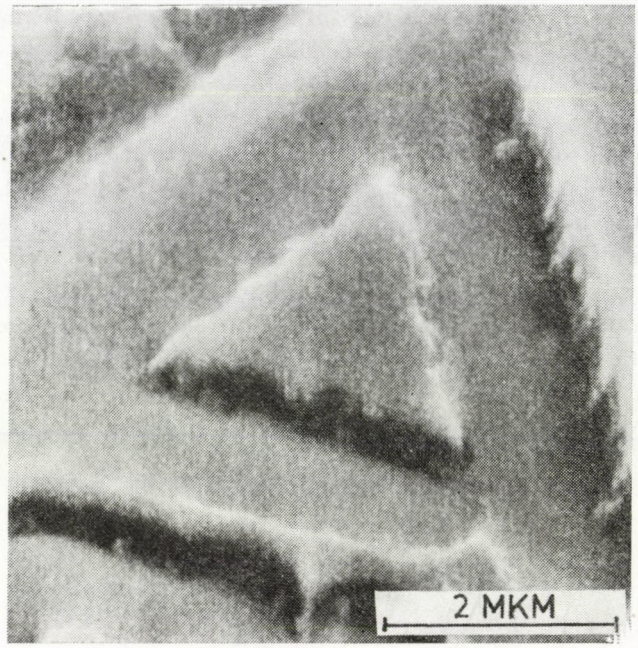

Fig. 19. Si small crystal on the surface of Si—Au alloys in the centre of a triangular cell

The dislocation density, according to the etch pits, is 10^5—10^6 cm^{-2} in good layers. In Si layers grown on single crystal sapphire substrates, it equals 10^8 cm^{-2} [9].

The dislocation density depends on the growing conditions. It diminishes with the increase of the temperature and with the reduction of the supersaturation (Fig. 18).

The mechanism of orientation

Small crystals of Si and Ge in Si—Au and Ge—Au systems prove to be a surface active impurity [10]. For this reason, and owing to their low density, these crystals must be on the surface of the liquid phase. Here they grow quickly being very mobile, and when their dimensions become commensurable with those of the cell, their orientation occurs under the action of capillary forces.

An example for the orientating action of such forces is shown in Fig. 19. Here a Si crystal is in the centre of a pattern cell. One can see that the crystal does not come into contact with the cell walls, being in strictly orientated position.

The orientation effect of capillary forces on macroscopic scale is dealt with in another paper [11].

Such are the main regularities of the new method for obtaining single crystal layers on non-orientated substrate.

Recently, the same principle has been developed elsewhere, too [12]. It can be estimated as an indication of its perspective.

REFERENCES

1. N. N. SHEFTAL, in: Growth of Crystals, Vol. **10**, Nauka, 1974. p. 195 (in Russian); Consultants Bureau, New York, 1976, p. 185.
2. N. N. SHEFTAL and A. N. BUZYNIN, Vestnik MGU, ser. geol., N 3, 102, 1972.
3. V. I. KLYKOV, N. N. SHEFTAL and N. P. KOKORISH. Manuscript depon. in VINITI N 642-76 from 1.03.76.
4. V. I. KLYKOV, R. N. SHEFTAL, and N. N. SHEFTAL, in: Process of Real Crystal Formation, Nauka, Moscow, 1977, p. 144.
5. N. N. SHEFTAL and V. I. KLYKOV, in: The Mechanism and Kinetics of Crystallization, Vol. 1, Tbilisi, 1977, 31 (Abstracts for 5th Conference on Crystal Growth).
6. V. I. KLYKOV and N. N. SHEFTAL, Vestnik MGU, ser. geol. N 1, 115, 1978.
7. N. N. SHEFTAL, N. P. KOKORISH and A. V. KRASILOV, Izv. AN SSSR, ser. fiz. **21** (1), 147, 1957.
8. E. I. GIVARGIZOV, The Growth of Whiskers and Lamellar Crystals from Vapour Phase, Nauka, Moscow, 1977 (in Russian).
9. S. A. GARJAINOV, The Dielectrical Isolation of the Elements of the Integral Schemes, Sov. Radio, Moscow, 49, 1975.
10. IU. V. NAIDICH, V. M. PEREVERTAILO and L. P. OBUSHCHAK, in: Physical-chemistry of the Condensed Phase, Overhard Materials and their Boundaries. Naukova Dumka, Kiev, 1975, p. 3.
11. E. HARTMANN, N. N. SHEFTAL and V. I. KLYKOV, Acta Phys. Hung., this issue, p. 185.
12. H. I. SMITH and D. C. FLANDERS, Appl. Phys. Lett., **32**, 349, 1978.

Acta Physica Academiae Scientiarum Hungaricae, Tomus 47 (1—3), pp. 185—188 (1979)

ON THE ORIENTATION EFFECT OF CAPILLARY FORCES

By

E. HARTMANN

RESEARCH LABORATORY FOR CRYSTAL PHYSICS OF THE HUNGARIAN ACADEMY OF SCIENCES
BUDAPEST, HUNGARY

N. N. SHEFTAL and V. I. KLYKOV

INSTITUTE OF CRYSTALLOGRAPHY, ACADEMY OF SCIENCES OF THE USSR, MOSCOW, USSR

The positions of crystals floating on the surface of a liquid in triangular and quadratic cells are investigated. It is demonstrated that the orientations of the crystals can be explained by capillary forces.

Studying artificial epitaxy [1] it was observed that during the growing process a small crystal of triangular form floating on the surface of the solution in a triangular cell takes a position at which the edges of the crystal and the cell walls are parallel to each other [2].

It is apparently obvious that the orientation of the crystal in the cell is determined by capillary forces. To prove that the orientation is due to no

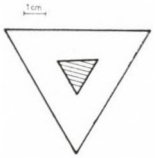

Fig. 1. The equilibrium position of a triangular body floating on the surface of a liquid in a triangular cell. The surface of the liquid is concave at the cell walls and convex at the edges of the body (or vice versa).

other forces, such as for instance the crystallisation pressure [1], the following experiments were carried out.

A triangular cell was made from microscopic slides (7 cm long). Then a 1 mm thick triangular aluminium plate was put on the surface of water in the cell. The plate oriented itself parallel to the cell walls as depicted in Fig. 1. This equilibrium position of the plate proved to be very stable. If the plate was moved out of this position after some vibrations it returned into this position again. The explanation of the experiment is very simple: this position

ensures the minimum of the water surface taking into consideration the curved parts of the water surface too.

A similar phenomenon was observed in the case of a quadratic glass cell with quadratic aluminium plate (Fig. 2). A thin NaCl crystal plate of quadratic form floating on the surface of saturated NaCl solution takes the same equilibrium position, i.e. the position in which the crystal edges are parallel with the cell walls. In this case the surface of the NaCl solution was convex at the edges of NaCl crystal, as it was shown by GYULAI [3] earlier.

The equilibrium positions of plates of various symmetry in cells of different symmetry show a well-determined regularity. The results of these observations will be published elsewhere [4].

In the above mentioned experiments the liquid surface at the cell walls was concave but at the edges of the floating body it was convex. If, conversely, the liquid surface at the cell walls is convex and at the edges of the floating plate is concave, the orientation of the plate in relation to the cell is the same as in the previous case. A convex surface of water at the cell walls could be produced by filling the cell with somewhat more water than the volume of the cell (Fig. 3). Owing to the surface tension the water did not overflow. An ice cube floating on a bulging water surface in a quadratic cell takes an equilibrium position, which is illustrated in Fig. 2.

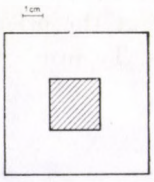

Fig. 2. The equilibrium position of a quadratic body floating on the surface of a liquid in a quadratic cell. The surface of the liquid is concave at the cell walls and convex at the edges of the body (or vice versa).

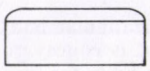

Fig. 3. The cell with bulging water surface (side view)

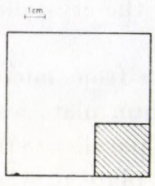

Fig. 4. The equilibrium position of a quadratic body floating on the surface of a liquid in a quadratic cell. The surface of the liquid is concave (or convex) both at the cell walls and at the edges of the body.

If the water surface at the cell walls was also concave (which is the usual case), the ice cube drifted to the corner of the cell (Fig. 4). In a triangular cell with a bulging water surface the aluminium plate usually drifted into the corner of the cell (Fig. 5) or sticked to the cell wall.

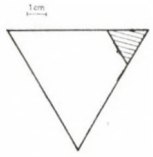

Fig. 5. The equilibrium position of a triangular body floating on the surface of a liquid in a triangular cell. The surface of the liquid is concave (or convex) both at the cell walls and at the edges of the body.

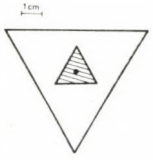

Fig. 6. The equilibrium position of a triangular body floating on the surface of a liquid in a triangular cell. The surface of the liquid is concave (or convex) both at the cell walls and at the edges of the body. The translational motion of the body is prevented.

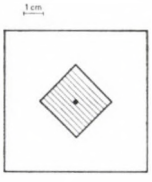

Fig. 7. The equilibrium position of a quadratic body floating on the surface of a liquid in a quadratic cell. The surface of the liquid is concave (or convex) both at the cell walls and at the edges of the body. The translational motion of the body is prevented.

If the liquid surface both at the cell walls and at the edges of the floating body is concave (or convex) and its translational motion is prevented, the floating body takes up orientation in the centre of the cell. This was shown in the following way. A hole was drilled in the centre of the Al plate. Water was poured into the cell so that the water surface bulged out. The Al plate was put on this bulging water surface and a needle was inserted in the hole so that the Al plate could rotate freely around the needle but could not shift from the centre of the cell. A triangular plate took an equilibrium position in a triangular cell as demonstrated in Fig. 6. In the case of a quadratic cell with a quadratic plate, the equilibrium position of the plate is as depicted

in Fig. 7. It should be mentioned that if the liquid was mercury, similar phenomena could not be observed, probably because of the big frictional forces.

These experiments indicate that the capillary forces may play an important part in the artificial epitaxy as well as in the growing of shaped crystals.

Acknowledgements

The authors thank Dr. L. MALICSKÓ for helpful discussions and Mrs. J. HORN for technical assistance.

REFERENCES

1. Processes of Real Crystal Formation. N. V. Belov (ed.) (In Russian). Izd. Nauka, Moscow, 1977.
2. V. I. KLYKOV, N. N. SHEFTAL and E. HARTMANN, Acta Phys. Hung., this issue, p. 167.
3. Z. GYULAI and S. BIELEK, Acta Phys. Hung., **1**, 199, 1952.
4. E. HARTMANN, Acta Phys. Hung., this issue, p. 189.

Acta Physica Academiae Scientiarum Hungaricae, Tomus 47 (1—3), pp. 189—190 (1979)

SYMMETRICAL CONFIGURATIONS BY CAPILLARY FORCES

By

E. HARTMANN

RESEARCH LABORATORY FOR CRYSTAL PHYSICS OF THE HUNGARIAN ACADEMY OF SCIENCES
BUDAPEST, HUNGARY

The equilibrium positions of aluminium plates of different shapes floating by capillary forces on water surface in glass cells of various forms are investigated. In the centre of the cells the floating plates have an equilibrium orientation for which the symmetry elements of the cell and those of the floating plate coincide with each other as far as possible.

It was shown in a previous paper that a triangular aluminium plate floating by capillary forces on the surface of water in a triangular glass cell takes an equilibrium position for which the edges of the plate are parallel with the walls of the cell [1].

This paper deals with the equilibrium position of plates of different symmetry in cells of various symmetry.

The glass cells were made from microscopic slides. The plates of given form were made from an aluminium sheet of 1 mm thick. This thickness was necessary to produce a well-expressed convex water surface at the edges of the floating Al plate, because the powers acting on the edges of the plate depend on the angle between the tangent and the vertical direction in the point of inflexion. According to BAKKER [2] the power (P) acting between two parallel plates, if the liquid surface at one plate is convex and at the other plate is concave:

$$P = -H(1 - \sin \gamma),$$

where H is the surface tension, γ is the angle between the tangent and the vertical direction in the point of inflexion.

To investigate extreme cases the equilibrium position of a non-magnetic needle in the cells was also studied.

The observed equilibrium positions are presented in Figs. 1a—4e.

In some cases every symmetry element of the cell and that of the Al plate completely correspond to each other (Figs. 1d, 2c, 3a and 4b). In Fig. 4c all symmetry elements of the plate (2mm) coincide with some elements of symmetry of the quadratic cell. In Figs. 3b and 4a the equilibrium positions are depicted at which one symmetry element of the cell and that of the plate is common.

Fig. 1.

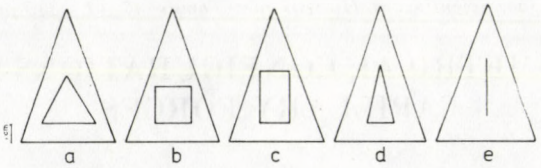

Fig. 2.

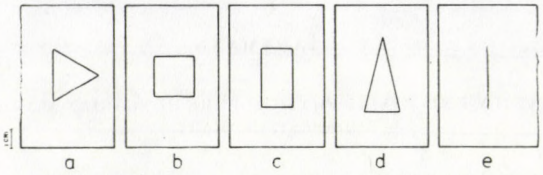

Fig. 3.

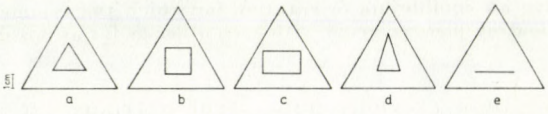

Fig. 4.

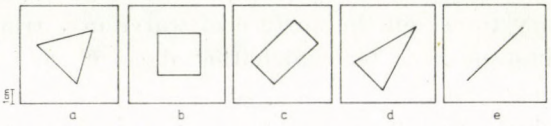

Figs. 1.—4. Equilibrium positions of Al plates on the surface of water in glass cells

Relying on these observations the following conclusion can be drawn: plates floating in the centre of the cells on the surface of a liquid filling the cells take an equilibrium orientation for which the symmetry elements of the cell and those of the floating plate coincide with each other as far as possible.

It should be mentioned that in nature other examples can be found, where interacting systems in equilibrium are placed symmetrically to each other, for instance an electric dipole in an electric field. Consequently, it seems to be possible that the principle observed in the case of capillary forces may also be extended to other phenomena. This principle would be similar to the Curie principle [3].

Acknowledgements

I should like to express my acknowledgement to Prof. N. N. SHEFTAL for valuable discussions. Thanks are due to Mrs. J. HORN for helpful technical assistance.

REFERENCES

1. E. HARTMANN, N. N. SHEFTAL and V. I. KLYKOV, Acta Phys. Hung., this issue, p. 185.
2. G. BAKKER, Kapillarität und Oberflächenspannung, (Handbuch der Experimentalphysik, Band 6.) Akademische Verlagsgesellschaft M.B.H., Leipzig, 1928, p. 82.
3. A. V. SHUBNIKOV, Uspekhi fiz. nauk, **59**, 591, 1956.

Acta Physica Academiae Scientiarum Hungaricae, Tomus 47 (1—3), pp. 191—193 (1979)

SOME RESULTS OF WORK ON ARTIFICIAL EPITAXY (DIATAXY)

By

N. N. SHEFTAL

INSTITUTE OF CRYSTALLOGRAPHY, ACADEMY OF SCIENCES OF THE USSR, MOSCOW, USSR

Some results of work on artificial epitaxy (diataxy) are discussed.

The initial idea of work on artificial epitaxy originated more than 15 years ago [1], based on the hypothesis that it is possible to control the formation of monocrystalline layers of arbitrary crystals, independent of their structure, on substrates of likewise arbitrary substances; on monocrystalline, polycrystalline or amorphous ones. This idea was founded on the one hand, on the experimentally confirmed ideal growth according to the mechanism of Kossel—Stranski and, on the other, on data on crystal growth from blocks and microcrystals. It was conjectured that the nucleation on artificial microrelief (consisting of densely arranged parallel "micronets", in which it is energetically advantageous to position the microcrystals in accordance with their form) promotes the formation of the first monocrystalline layer on the substrate, which, under favourable conditions, can grow further as a single crystal.

For some time experimental results, so it seemed, confirmed this idea. However, the development of experimental work on the production of layers, and likewise the experiments of HARTMANN [2, 3] indicated a number of new aspects of and a new mechanism for the process. Experiments of KLYKOV [4] by the VLS method brought to light the fact that microcrystals never arrange themselves directly on the substrate, but rather on a very thin layer of the solvent (crystallization from a melt has not yet been produced). Secondly, the orientations of small crystals, which are floating in the solution in the cell of the pattern are produced by forces of surface tension.

Thirdly, as is indicated by the experimental work of KLYKOV et al [4] a crystalline particle settles down on the substrate with an important face of the equilibrium form and one has therefore not succeeded in forcing of the formation of a new face under the influence of the form of the micropattern. Further, in agreement with the published work of HARTMANN [3] equilibrium is given by the symmetric position of the small crystal in the cell even if there is a lack of correspondence of the cell and the form of the crystal.In other words quadratic cells can orient a hexagonal crystal in conformity with its hexagonal nature, although worsely than hexagonal cells.

So microcrystals of germanium in rare cases orient themselves on a quadratic pattern, but silicon is practically not oriented at all. This can be explained by the fact that in germanium one encounters cubic faces, but in silicon there occur only octahedral ones.

We remark also that the smaller specific weight of silver in comparison to gold might be one of the reasons for the worse orientation when it is used as solvent.

Finally, it should be indicated that the liquid phase takes part in all our experiments. It is in this liquid where the microcrystals flow. In case of crystallization from gas phase, or from the melt it is possible to expect the orientation according to the original idea.

As for the general results of the work, one may think that a fundamentally new and important phenomenon has been established, namely artificial epitaxy, which gives new possibilities for directing the processes of growth of monocrystalline layers, and broadening the opportunity existing for this aim.

In recent time a related work, carried out with great vigour and on a high technical level, has appeared [5]. This work has so far been carried out only on model material (KCl) and no monocrystalline layers, but only individual parallel oriented microcrystals have been obtained.

All this gives additional support for the idea that orientation with the aid of an artificial grating will continue to develop.

REFERENCES

1. N. N. SHEFTAL (ed.), Growth of Crystals, Vol. **10**. Consultants Bureau, New York, 1976, p. 185.
2. E. HARTMANN, N. N. SHEFTAL and V. I. KLYKOV, Acta Phys. Hung., this issue, p. 185.
3. E. HARTMANN, Acta Phys. Hung., this issue, p. 189.
4. V. I. KLYKOV, N. N. SHEFTAL and E. HARTMANN, Acta Phys. Hung., this issue, p. 167.
5. H. I. SMITH and D. C. FLANDERS, Appl. Phys. Lett., **32**, 349, 1978.

Note added in proof

We have received a preprint of [3[where the authors made a note with reference to the English translation of my article on the same problem [1].

On account of this it is worth-while to notice the peculiarities of artificial epitaxy.

In order to solve the problem of growing monocrystalline layers of any crystal on any nonorienting substrate we rely on our ideas about the participation of microcrystals in processes of nucleation and growth of crystals [4], and also on the idea of the importance of the entrance angles for orientation [5]. We supposed that it is possible to compel the microcrystals having dimensions of approximately 0.1 μm to orient by deposition on nonorienting substrates by means of relief micropatterns on them. The micropatterns must correspond to our tasks and also the morphology of the precipitated crystals.

On the basis of this consideration we have obtained at first the oriented growth of the NH_4I crystals (from aqueous solution) on the optical diffraction crossgratings (600 scratches on the mm) [6].

Then we obtained a good orientation of germanium crystals on polycrystalline tungsten, by means of parallel scratches in three directions under the angles 60°. The scratches were made on the substrate by hand using emery paper of the small number (5).

The further experiments in crystallization were performed on special micropatterns. On these patterns we have obtained almost unbroken monocrystalline layers of silicon and germanium up to 15mm^2 on a quartz glass [7].

Thus ideas on microcrystals and entrance angles are confirmed and give us in principle the possibility to solve the problem of the artificial epitaxy.

I am grateful to Dr. E. I. GIVARGIZOV, who informed Prof. H. SMITH about my researches. I also express my gratitude to Prof. H. SMITH for sending me his preprint [3].

1. N. N. SHEFTAL, in: Growth of Crystals, Vol. **10**, Consultants Bureau, New York, 1976 p, 195.
2. N. N. SHEFTAL and E. G. KOLOMYTS, in: Growth of Crystals, Vol. **10**, Consultants Bureau, New York, 1976, p, 220.
3. M. W. GEIS, D. C. FLANDERS, HENRY I. SMITH and D. A. ANTONIADIS, Graphoepitaxy of Silicon on Fused Silica used Surface Micropattern and Laser Crystallization. Preprint published in Vacuum Science Technology, **16**(6) November/December, 1640, 1979.
4. N. N. SHEFTAL, in: Growth of Crystals, Vol. 1, Consultants Bureau, New York, 1958, p, 5.
5. N. N. SHEFTAL and V. I. KLYKOV, The Theses of Reports on the 5. Conference on Crystal Growth in USSR, Tbilisi, 1977, Vol. 1, p. 31.
6. N. N. SHEFTAL and A. N. BUZYNIN. Vestnik MGU, ser. geol. N 3, 102, 1972.
7. V. I. KLYKOV, N. N. SHEFTAL and E. HARTMANN. Acta Phys. Hung., this issue, p. 167.

Acta Physica Academiae Scientiarum Hungaricae, Tomus 47 (1—3), pp. 195—199 (1979)

THE EFFECT OF THE SOLIDIFICATION FRONT SHAPE ON CRYSTAL PERFECTION

By

V. N. EROFEEV and V. A. TATARCHENKO

THE SOLID STATE PHYSICS INSTITUTE, ACADEMY OF SCIENCES OF THE USSR, MOSCOW, USSR

The theoretical and experimental data on thermal conditions close to the solid-liquid interface in Czochralski grown alkali halide crystals are considered. The distribution of axial and radial temperature gradients in a growing crystal has been defined to depend on the crystallization front configuration. The crystallization front curvature affects the crystal structure perfection and the impurity distribution behaviour. The dislocation density was measured in KCl crystals. A radial distribution of Sr and Na in KCl crystals was measured.

The structural perfection of melt-grown crystals is predominantly due to the thermal conditions of growth. These control the thermal stresses arising in the crystal.

The theoretical calculations [1, 2] relate directly the density of dislocations to the temperature gradient: $\varrho = \frac{\alpha}{b} \nabla T$, where α is a linear coefficient of thermal expansion, b is the Burgers vector of dislocations, ∇T is an axial or radial temperature gradient.

Therefore, the determination of the temperature distribution in the crystal on the basis of the actual growth conditions is one of the most important problems.

In our works [3, 4], thermal conditions near the solid-liquid interface are investigated, and the distribution of axial and radial temperature gradients in a growing crystal is obtained by solving the steady state equations of thermal conduction using a computer, and from experimental measurements in NaCl crystals grown from the melt by the Czochralski method. The temperature gradients were measured by the technique of grown-in thermocouples [3].

Fig. 1 represents schematically the distribution of an axial temperature gradient and the form of the temperature field in crystals with a convex towards the melt (Fig. 1a) and concave (Fig. 1b) solidification front under actual conditions in the presence of heat loss from the side surface of the crystal. Solid lines show the isotherms whose geometry was determined from the experimental measurement of a radial temperature distribution. Dashed lines show heat fluxes. In a crystal with a convex solidification front, a maximum temperature gradient is observed not on the solid liquid interface, but at some distance away from it. At such solid-liquid interface geometry, the heat fluxes due to release of the latent heat of crystallization appear to be focussed on

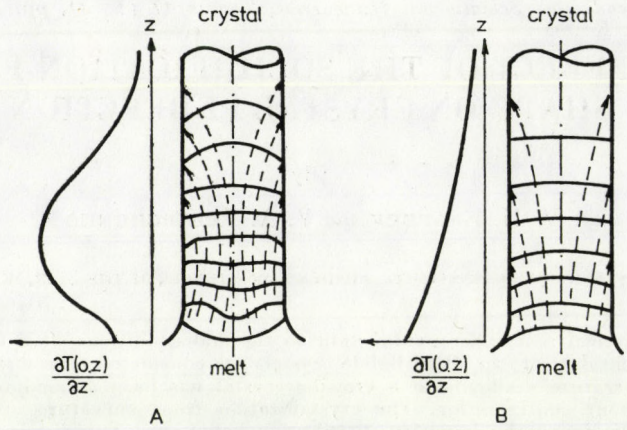

Fig. 1. **Distribution of the axial temperature gradient and a view of the temperature field in crystals with the convex (A) and concave (B) crystallization front**

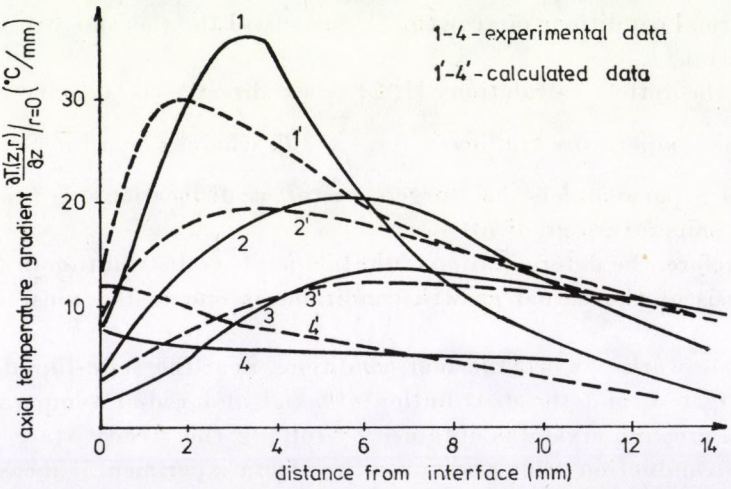

Fig. 2. **Experimental and calculated data on the axial temperature gradient dependence on a distance to the boundary interface as the crystal diameter increases and the crystallization front curvature decreases**

the growth axis. Convergence of the heat fluxes towards the growth axis and, hence, an increase of the axial gradient slope at the moment that the isotherms undergo a full convex-to-concave transformation. So, the maximum magnitude and position depend, 1) on the curvature of the initial isotherm, that is, on the curvature of the solidification front, and 2) on the rate of this transformation, that is, on the cooling rate of a crystal (on the crystal size).

These conclusions are confirmed by the experimental measurements. Fig. 2 represents the distribution of the axial temperature gradient along the

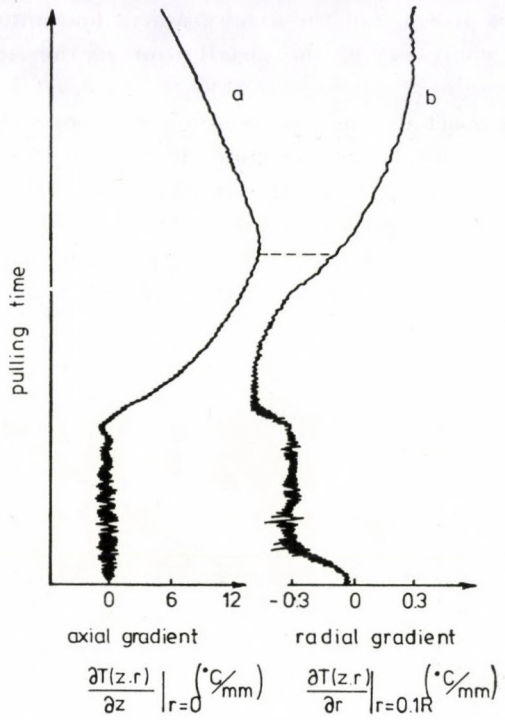

Fig. 3. Experimental data on synchronous measurements of axial (a) and radial (b) temperature gradients

crystal: the experimental data are solid lines, the calculated data are dashed lines. As the crystal radius is increased (2.5, 5 and 10 mm) and the solidification front curvature decreased, the magnitude of the gradient is descreased (curves 1, 2, 3 in Fig. 2) and its maximum position is displaced. In the case of a flat and concave front (curves 4 in Fig. 2) no peak is present.

A simultaneous determination of axial and radial gradients has shown that at the moment that the axial gradient has reached its maximal value, the radial gradient is zero (Fig. 3). To do this, two differential thermocouples were grown in the crystal.

The temperature distribution in a crystal with a convex or concave solidification front must determine the thermoelastic stress fields in each case, because the stress source is the incompatibility of thermal deformations expressed by means of second derivatives of temperature. From the calculations by INDENBOM [2], the stresses operating along the growth axis can be estimated from the second derivative of temperature $\sigma = \alpha E L^2 \partial^2 T/\partial Z^2$, where E is the Young modulus, L is a correction parameter depending on the cross dimensions of the crystal and on the geometry of the temperature field. It can easily be seen that the greatest value of σ corresponds to the case of a convex solid-

liquid interface. The presence of the axial gradient maximum is also disadvantageous, from the viewpoint of the distribution of the signs of the thermoelastic stresses arising in a growing crystal [5]. The crystal site near the axial gradient maximum is acted upon by the neighbouring crystal sites from above and from below, whereas at a monotonous decrease of the axial gradient (flat or concave solid-liquid interface) the stresses operating along the growth axis do not reverse their signs, and the contributions from the neighbouring sites partially compensate one another. The formation of the thermoelastic stress field can markedly be affected by the peculiarities of the radial temperature distribution taking place in crystals with a convex solidification

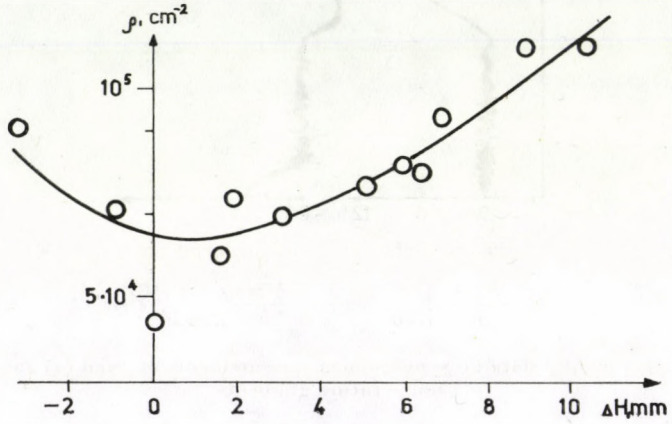

Fig. 4. Dependence of the dislocation density on the crystallization front sagging

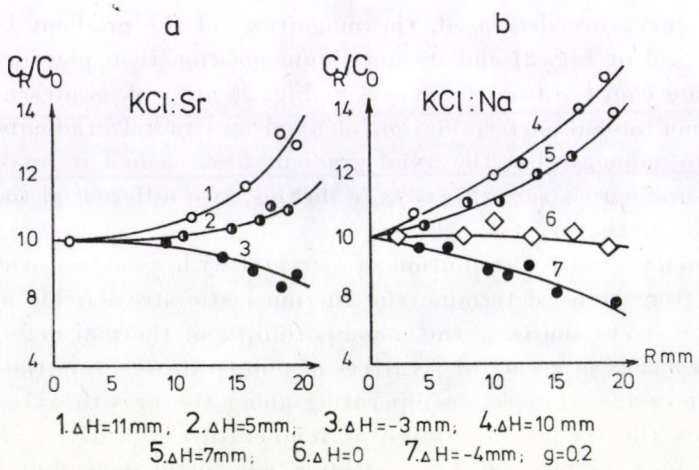

Fig. 5. Radial distribution of impurities in crystals with different sagging of the front crystallization; C_0 — the impurity concentration in the centre of the crystal cross-section; C_R — the impurity concentration along the cross-section radius

front. The presence of temperature maxima and minima restricts the occurrence of free thermal expansion of the adjoining layers and can give rise to essential thermoelastic stresses.

The qualitative conclusions are confirmed by the experimental observations. We have investigated the dislocation structure of alkali halide crystals grown from the melt by the Czochralski method, with respect to the solidification front shape. Fig. 4 represents the dislocation density ϱ in KCl crystals as a function of the magnitude of the solidification front sagging ΔH, $\Delta H = 0$ is a flat front, $\Delta H > 0$ is a convex solidification front, $\Delta H < 0$ is a concave front. The studies were performed on crystals with similar block structures. The dislocation density within the blocks was estimated from the etch pit concentrations. As seen in Fig. 4, crystals with a flat solid-liquid interface have the greatest structural perfection.

The solidification front shape affects the impurity distribution in a growing crystal, too. We have investigated a radial distribution of strontium and sodium in cross-sections of KCl by the ionic thermoconductivity and flame photometry techniques. The results of the measurements are represented in Fig. 5. The impurity concentration is increased from the cross-section centre towards the periphery in crystals with a convex solid-liquid interface, and from the periphery towards the centre in crystals with a concave solid-liquid interface. It is constant in the case of a flat interface. The non-uniformity of the impurity distribution is increased with an increase of the solidification front curvature. All the crystals under study were of the same size: 40 nm in diameter, parameter $g = 0.2$ [6].

So, the solidification front shape related to the thermal conditions of a crystal growth is one of the important parameters determining the structural perfection of a crystal.

REFERENCES

1. E. Billig, Proc. Roy. Soc., A**235**, 37, 1956.
2. V. L. Indenbom, Isv. Akad. Nauk SSSR, ser. fiz. **37**, 2258, 1973.
3. V. A. Borodin, V. N. Erofeev, S. A. Startsev and V. A. Tatarchenko, Isv. Akad. Nauk SSSR, ser. fiz., **40**, 1452, 1976.
4. V. A. Borodin, V. N. Erofeev, L. B. Davidova, A. V. Shdanov, S. A. Startsev and V. A. Tatarchenko, J. Crystal Growth (in print).
5. V. I. Goriletskii and L. G. Eidelman, Isv. Akad. Nauk SSSR, ser, fiz., **40**, 1552, 1976.
6. M. G. Milvidskii, Kristallografija, **6**, 803, 1961.
7. V. N. Erofeev, A. G. Melentjev, E. M. Nadgornii and G. I. Peresada, Fiz. tverd. tela (SSSR), **18**, 2252, 1976.

Acta Physica Academiae Scientiarum Hungaricae, Tomus 47 (1—3), pp. 201—207 (1979)

GROWTH AND PERFECTION OF Cr_3Si SINGLE CRYSTALS

By

M. JURISCH and G. BEHR

CENTRAL INSTITUTE OF SOLID STATE PHYSICS AND MATERIAL SCIENCES
ACADEMY OF SCIENCES OF GDR, DRESDEN, GDR

The crystal growth of Cr_3Si from the melt and the first results of characterization by different methods are reported.

1. Introduction

Usually the physical properties of intermetallic compounds sensitively depend on the exact concentration in the homogeneity range. Therefore high demands must be fulfilled by materials under investigation.

For comparative studies of physical, especially of electrical properties of V_3Si, Cr_3Si and some alloys in the quasibinary system $V_3Si—Cr_3Si$ single crystals of these substances corresponding to these demands were grown.

The intermetallic compound Cr_3Si is the "forefather" of the A-15-structure type, to which the superconductors of the highest transition temperature at present belong. But until now no superconductivity could be detected for Cr_3Si down to 10 mK. In the present paper the crystal growth of Cr_3Si from the melt and the first results of characterization are reported.

2. Growth of Cr_3Si single crystals

2.1. *Preliminary remarks*

Many papers are known about the constitutional diagram of the Cr—Si-system in the interesting concentration range. The papers agree regarding the fact that Cr_3Si is a congruently melting phase. In [1] it was supposed that the melting maximum at a temperature of approximately 1700 °C does not coincide with the stoichiometric concentration, but lies on the Cr-rich side. Different data are available on the homogeneity range of the compound: according to [2] a homogeneity range at 1000 °C exists between 18 and 31 at % Si according to [3] between 22...28 at % Si and according to [1] between 22.5...25.5 at % Si.

At melting temperature the vapour pressure of Cr and Si cannot be ignored. According to [1] the relative Si losses are greater than the Cr losses in the interesting concentration range. Polycrystalline samples are usually produced by direct melting of corresponding amounts of Si and Cr under inert

gas pressure, followed by annealing for homogeneization. To our knowledge results of a successful growth of Cr_3Si single crystals have so far not been reported in literature.

2.2. *Growth experiments*

As starting material for crystal growth powder compacts with a diameter of approx. 6 mm depending on the required crystal diameter up to 90 mm long were used. They were prepared from Cr/Si powder mixtures (particle size 45 . . . 80 μm) in Mo-containers at 1000 °C and kept 24 hours in a vacuum chamber of (1 . . . 3) mPa without precompaction. As starting material for the preparation of powder electrolytic Cr and semiconductor grade Si were applied. Using a planetary ball mill with agate as material for vessel and balls the purity of silicon could be maintained. But chromium powder could be produced only in a mill the material of which was stainless steel or a hard alloy. Therefore the purity of starting chromium was reduced during powder production. Depending on the vessel material Fe or W, Mo, Co were found, respectively, as main impurities. The oxygen content of the chromium and silicon powders amounted to 1 at %. It did not change after production of the powders and was found in the compacts, too. Calculating the concentration of the powder compacts silicon and chromium losses were accounted for by evaporation of the elements and of SiO, too, which forms by reduction of corresponding oxides during heat treatment over 1000 °C. The crystal growth from powder compacts was carried out by crucibleless rf-zone melting under a static atmosphere of 70 kPa Ar and 10 kPa H_2 for avoiding electric discharges. The inert gas was purified by titanium metal at 800 °C. The purity of the inert gas was controlled during melting by quadrupole-mass detector.

A two-step process of growing was used: during a first zone travel at a rate of 2.3 mm/min and a zone length of approx. 5 mm the powder compacts were transformed into nearly constant diameter rods. The compact was rotated during melting. For the process of single crystal growth the last zone of the obtained rod was melted once again, connected with a seed crystal and drawn opposite to the direction of the alloying process. The rate of drawing for all experiments amounted to 0.4 mm/min. The seed crystal rotated with 30 rpm. Changing the rate, the initial rod fluctuations of the diameter could be reduced. Depending on the diameter of the starting powder compacts single crystals ranging from 4 to 8 mm in diameter and 40 to 80 mm in length were grown.

2.3. *Methods used for characterization*

The contents of other than Cr_3Si phases was investigated by metallographic methods after electrolytically etching longitudinal and cross sections with 10% oxalic acid. As sufficiently sensitive chemical methods are lacking

the composition of single crystals was studied by measurements of resistivity ratio at room and liquid helium temperatures, by precision determination of lattice constants by means of Kossel technique and of density by a weighing method. It is necessary to underline that without calibration these methods cannot give concentration themselves. For this as a first approximation the relation between concentration and resistivity ratio for V_3Si [4] was used.

The resistivity ratio of intermetallic compounds depends on the deviation of stoichiometric concentration and temperature, but on concentration of atomically dissolved impurities and physical perfection, too. Therefore the impurity content and the real structure of specimens with different resistivity ratios were investigated. For investigations of the real structure the half width of rocking curves of elastically scattered neutrons was determined and Berg—Barrett and Lang topographs were obtained.

3. Results

By means of the described method single crystals were obtained only in those cases where the concentration of the starting compacts varied between 23.0...25.2 at % Si, supplying crystals between approx 23.5...25.4 at % Si. The given Si concentrations are real concentrations in the case of crystals, but expected concentrations for the compacts after the full reduction of oxides and evaporations of SiO (evaporation of elements is not accounted for). With concentrations deviating from the given range α-Cr or Cr_5Si_3 inclusions appeared, due to the constitutional suppercooling of the melt. A typical single crystal is shown in Fig. 1. During zone melting Cr and Si evaporate especially from the molten zone. But evaporation never disturbs the melting process. From the fact that composition of the single crystals was enriched in silicon compared with initial materials in every case it was concluded that the relative Cr-loss is greater than that of silicon in contrast to the findings in [1].

Owing to a superposition of zone melting effect, inhomogeneities of the initial material, zone volume and possibly concentration dependent evaporation losses the concentration along the crystal is not constant. Depending on the initial concentration two different types of concentration curves were obtained in the single crystals. For concentrations ranging from 23.3 to 24.8 at % Si the resistivity ratio increased from the beginning to the end of the crystals, indicating a decrease of deviation from the stoichiometric concentration. For compositions greater than 24.8 at % Si the opposite was observed: the deviation from stoichiometric concentration increased to the end of the crystals. Crystals with an initial concentration lower than 23.3 at % Si showed increasing deviation from stoichiometric concentration, too.

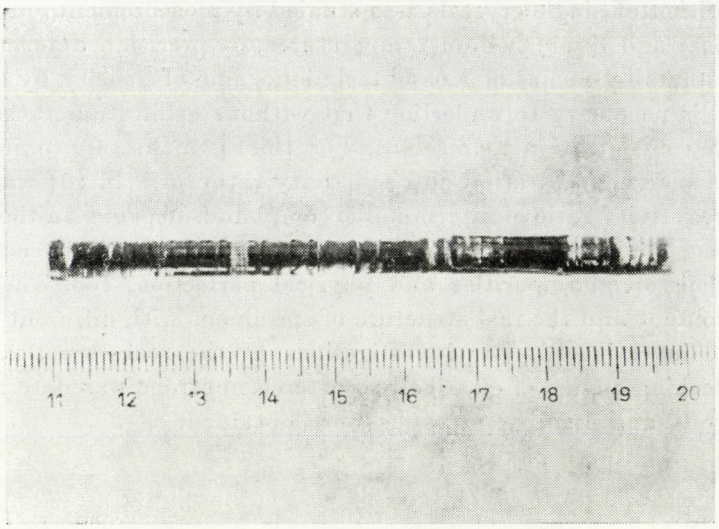

Fig. 1. Cr_3Si single crystal

The largest resistivity ratio corresponding to the stoichiometric composition was 20. This is lower than the value found for stoichiometric V_3Si with the same impurity level. The reason for this behaviour is not clear yet.

The observed concentration curves can be explained, supposing that the concentration of the melting point maximum does not coincide with the stoichiometric concentration, but is situated on the Cr-rich side of the homogeneity range. The position of the maximum was estimated between 23.7... 24.2 at % Si. The explanation given above is supported by the following findings: On the surface of crystals with the highest resistivity ratios corrugations could be observed. They were missing in crystals with lower values (Fig. 2). Corrugations are caused by the constitutional supercooling of the melt near the interface. If the concentrations of melting maximum and stoichiometric composition of the compound would coincide, no corrugations could be expected for melting near stoichiometric concentration. Furthermore, the rapid quenched zones exhibited Cr_5Si_3 inclusions for all crystals with concentrations greater than approx 24.0 at % Si.

The main impurities of single crystals grown from Cr-powder with a higher level of high-melting point elements are given in Table I. By optimization of the purification process of inert gas and by the utilization of a mill with a stainless steel container the impurity concentration could be reduced (Table I).

For single crystals on the Cr-rich side of the homogeneity range lattice constants and densities increase from (4.5580 $\pm$ 0.0002) Å and (6.4443 $\pm$

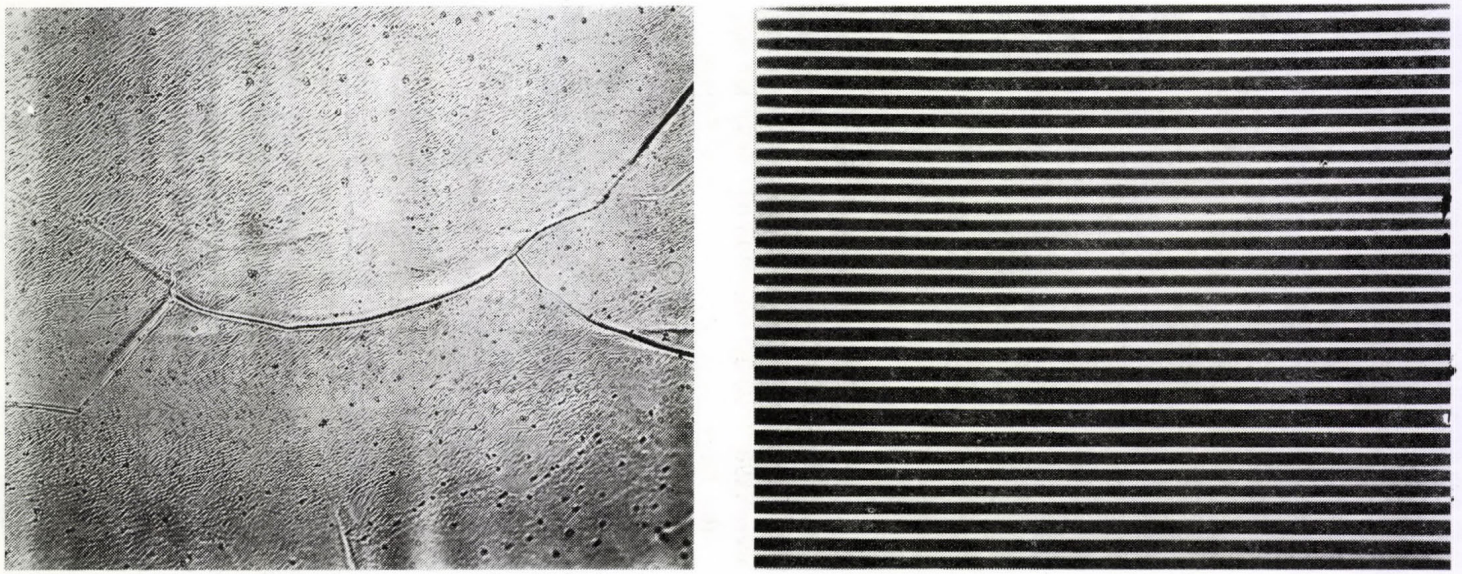

Fig. 2. Surface structure of Cr_3Si single crystals near (left) and apart (right) from the melting maximum. The resistivity ratios are $r_{4,2K}{}^{-1} = 1.7$ and 17, respectively.

Table I

Main impurities of Cr_3Si single crystals. Column 2 refers to Cr-powder from a hard-metal mill, column 3 to that from a stainless steel mill and after improvement of the purification line of inert gas

Impurity	Concentration in at. ppm	
W	400	2
Nb	20	6
Ni	10	20
Fe	200	300
V	100	6
Ti	50	1
Co	200	1
O	1000	50
N	300	20

0.0002) g/cm^3, respectively, for approximately stoichiometric material to (4.5600 $\pm$ 0.0002) Å and (6.4931 $\pm$ 0.0002) g/cm^3 for crystals with a concentration of about 23.5 at % Si. The temperatures for the measurements of lattice constants and densities were (298 $\pm$ 5) K and (296.0 $\pm$ 0.5) K, respectively. Until now no reliable results have been obtained on the Si-rich side of the homogeneity range. From these results it follows that like in the case of V_3Si a substitutional model of nonstoichiometric crystals should be valid. The observed lattice constants for stoichiometric crystals lie well between the results of FLÜKIGER et al [5], who measured (4.564 $\pm$ 0.002) Å and CHANG [6] (4.555 $\pm$ 0.001) Å. The results agree with the lattice constants of PJATKOVA [1].

The investigations of the real structure are not completed yet. But one can say that the single crystals are of high perfection. The half width of rocking curves measured with neutrons on crystals 40 mm long and 5 mm in diameter was is some cases lower than 25 min, characterizing the maximum desorientation between subgrains. The average desorientation of subgrains determined from the contrast width of Berg—Barrett topographs was in the range of some minutes. The subgrains are elongated in the growth direction. Until now no signs of a relation between real structure and deviation from stoichiometric concentration could be found.

Acknowledgement

The authors are indebted to Dr. WEISS (ZfK Rossendorf), Dr. ULLRICH (TU Dresden) and Dr. ZEDLER (ZFW Dresden) for their measurements of rocking curves, lattice constants and densities, respectively.

REFERENCES

1. T. M. PJATKOVA, V. I. SURIKOV, A. K. STOLZ, V. L. ZAGRJAZSKIJ and P. V. GELN, Izv. Akad. Nauk SSSR, Ser. neorg. mater, **7,** 1755, 1971.
2. H. J. GOLDSCHMIDT and J. A. BRAND, J. Less-common Metals, **3,** 34, 1961.
3. V. I. SVECNIKOV, JU. A. KOCERZINSKIJ and L. M. JUPKO, Sb. Voprosy fiziki metallov i metalloved, **19,** 212, 1964.
4. M. JURISCH, K.-H. BERTHEL and H.-J. ULLRICH, phys. stat. sol. (a), **44,** 277, 1977.
5. R. FLÜKIGER, F. HEINIGER, A. JUNOD, J. MÜLLER and P. SPITZLI, J. Phys. Chem. Sol., **32,** 459, 1971.
6. Y. A. CHANG, Trans. Metallurg. Soc. AIME, **242,** 1509, 1968.

Acta Physica Academiae Scientiarum Hungaricae, Tomus 47 (1—3), pp. 209—217 (1979)

STRUCTURE OF $PbO-B_2O_3-Fe_2O_3$ MELTS

By

Á. VÉRTES

CENTRAL RESEARCH INSTITUTE FOR PHYSICS, HUNGARIAN ACADEMY OF SCIENCES
BUDAPEST, HUNGARY

The analysis of the mathematical model of liquid phase epitaxial crystal growth has drawn attention to the relationship between the growth process and the structure of high temperature solutions. Parameters in the model are not fully reported in the literature and even ionic equilibria are unknown for the $PbO-B_2O_3-Fe_2O_3$ system which is the preferred solvent for magnetic bubble storage technology.

Electric conductivity measurements relating to the ionic equilibria are described and a relationship is derived between composition dependence of activation energies and possible polyion formation. The suppositions below are supported by experiments:

$$PbO = Pb^{2+} + O^{2-}$$

$$B_2O_3 + 3\ O^{2-} = 2\ BO_3^{3-}$$

$$Fe_2O_3 + 3\ O^{2-} = 2\ FeO_3^{3-}$$

Equilibria are controlled by oxide-ion activity; a decrease in O^{2-} activity leads to the polymerization of oxianions. This model enables us to suggest as a general form

$$3\ YO_3^{3-} + 5\ FeO_3^{3-} = Y_3Fe_5O_{12} + 12\ O^{2-}$$

for the surface integration step of YIG.

Introduction

In the past few years the use of PbO-based high temperature solutions has become increasingly widespread. The method of liquid phase epitaxy (LPE) [1] has become an important part of the technology of magnetic bubble domain based mass storage devices. The epitaxial growth of YIG-type magnetic garnets on a nonmagnetic gallium-gadolinium-garnet (GGG) substrate takes place in a supercooled high temperature solution. In most of the technologies the defect-free substrate is horizontally rotated. In the development of the technology the importance of the knowledge of the growth kinetics became rapidly clear.

GHEZ and GIESS [2] proposed a theoretical model for the growth rate which consists of two steps. First, the crystal constituents diffuse through the boundary layer to the rotating disc; secondly, they take part in a surface integration step which is described as a first order chemical reaction. This model gives the time dependence of the growth rate in the following form:

$$V_g(t) = \frac{D(c_L - c_e)}{\varrho' \delta}\left[\frac{1}{1+R} + 2\sum_{n=1}^{\infty}\frac{\exp\left(-\alpha_n^2 Dt/\delta^2\right)}{1+R+R^2\alpha_n^2}\right], \qquad (1)$$

where δ is the width of the boundary layer, D is the diffusion constant, k is the kinetic coefficient for the surface reaction, $R = D/(\delta, k)$, ϱ' is the density of the crystal, c_L, c_e are the real and equilibrium concentrations of the solution, respectively, α_n-s are the roots of the equation: $\tan \alpha + R\alpha = 0$. The width of the boundary layer is obtained from hydrodynamic calculations:

$$\delta = 1.6 D^{1/3} \eta^{1/6} \varrho^{-1/6} r^{-1/2}, \tag{2}$$

where η is the viscosity, ϱ is the density of the melt, r is the rate of the rotation.

Let us see which material parameters are involved in the model of GHEZ and GIESS. The width of the boundary layer depends on D, η and ϱ, the growth process is governed by D, k, ϱ' and c_e. In the usual kinetic experiments η, ϱ, ϱ' and c_e are supposed as being known from other measurements, while the diffusion and kinetic coefficients are determined as regression parameters. However, these estimated values seem to be valid only with regard to the order of magnitude [2, 3]. It was because of these uncertainties that they decided to analyse the model [4]. The main problems are related to the characteristics of the surface integration step, to the influence of the heat of crystallization, and to the neglect of convective transport. On the other hand the structure and transport properties of the melt phase should be studied.

The investigations can be divided into two groups. The first is based on the measurement of the LPE growth kinetics as a function of supercooling, growth temperature, rotation rate and orientation of the substrate [5, 6]. The results give direct information on the applicability of the model and on the validity of its assumptions. The other group concerns the physico-chemical investigation of the high temperature solution, where special interest is devoted

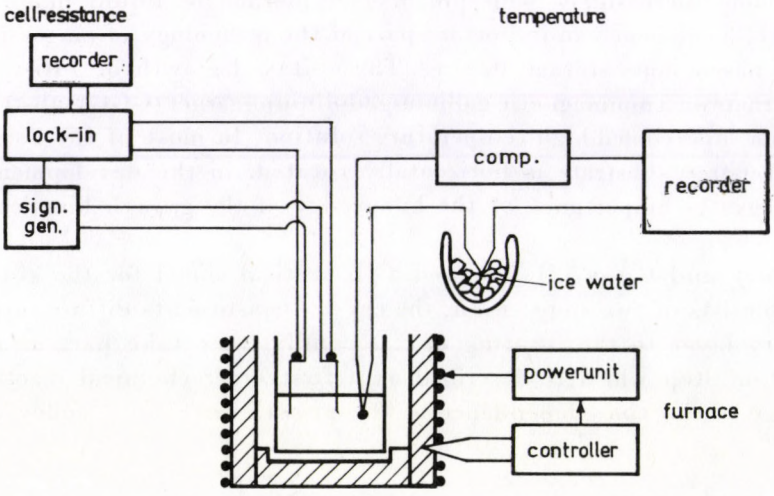

Fig. 1. Block scheme of experimental setup

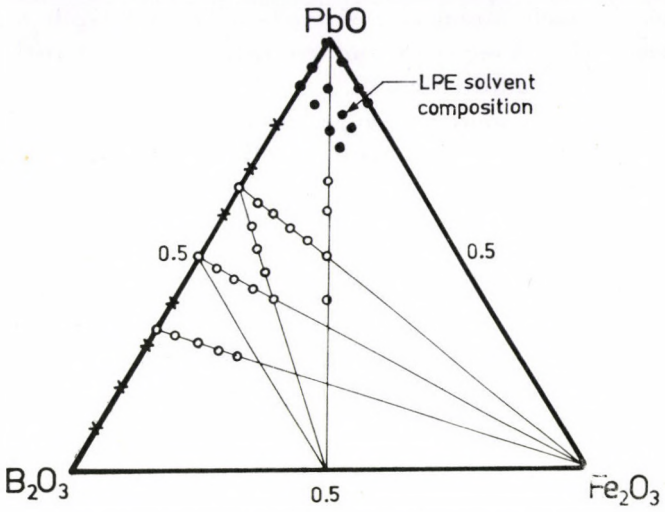

Fig. 2. Earlier measurements in the $PbO-B_2O_3-Fe_2O_3$ system [8—10] are characterized by much higher B_2O_3 content than in the LPE solvent (→). The compositions investigated by HIRASHIMA and YOSHIDA [8] (○) compared with our measurements (●)

to the diffusion constants of the components, the viscosity of the melt and to the solute — solvent interactions.

Our investigations are restricted to this second type of approach and to the $PbO-B_2O_3-Fe_2O_3$ ternary system.

Electric conductivity measurements

In order to describe the LPE growth process independent values of diffusion and kinetic coefficients are needed. Thus the question arises as to the real form of the crystal constituents in the melt. In other words: What types of ionic equilibria exist in the system? Earlier investigations of $PbO-B_2O_3-Fe_2O_3$ melts were focussed on the B_2O_3 rich glass forming region. The LPE solvent contains PbO as its main component and not more than 20 mol% of the other two oxides.

Experimental

The experimental setup (Fig. 1) is based on the AC voltage-drop method. The constant current driven by a current generator has 1 mA amplitude and 1 kHz frequency (it was earlier verified that this frequency is high enough to avoid the effects of electrode polarization). The voltage-drop is measured by a lock-in amplifier with potential wires leading directly to the electrodes. Two special requirements were taken into acount in the cell con-

struction: the extremely strong corrosiveness and the relatively high conductivity of the lead oxide. Frequency and geometrical characteristics of the cell were also investigated and optimized.

Fig. 2 shows the composition range of earlier measurements in the system [7—9] compared with ours. The result of HIRASHIMA and YOSHIDA [7—9] relate to glass technology, therefore their compositions are on the B_2O_3 rich side.

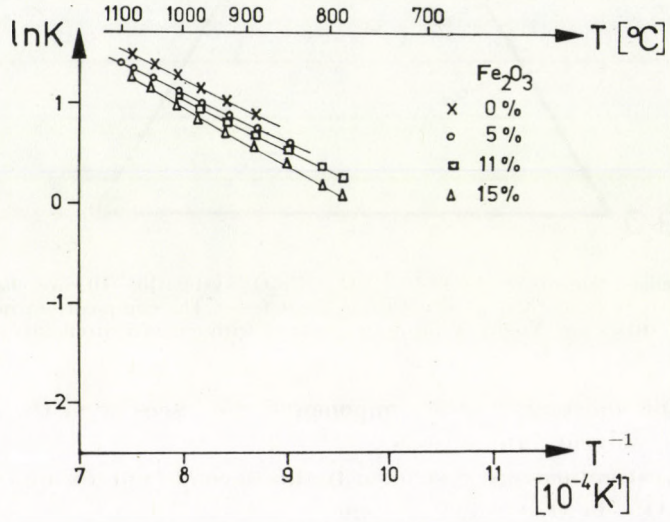

Fig. 3. Temperature dependence of electric conductivity in $PbO-Fe_2O_3$ systems

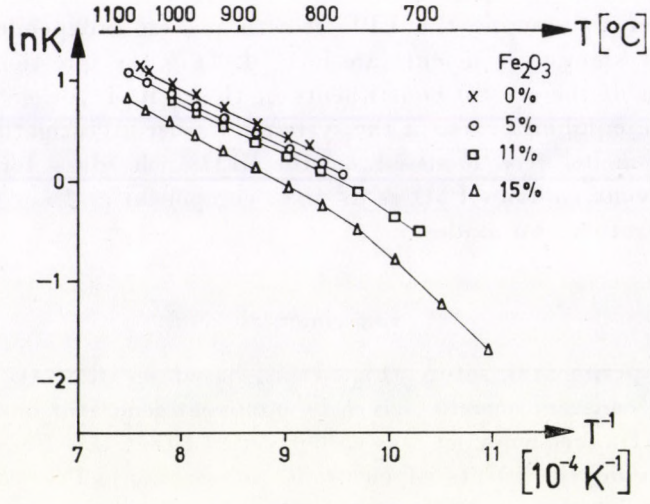

Fig. 4. Temperature dependence of electric conductivity in $(94-x)\%$ PbO — 6% B_2O_3 — $x\%$ Fe_2O_3 system. The slope of the curve of 15% Fe_2O_3 is not constant.

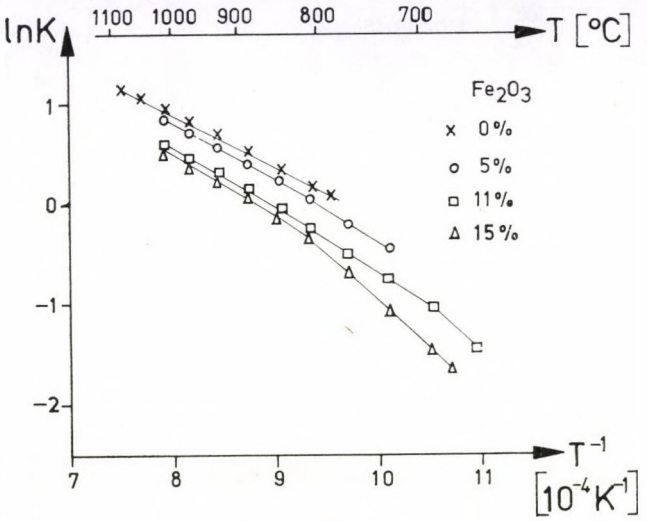

Fig. 5. Temperature dependence of electric conductivity in $(90-x)\%$ PbO – 10% B_2O_3 – $x\%$ Fe_2O_3 systems. In systems containing Fe_2O_3 the slopes of the curves are not constant.

The temperature dependence of specific conductivities on different compositions is shown in Figs. 3, 4 and 5 in Arrhenius-type plots. Activation energies (Figs. 6 and 7) are worked out by linear regression. It can easily be seen that the slope of the curves at high Fe_2O_3 content is not constant. This is probably due to the deviations described by ANGELL [10] but, in the absence of appropriate glass transition temperatures, we were not able to use his approximation.

Discussion

The interpretation of such measurements is usually made in a qualitative way, although there is a relation between the size of ions r_i and the equivalent conductance Λ. Let us combine the Stokes–Einstein and the Nernst equations:

$$\Lambda = \frac{F^2}{3N\pi\eta} \sum_i \frac{z_i x_i}{r_i}, \tag{3}$$

where N is the Avogadro number, F is the Faraday constant, z_i is the charge, r_i is the radius, x_i is the molar ratio of the i-th ion. This formula of course includes the approximations applied in the derivation of the Stokes–Einstein and Nernst equations. However, it is suitable as a means of explaining the effect of changing the composition. The appearance of new components has a direct influence by altering the $\sum_i z_i x_i / r_i$ sum and an indirect effect by changing the viscosity.

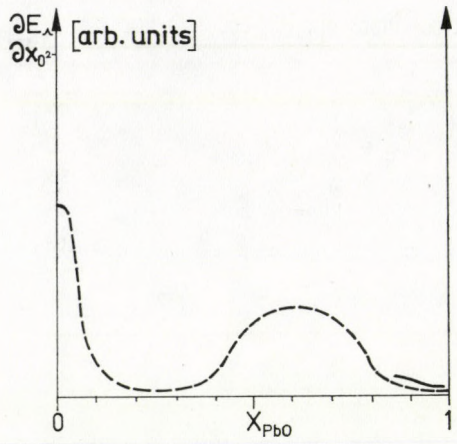

Fig. 6. Composition derivative of activation energies as a function of composition in PbO—B_2O_3 – – – and PbO—Fe_2O_3 —— systems. The "peaks" are due to polyion formation

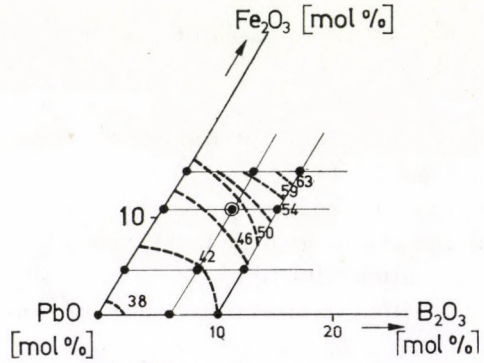

Fig. 7. Composition dependence of E_Λ in the ternary system. Equi-activation energy curves are indicated by dashed lines. The values are in kJ/mole. The composition indicated by a circle is due to the LPE solvent

In the case of polyion formation when n_i i-ions give n_j j-ions the change in the equivalent conductivity is:

$$\Lambda \frac{\partial \eta}{\partial x_i} + \eta \frac{\partial \Lambda}{\partial x_i} = \frac{F^2 n_i z_i}{3N\pi} \left(\frac{1}{r_j} - \frac{1}{r_i} \right), \tag{4}$$

where $n_j z_j = n_i z_i$ is involved because of charge conservation. This equation, in principle, gives the opportunity to make a rough estimation of the polyion size from $\Lambda(x_i)$, $\eta(x_i)$ data, but quantitative values have no real significance because of the approximations. Taking into account the Arrhenius type behaviour of the transport coefficients, one can obtain

$$\frac{\partial (E_\eta - E_\Lambda)}{\partial x_i} = \frac{n_i z_i}{\sum_1 \frac{z_1 x_1}{r_1}} \left(\frac{1}{r_j} - \frac{1}{r_i} \right) - \frac{\partial \ln (\eta_0 \Lambda_0)}{\partial x_i}, \tag{5}$$

where E_Λ, E_η are the activation energies, Λ_0, η_0 are the pre-exponential factors. Thus the relation between the composition dependence of activation energies and the size of polyions becomes evident. In a rough approximation one can neglect the term containing the pre-exponentials and the effects of the viscosity deviation. In Fig. 6 the composition dependence of $\partial E_\Lambda/\partial x_{O^{2-}}$ is shown for the $PbO-B_2O_3$ and $PbO-Fe_2O_3$ binary systems according to our own and other [11] measurements. In the $PbO-B_2O_3$ system there are two composition ranges where structure changes may occur, viz. between 35 and 80 mol% PbO and between 0 and 10 mol% PbO. In the context of Eq. (4) it means that one can expect polyion formation in these regions. Following the assumptions of BOCKRIS [11] the first range is due to a chain-like polyborate anion formation whereas at the B_2O_3 rich end a polyion network formation takes place.

Pure lead oxide in the melt phase is assumed to be in a completely dissociated form. This is in accordance with the high values of its specific conductivity. The question is whether or not free electrons or holes take part in conduction. In other words: Is the lead oxide a liquid semiconductor? Although lead chalcogenides behave as semiconductors in the melt phase too [12]; conductivity determinations of PbO in the region of its phase transition supported the idea of ionic conduction. So the equilibrium:

$$PbO \rightleftharpoons Pb^{2+} + O^{2-} \tag{6}$$

is moved almost completely to the right hand side.

The $PbO-B_2O_3$ system has been investigated over the whole composition range. Electrical conductivity measurements [11, 13, 14], EMF [15, 16] and calorimetric [17] investigations verify that with a value of less than 20 mol% B_2O_3 content, the O^{2-} ions — produced by complete dissociation of PbO — form monomer anions with the B_2O_3 in an acid-base equilibrium. The possible anions are BO_3^{3-} and perhaps BO_4^{5-}. In our range of interest the B_2O_3 content is lesss than 10 mol%, thus

$$B_2O_3 + 3\,O^{2-} \rightleftharpoons 2\,BO_3^{3-}. \tag{7}$$

The activation energy of conductivity in $PbO-Fe_2O_3$ systems does not vary with the composition up to 15 mol% Fe_2O_3 (see Fig. 6). This makes it probable that Fe_2O_3 does not form polyions. However, a decrease in conductivity with increasing Fe_2O_3 content in Fig. 2 should in the spirit of Eq. (3) be related to the decrease in the number of O^{2-} ions and to the appearance of larger ions, respectively. So Fe_2O_3 seems to take part in the acid-base reaction:

$$Fe_2O_3 + 3\,O^{2-} \rightleftharpoons 2\,FeO_3^{3-} \tag{8}$$

and to form the FeO_3^{3-} oxianion. The presence of FeO_3^{3-} ions is supported by the fact that $YFeO_3$ separates at much lower supercooling from the melt.

Activation energies for the ternary system are shown in Fig. 7 in the form of equi-activation energy lines. In the solvent region the lines go almost parallel with the straight lines of constant PbO content. This refers to the concept that B_2O_3 and Fe_2O_3 decrease the conductivity of PbO in a similar way. One can mention a sharp increase in activation energies above LPE solvent composition that is probably due to polyion formation.

Using this oxianion model one can suggest a similar mechanism for Y_2O_3 solvation in the form of YO_3^{3-} ions. The hypothesis is in good agreement with electrocrystallization experiments [18].

Another problem is the geometry of oxianions. The valence electron pair repulsion theory gives two versions: trigonal-planar and trigonal-pyramidal configurations [19]. To find the real geometry is far from our present possibilities.

The oxianion model has some consequences for the nature of the surface integration step, too. To understand the role of this reaction let us compare the coordination of metal atoms in the melt and in the crystal. The supposed trigonal-planar or trigonal-pyramidal geometry of the oxianions in the melt differ substantially from the octahedral coordination of metallic ions in the garnet crystal — as is known from X-ray diffraction measurements. This means that the torsion of bond angles during the integration is unavoidable. The formal equation prescribes bond breaking, too:

$$3\,YO_3^{3-} + 5\,FeO_3^{3-} = Y_3Fe_5O_{12} + 12\,O^{2-}. \tag{9}$$

This equation does not, of course, correspond to the real mechanism because of the low probability of coexistence of the large number of negative ions at the same place. However, it is useful to draw attention to the problem of O^{2-} accumulation and to its transport from the surface.

Acknowledgement

I am thankful to Dr. G. Konczos, Head of the Technological Department, Central Research Institute for Physics, Budapest, for his continuous help and interest in this work.

REFERENCES

1. D. Elwell and H. J. Schell, Crystal Growth from High Temperature Solutions, pp. 160—170, Academic Press, London, 1975.
2. R. Ghez and L. A. Giess, Mat. Res. Bull., **8**, 31, 1973.
3. S. Knight, B. S. Hewitt, D. L. Rode and S. L. Blank, Mat. Res. Bull., **9**, 895, 1974.
4. E. A. Giess and R. Ghez, Liquid Phase Epitaxy (in Epitaxial Growth, Ed. J. W. Matthews) Academic Press, London, 1975.
5. P. Görnert, S. Bornmann, F. Voigt and M. Wendt, Phys. Stat. Sol. (a), **41**, 505, 1977.
6. P. Görnert and S. Bornmann, Kristall und Technik, **13**, K41, 1978.
7. H. Hirashima and T. Yoshida, Yogyo-Kyokai-Shi, **79**, 316, 1971.
8. H. Hirashima and T. Yoshida, Xth International Congress on Glass, Kyoto, Japan, July, 1974.
9. H. Hirashima and T. Yoshida, Yogyo-Kyokai-Shi, **85**, 434, 1977.

10. C. A. ANGELL, J. Phys. Chem., **69**, 399, 1965.
11. J. O'M. BOCKRIS and G. W. MELLORS, J. Phys. Chem., **60**, 1321, 1956.
12. M. CUTLER, Liquid Semiconductors, pp. 7., Academic Press, New York, 1977.
13. H. HIRASHIMA and T. YOSHIDA, Yogyo-Kyokai-Shi, **82**, 30, 1974.
14. O. A. ESIN and V. L. ZIAZIEV, Russ. J. Inorg. Chem., **2**, 1998, 1957.
15. M. L. KAPOOR and M. G. FROHBERG, Can. Met. Quart., **12**, 137, 1973.
16. B. M. LEPINSKIH and O. A. ESIN, Russ. J. Inorg. Chem., **6**, 625, 1961.
17. J. L. HOLM and O. J. KLEPPA, Inorg. Chem., **6**, 645, 1967.
18. L. JASTRZEBSKI, H. C. GATOS and A. F. WITT, J. Electrochem. Soc., **124**, 633, 1977.
19. R. J. GILLESPIE, Molecular Geometry, Van Nostrand Reinhold Co., London, 1972.

Acta Physica Academiae Scientiarum Hungaricae, Tomus 47 (1—3), pp. 219—226 (1979)

INDUCED STRIATIONS IN LPE GARNET LAYERS

By

P. GÖRNERT and S. BORNMANN

CENTRAL INSTITUTE OF SOLID STATE PHYSICS AND MATERIAL SCIENCES
ACADEMY OF SCIENCES OF GDR, 69 JENA, GDR

At a given chemical composition of a solution the composition of the deposited material depends on the growth rate. Therefore well defined changes of the growth rate can be used to prepare single crystals or LPE layers with defined changes of the composition. In the case of garnet single crystals the growth rate has been modulated by the variation of the undercooling to generate induced striations, which are a tool in investigating and optimizing the growth process in high temperature solutions. During the course of liquid phase epitaxy experiments (LPE) of garnets the variations of the growth rate were produced by changing the rotation rate to generate a layered structure. By measuring the thickness of the layers optically one gets the dependences of the growth rate as a function of the time, rotation rate, and undercooling by one experiment with one substrate in each case.

Based on the work of LEVINSTEIN et al [1] and GIESS et al [2] the isothermal LPE dipping method with axial substrate rotation plays the dominant role in growing epitaxial garnet films on nonmagnetic substrates for applications in the microwave and memory technique. Besides this technical importance, the same technology is excellently suitable for studying both the elementary processes in the course of crystal growth and the relation between crystal growth, the real structure, and properties.

In this paper the possibility will be shown of measuring of the growth rate economically and exactly on the basis of induced striations in epilayers, the growth rate being one of the most important parameters of all problems linked with crystal growth.

Using the diffusion boundary layer approximation the steady state growth rate v in the solvent-solute binary system is given for diluted solutions by

$$v = \frac{D}{c_S} \frac{c_L - c_e}{\delta_{\text{eff}}}, \tag{1}$$

$\frac{\delta_{\text{eff}}}{D}$ represents the integral resistivity

$$\frac{\delta_{\text{eff}}}{D} = \frac{\delta}{D} + \frac{1}{k} \tag{2}$$

which contains the transport (δ/D) such as convection, diffusion and interfacial processes $(1/k)$ such as desolvation, adsorption, surface diffusion, incorporation. The meaning of symbols is explained in the list at the end of the text.

The so-called diffusion boundary layer thicknes δ (see Fig. 1) is proportional to the negative square root of the rotation rate $(\delta \sim r^{-1/2})$ according

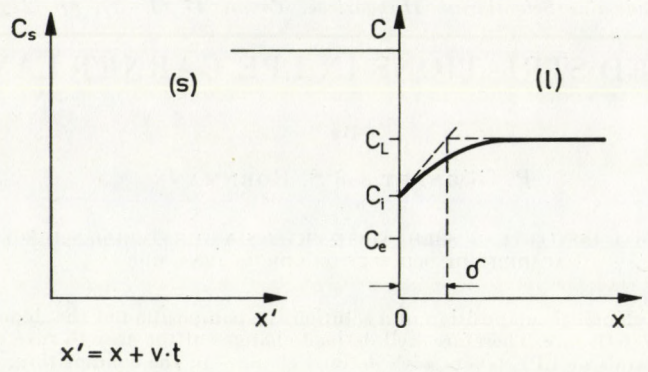

Fig. 1. The solute concentration c in front of the growing interface ($x > 0$) and in the solid state ($x < 0$)

to LEVICH [3] and BURTON et al [4]. The kinetic coefficient k is defined by mass conservation (see Fig. 1)

$$D \frac{c_L - c_i}{\delta} = k(c_i - c_e) . \tag{3}$$

The composition of the solid state is given by the composition of solute and by the growth rate. At constant solute composition variations of the growth rate can be accounted for according to Eqs. (1) and (2) by

(i) changes of the effective driving force $(c_L - c_e)$

(ii) changes of the hydrodynamical conditions or, strictly speaking, variations of the rotation rate in the case of LPE films.

For ideal solutions the relation between the driving force expressed in concentrations $(c_L - c_e) = \Delta c$ and in temperatures $(T_L - T_e) = \Delta T$ is defined by the solubility curve in the mathematical form

$$\Delta c = \frac{c_L \Phi}{RT^2} \Delta T , \tag{4}$$

where Φ is the activation energy of solution. Eq. (4) is well fulfilled in high temperature solutions for the growth of garnets. Φ is the sum of the binding energy of growth units and the interaction energy of solute with solvent molecules.

In the case of garnet single crystals grown by the slow cooling method quick variations of the growth temperature result in variations of the garnet composition which were revealed on crystal slices by chemical etching and called induced striations. The scheme of the experimental arrangement of our slow cooling experiments with the induced striation generator (programmer 2) is shown in Fig. 2. With the help of these induced striations as presented in

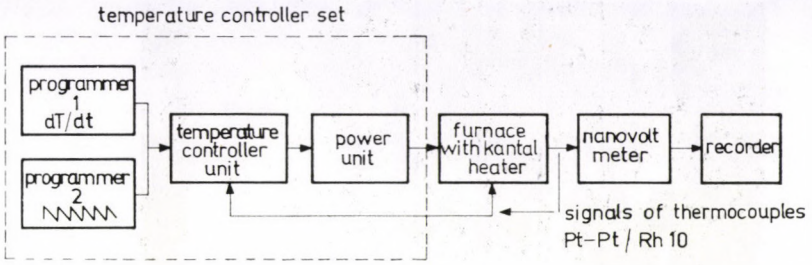

Fig. 2. Scheme of the experimental arrangement for crystal growth experiments by slow cooling

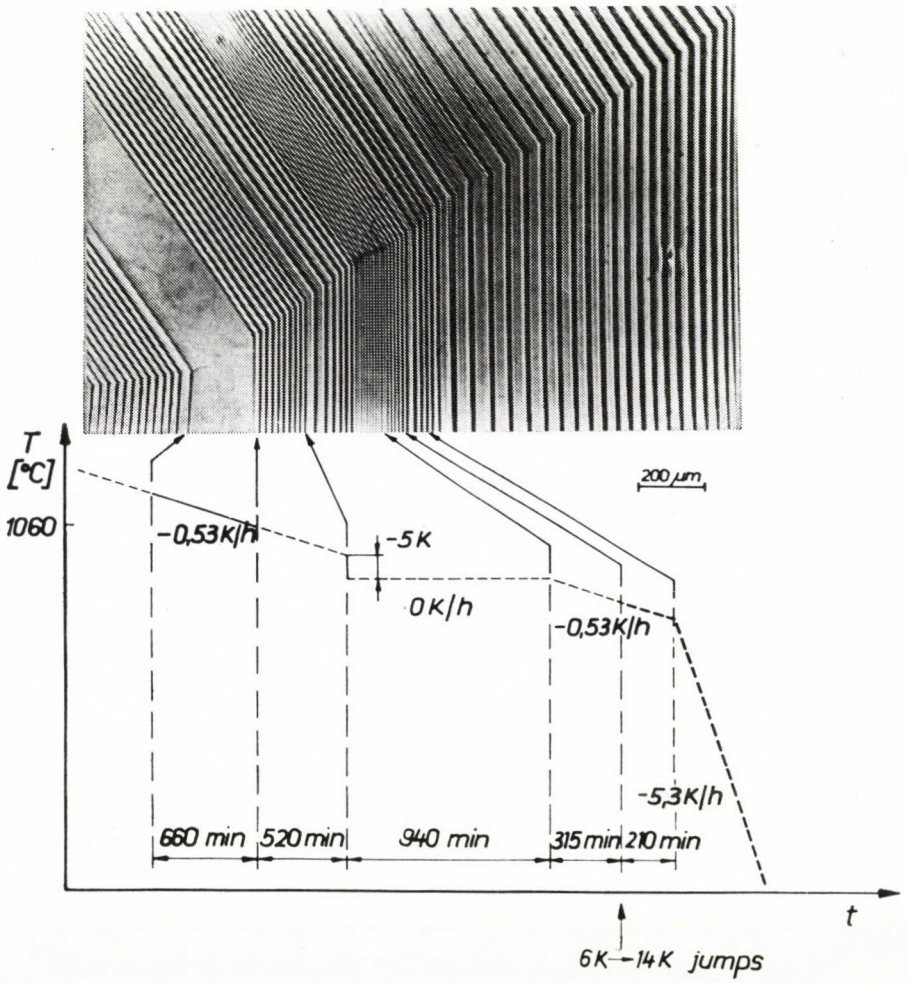

Fig. 3. Cooling program and induced striations in a Ga substituted YIG single crystal (optical micrograph of a chemically etched slice)

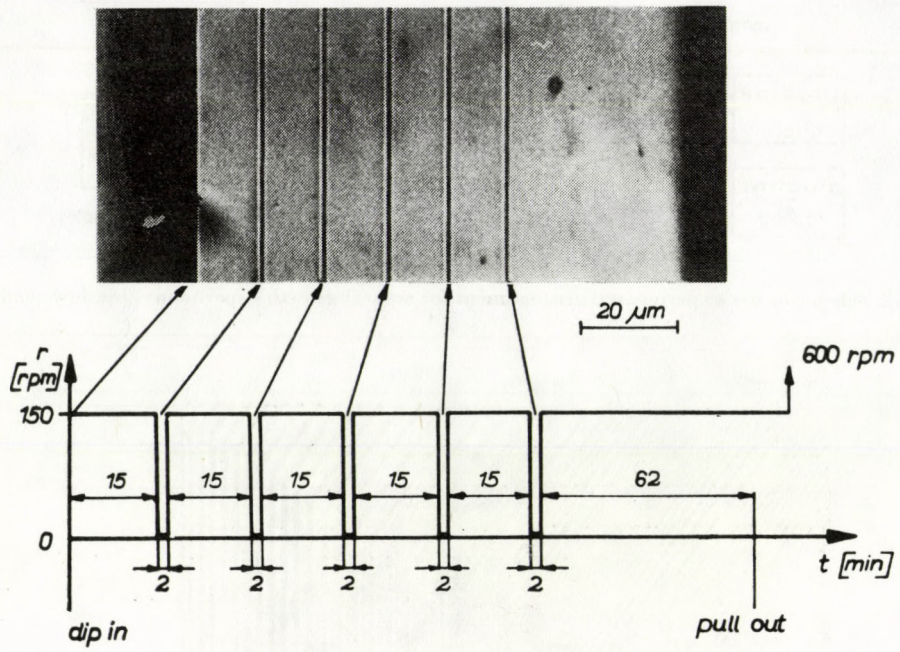

Fig. 4. Substrate rotation rate r versus time t and induced striations in a $(YSm)_3(FeGa)_5O_{12}$ epilayer on {111} GGG (optical micrograph, chemically etched); supercooling $\Delta T = (18 \pm 1.5)$ K

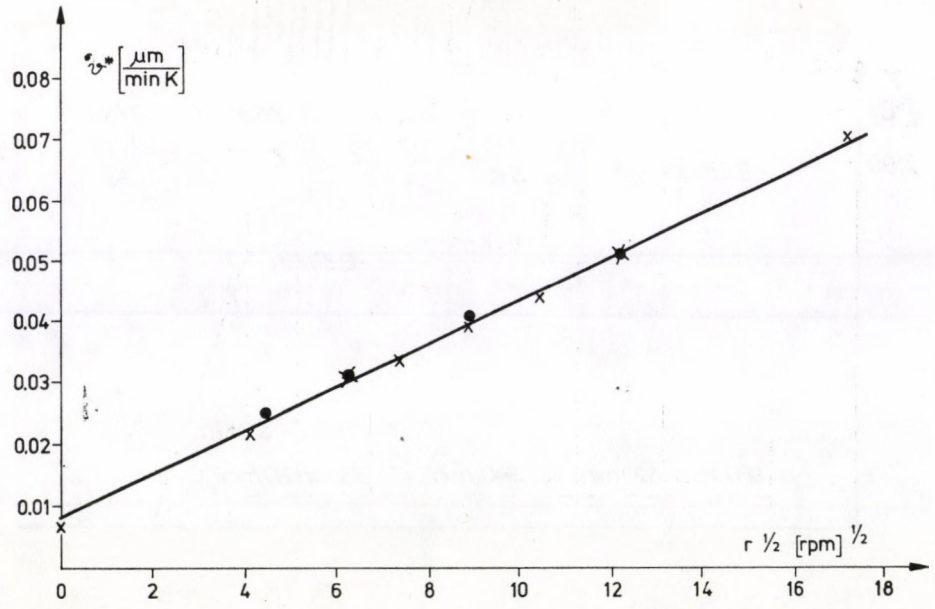

Fig. 5. Growth rate v^* normalized to 1 K undercooling of $(YSm)_3(FeGa)_5O_{12}$ films (×) and of a multilayer (●) grown on {111} GGG as function of the square root of the rotation rate $r^{1/2}$

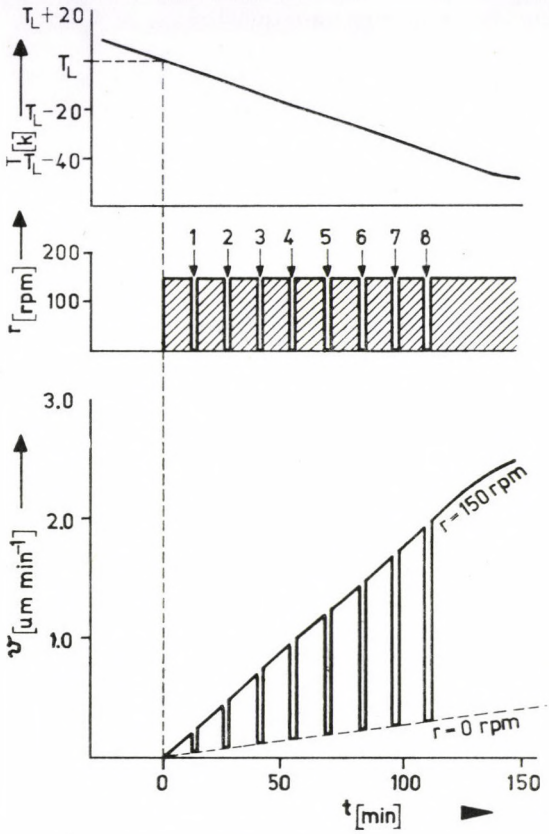

Fig. 6. Temperature T of the high temperature solution, rotation rate r of the substrate, and growth rate v of a multilayer as function of time t
T_L: liquidus temperature; $r = 0$ rpm corresponds to $r_{\text{eff}} = 5$ rpm given by thermal convection.

Fig. 3 we have investigated quantitatively the growth processes during garnet single crystal growth [5, 6]. A review [7] will be published elsewhere.

In the case of garnet epilayers induced striations as shown in Fig. 4 were generated by quick changes of the rotation rate [8]. The advantage of this method is that the transient time for changes of the rotation rate as well as for the formation of the diffusion boundary layer

$$\tau_1 = \frac{\delta^2}{D\gamma^2} \tag{5}$$

is in the range of seconds which was experimentally confirmed by DAVIES et al [9]. Using typical values $\delta \approx 3 \cdot 10^{-3}$ cm for $r = 150$ rpm and $D = 2 \cdot 10^{-6}$ cm^2/s we get $\tau_1 \approx 0.5$ s for $\gamma = \pi \cdot \gamma$ is equal to π for very large kinetic coefficients ($k \to \infty$) and $\pi/2$ for very large rotation rates ($r \to \infty$) [10].

The relaxation time for solute exhaustion [5]

$$\tau_2 = \frac{V \delta_{\text{eff}}}{FD} \tag{6}$$

is in the range of some hours. For typical values $\delta_{\text{eff}}/D \approx 1.5 \cdot 10^3$ s/cm, $V = 70$ cm^3, and $F = 2$ cm^2 we get $\tau_2 \approx 15$ h. That is why the growth rate of LPE films for atomic rough interfaces, as {111} in the garnet system, is nearly constant for dipping times ≈ 30 min if the growth temperature does not vary remarkably.

Using a rotation program with different rotation rates separated by induced striations we measure the growth rate as a function of the rotation rate by one experiment with one substrate (see Fig. 5).

If we combine the LPE dipping technique with a cooling one [11] as presented in Fig. 6 Eq. (1) can be written as

$$v = C\Delta T = Cbt, \tag{7}$$

where b is a constant cooling rate and t is time. The layer thickness which is marked by induced striations is

$$h = Cb\frac{t^2}{2}, \tag{8}$$

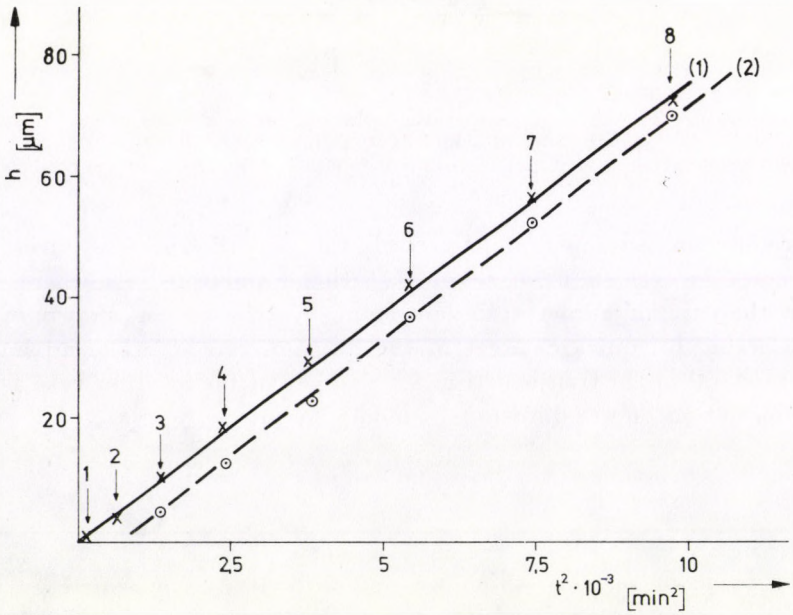

Fig. 7. Layer thickness h measured by induced striations as a function of time square t^2 for 1 (×) $(YSmCa)_3(FeGe)_5O_{12}$ and 2 (⊙) $(YSm)_3(FeGa)_5O_{12}$ garnet on {111} GGG substrates; cooling rate $b = 0.34$ K/min (1) and 0.45 K/min (2)

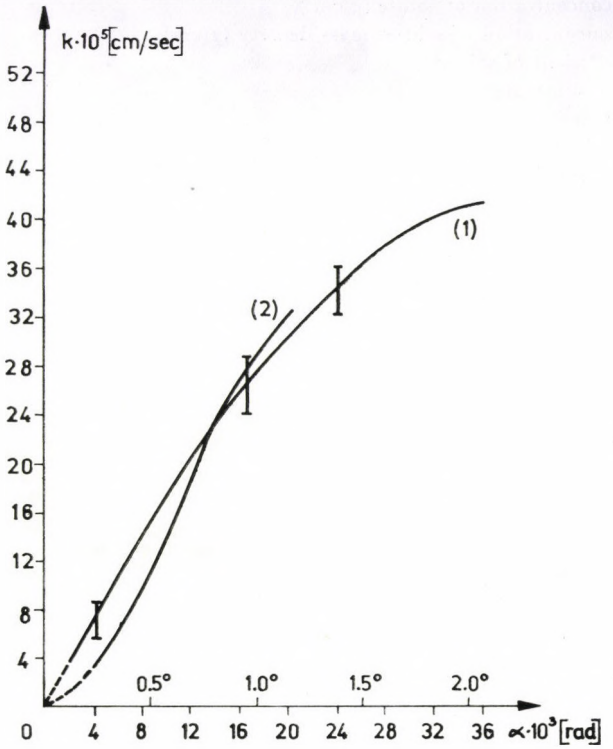

Fig. 8. The surface kinetic coefficient k of vicinal faces of {111} as a function of the vicinal angle α for two $(YSm)_3(FeGa)_5O_{12}$ samples

as shown in Fig. 7. From the slope of the $h(t^2)$ curves we calculate C and thus relation between growth rate and undercooling.

Knowing C we get the integral resistivity δ_{eff}/D. In the case of garnet substrates oriented in {111} the kinetic coefficient is in the order of 10^{-2} cm/s and the integral resistivity is equal to the resistivity of mass transport ($\delta_{\text{eff}}/D = \delta/D$) as is shown by the linear dependence of the growth rate on the square root of the rotation rate in Fig. 5.

By further experiments with other orientations as e.g. vicinal faces of {110} in the garnet system we have measured kinetic coefficients [12, 13] plotted in Fig. 8. These measurements form the basis for studying elementary reactions of the interface which is the aim of our work.

List of symbols

b constant cooling rate
C parameter defined by Eqs. (1) and (4)
c_e equilibrium concentration of solute (g/cm³)
c_i interfacial concentration of solute (g/cm³)

c_L bulk liquid concentration of solute (g/cm³)
c_S solid state concentration of solute; mass density (g/cm³)
D diffusion coefficient of solute
F surface of the substrate
h epilayer thickness
k kinetic coefficient
r rotation rate (rpm)
R gas constant
t time
T temperature (K)
ΔT undercooling (K)
v growth rate
V volume of the solution
x moving space coordinate
x' nonmoving space coordinate
γ angle characterizing transport and interfacial processes
δ diffusion boundary layer thickness
δ_{eff} effective diffusion boundary layer thickness
Φ activation energy of solution
τ_1 relaxation time for the formation of the diffusion boundary layer
τ_2 relaxation time for solute exhaustion

REFERENCES

1. H. J. LEVINSTEIN, S. LICHT, R. W. LANDORF and S. L. BLANK, Appl. Phys. Letters, **19,** 486, 1971.
2. E. A. GIESS, J. D. KUPTSIS and E. A. D. WHITE, J. Crystal Growth, **16,** 36, 1972.
3. V. G. LEVICH, Acta Physicochem. USSR, **17,** 257, 1942.
4. J. A. BURTON, R. C. PRIM and W. P. SLICHTER, J. Chem. Phys., **21,** 1987, 1953.
5. P. GÖRNERT and G. WENDE, phys. stat. sol., (a) **37,** 505, 1976.
6. G. WENDE and P. GÖRNERT, phys. stat. sol. (a) **41,** 263, 1977.
7. P. GÖRNERT, to be published.
8. P. GÖRNERT, S. BORNMANN, F. VOIGT and M. WENDT, phys. stat. sol., (a) **41,**, 505, 1977.
9. J. E. DAVIES, E. A. GIESS and J. D. KUPTSIS, Mater. Res. Bull., **10,** 65, 1975.
10. R. GHEZ and E. A. GIESS, Mater. Res. Bull., **8,** 31, 1973.
11. P. GÖRNERT and S. BORNMANN, Kristall und Technik, **13,** K 41, 1978.
12. R. HERGT and P. GÖRNERT, phys. stat. sol., (a) **46,** 427, 1978.
13. P. GÖRNERT and R. HERGT, phys. stat. sol., (a) **47,** 99, 1978.

Acta Physica Academiae Scientiarum Hungaricae, Tomus 47 (1—3), pp. 227—232 (1979)

CZOCHRALSKI-TYPE CRYSTAL GROWTH SYSTEM DEVELOPED AT THE CENTRAL RESEARCH INSTITUTE FOR PHYSICS

By

F. Tobisch

TECHNICAL DEPARTMENT, CENTRAL RESEARCH INSTITUTE FOR PHYSICS, HUNGARIAN ACADEMY OF SCIENCES, BUDAPEST, HUNGARY

An equipment for Czochralski-type crystal growth has been built in order to produce the basic material of bubble domain memory research carried out in the Central Research Institute for Physics.

The main technical data, construction of the different units and their functions are reported from the point of view of engineering.

Monocrystal substrates of various sizes are needed as basic material for the bubble domain memory research in progress at the Central Research Institute for Physics. A technological base for the production of such substrates has been elaborated at the Institute.

The substrates are made from the slices of monocrystal rods. The crystal rods are produced by Czochralski-type crystal pulling [1—2].

An equipment (Malvern Co.) had been purchased by the Institute to be used for the routine growth of crystals $1'' \times 4''$ in size.

As the next step crystals of $2''$ in diameter had to be grown, which required a larger equipment.

Three ways could be considered in order to acquire the larger equipment:

— to buy the complete system
— to buy only some units and to develop and build the rest
— to build locally the complete equipment.

Our own capacity for development and building proved to be insufficient for the installation of the complete equipment. Thus, it was decided that some units would be purchased, while the assembly and the incorporation of other required elements would be carried out at the Institute.

The equipment consists of the following main units (Fig. 1).

1. Mechanical unit — the driving mechanism to provide for the movements needed for growth
2. Work chamber — to provide for the atmospheric conditions of growth
3. Balance chamber — to house the balance weighing the crucible
4. Mechanical frame — to hold together the different units

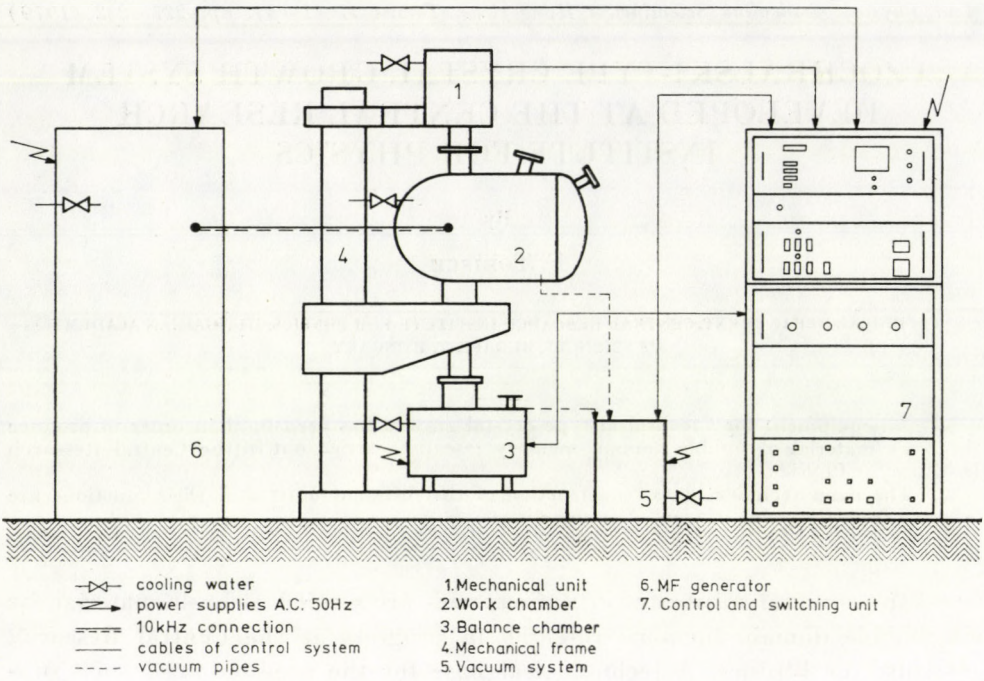

Fig. 1

5. Vacuum system — to provide for vacuum, if required
6. Generator — to provide for the growth temperature
7. Control and switching unit — to regulate and protect the process of growth.

The units are connected by power and low power cables, and by water and air conducting pipes.

The equipment is suitable for pulling Czochralski-type 2″ diameter 12″ long single crystal-bull, in vacuum or protective gas atmosphere.

The operational conditions are the following:

power supply	$3 \times 380/220$ V max. 50 kW, 50 Hz
cooling water	max. 50 litre/min 25 °C
heating water	min. 5 litre/min 60 °C
compressed air	max. 5 litre/min 30 °C $6 \cdot 10^5$ Pa
pressure free water outflow	

Fig. 2 shows the assembled equipment. The generator, the mechanical unit and the electronic balance were acquired commercially while the rest was built in our workshop.

Description of some of the units:

Mechanical unit

Fig. 3 shows the mechanical unit. It was bought along with the controller from the Leybold—Heraeus KG. (FRG). According to the Czochralski system the pulling rod rotates and moves in the axial direction. It is water-cooled and 20 mm in diameter. It can move 300 mm in the direction of pull, at a speed which can be set continuously from 0.2 to 100 mm/hour. The rotational speed is also continuously variable from 0.2 to 125 rpm. Both movements are electronically controlled to an accuracy of $\pm 0.5\%$. The fast speed can be raised from 50 to 30 000 mm/hour. Manual control is not provided for.

Work chamber

It is a double-walled, water-cooled, horizontally positioned cylindrical vessel. Its front lid can be opened. It has 6 non-water-cooled joints, 4 of 40 mm, and 2 of 10 mm in diameter as well as 4 double-walled main flanges. The upper flange can be connected to the mechanical unit while the lower one, which is connected through an adapter to the balance chamber, serves also for supporting the vessel. The 200 mm diameter flanges on the right and on the left side can be connected to the vacuum pump and the power supply, respectively. The water-cooled connector to the power supply is of special design for the elimi-

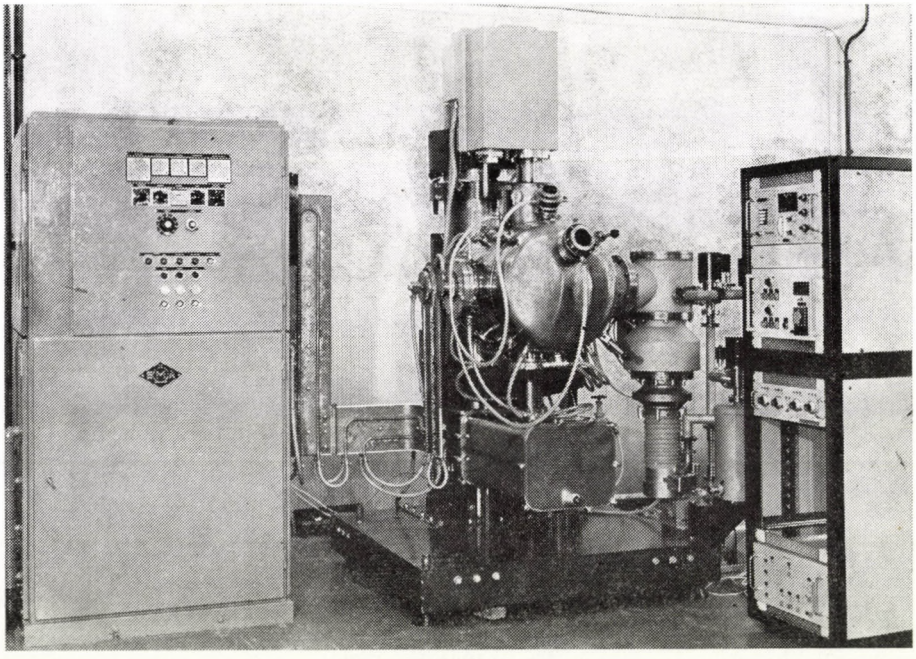

Fig. 2

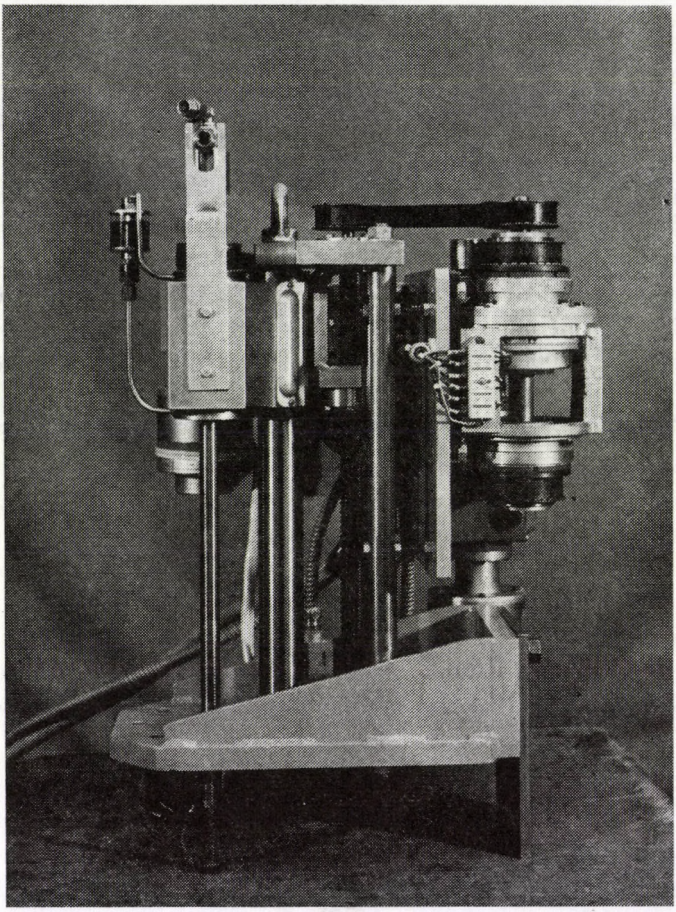

Fig. 3

nation of drift current losses. The chamber can be observed through 2 cooled, shielded windows with polarizers.

The lid is provided with quick locks, the chamber with a spring safety valve which acts as a safety valve for growth under overpressure and as manually operated air inlet valve in the case of operation under vacuum pressure.

Dimensions: inside diameter 490 mm, outside diameter 560 mm, width 900 mm, depth (length) 850 mm, height 1060 mm, mass (empty) abt. 300 kg.

Balance chamber

A stainless steel vacuum chamber is provided for the balance. The balance can be shifted in the x, y directions by ± 5 mm and set in the axial directions of the pulling rod to an accuracy of 1/100 mm. The weight can be read through

a large-sized window. The heat generated in the balance chamber is dissipated by a separate cooling circuit. The front and rear lids of the chamber can be opened by quick closing clamps. The electrical leads are introduced into the chamber through 3 current leadthrough with 21 poles.

Dimensions: width 450 mm, length 900 mm, height 360 mm, mass abt. 50 kg.

The crucible with the melt is weighed by a Mettler P15 type electronic digital balance to an accuracy of 10^{-3} N up to 150 N. The output signal of the balance is fed to the computer which controls the growth.

Mechanical frame

It holds the mechanical unit, the work chamber, the vacuum system, the balance chamber and the water distributor main in a fixed rigid position. Moreover, it absorbs the vibrations of the crystal puller. It consists of an angular base with a screwed-on tubular column to which the movable table and the consol supporting the mechanical unit can be fixed. The base frame can be moved on 4 rollers or propped up on lowered stands. The mechanical frame is of a welded construction, built with regard to adequate load capacity and to absorption of vibrations.

Height and position of the work chamber, the mechanical unit and the balance chamber can be set at will.

Dimensions: width 1350 mm, length 1350 mm, height 2500 mm, mass abt. 800 kg.

Vacuum system

It is a system of 200 mm in nominal diameter suitable for the generation of low and high vacuum. The forevacuum is produced by a rotational forevacuum pump, the high vacuum by water cooled-, and liquid N_2 traps and by oil diffusion pump. The system contains, in addition, electromagnetic valves (2 of 40 mm in diameter and 1 of 10 mm in diameter) and a 200 mm diameter electropneumatic valve protected from radiative heat by a water-cooled screen.

The vacuum system is controlled from a special control panel while the vacuum is being measured by use of a Tungsram (Hungary) product Pirani and Penning-type intsrument.

The vacuum equipment is made from stainless steel.

The final vacuum which can be achieved without warm water heating, with liquid N_2 is at least $1.33 \cdot 10^{-3}$ Pa as measured at the 200 mm diameter valve.

Generator

The induction generator is a rotating type purchased from the EMA firm (FRG). Its power output is max. 40 kW, frequency 10 kHz. The cooled electric

conductor connecting the generator with the vacuum chamber deserves closer attention because its geometrical dimensions form along with the induction coil of the chamber a terminal resistance matched to the generator. Cooling is needed for the high current densities.

Cooling water system

The water distributor and the out-flow tube are mounted on the rigid frame. The separate cooling-tapwater currents are protected from pressure failures by flow indicators.

Programmer and controller unit

This unit has also been developed at the Institute, however, as this work does not belong to the field of mechanical engineering, here it is to be noted only that individual blocks are provided for the electronics of the vacuum system, the generator and of the programmer-controller units.

The equipment is operated at the Solid State Research Institute of the Central Research Institute for Physics [3]. According to the present requirements, work is in progress to elaborate a system for the growth of 3″ size crystals on the principle of the described equipment so that also the mechanical unit will be built at the Institute.

REFERENCES

1. D. Matejka, P. Flisikowski, H. Kohler and R. Kilian, J. Crystal Growth, **41**, 262, 1977.
2. E. Buehler, J. Crystal Growth, **43**, 584, 1978.
3. J. Paitz and L. Gosztonyi, Acta Phys. Hung., this issue, p. 233.

Acta Physica Academiae Scientiarum Hungaricae, Tomus 47 (1—3), pp. 233—240 (1979)

THE GROWTH OF TWO INCH DIAMETER GGG CRYSTALS

By

J. PAITZ and L. GOSZTONYI

CENTRAL RESEARCH INSTITUTE FOR PHYSICS, HUNGARIAN ACADEMY OF SCIENCES
BUDAPEST, HUNGARY

The economical, technical and scientific aspects of the growth of two-inch diameter GGG crystals are discussed.

Introduction

The test whether a crystal is of practical use, is a long and complicated procedure. First, it has to be shown that the crystal properties have practical value and some kind of device can be made from the crystal. Secondly, it has to be pointed out that the fluctuation in the production does not influence the application or the crystal can be grown in device quality reproducibly. Thirdly, it must be proved that the crystal can be produced in large sizes and quantities which makes the production economical. The first and second question can be answered with small crystals on laboratory scale. In this paper, before dealing with the growth of large crystals, I want to touch a little bit closer the economy aspects of growth because this leads us to the answer of the third question. Not too much is published on these problems, perhaps because the costs of crystal production in general are only a smaller part of the endproduct.

Economy aspects

No matter what the actual crystal is, a crystal which is applied for an electronic device, the so-called electronic crystal, undergoes the following general procedure. After the crystal has been pulled there are five further steps in the production. The crystals are crystallographic oriented by X-ray or optical methods, slices are cut mainly by diamond saw. These slices are polished, epitaxial films are grown on the surface, a structure or electrodes are evaporated or sputtered on the surface. Finally, chips are cut from the plates. It can be shown that the larger the crystal the smaller the costs/chip. Table I shows how the time depends for every single step on a characteristic length of the crystal (here it is supposed that length and radius are proportional, which is generally true). It is obvious that by increasing crystal dimensions the working times decrease at least linearly. This is the stimulation for a crystal grower

Table I

Time dependence of various worksteps vs linear dimension of the crystal

Workstep	time/chip reverse proportional to
Growth	L^2
Orientation	L^3
Cutting	L
Polishing	L^2
Epitaxy	L^2
Dicing	L

to pull larger and larger crystals even if the price/crystalkilogram does not change. Another analysis would show that for large crystals the price/kilogram may even decrease.

GGG crystals

From its very beginning in 1970, bubble technology based on rare-earth iron garnets has required substrates of high crystalline quality. The initial crystals grown for use as substrates were typically 2 cm in diameter and 4 to 5 cm in length. As the film growth technology developed the requirements for the internal quality of the substrate increased and as the bubble technology has propagated from research stage into pilot plant operation, the need for larger diameter substrates has developed. Typical quality requirements today are <1 defect/cm^2 and a diameter of at least 2''. Table II summarizes the advantages of the increase of size, together with the requirements from the point of view of bubble devices. The total number of permitted defects is given for the various diameter substrates assuming the defect density to be less than

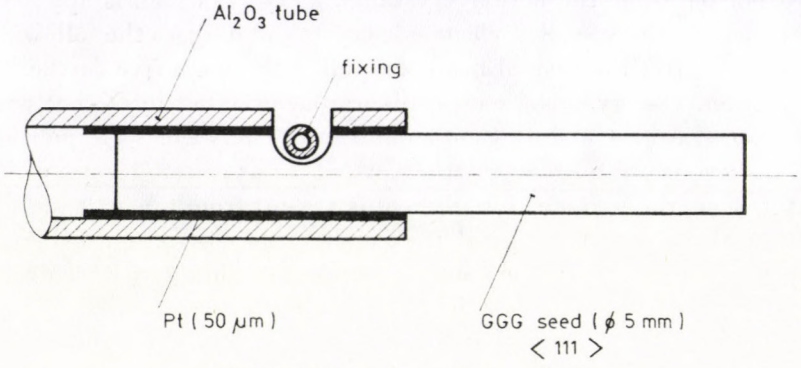

Fig. 1. Fixing the seed in seedholder

Table II

Number of defects and usable area for GGG substrates

Sub diameter	Sub area (cm^2)	Usable sub. area	%	Total defects
25 mm (1″)	5.07	3.60	71	3
32 mm (1.25″)	7.92	6.05	76.4	6
38 mm (1.5″)	11.40	9.13	80	9
50 mm (2″)	20.27	17.2	85	17
75 mm (3″)	45.60	40.9	90	40

$1/cm^2$. It should be noted that the defect count includes both material and polishing defects. Thus, the actual material defects required to meet the above specification are in the range of 0.4 to 0.6 defects/cm^2.

The use of large diameter substrates also allows for the more efficient use of the substrate surface, i.e. the precentage of usable surface area is larger. For comparison Table II includes even the 3″ diameter crystal.

Scaling

Because of quality problems mentioned above, the growth system had to be designed so that the results obtained in 20 mm diameter growth could be duplicated in 2″ diameter growth. Scaling factors which are believed to have a major influence on the crystal growth process and which were justified recently by BRANDLE are: 1) crystal diameter/crucible diameter ratio, 2) crucible diameter/height ratio, 3) growth rate, 4) rotation rate, 5) physical dimensions of the furnace. Once one of these parameters has been fixed, all the others can be scaled accordingly.

For smaller GGG crystals the general rule of thumb is that the crucible diameter should be about twice the crystal diameter. Therefore, a crucible diameter was selected for 2″ diameter growth so that the crystal diameter/crucible diameter

$$D = \frac{r \text{ crystal}}{R \text{ crucible}}$$

was in the range to 0.5 of 0.4. Furthermore, as has been pointed out by others [1], the crucible aspect ratio

$$A = \frac{H \text{ crucible}}{R \text{ crucible}}$$

should be approximately unity. This value of the aspect ratio for the crucible is a good compromise between the large melt volume, (i.e. maximum crystal

length) and thermal convection. In our experiments with 22 mm diameter GGG crystals it was pointed out that thermal conditions, that is the thermal isolator system and the position of the crucible in RF coil, must assure a free thermal convection throughout the growth. When the vertical thermal gradient in the crucible, which produces a free convection in the crucible, drops to a minimum the condition for plane growing interface can be preserved no longer. On the other hand with high aspect ratio due to the vertical gradient the melt is strongly overheated during the starting period of the growth.

The actual growth rate which can be sustained by growing crystals without interface breakdown is a strong function of the many physical parameters are of the growing system. If these physical parameters are scaled so that the ratio of the small to the large system is constant then the larger system should be able to sustain the same growth velocity as the small system. The actual time averaged growth rate of the crystal is a function of the crucible diameter, the ratio of the liquid to solid density and the crystal diameter. It is given by

$$h = P\left(\frac{R^2 k}{R^2 k - r_c^2}\right) = P\left(\frac{k}{k - D_t^2}\right),$$

where h = actual growth rate (cm/hr), P = pull rate (cm/h), R = crucible diameter (cm), k = ratio of the liquid to solid density, r_c = crystal diameter (cm). Thus once $D = \frac{r_{\text{crystal}}}{R_{\text{crucible}}}$ has been set, the value of P can be calculated, using as a basis the value of h, obtained in the smaller system (for 22 mm diameter crystals). In this manner one can be assured that the actual growth rate of the crystal has been maintained constant in the scaling process.

Recently, it has been shown that the meltback diameter of a GGG crystal can be related to the temperature gradient, rotation rate, crystal diameter and the crucible diameter [2, 3]. If the thermal system is designed to produce the same thermal gradient, then Carruthers' relationship can be

Table III

Growth parameters for GGG substrates

	⌀ 22 mm	⌀ 50 mm
Growth rate	0.7 cm/h	0.7 cm/h
Rotation rate	55 RPM	22 RPM
r_c/R	0.4—0.5	0.4—0.5
Melt mass	0.45 kg	5 kg
Crystal weight	250 g	2 kg
Length	120 mm	150 mm

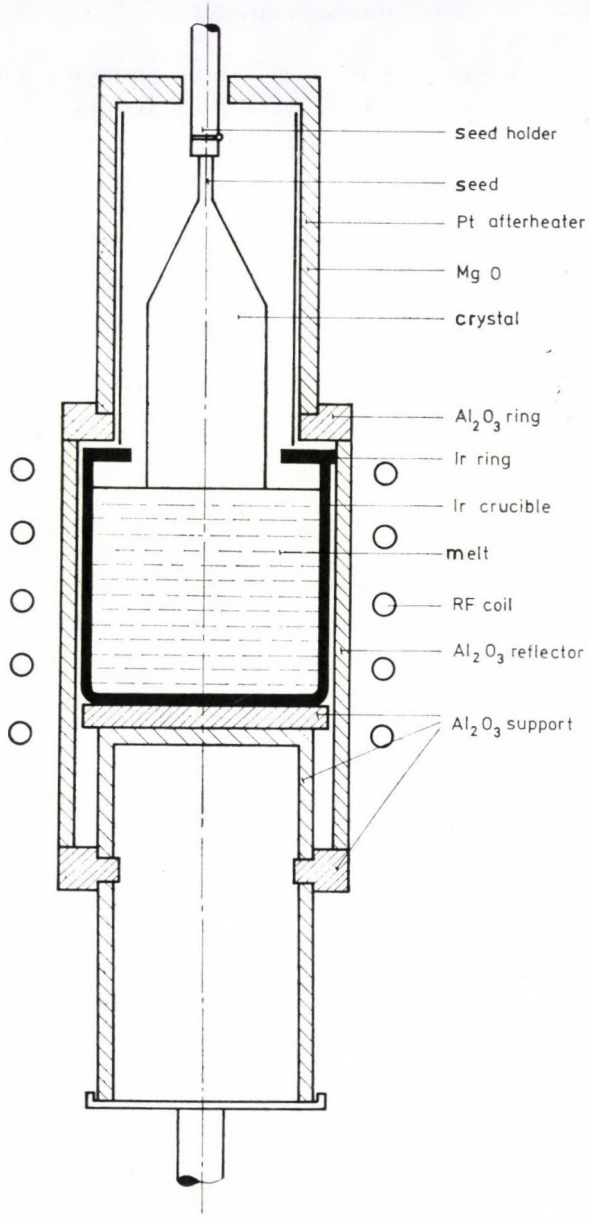

Fig. 2. Sketch of thermal setup for GGG growth

used to obtain the correct rotation rate necessary to produce interface inversion. A summary of the typical values for the growth of 22 mm and 50 mm crystals is given in Table III. Note that with the exception of the rotation rate all other parameters mentioned above have been scaled to produce the same value.

Starting material

The starting material was the same as for small crystals. Both Ga_2O_3 and Gd_2O_3 were of 5N purity. They were fired at some 1000 °C to remove traces of water. The oxides were mixed in a ball-mill with a ratio of congruent composition. For small diameter crystal growth the shift in the crystal composition away from the stoichiometric composition was obvious. Typical weight losses due to the evaporation of Ga_2O_3 in the melt were sufficient to shift the liquid composition from the stoichiometric to the congruent composition and even further out of the garnet phase. For a large crystal the melt to surface ratio is more favourable and the amount of loss is not sufficient to compensate for the difference between the stoichiometric and congruent composition. Therefore it is necessary to shift the starting melt composition away from the stoichiometric towards the congruent composition, in order to maintain a uniform lattice parameter over the entire crystal length [4, 5].

Another difference in the preparation of starting materials for large and small crystals is that after mixing and pressing tablets they have to be fired again. The charge for the big crucible is some 10 times more than for the small one and during the mixing and storing the absorbed water produces a considerable water concentration in the growing atmosphere, which leads to the cracking of the crystals.

Furnace

Although a bigger system was designed and built for pulling the large crystals [6] the first experiments were made in the Metals Research MSR 5 system. Seed of 5 mm diameter was cut out from a perfect crystal. It was inserted in an alumina tube with 50 μ platinum foil between the seed and the tube to prevent solid state reaction of the two different oxides (Fig. 1).

An iridium crucible of 100 mm in diameter by 100 mm in height and of 3 mm wall thickness was used. The starting material weighed 5 kg. The thermal setup is shown in Fig. 2. The whole setup was supported by a stainless steel disk and tube which was fixed to the electronic balance. The alumina crucible turned upside-down and the alumina ring served for the thermal insulation as well as support of the whole system. The crucible is covered by an iridium afterheater ring to reduce radiation loss of the free melt surface. Without this ring an unreasonable amount of power is needed for melting the entire charge of the crucible. The second afterheater is made of Pt—Rh alloy sheet which was mounted in a magnesia holder. The whole thermal setup was designed with the growth requirements in sight, on the other hand keeping the total weight of isulation crucible charge system below 10 kg (the maximum load of the balance is 10 kg!).

Growth

The whole growth procedure from dipping the seed to the heat treatment of the grown crystal is made under automatic control. The growth starts with extension of the seed that is a cylindrical crystal is grown with a diameter equal

Fig. 3. 2″ diameter GGG crystal

to the seed and 20 mm long. The extension can be grown at a rate of 7 mm/h and is enough for the dislocation to grow out, which can form at the seed crystal junction. The pulling rate is then slowed down to 3 mm/h and the diameter is increased to the nominal value. The decrease of the pulling rate is necessary to avoid interface breakdown in the central part of the crystal associated with the highly convex shape of the interface [7]. The rotation rate is constant during this period and is set to 30 rpm which is a little bit higher than that belonging to the inverison given in Table III. This is very important to avoid interface instability after the inversion occurred. Reaching the nominal diameter the pulling rate can be increased to 5 mm/h (this corresponds to a growth rate of 7 mm/h) and the rotation is slowed down gradually to 22 rpm during a period of 4 hours. Fig. 3 shows a GGG crystal of 50 mm in diameter weighing 1.6 kg.

REFERENCES

1. P. A. C. WHIFFIN and J. C. BRICE, J. Crystal Growth, **10,** 91, 1971.
2. J. PAITZ and G. CSATH, First Hungarian Conference on Crystal Growth, Budapest, 1976.
3. J. R. CARRUTHERS, J. Crystal Growth, **36,** 212, 1976.
4. C. D. BRANDLE, D. C. MILLER and J. W. NIELSEN, J. Crystal Growth, **12,** 195, 1972.
5. J. R. CARRUTHERS, M. KOKTA, R. L. BARNS and M. GRASSO, J. Crystal Growth, **19,** 204, 1973.
6. F. TOBISCH, A Czochralski Type Crystal Growth System Developed in the Central Research Institute for Physics (KFKI-1979-16).
7. J. PAITZ and L. GOSZTONYI, ECCG-2 Lancester, England, 10—15, Sept. 1979.

Acta Physica Academiae Scientiarum Hungaricae, Tomus 47 (1—3), pp. 241—245 (1979)

BUBBLE FILMS GROWN ON CALCIUM—GERMANIUM—GALLIUM GARNET (CGGG) SUBSTRATES

By

V. SMOKIN and JU. STAROSTIN

IECM, MOSCOW, USSR

The paper deals with the growing of $(SmLuCa)_3(SiLuFe)_5O_{12}$ films on substrates CGGG, with the phase balance, growth kinetics and its influence on the magnetic properties of the films.

CGGG as a substrate due to its low cost is much better suited for magnetic bubble films than traditionally used GGG. But the properties of the first bubble films $(LuCa)_3(SiLuFe)_5O_{12}$/CGGG [1] appeared to be unsatisfactory for practical use due to low values of the uniaxial anisotropy constant $K \lesssim 2 \cdot 10^3$ erg/cm^3 and Curie temperature ($T_c \lesssim 150$ °C).

This paper deals with: 1) growing $(SmLuCa)_3(SiLuFe)_5O_{12}$ CGGG films with orientation (iii), containing bubbles with operational diameter $d = 5 : 2$ μm and parameters, satisfying memory device requirements; 2) phase balance study, growth kinetics and its influence on magnetic properties of the films; 3) choice of a simple strategy of growing a set of films with identical characteristics; 4) probable direction of getting films with better parameters.

Films were grown by conventional dipping techniques from the $PbO—B_2O_3$ solution (weight of melt is 250 g, substrate diameter $-20 +25$ mm). The composition of the films was determined by micro-X-ray-spectral analysis. Stoichiometric relationships for the garnet were obtained from the values of T_c, magnetization $4\pi M$, lattice parameter a and data for bulk materials taking into account the not too high accuracy of the determination of the contents of the light elements (in our case Ca and Si) and also a considerable probability of introducing lutetium into octahedral sites.

As it follows from the obtained data the substitution of one formulae unit of iron for lutetium results in increasing the lattice parameter of the film a_f on the average by 0.18 Å. Within the limits of the error of measurement (± 0.05 f.u.) charge compensation between two and four-valent ions has taken place.

The stripe domain width W, bubble collapse field H_0, Curie temperature T_c, uniaxial (K) and magnetocrystalline (K_1) anisotropy, coercivity H_c were measured by magnetooptical methods; bond method, interference method and Vello—Coleiro method were used for measurements of the lattice spacings of

the films (a_f) and the substrates (a_c), film thickness (h) and domain wall mobility (μ_0), respectively. Saturation magnetization $4\pi M$ was calculated from the values H_0, W and h.

The main melts A, B, C for growing LPE films with bubble diameter $d = 5$, 3 and 2 μm are characterized with the following molar ratios constituting oxides [2] $R_1 = 28$; $R_2 = 0.120-0.15$; $R_3 = 10.4$; $R_4 = 0.165$; $R_5 = 1.15$; $R_{sm} = 0.037-0.065$.

The border of crystallization between the phases garnet-magnetoplumbit is in $R_1 = 35$ region for a melt homogeneized at 1120 °C, for 12 hours and stirred. Without stirring the melt exfoliation is taking place and the phase border moves to $R_1 = 30$.

Note that the values of R_1 (i.e. the iron to rare earth ratio) is increased and the value of the PbO/B_2O_3 ratio R_3 is decreased in comparison with the usually published values for lowering the octahedral lutetium content and introducing of the samarium.

Table I

Composition and parameters of magnetic bubble garnet films grown from different melts (A, B, C)

$A(Sm_{0,06}Lu_{1,96}Ca_{0,98})(Si_{0,98}Lu_{0,04}Fe_{3,98})O_{12}$
$B(Sm_{0,09}Lu_{1,98}Ca_{0,93})(Si_{0,93}Lu_{0,05}Fe_{4,02})O_{12}$
$C(Sm_{0,12}Lu_{2,02}Ca_{0,84})(Si_{0,84}Lu_{0,03}Fe_{4,17})O_{12}$

Parameter	A	B	C
h, μm	5.29	2.90	2.05
w, μm	5.40	2.95	1.85
H_0, Oe	94	158	212
4πM, G	189	306	394
T_c, °C	189	199	208
$A \cdot 10^{-7}$, $\frac{\text{ergs}}{\text{cm}}$	2.12	2.27	2.35
$K \cdot 10^{-3}$, $\frac{\text{ergs}}{\text{cm}}$	10.0	16.9	18.0
$K^1 \cdot 10^{-3}$, $\frac{\text{ergs}}{\text{cm}^3}$	3.7	3.0	4.3
q	6.3	4.5	2.9
H_c, Oe	0.25	0.35	0.55
a_f, Å	12.2457	12.253	12.2584
μ_0, $\frac{\text{m}}{\text{sec} \cdot \text{Oe}}$	17	10	7.5

Symbols:

L film thickness, w stripe domain width, H_0 bubble collapse field, $4\pi M$ magnetization, T_c Curie temperature, A exchange coefficient, K uniaxial anisotropy constant, K_1 cubic anisotropy constant, q quality factor, H_c coercive force, a_f film lattice parameter, μ_0 domain wall mobility

The typical compositions and parameters of the films grown on CGGG substrates are given in the Table I. The parameters given in the Table I closely meet the requirements of practical applications in magnetic memory devices.

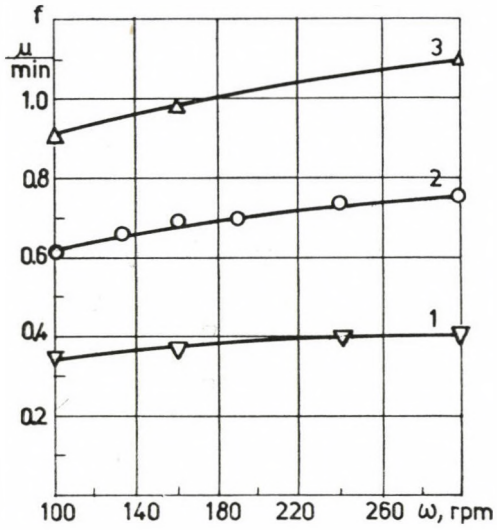

Fig. 1. Dependence of the LPE film growth rate (f) from the melt A on the rotation speed ω and the supercooling $\Delta T = 7$ °C (▽), 13 °C (○) and 19 °C (△). The curves 1, 2 and 3 are calculated with regard to diffusion-reaction model for $D = 4.3 \times 10^{-6}$ cm²/sec and $K = 5.4 \times \times 10^{-4}$ cm/sec

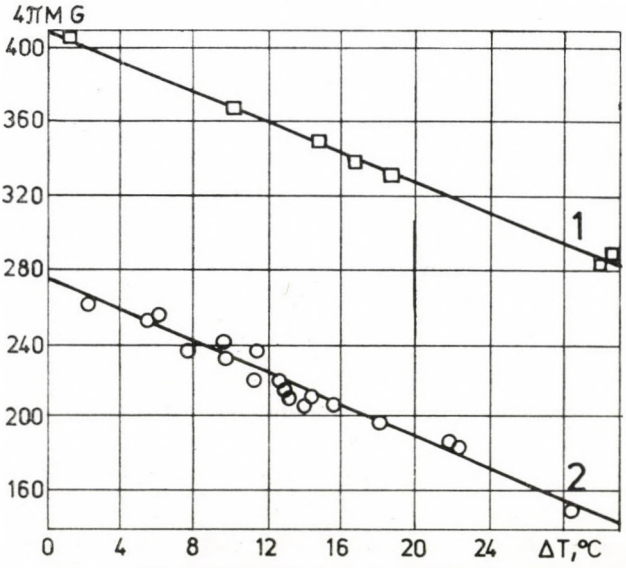

Fig. 2. Dependence of the magnetization $4\pi M$ on the supercooling ΔT for the films grown from the melts A(2) and B(1)

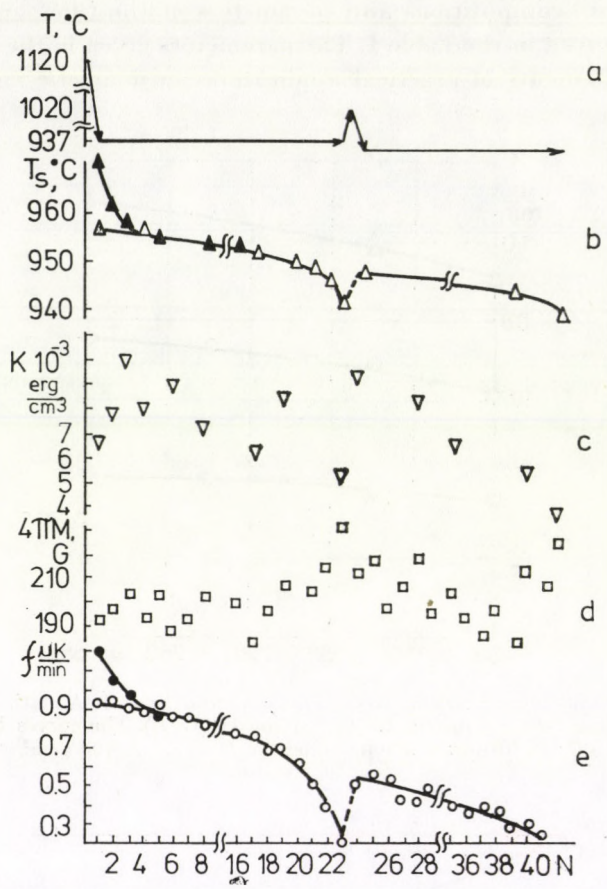

Fig. 3. Temperature program of growth for a set of films (a). The drift of the saturation temperature T_s — (b), anisotropy constant K — (c), magnetization $4\pi M$ — (d) and growth rate f — (e) from film to film (N). ▲ and ● mark previously unstirred melt.

Contents of octahedral Lu is reduced by 2—3 times in comparison with data in [1].

Fig. 1 shows the dependence of the growth rate for the melt A on the rotation speed for the three supercooling temperatures $\Delta T = 7$, 13 and 19 °C (curves 1, 2 and 3, respectively). The curves are calculated in accordance with the diffusion-reaction model with the diffusion coefficient of $D = 4.3 \times 10^{-6}$ cm²/sec and $K = 5.7 \times 10^{-4}$ cm/sec.

Fig. 2 shows the dependence of the magnetization $4\pi M$ on the supercooling ΔT for films grown from melt A (curve 2) and from melt B (curve 1). Here the speed of the lowering $4\pi M$ with the increase of ΔT is slower than that for the yttrium garnets which is explained by the increased octahedral lutetium contents.

The drift of the saturation temperature T_s, growth rate f, magnetization $4\pi M$ and anisotropy K were investigated in the process of growing a set of films (Fig. 3).

The melt that was not stirred previously is characterized by three (I, II, III) and the one that was stirred by two (II, III) separate regions. In region I T_s is reduced by $\sim$10 °C for the second sample due to stirring with rotating substrates and gradual enriching of surface layers with lead oxide. In region II the rate of growth at constant temperature T_g slowly (linearly) reduces due to irreversible reducing of T_s $\sim$0.3 °C/sample. At the same time the magnetization practically does not change which can be explained by the fact that garnet leaves the melt and there is only a weak dependence (Fig. 2). In region III (as a rule after the 16th sample) T_s and f decrease exponentially, $4\pi M$ increases, K falls, which is connected with melt ageing and can be removed with homogeneization at 1020 °C for 6 hours. After homogeneization a repeated growing of series of films without melt correction is possible.

The magnetic quality factor q is less than 3 only at $\Delta T \leq 6$ °C and $f \lesssim 0.25$ μm/min due to the reduced growth rate and a sharp deviation from 1 of the distribution coefficient of Sm related to Lu.

The apparent practical limit of bubble diameter $d = 2$ μm on substrates CGGG (see Table I: a_f, H_c and q) can be reduced to $d \sim 1.5$ m as a result of using Cd^{2+} and Na^{1+} instead of Ca^{2+}. Previous information shows that films $Eu_{0.20}$ $Lu_{2,05}$ $Cd_{0,75}$ $Si_{0,75}$ $Lu_{0,04}$ $Fe_{4,21}$ O_{12} have the following parameters: $h = 1.7$ μm; $w = 1.5$ μm; $H_0 = 280$ Oe; $4\pi M = 500$ Gs; $a_f = 12.252$ A.

On the other hand films $(Bi\ Eu\ Lu\ Ca)_3(Si\ Lu\ Mn\ Fe)_5O_{12}$/CGGG with orientation (110) being in compression $(a_f - a_s)/a_f \sim 3 \cdot 10^{-3}$ with bubble diameter of $d = \mu$m and showing orthorhombic anisotropy have been grown giving exceptionally good dynamic characteristics [3].

*

The authors express their gratitude to Prof. K. P. Belov and Dr. B. V. Mille for their kind gift of single crystals of CGGG and valuable advice and to M. I. Shypegin for measurements of lattice parameters.

REFERENCES

1. I. P. M. Damen, I. A. Pistorius and I. M. Robertson, Mat. Res. Bull., **12**, 73, 1977.
2. S. L. Blank and J. W. Nielsen, J. Cryst. Growth, **17**, 302, 1972.
3. D. I. Breed, W. T. Stacy, A. B. Voermans and H. Logmans, A. M. I. van der Heyden IEEE Trans. Magn., Mag — 13, 1087, 1977.

Acta Physica Academiae Scientiarum Hungaricae, Tomus 47 (1—3), pp. 247—253 (1979)

PRECISE ADJUSTMENT OF MAGNETIC PROPERTIES OF BUBBLE GARNET WAFERS BY ETCHING

By

I. FELLEGVÁRI

HUNGARIAN OPTICAL WORKS, BUDAPEST, HUNGARY

and

M. PARDAVI-HORVÁTH

CENTRAL RESEARCH INSTITUTE FOR PHYSICS, HUNGARIAN ACADEMY OF SCIENCES
BUDAPEST, HUNGARY

Chemical etching in phosphoric acid was employed for postgrowth modification of magnetic bubble domain collapse field (H_0) of epitaxially grown $(YSmCa)_3(FeGe)_5O_{12}$ magnetic garnet layers. The dependence of the etching process on the etching conditions, the etching rate and the magnetic and surface features of the layers was investigated. It is possible to achieve a pre-determined change in the collapse field solely by controlling the etching time at a given temperature. For etching at 140 °C the etching rate is $\Delta H_0/\Delta t = (0.500 \pm 0.05)$ Oe min^{-1} for a decrease in thickness 0.045 μm min^{-1}.

Introduction

Magnetic garnet layers grown by the liquid phase epitaxial method have four properties that determine the applicability of the layers for bubble domain memories. For 5 μm domain applications the following values of these properties are required: thickness: $h = (5 \pm 0.5)\mu$m, collapse field of bubble domains: $H_0 = (100 \pm 1)$ Oe, period of stripe domains: $p_0 = (10 \pm 1)$ μm, coercivity: $H_c \leq 0.5$ Oe.

One of the most important magnetic properties affecting the device performance is the collapse field, which must be controlled by the LPE growth process. However, experience shows that in epitaxial films this parameter varies from one layer to another, sometimes over a substantial range, even when the film growth conditions are controlled to the utmost. The real values vary after growth for 90.2% of our garnet films between 110 and 90 Oe. Modification is not possible when the collapse field is less than 100 Oe, but we were successful in finding a technique for modification when $101 \leq H_0 \leq 110$ Oe.

Thermal annealing is one of those techniques in which the collapse field changes as a result of changing the saturation magnetization of the film. This method is not suitable, however, for films containing Ge^{4+} ions, because of the hindered redistribution of Ge^{4+} between tetrahedral and octahedral positions.

Chemical etching is a simple and rapid method for tailoring the collapse field of existing films [1, 2, 3] because of the thickness dependence of the collapse field [4]:

$$H_0 = f(h), \tag{1}$$

$$H_0 = 4\pi M \left(1 + \frac{3l}{4h} - \sqrt{\frac{3l}{h}}\right). \tag{2}$$

On changing the thickness, e.g. by etching, the collapse field change is:

$$\frac{\Delta H_0}{\Delta h} = \frac{4\pi M}{2h} \sqrt{\frac{3l}{h}} \left(1 - \frac{1}{2}\sqrt{\frac{3l}{h}}\right), \tag{3}$$

where $4\pi M$ is the magnetization and l the characteristic length of the bubble garnet film.

For $\Delta H_0 = 1$ Oe, a thickness decrease of about 0.1 μm is required.

Experimental

Garnets are chemically stable materials. It is known [1, 5, 6, 7, 8] that phosphoric acid or its mixtures with sulphuric acid can be used for rare earth garnet etching but our experiments have shown that an etching mixture containing H_2SO_4 deteriorates. A great deal of precipitation took place which increased with increasing sulphuric acid contents. We investigated mixtures containing H_2SO_4 at different temperatures, but these mixtures were unsuitable because in all cases sulphuric vapour was observed. This was not prevented even by having kept the acid warm for thirty hours.

We also tried pure H_3PO_4 acid. We tried this at various temperatures from 128 °C to 170 °C: we observed no precipitation and no colouring. For this reason, in our investigations we used commercial 85% H_3PO_4 with a starting density of 1.7 g cm^{-3}, as our etchant.

The etching apparatus was a thermostat containing 20 l of 87% glycerine as the heating liquid. At temperatures above 160 °C, vacuum oil was used. The amount of etchant was 150 ml, it was contained in a glass beaker.

The crystal to be etched was held in a platinum holder which could be rotated during etching. The first stage in cleaning the crystals was by ultrasonic agitation in deionized water, this was followed by neutralization in 30% KOH solution. Any orthophosphoric acid remaining on the layers was neutralized by dint of neutralization.

The thickness of the magnetic garnet layer was determined interferometrically, the collapse field was measured photoelectrically based on the Faraday effect [9].

Results

The rate of etching depends on temperature. For precise and reproducible etching there is an optimum etching rate attainable at fixed temperature. First, we had to choose a suitable temperature for etching. The etching process is an endothermic one and when the temperature increases the speed of etching increases, too. That temperature must be chosen which yields the required etching rate, the rate being checked by measuring the decrease in thickness of the magnetic film. Phosphoric acid loses water on heating and polymers begin to form in it. The equilibrium of polymerization is reached after a long period. Etching probably results from the action of PO_4^{2-} ions, whose change is inversely proportional to the change of the polymerization rate. In order to reproduce the same degree of etching we have to know the equilibrium state. On the basis

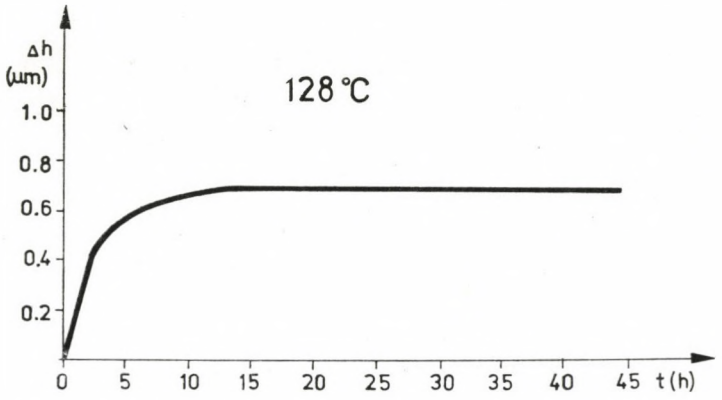

Fig. 1. Film thickness change (Δh) during chemical etching vs equilibration time (t). Etching time: 20 min, rotation speed of the wafer: 98 rpm

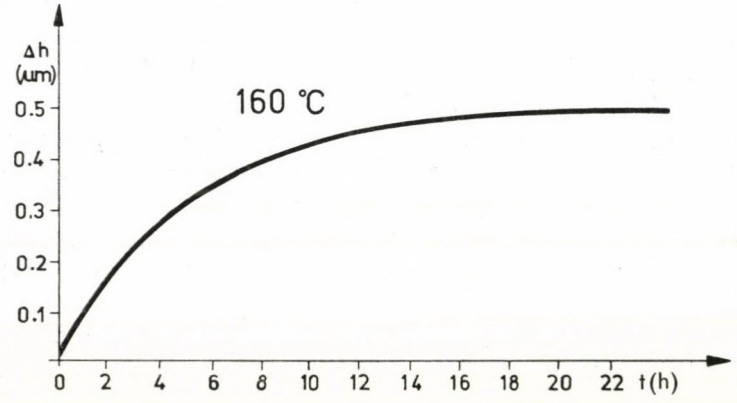

Fig. 2. Film thickness change (Δh) during etching vs equilibration time (t). Etching time: 2 min, rotation speed 90 rpm

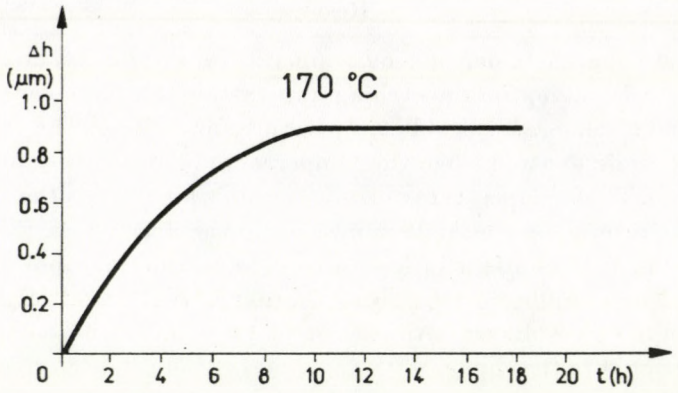

Fig. 3. Film thickness change (Δh) during etching vs equilibration time (t). Etching time: 1 min, rotation speed: 90 rpm

of our experiments it turned out that the etchant must be maintained at a chosen temperature for twenty four hours to reach the stationary polymerization rate. This period was long enough in all of our experiments, these being performed at 128, 140, 160 and 170 °C.

At 128 °C samples were taken periodically for 48 hours (Fig. 1). For the first 24 hours until reaching the equilibrium the etching effects varied considerably. After 24 hours we could get constant etching rates. In that the activity of the phosphoric acid is not too high at this temperature, we had to use an etching time of 20 min. For a 20 min etching time the thickness decrease was 0.7 μm. This rate of thickness decrease was constant for the next 24 hours. At 128 °C the speed of etching is 0.025 μm min^{-1}.

The etchant was held at 160 °C etching temperature for 24 hours to reach equilibrium. The etching effect increased in the first 20 hours and after that it did not change. The higher the temperature the higher the etching effect, so we needed only 2 min etching time for a measurable thickness change. The speed of the etching at 160 °C is 0.25 μm min^{-1} (Fig. 2).

At 170 °C etching temperature the equilibrium was attained in ten hours (Fig. 3). The speed of rotation of the crystals during etching was the same as in the previous cases, but the etching time was only 1 min. After ten hours the etching rate becomes constant, viz. 0.9 μm min^{-1}.

Our experiments showed that the temperature of 128 °C is too low, thus the speed of etching is too low. However, at 160 °C and at 170 °C etching is too rapid. In view of this, it seemed that etching at 140 °C would be suitable.

The investigation was started with the etchant having been kept at 140 °C for 24 hours. The etching rate was determined by measuring the etching time dependence of the thickness change (Fig. 4). The measured thickness decrease was directly proportional to the etching time. The speed of

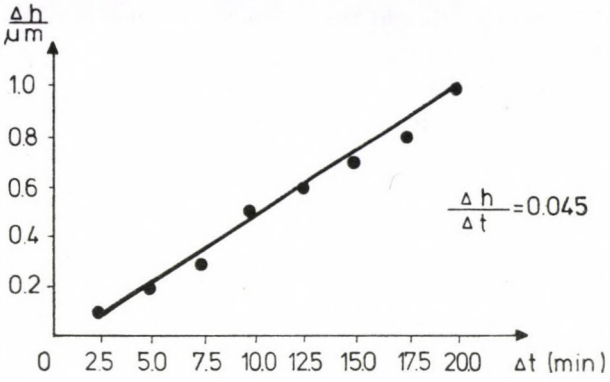

Fig. 4. Thickness decrease (Δh) of the epitaxial layer vs etching time (Δt). Etching temperature: 140 °C, rotation speed: 90 rpm

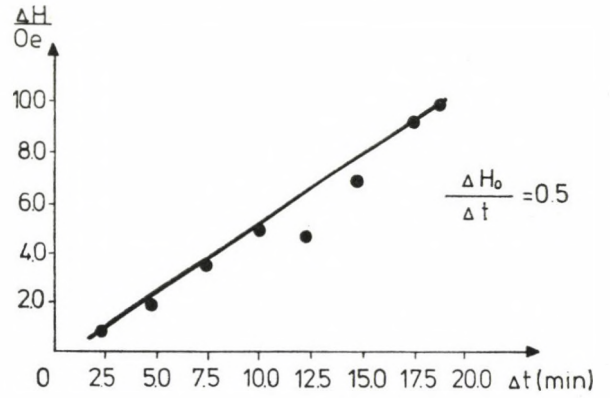

Fig. 5. Collapse field change (ΔH_0) vs etching time (Δt). Etching temperature: 140 °C, rotation speed: 90 rpm

etching was 0.045 μm min^{-1}. The straight line showing the proportionality was reproducible and the deviation from this line was found to be equal to the error of the measurements. This investigation gave us the connection between the thickness change and the etching time.

If the etching process caused deterioration in the surface of the as-grown film, it could not be used. The surface features were investigated microscopically and by Tallystep control of the surface irregularities. The speed of rotation of the crystals in the etchant was found to have a marked effect on the surface morphology. With a slow rotation rate, etching was slow and the surface became very rough. With faster rotation — for example 90 rpm — the etching rate varied over a wide range and was not reproducible. The best speed of rotation at 140 °C was 27 rpm. On increasing the temperature the surface roughness increased independently of rotation rate.

The detailed investigation of the magnetic properties of the garnet layers was started at this temperature. The change in thickness was proportional to the change in the collapse field (3). Because our most important target was the adjustment of the magnetic properties, we had to prove the validity of this relationship and to establish the reproducibility of the collapse field change.

Table I

Change of collapse field along the surface of the LPE layer

D [mm]	H_0 [Oe]	H_{01} [Oe]	ΔH_{01} [Oe]	H_{02} [Oe]	ΔH_{02} [Oe]	H_{03} [Oe]	ΔH_{03} [Oe]	$\Delta H_0/\Delta t$ [Oe min^{-1}]
0	110.4	109.4	1.0	108.4	1.0	107.3	1.1	1.0
2	110.7	109.6	1.1	108.6	1.0	107.6	1.0	1.0
4	111.2	110.2	1.0	109.1	1.1	108.0	1.1	1.1
6	110.9	109.8	1.1	108.8	1.0	107.7	1.1	1.1
8	110.5	109.4	1.1	108.3	1.1	107.2	1.1	1.1
10	109.6	108.6	1.0	107.5	1.1	106.3	1.2	1.1

D: distance along the diameter of the layer;
H_0: original value of collapse field;
H_{01}: value of collapse field after first etching (2 min);
H_{02}, H_{03}: value of collapse field after second and third etchings (2 min);
ΔH values: changes in collapse field values between subsequent etchings.

Table II

Relationship between collapse field and film thickness of LPE layers grown in succession

t [min]	h [μm]	h' μ[m]	Δh [μm]	H_0 [Od]	H_0' [Oe]	ΔH_0 [Oe]	$\Delta H_0/\Delta h$ [Oe μm^{-1}]
2.5	4.5	4.4	0.1	114.0	113.1	0.9	9.0
5.0	4.3	4.1	0.2	114.7	112.5	2.1	10.5
7.5	4.5	4.2	0.3	114.1	110.8	3.3	11.0
10.0	4.5	4.0	0.5	114.1	108.9	5.2	10.4
12.5	4.6	4.0	0.6	114.9	109.4	5.5	9.2
15.0	4.8	4.0	0.8	114.5	106.6	7.9	9.9
17.5	5.1	4.2	0.9	114.9	105.6	9.3	10.3
20.0	5.0	4.0	1.0	114.9	104.9	10.0	10.0

t: etching time;
h: original thickness of layer;
h': thickness after etching;
Δh: thickness change;
H_0: original value of collapse field;
H_0': value of collapse field after etching;
ΔH_0: change of collapse field.

One of the LPE layers was analysed after having been held in the acid for two minutes. This process was repeated three times for the same crystal. The collapse field was measured at six distinct points along the diameter of the layer. The changes were negligible bearing in mind the experimental errors (± 1 Oe in H_0 and ± 0.1 μm in h). We were able to prove that the collapse field alters uniformly on the surface (Table I). The epitaxial garnet layers used in the experiments for investigating the collapse field — film thickness relationship were grown in succession and had nearly identical properties (Table II). The first etching time was 2.5 min: it was increased by 2.5 min for every successive layer. Changes in the collapse field and the film thickness were measured simultaneously at the same point of the film. In this way we were able to determine the change of H_0 and film thickness with time, i.e. the desired decrease of the collapse field on decreasing the thickness:

$$\frac{\Delta H_0}{\Delta h} = \frac{\Delta H_0}{\Delta t} \cdot \frac{1}{\Delta h / \Delta t}. \tag{4}$$

The change in the collapse field with time (Fig. 4) shows that the collapse field and the etching time change in parallel, too. The equation of the straight line was calculated by the method of least squares. Its slope is:

$$\frac{\Delta H_0}{\Delta t} (0.500 \pm 0.05) \text{ Oe min}^{-1},$$

for $T = 140$ °C and a rotation rate of 27 rpm.

With the help of this relation we can modify in a precise way the collapse field by a predetermined value.

Our experiments have proved that a desired change in the collapse field of a bubble memory garnet layer can be achieved very accurately by controlling only the time of etching at a given temperature. The method is also applicable to smaller diameter bubble domain materials for which ultimate precision is needed in controlling the collapse field. The technique can be adapted very easily to multiwafer etching.

REFERENCES

1. S. J. Licht, J. Electr. Materials, **4,** 757, 1975.
2. T. Kasai, Japan. J. Appl. Phys., **14,** 1421, 1975.
3. J. E. Davies, IBM J. Res. Development, **522,** Nov. 1977.
4. H. Callen and R. M. Josephs, J. Appl. Phys., **42,** 1977, 1971.
5. D. C. Miller, J. Electr. Materials, **1,** 499, 1972.
6. D. C. Miller, J. Electrochem. Soc., **678,** 1973.
7. A. M. Szaplonczay and H. H. D. Quon, J. Mat. Sci., **7,** 1280, 1972.
8. T. Kasai, Japan J. Appl. Phys., **15,** 1391, 1976.
9. M. Balaskó and M. Pardavi-Horváth, Appl. Phys., **16,** 75, 1978.

Acta Physica Academiae Scientiarum Hungaricae, Tomus 47 (1—3), pp. 255—261 (1979)

ИСПОЛЬЗОВАНИЕ МЕТОДА ДТГ(М) ДЛЯ ИЗМЕРЕНИЯ ТЕМПЕРАТУРЫ КЮРИ НЕКОТОРЫХ МАГНИТНЫХ ОКСИДНЫХ МАТЕРИАЛОВ

Е. БЕРЕГИ

НАУЧНО-ИССЛЕДОВАТЕЛЬСКИЙ ИНСТИТУТ СВЯЗИ, Г. БУДАПЕШТ, ВЕНГРИЯ

Я. СТАТИС и Ш. ГАЛ

ПОЛИТЕХНИЧЕСКИЙ УНИВЕРСИТЕТ, Г. БУДАПЕШТ, ВЕНГРИЯ

Излагается возможность использования метода ДТГ (М) для измерения температуры Кюри некоторых магнитных оксидных материалов. Были рассмотрены следующие вещества:

$Y_3Fe_{5-x}Ga_xO_{12}$ где $x = 0; 0{,}4; 0{,}67; 0{,}9; 1{,}3$

$Y_3Fe_{5-x-y}Ga_xSc_yO_{12}$ где $x = 0{,}8; y = 0; 0{,}11; 0{,}18; 0{,}4.$

Измеренные методом ДТГ(М) температуры Кюри были сравнены с T_c, полученными обычным методом экстраполяции кривой $4\pi M_s(T)$, с литературными данными и с расчетными T_c, полученными использованием расчетной формулы T_c, представленной статистической теорией Gilleo. Сделан вывод, что метод можно рекомендовать для быстрого и надежного измерения T_c, для получения информации об однородности исследуемых магнитных систем и что он особенно важен при исследовании многофазовых магнитных систем.

В данной работе излагается возможность использования метода ДТГ(М) для измерения температуры Кюри некоторых магнитных оксидных материалов. Были рассмотрены следующие вещества:

$$Y_3Fe_{5-x}Ga_xO_{12} \quad \text{где} \quad x = 0; 0{,}4; 0{,}67; 0{,}9; 1{,}3$$

и

$$Y_3Fe_{5-x-y}Ga_xSc_yO_{12} \quad \text{где} \quad x = 0{,}8; y = 0; 0{,}11; 0{,}18; 0{,}4$$

Температура Кюри, как известно, одно из основных свойств, характеризующих ферромагнитные вещества. Она довольно чувствительна к структурным и композиционным изменениям. В результате этого измерения T_c могут быть использованы для определения и идентификации различных магнитных фаз в многофазовой системе.

Температура Кюри рассматриваемых материалов была измерена методом ДТГ (дифференциальный термогравиметрический анализ) в магнитном поле. Этот метод разработан в термолаборатории Политехнического Университета г. Будапешта.

Как известно, ДТГ представляет собой метод, с помощью которого можно регистрировать изменения веса вещества с изменением температуры. Так получают кривую в координатах вес-температура. Дифференцирование

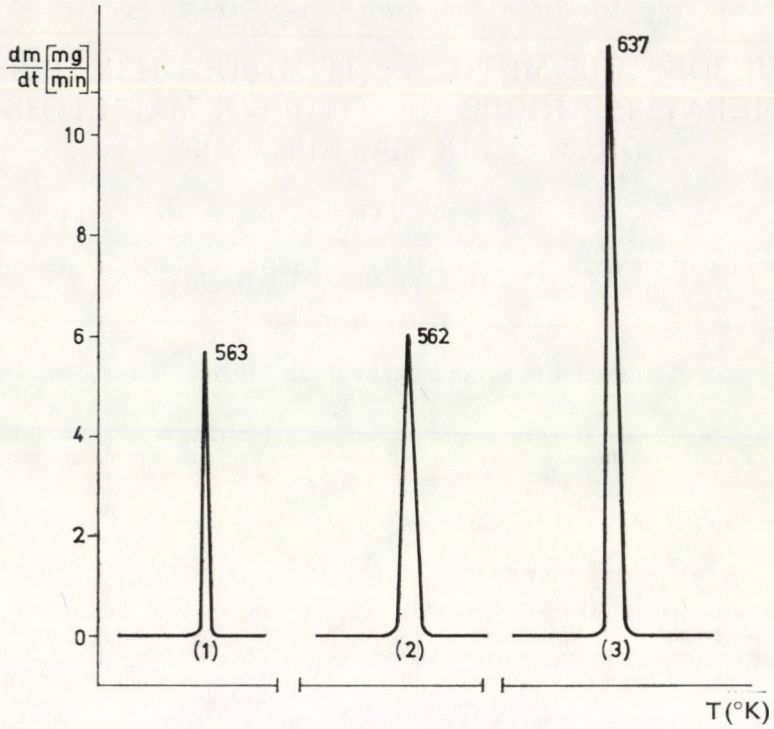

Рис. 1. Кривые ДТГ(М) монокристал. ЖИГ-а (1), поликристал. ЖИГ-а (2), Ni — сферы (3)

этой кривой во времени дает кривую ДТГ. Все измерения проводились на электронных термовесах марки «DuPont» в атмосфере воздуха и в магнитном поле, создаваемом постоянным магнитом, гексаферритом бария.

Как уже упоминалось, в нашем случае измерения кривых ДТГ велось в магнитном поле, но измерялся не вес образца, а сила взаимодействия между образцом и полем. Сила взаимодействия мгновенно автоматически компенсируется, так что положение образца в магнитном поле не меняется.

При достижении температуры Кюри образца намагниченность исчезает и кривая ТГ быстро растет. Этот переход состояния образца из ферромагнитного в парамагнитное на кривой ДТГ в магнитном поле проявляется в виде острого пика. Образцы в виде поликристаллических и монокристаллических сфер диаметром 1 мм помещались в платиновый тигель. Температура повышалась линейно со скоростью 10 ° С/мин от 20 °С до температуры Кюри образца.

Достоверность измерений была проверена на сферических образцах спектрально чистого Ni, монокристаллического и поликристаллического ЖИГ-а.

Ниже приведены температуры Кюри этих веществ и для сравнения указаны литературные данные [1]

Метод ДТГ (М)	(°К)	Литератур. данные (°К)
спектр. чист. Ni	637	631
монокр. ЖИГ	563	560
поликр. ЖИГ	562	560

Ниже на рис. 1 приведены кривые ДТГ(М) вышеупомянутых материалов.

Как вино из рисунка, пики, соответствующие температуре Кюри, исключительно резкие. Пик поликристаллического ЖИГ-а более широкий по сравнению с пиком монокристаллического ЖИГ-а, что по всей вероятности связано с влиянием межкристаллических границ образца.

На рис. 2 представлена серия пиков, соответствующих температуре Кюри галлий замещенных иттрий — железистых гранатов. Как видно из сравнения пиков, ширина их однозначно связана с величиной замещения ЖИГ-а немагнитными ионами. При замещении x=0,90—1,30 у пика появляется «плечо», характерное для составов с более низкими T_c, а при $x = 1{,}30$, как видно из графика, образец представляет систему твердых растворов гранатов.

Принимая во внимание, что уширение пиков наблюдалось для веществ с большим содержанием немагнитных ионов и измерялось для сфер, вес которых составлял всего 1—5 мг, для лучшего наблюдения негомогенности вещества были сняты кривые, характеризующие температуру Кюри для кристаллов с большим содержанием немагнитных ионов (см. рис. 3).

Как видно из рис. 3, наряду с основным пиком, характеризующим T_c вещества, и «плечами» существуют побочные пики. Это говорит о том, что в гранате присутствуют две (или больше) магнитные фазы с различными ком-

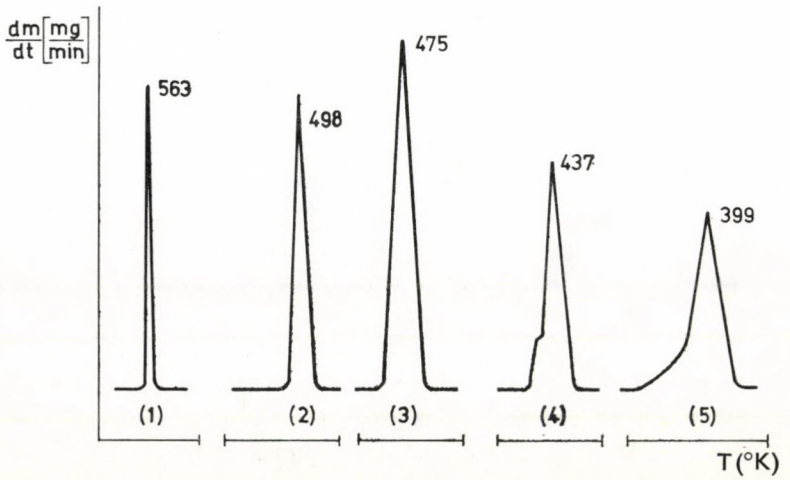

Рис. 2. Кривые ДТГ(М) монокристаллов $Y_3Fe_{5-x}Ga_xO_{12}$ с $x = 0$ (1); $x = 0{,}4$ (2); $x = 0{,}67$ (3); $x = 0{,}9$ (4); $x = 1{,}3$ (5)

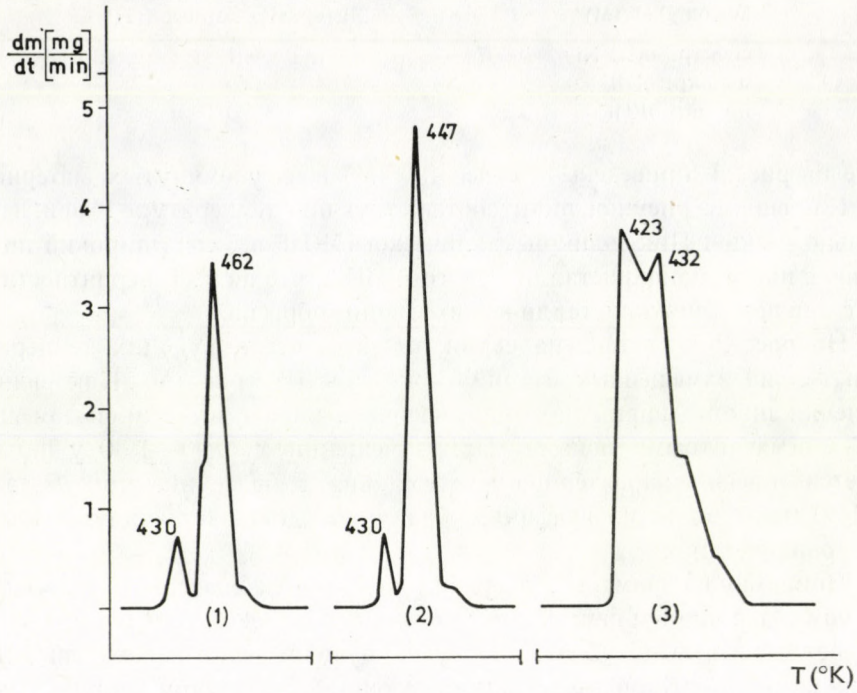

Рис. 3. Кривые ДТГ(М) монокристаллов $Y_3Fe_{5-x-y}Ga_xSc_yO_{12}$ с $x = 0{,}8$; $y = 0$ (1); $x = 0{,}8$; $y = 0{,}11$ (2); $x = 0{,}8$; $y = 0{,}18$ (3)

позиционными параметрами x и y, т. е. имеют преимущество две магнитные фазы с температурами Кюри:

	T_c главного пика (°К)	T_c побочного пика (°К)
1.	462	430
2.	447	430
3.	423	432

Аналогичные результаты, появление добавочного пика, наблюдались на кальций — ванадий — висмутовых феррогранатах; эксперименты в этой работе проводились на дериватографе методом ДТАМ [2]. Появление добавочного пика при $T_c = 430$ °К вероятно отражает схожесть условий выращивания упомянутых кристаллов, а также близость их композиций.

Для определения соответствия литературных и наших экспериментальных данных, нами были расчитаны T_c некоторых гранатов. Для расчетов была использована формула выведенная из модели Gilleo [3]. Далее, были использованы результаты химического анализа наших образцов (основанного на катионной хромотографии и последующем комплексометрическом анализе) и данные о распределении ионов галлия по двум подрешеткам монокристалли-

ческого граната, приведенные в работе [4]. Принимая во внимание, что концентрация ионов скандия далека от значения $y = 0{,}7$, при котором ожидается переход ионов из октаэдрической в тетраэдрическую подрешетку, все ионы Sc^{3+} приписывались октаэдрической подрешетке.

Таблица I

Образец	$X_a + X_d$*	X_d**	X_a**	y_d*	T_c расчет	T_c ДТГ(М)	T_c экстрап.
1.	0	0	0	0	560	563	—
2.	0	0	0	0	560	562	533
3.	0,48	0,47	0,01	0	518	498	—
4.	0,67	0,65	0,02	0	500	475	—
5.	0,9	0,85	0,05	0	480	437	—
6.	1,3	1,22	0,08	0	428	399	—
7.	0,8	0,768	0,032	0	486	462	—
8.	0,78	0,750	0,030	0,11	473	447	—
9.	0,80	0,768	0,032	0,18	460	423	418
10.	0,78	0,750	0,030	0,4	410	383	—

X_d, X_a — количество ионов Ga^{3+} соответственно в тетраэдрических и октаэдрических местах.

y_d — ионы Sc^{3+} в октаэдрической подрешетке

* Результаты химического анализа. Ошибка измерения $\pm 1\%$.

** Расчетные количества распределения ионов Ga^{3+} по двум подрешеткам; для расчетов были использованы данные работы [4].

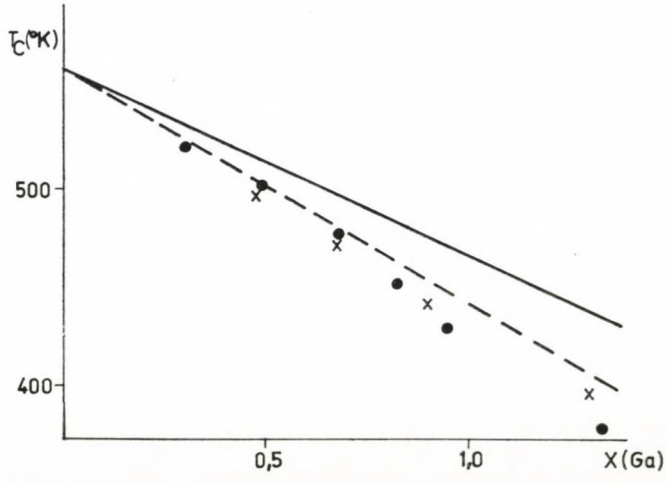

Рис. 4. Концентрация зависимость T_c для $Y_3Fe_{5-x}Ga_xO_{12}$. Сплошная кривая расчитана из формулы Gilleo на основе наших данных. Пунктирная кривая взята из [4] .... — экспериментальные данные, взятые из [4]. x — наши экспериментальные данные, метод ДТГ(М)

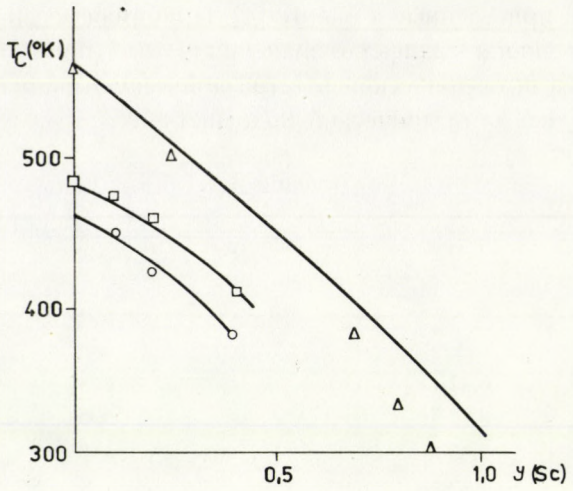

Рис. 5. Концентрационная зависимость T_c для $Y_3Fe_{5-y}Sc_yO_{12}$. Сплошная кривая — расчеты Gilleo [5] △ — экспериментальные данные из [5], ○ — наши экспериментальные данные для композиции $Y_3Fe_{4,2-y}Ga_{0,8}Sc_yO_{1,2}$ (метод ДТГ(М)), □ — наши расчеты

Предполагаемая концентрация ионов Ga^{3+} и Sc^{3+} по подрешеткам, расчитанные и измеренные T_c представлены в таблице I и на рис. 4, 5.

Как видно из рисунков, разбавление магнитных подрешеток немагнитными ионами приводит к уменьшению числа сверхобменных связей. При уменьшении числа связей на один ион T_c твердого раствора уменьшается. При малом разбавлении T_c изменяется линейно при увеличении x; при больших разбавлениях отклонение от линейности велико и связано со статистикой распределения ионов по подрешеткам.

Выводы

Измеренные вышеупомянутым методом температуры Кюри были сравнены с литературными данными, с T_c, полученными обычным методом экстраполяции кривой $4\pi M_s(T)$ и с расчетными данными, полученными использованием расчетной формулы T_c, представленной статистической теорией Gilleo.

Как мы видели, острота и ширина пиков могут дать информацию о химическом составе и гомогенности вещества.

Принимая во внимание, что согласованность наших опытных данных по измерению T_c, полученных с помощью метода ДТГ(М), с литературными данными хорошая, мы считаем, что этот метод можно рекомендовать для быстрого и надежного определения температуры Кюри и получения информаций об однородности исследуемых магнитных систем.

Следует также отметить, что ни магнитные, ни рентгеновские измерения не обладают такой чувствительностью, с какой мы встретились в случае метода ДТГ в магнитном поле.

ЛИТЕРАТУРА

1. Я. Смит, Х. Вейн, Ферриты, Издательство иностранной литературы, Москва, 1962.
2. I. Masiulanis, R. Moskalewicz, Science of Ceramics, Edited by K.I.D. Vries. Published by The Nederlandse Keramische Vereniging, Vol. **9**, 359, 1977.
3. M. A. Gilleo, Phys. Rev., **110**, 73, 1958.
4. P. Hansen, J. of Appl. Phys., **45**, 2728, 1974
5. S. Geller, Bell Syst. Techn. J., XLIII, 565, 1974.

Acta Physica Academiae Scientiarum Hungaricae, Tomus 47 (1—3), pp. 263—273 (1979)

CRYSTAL DEFECTS IN FLUX GROWN LITHIUM FERRITE, $LiFe_5O_8$ SINGLE CRYSTALS

By

E. Beregi, E. Sterk

RESEARCH INSTITUTE FOR TELECOMMUNICATION, BUDAPEST, HUNGARY

E. Pál and M. Farkas-Jahnke

RESEARCH INSTITUTE FOR TECHNICAL PHYSICS OF THE HUNGARIAN ACADEMY OF SCIENCES, BUDAPEST, HUNGARY

With the increase of frequencies in microwave communications lithium ferrite single crystals attract growing interest.

The characteristic crystal defects of a flux-grown $LiFe_5O_8$ single crystal were investigated by means of light microscopy, scanning electron microscopy and X-ray topography with respect to the technology. At the beginning of the growth process crystal grains with slightly different orientations and with boundaries containing dislocation groups were formed. Thermal stresses caused cracks. The curved cracks were accompanied by strain fields of helices partly decorated by precipitates visible on the topographs and also by light microscope. Far from the nucleation site of the crystal large perfect regions containing only straight small-angle boundaries could be found. Precipitates, presumably of $LiFeO_2$, were present in all parts of the crystal. Dislocation arrangements characteristic of stacking faults also appeared on the crystal.

1. Introduction

The trend of development of microwave devices is to increase frequency above 10 GHz which, owing to its high Curie temperature, fairly high magnetic anisotropy and narrow magnetic resonance linewidth (the lowest of all spinel-structure ferrites) focussed attention on lithium ferrite. Its single crystals are used in many types of microwave devices, such as filters, magneto-elastic delay lines and parametric amplifiers.

It has been found, however [1], that the essential parameter of gyromagnetic filters, namely the resonance linewidth ΔH of $Li_{0.5}Fe_{2,5}O_4$ single crystals is greatly influenced by the presence of submicroscopic lattice defects. Crystals applied for magnetoelastic purposes must also have fairly large perfect regions.

In devices single crystal spheres of 1 mm diameter or 0.2 mm thick discs of 2—3 mm diameter are used. Thus, for economical device fabrication it would be desirable to grow the crystals under conditions resulting in large defectless regions. Very few published works deal with the correlations between the occurrence of crystal defects and the parameters of the growth processes. Though the chemical reactions of Li-ferrite crystals are rather well known,

there are only few data on the origin of the crystal defects. It is important from both the theoretical and practical aspect to know the possible types and characteristics of the defects as a first step towards the improvement of crystal quality.

2. The structure of Li-ferrite [7—8]

Li-ferrite is a ferrimagnetic spinel crystal with eight ($Li_{0,5}Fe_{2,5}O_4$) formula units in the elementary cell. The metal ions are situated in the interstitial places of the fcc lattice built of oxygen ions. There are 64 tetrahedral and 32 octahedral coordinate sites.

In the spinels 8 tetrahedral "A" and 16 octahedral "B" sites are occupied by metal ions, forming the "A" and "B" sublattices, respectively. The cation distribution can be represented by the following formula:

$$Fe^{3+}\,[Fe^{3+}_{1,5}\,Li^{1+}_{0,5}]\,O_4,$$

where the unbracketed cations are on the "A" and the bracketed cations on the "B" sites. There is a ferrimagnetic coupling between the "A" and "B" sublattices.

At high temperatures the "B" sublattice contains both Li^{1+} and Fe^{3+} ions without any regularity. When the crystals are cooled slowly below 750 °C an ordering process of the "B" site cations takes place, i.e. three Fe^{3+} ions are followed by one Li^{1+} ion in the [110] direction. Since the number of Fe^{3+} ions in the "A" and "B" sublattices does not change during this ordering process, the latter does not affect the Curie temperature and magnetization, but influences significantly magnetic anisotropy, magnetostriction and even the resistivity of the crystals.

The magnetic properties of Li-ferrites are greatly influenced also by the stoichiometry of the compound. Above 1000 °C part of the lithium and oxygen ions volatilize which can lead to γ-Fe_2O_3 formation and after phase transition α-Fe_2O_3 can precipitate in the Li-ferrite lattice, thus lowering saturation magnetization. Oxygen loss causes the formation of Fe^{2+} ions which act like paramagnetic substituents increasing magnetic losses. Resistivity is also affected by the valence exchange process $Fe^{3+} \rightleftharpoons Fe^{2+}$.

Since superperiodicity and composition inhomogeneities, e.g. presence of Fe_2O_3 precipitates affect the physical properties of the crystal they have to be investigated in crystals to be used in devices.

3. Crystal growth process

Because of the high volatility of Li_2O and the high oxygen tension of the crystals, Li-ferrite single crystals are, as a rule, grown by the flux method. The composition of our melt is given in Table I.

Table I

Flux composition

Li_2CO_3	Fe_2O_3	B_2O_3	FbO
11.7 mol%	14.6 mol%	29.4 mol%	44.3 mol%

The diagram of the crystal growth apparatus is shown in Fig. 1. The volume of the Pt-crucible was 300 ml, the highest temperature at the top of the crucible 1050 °C; with a downward negative temperature gradient of 1.5 °C/cm. After 12 hours heating at 1050 °C the whole system was cooled slowly to 600 °C at a rate of 1 °C/h.

By this method one large crystal of 3 cm edge-length, 6 crystals of 1 cm average diameter and several smaller crystals were obtained.

As the thermal stresses were probably the highest at the bottom of the crucible, the large crystal grown there was expected to contain the greatest number and variety of defects characteristic of flux grown Li-ferrites. The large, as-grown surfaces of the plate like crystal were (111) planes.

According to chemical analysis the composition of the crystal corresponded to the formula $Li_{0.45}Fe_{2.52}O_4$ instead of the desired $Li_{0.5}Fe_{2.5}O_4$; the lattice constant was 0.8331 nm. The measured values of electric and magnetic parameters are listed in Table II together with those of YIG, $MgFe_2O_4$ and literature values for Li-ferrite crystals [2, 3, 4, 5]. No chemical inhomogeneities could

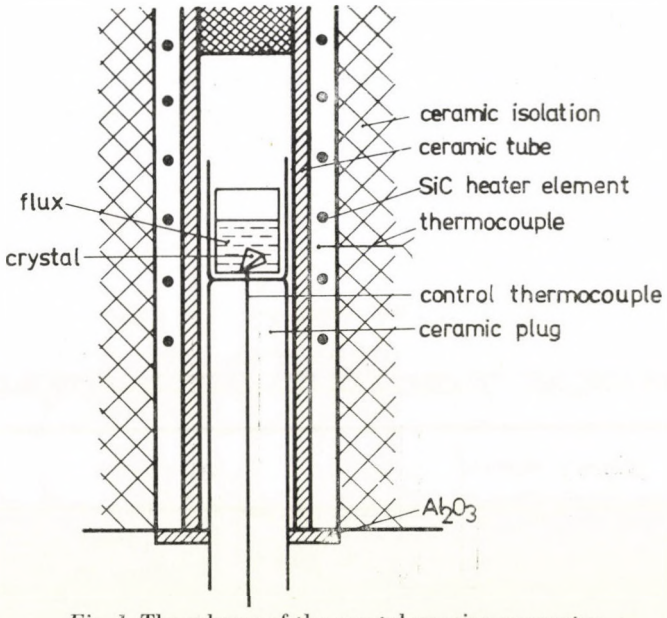

Fig. 1. The scheme of the crystal growing apparatus

Table II

Electric and magnetic parameters of YIG, $MgFe_2O_4$ and $LiFe_5O_8$

	YIG	$MgFe_2O_4$	$LiFe_5O_8$	The investigated $LiFe_5O_8$ crystal
T_c [K]	560	613* 653**	893* 893**	903* 903**
$4\pi M_S$ [T]	0.18	0.2* 0.12**	0.37	0.37
ΔH*** [A/M]	28	240* 160**	560—1500* 120**	560—1500* 80**
K_1/M [KA/M]	−3.2	−16* 29.6**	−23.2	
$\lambda_{100} \cdot 10^{-6}$	−1.0	−15	−22.4 −24.2	
ϱ [Ωcm]	10^8—10^{12}	10^5	10^5**	$4 \cdot 10^5$** $1 \cdot 10^4$*

* disordered ** ordered *** at 9.1 GHz

be detected by electron microprobe analyses with the JEOL JXA-type analyser. As the possible precipitates are $LiFeO_2$, PbO, α-Fe_2O_3, in this way we could exclude PbO and α-Fe_2O_3 precipitates; the presence of $LiFeO_2$ inclusions could not be revealed by this method, because the Li ion is not detectable by the device and the difference in iron content is not noticeable since the iron ratio of $LiFe_5O_8$ (s) and $LiFeO_2$ (o) is very small ($Fe_s\,wt\%/Fe_o\,wt\% < 1.2$.).

4. Investigation of defects

4.1 *Experimental*

For the investigation of the defect structure of the above mentioned large crystal light microscopy and X-ray topography were used before and after the etching processes. Light microscopic investigations were carried out

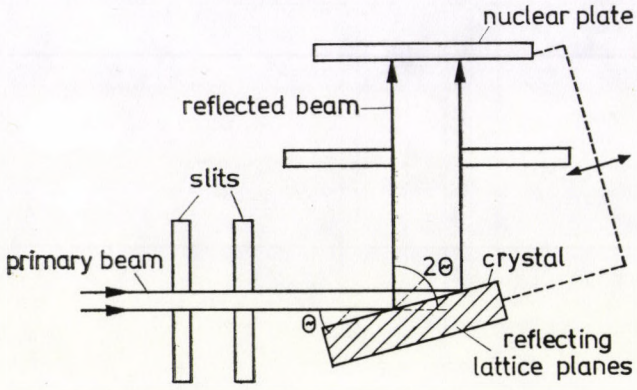

Fig. 2. The scheme of the back reflection Lang-type topographic camera

with Zeiss and Reichert microscopes, X-ray topographs were taken in reflection Lang-arrangement according to Fig. 2. using FeK_α radiation and 333, 620, 440 reflections.

The surface was treated before and during the intervals of the investigation of the defects as follows;

i) Mechanical polishing by Al_2O_3 suspension parallel to the largest as-

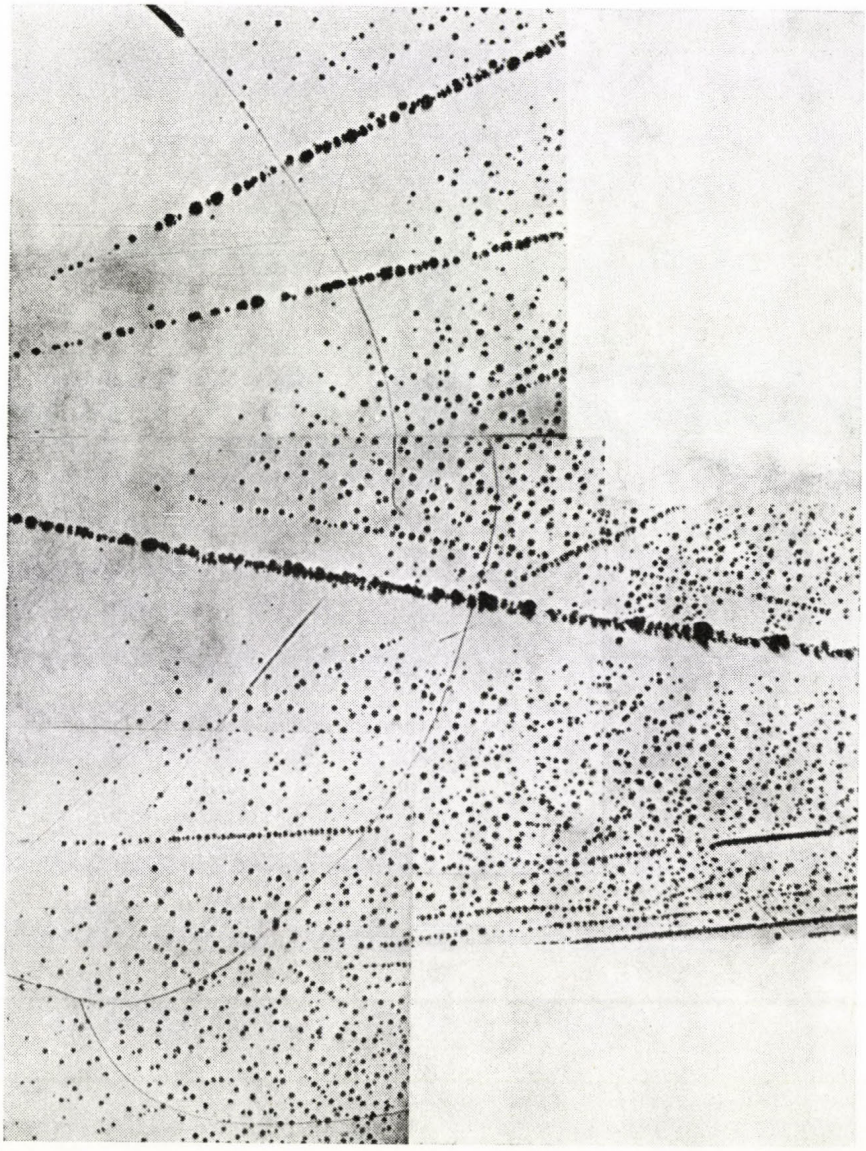

Fig. 3. Part of side "I" of the crystal plate after mechanical polishing, photographed under a Zeiss microscope

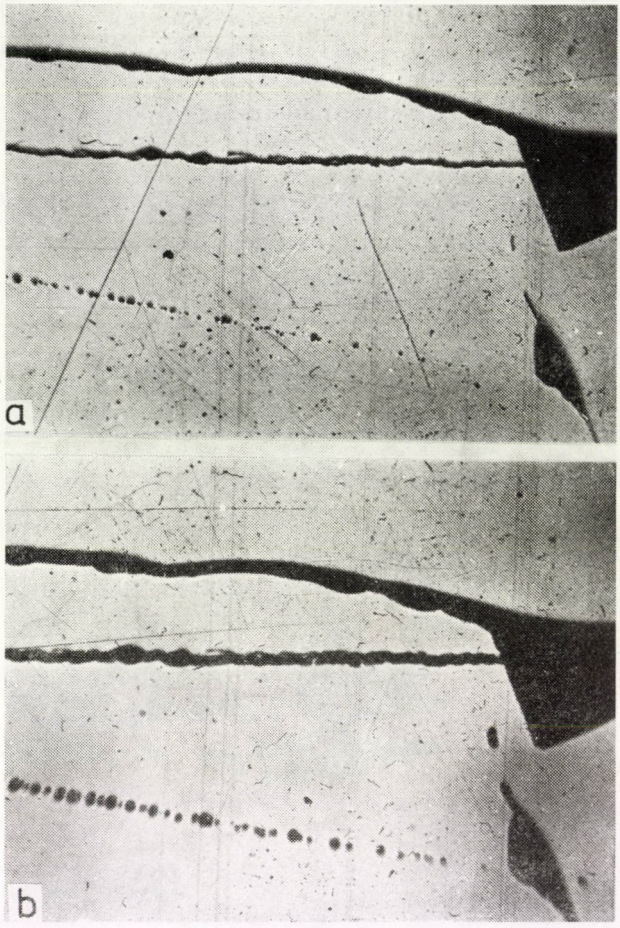

Fig. 4. Light microscope image of the same part of the crystal after etching in boiling azeotropic HCl for a) 4 min, b) 4 hours

grown (111) planes. The thickness of the abraded layer was less than 20 μm on each side of the crystal plate.

ii) Etching in boiling azeotropic HCl for 4 min to 4 hours. Thickness of the dissolved layer was less than 5 μm on each side.

iii) Etching in phosphoric acid at 200 °C for 8 min. Thickness of the dissolved layer was less than 10 μm on each side.

4.2. *Results*

I. After the first polishing the crystal was light microscopically examined. Already on the mechanically polished surfaces signs indicating different kinds of defects could be detected, such as continuous curved lines with black con-

trasts, as well as straight and curved lines of black dots. Besides these, a rather large region of the crystal was covered by statistically distributed black dots (Fig. 3).

II. The first time etching resulted in a weak pattern which did not change considerably when the time of etching was increased from 4 min to 4 hours (Fig. 4). X-ray topographs of a selected part of the crystal shown in Fig. 5a and 5b revealed a number of different types of faults which could be related to the light microscopic pattern. In the topographs lines of white contrast appeared corresponding to black continuous curved microscopic lines and were identified as cracks in the crystal; they were in most cases accompanied by lines of black contrasts and appeared in most, — but not in all — cases

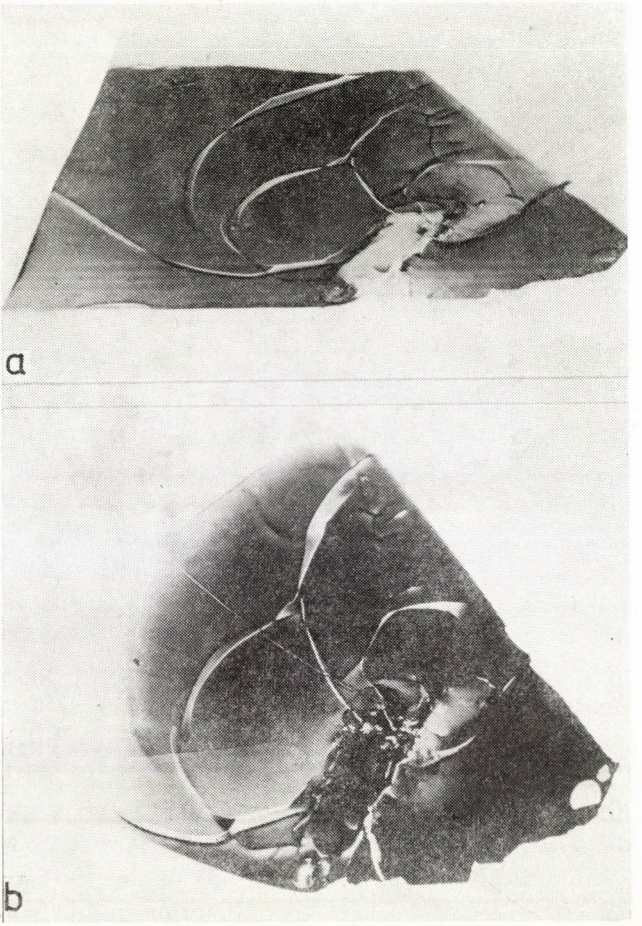

Fig. 5. Topographs of side "I" after the first etching a) (333) reflection; b) (620) reflection; defects: misoriented grains with dislocation network boundary (areas of different contrast on the right side of the crystal); small angle grain boundaries (straight line in Fig. 5b in the middle between regions of different contrast); cracks (white lines) and strain-fields with black contrast

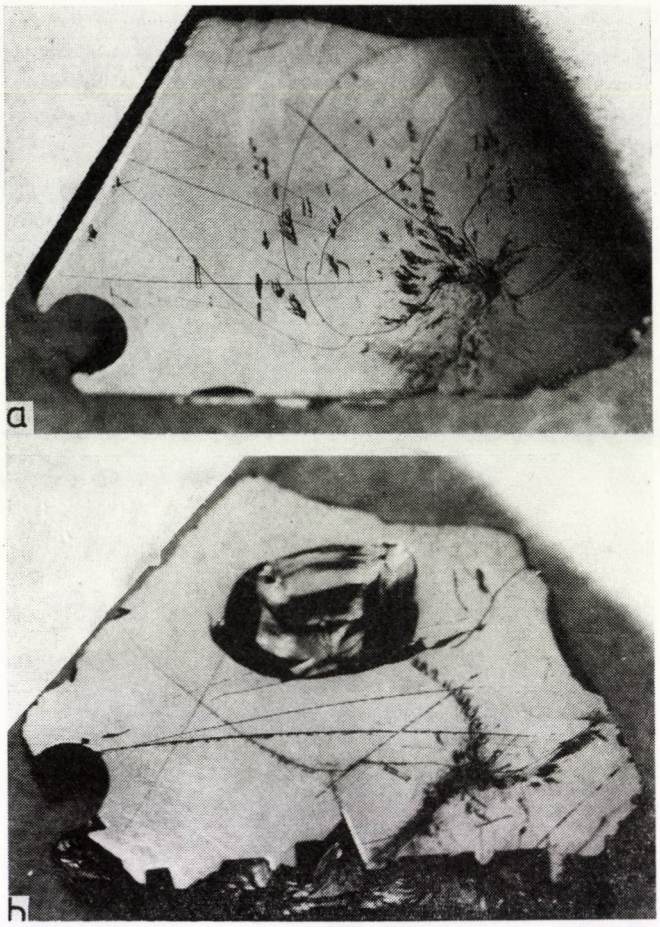

Figs. 6a, b. Photographs of both side of the crystal plate taken after the second etching

as curved dotted lines under the light microscope. This type of faults will be dealt with later.

The straight lines of black dots on the light microscopic pattern were identified as small angle grain boundaries. This was confirmed by the contrast difference between the regions on the two sides of such a line (Fig. 5b). The right apex of the crystal contained several large grains with considerable orientation difference (approx. 1°) as indicated by the great variation of contrasts on the different topographs. The boundary regions of these grains contain a large amount of dislocations. This part of the crystal was in contact with the bottom of the crucible where crystallization had begun.

Small parallel lines giving black-white contrasts were found almost everywhere in the crystal. They are similar to those found by MISHRA et al who identified them as $LiFeO_2$ precipitates [6].

III. After the second etching some of the characteristic features of the defects became more pronounced and could be distinguished under the light microscope and on the topographs as well. Photographs of both sides of the whole crystal are shown in Fig. 6a—6b. The side in Fig. 6a ("I" side) was already shown on two topographs and will be dealt with later. From the other side shown in Fig. 6b ("II" side) one of the strongly disoriented grains fell out during mechanical polishing. Some grains were missing also from the lower edge of the crystal. Some of the curved lines correlated fairly well with those on the "I" side, proving that they were built of dislocations going through the crystal plate almost perpendicularly to the surface.

Second etching revealed a great number of dislocation groups which were already visible under the light microscope. Parallel lines indicating the

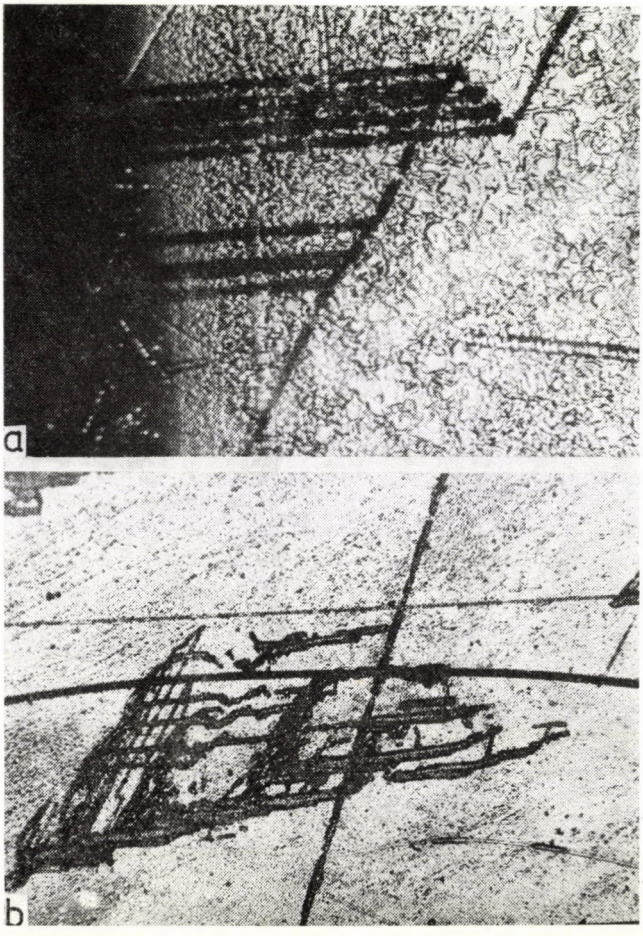

Fig. 7. Parallel dislocation lines indicating the presence of stacking faults. Light microscopic images taken after the second etching (a, b)

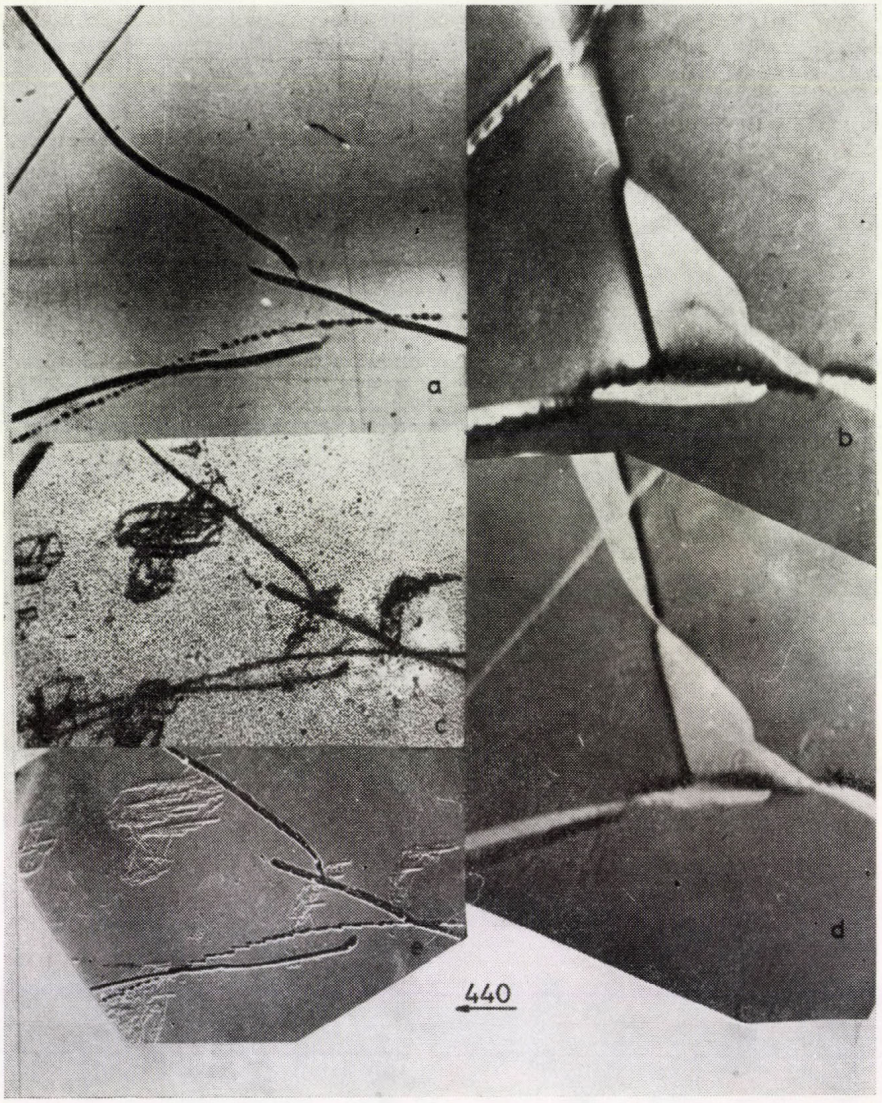

Fig. 8. Light microscopic images and topographs of a node of cracks and strain-field lines: a) light microscopic image, b) (440) topograph after the first etching; c) light microscopic image; d) (440) topograph; e) SEM image after the second etching. Note the change of contrast along the black lines. The strain-field of the decorated helices diminished as the precipitates were etched out

presence of stacking faults are shown in Fig. 7. Comparison of the details of topographs taken of the "I" side after the first and second etching shows interesting changes in some of the regions. In Fig. 8 the light microscopic pictures and topographs of a very interesting node of cracks and dotted lines, i.e. black lines, are shown before (8a, 8b) and after (8c, 8d, 8e) the second etching. Al-

ready before second etching there had been interesting differences between the light optical picture and the topograph of this region. The cracks were visible in both cases, but of the almost perpendicular black lines on the topograph only the one with a helix-like structure was visible also on the light optical picture. After second etching the contrast due to the strain-field decreased at that part of the topographic line and acted as a source of several groups of dislocations, as shown by light and by scanning electron microscopy (Fig. 8e) When the g vector of the reflection used for topographs is changed, the change in the contrast of the helical lines was not large, so the strain field must be due partly to precipitates on the helices. During second etching some of these precipitates were dissolved causing a decrease of the strain field and thereby the contrast on the topograph.

5. Conclusions

It was possible to detect and identify several types of crystal defects in one big flux-grown $LiFe_5O_8$ single crystal by means of the combination of repeated etching, light microscopy and X-ray topography.

At the beginning of the growth process crystal grains with slightly different orientations and with boundaries containing dislocation groups were formed. At a distance of this part the crystal has larger perfect regions containing only small angle grain boundaries. Precipitates of $LiFeO_2$ were present in all parts of the crystal. In the vicinity of cracks of thermal origin black lines due to the strain field of partly decorated helices are seen on the topographs; some of them are visible also under the light microscope. These helices can be useful for the formation of more perfect crystal regions since impurities from the sorrounding can precipitate along them.

REFERENCES

1. D. Lepore, J. Appl. Phys., **38,** 1421, 1967.
2. Ю. Яковлев, Известия АН СССР. Сер. физ., **32,** 1544, 1972.
3. Ю. Яковлев, Физика твердого тела, **13,** 1151, 1977.
4. E. Spence and I. Nielsen, J. Appl. Phys., **30,** 732, 1968.
5. Ken Ichi, J. Phys. Soc. Japan, **33,** 1581, 1972.
6. Raja K. Mishra, J. Amer. Ceram. Soc., **61,** 121, 1978.
7. G. O. White and C. E. Patton, J. of Magnetism and Magnetic Materials, **9,** 299, 1978.
8. J. Smit and H. P. I. Wijn,: Ferrites, John Wiley and Sons, Inc. New York, 1959.

Printed in Hungary

A kiadásért felel az Akadémiai Kiadó igazgatója **Műszaki szerkesztő:** Botyánszky Pál

A kézirat a kiadóba érkezett: 1979 VIII. 10. **A kézirat nyomdába érkezett: 1979. IX. 10. —Terjedelem: 24 (A/5) ív, 167 ábra**

80.7492 Akadémiai Nyomda, Budapest — Felelős vezető: Bernát György

NOTES TO CONTRIBUTORS

I. PAPERS will be considered for publication in Acta Physica Hungarica, only if they have not previously been published or submitted for publication elsewhere. They may be written in English, French, German or Russian.

Papers should be submitted to

Prof. I. Kovács, Editor
Department of Atomic Physics, Technical University
1521 Budapest, Budafoki út 8, Hungary

Papers may be either articles with abstracts or short communications. Both should be as concise as possible, articles in general not exceeding 25 typed pages, short communications 8 typed pages.

II. MANUSCRIPTS

1. Papers should be submitted in five copies.

2. The text of papers must be of high stylistic standard, requiring minor corrections only.

3. Manuscripts should be typed in double spacing on good quality paper, with generous margins.

4. The name of the author(s) and of the institutes where the work was carried out should appear on the first page of the manuscript.

5. Particular care should be taken with mathematical expressions. The following should be clearly distinguished, e.g. by underlining in different colours: special founts (italics, script, bold type, Greek, Gothic, etc.); capital and small letters; subscripts and superscripts, e.g. x^2, x_3; small *l* and 1; zero and capital O; in expressions written by hand: *e* and *l*, *n* and *u*, *v* and *v*, etc.

6. References should be numbered serially and listed at the end of the paper in the following form: J. Ise and W. D. Fretter, Phys. Rev., *76*, 933, 1949.

For books, please give the initials and family name of the author(s), title, name of publisher, place and year of publication, e.g.: J. C. Slater, Quantum Theory of Atomic Structures, I. McGraw-Hill Book Company, Inc., New York, 1960.

References should be given in the text in the following forms: Heisenberg [5] or [5].

7. Captions to illustrations should be listed on a separate sheet, not inserted in the text.

8. As per lst January 1980 the use of SI units has been made compulsory for all publications issued in Hungary. Please note that in papers submitted to Acta Physica after that date all measures should be expressed in SI units.

III. ILLUSTRATIONS AND TABLES

1. Each paper should be accompanied by five sets of illustrations, one of which must be ready for the blockmaker. The other sets attached to the copies of the manuscript may be rough drawings in pencil or photocopies.

2. Illustrations must not be inserted in the text.

3. All illustrations should be identified in blue pencil by the author's name, abbreviated title of the paper and figure number.

4. Tables should be typed on separate pages and have captions describing their content. Clear wording of column heads is advisable. Tables should be numbered in Roman numerals. (I, II, III, etc.).

IV. MANUSCRIPTS not in conformity with the above Notes will immediately be returned to authors for revision. The date of receipt to be shown on the paper will in such cases be that of the receipt of the revised manuscript.

Reviews of the Hungarian Academy of Sciences are obtainable at the following addresses:

AUSTRALIA
C.B.D. LIBRARY AND SUBSCRIPTION SERVICE, Box 4886, G.P.O., *Sydney N.S.W.2001*
COSMOS BOOKSHOP, 145 Ackland Street, *St. Kilda (Melbourne), Victoria 3182*

AUSTRIA
GLOBUS, Höchstädtplatz 3, *1200 Wien XX*

BELGIUM
OFFICE INTERNATIONAL DE LIBRAIRIE, 30 Avenue Marnix, *1050 Bruxelles*
LIBRAIRIE DU MONDE ENTIER, 162 Rue du Midi, *1000 Bruxelles*

BULGARIA
HEMUS, Bulvar Ruszki 6, *Sofia*

CANADA
PANNONIA BOOKS, P.O. Box 1017, Postal Station "B", *Toronto, Ontario M5T 2T8*

CHINA
CNPICOR, Periodical Department, P.O. Box 50, *Peking*

CZECHOSLOVAKIA
MAD'ARSKÁ KULTURA, Národní třida 22, *115 66 Praha*
PNS DOVOZ TISKU, Vinohradská 46, *Praha 2*
PNS DOVOZ TLAČE, *Bratislava 2*

DENMARK
EJNAR MUNKSGAARD, Norregade 6, *1165 Copenhagen*

FINLAND
AKATEEMINEN KIRJAKAUPPA, P.O. Box 128, *SF-00101 Helsinki 10*

FRANCE
EUROPERIODIQUES S. A., 31 Avenue de Versailles, *78170 La Celle St.-Cloud*
LIBRAIRIE LAVOISIER, 11 rue Lavoisier, *75008 Paris*
OFFICE INTERNATIONAL DE DOCUMENTATION ET LIBRAIRIE, 48 rue Gay-Lussac, *75240 Paris Cedex 05*

GERMAN DEMOCRATIC REPUBLIC
HAUS DER UNGARISCHEN KULTUR, Karl-Liebknecht-Strasse 9, *DDR-102 Berlin*
DEUTSCHE POST ZEITUNGSVERTRIEBSAMT, Strasse der Pariser Kommüne 3—4, *DDR-104 Berlin*

GERMAN FEDERAL REPUBLIC
KUNST UND WISSEN ERICH BIEBER, Postfach 46, *7000 Stuttgart 1*

GREAT BRITAIN
BLACKWELL'S PERIODICALS DIVISION, Hythe Bridge Street, *Oxford OX1 2ET*
BUMPUS, HALDANE AND MAXWELL LTD., Cowper Works, *Olney, Bucks MK46 4BN*
COLLET'S HOLDINGS LTD., Denington Estate, *Wellingborough, Northants NN8 2QT*
W.M. DAWSON AND SONS LTD., Cannon House, *Folkestone, Kent CT19 5EE*
H. K. LEWIS AND CO., 136 Gower Street, *London WC1E 6BS*

GREECE
KOSTARAKIS BROTHERS, International Booksellers, 2 Hippokratous Street, *Athens-143*

HOLLAND
MEULENHOFF-BRUNA B.V., Beulingstraat 2, *Amsterdam*
MARTINUS NIJHOFF B.V., Lange Voorhout 9—11, *Den Haag*
SWETS SUBSCRIPTION SERVICE, 347b Heereweg, *Lisse*

INDIA
ALLIED PUBLISHING PRIVATE LTD., 13/14 Asaf Ali Road, *New Delhi 110001*
150 B-6 Mount Road, *Madras 600002*
INTERNATIONAL BOOK HOUSE PVT. LTD., Madame Cama Road, *Bombay 400039*
THE STATE TRADING CORPORATION OF INDIA LTD., Books Import Division, Chandralok, 36 Janpath, *New Delhi 110001*

ITALY
EUGENIO CARLUCCI, P.O. Box 252, *70100 Bari*
INTERSCIENTIA, Via Mazzé 28, *10149 Torino*
LIBRERIA COMMISSIONARIA SANSONI, Via Lamarmora 45, *50121 Firenze*
SANTO VANASIA, Via M. Macchi 58, *20124 Milano*
D. E. A., Via Lima 28, *00198 Roma*

JAPAN
KINOKUNIYA BOOK-STORE CO. LTD., 17-7 Shinjuku-ku 3 chome, Shinjuku-ku, *Tokyo 160-91*
MARUZEN COMPANY LTD., Book Department, P.O. Box 5050 Tokyo International, *Tokyo 100-31*
NAUKA LTD. IMPORT DEPARTMENT, 2-30-19 Minami Ikebukuro, Toshima-ku, *Tokyo 171*

KOREA
CHULPANMUL, *Phenjan*

NORWAY
TANUM-CAMMERMEYER, Karl Johansgatan 41—43, *1000 Oslo*

POLAND
WĘGIERSKI INSTYTUT KULTURY, Marszalkowska 80, *Warszawa*
CKP I W ul. Towarowa 28 *00-958 Warsaw*

ROMANIA
D. E. P., *Bucureşti*
ROMLIBRI, Str. Biserica Amzei 7, *Bucureşti*

SOVIET UNION
SOJUZPETCHATI — IMPORT, *Moscow* and the post offices in each town
MEZHDUNARODNAYA KNIGA, *Moscow G-200*

SPAIN
DIAZ DE SANTOS, Lagasca 95, *Madrid 6*

SWEDEN
ALMQVIST AND WIKSELL, Gamla Brogatan 26, *101 20 Stockholm*
GUMPERTS UNIVERSITETSBOKHANDEL AB, Box 346, *401 25 Göteborg 1*

SWITZERLAND
KARGER LIBRI AG, Petersgraben 31, *4011 Basel*

USA
EBSCO SUBSCRIPTION SERVICES, P.O. Box 1943, *Birmingham*, Alabama 35201
F. W. FAXON COMPANY, INC., 15 Southwest Park, *Westwood*, Mass. 02090
THE MOORE-COTTRELL SUBSCRIPTION AGENCIES, *North Cohocton, N. Y. 14868*
READ-MORE PUBLICATIONS, INC., 140 Cedar Street, *New York, N. Y. 10006*
STECHERT-MACMILLAN, INC., 7250 Westfield Avenue, *Pennsauken* N. J. 08110

VIETNAM
XUNHASABA, 32, Hai Ba Trung, *Hanoi*

YUGOSLAVIA
JUGOSLAVENSKA KNJIGA, Terazije 27, *Beograd*
FORUM, Vojvode Mišiča 1, *21000 Novi Sad*

Index: 26.022
Acta Phys. Hung. Tom. 47. No. 1—3. Budapest, 26. VI. 1980 HU-ISSN 0001-6705

ACTA PHYSICA

ACADEMIAE SCIENTIARUM HUNGARICAE

TOMUS XLVII FASCICULUS 4

AKADÉMIAI KIADÓ, BUDAPEST

1979

ACTA PHYS. HUNG. APAHAQ 47 (4) 275—364 (1979)

ACTA PHYSICA

ACADEMIAE SCIENTIARUM HUNGARICAE

SZERKESZTI

KOVÁCS ISTVÁN

Az *Acta Physica* angol, német, francia vagy orosz nyelven közöl értekezéseket. Évente két kötetben, kötetenként 4—4 füzetben jelenik meg. Kéziratok a szerkesztőség címére (1521 Budapest XI., Budafoki út 8.) küldendők.

Megrendelhető a belföld számára az Akadémiai Kiadónál (1363 Budapest Pf. 24. Bankszámla 215-11488), a külföld számára pedig a „Kultura" Külkereskedelmi Vállalatnál (1389 Budapest 62, P.O.B. 149. Bankszámla 217-10990), vagy annak külföldi képviseleteinél.

The *Acta Physica* publish papers on physics in English, German, French or Russian, in issues making up two volumes per year. Distributor: "Kultura" Foreign Trading Company (1389 Budapest 62, P.O. Box 149) or its representatives abroad.

Die *Acta Physica* veröffentlichen Abhandlungen aus dem Bereich der Physik in deutscher, englischer, französischer oder russischer Sprache, in Heften, die jährlich zwei Bände bilden.

Bestellbar bei »Kultura« Außenhandelsunternehmen (1389 Budapest 62, Postfach 149) oder seinen Auslandsvertretungen.

Les *Acta Physica* publient des travaux du domaine de la physique en français, anglais, allemand ou russe, en fascicules qui forment deux volumes par an.

On peut s'abonner à l'Entreprise du Commerce Extérieur «Kultura» (1389 Budapest 62, P.O.B. 149) ou chez représentants à l'étranger.

«*Acta Physica*» публикуют трактаты из области физических наук на русском, немецком, английском и французском языках.

«*Acta Physica*» выходят отдельными выпусками, составляющими два тома в год.

Заказы принимает предприятие по внешней торговле «Kultura» (1389 Budapest 62, P.O.B. 149) или его заграничные представительства.

ACTA PHYSICA

ACADEMIAE SCIENTIARUM HUNGARICAE

TOMUS XLVII FASCICULUS 4

AKADÉMIAI KIADÓ, BUDAPEST
1979

ACTA PHYS. HUNG.

INDEX

Acta Physica Academiae Scientiarum Hungaricae, Tomus 47 (4), pp. 275–280 (1979)

TEMPERATURE DEPENDENCE OF INFRARED ACTIVE FUNDAMENTAL MODES OF ADAMANTANE*

By

S. P. SRIVASTAVA and I. D. SINGH

ANALYTICAL PHYSICS LABORATORY, INDIAN INSTITUTE OF PETROLEUM, DEHRA DUN-248 005, INDIA

(Received 19. VI. 1979)

The infrared lattice vibrational spectrum of adamantane in solid cubic phase has been recorded at different temperatures using a Beckman IR-12 grating spectrophotometer. Besides the fundamental absorption bands at the centre of the Brillouin zone, a few lattice bands involving the interaction of infrared radiation with more than one phonon have also been observed. In the absence of detailed dispersion curves, a tentative assignment of these multiphonon bands has been done. The shifts observed in the fundamental bands due to rise in temperature have been discussed in terms of volume-dependence and other anharmonic effects.

Introduction

The infrared studies of adamantane ($C_{10}H_{16}$) have been the subject of recent investigations [1—3] because it shows a first-order phase transition at 208 K. The high temperature phase is face-centred cubic T_d space group while the low temperature phase is tetragonal, the unit cell being primitive. The molecular point group is also T_d, justifying its class as globular hydrocarbons. It sublimes at about 540 K (sealed tube).

The normal coordinates of adamantane vibrations span the representation $5A_1 + A_2 + 6E + 7F_1 + 11F_2$ of the point group T_d. Only the F_2 vibrations are infrared active. In the solid phase, the vibrations are subjected to the intermolecular potential with the local symmetry of the molecular site and to a dynamic interaction with the symmetry of the unit cell group (factor group) for the modes at zero wave vector.

The normal coordinate analysis of adamantane using a valence force field has been done by SNYDER and SCHACHTSCHNEIDER [1] by recording the infrared spectrum of adamantane at —190 °C (below the transition temperature) while the mechanism of phase transition has been studied by WU et al [2] by recording the infrared spectra at 150 and 225 K. Above this temperature values of the infrared bands of adamantane have been published recently by LEE and SLUTSKY [3] and some lattice properties have also been studied by these

* A Summary of this paper was presented at the 'National Conference on Molecular Spectroscopy and Lasers' held at the Banaras Hindu University, Varanasi, India, January 29–31, 1979.

authors. The temperature-dependence of the cohesive energy and Grüneisen parameter of adamantane have been studied recently by us [4].

In this communication we report our measurements of the infrared spectra of adamantane at high temperatures. Besides the fundamental bands at the centre of the Brillouin zone, a few more bands involving the interaction of infrared radiation with more than one phonon have been observed. An attempt has been made to explain the occurrence of these multiphonon bands and also of the shifts observed in the fundamental bands due to temperature in terms of volume-dependence of the vibrational frequencies and anharmonic effects.

Experimental

The infrared spectra of adamantane at 298, 355, 435 and 468 K have been recorded on a Beckman IR-12 double beam grating spectrophotometer equipped with a "Heatable Vertical Liquid Cell". The spectra were recorded both in thin film and KBr pellet and were found to be identical. The whole spectrum was calibrated using a thin film of polystyrene and spectroscopically pure indene.

Under the experimental conditions the spectral resolution was 0.25 cm^{-1} at 1000 cm^{-1} and frequency accuracy was ± 0.5 cm^{-1}.

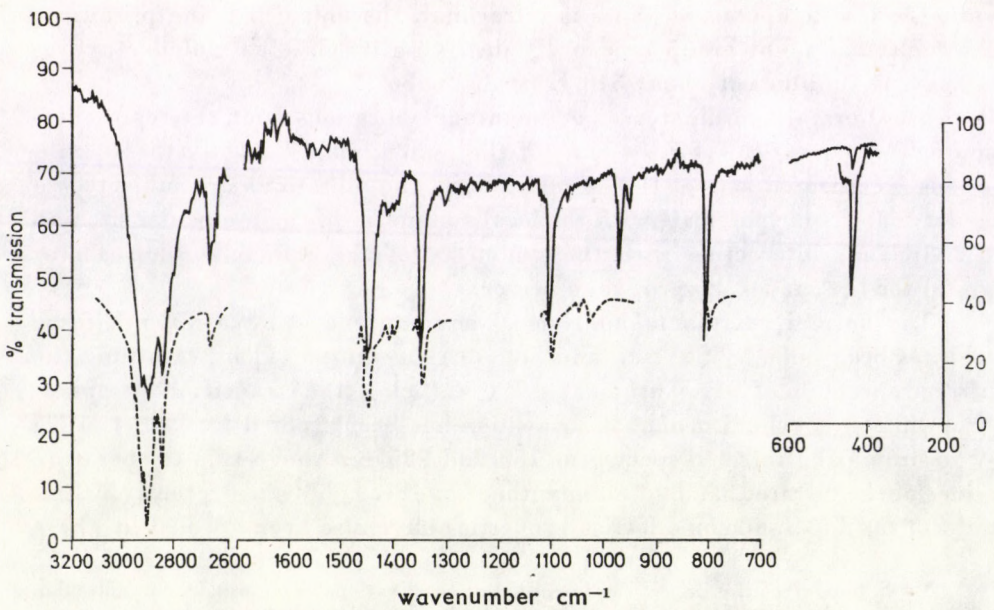

Fig. 1. Infrared absorption spectra of adamantane. —— 298, K ----- 435 K

The spectra recorded at 298 and 435 K have been reproduced in Fig. 1. Some of the results have also been verified on a Perkin-Elmer 577 model at 298 K in the low frequency region.

Results and discussion

The frequency values observed in Fig. 1 at 298 K are listed in Table I where these have been compared with those obtained from valence force field calculations and from measurements of other workers [1, 3].

Unlike previous studies, in the present investigation we have observed all the eleven infrared active F_2 vibrations as predicted by normal coordinate analysis. In the work of SNYDER et al [1], where they have measured the infrared spectra of adamantane in tetragonal phase (−196 °C), many more bands have been observed. Some of these bands are due to splittings of the fundamental vibrations, each vibration showing its triply degenerate character [2].

Table I

Infrared active fundamental and subsidiary bands (in cm^{-1}) of adamantane at 298 K

Observed			Calculated	
Present study	LEE and SLUTSKY [3]	SNYDER et al [1]	SNYDER et al [1]	CYVIN et al [6]
442.5	—	—	423	440
640	—	632	649	635
801.5	796	880	800	795
951	—	—	—	—
971	967	966	971	965
1105	1102.8	1101	1100	1100
1314	—	1289	1285	1305
1355	1351	1354	1354	1350
1415	—	—	—	—
1451.5	1447.5	1452	1459	1450
2020	—	—	—	—
2120	—	—	—	—
2120	—	—	—	—
2670	—	—	—	—
2700	—	—	—	—
2742	—	—	—	—
2848.5	2853.5	—	2856	2855
2911	—	—	2904	2910
2927	2923.5	—	2932	2935

Table II

Temperature dependence of fundamental bands of adamantane

298 K		355 K	435 K	468 K
Present study	LEE and SLUTSKY [3]**			
442.5	—	439	*	*
640	—	*	*	*
801.5	796	799.5	799	798.5
971	967	970.5	969	*
1105	1102.8	1103	1100	1100
1314	—	*	*	*
1355	1351	1354	1352	1352
1451.5	1447.5	1452.5	1452	1450.5
2848.5	2853.5	2848	2847	2847
2911	—	2908	2906	2906
2928	2923.5	2928	2927	2926

* The band becomes so broad that it is difficult to assign a proper frequency value.
** These authors have also made temperature-dependent studies. Since their measurements are not consistent with the present study and the conditions and accuracy of these measurements are not known either, a comparison with the present study is not possible.

However, two fundamental bands at 442.5 cm^{-1} and 640 cm^{-1}, which were predicted by the valence force field calculations, have also been observed in the present study. The band at 640 cm^{-1} (not shown in Fig. 1) was observed in CS_2 solution.

In Table II we have listed the values of the fundamental vibrations observed at different temperatures. In some of these cases, the observed bands become so broad with the rise in temperature that it was felt difficult to assign a proper value.

The effect of raising the temperature on the spectra is to shift the entire curve to low frequencies. It is generally believed [5] that the change in the peak position and width of the infrared active lattice band are caused by anharmonic forces in the crystal lattice. The thermal expansion of solids has also the same effect. Surprisingly, for the molecular crystal of adamantane with strong chemical bonds within a molecular group and with loose bindings such as the Van der Waal's type between the molecules, the lattice bands do not change much with temperature. Such an observation has also been made by LEE and SLUTSKY [3]. We may attribute this phenomenon to the fact that often the directions of shifts arising from the volume dependence and anharmonic effect are opposite, which results in a smaller temperature dependence [5]. The amount of shift due to these two effects can be separately calculated from the equations developed by MITRA [5] for ionic solids, but unfor-

tunately for adamantane, the data on thermal expansion coefficient at different temperatures are not available.

However, an indirect study on the volume dependence of the vibrational frequencies can be made by evaluating the Grüneisen parameters from the temperature dependence of the fundamental modes. For the i^{th} mode and K wave-vector vibration, we can define the mode Grüneisen parameter as

$$\gamma_i(\mathbf{K}) = -\left(\frac{1}{\alpha}\right)\frac{1}{\nu_i(\mathbf{K})}\left(\frac{\partial \nu_i(\mathbf{K})}{\partial T}\right)_P, \tag{1}$$

where α is the volume expansion coefficient and $\nu_i(\mathbf{K})$ the frequency of the i^{th} mode. Using the average value of α [4] and the temperature dependence of the fundamental modes as have been observed in Table II, we find the average value of $\gamma_i(\mathbf{K})$ as 0.4. The experimental value, obtained from the consideration of $3N_A$ modes (N_A being the Avogadro's number) is 6.3 [4]. Such a small value of the average $\gamma_i(\mathbf{K})$ thus indicated that the main contribution to γ is not from the fundamental vibrations but from the acoustic torsional modes.

Besides the fundamental modes, some more bands have been observed in the infrared spectrum of adamantane. The fundamental modes of vibration generally belong to the centre of the Brillouin zone. The symmetry classification and selection rules are derived from the factor group analysis and these constitute the $\mathbf{K} = 0$ modes of optical branches. The acoustic modes have zero frequencies in the factor group approximation and will have non-vanishing values at the zone boundary and thus may take part in the combinations and overtones. For the molecular modes, internal + internal, internal + external and internal + acoustic combinations are possible whereas the combinations external + external, external + acoustic and acoustic + acoustic give rise to the multiphonon combinations. In all these interactions the energy and wave vectors must be conserved.

The occurrence of the combination and overtones can be explained to be due to the interaction of two or more phonons with the radiation, through terms in the electric moment of second or higher orders in the molecular displacements. The combinations should give rise to continuous spectrum but the absorption peaks are found to occur because of the singularities in the phonon frequency distribution. These singularities arise from critical points in the Brillouin zone where the curves of frequency as a function of wave vector for the individual branches are flat. Such points are expected to occur at or near the edge of the Brillouin zone. For a given phonon branch this flattening of frequency as a function of phonon wave vector makes it possible to characterise that branch by a single frequency. The infrared spectrum can then be completely understood in terms of critical point phonons if these are known either from neutron scattering data or from a reliable theoretical calculation. Unfortunately, to our knowledge, no such data are available for adamantane.

In the absence of detailed dispersion curves, Wu et al [2] have made a tentative assignment of an extra band observed in their studies at 1104 cm^{-1}. Similar assignments could be done for the bands observed in the present case as well. For example, the band occurring at 2670 cm^{-1} could be assigned to be due to a two-phonon-process involving 1314 cm^{-1} and 1355 cm^{-1} fundamental vibrations (summation band) and that at 2700 as an overtone of 1355 cm^{-1} fundamental. The band at 2120 cm^{-1} appears to be due to the combination of 801.5 cm^{-1} and 1314 cm^{-1} fundamentals. The bands at 2020 and 2742 cm^{-1} probably appear to be due to interactions of external and acoustic modes because they could not be explained with the present set of fundamentals. However, in any case, a unique assignment is not possible because the combinations of other fundamentals might also become infrared active whereas these fundamentals themselves were not infrared active.

REFERENCES

1. R. G. Snyder and J. H. Schachtschneider, Spectrochim. Acta, **21**, 169, 1965.
2. P. J. Wu, L. Hsu and D. A. Dows, J. Chem. Phys. **54**, 2714, 1971.
3. W. Y. Lee and L. J. Slutsky, J. Phys. Chem., **79**, 2602, 1975.
4. S. P. Srivastava, I. D. Singh and P. L. Gupta, Acta Phys. Hung., **44**, 211, 1978.
5. S. S. Mitra, in "Optical Properties of Solids", Plenum Press, N. Y., 1969.
6. C. J. Cyvin, O. Ra and J. Brunvoll, Indian J. Pure Appl. Phys., **9**, 890, 1971.

Acta Physica Academiae Scientiarum Hungaricae, Tomus 47 (4), pp. 281—291 (1979)

STATIONARY BRANS-DICKE VACUUM SOLUTIONS FROM STATIC CYLINDRICALLY SYMMETRIC ZERO-MASS FIELDS

By

P. P. RAO and R. N. TIWARI

DEPARTMENT OF MATHEMATICS, INDIAN INSTITUTE OF TECHNOLOGY, KHARAGPUR 721302, (W. B.) INDIA

(Received 21. VI. 1979)

Stationary Brans-Dicke (BD) vacuum fields when the BD coupling constant $\omega \neq -3/2$ is obtained from static cylindrically symmetric zero-mass fields in three stages. The solution so obtained, in a way, can be said to belong to Majumdar—Papapetrou (MP) class.

Introduction

PERJÉS [1] has given a method for constructing stationary Einstein vacuum solutions from static axially symmetric Einstein—Maxwell solutions when both the electric and magnetic potentials are simultaneously present. This was later extended by RAO, TIWARI and RAO [2] to the case wherein stationary BD vacuum solutions for the coupling constant $\omega = 0$ can be obtained from those of static axially symmetric BD Maxwell solutions for $\omega = -3/2$. The present attempt is to extend the above result for the case when $\omega \neq -3/2$. We may mention that in our approach we have always kept MP class of solutions in the background. The solution generated here also, in a way, can be said to belong to this class.

In view of the above we have first obtained. using PERJÉS [3] result (derived here afresh), a generalized MP relation (in the sense that the metric component g_{44} is a function of both the electric and magnetic components of the four potential instead of only electrostatic potential as obtained by MAJUMDAR [4] and PAPAPETROU [5] for static cylindrically symmetric coupled zero-mass and electromagnetic fields. The relation so obtained enables one to generate the so called MP class of solutions from the static cylindrically symmetric zero-mass fields. Next as an extension of PERJÉS [1] result, we have obtained a theorem which converts any static cylindrically symmetric coupled zero-mass and electromagnetic fields to stationary zero mass fields. This technique thus takes over the MP class of solution obtained above to stationary zero mass field. In the third stage we have used a well known transformation by TABENSKY and TAUB [6] that has enabled us to take over the above stationary zero-mass solution to stationary solutions of BD vacuum fields for the BD coupling constant $\omega \neq -3/2$.

The present solution, in addition to having its origin in the cylindrically symmetric MP class of solutions (physical importance of which is rigorously discussed by HARTLE and HAWKING [7], also belongs to Kerr family (being stationary) and hence has a well established physical background.

1. MP class of coupled zero-mass and electromagnetic fields solution

The Einstein field equations for coupled zero-mass and electromagnetic field are:

$$R_{ij} = -kT_{ij} - \frac{k}{4\pi} v, i, v_{,j}, \tag{1}$$

with

$$T_{ij} = -\frac{1}{4\pi}\left(g^{sp} F_{si} F_{pj} - \frac{1}{4} g_{ij} F^{sp} F_{sp}\right), \tag{2}$$

$$F_{ij} = A_{i,j} - A_{j,i}, \tag{3}$$

$$F^{ij}_{;j} = 0, \tag{4}$$

$$g^{ij} v_{;ij} = 0, \tag{5}$$

where $k = \left(\frac{8\pi G}{c^4}\right)$ is the gravitational constant, A_i the electromagnetic four potential and v is the zero-mass scalar. Here and in what follows a subscript comma or a semi-colon after the unknown variable denotes partial differentiation or covariant differentiation, respectively.

We now solve the field equations (1)—(5) for the cylindrically symmetric Weyl's metric

$$ds^2 = e^{2\beta} dt^2 - e^{-2\beta}\left[e^{2\gamma}(d\varrho^2 + dz^2) + \varrho^2 d\Phi\right], \tag{6}$$

where α, β are functions of ϱ and z only and (ϱ, z, Φ, t) correspond to (x^1, x^2, x^3, x^4) co-ordinates, respectively.

The axial symmetry together with (3) implies that the only surviving components of F_{ij} are F_{13}, F_{14}, F_{23} and F_{24}, respectively. These can be expressed only in terms of the components A_3 and A_4 of the four potential A_i. For convenience we denote A_3 and A_4 by ξ and η, respectively.

The field equations (1)—(5) with respect to the metric (6) are:

$$\alpha_{,1} = \varrho(\beta_{,1}^2 - \beta_{,2}^2) + \frac{k\varrho}{8\pi}\left[\frac{e^{2\beta}}{\varrho^2}(\xi_{,1}^2 - \xi_{,2}^2) - e^{-2\beta}(\eta_{,1}^2 - \eta_{,2}^2)\right] + \frac{k\varrho}{8\pi}(v_{,1}^2 - v_{,2}^2), \tag{7}$$

$$\alpha_{,2} = 2\varrho\beta_{,1}\beta_{,2} + \frac{k\varrho}{4\pi}\left[\frac{e^{2\beta}}{\varrho^2}\xi_{,1}\xi_{,2} - e^{-2\beta}\eta, \eta_{,2}\right] + \frac{k\varrho}{4\pi} v_{,1} v_{,2}, \tag{8}$$

$$\beta_{,11}+\beta_{,22}+\frac{\beta_{,1}}{\varrho}=\frac{k}{8\pi}\left[\frac{e^{2\beta}}{\varrho^2}(\xi_{,1}^2+\xi_{,2}^2)+e^{-2\beta}(\eta_{,1}^2+\eta_{,2}^2)\right], \tag{9}$$

$$\xi_{,11}+\xi_{,22}-\frac{\xi_{,1}}{\varrho}=-2\beta_{,1}\xi_{,1}-2\beta_{,2}\xi_{,2}, \tag{10}$$

$$\eta_{,11}+\eta_{,22}+\frac{\eta_{,1}}{\varrho}=2\beta_{,1}\eta_{,1}+2\beta_{,2}\eta_{,2}, \tag{11}$$

$$\eta_{,2}\xi_{,2}-\eta_{,1}\xi_{,2}=0, \tag{12}$$

$$v_{,11}+v_{,22}+\frac{v_{,1}}{\varrho}=0. \tag{13}$$

Substituting (TAUBER [8])

$$\xi_{,1}\frac{e^{2\beta}}{\varrho}=\psi_{,2}, \qquad \xi_2\frac{e^{2\beta}}{\varrho}=-\psi_{,1}, \tag{14}$$

in (10), we get

$$\psi_{,11}+\psi_{,22}+\frac{\psi_{,1}}{\varrho}=2\beta_{,1}\psi_{,1}+2\beta_{,2}\psi_{,2}. \tag{15}$$

We now assume η to be functionally dependent on ψ, viz.,

$$\eta=\eta(\psi). \tag{16}$$

Using (16) in (11) and (15), we obtain

$$\eta=a\psi+b, \tag{17}$$

where a and b are arbitrary constants of integration. Eq. (17), is a linear relation between electric and magnetic potentials already obtained by PERJÉS [3]. In view of this, Eqs. (11) and (5) become identically the same.

Using (14) and (17) in (7)—(13) we get:

$$\alpha_{,1}=\varrho(\beta_{,1}^2-\beta_{,2}^2)+\frac{k}{8\pi}(1-a^2)\frac{e^{2\beta}}{\varrho}(\xi_{,1}^2-\xi_{,2}^2)+\frac{k\varrho}{8\pi}(v_{,1}^2-v_{,2}^2), \tag{18}$$

$$\alpha_{,2}=2\varrho\beta_{,1}\beta_{,2}+\frac{k}{4\pi}(1+a^2)\frac{e^{2\beta}}{\varrho}\xi_{,1}\xi_{,2}+\frac{k\varrho}{4\pi}v_{,1}v_{,2}, \tag{19}$$

$$\beta_{,11}+\beta_{,22}+\frac{\beta_{,1}}{\varrho}=\frac{k}{8\pi}(1+a^2)\frac{e^{2\beta}}{\varrho^2}(\xi_{,1}^2+\xi_{,2}^2), \tag{20}$$

$$\xi_{,11}+\xi_{,22}-\frac{\xi_{,1}}{\varrho}=-2\beta_{,1}\xi_{,1}-\beta_{,2}\xi_{,2}, \tag{21}$$

$$v_{,11}+v_{,22}+\frac{v_{,1}}{\varrho}=0. \tag{22}$$

which again can be expressed in an equivalent form:

$$\alpha_{,1} = \varrho(\beta_{,1}^2 - \beta_{,2}^2) - \frac{k\varrho}{8\pi}(1 + a^2)e^{-2\beta}(\psi_{,1}^2 - \psi_{,2}^2) + \frac{k\varrho}{8\pi}(v_{,1}^2 - v_{,2}^2), \tag{23}$$

$$\alpha_{,2} = 2\varrho\beta_{,1}\beta_{,2} - \frac{k\varrho}{4\pi}(1 + a^2)e^{-2\beta}\psi_{,1}\psi_{,2} + \frac{k\varrho}{4\pi}v_{,}v_{,2}, \tag{24}$$

$$\beta_{,11} + \beta_{,22} + \frac{\beta_{,1}}{\varrho} = \frac{k}{8\pi}(1 + a^2)e^{-2\beta}(\psi_{,1}^2 - \psi_{,2}^2), \tag{25}$$

$$\psi_{,11} + \psi_{,22} + \frac{\psi_{,1}}{\varrho} = 2\beta_{,1}\psi_{,1} + 2\beta_{,2}\psi_{,2}, \tag{26}$$

$$v_{,11} + v_{,22} + \frac{v_{,1}}{\varrho} = 0. \tag{27}$$

We denote Eqs. (18)–(22) as set A and Eqs. (23)–(27) as set B.

To arrive at the MP relation we assume β to be function of v and ψ, viz.,

$$\beta = \beta(v, \psi), \tag{28}$$

where v and ψ are independent of each other. In view of the assumption (28). Eqs. (26) and (27) when used in (25) give the following differential equation:

$$\left[\beta_{,\psi\psi} + 2\beta_{,\psi}^2 - \frac{k}{8\pi}(1 + a^2)e^{-2\beta}\right](\psi_{,1}^2 + \psi_{,2}^2) + \\ + 2(\beta_{,v}\beta_{,\psi} + \beta_{,\psi v})(v_{,1}\psi_{,1} + v_{,2}\psi_{,2}) + \beta_{,vv}(v_{,1}^2 + v_{,2}^2) = 0. \tag{29}$$

Since Eq. (29) is highly non linear and difficult to solve we assume the following differential conditions to satisfy it:

$$\left.\begin{aligned} &\beta_{,\psi\psi} + 2\beta_{,\psi}^2 - \frac{k}{8\pi}(1 + a^2)e^{-2\beta} = 0, && \text{(a)} \\ &\beta_{,v}\beta_{,\psi} + \beta_{,\psi v} = 0, && \text{(b)} \\ &\beta_{,vv} = 0 && \text{(c)} \end{aligned}\right\}. \tag{30}$$

It may be remarked here that there can be various other possibilities to satisfy Eq. (29), a detailed discussion regarding which is given by RAO and TIWARI [9]. The case considered here, however, in a sense can be said to be more general as compared to other cases. Consistency of the above Eqs. (30) demands that β must be independent of the scalar field v*. Thus the Eqs. (30b) and

* Dependence of β on both v and ψ leads to its imaginary value. Hence β depends only on ψ. For detailed discussion refer to TIWARI [10].

(30c) are identically satisfied whereas (30a) integrates to

$$g_{44} = e^{2\beta} = \frac{k}{8\pi}\left[(1 + a^2)\,\psi^2 + b\,\psi + c\right], \tag{31}$$

where b and c are arbitrary constants of integration. It may be noted here that in the relation obtained by MAJUMDAR [4] and PAPAPETROU [5], g_{44} is a function of electrostatic potential ψ only and is obtained as a special case of (31) when $a = 0$. Hence Eq. (31) may be called a generalized MP relation between the metric coefficient g_{44} and the electromagnetic potential ψ.

Making use of (31) and then substituting

$$\int \frac{d\psi}{(1 + a^2)\psi^2 + b\psi + c} = \frac{2x}{\sqrt{b^2 - 4c(1 + a^2)}}, \tag{32}$$

where x is a new variable, the set B (viz., Eqs. (23)—(27)) reduces to:

$$\alpha_{,1} = \varrho(x_{,1}^2 - x_{,2}^2) + \frac{k\varrho}{8\pi}(v_{,1}^2 - v_{,2}^2), \tag{33}$$

$$\alpha_{,2} = 2\,\varrho x_{,1} x_{,2} \frac{k\varrho}{4\pi} v_{,1} v_{,2}, \tag{34}$$

$$x_{,11} + x_{,22} + \frac{x_{,1}}{\varrho} = 0, \tag{35}$$

$$v_{,11} + v_{,22} + \frac{v_{,1}}{\varrho} = 0. \tag{36}$$

On integration Eq. (32) leads to

$$\psi = -\frac{b}{2(1 + a^2)} - \frac{\sqrt{b^2 - 4c(1 + a^2)}}{2(1 + a^2)} \coth x, \tag{37}$$

which when substituted in (31) gives

$$\beta = \frac{1}{2}\log\left[\frac{k}{8\pi}\,\frac{\{b^2 - 4c\,(1 + a^2)\}}{(1 + a^2)}\,\frac{e^{2x}}{(e^{2x} - 1)^2}\right]. \tag{38}$$

It can be verified that the field equations (33)—(36) correspond to the zero-mass field equations for the Weyl's metric:

$$ds^2 = e^{2x}\,dt^2 - e^{-2x}\left[e^{2z}(d\varrho^2 + dz^2) + \varrho^2\,d\Phi^2\right]. \tag{39}$$

Thus given any solution of zero-mass field for (39) one can always construct a corresponding coupled zero-mass and electromagnetic field solution for the metric (6) under the conditions (37) and (38).
Hence the theorem:

Theorem

Given any (α_0, x_0, v_0) as the zero-mass solutions for the metric (39), one can always generate the corresponding coupled zero-mass and electromagnetic solutions $(\alpha, x, v, \psi, \eta)$ for the same metric as:

$$\left.\begin{aligned} \alpha &= \alpha_0 , \\ x &= \frac{1}{2}\log\left[\frac{k}{8\pi}\,\frac{\{b^2 - 4c(1+a^2)\}}{(1+a^2)}\,\frac{e^{2x_0}}{(e^{2x_0}-1)^2}\right], \\ \psi &= -\frac{b}{2(1+a^2)} - \frac{\sqrt{b^2 - 4c(1+a^2)}}{2(1+a^2)}\coth x_0 , \\ \eta &= a\psi + b , \\ v &= v_0 . \end{aligned}\right\} \tag{40}$$

Example

When α_0, β_0 and v_0 are considered to be functions of ϱ only, it can be readily seen that the static cylindrically symmetric zero-mass fields for the metric (6), will have a solution set as:

$$\left.\begin{aligned} \alpha_0 &= \left(\frac{k}{8\pi}A^2 + B^2\right)\log\varrho + C , \\ \beta_0 &= B\log\varrho , \\ v_0 &= A\log\varrho , \end{aligned}\right\} \tag{41}$$

where A, B, C are arbitrary constants of integration. Now applying the theorem stated above, one can easily obtain the coupled zero-mass and electromagnetic fields solution for the metric (6) as:

$$\left.\begin{aligned} \alpha &= \left(\frac{k}{8\pi}A^2 + B^2\right)\log\varrho + C , \\ \beta &= \frac{1}{2}\log\left[\frac{k}{8\pi}\,\frac{\{b^2 - 4c(1+a^2)\}}{(1+a^2)}\,\frac{\varrho^{2\beta}}{(\varrho^{2\beta}-1)^2}\right], \\ \xi &= -\frac{16\pi BZ}{k\{b^2 - 4c(1+a^2)^{1/2}} + \text{constant} , \\ \eta &= -\frac{ab}{2(1+a^2)} - \frac{a\sqrt{b^2 - 4c\,(1+a^2)}}{2(1+a^2)}\left(\frac{\varrho^{2\beta}+1}{\varrho^{2\beta}-1}\right) + b , \\ v &= A\log\varrho . \end{aligned}\right\} \tag{42}$$

2. Stationary zero-mass field

PERJÉS [1] has generated the stationary source free gravitational field solutions from the static cylindrically symmetric Einstein—Maxwell fields. Using the same technique we, in this Section, have constructed the solutions of stationary zero-mass field from those of static cylindrically symmetric coupled zero-mass and electromagnetic fields.

The most general stationary symmetric line element is

$$ds^2 = -e^{\mu}(d\varrho^2 + dz^2) - \varrho^2\gamma d\Phi^2 + \frac{1}{\gamma}[dt - w d\Phi]^2, \tag{43}$$

where μ, γ and w are functions of ϱ and z only.

The zero-mass field equations for the metric (43) are:

$$\mu_{,1} = \frac{1}{2\varrho\gamma^2}[\varrho^2(\gamma_{,1}^2 - \gamma_{,2}^2) - (w_{,1}^2 - w_{,2}^2)] + \frac{\gamma_{,1}}{\gamma} + \frac{k}{4\pi}(v_{,1}'^2 - v_{,2}'^2), \tag{44}$$

$$\mu_{,2} = \frac{1}{\varrho\gamma^2}[\varrho^2\,\gamma_{,1}\gamma_{,2} - w_{,1}w_{,2}] + \frac{\gamma_{,2}}{\gamma} + \frac{k}{2\pi}\varrho v_{,1}' v_{,2}', \tag{45}$$

$$\gamma_{,11} + \gamma_{,22} + \frac{\gamma_{,1}}{\varrho} - \frac{\gamma_{,1}^2 + \gamma_{,2}^2}{\gamma} - \frac{w_{,1}^2 + w_{,2}^2}{\varrho^2\gamma} = 0, \tag{46}$$

$$w_{,11} + w_{,22} - \frac{w_{,1}}{\varrho} - \frac{2(w_{,1}\gamma_{,1} + w_{,2}\gamma_{,2})}{\gamma} = 0, \tag{47}$$

$$v_{,11}' + v_{,22}' + \frac{v_{,1}'}{\varrho} = 0. \tag{48}$$

where v' defines the zero-mass field.

It may be verified that if we substitute

with

$$\left.\begin{aligned} \alpha &= 2\mu - 2\log\gamma\,, \\ \beta &= -\log\gamma\,, \\ \xi &= -\left\{-\frac{8\pi}{k(1+a^2)}\right\}^{1/2} w\,, \\ v &= 2v'\,, \\ k &< 0\,, \end{aligned}\right\} \tag{49}$$

the static cylindrically symmetric coupled zero-mass and electromagnetic field equations of the set A (viz., Eqs. (18)—(22) of Section 1) go over to the stationary symmetric field equations for the metric (43) (viz., Eqs. (44)—(48)). Thus the theorem:

Theorem

Given any static cylindrically symmetric coupled zero-mass and electromagnetic solutions $(\alpha, \beta, \xi, \eta, v)$ for the metric (6), one can always construct a corresponding stationary zero-mass solutions (μ, γ, w, v') for the metric (43) where:

$$\left.\begin{aligned} \mu &= \frac{\alpha}{2} - \beta\,, \\ \gamma &= e^{-\beta}\,, \\ w &= -\left[-\frac{k(1+a^2)}{8\pi}\right]^{1/2} \xi\,, \\ v' &= \frac{1}{2}\, v\,, \end{aligned}\right\} \tag{50}$$

(of course with a change in gravitational constant k). The reverse process also holds good but it is unphysical.

Example

Using the solution (42) in the above stated theorem (viz., Eq. (50)) we get the stationary zero-mass solution for the metric (43) as:

$$\left.\begin{aligned} \gamma &= \left[\frac{k}{8\pi}\,\frac{\{b^2 - 4c\,(1+a^2)\}}{(1+a^2)}\right]^{-1/2} \frac{\varrho^{2\beta} - 1}{\varrho^{\beta}}\,, \\ \mu &= \frac{1}{2}\left(\frac{k}{8\pi} A^2 + B^2\right) \log \varrho + \log C' - \\ &\quad - \frac{1}{2} \log\left[\frac{k}{8\pi}\,\frac{\{b^2 - 4c(1+a^2)\}}{(1+a^2)}\,\frac{\varrho^{2\beta}}{(\varrho^{2\beta}-1)^2}\right], \\ w &= -\left[-\frac{k(1+a^2)}{8\pi}\right]^{1/2} \frac{16\pi\beta Z}{k\sqrt{b^2 - 4c\,(1+a^2)}}\,, \\ v' &= \frac{1}{2} A \log \varrho\,. \end{aligned}\right\} \tag{51}$$

3. BD stationary fields from the zero-mass stationary fields

TABENSKY and TAUB [6] have shown that, under the equation of state $\varrho' = p'$ (viz., ZELDOVICH fluid [11]), an irrotational perfect fluid can always be replaced by an equivalent zero-mass field (by a suitable relation between ϱ', p' and scalar field v') which, under a particular transformation, will go over to the BD vacuum fields when BD coupling constant $\omega \neq -3/2$ and vice-

versa. These transformations thus enable one to generate the solutions for the BD vacuum field equations when $\omega \neq -3/2$ from those of ZELDOVICH fluids via zero-mass fields. One can use these results even partially, namely, given any zero-mass field solution it will always be possible to generate the corresponding BD vacuum solution for $\omega \neq -3/2$ by using only part of the transformations relating zero-mass and BD scalar fields. This result of TABENSKY and TAUB [6] is independent of any symmetry imposed on the physical fields and hence the stationary zero-mass solution of the previous Section can be used to generate a corresponding stationary BD vacuum solution.

The transformation relations of TABENSKY and TAUB [6] are given as follows:

$$\varphi_{(BD)} = e^{\sqrt{2}\,\nu'/(\omega+3/2)^{1/2}},$$

$$\varphi_{(BD)}\, g_{\mu\nu(BD)} = g_{\mu\nu(\text{zero-mass})}\,.$$

Using these for the solution (51) obtained in Section 2, we get the stationary BD vacuum solution when $\omega \neq -3/2$ as:

$$\begin{aligned}
g^{11}_{BD} &= g^{22}_{BD} = -\frac{\varrho^{\frac{k}{16\pi}A^2+\frac{\beta^2}{8\pi}}\, c'(\varrho^{2\beta}-1)}{\left[\dfrac{k}{8\pi}\dfrac{\{b^2-4c(1+a^2)\}}{(1+a^2)}\right]^{1/2}\varrho^{\beta}}\cdot e^{-A\log\varrho/\sqrt{2}\,(\omega+3/2)^{1/2}}\\
g^{33}_{BD} &= -\left[\frac{k}{8\pi}\frac{\{b^2-4c\,(1+a^2)\}}{(1+a^2)}\right]^{-1/2}\times\\
&\qquad\times\left[\varrho^{2-\beta}\,(\varrho^{2\beta}-1)+\frac{4\beta^2 z^2\,\varrho^{\beta}}{\varrho^{2\beta}-1}\right]e^{-A\log\varrho/\sqrt{2}\,(\omega+3/2)^{1/2}},\qquad (52)\\
g^{44}_{BD} &= \left[\frac{k}{8\pi}\frac{\{b^2-4c\,(1+a^2)\}}{(1+a^2)}\right]^{1/2}\frac{\varrho^{\beta}}{\varrho^{2\beta}-1}\,e^{-A\log\varrho/\sqrt{2}(\omega+3/2)^{1/2}},\\
g^{34}_{BD} &= g^{43}_{BD} = \frac{2\beta z\,\varrho^{\beta}}{\varrho^{2\beta}-1}\,e^{-A\log\varrho/\sqrt{2}\,(\omega+3/2)^{1/2}},\\
\varphi_{BD} &= e^{A\log\varrho/\sqrt{2}\,(\omega+3/2)^{1/2}}.
\end{aligned}$$

It has been verified by direct substitution that the solution (52) satisfies the stationary BD vacuum field equations for the line element

$$ds^2 = -e^{\mu}(d\varrho^2+dz^2)-\varrho^2\gamma d\Phi^2-\frac{1}{\gamma^2}[dt-wd\Phi]^2\,. \qquad (53)$$

4. Conclusions

Combining the result of Sections 1, 2 and 3, we have the following final theorem:

Theorem

Given any static cylindrically symmetric zero-mass solutions one can always generate a corresponding stationary symmetric BD vacuum solution when $\omega \neq -3/2$ in three steps as follows:

Step 1. Generate static cylindrically symmetric coupled zero-mass and electromagnetic solutions from the corresponding static cylindrically symmetric zero-mass solutions using MP relation.

Step 2. Generate stationary zero-mass solutions from the static cylindrically symmetric coupled zero-mass and electromagnetic solutions obtained in Step 1.

Step 3. Generate BD stationary vacuum solutions from the stationary zero-mass solutions obtained in Step 2 using TABENSKY and TAUB's result.

Acknowledgement

Authors thank Prof. J. R. RAO for his continuous encouragement and interest throughout the work.

REFERENCES

1. Z. PERJÉS, Il Nuovo Cimento, **45B**, 600, 1968.
2. P. P. RAO, R. N. TIWARI and J. R. RAO, to appear in Indian J. Pure Appl. Math.
3. Z. PERJÉS, Acta Phys. Hung., **25**, 393, 1968.
4. S. D. MAJUMDAR, Phys. Rev., **72**, 390, 1947.
5. A. PAPAPETROU, Proc. Roy. Irish Acad., A **51**, 191, 1947.
6. R. TABENSKY and A. H. TAUB, Commun. Math. Phys., **29**, 61, 1973.
7. J. B. HARTLE and S. W. HAWKING, Commun. Math. Phys., **26**, 87, 1972.
8. G. TAUBER, Canad. J. Phys., **35**, 477, 1957.
9. P. P. RAO and R. N. TIWARI, Acta Phys. Hung. **45**, 285, 1978.
10. R. N. TIWARI, Indian J. Pure Appl. Math., **10**, 339, 1979.
11. YA. B. ZELDOVICH, Sov. Phys. JETP, **14**, 1143, 1962.

Appendix

The BD stationary vacuum field equations for the metric (53) are:

$$\frac{\gamma_{,2}^2 - \gamma_{,1}^2}{2\gamma^2} + \frac{\gamma_2 h_{,2} - \gamma_{,1} h_{,1}}{2\gamma h} + \frac{\mu_{,1}}{\varrho} - \frac{\gamma_{,1}}{\varrho} - \frac{(\mu_{,1} h_{,1} - \mu_{,2} h_{,2})}{2h} +$$

$$+ \frac{1}{2\gamma^2 \varrho^2 h}(w_{,1}^2 - w_{,2}^2) + \frac{3}{4}\frac{(h_{,2}^2 - h_{,1}^2)}{h^2} + \frac{1}{2}\frac{(h_{,11} - h_{,22})}{h} =$$

$$= -\omega\left(\frac{\varphi_{,2}^2 - \varphi_{,1}^2}{\varphi^2}\right) - \frac{(\mu_{,1}\varphi_{,1} - \mu_{,2}\varphi_{,2})}{\varphi} - \frac{(\varphi_{,22} - \varphi_{,11})}{\varphi},$$

$$\frac{(\mu_{,2} h_{,1} + \mu_{,1} h_{,2})}{4h} + \frac{\gamma_{,1}\gamma_{,2}}{2\gamma^2} + \frac{(\gamma_{,1} h_{,2} + \gamma_{,2} h_{,1})}{4\gamma h} - \frac{\mu_{,2}}{2\varrho} + \frac{\gamma_{,2}}{2\varrho\gamma} +$$

$$+\frac{h_{,2}}{2h\varrho}-\frac{w_{,1}w_{,2}}{2\gamma^2\varrho^2h}+\frac{3}{4}\frac{h_{,1}h_{,2}}{h^2}-\frac{1}{2\varrho h}-\frac{h_{,12}}{h}=$$

$$=-\omega\frac{\varphi_{,1}\varphi_{,2}}{\varphi^2}-\frac{\varphi_{,12}}{\varphi}+\frac{(\mu_{,2}\varphi_{,1}+\mu_{,1}\varphi_{,2})}{2\varphi},$$

$$w_{,11}+w_{,22}-\frac{w_{,1}}{\varrho}-\frac{3}{2}\left(\frac{w_{,1}^1h_{,1}+w_{,2}h_{,2}}{h}\right)-\frac{2}{\gamma}(w_{,1}\gamma_{,1}+w_{,2}\gamma_{,2})=$$

$$=-\frac{1}{\varphi}(w_{,1}\varphi_{,1}+w_{,2}\varphi_{,2}),$$

$$\frac{1}{\gamma}\left(\gamma_{,11}+\gamma_{,22}+\frac{\gamma_{,1}}{\varrho}\right)-\left(\frac{\gamma_{,1}^2+\gamma_{,2}^2}{\gamma^2}\right)+\frac{(h_{,11}+h_{,22})}{h}-\frac{3}{2h}(h_{,1}^2+h_{,2}^2)-$$

$$-\frac{(\gamma_{,1}h_{,1}+\gamma_{,2}h_{,2})}{2\gamma h}-\frac{1}{\varrho^2\gamma^2h}(w_{,1}^1+w_{,2}^2)=$$

$$=-\frac{\varphi_{,1}}{\varphi}\left(\frac{\gamma_{,1}}{\gamma}+\frac{h_{,1}}{h}\right)-\frac{\varphi_{,2}}{\varphi}\left(\frac{\gamma_{,2}}{\gamma}+\frac{h_{,2}}{h}\right),$$

$$-\frac{h_{,1}}{h}-\frac{\varrho h_{,11}}{2h}-\frac{\varrho h_{,22}}{2h}+\frac{3\varrho}{4h^2}(h_{,4}^2+h_{,2}^2)=$$

$$=-\left(-1\frac{\varrho h_{,1}}{2h}\right)\frac{\varphi_{,1}}{\varphi}+\frac{\varrho h_{,2}}{2h}\frac{\varphi_{,2}}{\varphi},$$

$$\varphi_{,11}+\varphi_{,22}+\frac{\varphi_{,1}}{\varrho}=\frac{\varphi_{,1}h_{,1}+\varphi_{,2}h_{,2}}{2h}.$$

Acta Physica Academiae Scientiarum Hungaricae, Tomus 47 (4), pp. 293—301 (1979)

FLOW OF 'DIPOLAR FLUIDS' THROUGH A CIRCULAR PIPE WITH CONSTANT TEMPERATURE GRADIENT

By

K. S. SHIRKOT and D. S. THAKUR

DEPARTMENT OF MATHEMATICS, HIMACHAL PRADESH UNIVERSITY, SIMLA-171005, INDIA

(Received 21. VI. 1979)

Dipolar fluids have been discussed by BLEUSTEIN and GREEN in quite a recent paper [1]. They have obtained explicit constitutive equations for homogeneous incompressible linear dipolar fluids. An application of this theory is made here to the problem of flow of dipolar fluids through a circular pipe with constant temperature gradient. It is found that the temperature distribution depends strongly on the ratio of the radius of the tube to the value of a material parameter l, with dimension of length. Numerical values for temperature for different values of radius in the pipe are given. Graphs are also drawn to compare our results with the classical ones. It is found that the temperature increases inside the pipe and is maximum at its axis.

1. Introduction

In their paper GREEN and RIVLIN [2] presented a theory of continuum in which stress multipoles of various orders were introduced. The theory of dipolar fluids is the simplest of multipolar fluids. It seems to be consistent to include dipolar stresses while considering fluids for which velocity gradients of higher orders than first are present in the constitutive equations. Also the boundary conditions follow in a natural way. Using this theory, SHIRKOT [3] has analysed the problem of Couette flow of dipolar fluids.

In the present paper, this theory of dipolar fluids is used to investigate the temperature distribution in a circular pipe with all at constant temperature gradient by using BLEUSTEIN and GREEN's [1] constitutive equations for homogeneous incompressible linear dipolar fluids when the fluid is flowing with the Poiseuille velocity distribution. Numerical values of the temperature for different values of the radius inside the pipe are sketched in the form of Tables. Graphs are drawn for showing the comparison with the classical case.

2. Basic equations

The constitutive equations have been derived by BLEUSTEIN and GREEN [1]. Here we mention only a brief outline. The constitutive equations for homogeneous incompressible linear dipolar fluids after some simplification can be put as follows:

$$\tau_{ij} + \varphi\delta_{ij} = 2\mu d_{ij}\,, \tag{2.1}$$

$$\sum_{(ij)k} + \psi_i \delta_{jk} + \psi_j \delta_{ik} = h_1 \delta_{ij} A_{kji} + h_3 A_{kji} + h_2(A_{ijk} + A_{jik}) + \gamma \delta_{ij} T_{,k}\,, \tag{2.2}$$

where τ_{ij} is ordinary stress tensor,

$$A_{ijk} = v_{i,jk} = A_{ikj}\,, \tag{2.3}$$

$$d_{ij} = \frac{1}{2}(v_{i,j} + v_{j,i}) = d_{ji}\,, \tag{2.4}$$

$$\delta_{ij} = 1 \text{ if } i = j \text{ and } \delta_{ij} = 0 \text{ if } i \neq j \tag{2.5}$$

and $\sum_{(ij)k}$ are the components of dipolar stress tensor with symmetry in the first two suffixes. φ and ψ are unknown functions, which govern the pressure p. $h_1, h_2, h_3, \mu, \alpha, \gamma$ and k are, in general, functions of temperature which are limited by the inequalities

$$\left.\begin{aligned} &(2h_1 + h_3) \geq 0\,,\ (2h_2 + h_3) \geq 0\,,\ \mu \geq 0\,, \\ &(h_3 - h_2) \geq 0,\ (5h_1 - 2h_2 + 2h_3) \geq 0\,, \\ &(5h_1 - h_2 + 2h_3)\frac{K}{T} + \frac{5}{4}\left(\gamma - \frac{\alpha}{T}\right)^2 \geq 0\,. \end{aligned}\right\} \tag{2.6}$$

The coefficients γ and α provide thermomechanical coupling. The rate of work equation is

$$\varrho r - \varrho(\dot{A} + \dot{T}S + \dot{S}T) - q_{i,i} + T_{ij} d_{ji} + \sum_{(ij)k} A_{kji} = 0\,, \tag{2.7}$$

where dot stands for material differentiation. In (2.7) A is the Helmholtz function and S the entropy, both per unit mass, $(T > 0)$ is the temperature, r is the heat supply function per unit mass per unit time, and ϱ is density

$$q_i = \alpha A_{ikk} + kT_{,i} \tag{2.8}$$

where q_i are the heat fluxes across the coordinate planes, per unit area of the planes per unit time. If the dipolar body forces per unit mass and the inertia terms are absent, we have

$$\tau_{i,\,j} \equiv \sigma_{ij} + \sum_{kij,k} \equiv \tau_{ji}\,, \tag{2.9}$$

where σ_{ij} is the monopolar stress tensor. Now the equations of motion governing the non-symmetric monopolar stress-tensor σ_{ij} are

$$\sigma_{ji,j} + \varrho f_i = \varrho \dot{\vartheta}_i\,, \tag{2.10}$$

where f_i is the monopolar body force per unit mass and ϱ is the mass density. We suppose f_i to be zero. Substituting for A_{ijk} and d_{ij} from (2.3) and (2.4) in (2.1) and (2.2) and using (2.9) we get the value of σ_{ij}. Substituting this in

(2.10) (with monopolar body forces absent) we write the equation of motion in the form

$$\mu(1 - l^2 \partial_i \partial_j) v_{k,jj} - p_{,k} = \varrho(1 - d^2 \partial_i \partial_j) + \\ + \varrho d^2 (v_{k,ij} v_{i,j} + v_{i,jj} v_{k,i}) , \tag{2.11}$$

where ∂_i is a gradient operator, the symbol l is intended to be suggestive of the fact that l has the dimension of length, and d is a material constant.

Also

$$l^2 = \frac{h_1 + h_3}{\mu} \geq 0 \quad \text{and} \quad p = \varphi - 2\psi_{i,i} .$$

As we have considered a homogeneous incompressible fluid case, we further have

$$v_{k,k} = d_{k,k} = 0 . \tag{2.12}$$

3. Solution of problem

We consider here the steady Poiseuille flow [1] of a homogeneous dipolar fluid through a straight circular pipe with walls kept at a uniform temperature gradient. We employ cylindrical coordinate system r, θ, z where $\hat{e}_r$, $\hat{e}_\theta$, $\hat{e}_z$. denote unit vectors in the coordinate directions. We suppose that the monopolar and dipolar body forces are zero and we look for the solutions of (2.11) and (2.12) in the form

$$\hat{v} = v(r)\, \hat{e}_z, \quad p = p(r, z) . \tag{3.1}$$

It is further assumed that

$$\varphi = \varphi(r, z), \ \hat{\psi} = \psi(r, z)\, \hat{e}_z , \tag{3.2}$$

so that

$$p(r, z) = \varphi(r, z) - 2 \frac{\partial}{\partial z} \psi(r, z) . \tag{3.3}$$

The condition will be similar at each section of the pipe and we may put

$$T = A_0 z + g(r) , \tag{3.4}$$

where A_0 is the prescribed temperature gradient. In (3.4), is a function to be determined from the solution of the probem subject to the condition, $g(r) = \\ = \text{constant} = g(R)$, at the boundary i.e.

$$g(r) = g(R) = \text{constant.} \tag{3.5}$$

From (2.2), (2.12), (3.1) and (3.2) we find that the non-zero physical components of the dipolar stress tensor are

$$\left.\begin{aligned} \underset{zrr}{\Sigma} &= \underset{rzr}{\Sigma} = -\psi + h_2 v'' \\ \underset{z\theta\theta}{\Sigma} &= \underset{\theta z\theta}{\Sigma} = -\psi + h_2 v' r^{-1} \end{aligned}\right\}, \tag{3.6}_1$$

$$\left.\begin{aligned} \underset{rrz}{\Sigma} &= (h_1 + h_3) v'' + h_1 v' r^{-1} + \gamma A_0 \\ \underset{\theta\theta z}{\Sigma} &= h_1 v'' + (h_1 + h_3) v' r^{-1} + \gamma A_0 \\ \underset{zzz}{\Sigma} &= -2\psi + h_1 (v'' + v' r^{-1}) + \gamma A_0 \end{aligned}\right\}, \tag{3.6}_2$$

where the prime denotes differentiation with respect to r. Eq. (3.1) satisfies (2.12) identically. Eq. (2.2) reduces to two scalar equations

$$\left.\begin{aligned} \frac{\partial p}{\partial r} &= 0 \\ (1 - l^2 D_r^2) D_r^2 \bar{v} &= \frac{1}{\mu} \frac{dp}{dz} \end{aligned}\right\}, \tag{3.7}$$

where D_r^2 is the differential operator

$$D_r^2 \equiv \left(\frac{d^2}{dr^2} + \frac{1}{r} \frac{d}{dr} \right). \tag{3.8}$$

The first equation of (3.7) shows that $p = p(z)$. From the second equation of (3.7) it then follows that $\left(-\frac{\partial p}{\partial z} \right) = C$, and thus the general solution to $(3.7)_2$ is written as

$$v = \frac{-Cr^2}{4\mu} + C_1 \log r + C_2 + C_3 I_0 \left(\frac{r}{l} \right) + C_4 K_0 (r/l), \tag{3.9}$$

where I_0 and K_0 are the modified Bessel's functions of first and second kind, respectively and C_1, C_2, C_3, C_4 are arbitrary constants.

Requiring the velocity to be finite at the centre of the tube, we obtain

$$C_1 = C_4 = 0 \tag{3.10}$$

and (3.9) reduces to

$$v = -\frac{Cr^2}{4\mu} + C_2 + C_3 I_0 \left(\frac{r}{l} \right). \tag{3.11}$$

The constants C_2 and C_3 are obtained with the help of boundary conditions as given by Eqs. (6.12) and (6.13) of BLEUSTEIN and GREEN [1]:

$$v[R] = 0\,,$$
$$T_{r\alpha}(R) = M_\alpha \quad \text{for} \quad \alpha = \theta, r, z\,; \tag{3.12}$$

where M_α are the prescribed dipolar tractions and R is the radius of the circular pipe. Since the only non-vanishing component of the dipolar traction T_{ij} is T_{rz} the solution for velocity finally becomes

$$v = \frac{CR^2}{4\mu}\left[1-\left(\frac{r}{R}\right)^2\right] - \frac{CR^2}{4\mu}\left[2+\frac{4\mu\eta_z}{(2h_1+h_3)C}\right]\left[\frac{\frac{l}{R}\left\{I_0(R/l) - I_0\left(\frac{r}{l}\right)\right\}}{\frac{R}{l}\frac{h_1+h_3}{2h_1+h_3}I_0\left(\frac{R}{l}\right) - \frac{h_3}{2h_1+h_3}I_0(R/l)}\right], \tag{3.13}$$

where η_z is given by $\eta_z = (M_z - \gamma A_0)$. (3.14)

We assume heat supply function and internal energy to be zero and constant, respectively. Now with the help of $(3.6)_2$, (2.1), (2.3) and (2.8), (2.7) reduces to

$$K\left(\frac{d^2g}{dr^2}+\frac{1}{r}\frac{dg}{dr}\right) = \mu(v')^2 + (h_1+h_3)(v''+v'r^{-1})^2 + \gamma A_0(v''+v'r^{-1}) - 2h_3 v' v'' r^{-1}, \tag{3.15}$$

putting the value of v given by (3.13) in (3.15), the differential equation determining $g(r)$ becomes

$$K\left(\frac{d^2g}{dr^2}+\frac{1}{r}\frac{dg}{dr}\right) = \mu\left[\frac{C^2r^2}{4\mu^2}+C_3^2\left\{\frac{I_1(r/l)}{l}\right\}^2 - CC_3\left\{\frac{r}{l}I_1\left(\frac{r}{l}\right)\right\}\right] + (h_1+h_3)\left[\frac{C^2}{\mu^2}+C_3^2\left\{\frac{I_0(r/l)}{l^2}\right\}^2 - \frac{2CC_3}{\mu l^2}\{I_0(r/l)\}\right] - \frac{h_3}{r}\frac{d}{dr}\left[\frac{C^2r^2}{4\mu^2}+C_3^2\left\{\frac{I_1(r/l)}{l}\right\}^2 - \frac{CC_3}{\mu}\left\{\frac{r}{l}I_1(r/l)\right\}\right] + \gamma A_0\left(\frac{d^2v}{dr^2}+\frac{1}{r}\frac{dv}{dr}\right), \tag{3.16}$$

where C_3 is given by [using (3.12) in (3.11)]

$$C_3 = \frac{\frac{CR^2}{4\mu}\left[2+\frac{4\mu\eta_z}{\eta(2h_1+h_3)C}\right]\frac{l}{R}}{\frac{R}{l}\frac{h_1+h_2}{2h_1+h_3}I_0(R/l) - \frac{h_3}{2h_1+h_3}I_1(R/l)}\,. \tag{3.17}$$

The solution of (3.16) which is free from singularities and satisfies the boundary conditions (3.5) is

$$K[g(r)-g(R)]=\frac{CR^2}{\tau\mu}\left[1-\left(\frac{r}{R}\right)^2\right]\gamma A_0-\frac{C^2R^4}{8\mu}\left[1-\left(\frac{r}{R}\right)^4\right]-$$

$$-\frac{C^2R^4}{8\mu}\left(\frac{2h_1+h_3}{h_1+h_3}\right)\left(\frac{l}{R}\right)^2\left[1-\left(\frac{r}{R}\right)^2\right]-\gamma A_0\frac{c^2R^2}{4\mu}\left[\left(2+\frac{4\mu\eta z}{(2h_1+h_3)C}\right)\times\right.$$

$$\left.\times\frac{\frac{l}{R}\{I_0(R/l)-I_0(r/l)\}}{\frac{R}{l}\left(\frac{h_1+h_3}{2h_1+h_3}\right)I_0(R/l)-\frac{h_3}{2h_1+h_3}I_1(R/l)}\right]+\frac{C^2R^4}{4\mu}\left[\left(2+\frac{4\mu\eta_z}{(2h_1+h_3)C}\right)\times\right.$$

$$\left.\times\frac{\left\{\frac{R}{l}I_1(R/l)-\frac{r}{l}I_1(r/l)\right\}-\frac{h_3}{h_1+h_3}\{I_0(R/l)+I_0(r/l)\}}{\left\{\frac{R}{l}\left(\frac{h_1+h_3}{2h_1+h_3}\right)I_0(R/l)-\frac{h_3}{2h_1+h_3}I_1(R/l)\right\}(R/l)^3}\right]$$

$$-\frac{C^2R^4}{32\mu}\left[\left(2+\frac{4\mu\eta_z}{(2h_1+h_3)C}\right)\times\right.$$

$$\left.\times\frac{\frac{h_1}{h_1+h_3}\{I_0^2(R/l)-I_0^2(r/l)\}+\frac{h_3}{h_1+h_3}\{I_1^2(R/l)-I_1^2(r/l)\}}{\left\{\frac{R}{l}\left(\frac{h_1+h_3}{2h_1+h_3}\right)I_0(R/l)-\frac{h_3}{2h_1+h_3}I_1(R/l)\right\}^2(R/l)^2}\right] \tag{3.18}$$

where we have used the relation $\mu l^2\equiv(h_1+h_3)$. Thus $T=A_0z+g(r)$ is determined.

4. Numerical values

We consider the motion for which $0<r/R<1$, and $M_z(R)=\gamma A_0=$ $=CR^2/4=$ constant and thus $\eta_z=0$.

Here it may be observed that the values of M_z will depend on the nature of the interaction of the fluid with the wall of the cylinder and is not necessarily zero. In this case (3.18) takes the form

$$\theta=\frac{C^2R^4}{4\mu kg(R)}\left[\frac{3}{16}-\left(\frac{r}{2R}\right)^2+\left(\frac{r}{2R}\right)^4-\frac{2h_1+h_3}{2(h_1+h_3)}\left(\frac{l}{R}\right)^2\{1-(r/R)^2\}\right.$$

$$-\frac{I_0(R/l)-I_0(r/l)}{\frac{2R}{l}\left\{\frac{R}{l}\left(\frac{h_1+h_3}{2h_1+h_3}\right)I_0(R/l)-\frac{h_3}{2h_1+h_3}I_1(R/l)\right\}}+$$

$$+\frac{2\{(R/l)\,I_1(R/l)-r/l\,I_1(r/l)\}-\frac{h_3}{h_1+h_3}\{I_0(R/l)-I_0(r/R)\}}{\left\{\frac{R}{l}\left(\frac{h_1+h_3}{2h_1+h_3}\right)I_0(R/l)-\frac{h_3}{2h_1+h_3}I_1(R/l)\right\}(R/l)^3}-$$

$$-\frac{\frac{h_1}{h_1+h_3}\{I_0^2(R/l)-I_0^2(r/l)\}+\frac{h_3}{h_1+h_3}\{I_1^2(R/l)-I_1^2(r/l)\}}{2\left\{R/l\left(\frac{h_1+h_3}{2h_1+h_3}\right)I_0(R/l)-\frac{h_3}{2h_1+h_3}I_1(R/l)\right\}^2(R/l)^2}\Bigg]. \quad (4.1)$$

Table I

Temperature as a function of R/l for $h_1/h_3 = 0.5$ (fixed) $r/R \rightarrow$

$R/l \downarrow$	0 (axis)	0.2	0.4	0.6	0.8	1 (Wall)
1	0.0193	0.0184	0.0155	0.0117	0.0065	0
2	0.0649	0.0612	0.0524	0.0356	0.0174	0
3	0.1056	0.0994	0.0819	0.0561	0.0267	0
4	0.1223	0.1244	0.1025	0.0699	0.0330	0
5	0.1488	0.1401	0.1156	0.0790	0.0377	0
∞	0.1875	0.1776	0.1491	0.1056	0.0531	0

Table II

Temperature as a function of h_1/h_3 for $R/l = 2$ (fixed) $r/R \rightarrow$

$h_1h_3 \downarrow$	0 (axis)	0.2	0.4	0.6	0.8	1 (Wall)
∞	0.0451	0.0427	0.0358	0.0251	0.0123	0
0.5	0.0649	0.0612	0.0424	0.0356	0.0114	0
0	0.0791	0.0747	0.0623	0.0345	0.0215	0
− 0.3	0.1066	0.1013	0.0841	0.0591	0.0294	0
− 0.4	0.1035	0.1233	0.1032	0.0728	0.0365	0

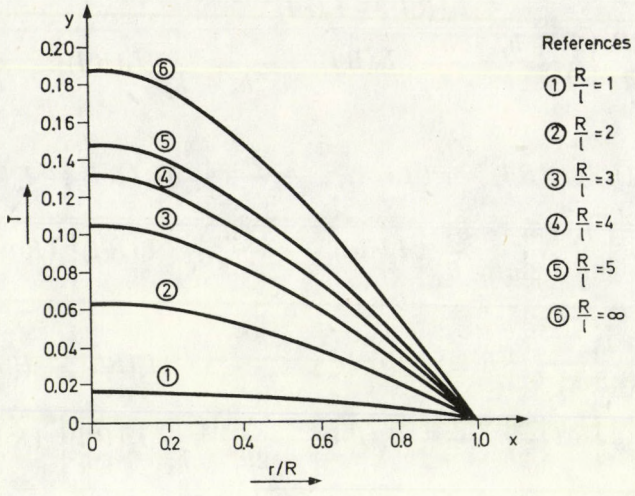

Fig. 1

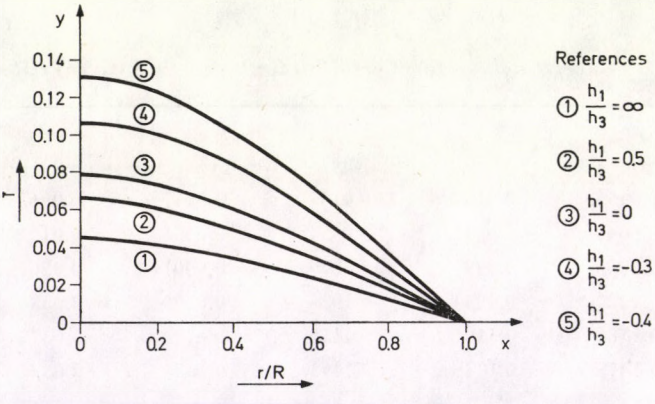

Fig. 2

Taking U_0 to be the mean velocity of flow and setting

$$\bar{R} = \frac{CR^2}{2\mu U_0}, \qquad \text{(modified Reynolds number)},$$

$$B_r = \frac{\mu U_0^2}{Kg(R)}, \qquad \text{(Brinkman number)},$$

$$\theta = \frac{g(r)-g(R)}{g(R)}, \text{ (dimensionless temperature)}.$$

From (3.1) we notice that θ is directly proportional to the Brinkman number and square of the modified Reynolds number. This also depends on R/l and h_1, h_3. Corresponding to the different values of R/l and h_1/h_3 the values of θ are given for $\bar{R} = 1$, $B_r = 1$ and $0 \leq r/R \leq 1$, in Table I and Table II, respectively.

5. Conclusion

In Fig. 1 temperature profiles are drawn for different values of R/l, keeping $\bar{R} = 1$, $B_r = 1$ and $h_1/h_3 = 0.5$, (fixed).The temperature profile is seen to vary sensitively to changes in R/l within the range $0 \leq R/l \leq 5$. As R/l tends to infinity, the classical solution is recovered.

In Fig. 2 the temperature profiles are drawn as a function of the ratio h_1/h_3 for R/l fixed, at the value 2. The temperature profile is seen to be insensitive to change in h_1/h_3.

REFERENCES

1. J. L. Bleustein and A. E. Green, Int. J. Engg. Sci., **5**, 323, 1967.
2. A. E. Green and R. S. Rivlin, Archs. Ration. Mech. Analysis, **15**, 325, 1964.
3. K. Shirkot, Proc. Camb. Phil. Soc., **66**, 197, July, 1969.

Acta Physica Academiae Scientiarum Hungaricae, Tomus 47 (4), pp. 303—312 (1979)

DEPENDENCE ON THE GEOMETRY AND ON THE BASIS SET OF LOCALIZED ORBITAL ENERGY AND MOMENT CONTRIBUTIONS

II. INTERACTION ENERGIES

By

E. KAPUY, C. KOZMUTZA and ZS. OZORÓCZY

QUANTUM THEORY GROUP, PHYSICAL INSTITUTE, TECHNICAL UNIVERSITY OF BUDAPEST, BUDAPEST

(Received 3. VII. 1979)

The Coulomb (J), the exchange (K) and the total (2J—K) interaction energy contributions between localized orbitals have been studied for molecules HF, H_2O, NH_3 and CH_4, respectively. Different basis sets (one of (*sp*/*s*) and another of (*spd*/*s*) type) were used for the calculations, which were carried out at the experimental and at the theoretical equilibrium geometries. Several regularities were found which could be related to the results obtained in earlier works for the localizability as well as for the spatial distributions of localized charge densities.

1. Introduction

Several localization criteria have been proposed recently for obtaining "separated" molecular orbitals [1—4]. The separation is implemented by the use of energetic or spatial criteria. In spite of the localization methods and procedures so different, no remarkable deviations were found between the localized charge densities determined for a large number of molecules [5]. There are certain questions, however, which have not yet been analyzed concerning the localizability of molecular orbital densities. In the present paper we discuss the Coulomb, the exchange and the total interaction energy contributions between localized orbitals. The molecules studied are the following: HF, H_2O, NH_3 and CH_4. Experimental and calculated equilibrium geometries were used: all details can be found in Part I of this series [6]. The HF—SCF calculations were carried out by the use of the basis sets 6-31G and 6-31G/d. A detailed description of the method, the geometries and total energies etc. are given in Part I.

2. Preliminary studies

Before analysing the results, we ought to mention some studies and conclusions for purposes similar to that of the present work.

The first paper dealing with the limits of the localized interpretation of molecular orbitals was published in 1976 [7]. The new measures proposed there for the localizability clearly show that the absolute and density overlaps of

even "well-localized" systems (e.g. CH_4,) remain still large after localization. In this paper we discuss whether these overlaps could be related to the interaction energy contributions, using different geometry data and basis sets with and without polarization functions.

Table I

Interaction energies between core and bond pair localized orbitals (in hartree)

		Coulomb	
		Basis 6-31G	Basis 6-31G/d
HF	exp	1.03833	1.04076
	calc	1.03695	1.04344
H_2O	exp	0.89440	0.89580
	calc	0.89938	0.90017
NH_3	exp	0.76563	0.76572
	calc	0.77726	0.76902
CH_4	exp	0.64391	0.64398
	calc	0.64743	0.64622
		Exchange	
		Basis 6-31G	Basis 6-31G/d
HF	exp	0.01929	0.01925
	calc	0.01926	0.01931
H_2O	exp	0.01471	0.01470
	calc	0.01481	0.01480
NH_3	exp	0.01120	0.01118
	calc	0.01140	0.01126
CH_4	exp	0.00824	0.00818
	calc	0.00832	0.00823
		Interaction	
		Basis 6-31G	Basis 6-31G/d
HF	exp	2.05737	2.06227
	calc	2.05464	2.06749
H_2O	exp	1.77409	1.77690
	calc	1.78395	1.78554
NH_3	exp	1.52006	1.52026
	calc	1.54312	1.52678
CH_4	exp	1.27958	1.27978
	calc	1.28654	1.28421

Secondly, the spatial distribution of localized orbitals has also been analyzed [8]. Several interesting results were found. Namely, the tail populations remain quite large after localization and the principal lobe contains a charge density whose extent depends on the type of localized orbitals (bond or lone pair). The present study investigates whether there are relationships between the interaction energy contributions and the spatial distributions obtained for the individual localized molecular orbitals.

A detailed study published on the basis set dependence of localized orbital densities for molecule H_2O has shown that there are systematic changes in the localized orbitals by enlarging the basis set [9]. The interaction energies obtained between localized orbitals have also been analyzed. In this paper we investigate how the conclusions found for H_2O can be extended for other systems as well.

3. Interaction energies between core and valence shell orbitals

The Coulomb, the exchange and the total interaction energies obtained for interactions between the cores and the bond pair localized orbitals are given in Table I. The same quantities resulting for the interactions between the cores and the lone pair orbitals are presented in Table II. It is remarkable that the core/bond pair interaction energies (all of Coulomb, exchange and the total ones) are larger at the calculated than at the experimental geometries for each molecule using the more relevant basis 6-31G/d. These results are in agreement with earlier studies [10], i.e. the increasing nuclear potential (as going from the experimental to the calculated equilibria) is followed by the increase of the total electron charge density. It is interesting, however, that while the core/lone pair exchange interaction energies are also slightly larger at the theoretical than at the experimental equilibrium geometries for each molecule studied (using basis 6-31G/d), it does not apply to the Coulomb and the total interaction energy contributions. These latter quantities are systematically smaller at the calculated than at the experimental equilibrium position of nuclei for HF, H_2O and NH_3. The results show that the increasing total electron charge density as going from the experimental to the calculated equilibrium geometries is not followed by the increase of each localized orbital energy contribution. The decrease of the core/lone pair interaction energies suggests that although the bond lengths are found to be shorter at the calculated than at the experimental equilibrium geometries of molecules by the use of basis sets near (or approaching) the Hartree—Fock limit, the lone pair localized charge densities (more precisely the centres of the charge distributions) are certainly displaced farther away from the cores at the calculated than at the experimental equilibrium positions of the nuclei. It should be noted,

Table II

Interaction energies between core and lone pair localized orbitals (in hartree)

		Coulomb	
		Basis 6-31G	Basis 6-31G/d
HF	exp	1.21914	1.21838
	calc	1.21915	1.21836
H_2O	exp	1.03902	1.03873
	calc	1.03813	1.03847
NH_3	exp	0.86969	0.87183
	calc	0.86352	0.87133
		Exchange	
		Basis 6-31G	Basis 6-31G/d
HF	exp	0.02585	0.02590
	calc	0.02584	0.02591
H_2O	exp	0.01984	0.01996
	calc	0.01995	0.02000
NH_3	exp	0.01507	0.01521
	calc	0.01605	0.01527
		Interaction	
		Basis 6-31G	Basis 6-31G/d
HF	exp	2.41243	2.41086
	calc	2.41246	2.41081
H_2O	exp	2.05820	2.05750
	calc	2.05631	2.05694
NH_3	exp	1.72431	1.72845
	calc	1.71099	1.72739

however, that these smaller or larger energy contributions obtained for the core/lone pair interactions may also be due to the different extent of lone pair charge densities at the theoretical and the experimental equilibrium geometries. It is expected that a further analysis including the first and second order electric moments of localized orbitals will also provide information about the behaviour of localized charge densities at different geometries (see Parts III and IV of this series to be published later).

Comparing the results obtained by basis sets 6-31G and 6-31G/d at the experimental geometries, several regularities can be found. As to the values of core/bond Coulomb interaction energies, they are always larger obtained

by basis sets with than without polarization functions. The deviation, however, is systematically decreasing as going from molecule HF (about 0.0024 a.u., 0.2%) to molecule CH_4 (only 0.00007 a.u., 0.01%). These results suggest that the inclusion of d-type polarization function is more important on that heavy atom which contains more and more lone pair orbitals. The results obtained for the exchange interaction energies between cores and bond orbitals, however, do not suggest a similar conclusion: the largest deviations between the values resulting by basis 6-31G and 6-31G/d are found for molecules HF and CH_4 and the smallest ones for H_2O and NH_3. All deviations, however, obtained for the exchange terms are less than 0.00006 a.u. (about 0.1—1.0%), and these discrepancies may be due to different effects. The exchange interactions, on the other hand, have been found to be rather sensitive also to the molecular environment by another study of localized molecular orbitals [11].

Investigating the same quantities at the calculated equilibrium geometries, larger differences have been found than at the experimental ones for the values obtained by the use of basis sets 6-31G and 6-31G/d. This is expected because the theoretically determined equilibrium bond lengths and both angles by an (*sp*/*s*) type basis set are rather far from the Hartree—Fock limiting values [12].

The interaction energies between core and lone pair localized orbitals do not differ much at the experimental equilibrium geometries whether they have been calculated by the 6-31G or the 6-31G/d basis sets (see Table II). It is interesting, however, that these deviations do not show the regularities similar to those found for the core/bond interactions. As to the Coulomb terms, their deviations obtained by the two basis sets used are less than 0.002 a.u. (about 0.25%). The differences obtained for the exchange parts of core/lone pair interaction are found to be about 0.00005—0.0014 a.u. (0.2—1.0%), and the values obtained by the use of 6-31G basis are always smaller than by using the 6-31G/d basis set.

It is remarkable that the core/lone pair interaction energies obtained at the calculated equilibrium geometries by basis sets of (*sp*/*s* and *spd*/*s*) types show smaller deviations than the core/bond interactions do for molecules HF and H_2O (see Table I and Table II, respectively). The opposite result was found, however, for the localized orbital interaction energies for NH_3. These results suggest that the statement "lone pairs have a more atomic nature" [3] depends strongly on the molecular system.

4. Interaction energies between valence shell localized orbitals

The Coulomb, the exchange and the total interaction energy contributions between two bond orbitals are presented in Table III. The same quantities between bond and lone pair orbitals are given in Table IV, while those

Table III

Interaction energies between bond pair localized orbitals (in hartree)

		Coulomb	
		Basis 6-31G	Basis 6-31G/d
H_2O	exp	0.56495	0.56867
	calc	0.56596	0.57158
NH_3	exp	0.48309	0.48320
	calc	0.48473	0.48533
CH_4	exp	0.40519	0.40282
	calc	0.40786	0.40453
		Exchange	
		Basis 6-31G	Basis 6-31G/d
H_2O	exp	0.03441	0.03412
	calc	0.03516	0.03432
NH_3	exp	0.02626	0.02486
	calc	0.02669	0.02496
CH_4	exp	0.01871	0.01670
	calc	0.01836	0.01679
		Interaction	
		Basis 6-31G	Basis 6-31G/d
H_2O	exp	1.09549	1.10322
	calc	1.09676	1.10884
NH_3	exp	0.93992	0.94154
	calc	0.94277	0.94570
CH_4	exp	0.79167	0.78894
	calc	0.79686	0.79227

obtained between two lone pair orbitals are summarized in Table V. The values are given both at the experimental and the calculated equilibrium molecular geometries, determined by basis sets 6-31G and 6-31G/d. The regularities found can be summarized as follows.

Investigating the Coulomb interaction energies, it can be seen that those found for all of the valence shell orbital interactions are larger at the calculated than at the experimental geometries of each molecule studied (using basis 6-31G/d). A similar conclusion holds for the exchange as well as for the total interaction energy contributions. These results confirm that the increasing nuclear potential as going from the experimental to the theoretical

equilibrium geometries is followed by a remarkable and well-defined increase of electron charge density in the valence shell. The Coulomb parts of the bond/bond and bond/lone pair interaction energies are less sensitive to the enlargement of the basis set than are the exchange terms of the interaction energy contribution. The Coulomb and the exchange parts determined for the bond/lone pair interactions have a similar sensitivity to the increase of basis set size. It is interesting that, while the total interaction energy contributions obtained for the bond/lone pair interactions are always increased by the inclusion of the *d*-type functions into the basis, those between two lone pair orbitals decrease both for HF and H_2O. The same quantities, on the other hand, obtained for

Table IV

Interaction energies between bond and lone pair localized orbitals (in hartree)

		Coulomb	
		Basis 6-31G	Basis 6-31G/d
HF	exp	0.71782	0.72130
	calc	0.71720	0.72259
H_2O	exp	0.61237	0.61463
	calc	0.61455	0.16667
NH_3	exp	0.51669	0.51714
	calc	0.53023	0.51900
		Exchange	
		Basis 6-31G	Basis 6-31G/d
HF	exp	0.05617	0.05624
	calc	0.05616	0.05632
H_2O	exp	0.04534	0.04519
	calc	0.04546	0.04536
NH_3	exp	0.03539	0.03485
	calc	0.03995	0.03512
		Interaction	
		Basis 6-31G	Basis 6-31G/d
HF	exp	1.37947	1.38636
	calc	1.37824	1.38886
H_2O	exp	1.17940	1.18407
	calc	1.18364	1.18798
NH_3	exp	0.99799	0.99943
	calc	1.02051	0.00288

Table V

Interaction energies between lone pair localized orbitals (in hartree)

		Coulomb	
		Basis 6-31G	Basis 6-31G/d
HF	exp	0.79143	0.79098
	calc	0.79136	0.79109
H_2O	exp	0.66808	0.66633
	calc	0.76051	0.66701
		Exchange	
		Basis 6-31G	Basis 6-31G/d
HF	exp	0.07011	0.07059
	calc	0.07008	0.07064
H_2O	exp	0.05681	0.05791
	calc	0.05826	0.05830
		Interaction	
		Basis 6-31G	Basis 6-31G/d
HF	exp	1.51275	1.51137
	calc	1.51264	1.51154
H_2O	exp	1.27935	1.27475
	calc	1.28276	1.27572

the bond/bond interactions do depend on the molecular system: they are larger for H_2O by the use of basis 6-31G/d than by that of basis 6-31G by about 0.008 a.u., for NH_3 by only about 0.002 a.u., but a smaller value was found for CH_4 by basis 6-31G/d than by basis 6-31G, by about 0.03 a.u. (see Table III). These results suggest that the bond/bond interaction energies are the most sensitive to the molecular system.

The interaction energy contributions obtained for the bond/bond and lone pair/lone pair interactions do not differ much whether the basis 6-31G or 6-31G/d was used: the discrepancies found are similar at the experimental and the calculated equilibrium geometries (see Table III. and Table IV, respectively). This does not apply to the bond/lone pair interaction energies: the deviations between the results obtained by the use of basis sets with and without *d*-type polarization functions are larger at the theoretically determined total energy minima than at the experimental equilibrium geometries. These results thus also suggest that the bond and lone pair charge densities change in the opposite direction by enlarging the basis set.

5. Conclusion

The behaviour of localized charge distributions at the experimentally and theoretically determined molecular equilibrium geometries was investigated. Several regularities were found due also to the different basis sets used. The results obtained can be related to those of some earlier works. The question is, however, whether the conclusions resulting from this study are in a total agreement with the earlier ones or we should modify the picture obtained so far on the localized charge densities of molecules.

As to the results obtained in the study of the localizability, the regularities found there (in [7]) are in agreement with those of this work: the absolute and the density overlaps and the interaction energies between the localized orbitals do characterize suitably the individual type of interactions. It should be noted, however, that these overlaps are expected to have a slightly different extent at the calculated than at the experimental geometries. Thus the absolute as well as the density overlaps, e.g., are certainly smaller between cores and lone pairs but larger between cores and bond orbitals at the calculated than at the experimental equilibrium geometries.

As to the correlation with the spatial distributions of localized orbitals [9], it seems that the tail populations can be related to the exchange interaction terms while the Coulomb interaction energies certainly depend rather on the principal lobes (see, e.g., the similar sensitivities for the molecular system or those of the individual type of interactions). A study on the spatial distribution of localized orbital densities including also polarization functions would be of interest.

The conclusions obtained on the basis set dependence of H_2O localized orbitals [9] are in general valid even for other systems, as it has been found in this work. Two regularities are worth mentioning. The core/bond and core/lone pair interactions do change always into the opposite direction: whether the basis set is enlarged or the geometry is changed for any system investigated. It is also remarkable that in the valence shell the bond/lone pair interaction energies were found to be the less sensitive to the molecular system, to the basis set as well as to the geometry variations.

REFERENCES

1. C. Edmiston and K. Ruedenberg, Rev. Mod. Phys., **35**, 457, 1963.
2. S. F. Boys, Quantum Theory of Atoms, Molecules and the Solid State, P. O. Löwdin, Ed. Academic Press New York, 1966.
3. W. England, L. S. Salmon and K. Ruedenberg, Topics in Current Chemistry, **23**, 31, 1971.
4. H. Weinstein, R. Pauncz and M. Cohen, Advan. At. Mol. Phys., **7**, 97, 1971.
5. W. von Niessen, J. Chem. Phys., **56**, 4290, 1972.
6. E. Kapuy, C. Kozmutza, Zs. Ozóróczy and J. Pipek, Acta Phys. Hung., **46**, 333, 1979.
7. R. Daudel, M. E. Stephens, E. Kapuy and C. Kozmutza: Chem. Phys. Letters, **40**, 194, 1976.

8. M. E. STEPHENS, E. KAPUY and C. KOZMUTZA, Theoret. Chim. Acta (Berl.) **45,** 111, 1977.
9. E. KAPUY, C. KOZMUTZA, R. DAUDEL and M. E. STEPHENS, Theoret. Chim. Acta (Berl.) **50,** 31, 1978.
10. E. KAPUY, C. KOZMUTZA and R. DAUDEL, Chem Phys. Letters (submitted for publication).
11. E. KAPUY, C. KOZMUTZA, R. DAUDEL and M. E. SPEPHENS, Theoret. Chim. Acta (Berl.) (in press).
12. S. BELL, J. Chem. Phys., **68,** 3014, 1978.
13. R. DAUDEL, M. E. STEPHENS, I. G. CSIZMADIA, C. KOZMUTZA, E. KAPUY and J. D. GODDARD, Int. J. Quant. Chem. **11,** 665, 1977.

Acta Physica Academiae Scientiarum Hungaricae, Tomus 47 (4), pp. 313–317 (1979)

FREE CONVECTION FLOW PAST A VERTICAL INFINITE POROUS PLATE IN A ROTATING FLUID

By

V. M. SOUNDALGEKAR

DEPARTMENT OF MATHEMATICS, I.I.T., POWAI, BOMBAY-76, INDIA

and

I. POP

FACULTY OF MATHEMATICS, UNIVERSITY OF CLUJ, CLUJ CP 253, ROMANIA

(Received 3. VII. 1979)

An exact analysis of free convection flow past a vertical infinite porous plate in a rotating fluid is presented. The plate and the fluid are assumed to rotate in a solid body rotation in a steady state. Exact solutions for the velocity and temperature fields have been derived. The effects of E, the Ekman number, on the flow characteristics are discussed.

1. Introduction

Rotating fluids received the attention of many research workers because of their applications in cosmical and geophysical sciences. It is well-known that in a rotating fluid near a flat plate Ekman layer exists wherein the viscous and Coriolis forces are of the same order of magnitude. BATCHELOR [1] studied the Ekman layer flow on a horizontal plate. The effect of suction on such a flow was studied by GUPTA [2], SOUNDALGEKAR and POP [3], etc. On the other hand GREENSPAN and HOWARD [4], SOUNDALGEKAR and POP [5], POP and SOUNDALGEKAR [6], GUPTA and POP [7] and others have analysed an unsteady rotating flow past an impermeable or permeable plate under the assumption of a rigid body rotation. The spin-up phenomenon was discussed by GREENSPAN and HOWARD [4]. If now, a vertical porous infinite plate is made to rotate with the fluid in a state of rigid rotation, how do the free convection effects affect the flow? As we are aware this problem has not been studied in the literature. Such a phenomenon has many applications in the technological field. Hence it is now proposed to study the free convection effects on the flow past an infinite vertical porous plate rotating in a fluid in rigid body rotation. In Section 2 the mathematical analysis is presented followed by a discussion in Section 3.

2. Mathematical analysis

Consider a Cartesian co-ordinate system rotating uniformly with a fluid in a rigid state of rotation with angular velocity Ω about z-axis taken positive in the direction normal to the plate. The vertical plate is assumed to coin-

cide with the plane $z = 0$. Then the flow is governed by the following equations:

$$\frac{D\mathbf{V}}{Dt} + 2\Omega\mathbf{k}\times\mathbf{V} + \nabla\left[p/\varrho - \frac{1}{2}\Omega^2(x^2+y^2)\right] = \nu\nabla^2 + g\beta(T - T_\infty)\,\mathbf{i}, \quad (1)$$

$$\nabla\cdot\mathbf{V} = 0\,, \quad (2)$$

$$\frac{DT}{Dt} = \frac{\varkappa}{\varrho C_p}\nabla^2 T + \frac{\mu}{\varrho C_p}\Phi\,. \quad (3)$$

Here $\mathbf{V}$ is the velocity vector with components (u, v, w) in the (x, y, z) directions, respectively, $\mathbf{i}$ and $\mathbf{k}$ are the unit vectors along x and z axes, p is the pressure, μ is the dynamic viscosity, ν is the kinematic viscosity, g is the acceleration due to gravity, β is the coefficient of volume expansion, T is the temperature of the fluid, T_∞ is the ambient temperature,

$$\nabla = \frac{\partial}{\partial x}\mathbf{i} + \frac{\partial}{\partial y}\mathbf{j} + \frac{\partial}{\partial z}\mathbf{k}\,,$$

ϱ is the density, C_p is the specific heat at constant pressure, D/Dt is the convective derivative, $\varkappa$ is the thermal conductivity of the fluid and Φ is the viscous dissipation term defined in SCHLICHTING [8]. Let O be a fixed point in the plane $z = 0$ and Ox, Oy be measured along the plate in two perpendicular directions to z-axis. As the plate is infinite in extent and the flow is steady, the physical variables are functions of z only. Hence

$$\frac{\partial}{\partial x}, \frac{\partial}{\partial y}, \frac{\partial}{\partial t} = 0\,.$$

Then from Eq. (2) it follows:

$$\frac{\partial w}{\partial z} = 0\,, \quad (4)$$

and for constant suction it yields

$$w = -w_0\,, \quad (5)$$

where w_0 is the constant suction velocity and the negative sign indicates that the suction is towards the plate. If the flow of the fluid is slow, viscous dissipation effects can be neglected. Hence in view of these assumptions and Eq. (5), Eqs. (1) and (3) reduce to the following set of equations:

$$-w_0\frac{\partial u}{\partial z} - 2\Omega v = \nu\frac{\partial^2 u}{\partial z^2} + g\beta(T - T_\infty)\,, \quad (6)$$

$$-w_0\frac{\partial v}{\partial z} + 2\Omega u = \nu\frac{\partial^2 v}{\partial z^2}\,, \quad (7)$$

$$-w_0 \frac{\partial T}{\partial z} = \frac{\varkappa}{\varrho C_p} \frac{\partial^2 T}{\partial z^2} . \tag{8}$$

The boundary conditions of the problem are

$$u = 0, \quad v = 0, \quad T = T_w \text{ at } z = 0 ,$$
$$u \to 0, \quad v \to 0, \quad T \to T_\infty \text{ as } z \to \infty , \tag{9}$$

where T_w is the temperature of the plate.

Introducing the dimensionless quantities

$$Z = w_0 z/\nu, \quad U = \frac{u}{w_0} + i\frac{v}{w_0}, \quad \Theta = (T - T_\infty)/(T_w - T_\infty) ,$$
$$P = \varrho C_p/\varkappa , \quad G = \nu g\beta(T_w - T_\infty)/w_0^3 , \quad E = \Omega\nu/w_0^2 , \tag{10}$$

where $i = \sqrt{-1}$, P is the Prandtl number, G is the Grashoff number and E is the Ekman number, the Eqs. (6), (7) and (8) become

$$\frac{d^2 U}{dZ^2} + \frac{dU}{dZ} - 2iEU = -G\Theta , \tag{11}$$

$$\frac{d^2 \Theta}{dZ^2} + P\frac{d\Theta}{dZ} = 0 , \tag{12}$$

subject to the boundary conditions:

$$U = 0, \quad \Theta = 1 \text{ at } Z = 0 ,$$
$$U \to 0, \quad \Theta \to 0 \text{ as } Z \to \infty . \tag{13}$$

The solutions of Eqs. (11) and (12) under the boundary conditions (13)' are the following:

$$U = \frac{u}{w_0} + i\frac{v}{w_0} = \frac{G}{P(P-1) - 2iE}(e^{-\lambda Z} - e^{-PZ}) , \tag{14}$$

$$\Theta = e^{-PZ}, \tag{15}$$

where

$$\lambda = \frac{1}{2}[1 + (1 + 8iE)^{1/2}] .$$

On separating the real and imaginary part in (14) we get

$$\frac{u}{w_0} = \frac{G}{P^2(P-1)^2 + 4E^2}[P(P-1)e^{-\lambda_r Z}\cos(\lambda_i Z) +$$
$$+ 2Ee^{-\lambda_r Z}\sin(\lambda_i Z) - P(P-1)e^{-PZ}] , \tag{16}$$

$$\frac{v}{w_0} = \frac{G}{P^2(P-1)^2 + 4E^2}\left[2Ee^{-\lambda_r Z}\cos(\lambda_i Z) - \right.$$
$$\left. - P(P-1)e^{-\lambda_r Z}\sin(\lambda_i Z) - 2E\,e^{-PZ}\right], \tag{17}$$

where

$$\lambda_r = \frac{1}{2} + \frac{1}{2}\left[\frac{1}{2}(1 + (1 + 64E^2)^{1/2}\right]^{1/2},$$

$$\lambda_i = \frac{1}{2}\left[\frac{1}{2}\left((1 + 64\,E^2)^{1/2} - 1\right)\right]^{1/2}.$$

3. Results

Fig. 1. shows the velocity components u/Gw_0 and v/Gw_0 for different values of E, the Ekman number, in case of air ($P = 0.71$) and water ($P = 7$). We observe from this Figure that the axial velocity u/Gw_0 for air is negative at small values of E, whereas at large values of E it is positive for both air and water. Contrary the transverse velocity v/Gw_0 is always positive.

Knowing the velocity field we can now calculate the skin friction at the plate which is given by

$$\tau^+ = \mu\left(\frac{\partial u}{\partial z} + i\frac{\partial v}{\partial z}\right)_{z=0}, \tag{18}$$

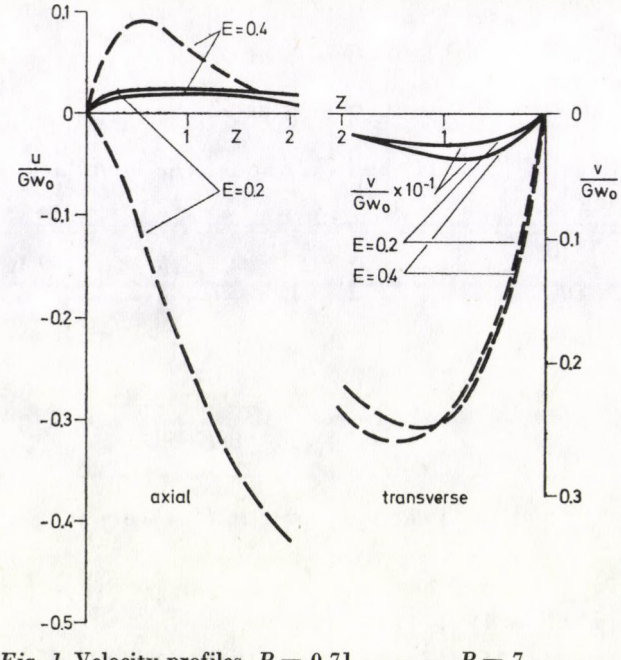

Fig. 1. Velocity profiles, $P = 0.71$ — — —, $P = 7$ ———

Table I

Values of τ_{xz}/G and τ_{yz}/G

	τ_{xz}/G			$-\tau_{yz}/G$		
P \ E	0	0.2	0.4	0	0.2	0.4
0.71	1.5082	1.0555	0.7949	0	0.4334	0.4549
7	0.1428	0.1405	0.3140	0	0.0065	0.0103

and in dimensionless form we have

$$\tau_{xz} = \tau_{yz} = \frac{\tau^+}{\varrho w_0^2} = \left.\frac{\partial U}{\partial Z}\right|_{Z=0} . \tag{19}$$

From (19) we obtain the components of the skin friction at the plate in the x and y directions of the form:

$$\tau_{xz} = G\frac{P(P-1)(P-\lambda_r) + 2E\lambda_i}{P^2(P-1)^2 + 4E^2} ,$$
$$\tau_{yz} = G\frac{2E(P-\lambda_r) - P(P-1)\lambda_i}{P^2(P-1)^2 + 4E^2} . \tag{20}$$

The numerical values of τ_{xz}/G and τ_{yz}/G are entered in Table I. From this Table we conclude that τ_{xz}/G decreases due to increase of E, the Ekman number for both air and water. But τ_{yz}/G increases with increasing E for both air and water.

The rate of heat transfer is given by

$$q^+ = -\varkappa \left.\frac{\partial T}{\partial z}\right|_{z=0} , \tag{21}$$

and in view of the relations (10) it reduces to

$$q = \frac{\nu q^+}{\varkappa (T_w - T_\infty) w_0} = -\left.\frac{\partial \Theta}{\partial Z}\right|_{Z=0} . \tag{22}$$

From (15) and (22) it follows:

$$q = P , \tag{23}$$

and hence the rate of heat transfer is equal to the Prandtl number of the fluid.

REFERENCES

1. G. K. Batchelor, An Introduction to Fluid Dynamics, Cambridge Univ. Press, 1970.
2. A. S. Gupta, Phys. Fluids, **15**, 930, 1972.
3. V. M. Soundalgekar and I. Pop, Z. angew. Math. Mech., **53**, 718, 1973.
4. H. P. Greenspan and L. N. Howard, J. Fluid Mech., **17**, 385, 1963.
5. V. M. Soundalgekar and I. Pop, Bull. Math. Soc. Sci. Math. R. S. Roumanie. **14 (62)** 375, 1970.
6. I. Pop and V. M. Soundalgekar, J. Inst. Maths Applics, **15**, 85, 1975.
7. A. S. Gupta and I. Pop, Bull. Math. Soc. Sci. Math. R. S. Roumanie, **19 (67)**, 291, 1975.
8. H. Schlichting, Boundary Layer Theory, 4th edn., McGraw-Hill, 1960.

Acta Physica Academiae Scientiarum Hungaricae, Tomus 47 (4), pp. 319—323 (1979)

SOME OPTICAL PROPERTIES OF BISMUTH FILMS

By

S. MAHMOUD*, A. H. ABOU EL ELA, A. H. EID* and M. A. MAHMOUD

PHYSICS DEPARTMENT, ISLAMIC GIRLS COLLEGE, NASR CITY and
PHYSICS DEPARTMENT,* NATIONAL RESEARCH CENTRE, CAIRO, EGYPT

(Received in revised form 5. VII. 1979)

The optical properties of thin bismuth films have been investigated in the near IR region. The results are compared with those obtained elsewhere on various bismuth samples and the value of the lattice dielectric constant was found to be 90 ± 5.

1. Introduction

Measurements of the optical properties of bismuth films in the infrared range of spectrum allow to obtain information concerning the electronic energy band structure as well as the carrier independent part of the dielectric constant and the relaxation mechanisms of charge carriers. The data available [1—4] on the optical properties of bismuth films are insufficient and could not be satisfactorily interpreted, since they contain contradictions. It is well established that the electrical and optical properties of bismuth films are sensitive and change substantially in the presence of very small metallic impurities (0.1—1%). This indicates that, in some respects, bismuth films are analogous to semiconductors, even though their electrical conductivity is higher than that of the majority of semiconducting materials.

In the present contribution measurements of the optical properties of evaporated bismuth films were carried out in the infrared range (2.5—40 μm) and the values of the optical and electrical constants are calculated.

2. Experimental

Bismuth films of different thicknesses (20—300 nm) were prepared by vacuum evaporation of highly pure bismuth (99.999%) in a vacuum of $\sim 10^{-4}$ Pa at an evaporation of about 2 nm/s, onto KBr discs as substrate. Film thickness was measured by TOLANSKY interference method [6]. Transmission measurements were carried out using a double beam infrared spectrophotometer type Beckmann 4220, which gives values of transmission accurate to about $\pm 1\%$.

3. Results and discussion

a) *Optical properties*

The results of mesurements of the transmission of bismuth films of different thicknesses are shown in Fig. 1. All samples show a transmittance maximum which shifts towards longer wavelengths on increasing film thickness. For thick films ($d > 150$ nm) the maximum occurs near 30 μm.

The problem of a plane monochromatic wave, of wavelength λ passing at normal incidence from vacuum into a homogeneous plane parallel specimen of index $n - ik$ and thickness d, on a substrate of index n_1, was treated by classical electromagnetic theory. According to TUBBS [7] and BRATTAIN [8], for thick absorbing film ($4\pi kd > \lambda$), the equations for the reflected and transmitted intensities are

$$R = \frac{(n-1)^2 + k^2}{(n+1)^2 + k^2}, \tag{1}$$

$$T = \frac{16n,(n^2 + k^2)}{[(n+1)^2 + lk^2][(n_1 + n)^2 + k^2]} \exp\left(-\frac{4\pi k\, d}{\lambda}\right). \tag{2}$$

Eq. (2) allows to calculate the value of the extinction coefficient k and the refractive index can be estimated from the preexponential factor by using the experimental values of T, d, n_1 and k.

Fig. 2 shows the dependence of the calculated values of k and n for thick bismuth films ($d > 150$ nm) on the wavelength, compared with the data of MARKOV and LINDSTREM [2] for an evaporated bismuth layer about 1 μm thick (deposited onto rock salt substrate), the data of MARKOV and KHAIKIN [3] for electrolytically polished bismuth and HODGSON's data [1] on mechanically polished bismuth. It is readily seen that the results differ considerably from each other, however, our result for 260 nm film is close to that for electropolished bismuth. These differences can be explained by the differences in surface structure. Mechanical polishing of bismuth produces a cold-worked surface layer of varying structure, while electropolishing does not leave a surface layer of different structure. Evaporated bismuth layers have a structure different from that of bulk bismuth. Moreover, the observed increase in the refractive index for thinner film (160 nm) with decreasing wavelength is in agreement with the observations of ALEKSEEVSKI and POTAPOV [9] and SCHULZ's data [10], who found that n has a maximum value at $\lambda = 2$ μm where it reaches 20.

The absorbance (energy absorbed) A can be calculated using the well known expression [11]

$$A = \frac{4n}{(n+1)^2 + k}. \tag{3}$$

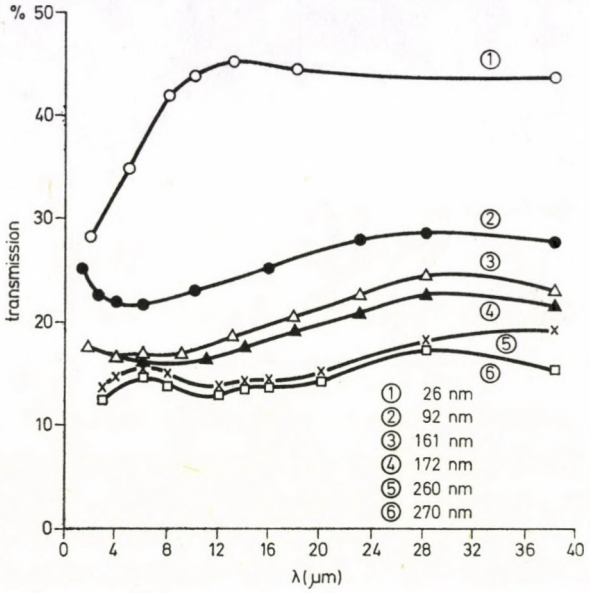

Fig. 1. The dependence of the transmittance of evaporated bismuth films on the wavelength

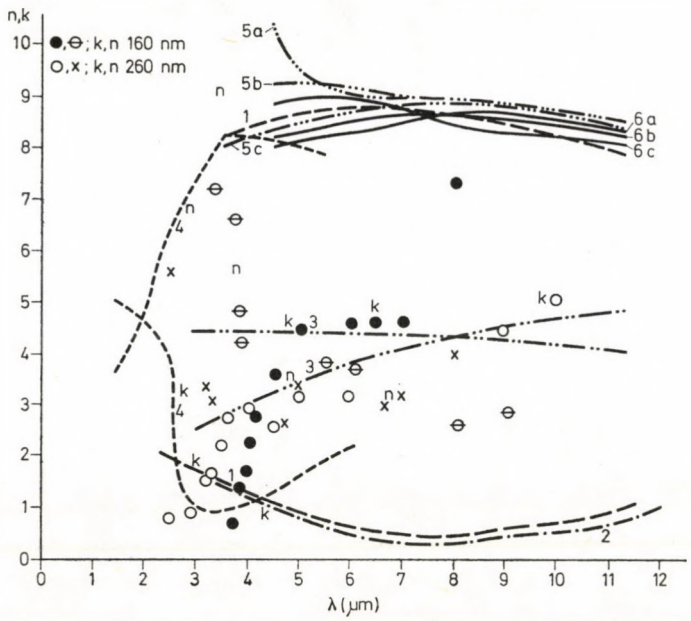

Fig. 2. The dependence of the extinction coefficient and the refractive index on the wavelength: 1. MARKOV and LINDSTREM [3], n and K for 890 nm film; 2. MARKOV and LINDSTREM [2], for 560 nm film; 3. MARKOV and KHAIKIN [3], for electrolytically polished Bi; 4. HODGSON [1], for mechanically polished Bi; 5. MARKOV and LINDSTREM [2], n for (a) 220 nm, (b) 560 nm, (c) 690 nm; 6. MARKOV and LINDSTREM [2] n for different temperatures: (a) −90 °C, (b) 20 °C, (c) 200 °C. Present measurements; ●, ⊖: k and n for 160 nm film; ○, ×: k and n for 260 nm film

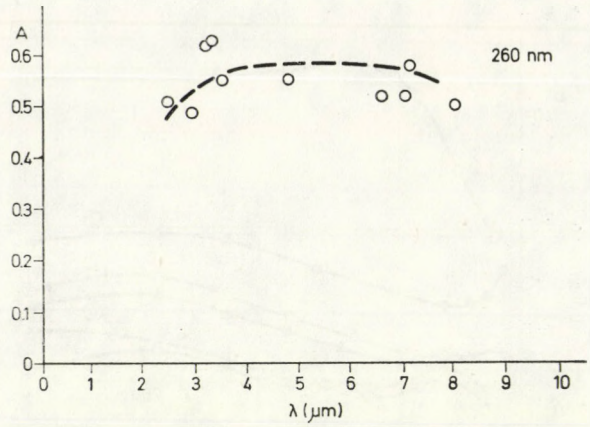

Fig. 3. **The variation of the absorbance (energy absorbed) with the wavelength**

The curve $A(\lambda)$ in Fig. 3 shows an evident drop at low wavelengths $\lambda < 2$ μm, which corresponds to the short wavelength edge of the absorption band. For longer wavelengths A remains nearly constant which shows that the band gap E_g lies in the long wavelength range, in contradiction with HODGSON's measurements [1], who suggests that $E_g \approx 0.3$ eV (corresponding to $\lambda \sim 3.5$ μm), which is doubtful. NANNEY [12] had shown that for bismuth crystal the band gap corresponds to a wavelength ~ 65 μm.

b) *The lattice dielectric constant*

On the assumption that conduction within bismuth is by different groups of electrons and holes, the contribution of free carriers to the optical constants is given by Drude theory

$$\varepsilon = n^2 - k^2 = \varepsilon_l - \sum_r \frac{Ne}{m^* \varepsilon_0} \left(\frac{\tau^2}{1 + \omega^2 \tau^2} \right), \tag{4}$$

when $\langle \omega\tau \rangle^2 \gg 1$, then

$$\varepsilon = \varepsilon_l - \frac{e^2}{4\pi^2 c^2 \varepsilon_0} \sum_r \frac{N}{m^*} \lambda^2, \tag{5}$$

where ε_l is the lattice dielectric constant or the carrier independent part of the dielectric constant, τ is the relaxation time, e is the charge of the electron, ε_0 is the permittivity of free space, N is the concentration of the charge carriers in the metal, m^* is the effective mass, λ is the wavelength and c is the velocity of radiation. Thus for that part of infrared where $\langle \omega\tau \rangle^2 \gg 1$, graphs of ε versus λ^2 should be represented by a straight line if (N/m^*) does not change

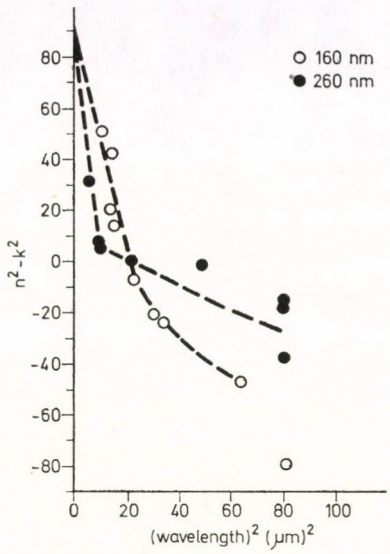

Fig. 4. The dependence of the real part of dielectric constant $\varepsilon = n^2 - k^2$ on the wavelength (λ^2)

with thickness. Fig. 4 shows the variation of $\varepsilon = n^2 - k^2$ with λ^2 for $d = 160$ and 260 nm. The change of ε with λ^2 is seen to approach linearity as $\lambda^2 = 0$. The intercept on the ordinate axis gives $\varepsilon_l = 90 \pm 5$, which is in agreement with the value calculated by BOYLE and BRAILSFORD [13] ($\varepsilon_l = 100$).

REFERENCES

1. J. N. HODGSON, Proc. Phys. Soc., B**67**, 269, 1954.
2. M. N. MARKOV and I. S. LINDSTREM, Optics and Spect., **7**, 228, 1959.
3. M. N. MARKOV and A. S. KHAIKIN, Optics and Spect., **9**, 253, 1960.
4. L. HARRIS and J. PIPER, J. Opt. Soc. Am., **33**, 11, 1963.
5. A. P. LENHAM, D. M. TREHERNE and R. J. METCALFE, J. Opt. Soc. Am. **65**, 9, 1965.
6. S. TOLANSKY, Introduction to Interferometry, Longmans Group, 1955.
7. M. R. TUBBS, Proc. Roy. Soc. London, A**228**, 566, 1964.
8. W. H. BRATTAIN and H. B. BRIGGS, Phys. Rev., **75**, 1705, 1949.
9. N. E. ALEKSEEVSKI and E. V. POTAPOV, Sov. Phys. JETP, **33**, 283, 1957.
10. L. G. SCHULZ, J. Opt. Soc. Am., **43**, 406, 1953.
11. L. N. SHKLIAREVSKI, A. A. AVDEENKO and V. G. PADALKA, Optics and Spect., **6**, 336, 1959.
12. C. NANNEY, Phys. Rev., **129**, 109, 1963.
13. W. S. BOYLE and A. D. BRAILSFORD, Phys. Rev., **120**, 1943, 1960.

Acta Physica Academiae Scientiarum Hungaricae, Tomus 47 (4), pp. 325—334 (1979)

CORRECTION TO LATTICE THERMAL CONDUCTIVITY DUE TO THREE PHONON NORMAL PROCESSES IN THE PRESENCE OF DISLOCATIONS IN THE FRAME OF THE GENERALIZED CALLAWAY INTEGRAL*

By

A. F. SALEH, R. H. MISHO and K. S. DUBEY

DEPARTMENT OF PHYSICS, COLLEGE OF SCIENCE, UNIVERSITY OF BASRAH, BASRAH, IRAQ

(Received in revised form 12. VII. 1979)

The contribution of the correction term due to the three phonon normal processes to the total lattice thermal conductivity of an insulator having dislocations, has been studied in the frame of the Generalized Callaway integral by obtaining for it an analytical expression, for the first time. To test the applicability of the expression obtained, the contribution of the correction term to the total lattice thermal conductivity has been calculated for the sample of NaF having dislocations in the entire temperature range 1—5 °K.

I. Introduction

Phonon-phonon scattering processes play a very important role in the study of the lattice thermal conductivity of an insulator at low as well as at high temperatures. Phonon-phonon scattering processes can be divided into two processes: normal processes (N-processes) in which momentum is conserved and umklapp processes (U-processes) in which momentum does not conserve. CALLAWAY [1] was the first to distinguish the role of the three phonon normal processes from the three phonon umklapp processes in the study of the lattice thermal conductivity of an insulator. Considering the special role of the three phonon N-processes and assigning a displaced Planck distribution function [1] for it, CALLAWAY [1] obtained an expression for the lattice thermal conductivity of an insulator which can be expressed as a sum of two parts. The first part is due to the combined scattering relaxation rate while the second part is very complicated and is known as the correction term [1] (ΔK) due to the three phonon normal processes, which reduces to zero in the absence of the three phonon N-processes. It is found that the contribution of the correction term (ΔK) is usually small enough compared to the total lattice thermal conductivity.

The contribution of the correction term (ΔK) due to the three phonon N-processes to the total lattice thermal conductivity has been calculated by several authors [2—11] to study the role of the three phonon N-processes at low as well as at high temperatures. But their studies are confined to a sample

* Part of M. Sc research thesis which will be submitted by the first author Miss SALEH.

having perfect structure only, i.e. the previous workers studied ΔK for a sample having boundary scattering, point defect scattering and phonon-phonon scattering processes only. Recently, the authors [12] have studied the contribution of ΔK for a sample having dislocations. They calculated the contribution of the correction term (ΔK) to the total phonon conductivity of NaF in the temperature range 1—10 °K and it was found that to calculate the value of ΔK one has to go through the numerical integration of several complicated integrals at each temperature. Therefore, a simple analytical expression is necessary.

The aim of the present work is to study ΔK for a sample having dislocations by obtaining for it an analytical expression in the frame of the generalized [13] CALLAWAY integral. To test the applicability of the expression obtained, the contribution of the correction term has also been calculated for NaF in the temperature range 1—5 °K in the frame of the expression reported in the present work.

II. Theory

According to DUBEY [13], the contribution of the correction term (ΔK) in the frame of the generalized CALLAWAY integral can be expressed as

$$\Delta K = C\,[2(T_1 + T_2) + (L_1 + L_2)]^2\,[2(T_1' + T_2') + (L_1' + L_2')]^{-1}, \tag{1}$$

where

$$S_1 = \left(\frac{1}{V_{S_1}^3}\right)\int_0^{\Theta_i/T} \tilde{C}_{N,S}^{-1}\,(\tilde{C}_{R,S}^{-1} + \tilde{C}_{N,S}^{-1})^{-1}\,(1 + R_i\,x^2)^3\,x^4 e^x (e^x - 1)^{-2}\,dx, \tag{2}$$

$$S_1' = \left(\frac{1}{V_{S_1}^5}\right)\int_0^{\Theta_i/T} \tilde{C}_{N,S}^{-1}\,\tilde{C}_{R,S}^{-1}\,(\tilde{C}_{N,S}^{-1} + \tilde{C}_{R,S}^{-1})^{-1}\,(1 + R_i\,x^2)^4 \times$$
$$\times\,(1 + 3\,R_i\,x^2)\,x^4\,e^x\,(e^x - 1)^{-2}\,dx\,, \tag{3}$$

$$T_2 = \left(\frac{1}{V_{T_2}^3}\right)\int_{\Theta_1/T}^{\Theta_2/T} \tilde{C}_{N,T}^{-1}\,(\tilde{C}_{N,T}^{-1} + \tilde{C}_{R,T}^{-1})^{-1}\,(1 + R_2\,x^2)^3\,x^4\,e^x\,(e^x - 1)^{-2}\,dx\,, \tag{4}$$

$$C = \frac{K_B}{6\pi^2}\left(\frac{K_B\,T}{\hbar}\right)^3. \tag{5}$$

S represents T and L, $i = 1$ and 3 for $S = T$ and L, respectively, K_B is the Boltzmann constant, $\hbar$ is the Planck constant divided by 2π, V's are the velocities of phonons, θ's are the characteristic temperatures, R's are the constants depending on the dispersion curve of the sample, suffixes T and L are used to differentiate transverse and longitudinal phonons, respectively, $\tilde{C}_N^{-1}$ is the scattering relaxation rate [14] due to the three phonon normal processes and $\tilde{C}_R^{-1}$ is the same due to all momentum non-conserving processes. A similar expression can also be written for L_2, T_2' and L_2'. (For more details, see [8].)

Since our study is limited to low temperatures only, the expression used for $\tilde{C}_N^{-1}$ and $\tilde{C}_R^{-1}$ can be expressed as

$$\tilde{C}_{N,T}^{-1} = B_1 w T^4 ,$$

$$\tilde{C}_{N,L}^{-1} = B_3 w^2 T^3 ,$$

$$\tilde{C}_R^{-1} = \tilde{C}_B^{-1} + \tilde{C}_{pt}^{-1} + \tilde{C}_u^{-1} + \tilde{C}_{\text{dis}}^{-1} ,$$

$$C_B^{-1} = \frac{V}{L'} ,$$

$$\tilde{C}_{pt}^{-1} = A w^4 ,$$

$$\tilde{C}_{\text{dis}}^{-1} = a w ,$$

$$\tilde{C}_{u,T}^{-1} = B_2 w T^4 e^{-\Theta/\alpha T} ,$$

$$\tilde{C}_{u,L}^{-1} = B_4 w^2 T^3 e^{-\Theta/\alpha T} ,$$

where $\tilde{C}_B^{-1}$, $\tilde{C}_{pt}^{-1}$, $\tilde{C}_{\text{dis}}^{-1}$ and $\tilde{C}_u^{-1}$ are the scattering relaxation rates due to boundary [15], point defect [16], dislocation [16] and the three phonon umklapp processes, respectively, L' is the CASIMIR [14] length of the crystal, A is the point defect scattering strength, B_1 and B_2 are the three phonon normal and umklapp processes, scattering strengths, respectively, for transverse phonons, B_3 and B_4 are the same for longitudinal phonons, θ is the Debye temperature of the sample, α is a constant [16] and a is the dislocation scattering strength. Thus $\tilde{C}_N^{-1}$ and $\tilde{C}_R^{-1}$ can be expressed as

$$\tilde{C}_{N,T}^{-1} = B_1 w T^4 = b_1 x , \tag{6}$$

$$\tilde{C}_{L,T}^{-1} = B_3 w^2 T^3 = b_3 x^2 , \tag{7}$$

$$\begin{aligned} \tilde{C}_{R,T}^{-1} &= \tilde{C}_B^{-1} + A w^4 + B_2 w T^4 e^{-\Theta/\alpha T} + a w \\ &= \tilde{C}_B^{-1} + D x^4 + b_2 x + y x , \end{aligned} \tag{8}$$

$$\begin{aligned} \tilde{C}_{R,L}^{-1} &= \tilde{C}_B^{-1} + A w^4 + B_4 w^2 T^3 e^{-\Theta/\alpha T} + a w \\ &= \tilde{C}_B^{-1} + D x^4 + b_4 x^2 + x y . \end{aligned} \tag{9}$$

At low temperatures, the contributions of T_2, L_2, T_2', L_2' are negligibly small compared to the contributions of T_1, L_1, T_1' and L_1' due to their limits of integration and one can neglect their contributions. At the same time, it is necessary to mention here that through the numerical analysis of the above expression for $\tilde{C}_R^{-1}$, it is found that at low temperatures, either $\tilde{C}_{\text{dis}}^{-1}$ dominates over $\tilde{C}_B^{-1}$ or $\tilde{C}_{\text{dis}}^{-1}$ is dominated by $\tilde{C}_B^{-1}$. Therefore, the analytical expressions are obtained under two different approximations, i.e. $\tilde{C}_{\text{dis}}^{-1} \ll \tilde{C}_B^{-1}$ and $\tilde{C}_B^{-1} \ll \tilde{C}_{\text{dis}}^{-1}$.

(A) If $\bar{C}_B^{-1} \gg \bar{C}_{\text{dis}}^{-1}$

Under the above approximation, the expression for T_1 can be approximated as

$$T_1 = b_1 \bar{C}_B V_{T_1}^{-3} \int_0^{\Theta_1/T} \left[x^5 - \frac{y x^6}{\tau_B^{-1}} - \frac{b_1 x^6}{\tau_B^{-1}} - \frac{b_2 x^6}{\tau_B^{-1}} - \frac{D x^9}{\tau_B^{-1}} \right] \times \\ \times (1 + R_1 x^2)^3 e^x (e^x - 1)^{-2} dx , \tag{10}$$

which reduces to

$$T_1 = b_1 \bar{C}_B I_5 V_{T_1}^{-3} [X_5^7(R_1) - D\bar{C}_B F_5^9 X_9^{11}(R_1) - (b_1 + b_2 + y) \tau_B F_5^6 X_6^8(R_1)], \tag{11}$$

where

$$X_n^m(R_i) = 1 + 3R_i F_n^m + 3R_i^2 F_n^{m+2} + R_i^3 F_n^{m+4},$$

$$F_n^m = \frac{I_m}{I_n},$$

$$I_r = \int_0^{\Theta_s/T} x^\gamma e^x (e^x - 1)^{-2} dx, \; m, n \text{ and } r \text{ integers}.$$

In a similar way, one can also simplify L_1, T_1' and L_1' as stated in the Appendix through Eqs. (A1—A3).

Hence, the expression ΔK can be expressed as

$$\Delta K = C \left[\frac{2G_1}{V_{T1}^3} + \frac{G_2}{V_{L1}^3} \right]^2 \left[\frac{2G_3}{V_{T1}^5} + \frac{G_4}{V_{L1}^5} \right]^{-1}, \tag{12}$$

where

$$G_1 = A_1 I_5 [X_5^7(R_1) - D_1 F_5^9 X_9^{11}(R_1) - (A_1 + A_2 + y_1) F_5^6 X_6^8(R_1)], \tag{13}$$

$$G_2 = A_3 I_6 [X_6^8(R_3) - D_1 F_6^{10} X_{10}^{12}(R_3) - (A_3 + A_4) F_6^8 X_8^{10}(R_3) - \\ - y_1 F_6^7 X_7^9(R_3)], \tag{14}$$

$$G_3 = A_1 I_5 [Y_5^7(R_1) - A_1 F_5^6 Y_6^8(R_1) - D_1^2 F_5^{13} Y_{13}^{15}(R_1) - \\ - D_1(A_1 + 2A_2 + y_1) F_5^{10} Y_{10}^{12}(R_1) - A_2(A_2 + A_1) F_5^7 Y_7^9(R_1) - \\ - y_1 (A_1 + 2A_2 + y_1) F_5^7 Y_7^9(R_1)], \tag{15}$$

$$G_4 = A_3 I_6 [Y_6^8(R_1) - (A_3 + Y_1^2) F_6^8 Y_8^{10}(R_1) - D_1(2A_4 + A_3) \times \\ \times F^{12} Y_2^{14} - (R_1) - 2y_1 D_1 F_6^{11} Y_{11}^{13}(R_1) - D_1^2 F_6^{14} Y_{14}^{16}(R_1) - \\ - A_4(A_3 + A_4) F_6^{10} Y_{10}^{12}(R_1) - y_1(A_3 + 2A_4^2) F_6^9 Y_9^{11}(R_1)], \tag{16}$$

where

$$A_i = b_i \bar{C}_B, \quad D_1 = D\bar{C}_B, \quad y_1 = y\bar{C}_B$$

and where

$$Y_n^m(R_i) = 1 + 7R_i F_n^m + 18R_i^2 F_n^{m+2} + 22R_i^3 F_n^{m+4} + 7R_i^4 F_n^{m+6} + 3R_i^5 F_n^{m+8}.$$

At low temperature, $\tilde{C}_u^{-1}$ is very small compared to $\tilde{C}_R^{-1}$ and one can neglect its contribution compared to other scattering relaxation rates. On further simplification of Eq. (12) the expression for ΔK reduces to

$$\Delta K = 3Cb_1 I_5 \tilde{C}_B^2 (Z_1 + Z_2) \Big/ \left[\left(1 + \frac{a}{2}\right) V_s Z_3 \right], \tag{17}$$

where

$$Z_1 = M\left[M - 2D_1 F_5^9 \left(1 + \frac{P^3 F_9^{10}}{2}\right) - 2A_1 F_5^6 \left(1 + \frac{P^2 a^3 F_6^8}{2}\right) - \right.$$
$$\left. - 2y F_5^6 \left(1 + \frac{Pa^3 F_6^7}{2}\right)\right], \tag{18}$$

$$Z_2 = 6R_1 F_5^7 \left[\left(1 + \frac{a^3 PC' F_7^8}{2}\right) - D_1 F_7^{11} \left\{ \left(1 + F_5^9 F_{11}^7\right) + \frac{a^3 P F_5^6}{2} \times \right.\right.$$
$$\times (1 + F_6^{10} F_{11}^7) + \frac{a^3 PC' F_{11}^{12}}{2} (1 + F_5^9 F_{12}^8) + a^6 P^2 C' \frac{F_{11}^{12} F_5^{10}}{2} \times$$
$$\left.\times (1 + F_{10}^6)\right\} - A_1 F_7^8 \{(1 + F_5^6 F_8^7) + a^3 P F_5^6 (1 + C')/2 + a^3 P^2 F_5^7/2 \times$$
$$\times (1 + C' F_8^{10} F_7^5) + a^6 P^2 C' F_5^8 (1 + F_8^{10} F_8^6)/4\} - y_1 F_7^8 \left\{ (1 + F_5^6 F_8^7) + \right.$$
$$+ \frac{Pa^3 C' F_8^9}{2} (1 + F_9^8 F_5^6) + \frac{Pa^3 F_5^6}{2} (1 + F_6^7 F_8^7) + \frac{a^6 P^2 C' F_8^9 F_5^6}{2} \times$$
$$\left.\left.\times (1 + F_6^7 F_9^8)\right\}\right], \tag{19}$$

$$Z_3 = M_1 - A_1 F_5^6 \left(1 + \frac{P^2 a^5 F_6^8}{2}\right) + 7R_1 F_5^7 \left[\left(1 + \frac{C' Pa^5 F_7^8}{2}\right) - \right.$$
$$\left. - A_1 F_5^8 \left(1 + \frac{P^2 a^5 C' F_7^8}{2}\right)\right], \tag{20}$$

$$P = \frac{b_3}{b_1}, \quad C' = \frac{R_3}{R_1}, \quad a = \frac{V_{T1}}{V_{L1}}, \quad M = 1 + \frac{a^3}{2} P F_5^6.$$

$M_1 = (1 + a^5 P F_5^6/2)$ and V_s is the average phonon velocity based on the two mode conduction of phonons proposed by HOLLAND [17]. In the absence of dislocations, i.e. $a = 0$, the expression for ΔK stated in Eq. (17) reduces to

$$\Delta K = \frac{2Cb_1 I_5 \tilde{C}_B^2}{V} \left[\frac{Z_1 + Z_2}{Z_3} \right], \tag{21}$$

$$Z_1 = M\left[M - 2D_1 F_5^9\left(1 + \frac{Pa^3 F_9^{10}}{2}\right) - 2A_1 F_5^6\left(1 + \frac{P^2 a^3 F_6^8}{2}\right)\right], \quad (22)$$

$$Z_2 = 6R_1 F_5^7\left[\left(1 + \frac{Pa^3 F_7^8 C'}{2}\right) - D_1 F_7^{11}\left\{1 + F_5^9 F_{11}^7 + \frac{Pa^3 F_{11}^{12} C'}{2} \times\right.\right.$$

$$\times (1 + F_5^9 F_2^8) + \frac{Pa^3 F_5^6}{2}(1 + F_6^{10} F_{11}^7) + \frac{P^2 a^6 F_5^6}{2} F_{11}^{12} \times$$

$$\left.\left. \times (1 + F_6^{10} F_{12}^6)\right\} - A_1 F_8^7\left\{\left(1 + F_5^6 F_8^7 + \frac{Pa^3 F_5^6}{2}(1 + C') + \right.\right.\right.$$

$$\left.\left.\left. + \frac{P^3 a^6 C' F_5^8}{4}(1 + F_8^{10} F_5^6) + \frac{P^2 a^3 F_5^7}{2}(1 + F_8^{10} F_7^5 C')\right\}\right], \quad (23)$$

$$Z_3 = \left[\left(1 + \frac{a^3 P F_5^6}{2}\right) - A_1 F_5^6\left(1 + \frac{P^2 a^5 F_6^8}{3}\right) - 7R_1 F_5^7 \times\right.$$

$$\left. \times \left\{\left(1 + \frac{Pa^5 C' F_7^8}{2}\right) - b_1 F_5^8\left(1 + \frac{P^2 a^5 C' F_8^{10}}{2}\right)\right\}\right], \quad (24)$$

which is the same as obtained by DUBEY [9] for a sample having perfect structure, i.e. a sample having no dislocations. At the same time, if one does not consider the dispersion of phonons, i.e.

$$R_1 = R_3 = 0, \quad V_{T1} = V_{L1} = V_s$$

(in the frame of the CALLAWAY integral), the expression for ΔK stated in Eq. (17) reduces to

$$\Delta K = 9.8 \times 10^2 \frac{Cb_1 \tilde{C}_B^2}{V_s}\left[1 - 8.78 \times 10^3 \, D\tilde{C}_B - \right.$$

$$\left. - 1.23 \times 10^2 b_1 \tilde{C}_B - 13.3 \, \tilde{C}_B a\right], \quad (25)$$

which is the same as obtained by the authors [18] for a sample having dislocations in the frame of the CALLAWAY theory.

Neglecting the dispersion of phonons, the expression obtained for ΔK reduces to

$$\Delta K = 9.8 \times 10^2 \frac{Cb_1 \tilde{C}_B^2}{V_s}\left[1 - 8.78 \times 10^3 \, D\tilde{C}_B - 1.23 \times 10^2 b_1 \tilde{C}_B\right] \quad (26)$$

for a sample having no dislocations, which is the same as obtained by DUBEY [10] for a pure sample in the frame of the CALLAWAY integral.

(B) If $\tilde{C}_{\text{dis}}^{-1} \gg \tilde{C}_B^{-1}$

For this case, the simplified forms or T_1, L_1, T_1' and L_1' are given in the Appendix through Eqs. (A_4—A_7). Using these equations, the expression for ΔK can be expressed as

$$\Delta K = \frac{3b_1 Cy^{-2} F_5^4 I_4}{(1 + a/2) V_s} \left[\frac{Z_1 + Z_2}{Z_3} \right], \tag{27}$$

where

$$Z_1 = M_2 \Big[M_2 - 2\tilde{C}_{B1}^{-1} F_4^3 \left(1 + \frac{Pa^3 F_3^4}{2}\right) - 2C_2 \left(1 + \frac{P^2 a^3 F_4^6}{2}\right) -$$

$$- 2D_2 F_4^7 \left(1 + \frac{Pa^3 F_7^8}{2}\right) \Big], \tag{28}$$

$$Z_2 = 6R_1 F_4^6 \Big[\left(1 + \frac{Pa^3 F_6^7 C'}{2}\right) - \tilde{C}_{B1}^{-1} F_6^5 \Big\{ 1 + F_4^3 F_5^6 + \frac{Pa^3 C' F_5^6}{2} \times$$

$$\times (1 + F_4^3 F_6^7) + \frac{Pa^3 F_4^5}{2} (1 + F_5^4 F_5^6) + \frac{P^2 a^6 C' F_4^6}{4} (1 + F_6^7 F_6^4) \Big\} -$$

$$- C_1 \Big\{ 2 + \frac{Pa^3 F_4^5}{2} (1 + C' F_6^7 F_5^4) + \frac{P^2 a^6 C' F_4^7}{4} (1 + F_7^5 F_6^8) +$$

$$+ \frac{P^2 a^3 F_4^6}{2} (1 + F_6^8 F_6^4 C') \Big\} - D_2 F_6^9 \Big\{ 1 + F_4^7 F_9^6 + \frac{Pa^3 F_9^{10} C'}{2} \times$$

$$\times (1 + F_{10}^7 F_4^7) + \frac{Pa^3 F_4^5}{2} (1 + F_5^8 F_9^6) + \frac{P^2 a^6 F_4^5 F_9^{10} C'}{4} (1 + F_5^7 F_{10}^8) \Big\} \Big], \tag{29}$$

$$Z_3 = M_1 + 7R_1 F_5^7 (1 - C_1) + \frac{7Pa^5 F_5^9}{2} (1 - C_1 P_6^9 F_8^5) -$$

$$- C_1 \left(1 + \frac{P^2 a^5 F_5^7}{2}\right); \tag{30}$$

where

$$C_i = \frac{b_i}{y}, \quad i = 1, 2, 3, \text{ and } 4, \quad D_2 = D/y, \quad \tilde{C}_B^{-1} = \tilde{C}_{B1}^{-1}/y \, .$$

Neglecting the dispersion of phonons i.e. in the frame of the CALLAWAY expression, Eq. (27) reduces to

$$\Delta K = 31.862 \frac{Cb_1}{y^2} \left[1 - 0.458 \frac{\tilde{C}_B^{-1}}{y} - 3.42 \frac{b_1}{y} - 572.55 \frac{D}{y} \right], \tag{31}$$

which is same as obtained by the authors [18] for a sample having dislocation ($\tilde{C}_{\text{dis}}^{-1} \gg \tilde{C}_B^{-1}$) in the frame of the CALLAWAY expression.

III. Results and discussion

To test the applicability of the expression obtained, the contribution of the correction term ΔK (due to the three phonon normal processes in the presence of dislocations) has been calculated in the temperature range 1—5 °K for NaF in the frame of the expression reported in the present work using the constants listed in Table I. The results obtained are reported in Table II. To have a comparative study between the results obtained in the frame of the expression reported and the frame of Eq. (1) i.e. numerical integration of the generalized form of the CALLAWAY integral), the value of ΔK is also reported

Table I

Constants used in the calculation of the phonon conductivity correction term ΔK for MaF in the temperature range 1—5 °K

$\tilde{C}_B^{-1} = 6.2 \times 10^5$ sec^{-1}	$V_{L_1} = 3.39 \times 10^5$ cm/sec
$A = 6.4 \times 10^{-4}$ sec^3	$V_{T_1} = 6.29 \times 10^5$ cm/sec
$a = 1.7 \times 10^{-8}$	$r_1 = 1.54 \times 10^{-28}$ sec^2
$B_1 = 1.0 \times 10^{-12}$ sec deg^{-4}	$r_3 = 1.8 \times 10^{-29}$ sec^2
$B_3 = 1.0 \times 10^{-24}$ sec deg^{-3}	$\Theta_1 = 158$ °K
$\Theta_3 = 256$ °K	$\Theta = 425$ °K

Table II

Phonon conductivity correction term ΔK for NaF sample having dislocations. K is the total lattice thermal conductivity, $(\Delta K)_{\text{Gen. Call.}}$ is the value of ΔK based on numerical integration, $(\Delta K)_{\text{present}}$ is the value of ΔK obtained in the frame of the expression reported in the present work. K and ΔK are expressed in watt/deg/cm

T (°K)	K	$(\Delta K)_{\text{Gen. Call.}}$	$(\Delta K)_{\text{present}}$
1	1.62×10^{-1}	1.385×10^{-7}	1.382×10^{-7}
2	1.27	3.393×10^{-5}	3.370×10^{-5}
3	4.21	8.266×10^{-4}	8.107×10^{-4}
4	9.75	7.740×10^{-3}	7.355×10^{-3}
5	18.43	4.240×10^{-2}	3.705×10^{-2}

in the frame of Eq. (1). With the help of Table II, one can see that the value of ΔK in the frame of expression obtained is very close to those obtained in the frame of numerical integration of the generalized CALLAWAY integral. Thus, it can be concluded that the analytical expression reported in the present work gives good response to the phonon conductivity correction term. At the same time, it should be stated here that one can have the value of ΔK without going through the numerical integration of the complicated integrals.

With the help of Eq. (18), it can be seen that for $\bar{C}_B^{-1} \gg \bar{C}_{\text{dis}}^{-1}$, ΔK is proportional to the product of the three phonon normal processes scattering strength and square of the boundary scattering relaxation time i.e. $\Delta K \alpha B_1 \bar{C}_B^{-2}$, which indicates that for $\bar{C}_B^{-1} \gg \bar{C}_{\text{dis}}^{-1}$, ΔK mainly depends on $\bar{C}_B^{-1}$ and $\bar{C}_{3ph\,N}^{-1}$. At the same time, with the help of Eq. (27), it is very clear that for $\bar{C}_B^{-1} \ll \bar{C}_{\text{dis}}^{-1}$, ΔK is proportional to the the three phonon normal processes scattering strength and inversely proportional to the square of the dislocation scattering strength, i.e. $\Delta K \alpha B_1/a^2$ which shows that for $\bar{C}_{\text{dis}}^{-1} \gg \bar{C}_B^{-1}$, ΔK depends mainly on $\bar{C}_{3phN}^{-1}$ and $\bar{C}_{\text{dis}}^{-1}$. It is interesting to note that under special conditions, the expression obtained reduced to an expression which is similar to previous findings of the earlier workers which can be seen in Eqs. (21), (25), (26) and (31).

The entire work can be summarized as follows:

(a) The phonon conductivity correction term ΔK due to the three phonon normal processes in the presence of dislocation has been studied in the frame of the generalized CALLAWAY integral by obtaining analytical expression for the first time.

(b) The phonon conductivity correction term ΔK has been calculated in the temperature range 1—5 °K for NaF in the frame of the expression obtained and it is found to give very good response to the ΔK.

(c) For $\bar{C}_{\text{dis}}^{-1} \gg \bar{C}_B^{-1}$, ΔK depends mainly on $\bar{C}_{3ph}^{-1}$ and $\bar{C}_{\text{dis}}^{-1}$ whereas for $\bar{C}_B^{-1} \gg \bar{C}_{\text{dis}}^{-1}$ it depends mainly on $\bar{C}_{3ph,N}^{-1}$ and $\bar{C}_B^{-1}$.

(d) In the limiting cases, the expression obtained shows similarity with expressions reported by previous workers for ΔK.

Acknowledgement

The authors wish to express their thanks to Dr. R. A. RASHID, Head of Department of Physics, for his interest in the present work.

REFERENCES

1. J. CALLAWAY, Phys. Rev., **113,** 1046, 1959.
2. B. K. AGRAWAL and G. S. VERMA, Phys. Rev., **128,** 603, 1962.
3. J. CALLAWAY and C. V. BAEYER, Phys. Rev., **120,** 1149, 1960.
4. Y. P. JOSHI, M. D. TIWARI and G. S. VERMA, Physica, **47,** 213, 1970.
5. K. S. DUBEY and G. S. VERMA, Proc. Phys. Soc. (Japan), **32,** 1202, 1972.
6. K. S. DUBEY, Ind. J. Pure Appl. Phys., **11,** 265, 1973.
7. R. N. SAMUEL, R. H. MISHO and K. S. DUBEY, Current Science, **46,** 220, 1977.
8. K. S. DUBEY, J. de Physique, **37,** 267, 1976.
9. K. S. DUBEY, Solid State Comm., **23,** 1963, 1977.
10. K. S. DUBEY, Phys. Stat. Solidi, (b) **79,** K119, 1977.
11. K. S. DUBEY, Phys. Stat. Solidi, (b) **81,** K83, 1977.
12. A. F. SALEH, R. H. MISHO and K. S. DUBEY, Ind. J. Phys., 1979. (in press).
13. K. S. DUBEY, Phys. Stat. Solidi, (b) **63,** K35, 1974.
14. C. HERRING, Phys. Rev., **95,** 954, 1954.
15. H. B. G. CASIMIR, Physica, **5,** 495, 1938.
16. P. G. KLEMENS, Solid State Physics, **7,** 1, 1958.
17. M. G. HOLLAND, Phys. Rev., **132,** 2461, 1963.
18. A. F. SALEH, R. H. MISHO and K. S. DUBEY, Solid State Comm., **32,** 537, 1979.

Appendix

Similar to T_1 (a stated in Eq. (11)), the terms L_1, T_1' and L_1' can also be simplified for $\tilde{C}_B^{-1} \gg \tilde{C}_{\text{dis}}^{-1}$ as

$$L_1 = b_3 \tilde{C}_B I_6 V_{L1}^{-3} [X_6^8(R_3) - D\tilde{C}_B F_6^{10} X_{10}^{12}(R_3) - (b_3 + b_4) \tilde{C}_B \times \times F_6^8 X_8^{10}(R_3) - a\tilde{C}_B F_6^7 X_7^9(R_3)], \quad \text{(A1)}$$

$$T_1' = b_1 I_5 V_{T1}^{-5} [Y_5^7(R_1) - b_1 \tilde{C}_B F_5^6 Y_6^8(R_1) - D^2 \tilde{C}_B^2 F_5^{13} Y_{13}^{15}(R_1) \times - D\tilde{C}_B^2 F_5^{10} Y_{10}^{12}(R_1)(2b_2 + b_1 + 2a) - b_2(b_2 + b_1) \tilde{C}_B^2 F_5^7 Y_7^8(R_1) - - a(2b_2 + b_1) \tilde{C}_B^2 F_5^7 Y_7^9(R_1) - a^2 \tilde{C}_B^2 F_5^7 Y_7^9(R_1)], \quad \text{(A2)}$$

$$L_1' = b_3 I_6 V_{L1}^{-5} [Y_6^8(R_3) - b_3 \tilde{C}_B F_6^8 Y_8^{10}(R_3) - D^2 \tilde{C}_B^2 F_6^{14} Y_{14}^{16}(R_3) - - D(b_3 + 2b_4) F_6^{12} Y_{12}^{14}(R_3) - 2Da F_6^{11} Y_{11}^{13}(R_3) - b_4(b_3 + b_4) \times \times F_6^{10} Y_{10}^{12}(R_3) \tilde{C}_B^2 - a(b_3 + 2b_4) \tilde{C}_B^2 F_6^9 Y_9^{11}(R_3) - a^2 \tilde{C}_B^2 F_6^8 Y_8^{10}(R_3)]. \quad \text{(A3)}$$

Similarly for $\tilde{C}_{\text{dis}}^{-1} \gg \tilde{C}_B^{-1}$,

$$T_1 = \frac{b_1 I_4}{V_{T1}^3 y} \left[X_4^6(R_1) - \frac{\tilde{C}_B^{-1}}{y} F_4^3 X_3^5(R_1) - \frac{(b_1 + b_2)}{y} X_4^6(R_1) - - \frac{D}{y} F_4^7 X_7^9(R_1) \right], \quad \text{(A4)}$$

$$L_1 = \frac{b_3 I_5}{V_{L1}^3 y} \left[X_5^7(R_3) - \frac{\tilde{C}_B^{-1}}{y} F_5^4 X_4^6(R_3) - \frac{(b_3 + b_4)}{y} F_5^6 X_6^8(R_3) - - \frac{D}{y} F_5^8 X_8^{10}(R_3) \right], \quad \text{(A5)}$$

$$T_1' = \frac{b_1 I_5}{V_{T1}^5} \left[Y_5^7(R_1) - F_5^3 Y_3^5(R_1) \frac{\tilde{C}_B^{-1}}{y} - \frac{2D}{y} \frac{\tilde{C}_B^{-1}}{y} Y_7^9(R_1) - - \frac{2b_2 + b_1}{y} \frac{\tilde{C}_B^{-1}}{y} Y_4^6(R_1) F_5^4 - \frac{D^2}{y^2} F_5^{11} Y_{11}^{13}(R_1) - - \frac{2b_2 + b_1}{y} \frac{D}{y} F_5^8 Y_8^{10}(R_1) - \frac{b_2(b_2 + b_1) + b_1}{y^2} Y_5^7(R_1), \right. \quad \text{(A6)}$$

$$L_1' = \frac{b_3 I_6}{V_{L1}^5} \left[Y_6^8(R_3) - \frac{\tilde{C}_B^{-2}}{y^2} F_6^4 Y_4^6(R_3) - \frac{b_3}{y} F_6^7 Y_7^9(R_3) - - 2\frac{D}{y} \frac{\tilde{C}_B^{-1}}{y} F_6^8 Y_8^{10}(R_3) - \frac{(2b_4 + b_3)}{y} \frac{\tilde{C}_B^{-1}}{y} Y_6^8(R_3) - \frac{D^2}{y^2} F_6^{12} Y_{12}^{14}(R_3) - - \frac{D}{y} \frac{2b_4 + b_3}{y} F_6^{10} Y_{14}^{12}(R_3) - \frac{b_4(b_3 + b_4)}{y^2} F_6^8 Y_8^{10}(R_3) \right]. \quad \text{(A7)}$$

Acta Physica Academiae Scientiarum Hungaricae, Tomus 47 (4), pp. 335—343 (1979)

NEUERE UNTERSUCHUNGEN IM PROBLEMENKREIS DES HAGEN-POISEUILLESCHEN STRÖMUNGSGESETZES

Von

M. MIKOLÁS und L. BARDÓCZ

LEHRSTUHL FÜR MATHEMATIK, FAKULTÄT FÜR BAUWESEN DER TECHNISCHEN UNIVERSITÄT BUDAPEST UND ABTEILUNG FÜR ISOLATIONSTECHNIK DES FORSCHUNGSINSTITUTES FÜR ELEKTROINDUSTRIE IN BUDAPEST

(Eingegangen 25. VII. 1979)

Mit einer neuartigen geometrischen und analytischen Begründung wird eine Verallgemeinerung des Hagen-Poiseuille-Gesetzes behandelt, die bei vielen, in der Physik und Technik vorkommenden Kanalformen bzw. Flüssigkeitstypen eine feinere Beschreibung des Strömungsvorganges ermöglicht.

1. Einleitung

Wie bekannt, ist das Gesetz von Hagen und Poiseuille, das seit seiner Entdeckung (1839) auf verschiedenen Gebieten der Physik, Chemie und Biologie oft benutzt wurde, während der letzten Jahrzehnte auch in der Technik zu einer wesentlichen Unterstützung geworden. (Vgl. z. B. [1]—[3], [16], [17].) Man muss aber beachten, dass die genannte Regel nur den elementarsten Fall: Newtonsche Flüssigkeiten und zylindrische Kanäle mit Kreisdurchschnitt betrifft, wogegen die übrigen Fälle in der Fachliteratur meistens mit Hilfe unzuverlässiger Approximationsformeln behandelt werden. (S. [16], 120 und 137—138; [17], 200.)

Im Folgenden soll nun eine derartige starke Erweiterung des Hagen-Poiseuille-Gesetzes abgeleitet werden, die aller Wahrscheinlichkeit nach geeignet ist, den Strömungsvorgang in den praktisch wichtigsten Fällen exakter widerzuspiegeln. Die Resultate entstanden im Laufe einer im Jahre 1977 begonnenen Kooperation zwischen den, im Titel angegebenen zwei Institutionen, welche u.a. zum Ziele hatte, eine unlängst erfundene Isolationstechnologie für Anker gewisser Elektromotoren, wobei die Isolierschichten durch Spritzguss und unter Verwendung spezieller Kunststoffe hergestellt werden, mathematisch zu begründen.

Bemerkt sei noch, dass viele Mitteilungen der neueren Fachliteratur die Weiterentwicklung des Problemenkreises in anderen Richtungen, nämlich die Untersuchung von Hagen-Poiseuille-Strömungen (in Rohren mit kreisförmigen oder annularen Durchschnitten) bei temperaturabhängiger Viskosität, zeitabhängiger Druckverteilung, für einige Gasgemische, oder in Bezug auf Stabilität zum Gegenstand haben. (Vgl. z. B. [4]—[7], [9]—[10], [13]—[15], [18].)

2. Richtung der Verallgemeinerung, geometrische Grundlage

Das nach Hagen und Poiseuille benannte klassische Gesetz für stationäre Rohrströmungen und Newtonsche Flüssigkeiten lautet:

$$\dot{V} = \frac{\pi R^4}{8\eta l}(p_1 - p_2)\,, \tag{1}$$

wobei $\dot{V}$ den »Volumenstrom«, d.h. das pro Zeiteinheit durch einen Rohrquerschnitt strömende Flüssigkeitsvolumen, $p_1 - p_2$ den Druckabfall entlang des ganzen Rohres, R und l den Radius bzw. die Länge des zylindrischen Rohres, η aber die dynamische Viskosität der Flüssigkeit bezeichnet. Dass die Flüssigkeit «Newtonsch« ist, bedeutet bekanntlich folgende Beziehung zwischen der Schubspannung τ und dem Geschwindigkeitsgradienten dv/dr $(0 < r \leq R)$:

$$\tau = \eta \frac{dv}{dr}\,. \tag{2}$$

Wir möchten gleich hervorheben, dass man — unter Beibehaltung der Rohrform — relativ einfach auf den Fall Nicht-Newtonscher Flüssigkeiten übergehen kann. Wir haben nämlich nur $\dot{V}$ als Integral der Geschwindigkeit auf dem Rohrquerschnitt zu betrachten, dann nach passender Teilintegration in Bezug auf die Variable r den Gradienten dv/dr mit seinem aus dem beliebig vorgegebenen Fliessgesetz gewonnenen Ausdruck (als Funktion von τ) zu ersetzen, und schliesslich anstatt r nach τ zu integrieren. (Die Schubspannung ist in unserem Fall einfach proportional r; vgl. z. B. [1], 104—105). Von diesem Grundgedanken werden wir auch im weiteren Gebrauch machen; da aber die Hauptschwierigkeit einer Ausdehnung von (1) in der komplizierten Abhängigkeit der Strömungsparameter von der Kanalform liegt, so wollen wir uns vor allem auf die Untersuchung der Schubspannung bei gewissen allgemeineren Kanaltypen konzentrieren.

Es wird wieder die in einem zylindrischen Rohr der Länge l stationär ablaufende Strömung einer Newtonschen Flüssigkeit geprüft, aber der Rohrquerschnitt $\mathfrak{B}$ ist ein Bereich allgemeiner Art, dessen Rand aus folgenden Teilen besteht: (I) aus einem Stück einer geschlossenen, abteilungsweise glatten ebenen Kurve $\mathcal{C}$, welche ein Symmetriezentrum O besitzt und in einem, O als Anfangspunkt enthaltenden Polarsystem die Gleichung $r = f(\varphi)$ mit $r > 0$ hat;* (II) aus einer anderen Kurve $\mathcal{C}_\varepsilon$, welche aus $\mathcal{C}$ durch eine Ähnlichkeitstransformation mit dem Verhältnis $1 : \varepsilon$ und mit O als Ähnlichkeitszent-

* Somit wird die Funktion $f(\varphi)$ eindeutig und abteilungsweise stetig-differenzierbar vorausgesetzt.

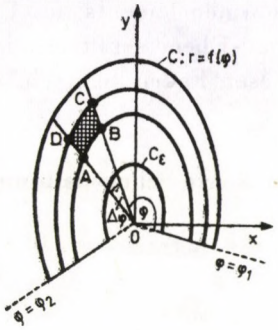

Fig. 1. Durch Affinität erzeugter allgemeiner Rohrquerschnitt und zugehöriges Polarsystem

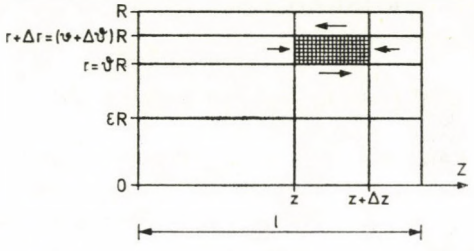

Fig. 2. Einem festen Polarwinkel zugehöriger Kanalquerschnitt in Strömungsrichtung

rum erzeugt wird; ferner (III) aus gewissen Strecken $\varphi = \varphi_1$ (konst.), $\varphi = \varphi_2$ (konst.) (siehe Fig. 1). Wir betrachten nebst dem $r\varphi$-Polarsystem auch ein rechtwinkliges xy-Koordinatensystem mit dem gleichen Anfangspunkt und ergänzen letzteres mit einer in Strömungsrichtung liegenden z-Achse zu einem räumlichen Descartessystem. Wenn man das Rohr durch eine die z-Achse enthaltende, mit einem festen Wert von φ gekennzeichnete Ebene schneidet, so entspringt ein Rechteck der Länge l und Breite $(1-\varepsilon)R$, wobei R diesmal eine Abkürzung für $r(\varphi)$ ist. (Vgl. Fig. 2.)

Wir setzen noch voraus, dass die Stromlinien zur z-Achse parallel sind, und der Druck p nur von z abhängt, ferner linear längs des Rohres abnimmt; der Anfangswert von p wird mit p_1, sein Endwert (Minimum) mit p_2 bezeichnet. Denkt man sich nun den Strömungsraum mittels geeigneter, aus der zu $\mathcal{C}$ gehörigen Grenzfläche durch Affinitäten erzeugten Flächen, sowie zur xy-Ebene paralleler und die z-Achse enthaltender Ebenen in Volumenelemente zerlegt (in den Figuren 1—2 sind die den Rand eines solchen Elements charakterisierenden Polarkoordinaten und z-Koordinaten der Reihe nach mit $r = \vartheta R$ $[\varepsilon \leq \vartheta \leq 1]$, $r + \Delta r = (\vartheta + \Delta\vartheta)R$, φ, $\varphi + \Delta\varphi$ bzw. mit z und $z + \Delta z$ bezeichnet, ferner bedeutet $ABCD$ den entsprechenden elementaren Teil des Querschnittes $\mathfrak{B}$ in der xy-Ebene), dann greifen Schubspannungen entlang der

Randflächen eines jeden Volumenelements an. Es erhebt sich die Frage: wie hängt die entlang eines zur xy-Ebene senkrechten Stromfadens $\mathfrak{s}$ auftretende Schubspannung* von den diesen Faden kennzeichenden Polarkoordinaten ab?

3. Generalisierte Schubspannungsformel

Um die Antwort zu finden, betrachten wir zunächst einen veränderlichen Punkt Q der durch die Gleichung $r = \vartheta f(\varphi)$ $(\varphi_1 \leqq \varphi \leqq \varphi_2)$ dargestellten ebenen Kurve und schreiben wir für den Wert von τ entlang des zu Q gehörigen Stromfadens kurz $\tau_{\vartheta R}$ $(R = f(\varphi))$. Setzt man voraus, dass $\tau_{\vartheta R}$ eine stetige Ortsfunktion ist und sogar stetige Ableitungen nach den Polarkoordinaten besitzt, so ist diese Grösse bezüglich eines kurzen Kurvenstückes annähernd konstant. Daher ergibt die Gleichgewichtsbedingung für die an ein beliebiges Volumenelement wirkenden gesamten Kräfte:

$$\begin{aligned} &\Delta p \cdot (\text{Inhalt von } ABCD) \approx \\ &\approx \Delta z \left[(\text{Bogenlänge von } \widehat{CD}) \cdot \tau_{(\vartheta+\Delta\vartheta)R} - (\text{Bogenlänge von } \widehat{AB}) \cdot \tau_{\vartheta R}\right], \end{aligned} \tag{3}$$

wo $\Delta p = p(z + \Delta z) - p(z)$ ist. Die dabei implizit gemachte Annahme, dass die zu $\overline{AD}$ und $\overline{BC}$ gehörigen »Seitenflächen« schubspannungsfrei sind, ist offenbar berechtigt; denn die innere Reibung tritt erfahrungsgemäss nur zwischen solchen Stromfäden auf, die sich nebeneinander nicht mit der gleichen Geschwindigkeit bewegen, die also verschiedene Abstände vom Rande des Strömungsraumes haben.

Es ist nun wesentlich, dass die Bogenlänge eines durch ebene Polarkoordinaten gekennzeichneten, stückweise glatten Kurvenstückes, oder der Inhalt einer Flächengestalt des Types $ABCD$ in der Form einfacher Integrale ausgedrückt werden können. (Vgl. z. B. [11], 203 und 227—228.) Mithin erhält man für die Bogenlänge Δs des mit φ und $\varphi + \Delta\varphi$ bestimmten Stückes von $\mathfrak{C}$ die Formel:

$$\Delta s = \int_{\varphi}^{\varphi+\Delta\varphi} \sqrt{[f(\Phi)]^2 + [f'(\Phi)]^2}\, d\Phi\,, \tag{4}$$

während der Inhalt ΔI des zum Zentriwinkel $\Delta\varphi$ gehörigen Teilgebietes (Sektors) von $\mathfrak{B}$ die Darstellung

$$\Delta I = \frac{1}{2}\int_{\varphi}^{\varphi+\Delta\varphi} [f(\Phi)]^2\, d\Phi \tag{5}$$

* Hierunter versteht man natürlich den Grenzwert der auf eine den $\mathfrak{s}$ enthaltende Fläche $\mathfrak{S}$ bezogenen Schubspannung für den Fall, wo $\mathfrak{S}$ auf $\mathfrak{s}$ zusammenschrumpft.

zulässt (Fig. 1). Da aber die erste Polarkoordinate eines beliebigen Punktes von $\widehat{AB}$ bzw. $\widehat{CD}$ aus derjenigen des entsprechenden Punktes von $\mathcal{C}$ durch Multiplizieren mit ϑ bzw. mit $\vartheta + \Delta\vartheta$ entsteht (vgl. Fig. 2), so ergeben sich:

$$\text{Bogenlänge von } \widehat{AB} = \vartheta \Delta s,$$
$$\text{Bogenlänge von } \widehat{CD} = (\vartheta + \Delta\vartheta)\Delta s,$$
$$\text{Inhalt von } ABCD = \Delta\vartheta(2\vartheta + \Delta\vartheta)\Delta I,$$

womit (3) der Beziehung

$$\frac{(\vartheta + \Delta\vartheta)\tau_{(\vartheta+\Delta\vartheta)R} - \vartheta\tau_{\vartheta R}}{\Delta\vartheta} \approx (\vartheta + \Delta\vartheta)\frac{\Delta p}{\Delta z} \cdot \frac{\Delta I}{\Delta s} \tag{6}$$

äquivalent wird.

Wenn man in (6) die Grenzübergänge $\Delta\vartheta \to 0$ und $\Delta\varphi \to 0$ ausführt und beachtet, dass die vorausgesetzte lineare Beziehung des Druckes mit z die Formel

$$\frac{\Delta p}{\Delta z} = -\frac{p_1 - p_2}{l} \; (<0) \tag{7}$$

zur Folge hat, dann entsteht

$$\frac{\partial(\vartheta\tau_{\vartheta\Delta})}{\partial\vartheta} = -2\vartheta\frac{p_1 - p_2}{l}\frac{dI}{ds},$$

d. h. wegen

$$\frac{dI}{d\varphi} = \frac{1}{2}[f(\varphi)]^2, \quad \frac{ds}{d\varphi} = \sqrt{[f(\varphi)]^2 + [f'(\varphi)]^2},$$

$$\frac{dI}{ds} = \frac{dI}{d\varphi} : \frac{ds}{d\varphi} = \frac{1}{2}\frac{R^2}{\sqrt{R^2 + (R')^2}}$$

die Differentialgleichung

$$\frac{\partial(\vartheta\tau_{\vartheta R})}{\partial\vartheta} = -\vartheta\frac{p_1 - p_2}{l}\frac{R^2}{\sqrt{R^2 + (R')^2}} \quad \begin{pmatrix} \varepsilon \leq \vartheta \leq 1 \\ R = f(\varphi) \end{pmatrix}. \tag{8}$$

Die Auflösung von (8) liefert:

$$\vartheta\tau_{\vartheta R} = -\frac{\vartheta^2}{2}\frac{p_1 - p_2}{l}\frac{R^2}{\sqrt{R^2 + (R')^2}} + K,$$

wobei K von ϑ nicht abhängt; diese Grösse muss sogar 0 sein, wie es für $\vartheta \to +0$ unmittelbar ersichtlich ist. (Genauer: $K \to 0$ als $\varepsilon \to +0$.)

Wird noch $r = \vartheta R$ gesetzt und anstatt τ_r einfach τ geschrieben, so folgt schliesslich die gesuchte Darstellung der Schubspannung:

$$\tau = -\frac{p_1 - p_2}{2l} r\left[1 + \left(\frac{R'}{R}\right)^2\right]^{-1/2} \begin{pmatrix} \varepsilon R \leq r \leq R \\ R = f(\varphi), \quad \varphi_1 \leq \varphi \leq \varphi_2 \end{pmatrix}. \tag{9}$$

Wir bemerken, dass (9) im Falle $R =$ konstant, $\varepsilon = 0$ in die Formel

$$\tau = -\frac{p_1 - p_2}{2l} r \quad (0 \leqq r \leqq R),$$

d. h. in eine wohlbekannte elementare Relation aus der Theorie laminarer Rohrströmungen übergeht. (Vgl. z. B. [1], 97.]

4. Erweitertes Strömungsgesetz für Newtonsche Flüssigkeiten

Im Besitz von (9) ist es schon nicht schwer, denjenigen Zusammenhang zwischen dem Volumenstrom $\dot{V}$ und dem »Druckabfall« $p_1 - p_2$ abzuleiten, der im vorliegenden Fall der Hagen-Poiseuilleschen Regel (1) entspricht. Wir haben nur eine bekannte Formel der Vektoranalysis, sowie die in der Einleitung erwähnte Grundidee zu verwenden.

Tatsächlich gilt die Darstellung

$$\dot{V} = \iint_{(\sigma)} v \, dx \, dy \,, \tag{10}$$

bei welcher σ den Durchschnitt des behandelten zylindrischen Rohres, $v = v(x, y)$ die Strömungsgeschwindigkeit bezeichnet.

Auf Grund der Koordinatentransformation

$$\begin{cases} x = r \cos \varphi \,, \\ y = r \sin \varphi \,, \end{cases}$$

deren Funktionaldeterminante einfach r beträgt, geht (10) über in:

$$\dot{V} = \int_{\varphi_1}^{\varphi_2} \left[\int_{\varepsilon R}^{R} v(r, \varphi) \, r \, dr \right] d\varphi \,; \tag{11}$$

und das innere Integral lässt sich mit partieller Integration, sowie unter Benützung von (2) und (9) auf folgende Weise umformen:

$$\int_{\varepsilon R}^{R} rv \, dr = \left[\frac{1}{2} r^2 v \right]_{r=\varepsilon R}^{r=R} - \frac{1}{2} \int_{\varepsilon R}^{R} r^2 \frac{\partial v}{\partial r} \, dr =$$

$$= -\frac{1}{2\eta} \int_{\varepsilon R}^{R} r^2 \tau \, dr = \frac{1}{2\eta} \frac{p_1 - p_2}{2l} \left[1 + \left(\frac{R'}{R} \right)^2 \right]^{-1/2} \cdot \frac{R^4 - (\varepsilon R)^4}{4} \,.$$

Demnach gelangt man aus (11) unmittelbar zur gehofften *Verallgemeinerung von* (1) für Durchschnitte vom in Fig. 1 angedeuteten Typus:

$$\dot{V} = \frac{p_1 - p_2}{16 \eta l} (1 - \varepsilon^4) \int_{\varphi_1}^{\varphi_2} R^4 \left[1 + \left(\frac{R'}{R} \right)^2 \right]^{-1/2} d\varphi \quad (R = f(\varphi)). \tag{12}$$

Wird hierin $R =$ konstant gewählt und $\varepsilon R = R_0 \geq 0$ gesetzt (*Kreisbogengrenzen*), so entspringt die Beziehung:

$$\dot{V} = \frac{p_1 - p_2}{16\eta l}(R^4 - R_0^4)(\varphi_2 - \varphi_1)\,, \tag{13}$$

welche im Falle eines *Vollkreises* ($R_0 = 0$, $\varphi_1 = 0$, $\varphi_2 = 2\pi$) genau (1) liefert.

Der andere wichtigste Spezialfall von (12) ist derjenige eines *Rechtecks* mit den Seiten $2a \geq 2b$ (Fig. 3). Dann hat man offensichtlich $\varepsilon = 0$ zu setzen,

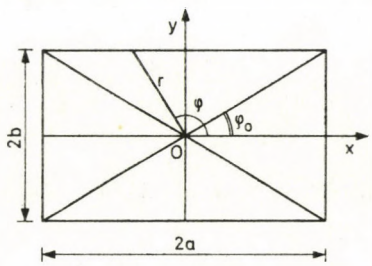

Fig. 3. Fall eines rechteckförmigen Durchschnittes

und es ist zweckmässig den Neigungswinkel φ_0 als Hilfsgrösse einzuführen, den die längere Symmetrieachse mit der Diagonale einschliesst.

Es gilt für diesen Winkel:

$$\varphi_0 = \operatorname{arc\,tg}\frac{b}{a} = \operatorname{arc\,ctg}\frac{a}{b}\,, \tag{14}$$

und mit Hilfe der Polardarstellungen der vier Rechtecksseiten:

$$r = \frac{a}{\cos\varphi}\,(-\varphi_0 \leq \varphi \leq \varphi_0);\quad r = \frac{b}{\sin\varphi}\,(\varphi_0 \leq \varphi \leq \pi - \varphi_0);$$

$$r = -\frac{a}{\cos\varphi}\,(\pi - \varphi_0 \leq \varphi \leq \pi + \varphi_0);\quad r = -\frac{b}{\sin\varphi}\,(\pi + \varphi_0 \leq \varphi \leq 2\pi - \varphi_0)$$

lässt sich das Integral in (12) explizit ausrechnen.

Zunächst erhält man:

$$\dot{V} = \frac{p_1 - p_2}{4\eta l}\left(a^4\int_0^{\varphi_0}\frac{d\varphi}{\cos^3\varphi} + b^4\int_{\varphi_0}^{\pi/2}\frac{d\varphi}{\sin^3\varphi}\right), \tag{15}$$

und beide letzten Integrale können durch die Substitution $u = \operatorname{tg}(\varphi/2)$ in geschlossener Form dargestellt werden. So ergeben sich:

$$\int_{\varphi_0}^{\pi/2}\frac{d\varphi}{\sin^3\varphi} = \frac{1}{8}\left(\operatorname{ctg}^2\frac{\varphi_0}{2} - \operatorname{tg}^2\frac{\varphi_0}{2}\right) - \frac{1}{2}\ln\left|\operatorname{tg}\frac{\varphi_0}{2}\right|, \tag{16}$$

$$\int_0^{\varphi_0} \frac{d\varphi}{\cos^3\varphi} = \frac{1}{8}\left[\operatorname{ctg}^2\left(\frac{\pi}{4}-\frac{\varphi_0}{2}\right) - \operatorname{tg}^2\left(\frac{\pi}{4}-\frac{\varphi_0}{2}\right)\right] - \\ - \frac{1}{2}\ln\left|\operatorname{tg}\left(\frac{\pi}{4}-\frac{\varphi_0}{2}\right)\right|, \tag{17}$$

ferner lassen sich die Werte (16)—(17) — hinsichtlich von (14) — einfach mit a, b ausdrücken. Mithin resultiert die in den Seitenlängen völlig symmetrische, elegante Formel:

$$\dot{V} = \frac{p_1 - p_2}{8\eta l}\left[a^4 W\left(\frac{b}{a}\right) + b^4 W\left(\frac{a}{b}\right)\right], \tag{18}$$

wo

$$W(x) = x\sqrt{x^2+1} + \ln\left(x + \sqrt{x^2+1}\right) \tag{19}$$

zu verstehen ist.

Insbesondere für $a = b$, d. h. wenn der Durchschnitt ein *Quadrat* ist, geht (18) über in

$$\dot{V} = \frac{\left[\sqrt{2} + \ln\left(\sqrt{2}+1\right)\right] a^4}{8\eta l}\left(p_1 - p_2\right), \tag{20}$$

das als ein eigentümliches Gegenstück von (1) aufgefasst werden kann.

Weitere Beispiele zeigen, dass (12) auch im Falle von nicht-zentralsymmetrischen Durchschnitten mit $\varepsilon = 0$, bzw. für Rohrquerschnitte, bei welchen das Symmetriezentrum von $\mathcal{C}$ mit dem Ähnlichkeitszentrum nicht zusammenfällt, unter passenden Einschränkungen zur approximativen Beschreibung des Strömungsvorganges geeignet ist.

5. Fall von Nicht-Newtonschen Flüssigkeiten, Weiterentwicklung der Resultate

Die Methode der Ableitung von (12) gestattet uns offenbar, das gefundene Strömungsgesetz auch auf gewisse Nicht-Newtonsche Flüssigkeiten auszudehnen. Der Kern dieser Methode besteht nämlich darin, dass der gewünschte Ausdruck von $\dot{V}$ nicht durch die vorläufige Bestimmung der Geschwindigkeit aus ihrem radialen Gradienten, wie es in der Fachliteratur allgemein üblich ist (vgl. z. B. [8], 189—190), sondern mittels der direkten Benützung des Fliessgesetzes für $\partial v/\partial r$ und der Schubspannungsformel (9), auf Grund einer passenden Umformung der Integraldarstellung (10) gewonnen wird.

Nehmen wir nun anstatt (2) die Gültigkeit eines sog. (zweigliedrigen) *Potenzgesetzes*

$$\frac{\partial v}{\partial r} = \varkappa\tau - \lambda|\tau|^N \tag{21}$$

mit vorgegebenen Konstanten $\varkappa$, λ, N an, das bekanntlich für eine breite Klasse von Nicht-Newtonschen Flüssigkeiten zutrifft (»pseudoplastische Media« mit $\varkappa = 0$, $\lambda > 0$, $N > 1$; »dilatante Media« mit $\varkappa = 0$, $\lambda > 0$, $N < 1$), so bekommen wir durch Einsetzen von (21) in die Formel [vgl. (11)]:

$$\int_{\varepsilon R}^{R} vr\,dr = -\frac{1}{2}\int_{\varepsilon R}^{R} r^2 \frac{\partial v}{\partial r}\,dr\,, \tag{22}$$

ferner durch Anwendung von (9) und Ausführung der Integration nach r die Darstellung:

$$\dot{V} = \frac{\varkappa(1-\varepsilon^4)}{16l}(p_1 - p_2)\int_{\varphi_1}^{\varphi_2} R^4\left[1+\left(\frac{R'}{R}\right)^2\right]^{-1/2} d\varphi + \\ + \frac{\lambda(1-\varepsilon^{N+3})}{2(N+3)}\left(\frac{p_1-p_2}{2l}\right)^N \int_{\varphi_1}^{\varphi_2} R^{N+3}\left[1+\left(\frac{R'}{R}\right)^2\right]^{-N/2} d\varphi \qquad (R=f(\varphi)). \tag{23}$$

Es ist eindeutig, dass (12) dem Spezialfall $\lambda = 0$ und der Bezeichnung $\varkappa = 1/\eta$ entspricht; im Nicht-Newtonschen Fall $\lambda \neq 0$ ist (23) wieder als eine Approximationsformel anzusehen.

Auf die Diskussion des Labilwerdens bzw. der Turbulenz der Strömung, sowie des Begriffs der Reynoldszahl und eines instationären Strömungsablaufs für nicht kreisförmige Rohrdurchschnitte, welche nebst mathematischen Überlegungen auch experimentelle Nachweise erfordert, werden wir an anderer Stelle eingehen. Schliesslich sei erwähnt, dass sich eine vorläufige Ankündigung in englischer Sprache über die obigen Ergebnisse in [12] befindet.

LITERATUR

1. E. Becker, Technische Strömungslehre, 2. Auflage, Teubner Verlag, Stuttgart 1970.
2. F. R. Eirich, Rheology-Theory and Applications, Vol. I—III., Academic Press, New York, 1956.
3. J. D. Ferry, Viscoelastic Properties of Polymers, Wiley, New York, 1961.
4. W. D. George und J. D. Hellums, J. Fluid Mech., **51**, 687, 1972.
5. D. F. Hays, Int. J. Heat Mass Transfer, **9**, 165, 1966.
6. D. K. Hennecke, Wärme- u. Stoffübertr., **1**, 177, 1968.
7. T. C. Ho und M. M. Denn, J. Non-Newtonian Fluid Mech., **3**, 179, 1977.
8. G. Joos, Theoretische Physik, 7. Auflage, Akad. Verlagsgesellschaft, Leipzig 1950.
9. P.-A. Mackrodt, Z. Angew. Math. Mech., **53**, T 111, 1973.
10. H. Maki, Phys. Fluids, **22**, 203, 1979.
11. H. Mangoldt und K. Knopp, Einführung in die höhere Mathematik, Bd. III., 9. Auflage, Hirzel Verlag, Leipzig 1951.
12. M. Mikolás und L. Bardócz, Z. Angew. Math. Mech., **59**, T 120, 1979.
13. V. Panaitescu, Stud. Cercet. Mec. Apl., **35**, 187, 1976.
14. S. Prakash, J. Appl. Mech., **36**, 309, 1969.
15. H. Salwen und Ch. E. Grosch, J. Fluid Mech., **54**, 93, 1972.
16. G. Schenkel, Kunststoff-Extrudertechnik, 2. Auflage, Hanser Verlag, München, 1963.
17. L. Sors, L. Bardócz und I. Radnóti, Műanyagalakító szerszámok (ung.), 2. Auflage, Műszaki Könyvkiadó, Budapest, 1977.
18. V. V. Struminskij, Prikl. Mat. Mekh., **39**, 144, 1975.

Acta Physica Academiae Scientiarum Hungaricae, Tomus 47 (4), pp. 345—352 (1979)

KINETICS OF CRYSTAL GROWTH IN AMORPHOUS SOLID AND SUPERCOOLED LIQUID $TeSe_{20}$ USING DTA AND d.c. CONDUCTIVITY MEASUREMENTS*

By

M. F. KOTKATA**

INTERNATIONAL CENTRE FOR THEORETICAL PHYSICS, TRIESTE, ITALY

E. A. MAHMOUD and M. K. EL-MOUSLY

PHYSICS DEPARTMENT, FACULTY OF SCIENCE, AIN SHAMS UNIVERSITY, CAIRO, EGYPT

(Received in revised form 30. VII. 1979)

Curves of reaction rate versus temperature for constant heating rates ($\Phi = 1-10$ °C/min) constructed by analytical methods have been used to demonstrate the crystallization kinetics of amorphous solid $TeSe_{20}$. The devitrification process takes place with predominance of random nucleation and one-dimensional growth, and is limited by combined switching and splitting of the chemical bonds. The mean value for the activation energy of the amorphous-crystal transformation, $\bar{E}$, is found to be 64 Kcal/mole. While the quantity E calculated on the basis of d.c. conductivity changes during different isothermal crystallization (120—175 °C) in supercooled liquid $TeSe_{20}$ amounts to 11.5 Kcal/mole and suggests the existence of mixed chains in the liquid alloys.

I. Introduction

The binary chalcogenide system Se-Te is of particular interest because the components are isomorphous and the phase diagram is very simple with total miscibility [1]. To satisfy the local valence requirements in the Se-Te alloys, any structural groupings other than rings or chains would appear to be excluded. The atoms within the chains are connected to each other by covalent bonds (main bonds), whereas the bonding between the chains shows covalent as well as Van der Waals character (weak bonds). Raman studies [2] have indicated that Te has a great effect in reducing the Se_8-ring concentration. Also, the viscosity of Se is increased by the addition of Te and is attributed to an enhanced interaction between chains [3]. An analysis of Mössbauer experimental data made by POOLCHAND and SURANYI [4] suggests that the binding of Se-Te bond is stronger than the average of the Se-Se and Te-Te bonds. This means that doping of Te in Se shows the tendency to form as many Se-Te bonds as possible [5], i.e. the weak bonds between the chains are attenuated.

In the present article, an attempt has been made to assess the applicability of using the DTA measurements to investigate the kinetics of devitri-

* Published in the ICTP Internal Report, Miramare-Trieste, IC/79/66, July 1979.

** Permanent address: Physics Department, Faculty of Science, Ain Shams University, Cairo, Egypt.

fication of amorphous solid $TeSe_{20}$. Also, kinetic calculations of the crystal growth in supercooled liquid $TeSe_{20}$ have been considered by continuously following the changes in d.c. conductivity at different isotherms.

II. Experimental arrangements

1. *Sample preparation*

The exact proportions of high purity (99.999%) Se and Te required for preparing 6 gm of $TeSe_{20}$ were enclosed in a vacuum-sealed (10^{-4} Torr) quartz tube about 12 mm in diameter. The tube was heated at 800 °C for 8 hours in an electric oven and shaken several times during the heating to ensure complete mixing. The molten material was then rapidly quenched in icy water. This method of preparation leads to the formation of $TeSe_{20}$ in the amorphous state as verified by the presence of a halo pattern in the X-ray diffraction. To increase the degree of order in the structure, annealing between T_g and T_m is required. A comparison of the diffraction patterns of a particularly crystallized $TeSe_{20}$ and hexagonal Se revealed primarily a slight shift in the Bragg angles of the characteristic diffraction peaks.

2. *DTA measurements*

The apparatus used for the differential-thermal-analysis (DTA) has been made locally. It is provided with accurate equipment for controlling and recording. The experimental conditions adopted were in accordance with the recommendations made by MACKENZI [6]. The DTA sample tube, made of pyrex glass of 3 mm in diameter, was filled with the amorphous material which had been ground into powder form. The differential temperature has been measured between the centres of the reference (α-aluminium oxide) and the active ($TeSe_{20}$) sample tubes. The sample temperature and the differential temperature have been recorded on the same chart using a two-channel recorder.

Crystallization during heating, or cooling, results in an exothermic peak and melting of crystalline material yields an endothermic peak. The glass transition point T_g, for a freshly prepared sample, takes the from of a step in the DTA trace. Such a step tends to a little peak if the sample has been aged. A typical DTA trace, with a scan rate of $\varphi = 11.3$ °C/min, is shown in Fig. 1 for $TeSe_{20}$ amorphous sample aged at room temperature for four weeks: the glass transformation temperature $T_g = 62$ °C and the maximum crystallization velocity is attained at 168 °C in contrast to pure Se, the beginning of crystallization and the subsequent melting are displaced towards higher temperatures ($T_m = 220$ °C for Se and 240 °C for $TeSe_{20}$).

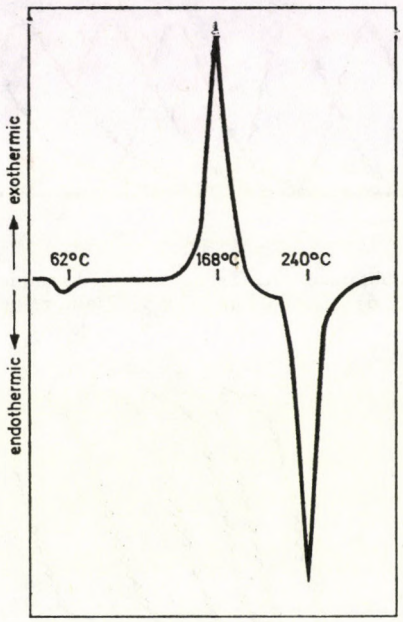

Fig. 1. A typical DTA trace obtained with scan rate of 11.3 °C/min for $TeSe_{20}$ amorphous sample aged four weeks at room temperature

3. *d.c. conductivity measurements*

For electrical conductivity measurements in supercooled liquid $TeSe_{20}$, the quenched material has been fabricated in the following way: i) About 2 gm of the material was sealed under vecuum (10^{-4} Torr) in a pyrex glass tube ($\sim$10 mm in diameter) provided with two tungsten electrodes near the base. ii) The tube was heated at 300 °C $\pm$ 2 °C for one hour, then quickly transferred to a preheated oven adjusted to the required temperature of annealing. The electrical conductivity has been measured accurately using an electrometer with an error less than 2.5%, and applying small stable voltage (less than 5 V)

III. Kinetics of crystal growth in amorphous solid $TeSe_{20}$

Fig. 2 shows exothermic curves of different scan rates, $\varphi = 1-10$ °C/min, obtained on 0.1 gm powdered samples with non-aged amorphous $TeSe_{20}$. It is clearly seen that the position of the exotherm, which is associated with the devitrification, shifts towards higher temperature with the increase of scan rate. This suggests that the crystallization should be considered as a rate process which cannot be characterized by a definite critical temperature independent of scan rate.

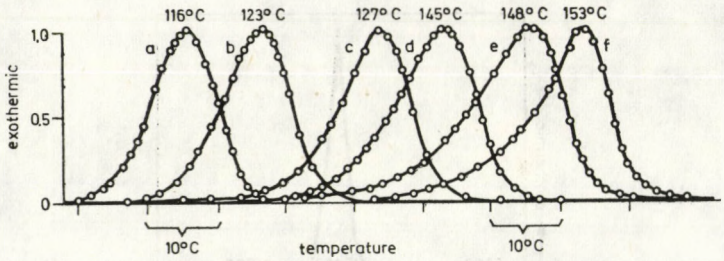

Fig. 2. Exothermic curves obtained with $TeSe_{20}$ non-aged samples scanned at: a) 0.85, b) 1.6, c) 2.2, d) 5.5, e) 8.5 and f) 9.8 °C/min, respectively

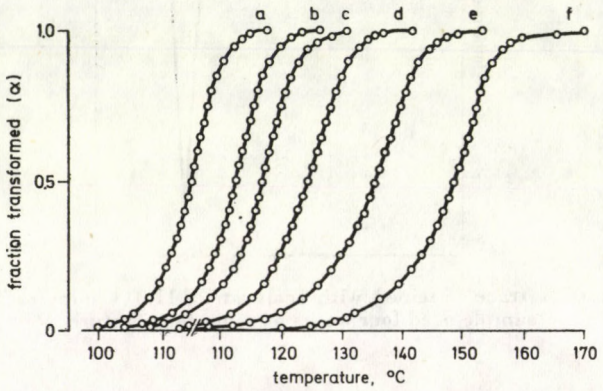

Fig. 3. Fraction reacted, α, versus temperature as calculated from the relevant area under the DTA peaks, for the various scan rates of Fig. 2

The complex process of devitrification of $TeSe_{20}$ can be described by the following kinetic equation formally derived by AVRAMI [7]:

$$-\ln(1-\alpha) = Kt^n + K_0 t^n \exp(-E/RT) . \qquad (1)$$

The desired parameters to be determined are n and E. The order of the reaction, n, has been calculated from the DTA trace by measuring the shape index according to KISSINGER [8] and the base line has been corrected by using the SCOTT and RAMACHANDRARAO method [9]. This gives a nearly constant value for the power index of $\bar{n} = 1 \pm 0.1$. That is, the process of devitrification of amorphous $TeSe_{20}$ takes place with one-dimensional growth.

The transformed fraction, α (the ratio of the new phase to the total volume) in time t can be calculated from the part of the area under the DTA curve up to the time t [10, 11]. Therefore, α is known as a function of temperature, and so the procedure of evaluation of kinetic data is the same as in the case of thermogravimetric measurements described earlier by SATAVA [12].

The results of $\alpha = f(T)$ are given in Fig. 3 for the different scan rates studied. The obtained curves are sigmoid in shape, indicating an autocatalytic

reaction which is often observed among various kinds of solid reactions. An estimate of the complex activation energy of crystallization, E, can be made by using PILOYAN's method [13]. This is based on the differential form of the model relation for α, $f(\alpha)$, and on BORCHARD's assumption [11] that the reaction rate, $d\alpha/dt$, is proportional to the temperature deflection, ΔT, as detected by DTA. Thus, Eq. (1) can be differentiated to yield:

$$\begin{aligned} d\alpha/dt &= A(1-\alpha)[-\ln(1-\alpha)]^n \exp(-E/nRT), \\ &= A' f(\alpha), \end{aligned} \tag{2}$$

where A and A' are constants. Eq. (2) may be written in the form:

$$\int_0^{\alpha} \frac{1}{f(\alpha)}\, d\alpha = \int_0^t A'\, dt = g(\alpha)\,. \tag{3}$$

For a constant rate $\varphi = dT/dt$, during the DTA measurements, is

$$g(\alpha) = [-\ln(1-\alpha)]^{1/n} = \frac{A}{\varphi}\int_{T_0}^{T_1} \exp -\left(-\frac{E}{nRT}\right) dT\,. \tag{4}$$

If $T_0 \ll T_1$, then

$$\log g(\alpha) = \text{constant} + \log\left[P\left(-\frac{E}{nRT}\right)\right]. \tag{5}$$

To a first approximation, SESTÁK [14, 15] assumed that: $P(E/nRT) \simeq \exp(E/nRT)$. That is a, plot of $\log g(\alpha)$ versus $1/T$ should give a straight line over the whole range of α $(0 < \alpha < 1)$ that corresponds to the correct mechanism of the process. Therefore, the function $\log g(\alpha)$ has been evaluated [12] and the probable reaction mechanism is determined by comparing the experimental

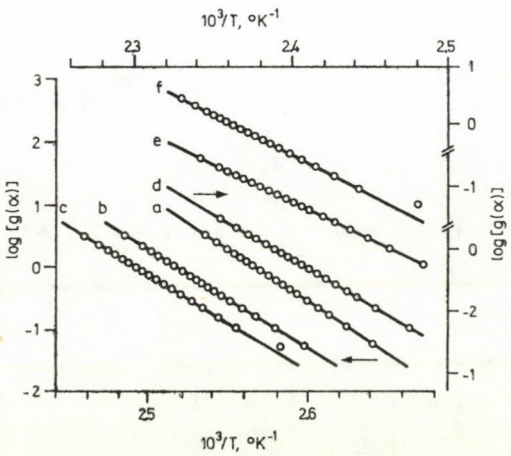

Fig. 4. Plots of the function $\log g(\alpha)$ versus temperature, where the fitting kinetic equation is: $-\ln(1-\alpha) = Kt$, for the scan rates investigated

data with kinetic equations [16]. Fig. 4 shows the plot of $\log g(\alpha) = f(l/T)$ for the probable mechanism of devitrification of $TeSe_{20}$. The fitting of the lines in Fig. 4 corresponds to a kinetic equation of the type: $-\ln(1-\alpha) = Kt$, for all values of φ. That is, the rate-controlling process takes place with predominance of random nucleation.

The activation energies E calculated from slopes of those lines in Fig. 4 are plotted as a function of φ and given in Fig. 5. It shows the dependence of

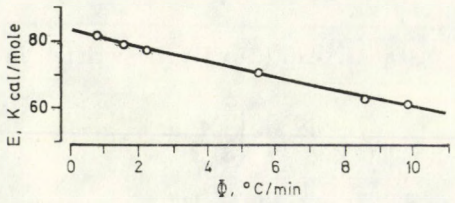

Fig. 5. Dependence of the activation energy for crystallization of amorphous solid $TeSe_{20}$ on the heating rate Φ. $\bar{E} = 64$ Kcal/mole

the activation energy of crystallization E on the heating rate φ. However, this is limited by combined switching and splitting of the chemical bonds which are necessary to convert the complex structure of the initial amorphous material (chains and rings of Se_8 and Se_6Te_2 [2]) to the chain structure of the solid solution of $TeSe_{20}$. From the data of Fig. 5, an average value of $\bar{E} =$ 64 Kcal/mole has been calculated.

Comparison of the kinetic parameters computed from the DTA measurements for the devitrification of amorphous solid $TeSe_{20}$ with literature data obtained for the same composition using other measurements (electrical conductivity, thermal conductivity, or density [17]), shows the good applicability of the method described.

IV. Kinetics of crystal growth in supercooled liquid $TeSe_{20}$

In Fig. 6 the d.c. conductivity σ of $TeSe_{20}$ is plotted versus the annealing time, t, at different isotherms in the temperature range of 120—175 °C. It shows conductivity decrease due to the decrease in the temperature of the sample from 300 °C to the temperature at which the crystallization starts (part ab); then it increases by 3 or 4 orders till it attains a certain limiting value characterizing the crystalline state at the temperature of the oven (part bc). The big change in σ during the part bc is due mainly to the transformation of the supercooled liquid $TeSe_{20}$ to hexagonal structure as indicated by X-ray diffraction. Fig. 7 shows the total time necessary for the completion of the process, τ, as a function of the annealing temperature. It shows that τ decreases with increasing temperature up to 150 °C, then it increases.

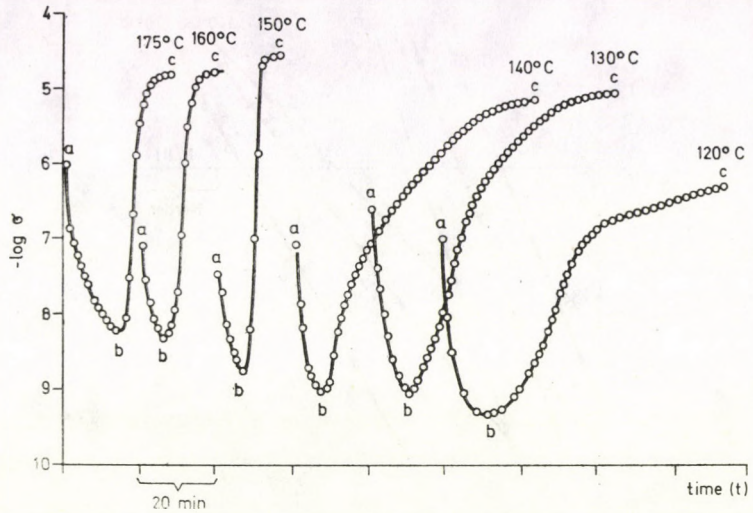

Fig. 6. The time-dependence of the electrical conductivity σ during different isothermal crystallization in supercooled liquid $TeSe_{20}$

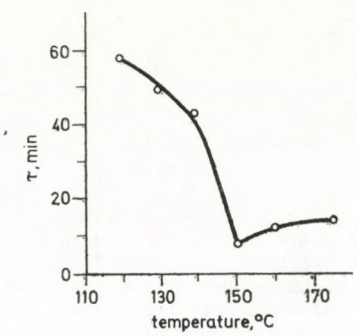

Fig. 7. The temperature-dependence of the total time of transformation τ

To determine the kinetics order, n, or the activation energy of liquid-crystal transformation E, at isothermal annealings, the AVRAMI equation, Eq. (1), is applied. The fraction volume, α, can be evaluated on the basis of changes in electrical conductivity σ during the part bc of the curves in Fig. 6 [18]. At any intermediate point between b and c the measured value of σ is a resultant of the conductivities of two phases, liquid and crystalline.

Fig. 8 shows that the AVRAMI plots, $\ln [-\ln (1 - \alpha)]$ versus $\ln (t)$, yield straight line relationships for the different annealing temperatures. Values of the kinetic parameter n, as calculated from the lines' slopes are drawn in the Figure. The changes of n in such a manner indicate that different crystallization mechanisms are dominant in various ranges of temperature. A plot of $\ln (K) = f(1/T)$ could be fitted with a straight line to give an activation energy

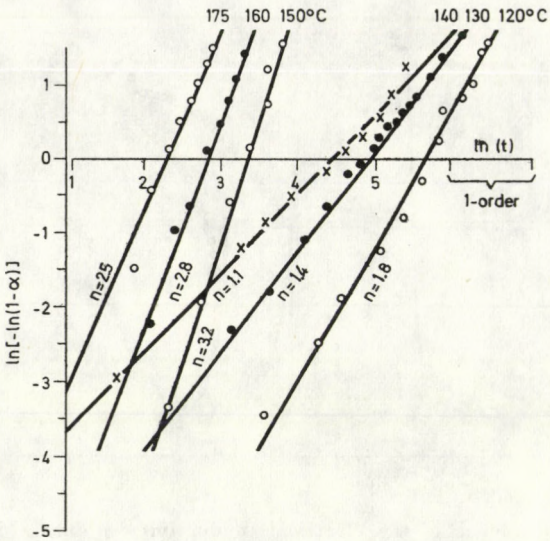

Fig. 8. AVRAMI plots for different annealing temperatures in the range of 120—175 °C

of 11.5 Kcal/mole in the temperature range considered. This value is signifi, cantly less than that for the crystallization from the amorphous solid phase- $\bar{E}$ = 64 Kcal/mole, reflecting the existence of mixed chains in the liquid alloys.

Acknowledgements

The authors wish to thank Dr. N. S. FELIX, National Research Center, Cairo, for his generous offer to provide the convenience of his DTA instruments. One of the authors (M.F.K.) wishes to express his thanks to Prof. M. P. TOSI, ICTP, for helpful discussions. He is also grateful to Prof. ABDUS SALAM, the International Atomic Energy Agency and UNESCO for hospitality at the International Centre for Theoretical Physics, Trieste.

REFERENCES

1. E. GRISON, J. Chem. Phys., **19,** 1109, 1951.
2. J. SCHOTTMILLER, M. TABAK, G. LUCOVSKY and A. WARD, J. Non-Cryst. Solids, **4,** 80, 1970.
3. H. P. D. LANYON, The Physics of Selenium and Tellurium, Ed. W. C. Cooper, Pergamon Press, 1969, p. 205.
4. P. BOOLCHAND and P. SURANYI, Phys. Rev., **B7,** 57, 1973.
5. H. THURN and J. RUSKA, J. Non-Cryst. Solids, **22,** 331, 1976.
6. R. C. MACKENZI, Differential Thermal Analysis, Academic Press, New York, 1970.
7. M. AVRAMI, J. Chem. Phys., **8,** 212, 1940.
8. H. E. KISSINGER, Anal. Chem., **29,** 1702, 1957.
9. M. G. SCOTT and P. RAMACHANDRARAO, Mat. Sci. and Engin,. **29,** 137, 1977.
10. H. J. BORCHARD and F. DANIELS, J. Am. Chem. Soc., **79,** 41, 1957.
11. H. J. BORCHARD, J. Inorg. Nucl. Chem., **12,** 252, 1960.
12. V. SATAVA and F. J. SKVÁRA, J. Am. Ceram. Soc., **52,** 591, 1969.
13. F. O. PILOYAN, I. O. RYABCHIKOV and O. S. NOVIKOVA, Nature, **212,** 1229, 1966.
14. J. SESTÁK, Thermochimica Acta, **3,** 150, 1971.
15. J. SESTÁK, Phys. and Chem. of Glasses, **15,** 137, 1974.
16. J. H. SHARP, H. W. BRINDLEY and N. N. ACHAR, J. Am. Ceram. Soc., **49,** 379, 1966.
17. M. K. EL-MOUSLY, Neorg. Mater. (USSR), **13,** 1587, 1977.
18. M. K. EL-MOUSLY, M. F. KOTKATA and S. A. SALAM, J. Phys., C **11,** 1077, 1978.

Acta Physica Academiae Scientiarum Hungaricae, Tomus 47 (4), pp. 353—356 (1979)

THERMAL CONDUCTIVITY OF LIQUID SELENIUM AND Se—Tl—S ALLOYS

By

A. H. ABOU EL ELA, H. H. A. LABIB* and K. A. H. SHARAF

PHYSICS DEPARTMENT, ISLAMIC GIRLS COLLEGE, NASR CITY and
PHYSICS DEPARTMENT,* FACULTY OF EDUCATION, AIN SHAMS UNIVERSITY, CAIRO, EGYPT

(Received in revised form 30. VIII. 1979)

Measurements of the thermal conductivity of liquid selenium were carried out above the melting point. The thermal conductivity increases with the temperature, which is attributed to the photon component of thermal conductivity. Moreover, the effect of thallium and sulphur on the thermal conductivity of selenium was investigated. It was found that the addition of thallium and sulphur increases the thermal conductivity.

1. Introduction

The temperature dependence of the thermal conductivity of selenium has not been studied completely. Most of the available data refer mainly to measurements at room temperature and lower [1—3]. ABDULLAEV et al [4] had studied the variation of the thermal conductivity of selenium near the softening ($T_g \sim 31$ °C) and the melting points. They showed that for amorphous selenium near T_g there is a discontinuity in thermal conductivity involving a sharp increase of about 40%. Heat treatment and addition of cadmium remove this discontinuity. Moreover, in the crystalline state the thermal conductivity increases with temperature up to the melting point where it decreases abruptly.

The aim of the present contribution is to study the thermal conductivity of pure selenium in the liquid state and the effect of thallium and sulphur additives, since the introduction of admixtures changes the intermolecular bonds and hence the magnitude of thermal conductivity.

2. Experimental

Selenium and Se—Tl—S samples were prepared from highly pure elements (99.999%). Two Se—Tl—S systems were prepared with the following composition (atom. %):

	Se	Tl	S
System 1	56.86	3.14	40
System 2	51.4	6.6	42

The synthesis of the samples was carried out under high vacuum in silica tubes at 450 °C for more than 6 hours. Then the tubes were quenched in air to obtain the sample in a glassy state. The solid glassy material is then heated in inert atmosphere until it melts, then transferred to the thermal conductivity measuring system.

Measurements of the thermal conductivity were carried out using the concentric cylinder method, where the material in liquid state was poured into the cylindrical gap between two concentric graphite cylinders kept in nitrogen atmosphere. The heater was inside the inner cylinder and the thermal conductivity was calculated using the formula

$$K = Q \ln (d_2/d_1)/2\pi L(t_1 - t_2),$$

where d_1 and d_2 are the diameters of the inner and outer cylinders, t_1 and t_2 are the temperatures on both sides of the sample, L is the length of the cylinders and Q is the quantity of heat generated.

3. Results and discussion

The temperature dependence of the thermal conductivity of liquid selenium and its admixtures with thallium and sulphur are shown in Fig. 1. The thermal conductivity of selenium increases rapidly with temperature, moreover, the addition of thallium and sulphur produces an additional rise of thermal conductivity (curves b and c). When the concentration of thallium

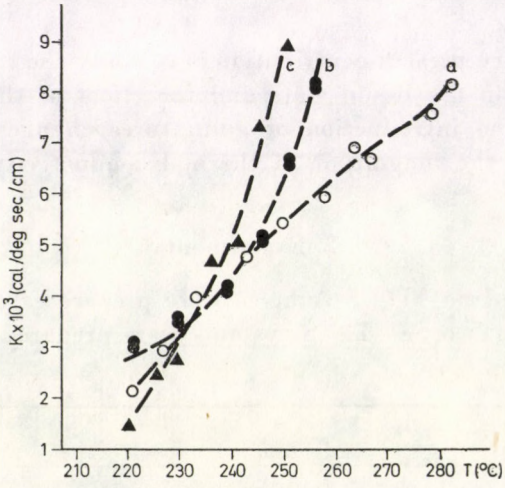

Fig. 1. Temperature dependence of the thermal conductivity of liquid selenium and its admixtures with thallium and sulphur: (a) Liquid selenium (○); (b) $Se_{0.5686}$ $Tl_{0.0314}$ $S_{0.40}$ (●); (c) $Se_{0.514}$ $Tl_{0.066}$ $S_{0.42}$ (▲)

increases from 3.14 atom. % to 6.6 atom. %, the thermal conductivity increases by about 50% at high temperatures.

The thermal conductivity in solid semiconductors can be adequately explained by transport due to phonons and free electrons. In liquid semiconductors, however, it is necessary to invoke an additional process involving photon transport [5]. The thermal conductivity of a liquid semiconductor can be described in the form [6]

$$K = K_a + K_e + K_m + K_r , \tag{1}$$

where K_a is the contribution of atomic motion and is given by

$$K_a = \frac{9kv}{\pi a} , \tag{2}$$

where a is the atomic radius, v is the vibration frequency $\simeq 3 \times 10^{12}$ s^{-1}, and k is Boltzmann's constant. The value of K_a is about 1.5×10^{-3} Cal · cm^{-1} · deg^{-1} · s^{-1}, K_e is the electron contribution, K_m is the bipolar contribution and K_r is the photon component of thermal conductivity.

In non-metallic materials like selenium the electronic and bipolar contributions are relatively small, therefore, it is suitable to attribute the difference between the measured values of thermal conductivity of liquid selenium (curve a) and the sum $(K_a + K_e + K_m)$ to the radiation contribution to heat transport. DRABBLE and GOLDSMID [7] had shown that for pure selenium above 350 °K other mechanisms of thermal conduction cannot play an important role. CZERNY [8] and GENZEL [9] had derived theoretically the equation of K_r for the case where the optical absorption coefficient α is small

$$K_r = \frac{16}{3} n^2 \frac{\sigma T^3}{\alpha} , \tag{3}$$

where n is the refractive index, σ is the Stefan—Boltzmann's constant. DIXON and ERTL [10] had proved the utility of Eq. (3) to explain the increase of thermal conductivity with temperature for liquid Tl_2Te.

The increase of thermal conductivity with the concentration of thallium and sulphur admixtures may be attributed to a change in intermolecular bonds in the liquid system. Viscosity measurements of KEEZER and BAILEY [11] indicate that polymerization equilibrium of selenium is displaced by thallium additive towards shorter chains. Moreover, liquid sulphur consists essentially of long chains [12] (diradical S_x) beside S_8.

REFERENCES

1. G. K. WHITE, S. B. WOOD and T. M. ELFORD, Phys. Rev., **112**, 1, 1958.
2. A. V. IOFFE and A. F. IOFFE, J. Tech. Phys. USSR, **22**, 12, 1952.
3. J. C. LASJAUNIAS and R. MAYNARD, J. Non-Cryst. Solids, **6**, 101, 1971.

4. G. B. ABDULLAEV, S. I. MEKHTIEVA, D. SH. ABDINOV, G. M. ALIEV and S. G. ALIEVA, Phys. Stat. Solidi, **13**, 315, 1966.
5. V. I. FEDOROV and L. S. STILBANS, High Temp., **11**, 206, 1967.
6. M. CUTLER, Liquid Semiconductors, Academic Press, 1977.
7. J. R. DRABBLE and H. J. GOLDSMID, Thermal Conduction in Semiconductors, Pergamon Press, 1961.
8. V. M. CZERNY and L. GENZEL, Glass. Tech. Ber., **25**, 387, 1952.
9. L. GENZEL, Zeit. Phys., **135**, 177, 1953.
10. A. J. DIXON and M. E. ERTL, J. Phys. D: Appl. Phys., **4**, 83, 1971.
11. R. C. KEEZER and M. W. BAILEY, Mat. Res. Bull., **2**, 185, 1967.
12. G. GEE, Trans. Faraday Soc., **48**, 515, 1952.

Acta Physica Academiae Scientiarum Hungaricae, Tomus 47 (4), pp. 357—360 (1979)

NON EXISTENCE OF AXIALLY SYMMETRIC FIELDS IN ROSEN'S BIMETRIC THEORY OF RELATIVITY

By

T. M. KARADE and Y. S. DHOBLE*

DEPARTMENT OF MATHEMATICS, NAGPUR UNIVERSITY, NAGPUR-440 010, INDIA

(Received in revised form 3. IX. 1979)

In ROSEN's bimetric theory of gravitation the non existence of the axially symmetric massive scalar meson field (together with electromagnetic field) is established.

I. Introduction

A new theory of gravitation proposed by ROSEN [1] displays the attractive features of general relativity without singularity. This bimetric theory of relativity is based on two metric tensors g_{ij} (a Riemann tensor describing the gravitational field) and γ_{ij} (a tensor of flat space-time which describes inertial forces).

The field equations of bimetric relativity are

$$K_{ij} = -8\pi k T_{ij}, \tag{1}$$

where

$$K_{ij} = N_{ij} - \frac{1}{2} N g_{ij} ,$$

and

$$N_j^i = \frac{1}{2} \gamma^{\alpha\beta} (g^{hi} g_{hj|\alpha}) \,|\, \beta , \tag{2}$$

where bar (|) stands for covariant differentiation with respect to γ_{ij} and $k = (g/\gamma)^{1/2}$, and T_{ij} is the energy momentum tensor of matter or other non gravitational fields. In an earlier work, the authors [2] have shown that nonexistence of static plane symmetric massive scalar field is established in bimetric relativity for a plane symmetric metric. This is not the case in respect of Einstein's general relativity. In this paper, we have pointed out that the non existence of a cylindrically symmetric massive scalar field is valid both in Einstein's general relativity and Rosen's bimetric relativity.

* Permanent address: Y. S. DHOBLE, Department of Agriculture Engineering, College of Agriculture, Nagpur-440100, India.

Here we consider an axially symmetric Einstein—Rosen space-time

$$ds^2 = e^{2\alpha-2\beta}(dT^2 - dR^2) - R^2 e^{-2\beta} d\varphi^2 - e^{2\beta} dZ^2, \tag{3}$$

with the conventions

$$x^1 = R,\ x^2 = \varphi,\ x^3 = Z,\ x^4 = T.$$

The unknown variables α and β are functions of R and T only. For the importance of this metric (3), one may refer to KARADE [3]. The flat space-time corresponding to (3) is

$$d\sigma^2 = dT^2 - dR^2 - R^2 d\varphi^2 - dZ^2 = \gamma_{ij}\, dx^i\, dx^j . \tag{4}$$

From (4), one finds easily that

$$\gamma_{11} = \gamma_{33} = -\gamma_{44} = -1 \text{ and } \gamma_{22} = -R^2 .$$

The γ-Christoffel symbols of the second kind are defined as

$$\Gamma^i_{jk} = \frac{1}{2}\gamma^{ih}\left(\frac{\partial \gamma_{jh}}{\partial x^k} + \frac{\partial \gamma_{kh}}{\partial x^j} - \frac{\partial \gamma_{jk}}{\partial x^h}\right).$$

From (4), we then obtain the non vanishing Γ-symbols as

$$\Gamma^2_{12} = \Gamma^2_{21} = \frac{1}{R} \quad \text{and} \quad \Gamma'_{22} = -R.$$

The straightforward calculations for the line element (3) yield

$$K^4_4 = 0 . \tag{5}$$

From (1) and (5), we derive

$$T^4_4 = 0 . \tag{6}$$

II. Massive meson field coupled with an electromagnetic field

The matter tensor for the massive scalar meson field is given by

$$M_{ij} = \frac{1}{4\pi}\left[V_i V_j - \frac{1}{2} g_{ij}(V_s V^s - m^2 V^2)\right],$$

where V_i stands for $\dfrac{\partial V}{\partial x^i}$ and the electromagnetic field is specified by the stress tensor

$$E_{ij} = \frac{1}{4\pi}\left[-F_{is} F^s_j + \frac{1}{4} g_{ij} F_{sp} F^{sp}\right], \tag{7}$$

where F_{ij} is a Maxwell electromagnetic tensor given by

$$F_{ij} = A_{i\underset{|}{}j} - A^{*}_{j|i} = A_{i,j} - A_{j,i}\,, \tag{8}$$

where A_i is a four vector potential and (,) stands for partial differentiation. The energy tensor, for a massive scalar field coupled with electromagnetic field will be

$$T_{ij} = \frac{1}{4\pi}\left[-F_{is}\,F^{s}_{j} + \frac{1}{4}\,g_{ij}\,F_{sp}\,F^{sp}\right] + \\ + \frac{1}{4\pi}\left[V_i\,V_j - \frac{1}{2}\,g_{ij}(V_s\,V^s - m^2\,V^2)\right]. \tag{9}$$

Then from (6) and (9), we get

$$-g^{11}\,V'^2 + g^{44}\,V^{\cdot 2} + m^2\,V^2 + g^{11}g^{22}(F_{12})^2 + g^{11}g^{33}(F_{13})^2 - \\ - g^{11}g^{44}(F_{14})^2 - g^{22}g^{44}(F_{24})^2 - g^{33}g^{44}(F_{34})^2 = 0\,, \tag{10}$$

where $V' = \partial v/\partial R$ and $V^{\cdot} = \partial V/\partial t$ etc. All the terms on l.h.s. of (10) are positive. Therefore to satisfy the identity (10), each of its terms must vanish separately, implying that

$$V' = V^{\cdot} = 0,\ m = 0,$$

$$F_{12} = F_{13} = F_{14} = F_{24} = F_{34} = 0. \tag{11}$$

It is seen that all the components of F_{ij} vanish except F_{23}. But because of the axial symmetry imposed, the four vector potential A_i will not depend upon Φ and Z, i.e.,

$$A_{2,3} = 0 = A_{3,2}\,.$$

Hence by (8)

$$F_{23} = A_{2,3} - A_{3,2} = 0\,. \tag{12}$$

The Maxwell electromagnetic tensor being zero, its contribution to T_{ij} is nil. It is interesting to note that (from 11 and 12) the contribution of scalar meson fields to T_{ij} is also nil. In short T_{ij} turns out to be zero and consequently gives an empty space-time. Therefore we arrive at a theorem:

"In ROSEN's bimetric relativity, the only possible solution of the axially symmetric distribution-scalar meson, massive meson and Maxwell electromagnetic fields is a vacuum solution."**

It has been observed that the above theorem does not hold good for the axial symmetry revealed through MARDER's metric [4] which involves three parameters.

* In bimetric theory ordinary differentiation of general relativity is replaced by γ-differentiation.

** Axially symmetric vacuum solutions for bimetric relativity are developed and their significance etc. will appear in the next paper.

In general relativity, the work of ROY and RAO [5] shows that the axially symmetric massive scalar field (also coupled with electromagnetic fields) is non existent. But it does admit scalar field and electromagnetic field.

Acknowledgement

The authors express their gratitude to the Referee for his kind suggestions and encouragement.

REFERENCES

1. N. ROSEN, Bimetric Theory of Gravitation, Topics in Theoretical and Experimental Gravitation Physics, Edited by V. De Sabbata and J. Weber, Plenum Press, New York, 273, 1977.
2. T. M. KARADE and Y. S. DHOBLE, communicated for publication, 1979.
3. T. M. KARADE, Rev. Roum. Phys. (Rumania), **23**, 425, 1978.
   Reprinted: POST-RAAG Reports No. 79 (Japan) 1978.
4. L. MARDER, Proc. Roy. Soc. Ser. A, **244**, 524, 1958.
5. A. R. ROY and J. R. RAO, Commun. math. Phys., **27**, 162, 1972.

RECENSIONES

SURAJ N. GUPTA: **Quantum Electrodynamics**

Gordon and Breach Science Publishers, London—New York—Paris, 1977, p. 226.

The book contains a comprehensive treatment of the well established facts of quantum electrodynamics in an extremely concise and coherent way. The first chapter describes the classical theory of fields based on variational principles, discusses the derivation of the canonical and symmetrical energy-momentum tensor. The second chapter summarizes the principles of quantum field theory (including indefinite metric problems), describes the properties of the different pictures and presents as an example the quantization of a scalar field. Chapter 3 is devoted to the quantization of the photon and electron field, treats their interaction and the C, T transformations. Chapter 4 deals with the properties of the scattering operator. Chapter 5 describes some cross sections and lifetimes. The following 34 pages contain regularization and renormalization problems. Chapter 7 treats some special topics including damping effects, two particle potentials, infrared divergences, etc. The orientation in these topics is facilitated by means of a comprehensive index.

The book is highly recommended to interested students who have studied a preliminary course of electrodynamics and quantum mechanics.

K. L. NAGY

Strongly Coupled Plasmas

Editors: G. Kalman and P. Carini, NATO Advanced Study Institutes Series; Series B: Physics, Volume 36, Plenum Publishing Corp., New York—London, 1978

The Advanced Study Institute on Strongly Coupled Plasmas was held on the Campus of the Université d'Orléans, Orléans-la-Source, France, from July 6th to July 23rd, 1977. 15 invited speakers and 50 other participants attended the Institute.

The present volume contains the texts of most of the lectures and of some of the numerous seminars held at the Institute.

Strongly coupled Coulomb systems occur in a great variety of physical situations: stellar and planetary interiors, solid and liquid metals, semiconductors, laser—compressed plasmas, and gas discharges. All these systems, however, resist analysis by traditional plasma perturbation techniques because of their high potential energy — kinetic energy ratio.

The Volume presents an up-to-date review of the various methods designed to deal with the strongly coupled plasma problem. The contributions reflect a full range of approaches and points of view, from formal statistical mechanics and kinetic theory to applied solid state and plasma physics. Numerous theoretical schemes addressing related equilibrium and non-equilibrium problems are reviewed, along with the abundance of computer-generated data on classical charged-particle behaviour.

The book definitely is of high value, because not only is it almost unique in its coverage of an important subject area, but it also contains a wealth of information that otherwise is difficult to find.

J. SZABÓ

Theoretical Methods in Medium-Energy and Heavy-Ion Physics

Editors: K. W. McVoy and W. A. Friedman, NATO Advanced Study Institutes Series; Series B: Physics, Volume 38, Plenum Publishing Corp., New York—London, 1979

This volume contains the Proceedings of the NATO Advanced Institute on Theoretical Nuclear Physics held at the University of Wisconsin, Madison, USA, June 12—23, 1978. It was a topical Institute focusing attention to two up-to-date fields of theoretical nuclear physics: heavy-ion (HI) reactions (Part I) and pion-nucleon reactions (Part II).

Part I begins with a thorough *survey of the current experimental situation in HI reactions* (D. K. Scott). It is followed by a lecture on *semi-classical approximation for HI-s* (R. Schaeffer) in which it is shown that the objections against the semiclassical approximation do not hold when complex contributions are included. Then a pedagogical lecture is presented on *the time-dependent meanfield approximation* (J. W. Negele), which turns out to be a well motivated and successful first approximation for a variety of problems of interest ranging from HI collisions through fission to pion condensation. This is followed by a lecture on the *transport theory of deeply inelastic HI reactions* (H. A. Weidenmüller) outlined in a compact and elegant manner, giving some examples for transport equations, the general aspects of nuclear transport theory, and a survey of theoretical approaches. The next lecture shows that the multiple scattering theory is applicable as a theoretical tool for describing *reactions between HI-s at high energy* (J. Hüfner). The last lecture of Part I discusses *models of high energy nuclear collisions* (N. K. Glendenning) and by performing statistical mechanical calculations it presents arguments that the study of the products of nuclear collisions at c.m. energies $\gtrsim$ 5 GeV/nucleon will be able to make a statement concerning the asymptotic form of the hadron spectrum.

Part II begins with a lecture on the non-relativistic *multiple scattering theory* (W. R. Gibbs) presenting also results for the scatterings $\pi^- - {}^4\mathrm{He}$ at $E = 110$ MeV and $\pi^\pm - {}^4\mathrm{He}$ at $E = 75$ MeV, and for charge exchange reaction ${}^{13}\mathrm{C}/\pi^+, \pi^\circ/{}^{13}\mathrm{N}$. In the lecture on the *field theory aspects of meson-nucleus physics* (L. S. Kisslinger) the differences between the theory involved in pion-nucleus vs conventional nuclear physics are emphasized and some tools for carrying out relativistic calculations are developed. The next lecture is on the *pion-nucleus scattering in the isobar formalism* (E. J. Moniz) in which the isobar-hole formalism for pion reactions is described and applied in detail to $\pi - {}^{16}\mathrm{O}$ scattering. The last lecture of Part II makes us familiar with the *application of three body techniques to pion-nucleus scattering* (A. W. Thomas).

All lecturers developed their subjects in a careful, coherent sequence. As a result, this book is an excellent introduction into these two rapidly expanding fields of nuclear physics.

B. Apagyi

Highly Conducting One Dimensional Solids

Edited by Jozef T. Devreese, Roger P. Evrard and Victor E. von Doren (Plenum Publishing Corp., New York—London, 1979

Research in the field of highly conducting quasi one dimensional materials has rapidly developed in the last decade. The reasons for this are manifold. The discovery of organic charge transfer salts in which donors and acceptors form segregated only weakly interacting chains and the synthesis of platinum mixed valency complexes in which well separated chains of platinum occur, yielded model systems with properties approaching ideal one dimensional conductors. Another impetus came from the suggestion of A. W. Little in 1964 that such quasi one-dimensional systems may show a new type of superconductivity which could lead to superconductivity persisting to temperatures well above ambient. In 1973 a group at Pennsylvania (Philadelphia, USA) led by A. J. Heeger found a large increase in the conductivity around 60 K in the organic charge transfer salt TTF—TCNQ, which they attributed to superconducting fluctuations. Although the question whether high temperature superconductivity may be obtained or not remains open, the enormous amount of both experimental and theoretical work which followed revealed a number of other phenomena particular to quasi one-dimensional systems. Perhaps the most spectacular of these are the lattice instabilities predicted

long ago by PEIERLS but for which clear evidence was only recently found in quasi one-dimensional systems. These lattice instabilities lead to charge and supposedly spin density waves which are not necessarily commensurate with the lattice periodicity.

The book contains eight reviews by the most prominent physicists of the field. A clear introduction is given by A. J. BERLINSKY. In a critical review H. GUTFREUND and W. A. LITTLE conclude that although all superconductors known at present are believed to be determined by the usual phonon mechanism all objections to the possibility to synthesize an excitonic type of superconductor with possibly high transition temperature can be answered. Our knowledge on lattice instabilities is based to a great extent on the X-ray scattering experiments performed at the Université Paris Sud Orsay in France and the neutron scattering experiments at Brookhaven National Laboratory in the United States. The review by R. COMÉS and G. SHIRANE gives a detailed description of this work. Despite the extensive experimental work on TTF—TCNQ and related systems in which almost all tools available to solid state physicists were used there is yet no agreement between different research groups on the nature of the basic interactions. The review by A. J. HEEGER gives a clear survey of the experimental situation on TTF—TCNQ and discusses the relation of theories developed for ideal systems to the experimental findings. A chapter by T. SCHULTZ and R. A. CRAVEN summarizes the work performed at the IBM Watson Research Center Yorktown Heights U.S. on a series of organic alloys based on TTF—TCNQ. The two chapters discussing the theory of lattice instabilities by L. I. SHAM and the theory of a one-dimensional electron gas by V. J. EMERY are excellent reviews. The final chapter by J. BARDEEN gives a brief account of the most important problems raised in the past few years and comments on some of the controversial points from the viewpoint of a theoretician.

The book is of great value both to experts and those who intend to enter the field and is highly recommended. We note, however, that the experimental sections deal almost exclusively with the KCP (a particular platinum complex) and TTF—TCNQ systems, although by now a large number of other highly conducting quasi one-dimensional salts are known. This concentration while having the advantage of a comprehensive treatment of these materials masks somewhat the much larger scope of the field.

A. JÁNOSSY

D. M. PISELLO: Gravitation, Electromagnetism and Quantized Charge

Ann Arbor Sci. Publishers, 1979, $ 12

This book presents essentially an elaboration of some ideas put forward by D. FINKELSTEIN and others on the possible homotopic nature of electric charge. Simple examples are worked out of the homotopy properties of certain complex-valued functions representing electrically charged physical states. The effects of the work which has been obviously spent on the preparation of the book are largely demolished by claims which are liable to be ridiculed by many readers. On p. 83 one finds: "Quantum mechanics is not revolutionary".

Once again, the publication of this book stirs the superficiality of our understanding of quantized material properties. There remains a tantalizing need for a decisive development towards a well-established theory of these properties.

Z. PERJÉS

Synergetics, Far from Equilibrium

Editors: A. Pacault and C. Vidal, Springer-Verlag, Berlin, Heidelberg, New York, 1979. pp. 105, 109 figures

Synergetics is declared an interdisciplinary field of the particular parts of natural sciences which is concerned with the cooperation of individual parts of a system that produces macroscopic spatial, temporal and functional structures. We have learned already from the two volumes of HAKEN'S (Synergetics: An Introduction; Synergetics: A Workshop, both published by Springer-Verlag) that this interdisciplinary field deals with deterministic as well as stochastic models of phenomena. This third volume gathers most of the lectures and commu-

nications presented at the meeting on "Far from Equilibrium, Instabilities and Structures" held in Bordeaux from 27th to 29th September, 1978. Since in the last decade Synergetics has become the "latest fashion" of the interdisciplinary field of some macroscopic natural sciences, the Bordeaux meeting was only part of a series of several other conferences such as Elmau 1972, London 1974, Dortmund 1976, Elmau 1977 and Tokyo 1978.

Undoubtedly, the research fields of Synergetics (laser emission, chemical reactions, fluid motion, etc.) are very important and interesting fields of natural sciences. However, by the subtitle of this volume: "Far from Equilibrium" the nonequilibrium state of the investigated systems is not uniquely and well defined, although most of the topics treated in this volume belong to the well-known fields of physics and chemistry. Indeed, the examples given are related mainly to thermohydrodynamics and chemistry, nevertheless on account of the given examples the meaning of "far" cannot be uniquely defined, We are even sure, for example, that the macroscopic evolution criterium of Prigogine and Glansdorff, which is undoubtedly the only complete theory for the investigated properties of instabilities and dissipative structures, is valid only for systems not so far from equilibrium. In fact, the characteristic matrix of the second variation $\delta^2 S$ of the entropy S contains material coefficients (specific heats etc.) but in this theory we consider them as constant quantities. However, there are several hundred experimental facts showing that this condition is not fulfilled but the system is not so far from the adequate equilibrium state. On the other hand, theories other than Prigogine's and Glansdorff's are not complete but rather special ones.

Apart from the above, it is real pleasure to see such a volume containing very important applications of interdisciplinary sciences in a well summarized way.

I. GYARMATI

Printed in Hungary

A kiadásért felel az Akadémiai Kiadó igazgatója Műszaki szerkesztő: Botyánszky Pál

A kézirat a kiadóba érkezett: 1979. X. 12. A kézirat a nyomdába érkezett: 1979. X. 16. — Terjedelem: 8 (A/5) ív, 20 ábra

80.7613 Akadémiai Nyomda, Budapest — Felelős vezető: Bernát György

NOTES TO CONTRIBUTORS

I. PAPERS will be considered for publication in Acta Physica Hungarica, only if they have not previously been published or submitted for publication elsewhere. They may be written in English, French, German or Russian.

Papers should be submitted to

Prof. I. Kovács, Editor
Department of Atomic Physics, Technical University
1521 Budapest, Budafoki út 8, Hungary

Papers may be either articles with abstracts or short communications. Both should be as concise as possible, articles in general not exceeding 25 typed pages, short communications 8 typed pages.

II. MANUSCRIPTS

1. Papers should be submitted in five copies.

2. The text of papers must be of high stylistic standard, requiring minor corrections only.

3. Manuscripts should be typed in double spacing on good quality paper, with generous margins.

4. The name of the author(s) and of the institutes where the work was carried out should appear on the first page of the manuscript.

5. Particular care should be taken with mathematical expressions. The following should be clearly distinguished, e.g. by underlining in different colours: special founts (italics, script, bold type, Greek, Gothic, etc.); capital and small letters; subscripts and superscripts, e.g. x_2, x^3; small l and 1; zero and capital O; in expressions written by hand: e and l, n and u, ν and v, etc.

6. References should be numbered serially and listed at the end of the paper in the following form: J. Ise and W. D. Fretter, Phys. Rev., *76*, 933, 1949.

For books, please give the initials and family name of the author(s), title, name of publisher, place and year of publication, e.g.: J. C. Slater, Quantum Theory of Atomic Structures, I. McGraw-Hill Book Company, Inc., New York, 1960.

References should be given in the text in the following forms: Heisenberg [5] or [5].

7. Captions to illustrations should be listed on a separate sheet, not inserted in the text.

8. As per 1st January 1980 the use of SI units has been made compulsory for all publications issued in Hungary. Please note that in papers submitted to Acta Physica after that date all measures should be expressed in SI unit

III. ILLUSTRATIONS AND TABLES

1. Each paper should be accompanied by five sets of illustrations, one of which must be ready for the blockmaker. The other sets attached to the copies of the manuscript may be rough drawings in pencil or photocopies.

2. Illustrations must not be inserted in the text.

3. All illustrations should be identified in blue pencil by the author's name, abbreviated title of the paper and figure number.

4. Tables should be typed on separate pages and have captions describing their content. Clear wording of column heads is advisable. Tables should be numbered in Roman numerals (I, II, III, etc.).

IV. MANUSCRIPTS not in conformity with the above Notes will immediately be returned to authors for revision. The date of receipt to be shown on the paper will in such cases be that of the receipt of the revised manuscript.

Reviews of the Hungarian Academy of Sciences are obtainable at the following addresses:

AUSTRALIA
C.B.D. LIBRARY AND SUBSCRIPTION SERVICE, Box 4886, G.P.O., *Sydney N.S.W. 2001*
COSMOS BOOKSHOP, 145 Acland Street, *St. Kilda (Melbourne), Victoria 3182*

AUSTRIA
GLOBUS, Höchstädtplatz 3, *1200 Wien XX*

BELGIUM
OFFICE INTERNATIONAL DE LIBRAIRIE, 30 Avenue Marnix, *1050 Bruxelles*
LIBRAIRIE DU MONDE ENTIER, 162 Rue du Midi, *1000 Bruxelles*

BULGARIA
HEMUS, Bulvar Ruszki 6, *Sofia*

CANADA
PANNONIA BOOKS, P.O. Box 1017, Postal Station "B", *Toronto, Ontario M5T 2T8*

CHINA
CNPICOR, Periodical Department, P.O. Box 50, *Peking*

CZECHOSLOVAKIA
MAD'ARSKÁ KULTURA, Národní třida 22, *115 66 Praha*
PNS DOVOZ TISKU, Vinohradská 46, *Praha 2*
PNS DOVOZ TLAČE, *Bratislava 2*

DENMARK
EJNAR MUNKSGAARD, Norregade 6, *1165 Copenhagen*

FINLAND
AKATEEMINEN KIRJAKAUPPA, P.O. Box 128, *SF-00101 Helsinki 10*

FRANCE
EUROPERIODIQUES S. A., 31 Avenue de Versailles, *78170 La Celle St.-Cloud*
LIBRAIRIE LAVOISIER, 11 rue Lavoisier, *75008 Paris*
OFFICE INTERNATIONAL DE DOCUMENTATION ET LIBRAIRIE, 48 rue Gay-Lussac, *75240 Paris Cedex 05*

GERMAN DEMOCRATIC REPUBLIC
HAUS DER UNGARISCHEN KULTUR, Karl-Liebknecht-Strasse 9, *DDR-102 Berlin*
DEUTSCHE POST ZEITUNGSVERTRIEBSAMT, Strasse der Pariser Kommüne 3—4, *DDR-104 Berlin*

GERMAN FEDERAL REPUBLIC
KUNST UND WISSEN ERICH BIEBER, Postfach *46, 7000 Stuttgart 1*

GREAT BRITAIN
BLACKWELL'S PERIODICALS DIVISION, Hythe Bridge Street, *Oxford OX1 2ET*
BUMPUS, HALDANE AND MAXWELL LTD., Cowper Works, *Olney*, Bucks *MK46 4BN*
COLLET'S HOLDINGS LTD., Denington Estate, *Wellingborough*, Northants *NN8 2QT*
W.M. DAWSON AND SONS LTD., Cannon House *Folkestone, Kent CT19 5EE*
H. K. LEWIS AND CO., 136 Gower Street, *London WC1E 6BS*

GREECE
KOSTARAKIS BROTHERS, International Booksellers, 2 Hippokratous Street, *Athens-143*

HOLLAND
MEULENHOFF-BRUNA B.V., Beulingstraat 2, *Amsterdam*
MARTINUS NIJHOFF B.V., Lange Voorhout 9—11, *Den Haag*
SWETS SUBSCRIPTION SERVICE, 347b Heereweg, *Lisse*

INDIA
ALLIED PUBLISHING PRIVATE LTD., 13/14 Asaf Ali Road, *New Delhi 110001*
150 B-6 Mount Road, *Madras 600002*
INTERNATIONAL BOOK HOUSE PVT. LTD., Madame Cama Road, *Bombay 400039*
THE STATE TRADING CORPORATION OF INDIA LTS. Books Import Division, Chandralok, 36 Janpath, *New Delhi 110001*

ITALY
EUGENIO CARLUCCI, P.O. Box 252, *70100 Bari*
INTERSCIENTIA, Via Mazzé 28, *10149 Torino*
LIBRERIA COMMISSIONARIA SANSONI, Via Lamarmora 45, *50121 Firenze*
SANTO VANASIA, Via M. Macchi 58, *20124 Milano*
D. E. A., Via Lima 28, *00198 Roma*

JAPAN
KINOKUNIYA BOOK-STORE CO. LTD., 17-7 Shinjuku-ku 3 chome, Shinjuku-ku, *Tokyo 160-91*
MARUZEN COMPANY LTD., Book Department, P.O. Box 5050 Tokyo International, *Tokyo 100-31*
NAUKA LTD. IMPORT DEPARTMENT, 2-30-19 Minami Ikebukuro, Toshima-ku, *Tokyo 171*

KOREA
CHULPANMUL, *Phenjan*

NORWAY
TANUM-CAMMERMEYER, Karl Johansgatan 41—43, *1000 Oslo*

POLAND
WĘGIERSKI INSTYTUT KULTURY, Marszałkowska 80, *Warszawa*
CKP I W ul. Towarowa 28 *00-958 Warsaw*

ROUMANIA
D. E. P., *Bucureşti*
ROMLIBRI, Str. Biserica Amzei 7, *Bucureşti*

SOVIET UNION
SOJUZPETCHATJ — IMPORT, *Moscow*
and the post offices in each town
MEZHDUNARODNAYA KNIGA, *Moscow G-200*

SPAIN
DIAZ DE SANTOS, Lagasca 95, *Madrid 6*

SWEDEN
ALMQVIST AND WIKSELL, Gamla Brogatan 26, *101 20 Stockholm*
GUMPERTS UNIVERSITETSBOKHANDEL AB, Box 346, *401 25 Göteborg 1*

SWITZERLAND
KARGER LIBRI AG, Petersgraben 31, *4011 Basel*

USA
EBSCO SUBSCRIPTION SERVICES, P.O. Box 1943, *Birmingham, Alabama 35201*
F. W. FAXON COMPANY, INC., 15 Southwest Park, *Westwood, Mass. 02090*
THE MOORE-COTTRELL SUBSCRIPTION AGENCIES, *North Cohocton, N. Y. 14868*
READ-MORE PUBLICATIONS, INC., 140 Cedar Street, *New York, N. Y. 10006*
STECHERT-MACMILLAN, INC., 7250 Westfield Avenue, *Pennsauken* N. J. 08110

VIETNAM
YXUNHASABA, 32, Hai Ba Trung, *Hanoi*

YUGOSLAVIA
JUGOSLAVENSKA KNJIGA, Terazije 27, *Beograd*
FORUM, Vojvode Mišiča 1, *21000 Novi Sad*

Index: 26.022
Acta Phys. Hung. Tom. 47. No. 4. Budapest, 30. VI. 1980 HU-ISSN 0001-6705